Università degli Studi di Napoli "Federico II"

Scuola Politecnica e delle Scienze di Base
Area Didattica di Scienze Matematiche Fisiche e Naturali

Dottorato di Ricerca in Fisica

Ciclo XXXIV

2018-2021

Tesi di Dottorato

Unveiling the evolutionary history of the Magellanic Clouds and beyond through detection and analysis of stellar over-densities: clusters and streams.

Tutori:
Vincenzo Ripepi
Giuseppe Longo

Candidato: Massimiliano Gatto
Matricola: DR994143

Contents

List of Figures

List of Tables

List of publications

This thesis is based on the following publications:

- **Gatto M.,** Ripepi V., Bellazzini M., Cignoni M, Cioni M-R.L., Dall'ora M., Longo G., Marconi M., Schipani P., Tosi M. : **"A search for star clusters in the outskirts of the Large Magellanic Cloud: indication of clusters in the age gap."**, Monthly Notices of the Royal Academy Society, Vol.499, p.4114-4139 (2020).

- **Gatto M. ,** Napolitano N.R., Spiniello C., Longo G., Paolillo M.: **"COSTA: the Cold Stream finder Algorithm. Searching for kinematical substructures in the phase space of discrete tracer."** Astronomy & Astrophysics, Vol.644, p.A134 (2020).

- **Gatto M.,** Ripepi V., Bellazzini M., Tosi M., Cignoni M., Tortora C., Leccia S., Clementini G., Grebel E.K., Longo G., Marconi M., Musella I.: **"STEP Survey II: structural analysis of 170 Star Clusters in the Small Magellanic Cloud"**, Monthly Notices of the Royal Academy Society, Vol.507, p.3312-3330 (2021).

- **Gatto M.,** Ripepi V., Bellazzini M., Tosi M., Tortora C., Cignoni M., Spavone M., Dall'ora M., Clementini G., Cusano F., Longo G., Musella I., Marconi M., Schipani P.: **"YMCA-1: A New Remote Star Cluster of the Milky Way?"**, Research Notes of the American Astronomical Society, Vol.5, p.159 (2021).

- **Gatto M.,** Ripepi V., Bellazzini M., Tortora C., Tosi M., Cignoni M., Longo G.: **"Discovery of NES, an extended tidal structure in the North-East of the Large Magellanic Cloud"**, submitted on the Astrophysical Journal.

- **Gatto M.,** Ripepi V., Bellazzini M., Dall'ora M., Tosi M., Tortora C., Cignoni M., Cioni M.-R. L., Cusano F., Longo G., Marconi M., Musella I., Schipani P., Spavone M.: **"Deep**

VLT photometry of the faint stellar system in the Large Magellanic Cloud periphery YMCA-1.", submitted on the Astrophysical Journal Letter.

During my PhD project, I also contributed to the following works:

- Marconi M., Molinaro R., Ripepi V., Leccia S., Musella I., De Somma G., **Gatto M.,** Moretti M.I.: **"A theoretical scenario for Galactic RR Lyrae in the Gaia database: constraints on the parallax offset"**, Monthly Notices of the Royal Academy Society, Vol.500, p.5009-5023 (2021).

- Ripepi V., Catanzaro G., Molinaro R., **Gatto M.,** De Somma G., Marconi M., Romaniello M., Leccia S., Musella I., Trentin E., Clementini G., Testa V., Cusano F., Storm J.: **"Cepheid Metallicity in the Leavitt Law (C- MetaLL) survey: I. HARPS-N@TNG spectroscopy of 47 Classical Cepheid and 1 BL Her variables"**, Monthly Notices of the Royal Academy Society, Vol.508, p.4047-4071 (2021).

- Chaturvedi, A.; Hilker, M.; Cantiello, M.; Napolitano, N.R.; van de Ven, G.; Spiniello, C.; Fahrion, K.; Paolillo, M.; **Gatto, M.;** Puzia, T.: **"The Fornax Cluster VLT Spectroscopic Survey III – Kinematical characterisation of globular clusters across the Fornax galaxy cluster"**, Astronomy & Astrophysics, Vol.657, p.A93 (2022).

- Napolitano, N. R. ; **Gatto, M. ;** Spiniello, C. ; Cantiello, M. ; Hilker, M. ; Arnaboldi, M. ; Tortora, C.; Chaturvedi, A.; D'Abrusco, R. ; Li, R.; Paolillo, M. ; Peletier, R.; Saifollahi, T. ; Spavone, M. ; Venhola, A. ; Pota, V. ; Capaccioli, M. ; Longo, G.: **"The Fornax Cluster VLT Spectroscopic Survey IV – Cold kinematical substructures in the Fornax core from COSTA"**, Astronomy & Astrophysics, Vol.657, p.A94 (2022).

Abstract

One of the key questions in astrophysics concerns how galaxies evolve, or more precisely, which are the physical processes that drive the morpho-chemo-physical evolution in a galaxy during its cosmic life, from the moment of its formation till the present time. In the framework of the hierarchical building block described by the ΛCDM paradigm, the evolution of a galaxy is also affected by the manifold of close encounters, interactions, and mergers it undergoes with its neighbor galaxies. Thus, reconstructing the whole evolutionary path of a galaxy, including its interaction history, is pivotal to link the galaxy properties we observe at high red-shift to their physical characteristics observed in the local Universe, and to improve galaxy formation and evolutionary models.

The Magellanic Clouds (MCs), composed of the Large Magellanic Cloud (LMC) and the Small Magellanic Cloud (SMC), are the closest example of a three-body interacting system composed of the Milky Way (MW), the LMC and SMC. Therefore, the unique opportunity provided by their relative proximity allowed us to analyse with matchless detail the dynamical and morphological evolution that a galaxy experience as a consequence of the mutual gravitational interaction with its neighbors. In addition, the MCs likely represent the massive members of a group of galaxies in the first infall into the MW halo and thus they are the ideal test-bed to investigate the pre-processing of groups prior the capturing by a massive galaxy, such as the MW.

In this thesis, I made use of astrometric, kinematics (proper motions and radial velocities) and photometric data, with the main goal of unveiling the evolutionary path of the MCs and their intense interaction history. To this aim, I developed new algorithms or improved existing techniques to take full advantage of the datasets I worked with. The majority of the works presented in this thesis are based on two complementary deep and highly accurate surveys which explored more than 160 square degrees within the MCs and their outskirts: the STEP and YMCA survey (PI: V. Ripepi), which were carried out with the VLT survey telescope (VST) since Dec.

2011 up to the last year, when the last tile has been observed. The photometry obtained with these surveys allows us to resolve the MC stars singularly down to about 1.5-2 magnitudes below the main-sequence turn-off of the oldest stellar population, permitting us to probe even the early stages of MCs evolution. The deep photometry is combined with the wide spatial coverage of the two surveys, which, in the case of YMCA also cover a significant part of the peripheries of the MCs, regions that have not been explored before employing deep and wide-field photometry. When I started my Ph.D. project, the STEP survey was already completed and the catalog available, while the YMCA survey was just starting the observations. As part of my thesis, I carried out the photometric measurements for the YMCA survey, including the construction of the procedures needed to calibrate and make available the catalog.

We tackled the reconstruction of the MCs evolutionary history by using two complementary approaches. The first one, which concerns the major part of this thesis, consisted of a deep analysis of the properties of the MCs star cluster (SC) system to get insights into their past evolution. We take advantage of the exclusive YMCA observations to try to obtain for the first time a complete census of SCs, till the smallest masses, in the areas imaged by the survey. To this aim, we developed a procedure to discover even the faintest, low-luminous, and sparse still unknown SCs. Our SC finding algorithm needs only the star coordinates as input parameters, and searches for local over-densities in the sky, based on density maps obtained through a Kernel Density Estimation (KDE) algorithm. In practice, we search for small regions in the sky (of the order of tens of arcsec) with a number of stars significantly higher than the local average field. The procedure also automatically derives the centre of each over-density and estimates its radius. This algorithm has been tested on a suite of Montecarlo simulations and artificial generated SCs to demonstrate its robustness. On this basis, we estimated an efficiency of the procedure of about 90%, achieved even in the worst possible case, that is poorly populated SCs embedded in regions with a high density of field stars. We ran the searching algorithm in the outermost and poorly studied regions of the LMC by taking advantage of the catalog provided by the majority of the YMCA tiles (65 and 12 sq. deg. towards East and West of the LMC, respectively) and to the STEP tiles close to the West of the LMC. As result, we detected 55 high reliable candidate SCs, of which 35 (60% of the sample) were new discoveries, in a total area of 79 square degrees in the LMC surrounding in a range of distances between $\sim$ 4 kpc and $\sim$ 13 kpc. We exploited the colour-magnitude diagrams (CMDs) of the detected SCs, after having properly de-contaminated from field or foreground stars with a customized procedure, to estimate their properties, such as age, reddening and metallicity via isochrone fitting. The

age distribution of the newly discovered SCs revealed a peak at about 2-3 Gyr which strongly indicates that a past close encounter between the LMC and SMC enhanced the star cluster formation activity. Even more interestingly, we detected for the first time the presence of tens of candidate SCs formed during the so-called "age-gap", an interval ranging from 4 to 10 Gyr in the LMC, which was thought to be almost totally devoid of SCs. Among the known SCs included in our photometry, the new age estimate obtained for KMHK 1762, based on the accurate and deep YMCA photometry, indicated that it is much older than previously evaluated, making it one of the very few (the third) confirmed LMC age gap SC ever discovered. Our findings allow us to suggest a possible solution for the age gap problem, which has puzzled the researchers for three decades. We propose that the age gap is not a real physical feature, but instead, the result of an observational bias, originated by the combination of too shallow photometry carried out by past surveys and a limited investigation of the LMC outskirts, where the lower field stellar density makes it easier to spot even the faint and sparse SCs.

In the context of the analysis of the YMCA tiles through the cluster searching algorithm, we also discovered a peculiar SC likely belonging to the LMC (YMCA-1), which, based on the YMCA data appeared distant, old and very metal-poor. The follow-up deep photometry ($g \sim$27 mag) with FORS2@VLT which we obtained for YMCA-1 allowed us to confirm that it is old and metal-intermediate ($t \sim 11.7$ Gyrs, $Fe/H \sim -1.12$ dex). It is placed at about 55 kpc from the sun, which is sufficiently close to the LMC to suggest it belongs to this galaxy, even if we cannot rule out completely its belonging to the MW halo. It is also a faint and very compact ($L_g = 10^{2.1\pm0.3} L_\odot$, $r_h = 3.5\pm0.3$ pc). These characteristics make YMCA-1 an exceptional object among the old LMC SC population. Indeed, YMCA-1 has age and metallicity similar to those of the other 15 known old LMC GCs, but structural characteristics are completely dissimilar, as it is two or three order of magnitudes fainter. In particular, it resides in a transition region of the M_V-r_h plane, in between the ultra-faint dwarf galaxies and the classical old clusters, and close to SMASH-1, another faint stellar system recently discovered in the LMC surroundings.

Regarding the SMC SC system, we took advantage of the STEP survey photometric catalogue to perform a deep analysis of 170 already known SMC SCs located in the main body of the galaxy. We derived their surface brightness profiles (SBPs) and obtained their main structural parameters by fitting their SBPs with Elson, Fall & Freeman (EFF) and King models. In addition, we also exploited their CMDs to estimate the ages for a subsample of 134 SCs. It was the first time that such a large sample of SCs in the SMC was homogeneously characterized in terms of their sizes, ages, luminosities and masses, exploring also a wider region of the parameter space, down

to hundreds of solar masses. The outcomes of this work confirmed the existence of a physical mechanism that induces an increase of the core radius after 0.3-1.0 Gyr. In the light of the very large mass interval investigated in our work, we suggested that the process driving the inner expansion is mass-dependent, as none of the SCs having $\log(M/M_{\odot}) \leq 3.5$ dex analysed in this work undergoes the expansion. This result represents a strong constraint for the different physical mechanisms proposed to explain such an expansion.

In addition to the study of the past evolution of the LMC with SCs, we also focused our attention on the detection of faint low-luminous sub-structures originated by recent or past tidal stripping events. These stellar tides represent coherent structures in both position and velocities, and thus they can be revealed as over-densities in the phase-space of the LMC stars. In this context, we exploited the exquisite results from the *Gaia* early data release 3 (EDR3) to search for over-densities in the six-dimensional parameters space constituted by photometric, kinematics and astrometric information by means of an unsupervised Gaussian Mixture Modelling (GMM) clustering algorithm. The GMM was able to disentangle the LMC, SMC and MW stellar populations, thus returning a genuine sample of LMC stars which was used to investigate the low surface outer regions of the LMC. In this context, we reported the discovery of a new diffuse stellar sub-structure protruding up to ~ 20 degrees from the LMC centre to its North-Eastern side, which we called the North-East structure (NES). Particularly noteworthy is that the NES is placed in a region where N-body simulations predict a bending of the LMC disc due to tidal stresses induced by the MW.

In the final part of this thesis, we studied the possibility of recovering the faint tidal signatures of merger events for more distant systems, where it is not possible to resolve the galaxies' individual stars any longer. To this aim, we developed the COld STream finder Algorithm (COSTA) that, through a deep friend-of-friend approach, analyze the position and radial velocity of discrete tracers (as could be globular clusters and/or planetary nebulae) to look for cold kinematic substructures in the phase-space. We applied COSTA to the relatively distant Fornax cluster since previous photometric surveys demonstrated that many interactions between the galaxy members are still ongoing. COSTA detected 13 cold substructures and for the first time it kinematically confirmed a stream already discovered in the deep photometry of the Fornax cluster.

It is worthwhile to point out that the procedure developed and described in this thesis can be easily generalized for any stellar system, from the MW to the edge of the local Universe (~ 50 Mpc), to decipher the evolutionary path of the systems investigated and unveil their history of mass assembly through the manifold interactions they experienced.

Chapter 1

Introduction

In the hierarchical formation scenario described by the ΛCDM model, massive dark matter halos grow in a bottom-up manner gathering mass through the merging of many smaller subhalos [White and Rees, 1978]. This process, known as the *merger tree* (see Figure 1.1), is still ongoing, as demonstrated by cosmological simulations [Cooper et al., 2010, Naab et al., 2007, 2009, Oser et al., 2010, 2012]. In this scenario, at very high redshift, overdense regions of dark matter which overcome a critical value experience a gravitational collapse, thus originating the first sub-halos. Within these dark matter sub-halos, the gas bound in the potential well begins to cool and condense, forming the stars and in turn the galaxies [White and Rees, 1978]. Thus, galaxies form and evolve within dark matter halos, which also contain the most mass in the Universe. Therefore, understanding the physical mechanisms driving the formation and evolution of galaxies is one of the key questions in astrophysics.

Two different approaches can be adopted to shed light on the physical mechanisms which play a role in shaping the galaxies during their lifetime. The first one is to investigate how the average properties of galaxies change as a function of the redshift. Indeed, it is possible to investigate the variation of the luminosity function [Hagen et al., 2015, Parsa et al., 2016], size [e.g., Bluck et al., 2012, Buitrago et al., 2008, McLure et al., 2013, Roy et al., 2018], number density [e..g, Cassata et al., 2013], stellar mass [e.g., Roy et al., 2018], star formation rate [e.g., Lapi et al., 2017], as a function of the redshift, just to mention a few quantities. Higher redshift means larger distances and therefore also longer look-back times. This approach allows us to build and analyze a very large statistical sample of galaxies of different morphological type[1]. However,

[1]Actually, at very high redshift, i.e. $z > 3$, the large distances of the galaxies involved make this task not

this strategy only permits us to determine the global physical characteristics of galaxies, as at high redshifts only the integrated properties of the galaxies, i.e. the average light emanated by billions of stars, can be collected and studied. On the opposite, the study of the nearby Universe (i.e., up to $\sim 100 - 200$ Mpc) allows us to take advantage of the higher spatial resolution, to perform a spatial-dependent analysis of the galaxies' chemical, physical and kinematic properties, allowing us to build a more detailed picture of a stellar system. In particular, for the galaxies belonging to the Local Group (LG)[2], we can even resolve the galaxy stars singularly till the early evolutionary stages such as the Main Sequence (MS), thanks to both advanced ground-based and space telescopes. We can thus use the physical and chemical information held by stars to unveil the host galaxy's formation and evolutionary history, that is, for example, the history of its interactions, and/or its chemical evolution. This second approach, also known as *Galactic Archaeology* is at the basis of this thesis.

1.1 Galaxy evolution

One of the most relevant physical mechanisms driving the galaxy evolution in the late Universe is galaxy-galaxy interactions. As predicted by galaxy formation models, most galaxies should be surrounded by an extended halo, made by an old and metal-poor stellar population, largely inhabited by the debris of past merging events [Annibali et al., 2016, Bullock and Johnston, 2005, Cooper et al., 2010, 2015]. The accretion of galaxy halos is one of the predictions of the hierarchical scenario, as the mass assembly is expected to occur either through the mergers with other galaxies [Liu et al., 2015, Malumuth and Richstone, 1984, Merritt, 1985, Nipoti, 2017, Ostriker and Tremaine, 1975, White, 1976] or through the tidal stripping of stars from their neighbor galaxies [Gallagher and Ostriker, 1972, Gregg, 1998, Moore et al., 1996, Read et al., 2006, Willman et al., 2004]. Therefore, the research of tidal signatures in the form of debris of a still ongoing or past merger event is a valuable tool for studying the mechanisms that supply mass in the galaxy outskirts and in turn to improve our knowledge of the galaxy evolution in a merger context. In addition, as the dynamical times are longer at large galactocentric distances [Bullock and Johnston, 2005], galaxy halos and their characteristic underlying old stellar populations may also preserve the physical and kinematics information about past mergers [e.g., Amorisco et al., 2014], making them an ideal target to disclose the interaction

straightforward even with the modern technologies.

[2]The Local Group is the galaxy group whose our Galaxy belongs to. It has a spherical radius of roughly 1 Mpc.

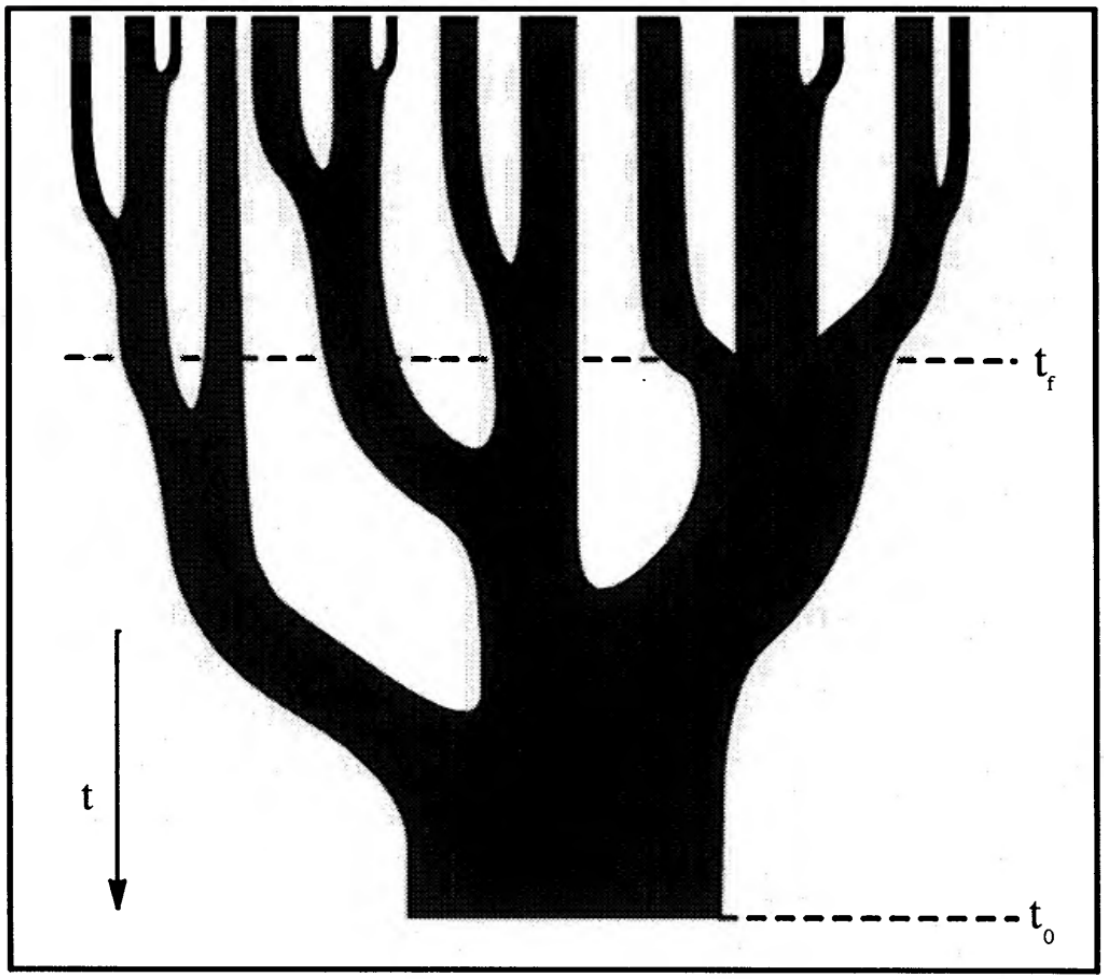

Figure 1.1: This illustration depicts a classical "merger tree" showing the progenitors of a dark matter halo selected at the current time. Time increases from top to bottom in the panel. The thickness of the branches indicate the masses of the sub-halos. The horizontal shaded line at the middle of the figure shows the masses of the parent halos at a given time. Image taken from Lacey and Cole [1993].

history of a stellar system. In recent years, the number of newly detected stellar streams and other sub-structures within the galaxies of the LG has noticeably increased, showing that debris of galaxy interaction events could be almost ubiquitous. Some remarkable examples in the Milky Way (MW) are the Sagittarius stream [Ibata et al., 2001b, 1997, Majewski et al., 2003], the Helmi stream [Helmi and White, 1999], the Gaia-Enceladus stream [e.g, Belokurov et al., 2018, Deason et al., 2018, Haywood et al., 2018, Helmi et al., 2018]. Many other substructures have been detected in the MW satellites [e.g., Belokurov et al., 2006, Carlin and Sand, 2018, Mackey et al., 2016] but also around external galaxies such as M31 [e.g., Ibata et al., 2001a, McConnachie et al., 2009].

Despite the wealth of information provided by tidal structures, debris originating through

close encounters between galaxies are expected to have a very low surface brightness (i.e. 28-30 mag/arcsec^2 in the $V-$band) and extend for many kpc [Cooper et al., 2010] Therefore, only deep photometric surveys combined with a wide spatial coverage of the galaxy outskirts are able to unveil the remnants of close encounters between galaxies. To overcome the complexities of tidal stream detection, approaches complementary to each other can be adopted to reconstruct how galaxies have evolved during their cosmic time. For example, a widely appropriate expedient is taking advantage of the galaxy star cluster (SC) system to reconstruct the whole evolutionary history of the hosting galaxy. Indeed, considering SCs as a coeval system, they preserve all the physical properties of the parent galaxy and the chemical status of the interstellar medium (ISM) at the moment of their formation [Ashman and Zepf, 2008]. It is thus suitable to use SCs as a surrogate of the galaxy stellar population and use them to reconstruct the whole galaxy star formation history (SFH) and/or its chemical enrichment. Moreover, it is currently accepted that a fraction of the SCs inhabiting the outermost regions of the galaxies have been captured from external dwarf galaxies, hence they represent a useful tool to investigate the interaction history of their hosting galaxy with its satellites [e.g., Kruijssen et al., 2019, Mucciarelli et al., 2021].

Amongst the tens of dwarf galaxies belonging to the LG, I focus most of my attention on the two massive dwarf satellites of our Galaxy, the Large Magellanic Cloud (LMC) and the Small Magellanic Cloud (SMC), which also constitute the galaxy binary system closest to the MW, known as Magellanic Clouds (MC).

1.2 The Magellanic System

The LMC and SMC are two gaseous-rich interacting dwarf galaxy satellites of the MW located in the Galactic Southern hemisphere. They represent the main stellar component of a network of stars and gaseous filaments commonly known as the Magellanic System (MS) which also includes: (i) an extended stream of HI gas that covers about 200°($\sim$ 175 kpc at the MS distance) around the Galactic South pole of the MW [Brüns et al., 2005, D'Onghia and Fox, 2016, Mathewson et al., 1974, Nidever et al., 2010, Putman et al., 2003] named the Magellanic Stream; (ii) the Magellanic Stream counterpart, dubbed the Leading Arm, which is located ahead of the LMC [Putman et al., 1998]; (iii) the Magellanic Bridge (MB) that connects the two galaxies from the East of the SMC to the South-West of the LMC (see §1.2.2.1 for a detailed description of the MB). The interaction signatures are striking, the most evident one is the already mentioned Magellanic Stream, also visible in Fig. 1.2 in its whole extension, or the MB. The LMC and

SMC also show a disturbed morphology [Belokurov and Erkal, 2019, Mackey et al., 2016, 2018, Petersen et al., 2021, Pieres et al., 2017]; a complex kinematics [e.g., Cullinane et al., 2022, Olsen et al., 2011]; enhanced periods of star formation or star cluster formation [Glatt et al., 2010, Harris and Zaritsky, 2009, Mazzi et al., 2021, Nayak et al., 2016, Nayak et al., 2018, Pietrzyński and Udalski, 2000, Rubele et al., 2012], that collectively constitute a strong evidence of their mutual gravitational interaction and of the tidal stresses induced by the MW. The MS not only represents the closest example of a three-body tidal interaction, made by the MCs and the MW, but from a cosmological point of view they also represent a rare stellar system. Indeed, cosmological simulations foresee that the odds of finding an LMC-SMC binary system still orbiting a MW-like galaxy at the current cosmic time are negligible [$\ll$1%, Boylan-Kolchin et al., 2011, González et al., 2013, Liu et al., 2011]. Therefore, the MCs are an ideal testbed to constrain galaxy evolutionary theories in a merger context and to probe with a matchless detail the mass assembly of the MW halo, via the accretion of an ongoing binary galaxy system.

In the last decades, great advances in the knowledge of the past evolution of the MS have been achieved. For example, even though the MCs were traditionally believed to have been MW satellites for a Hubble time [Bekki and Chiba, 2005, Connors et al., 2004, 2006, Gardiner and Noguchi, 1996, Gardiner et al., 1994, Heller and Rohlfs, 1994, Lin and Lynden-Bell, 1982, Lin et al., 1995, Mastropietro et al., 2005, Moore and Davis, 1994, Murai and Fujimoto, 1980, Yoshizawa and Noguchi, 2003], nowadays a large consensus exists about the hypothesis that the MCs approached to the MW only recently. In particular, they are on their first passage around the Galaxy, and currently, they just passed the pericenter and are moving towards the apocenter. This is supported by recent and more precise measurements of their proper motions [PM, Kallivayalil et al., 2006a,b, 2013, Vieira et al., 2010] obtained through observations carried out with the Hubble Space Telescope (HST) spanning a time interval of about 7 years and also thanks to the *Gaia* data release 1 [DR1, van der Marel and Sahlmann, 2016]. Based on these new findings, the idea of the MCs as interacting binaries for a Hubble time has been challenged [Besla et al., 2012, Diaz and Bekki, 2012], but also the origin of some tidal structures was re-interpreted. For instance, formerly the origin of the Magellanic Stream was ascribed to the tidal influence of the MW, while the current scenario based on the more accurate proper motions (PMs) is different, attributing its formation to the gas tidally stripped from the SMC because of a close past encounter, happened some Gyr ago, with its larger companion, the LMC [e.g., Diaz and Bekki, 2012].

A further breakthrough in the comprehension of the MS achieved in the past years concerns

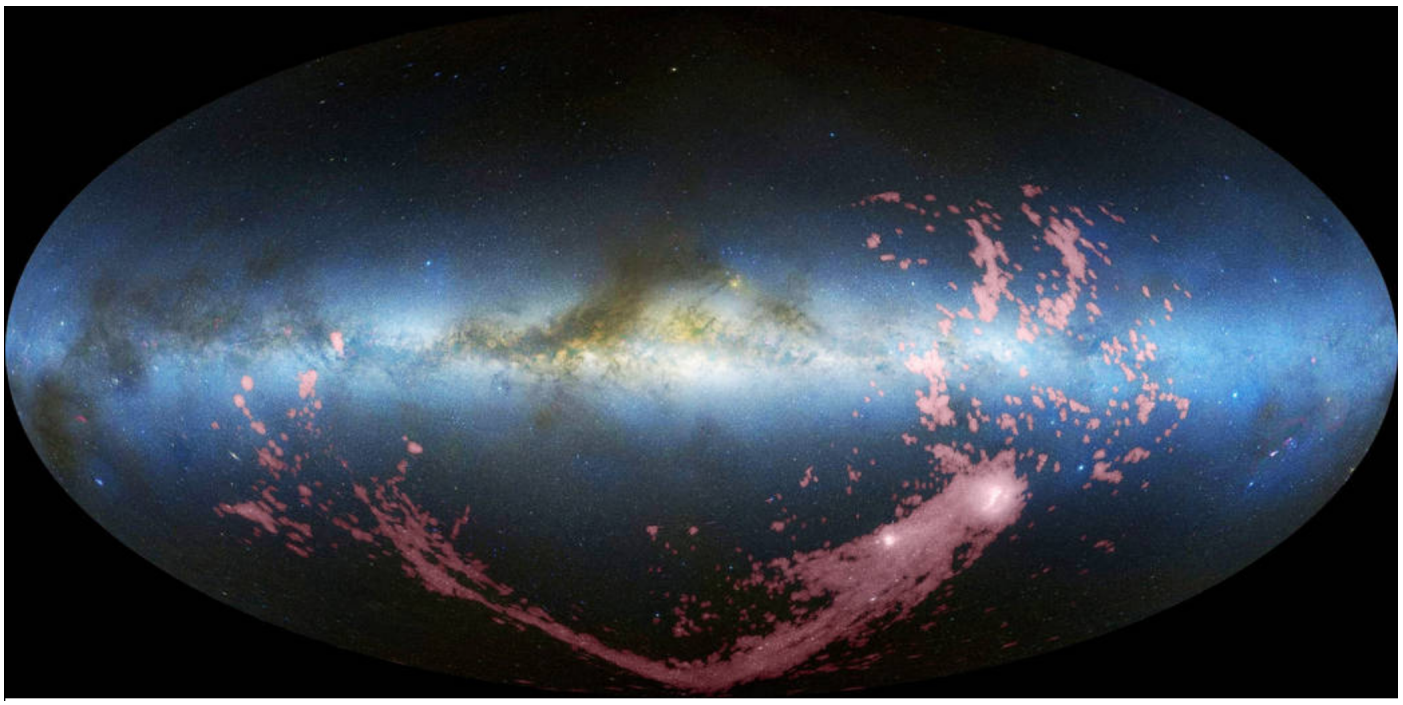

Figure 1.2: Image showing the Magellanic stream and the MCs in HI (red colours), with an optical all-sky image in Aitoff projection. Image taken from Mellinger [2009].

the dramatic increase of the evidence suggesting that the LMC entered into the MW halo with its own system of dwarf satellites, besides the SMC. The possibility that some MW galaxy satellites were connected with the MS was first proposed by Lynden-Bell [1976], and then discussed by other authors [D'Onghia and Lake, 2008, Nichols et al., 2011, Sales et al., 2011], on the basis of the discovery of the presence of several ultra-faint dwarf (UFDs) galaxies and globular clusters (GCs) along the MS orbital plane. Moreover, the existence of satellites of satellites is a strong prediction of the hierarchical paradigm in which large and massive structures form via the accretion of smaller ones. The availability of accurate PMs and parallax for more than 1 billion stars provided by the *Gaia* space mission [Gaia Collaboration et al., 2016, Lindegren et al., 2016] delineated a turning point for the research of LMC satellites. Kallivayalil et al. [2018] exploited the second data release of the *Gaia* space mission [DR2, Gaia Collaboration et al., 2018a] to obtain accurate PM measurements for 13 ultra-faint dwarf galaxies recently discovered in the MW halo. They concluded that 4 dwarf galaxies share the same orbital properties of the LMC, suggesting that they are likely dwarf satellites belonging to the MS rather than dwarf galaxies of the MW as commonly assumed. Many different authors took advantage of the capabilities of the *Gaia*

spacecraft, making the number of candidate LMC satellites increase [Pace and Li, 2019, Pardy et al., 2020, Patel et al., 2020], and showing up a picture in which the LMC is the massive member of a sub-group of galaxies only recently penetrated in the MW halo.

A recent outstanding outcome corroborates the hypothesis that the LMC also experienced mergers in the past by "cannibalizing" less massive dwarf galaxies. Indeed, Mucciarelli et al. [2021] discovered that the old LMC GC NGC 2005 has a chemical composition not compatible with an LMC origin, hence it is likely the only survivor of a past merger between the LMC and one of its dwarf satellites now completely dissolved. Although in the past different works detected signatures of likely ancient galaxies now absorbed by the LMC [e.g., Armstrong and Bekki, 2018], if confirmed, this result would be the first observational evidence that the process of mass assembly has operated also at the small scales.

In addition to the critical importance of the MS in constraining galaxy evolution theories as described above, the MCs have also been essential for many other astrophysical fields. For example, the MCs hold a very conspicuous system of SCs, constituted by several thousands of members (see §1.2.4 for a detailed discussion) suitable for investigating their properties in great detail, thanks to the relative proximity of the MS. The SC system of the MCs has still pivotal importance for improving stellar evolutionary models thanks to the analysis of their colour-magnitude diagrams (CMDs). In particular, the comparison between the position of their SC stars on the CMD and the theoretical isochrones built thanks to the current know-how of the time-evolution of the single stellar populations (SSP) has been critical to making progress in some particular aspects of the evolution of the stars, such as: (i) the overshooting [Mucciarelli et al., 2007]; some post-evolutionary phases as the thermal pulsing asymptotic giant branch [Girardi and Marigo, 2007, Lebzelter and Wood, 2007, Lebzelter et al., 2008]; the impact of the rotation of stars on their position on the CMD [e.g., Carini et al., 2020], just to mention a few. Moreover, the MCs system of SCs also includes massive (of the order of $10^5 M_{\odot}$) clusters spanning all the range of ages, from the still SC forming regions as the 30 Doradus complex up to the old GCs ($\log(t) \sim 10^{12}$ dex). They also cover at least 2 dex in metallicity, thus the parameters space covered by these objects extends over a wider region with respect to the MW SC system. This occurrence makes them ideal probes to study the physical processes that affect their evolution during the cosmic time and to investigate how their observables (luminosity, color, structural parameters, etc.) evolve as they get older (a more detailed introduction about the SC dynamical evolution is in §1.2.5).

Finally, also from a cosmological point of view, the MCs play remarkable importance as

they provide the first anchor for the cosmic distance ladder thanks to the period-luminosity relationship [Leavitt and Pickering, 1912] applied to the large sample of LMC-SMC standard candles, such as Cepheids and RR Lyrae stars [e.g., Jacyszyn-Dobrzeniecka et al., 2016, 2017, Ripepi et al., 2017, and references therein]. The accuracy of this relationship, and the analysis of its dependence by other physical parameters, as the metallicity, is a crucial step to decrease the uncertainty for the estimate of the Hubble constant [e.g., Ripepi et al., 2021, and references therein] and to resolve the puzzle of the Hubble tension as well [see, Planck Collaboration et al., 2020, Riess et al., 2021, and references therein].

In the following sections I discuss the LMC and SMC in more detail, describing the state-of-the-art of our knowledge about their evolutionary history, and the questions still open.

1.2.1 The Large Magellanic Cloud

The LMC, depicted in Fig. 1.3, is the greatest and most massive satellite of the MW, and it is the fourth massive galaxy of the Local Group (after the MW, M31 and M33). Its relative proximity with the MW [$\sim$ 50 kpc de Grijs et al., 2014] makes it possible to resolve its stellar population down to the very faint magnitudes, and in turn to probe its evolutionary history with unequaled detail. The LMC is a dwarf galaxy with a planar structure composed by a non constant inclination of the disc that varies with the galacto-centric distance. Indeed, the LMC's disc has an average inclination of $\sim 25-30^{\circ}$ [e.g., Choi et al., 2018b, Cusano et al., 2021, Mackey et al., 2016, van der Marel and Kallivayalil, 2014] but it dramatically increases up to $\sim 40^{\circ}$ close to the LMC centre [Choi et al., 2018b]. The LMC is oriented in such a way that its North-East side is spatially closer to us and its disc rotates in a counter-clock way with a rotational velocity of about 70 km s^{-}1 [Gaia Collaboration et al., 2018b, 2021b]. The LMC also possesses a few spiral arms [see e.g., de Vaucouleurs, 1955, de Vaucouleurs and Freeman, 1972b, Mazzi et al., 2021]. It is a gaseous rich and metal-poor galaxy with respect to the MW. Its metal content spans about 2 dex in metallicity, and it also shows a negative metallicity gradient from the centre to the periphery [Choudhury et al., 2016, 2021, Cioni, 2009, Grady et al., 2021, Skowron et al., 2021].

The LMC possesses a mix of young and intermediate-age old stellar populations. The former component is centrally concentrated and it mainly traces the thin off-centred bar and the spiral arms [e.g., El Youssoufi et al., 2019, Gaia Collaboration et al., 2021b]. The LMC is still actively forming stars at a rate of about 0.1-0.2 $M_{\odot}$/yr [Mazzi et al., 2021], and therefore hosts several clumpy star-forming regions, of which 30 Doradus, one of the most active starburst region known

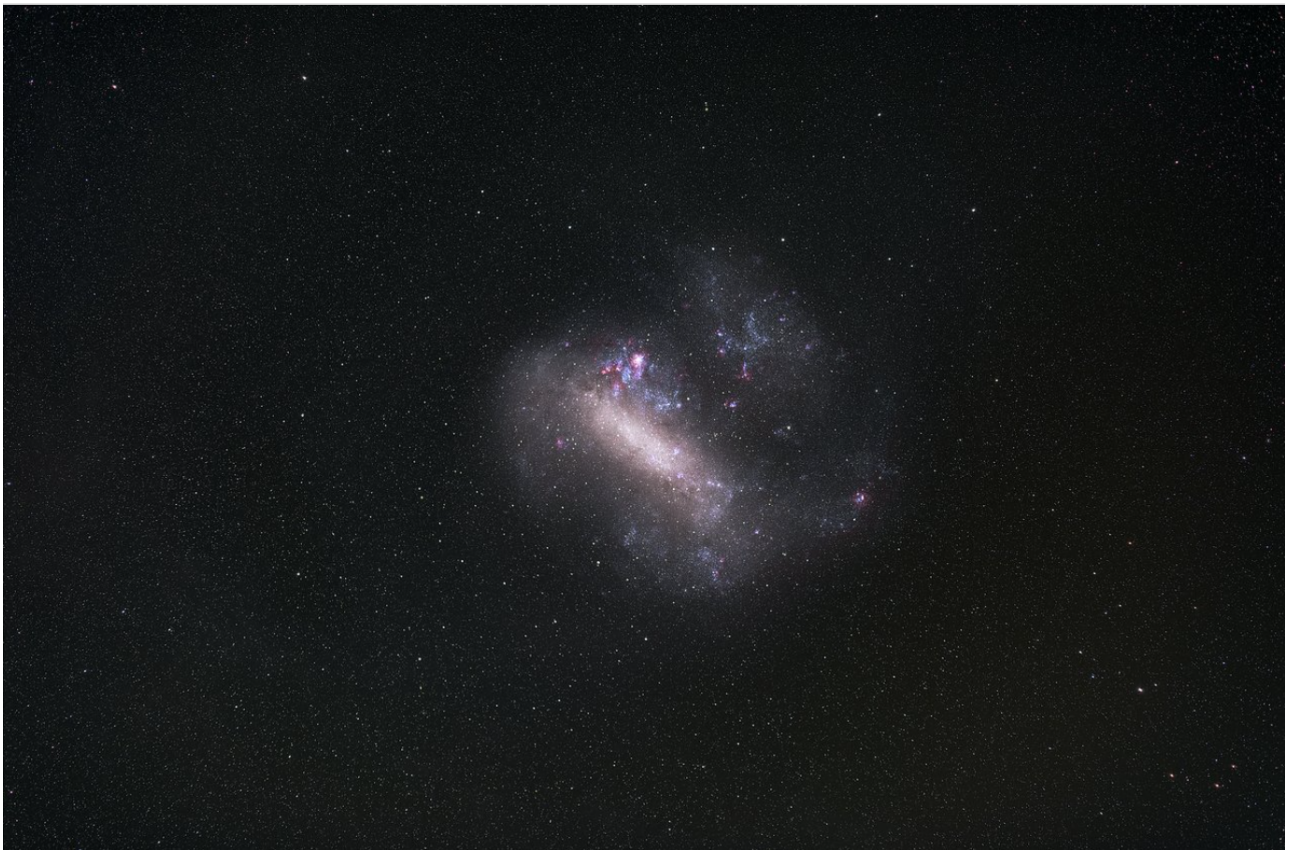

Figure 1.3: Image of the LMC taken from the European Southern Observatory (ESO) "La Silla". From this picture it is recognizable the irregularity of the LMC. It is visible the central bar and also other LMC structures, such as the 30 Doradus complex at the centre of the image. Credit Zdenek Bardon - ESO

in the LG, is the most remarkable example [see e.g., Cignoni et al., 2016, De Marchi et al., 2011, van Gelder et al., 2020]. On the other hand, the oldest stellar population is more evenly distributed, and extends farther out from its optical centre. Thus, the latter is an optimal component to trace the faintest luminous outermost regions of the LMC and to probe either the size of the LMC or the existence of an extended halo. The extension of the LMC disc reaches at least up to 16° (about 14 kpc at the LMC distance) to the North, following an exponential profile with a scale length of 1.15 kpc [Saha et al., 2010], and up to $\sim$ 10° -14° to the South (9-12 kpc) [Mackey et al., 2018], but the presence of LMC stars has been detected even at larger distances. For example, Nidever et al. [2019] disclosed a very faint surface brightness (down to 34 mag arcsec^2) old ($\sim$ 9 Gyrs) and metal-poor population up to 21° (18.5 kpc) from the LMC centre, following an exponential profile which breaks at 13° -15°. Belokurov and Koposov [2016] revealed blue horizontal branch (BHB) LMC stars out to about 30° (26 kpc). The picture that emerged from these pioneering works is that the LMC is much more extended than previously thought, despite is still not clear if these faint structures represent a stripped outer disc material or rather an accreted extended halo.

The LMC's evolution has been continuously affected by the mutual dynamical interaction with the SMC and more recently also by the gravitational potential of the MW as well. Indeed,

the LMC presents numerous features witnessing its turbulent past evolution. For example, its disc revealed to be warped, flared and twisted [Besla et al., 2016, Choi et al., 2018b, Mackey et al., 2016, Olsen and Salyk, 2002, van der Marel, 2001], it contains an off-centred bar [e.g., El Youssoufi et al., 2021, Subramaniam and Subramanian, 2009, Zhao and Evans, 2000], a ring-like stellar over-density [Choi et al., 2018a]. Moreover several faint substructures have been recently detected in its periphery [Belokurov and Erkal, 2019, El Youssoufi et al., 2021, Mackey et al., 2016, 2018, Petersen et al., 2021, a more detailed description of the substructures revealed in the LMC periphery is in discussion about the LMC substructures in §1.2.3.1 and §1.2.3.2], whose origin have been ascribed by N-body simulations to the combined tidal effect of the MW and SMC [e.g., Belokurov and Erkal, 2019, Cullinane et al., 2022]. The adversity of resolving such a three-body problem to explain the wealth of tidal signatures observed today in the LMC is even more complicated considering that other invisible actors may have played a crucial role in shaping the chemo-physical and kinematic properties of the LMC. Indeed, some evidence strongly suggests that the LMC has experienced direct collisions with dwarf galaxy satellites now completely dissolved, but that contributed to the assembly mass of its stellar population [see e.g., Armstrong and Bekki, 2018, Olsen et al., 2011] and its SC system [Mucciarelli et al., 2021, see also discussion in §1.2]. Thus, it is not surprising that these occurrences, combined with its vicinity, make the LMC one of the most interesting targets for investigating the theories of galaxy evolution in the ΛCDM paradigm, by studying the photometry, spectroscopy, and kinematics of its resolved stars.

1.2.2 The Small Magellanic Cloud: a tidal stripping galaxy

The SMC, depicted in Fig. 1.4, is a dwarf irregular galaxy, located at slightly larger distance with respect to the LMC [$\sim$ 60 kpc, de Grijs and Bono, 2015]. It has a total estimated dynamical mass of $M \sim 10^9 M_\odot$ [Di Teodoro et al., 2019] and being of about two orders of magnitudes less massive than its companion, the scars of the tidal forces generated by the mutual gravitational interaction with the LMC are much more prominent in its morphology, kinematics of the star and the gas. The status of the SMC is that of an ongoing tidally disrupting galaxy, stretched in the direction of the LMC. Stars and gas seems to be disconnected from a geometrical and kinematic point of view, and even the young and intermediate-age old stellar populations are off-set between each other [Mackey et al., 2018], suggesting past disturbances also to the reservoir of gas.

The SMC displays several distinct morphological features, the most striking one is a central

Figure 1.4: Infrared image of the SMC taken with the VISTA telescope. The SMC has not a defined morphology and it is stretched in the direction of the LMC. At the right of the image stands out the the very bright 47 Tucanae globular cluster. Credit: ESO - VISTA VMC.

bar where most of the stars and SCs reside. It also possesses an Eastern elongated structure made of stripped stars known as the Wing, first observed by Shapley [1940], that departs from the Northern edge of the bar and extends toward the LMC and likely represents an ongoing tidally stripped process [Besla et al., 2010, 2012, Cioni, 2009, Diaz and Bekki, 2012, Gonidakis et al., 2009, Gordon et al., 2009, Zaritsky and Harris, 2004]. Another remarkable feature is the Magellanic Bridge (MB) made of HI gas [Hindman et al., 1963] and stars that connect the South-East side of the SMC to the South-West side of the LMC (see §1.2.2.1 for a detailed description of the MB).

The young stellar population is highly irregular [e.g., El Youssoufi et al., 2021] and disturbed [Massana et al., 2020] and it is mostly located within the bar and the Eastern wing [El Youssoufi et al., 2019]. Alike to the LMC, the older stellar component is more smoothly distributed [see e.g., Haschke et al., 2012, Jacyszyn-Dobrzeniecka et al., 2017, Zaritsky et al., 2000]. The actual

3D shape of the SMC is still unclear but it can roughly be approximated as a triaxal spheroid or ellipsoid with a considerable extension along the line of sight [e.g., Deb et al., 2015, Gardiner and Hawkins, 1991, Jacyszyn-Dobrzeniecka et al., 2017, Muraveva et al., 2018, Ripepi et al., 2017, Scowcroft et al., 2016, Subramanian and Subramaniam, 2012]. To map the three-dimensional structure of the SMC Cepheids and RR Lyrae stars are commonly used as distance indicators, and as tracers of the young (50-500 Myr) and old ($\geq$ 10 Gyr) stellar population, respectively. The picture that emerged from these studies confirmed that the SMC is an ellipsoid rather than a flat disk galaxy [Jacyszyn-Dobrzeniecka et al., 2016, Ripepi et al., 2017, Scowcroft et al., 2016] , confirmed also by the absence of any rotational signal in the PMs obtained by the *Gaia* satellite [Gaia Collaboration et al., 2018b, 2021b]. The SMC is tilted with its East side closer to us of about 20 kpc with respect to the West side [Scowcroft et al., 2016] and possesses an elongation along the line of sight of more than 25–30 kpc [Ripepi et al., 2017]. Ripepi et al. [2017] also found evidence for the presence of a counter-bridge, predicted by N-body models of an LMC-SMC encounter [Diaz and Bekki, 2012]. Unlike the stars, the gas component might possess a circular motion typical of a rotating disc [Hindman et al., 1963, Kerr et al., 1954, Stanimirovic et al., 1999, Staveley-Smith et al., 1997], documenting the current complex geometrical structure of the SMC.

Thanks to the recent deep surveys, several low surface brightness substructures in the SMC periphery were unveiled. Just to mention the most noticeable ones, Pieres et al. [2017] through the analysis of Dark Energy Survey [DES; Dark Energy Survey Collaboration et al., 2016] data discovered a stellar over-density at 8° from North of the SMC centre, that they called Small Magellanic Cloud Northern Over-Density (SMCNOD). The SMCNOD contains mainly intermediate-age stars (6 Gyr, Z=0.001) and a small component of younger stars (1 Gyr, Z=0.01) that likely were originally part of the SMC disc removed by tidal stripping events during previous close encounters between the LMC and the SMC. Martínez-Delgado et al. [2019] revisited a shell-like over-density at about 2° from the SMC centre, to the North-East side, using Survey of the MAgellanic Stellar History [SMASH; Nidever et al., 2017] data. They only revealed the presence of a young population ($\sim$15 Myrs), suggesting that it likely represents a recent star formation event, probably triggered by the most recent LMC-SMC encounter that happened about 150 Myr ago. Piatti [2022a] re-analyzed the shell-like over-density revealing that the substructure is more extended along the line-of-sight than previously thought. They also revisited the Martínez-Delgado et al. [2019]'s hypothesis speculating that this feature is likely another tidally stripped/formed stellar structure from gas pulled out from the SMC main body because of the gravitational in-

teraction with the LMC and/or MW. Finally, Massana et al. [2020] identified a tidally stellar structure with SMASH data, that extends up to 12° from the SMC centre and has an estimated surface brightness of ~ 31.9 mag/arcsec^2).

1.2.2.1 The Magellanic Bridge

The MB connects the East side of the SMC to the South-West of the LMC, and therefore its line-of-sight distance varies from $\sim$ 50 kpc to $\sim$ 60 kpc. It was unveiled for the first time as a HI signature by Hindman et al. [1963], but later many works also reported the presence of both a young and older stellar component. The MB is likely the product of the most recent direct collision between the SMC and the LMC happened about 150 Myr ago [e.g., Besla et al., 2012, Zivick et al., 2018, 2019], hence the intermediate-age old stars detected in the MB [see e.g., Bagheri et al., 2013, Carrera et al., 2017, Dobbie et al., 2014, Nidever et al., 2013, Noël et al., 2013, 2015, Skowron et al., 2014] have been tidally stripped from the SMC, while the young stellar component is likely born-in-situ from the tidally stripped SMC gas material [e.g., Demers and Battinelli, 1998, Harris, 2007, Irwin et al., 1985, Mackey et al., 2017, Noël et al., 2015, Skowron et al., 2014]. This was confirmed by Noël et al. [2015] as they reported that young and intermediate-old age stars have distinct spatial distributions, with the former component mirroring the HI distribution.

Recently, also the PMs of red giant branch (RGB) stars in the MB have been constrained, confirming an overall flow of stars from the SMC towards the LMC [Schmidt et al., 2020], as also confirmed through the recent PMs provided by *Gaia* Early Data Release 3 [Gaia Collaboration et al., 2021a,b]. The MB also hosts a population of young SCs [Bica et al., 2015] whose estimated ages, namely between $7.3 \leq \log(t) \leq 8.3$, were sufficiently young to suggest an in-situ formation.[3]

1.2.3 Stellar sub-structures in the MC outskirts as proxy of their interaction history

As already anticipated in the discussion in §1.1, the outskirts of a galaxy may hold numerous evidence of the past mergers, due to the longer dynamical times that delay the mixing processes amongst the stars [Bullock and Johnston, 2005]. Indeed, N-body simulations foresee the existence of a very complex system of stellar tails, streams, and other faint substructures located in the halo of interacting galaxies and originated by the tidal stresses and past mergers experienced

[3] Bica et al. [2015] analyzed 14 SCs and young associations within the MB.

by a galaxy [Bullock and Johnston, 2005, Cooper et al., 2010]. These tidal signatures have very low surface brightness magnitudes [Cooper et al., 2010, and references therein], making not straightforward revealing them.

In the last decade, thanks to recent deep panoramic surveys targeting the MCs, several tidal structures generated by the mutual gravitational interaction between the MCs and the MW were unveiled [e.g., Belokurov and Koposov, 2016, Choi et al., 2018a, El Youssoufi et al., 2019, 2021, Mackey et al., 2016, 2018, Petersen et al., 2021, Pieres et al., 2017]. These discoveries aided to reconstruct the interaction history of the MCs, whose morphology and kinematics have been shaped in the last Gyrs by their mutual gravitational influence and by the tidal stresses induced by the MW [e.g., Belokurov and Erkal, 2019, Besla et al., 2012]. Even more valuable, the Early Data Release 3 (EDR3) of the *Gaia* mission [Gaia Collaboration et al., 2016, 2021a] made it possible to kinematically characterize the already known tidal substructures [Cullinane et al., 2022, Omkumar et al., 2021, Schmidt et al., 2020], to unveil the response of the MW halo to the LMC [Belokurov et al., 2019, Conroy et al., 2021, Garavito-Camargo et al., 2019, Vasiliev et al., 2021], but also to discover new stellar streams predicted by N-body models [Belokurov and Erkal, 2019, Petersen et al., 2021].

In the following sections, I describe the stellar sub-structures recently revealed in the periphery of the MCs, the progress made to shed light on their origin, and the questions still open within the scientific community.

1.2.3.1 The Northern Tidal Arm in the LMC: an unexpected thin over-density

Amongst the numerous sub-structures revealed in the last years, one of the most striking is the Northern Tidal Arm (NTA), an arm-like stellar over-density located to the North of the LMC, revealed by Mackey et al. [2016] by exploiting the public DES survey . Fig. 1.5 displays a spatial density map of old MSTO stars associated with the LMC by Mackey et al. [2016] where the NTA over-density is visible to the North of the outer LMC disc. Mackey et al. [2016] described it as an over-density that emerges from the LMC outer disc at about 13.5° North of the LMC centre, and extends for more than 10 kpc towards the East. It is about 1.5 kpc wide, making it the shape of a thin arm and has a total integrated magnitude in the $V-$band of $M_V \sim -7.4$ mag. The study of the NTA stellar population ledMackey et al. [2016] to conclude that it likely consists of stars tidally stripped from the LMC outer disc because of an external gravitational potential.

Belokurov and Erkal [2019] were able to trace the NTA in all its extension (i.e. 20°) by using a CMD selection of red giant branch (RGB) stars with *Gaia* DR2 [Gaia Collaboration et al.,

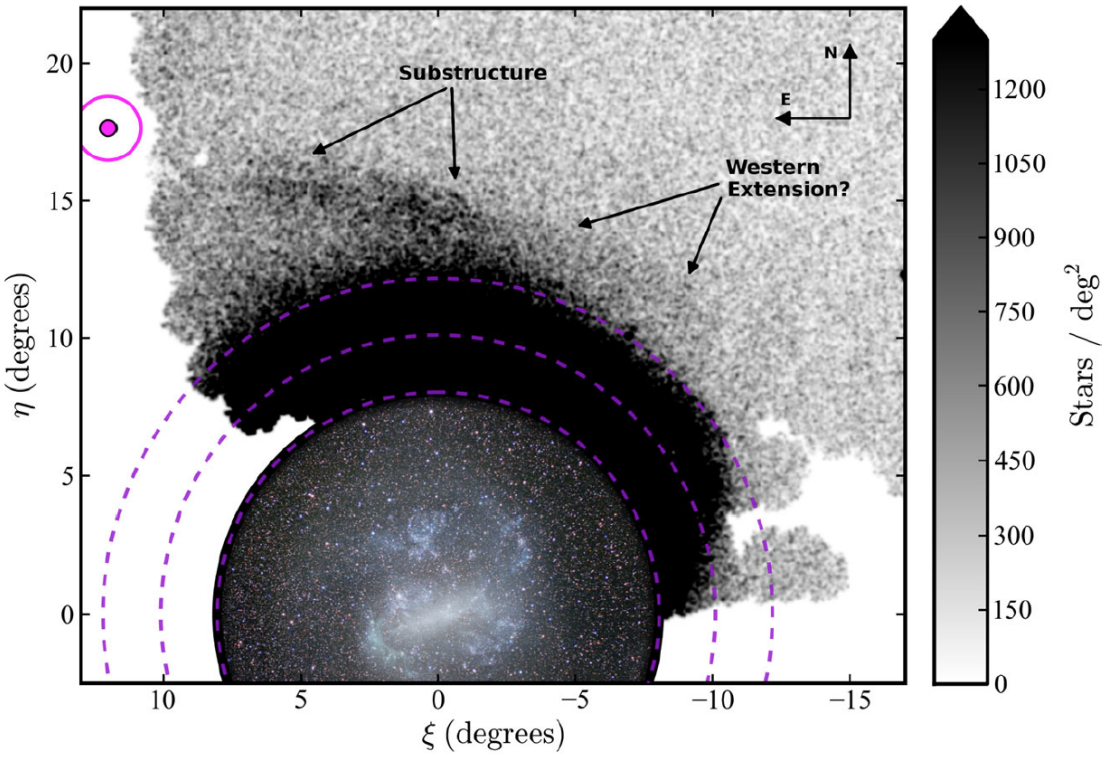

Figure 1.5: Spatial density map of LMC old main-sequence turn-off stars. The size of the bin is $2' \times 2'$. A Gaussian kernel with $\sigma = 3'$ was applied to smooth the image. In this figure, North is up and East is to the left as indicated. The coordinates (ξ, η) are in a tangent-plane (gnomonic) projection centred on the LMC. Three purple dashed circles mark angular distance of 8° , 10° , and 12° from the LMC centre. A wide-field optical image of the LMC (credit: Yuri Beletsky) fills the inner 8° . The NTA is clearly visible to the North of the outer LMC disc stretching towards the Carina dwarf, marked with a magenta point, and surrounded by a circle which indicates a radius of 1°. Image taken from Mackey et al. [2016].

2018a]. Mackey et al. [2016] and Belokurov and Erkal [2019] ran N-body simulations of an MW-LMC interaction to understand the origin of the NTA. They concluded that the tidal influence of the MW is strong enough to twist the Northern half part of the LMC disc. Nonetheless, the outcomes of these simulations predict as a consequence of the MW stress a more diffuse twisted stream in the North-Eastern side LMC, rather than a thin and horizontal arm as observed so far.

Recently, Cullinane et al. [2022] obtained radial velocities and metallicities of the NTA stars through spectroscopic observations of different regions along the arm in the context of the Magellanic Edges Survey (MagES). They also took advantage of the PMs from the *Gaia* EDR3 [Gaia Collaboration et al., 2021a] in order to have all the components of the 3D velocity vector along the NTA. Combining metallicity and kinematics measurements they unquestionably confirmed that the NTA consists of LMC outer disc material tidally distorted by an external gravitational potential. They also ran a set of N-body simulations of a LMC-MW interaction to shed light on the NTA origin. Alike the previous works, their best model that qualitatively matches with the observations also foresee a much more diffuse substructure, namely the half part of the North-East outer LMC disc twisted in the direction of the Galactic disc. However, at present, such a diffuse stellar structure has not been detected in the position predicted by N-body simulations yet. Finally, some peculiar kinematics features observed in the NTA, such as very large negative radial velocities, cannot be ascribed to the solely MW interaction. Therefore, they suggest that the MW gravitational attraction combined with past recurring close passages of the SMC shaped the morphology and kinematics of the NTA.

1.2.3.2 The outer disc of the LMC: a network of tidal stellar sub-structures

Besides the thin over-density discovered to the North of the LMC, other tidal structures ascribed to the dynamical interactions with the SMC and/or the MW surround the LMC. Analyzing deep optical images of the LMC disc, Besla et al. [2016] spotlighted the presence of stellar arcs and multiple spiral arms to the North of the LMC (within 10° from the LMC centre). They used numerical simulations to unveil the nature of all the features depicted to the Northern side of the LMC (including the NTA) and concluded that repeated close interactions between the MCs produced such tidal sub-structures. Afterward, Mackey et al. [2018] revealed two large stellar substructures to the South of the LMC, as well as in the Intra-cloud regions, and they also observed that the LMC outer disc is truncated at West and South side (in the directions facing the SMC) with respect to its extension to the North. An even more complex network of

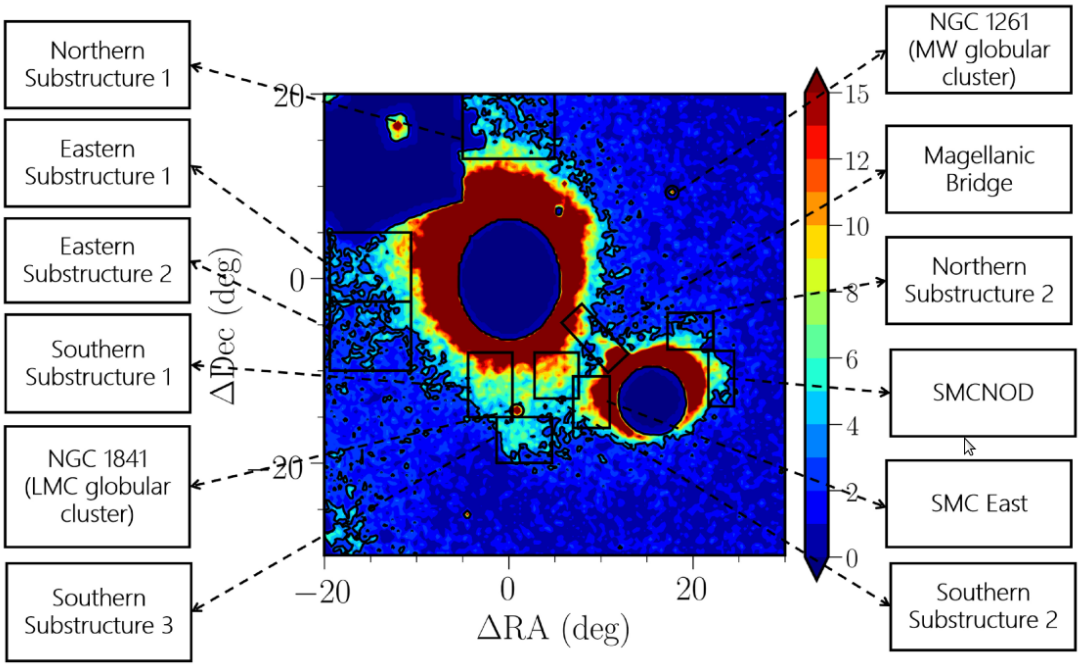

Figure 1.6: Morphological features in the outskirts of the MCs identified by El Youssoufi et al. [2021]. The size of the bin size is 0.09 deg^2. The main morphological features are listed at the sides of the figure. Image taken from El Youssoufi et al. [2021].

tidal features in the South of the LMC, reminiscing of spiral arms, were disclosed by Belokurov and Erkal [2019] by using a RGB sample taken from the *Gaia* DR2. They noticed that one of the substructures depicted by Mackey et al. [2018] is curving clockwise, in the direction of the SMC, but in addition, in the same region they discovered a new thin stellar stream that wraps around the South LMC disc and seems to connect with the SMC. They also retrieved the West truncation of the LMC outer disc as well.

N-Body simulations showed up that the combined effect of the MW and the SMC is needed to explain all these observed features [Belokurov and Erkal, 2019]. Recently, El Youssoufi et al. [2021] explored the periphery of both the MCs by using near-infrared photometry from the Vista Hemisphere Survey [VHS, McMahon et al., 2013]. They confirmed all the stellar tidal sub-structures described above to the North and South of the LMC, as well as the disc truncation at its Western side. Fig. 1.6 depicts the main morphological features in the MCs. Furthermore, they also discovered a new stellar sub-structure to the East of the LMC, up to 20° from the LMC centre, in the direction of the Galactic disc. They speculated that it could have formed by the tidal forces generated by the MW.

To conclude the description of the main stellar tides revealed in the last years within the LMC periphery, Petersen et al. [2021] used an N-body model to examine the ongoing tidal interaction of the LMC with the MW. Their model foresees an extended structure made by tidally stripped stars to the North-East of the LMC, stretched towards the Galactic disc. They also detected the leading arm of such a structure, beyond 25° from the LMC centre, adopting as population tracers a sample of RR Lyrae stars provided by the *Gaia* DR2 [Clementini et al., 2019, Holl et al., 2018] and employing the PMs measurements from *Gaia* EDR3. They revealed signatures of such a stream even at 70° from the LMC centre, in the Northern hemisphere, demonstrating that the LMC halo is more extended than previously thought.

1.2.4 The star cluster system of the MCs as proxy of their interaction history

The stars contain all the chemo-physical information about the entire evolutionary history of a galaxy, hence this can be reconstructed through the examination of its stellar component, either by means of the derivation of the SFH of the field or by using its SC system as surrogate of the stellar field population. SCs have always been pivotal stellar systems to understand many physical mechanisms in different astrophysical fields. Being an (approximately) coeval system of stars of different masses it is the ideal laboratory to test stellar evolutionary models and to understand the weight of physical phenomena happening inside stars, such as overshooting, mass loss rate, rotation, diffusion, mixing of chemical elements, amongst the others. In addition, considering all the SCs tied to a galaxy as a physical system, the different ages, masses and metallicities of its members offer an excellent benchmark to reconstruct the physical evolution of its hosting galaxy. The usefulness of approximating them as a SSP allows us to use their properties to derive the past star formation rate (SFR) and the chemical evolution of a galaxy ISM. Moreover, the episodic enhancements in the star cluster formation (SCF) represents tangible clues of the past close encounters and/or mergers experienced by a galaxy. Overall, the sub-population of the SCs captured from dwarf galaxy satellites is a direct witness, even in case of current dissolved stellar systems, of the mass assembly rate, aiding to comprehend the history of the interactions of a galaxy [see e.g., Kruijssen et al., 2019, Mucciarelli et al., 2021].

One of the main topics addressed in this thesis is the investigation of the MCs SC system with the aim of unveiling their past evolution. This is achieved: a) through a deep study of a large sample of already catalogued SCs whose main characteristics such as age, metallicity, structural

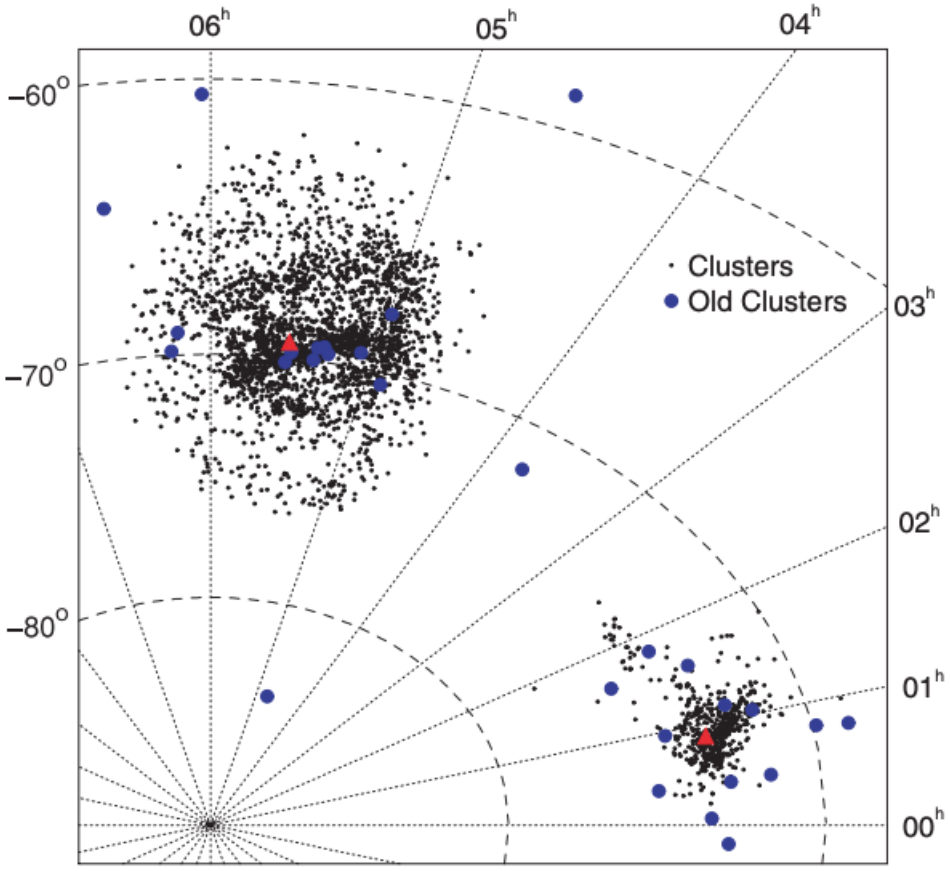

Figure 1.7: Objects catalogued as star cluster by Bica et al. [2008] in the LMC, the SMC and within the Bridge. Every small dot represents a SC whereas blue circles indicate SCs older than 4 Gyrs. The red triangles mark the position of the LMC and SMC centroids. Image taken from Bica et al. [2008].

parameters etc. have not been studied in detail so far; b) via an extensive research of unknown SCs in the outskirts of the MCs, in order to build a complete census of these objects, allowing us to study the MC SC system without selection biases. The SC system of the MCs has always been one of the most studied for the following reasons: (i) they are sufficiently close to let their individual stars be resolved by medium-size telescopes; (ii) many SCs are populous so that also the post main sequence evolutionary phases are well populated; (iii) the SCs in the Magellanic system are numerous. Indeed, the most recent updated catalogues by Bica et al. [2008] and Bica et al. [2020] contains more than 4000 objects comprising SCs and young associations. A not negligible subsample of MC SCs is also as massive as the old GCs of the MW, but with the peculiarity that, unlike the Galactic GCs, they span a very broad range of ages, from 10^6 to

10^{10} yrs, making suitable to use them to probe a wide parameter space and to analyze how their physical properties evolve during their lifetime (see also §1.2.5). Figure 1.7 shows the spatial position of the MCs SCs reported in the Bica et al. [2008] catalogue, as well as that of the SCs older than 4 Gyrs (blue points).

In the next sections I describe the state-of-art of the MCs SC system and the still open questions that I face in the present thesis.

1.2.4.1 Age distribution of star clusters in the Magellanic system

In recent years several authors tried to unveil the interaction history of the MCs by using the age distribution of their SC system as a tool [Baumgardt et al., 2013, Glatt et al., 2010, Nayak et al., 2016, Nayak et al., 2018, Piatti, 2021a, Piatti et al., 2015a,b, 2016, 2018, Pieres et al., 2016, Pietrzyński and Udalski, 2000]. Taking advantage of a conspicuous sample of SCs with homogeneously estimated ages, different authors reported the presence of peaks in the SCs age distribution, suggesting that the origin of these enhancements in the SCF were repeated close encounters between the LMC and the SMC. Indeed, SCs may form through strong shock compression produced by the re-distribution of the gas in response to a nearby encounter between two galaxies. Therefore, recurrent close passages induce episodic star formation events in the galaxies involved.

Pietrzyński and Udalski [2000] used the second data release of the Optical Gravitational Lensing Experiment [OGLE II, Udalski et al., 1997], to estimate ages for about 600 SCs younger than $\sim$ 1.2 Gyrs in the central parts of the LMC through the isochrone matching procedure. They revealed three important peaks of SCF, centred at $\sim$ 7 Myrs, $\sim$ 125 Myrs and $\sim$ 800 Myrs. Nevertheless, the adoption of a LMC distance modulus (DM) of a considerably lower value with respect to that accepted today (i.e DM = 18.24 mag vs $\mathrm{DM_{LMC}} \simeq 18.49$ mag) could have affected their age determination. Glatt et al. [2010] increased noticeably the sample of SCs studied in the MCs by using data from the Magellanic Cloud Photometric Surveys (MCPS). They derived ages of 324 and 1193 SCs younger than 1 Gyr in the SMC and LMC, respectively, through a visual isochrone fitting procedure. In this way, they were able to obtain and compare SCF periods of both the MCs adopting a homogeneous sample of SCs. They found that the MCs had a very similar burst of SC formation episodes, at 160 Myrs and 630 Myrs for the SMC and 125 Myrs and 800 Myrs for the LMC, strengthening the hypothesis that a nearby passage between the MCs originated these two peaks. Nayak et al. [2016] and afterwards Nayak et al. [2018] implemented a semi-automated quantitative method to retrieve age and reddening of 1072 LMC and 468 SMC

SCs, respectively, using data from the OGLE III. They found a major cluster formation episode at about 125 Myrs in the LMC and at about 130 Myrs in the SMC, in agreement with previous works. In the last years, the number of LMC and SMC SCs with estimated ages has considerably increased, finding consistent results with previous literature about episodic enhancements in the SCF at similar periods in both the MCs [Baumgardt et al., 2013, Chiosi et al., 2006, Perren et al., 2017, Piatti et al., 2015a,b, 2016]. At the same time, the search for still undiscovered SCs intensified thanks to the availability of wide-field surveys ensuring deeper photometry and higher spatial resolution in combination with a wide-spatial covering of the MCs [Gatto et al., 2020, Piatti, 2021a, Piatti et al., 2018, Pieres et al., 2016, Ripepi et al., 2014, Sitek et al., 2016, 2017], making the number of SCs associated with the MCs significantly expand. For example,Piatti et al. [2016] investigated a region of $0.4^\circ \times 0.4^\circ$ within the SMC bar, enlarging the number of known SCs by about 55%, demonstrating that a noticeable fraction of SCs is still missing.

Overall, the temporal picture emerging from these works revealed that the SCF histories of the MCs are coupled in the last Gyrs, suggesting that the interplay between the LMC and the SMC played a major role in the SF activity of the MCs. Furthermore, the spatial distribution depicted from the above mentioned works demonstrated that into the LMC most of the young SCs trace the central bar and the spiral arms, with the very young objects (< 10 Myrs) found in the supergiant shells of HII. On the opposite, older LMC SCs follow a smoother distribution and are located also at larger galacatocentric distances. Alike the LMC, most of the young SCs in the SMC reside in the bar and in the bridge connecting the MCs, whereas older SCs are more evenly distributed.

Despite the many similarities in the MCs SC system underlined above, some remarkable differences are present, in particular concerning the intermediate-age old SC population. For example, regarding the age distribution of the oldest SC members, the LMC hosts at least 15 confirmed SCs as old as the galaxy itself [e.g., Bica et al., 2008, Mackey and Gilmore, 2004, Olsen et al., 1998], namely $\sim 12 - 13$ Gyrs old and thus coeval with the oldest Galactic GCs (GGCs), indicating that the LMC and the MW might have formed at the same time. On the other hand, the SMC has only 1 old known SC, NGC 121, whose estimated age of 10 Gyrs [Glatt et al., 2008a, Mighell et al., 1998, Shara et al., 1998] is also relatively younger with respect to the LMC oldest population. A further striking difference between the LMC-SMC SCF histories is the almost total lack of LMC SCs in a period ranging in the time interval 4-10 Gyrs, known as "the age gap", which was first noticed by Da Costa [1991]. To date, only the SC ESO121-03 with an estimated age of $t \simeq 9$ Gyrs [Mackey et al., 2006, Mateo et al., 1986] is known to inhabit the age

gap. The SMC does instead possess numerous intermediate-age SCs which makes the age gap a peculiarity of the LMC alone [e.g., Glatt et al., 2008b, Mighell et al., 1998, Rich et al., 2000]. The age gap makes the SC formation/evolutionary history of the LMC anomalous compared to those in the MW, the SMC and other galaxies, where no similar gaps are found. The LMC age gap problem is one of the open questions faced in this thesis, therefore we discuss this subject in detail in the next sections.

Before concluding, it is worth noticing that the majority of the recent works specialized in looking for new SCs and devoted to the study of the properties of already known SCs, focused only in the central regions of the MCs [e.g., Nayak et al., 2016, Palma et al., 2016, Piatti et al., 2015a, 2018]. The photometry adopted in many works was also too shallow to allow a detailed analysis of SCs older than 1-1.5 Gyrs [Glatt et al., 2010, Nayak et al., 2016, Pietrzyński and Udalski, 2000], as the MS of these objects become fainter and fainter as the age increases. Only in recent years, the availability of wide-field photometric surveys allowed us to explore the outskirts of the MCs. For example, Pieres et al. [2016] availed of data from the public DES survey to explore the Northern region of the LMC to search for undiscovered SCs and to carefully analyse known SCs. They visually identified a total of 255 SCs, of which 109 ($\simeq$ 40%) were new discoveries, and thus evidenced that the census of the SCs in the MCs is still fairly incomplete, not solely in the outskirts as we see in §4.4.

1.2.4.2 The Age Gap

Since the first photometric investigations of the intermediate-age LMC SC candidates aimed at estimating their ages, it became clear that the LMC was lacking massive SCs in a broad interval of ages ranging between $\sim$ 2.5-3 Gyrs up to $\sim$ 10 Gyr [Da Costa, 1991, Jensen et al., 1988]. As already mentioned in the previous section, this feature is dubbed the "age gap" in the LMC SC formation history. The only exception known to date is represented by the SC ESO121-03, with an estimated age of about 9 Gyrs [Mateo et al., 1986][4] At the edges of this quiescent period of SCF, it is known that the LMC experienced two main SC forming episodes. The first one formed the old population of LMC GCs and corresponds to the time interval of 10-13 Gyrs ago (see also §1.2.4.1). The second started at the end of the gap and it is still occurring in the central regions of the LMC, such as the central bar, the inner disc or the spiral arms, as manifested by the numerous supergiant shells of HII regions in the LMC (see §1.2.4.1).

To further investigate this puzzling feature, several works followed-up with deep photometry

[4]The most recent age estimate derived by Mackey et al. [2006] is 9.0 ± 0.8 Gyr.

down to the MSTO magnitudes, the still poorly unstudied intermediate-age SCs in order to unambiguously derive their ages and in turn establish whether or not the age gap was a real period of quiescent SCF [Bica et al., 1998, Geisler et al., 1997, 1999]. Sarajedini [1998] claimed that 3 LMC SCs, namely NGC 2155, SL 663, and NGC 2121, were 4 Gyrs years old, which is inside the age gap period. They retrieved data from the HST archive and adopted the usual isochrone fitting procedure to estimate their ages. In particular, they noticed that all these 3 SCs possess many stars in the so-called Hertzsprung gap[5], which is a locus of the CMD that becomes populated of stars only for SCs older than 2.5 Gyrs (reference). However, Rich et al. [2001] analysed the same 3 SCs on the basis of longer integration time observations carried out with the HST. They detected the characteristic Hertzsprung gap, which was not resolved by Sarajedini [1998] because of poorer photometry. In fact, their ages resulted to be younger by about 0.8 Gyrs with respect to Sarajedini [1998]'s assessment (i.e. 3.2 Gyrs), so that these SCs lie at the young edge of the age gap and not inside it. Thus this result appears to confirm the scenario of two main episodes of SCF separated by a broad quiescent period.

In the most recent years, and particularly during the last decade, the number of projects surveying different regions of the LMC to look for new SCs has remarkably increased, leading to the discovery of hundreds of new SCs in the MCs [Piatti, 2021a, Piatti et al., 2015a, 2018, Sitek et al., 2016]. As discussed in §1.2.4.1, most of these works targeted only the central regions of the LMC, where confusion due to crowding makes it extremely difficult to obtain deep and accurate photometry, needed to unambiguously detect old SCs, and thus bringing modest advances in the comprehension of the age gap feature. One of the few exceptions was the extensive research made by Pieres et al. [2016] in the outer Northern side of the LMC, up to distances of 10 kpc, which increased the number of known SCs in those observed fields by more than 40%. They also provided an estimate of their main parameters, i.e. age, metallicity, distance modulus and reddening, for a sub-sample of 117 SCs by adopting a maximum-likelihood approach to estimate the relevant SC parameters. Besides the confirmation of ESO121-03 as a genuine member of the age gap, they also revisited the age of NGC 1997 to be $\sim 4.5 \pm 0.1$ Gyrs, about 2 Gyrs older than previous evaluations [Palma et al., 2016, Piatti et al., 2009], thus within the age gap, although it is very close to its younger edge. At the light of this striking result, to solve the

[5]For stars more massive than $M \geq 1.5\ M_{\odot}$, the stellar evolutionary phase following the hydrogen core exhaustion consists in a rapid contraction of the star. Usually, a very few stars are observed in this phase, for the time spanned by massive stars in this non-equilibrium status is relatively short, resulting in a gap between the main sequence and the sub-giant branch phase.

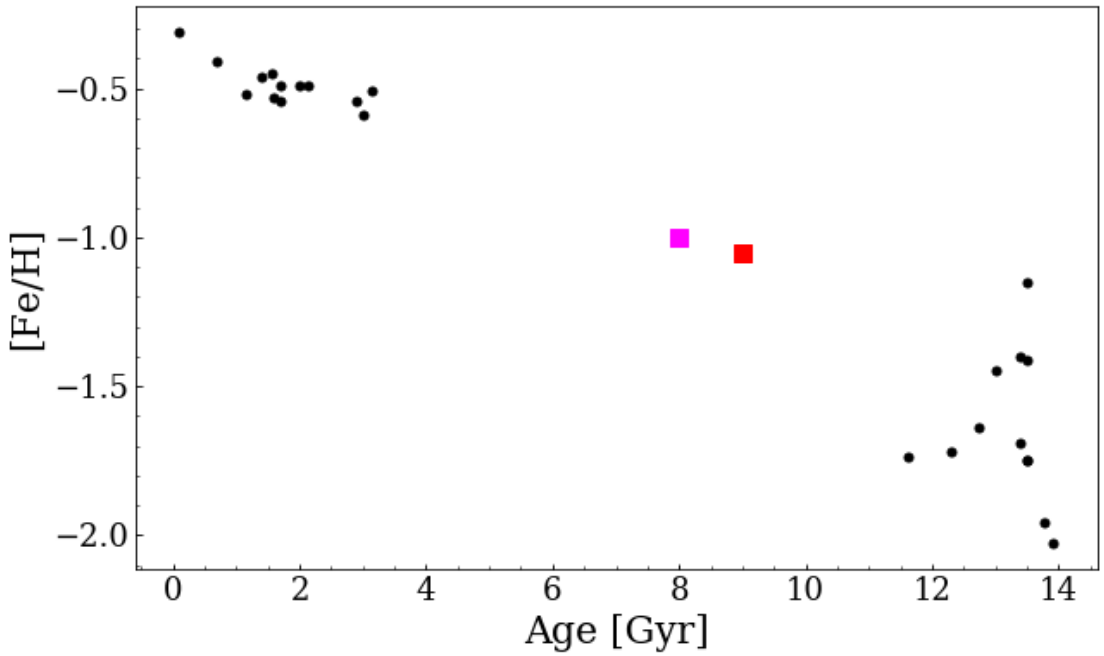

Figure 1.8: Metallicity as a function of the age for the LMC analyzed by Song et al. [2021] and Mucciarelli et al. [2021]. The red, blue and magenta squares indicate the SC ESO121-03 and KMHK 1592, respectively.

age gap puzzle it is necessary to massively explore the farthest regions of the LMC to detect and analyze new SCs. In addition, deeper and more accurate photometry is needed to study the known intermediate-age SCs to better assess their ages. At the moment of writing this thesis, Piatti [2022b] estimated the age of KMHK 1592 to be 8.0 ± 0.5 Gyrs through deep photometric observations carried out with the GEMINI telescopes, being the second LMC SC well within the age gap. Piatti [2022b] interpreted its presence in the LMC as a capture from an external galaxy, like for example the SMC.

From the observational context described above, it appears that the age gap is a real feature. However, its existence is difficult to explain by considering that: (i) the age distribution of SMC SCs shows numerous objects in the 3-10 Gyrs range interval, despite that in the last couple of Gyr the MCs SCF shows a common behaviour (see §1.2.4.1); (ii) the analysis of the LMC star formation histories (SFH) revealed that the stellar field counterpart does not present a zero star formation in that period [Carrera et al., 2011, Holtzman et al., 1999, Mazzi et al., 2021, Olsen, 1999, Piatti and Geisler, 2013, Tosi, 2004]. In principle, we can deduce that the SCF of the LMC was roughly absent in the age gap and thus decoupled from the field SF. However, since most stars should form in SCs [e.g., Lada and Lada, 2003], this statement is in disagreement with the

presence of stars formed during the age gap in the LMC field. On this basis, we could hypothesise that all the SCs in the age gap have been destroyed. Nevertheless, this hypothesis is at odds with the quite sharp increase at about 3 Gyr of the LMC SC population, which comprises several tens of SCs in the 1-3 Gyr age range. It is therefore difficult to explain the abrupt change in the age distribution at the edge of the age gap with solely disruption mechanisms [Da Costa, 2002].

It is worth noticing that the presence of such a long period of roughly zero SCs formation also prevents deriving an age-metallitic relation (AMR) in this broad time interval through the analysis of the LMC SC system. This is unfortunate, as the AMR is a powerful tool to understand the chemical evolution of a galaxy. Furthermore, the gap in the age distribution of LMC SCs is also mirrored in a similar gap in the metallicity [Rich et al., 2001]. This is illustrated in Fig. 1.8 which displays the AMR built with the LMC SCs spectroscopically analyzed by Song et al. [2021] and Mucciarelli et al. [2021]. There is a dual behaviour of the SCs in the LMC: the old LMC GCs are all very metal-poor, with [Fe/H ≤ -1.5 dex, while the young SCs have an average of [Fe/H $\simeq -0.7$ dex, with a few SCs having [Fe/H ≤ -1.0 dex. It stands out the presence of the SC ESO121-03 in between the two sup-populations (red square in the figure), and the very recent estimation of KMHK 1592 (magenta square). Unlike the LMC, SC of intermediate metallicity (and age) are known in the SMC [e.g., Da Costa and Hatzidimitriou, 1998]. Concluding, on the basis of the above discussion, it is crucial to detect, if any, as much as possible age gap members. Even the inclusion of a few new age gap members would not only help us in understanding this puzzling feature, but would also provide a significant improvement in the knowledge of the LMC chemical evolution.

1.2.4.3 Inconsistencies between the star formation and the star cluster formation histories in the LMC

Due to their relative proximity, the SFH of the MCs can be determined in high detail by studying their resolved stellar populations. Indeed, several efforts were devoted to reconstruct the MCs evolutionary history based on the analysis of their SFH [see e.g., Carrera et al., 2011, Cignoni et al., 2013, Harris and Zaritsky, 2004, Harris and Zaritsky, 2009, Piatti and Geisler, 2013, Rubele et al., 2012, 2015, 2018, Weisz et al., 2013]. In this context, it is important to compare the SFHs obtained through the star field and the SCs as the stars are thought to mostly form in clusters [Lada and Lada, 2003] and therefore we expect that in a galaxy the two sub-populations do exhibit a similar SFH. The above discussed age gap in the LMC SCs system (see §1.2.4.2) raises the obvious question of whether or not a similar gap is detectable in the star field. More

generally, we want to understand if the SFHs of SCs and field populations agree to each other, as this would have important consequences in our understanding of galaxy formation and evolution. For example, in more distant galaxies, where it is impossible to resolve individually the field stars, their SC system might be adopted as a proxy to study the galaxy's SFH.

Early works devoted to the study of the MCs SFH were space-limited, meaning that only a relatively small portion of the galaxy was probed, hence they were able to derive only a local SFH rather than an overall picture of the MCs SFH [Gallagher et al., 1996, Geha et al., 1998, Holtzman et al., 1999, Olsen, 1999, Smecker-Hane et al., 2002]. These works were based on HST observations in order to reach magnitudes fainter than the oldest MSTO, which were difficult to obtain with ground-based telescopes, at the expense of a tiny field-of-view (FoV). In the LMC, these observations mainly probed the bar or the inner disk, but in the limited area investigated by these works, the results were often in disagreement [see e.g., Dolphin, 2000, Geha et al., 1998, for what concerns the age gap period].

A significant advance was due to Harris and Zaritsky [2004], Harris and Zaritsky [2009] who obtained homogeneous photometry for about 4 million of stars covering an area of about 4×4.5 square degrees in the SMC and more than 20 million of stars covering an area of about 7×7 square degrees in the LMC (Magellanic Cloud Photometric Survey, or MCPS). On this basis, these authors were able to measure for the first time the spatially resolved SFH of the SMC and LMC, respectively. In more detail, they found a similar SF activity for both the LMC and the SMC in the last 3 Gyrs. Interestingly, both MCs experienced bursts of SF at about 2 Gyr, 0.5 Gyr, 0.1 Gyr, that is, close to the peaks revealed in the SC age distribution of both MCs (see §1.2.4.1). Harris and Zaritsky [2009] also disclosed two major SF events in the LMC. The former approximately 12 Gyrs ago, when also the old GCs in the LMC formed (see §1.2.4.1), and the latter which started about 5 Gyrs ago and it is still ongoing at an average rate of 0.2 $M_{\odot}$/yr. These two events are separated by a quiescent period of about 7 Gyrs, which therefore confirmed the age gap also in the field. However, at odds with Harris and Zaritsky [2009]'s work, Piatti and Geisler [2013] detected a not negligible presence of stars born between 5 and 12 Gyrs, based on Washington CT1 photometry for about 5.5 million stars distributed throughout the LMC main body. This outcome implied that the SF in the SC population in the LMC is in disagreement with that of stellar field for a relatively broad period of the galaxy's life.

Recently, both the MCs have been the targets of different surveys that covered their whole main body with sufficiently deep photometry to derive spatially-resolved SFHs throughout the two galaxies. In particular, the near-infrared VISTA survey of the Magellanic Clouds [VMC,

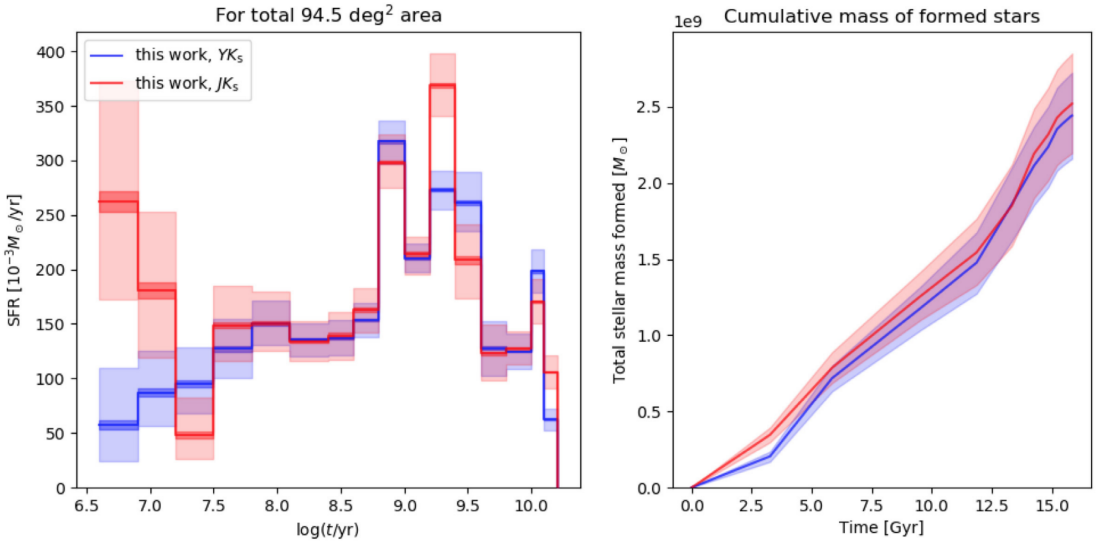

Figure 1.9: *Left:* Total SFR as function of the look-back time integrated over the total area covered by Mazzi et al. [2021]. Red and blue lines show the solutions obtained by adopting the filters Y-Ks and J-Ks, respectively. The shaded areas indicate the confidence regions. *Right:* Cumulative mass of formed stars, for the two different solutions. Image taken fromMazzi et al. [2021].

Cioni et al., 2011] observed the LMC and SMC and made it possible to estimate the age, metallicity (and hence to derive an AMR), the average distance modulus and reddening in sub-region as small as ~ 0.12 deg^2. Concerning the LMC, in a pilot work devoted to the study of 4 VMC tiles,Rubele et al. [2012] found two main peaks of SF at $\log(t) \sim 9.3$ and $\log(t) \sim 9.7$ in most of their sub-regions within the LMC inner disc. In particular, the latter peak is within the well-known age gap, in disagreement with Harris and Zaritsky [2009]. They also found that the LMC bar formed stars at a constant rate within the time interval $\log(t) \sim 8.4$-$\log(t) \sim 9.7$. Finally, Mazzi et al. [2021] gave an overall picture of the SFR within 96 square degrees in the LMC by using 63 VMC tiles. Figure. 1.9 shows the total SFH in the LMC as estimated by Mazzi et al. [2021]. They found out that the major period of SF in the LMC was between 4 and 0.5 Gyrs ago with rates of about 0.3 $M_\odot$/yr, while in the other periods the SFR is typically half that value.

In summary, the current scenario reports of tightly correlated SFHs between the LMC and SMC in the last 3-4 Gyrs, thus suggesting that the two galaxies might have become a close binary system only in the last Gyrs. A further clue reinforcing this hypothesis is the difference in the ancient SFHs ($t \geq 10$ Gyrs) between the LMC and SMC, which might suggest that the MCs were not companions at the moment on their formation. The enhanced episodes of SF, observed also as peaks in the SC age distribution of both MCs (see §1.2.4.1), are additional strong evidences of

close encounters between the LMC and SMC, as also predicted by N-body models and numerical simulations [Bekki and Chiba, 2005, Besla et al., 2012, Zivick et al., 2018, 2019].

Coming back to the question we posed at the beginning of this section, from the results discussed above, it appears that the LMC SF activities of SC and field were different during the age gap period, whereas they were strongly similar outside this interval. As it is thought that most stars of a galaxy did form in SCs [Lada and Lada, 2003], the question we should answer now is: "What did happen to all SCs that formed the observed stars in the LMC during the age gap?". In §1.2.4.2 we already addressed the improbability of their overall disruption based on the fact that a sharp increase at about 3-4 Gyrs of the SC age distribution is visible. More likely, a combination of a lower rate of SF and an increased disruption mechanism could account for the gap observed in the SC age distribution, but the only way to solve this puzzle is to complete the census of SCs in the LMC and to accurately analyze their ages to definitively prove whether the age gap is real or not.

To conclude, the LMC represents a peculiar case in which the SFHs retrieved from the SC system and field stars do not match throughout its life.

1.2.5 The SC system of the MCs as test-bed of the star cluster dynamical inner evolution

The MCs are an ideal laboratory for probing the inner dynamical evolution of SCs. Indeed in both MCs they are numerous (several thousand), span the entire interval of ages, from the newborn systems to the old GCs, and also show a wide interval of metallicities ($\sim$2 dex). Unlike the MW, the SC system of the MCs also contains very massive ($\log(M/M_{\odot}) \sim 5$ dex) young ($t \leq$ 1 Gyr) or intermediate age (1 Gyr $\leq t \leq$ 7-10 Gyrs) SCs. Therefore, the MCs SCs are suitable to explore a wider region of the parameter space, and in turn, to investigate in more detail the evolutionary processes working in a SC over cosmic time.

SCs evolve dynamically since the moment of their formation due either to internal and external processes. Among the former we mention: (i) gas expulsion from supernovae explosion of the massive stars; (ii) "evaporation" of the outer stars which overtake the escaping velocity; (iii) mass segregation; (iv) energy transfer from the inner to the outer SC regions because of a subpopulation of stellar mass black holes. The most important external processes include: (i) the gravitational field of the hosting galaxy; (ii) disc or bulge shocking; (ii) merger of binary SCs. It is likely that a combination of both internal and external mechanisms shape the properties of

SCs during their lifetime.

Key progress in this field has been achieved in the last decades thanks to several studies investigating the SCs in the MCs. For instance, Elson et al. [1989] discovered a trend between the age of SCs and the core radius r_c[6], that is, the older the SC, the larger the observed spread in core radius. This relationship was confirmed by subsequent works in the LMC [Carvalho et al., 2008, Elson, 1991, 1992, Mackey and Gilmore, 2003a,b, Santos et al., 2020] but also in other galaxies like M33, M51, M83, NGC 628 and NGC 1313 [Bastian et al., 2012, Chandar et al., 2016, Ryon et al., 2015, 2017, San Roman et al., 2012]. Mackey and Gilmore [2003a] investigated the possibility that a bias due to some selection effects could artificially generate this trend, but they ruled it out, concluding that the apparent behaviour reflects a real physical process.

The currently accepted scenario foresees that all SCs form with small core radii ($\sim$ 2-3 pc), then some of them remain compact, while others, after hundreds of Myrs, expand their inner regions. Some of the processes invoked to explain this phenomenon are: (i) energy transfer from the inner to outer regions because of stellar mass black holes [Mackey et al., 2007, 2008, Merritt et al., 2004]; (ii) mass loss due to stellar evolution [Mackey et al., 2007, 2008]; (iii) residual gas expulsion [Banerjee and Kroupa, 2017, Baumgardt and Kroupa, 2007, Goodwin and Bastian, 2006, Kroupa et al., 2001]; the presence of a central intermediate-mass black hole (IMBH) [Baumgardt et al., 2004a,b]. Of course, the combination of two or three of the above mechanisms could provide the observed expansion anyhow [e.g., Bastian et al., 2008]. However, up-to-date the physical mechanism driving the core expansion is still debated.

Unfortunately, previous works devoted to the characterization of a complete set of structural SC parameters (age, size, mass) were limited to the study of the massive MC SCs [e.g., Carvalho et al., 2008, Mackey and Gilmore, 2003a,b], as they do not suffer from stochastic issues which make it not straightforward to derive their total mass (see §7.4 for a detailed discussion). Therefore we still lack a homogeneous analysis of MC SCs down to the small mass scales in order to probe whether or not the evolutionary patterns observed up to now in the literature are mass-dependent and in what measure. In this context, in this thesis, we also investigate the physical mechanisms that govern the inner evolution of the SCs through a wide and deep analysis of a sample of MC SCs spanning a very broad range of masses, down to the hundreds of solar masses.

[6]The core radius is the distance from the cluster centre where the surface brightness drops down to half its central value.

1.3 Beyond the Magellanic Clouds

In the §1.2 we underlined the huge improvements that an interacting stellar system like the MCs (where the LMC is likely the massive member of a group of galaxies recently entered in the MW halo), that is close enough to resolve its stellar population, can provide to our knowledge of formation and evolution of galaxies. However, the galaxies where we can resolve and study even the MS stars are restricted to the LG, while beyond that there is an enormous amount of galaxies inhabiting a variety of environments, from small groups to galaxy clusters composed of thousands of members. Even if we cannot resolve their stellar content, for the closest galaxies up to 20-30 Mpc, it is often possible to adopt their GCs system as discrete tracers to investigate the kinematics of galaxies and galaxy clusters. More in detail, particularly interesting are the so-called intra-cluster GCs, which is a sub-population of GCs that have been stripped out from the parent galaxies by the tidal forces of other cluster galaxy members. Therefore, the kinematics of these intra-cluster GCs can be used as a proxy for the kinematics of the entire galaxy cluster, allowing us to study the interaction between galaxies in an environment completely different from that of the LG.

In this context, even if the main goal of this thesis is the investigation of the evolutionary and interaction history of the MCs, the final part of this work is devoted to the study of the intra-cluster discrete stellar tracers of the Fornax cluster core, the closest galaxy cluster in the Southern hemisphere.

1.3.1 Galaxy clusters as extreme environments of galaxy evolution

Galaxies are not uniformly distributed in the Universe, but they tend to agglomerate in over-structures such as the galaxy clusters, which represent the most massive, gravitationally bound and virialized systems in the Universe. Galaxy clusters can contain up to thousands of galaxies bound together by a common deep gravitational potential originated by a very massive dark matter halo with masses of the order of $10^{14} - 10^{15} M_{\odot}$. In these extremely dense environments, galaxy encounters are the main actors in shaping the properties of galaxy members. Indeed, in clusters the galaxies are continuously affected by their mutual gravitational interactions, which strongly influence their morphology, SFR, kinematics, just to mention a few. This whirl of galaxy encounters usually lead to the formation close to the cluster centre (i.e. the cluster core) of an anomalously bright galaxy, called the brightest central galaxy (BCG), or sometimes dubbed as the central dominant (cD), surrounded by a very extended halo. The BCGs are early-type like

galaxies, but with a remarkable high luminosity and mass ($M_\star \geq 10^{12} M_\odot$) and with a size many times larger than a common elliptical galaxy. These galaxies are the archetypes of the hierarchical growth scenario described in §1.1, as their evolution has been primarily shaped by their outstanding merging histories [Iodice et al., 2016, Ruszkowski and Springel, 2009, Weinzirl et al., 2014]. Semi-analytic models and numerical simulations demonstrated that the BCGs assembled the bulk of their mass and accreted their stellar halo in the last Gyrs, especially via minor merger events [Amorisco, 2019, De Lucia and Blaizot, 2007]. As these processes are expected to be still in action at the present epoch, it is important to search for observational signatures of such events in the cluster core, in order to test models of galaxy formation and evolution, especially in dense environments.

1.3.2 Discrete tracers in the intra-cluster regions to look for faint tidally signatures

In a cluster of galaxies, and especially within the cluster core, the huge number of tidal events has the effect of stripping material from the smaller galaxies (in the form of stars and GCs) that flows towards the massive one, in a process that is still ongoing. Some of the stripped material becomes gravitationally bound to the BCG or to other massive galaxies within the cluster but some fraction of it is freely moving in the common deep potential well of the galaxy cluster.

Recent surveys devoted to the analysis of the nearest galaxy clusters, detected and studied such a population of intra-cluster objects made of stars and GCs not bound to any galaxy member of the cluster [Arnaboldi et al., 2002, D'Abrusco et al., 2016, Mihos et al., 2017, Romanowsky et al., 2012, Tutukov and Fedorova, 2011, Zibetti et al., 2005]. The ensemble of these objects, which is dubbed the intracluster light (ICL), represents the remnant debris of past or ongoing stripping events witness of the dramatic galaxy-galaxy interactions occurred in a galaxy cluster. As already mentioned before, at larger cluster-centric radii the longer dynamical time preserves the kinematics of these tidal structures for a longer time [Bullock and Johnston, 2005]. Therefore, the intra-cluster regions are the ideal place to search for the debris of merger events, aiming at constraining the mechanisms driving the formation and evolution of the galaxies in dense environments.

Early investigations of such remnants were based on photometric observations. However, this approach is challenging because of the faint surface brightness of the debris, typically below $\mu \sim 27$ mag/arcsec^2 in the V-band for the brightest part of these substructures [e.g., Cooper

et al., 2010]. Nonetheless, most of the accreted mass provided by the fainter events have generally a surface brightness of the order of 30 mag/arcsec^2 or even below [Cooper et al., 2010], making it unsuitable to study these signatures from deep photometric analysis. A useful complementary approach is to adopt discrete kinematics tracers in the intra-cluster regions as a proxy of the underlying stellar population. GCs or planetary nebulae (PNe)[7] are suitable tracers as they are easily observable out to large distances due to their intrinsic luminosity or emission line dominated spectra [Cortesi et al., 2011, Douglas et al., 2007, Durrell et al., 2003, Merrett et al., 2003, Richtler et al., 2011, Romanowsky et al., 2012, Shih and Méndez, 2010]. Their radial velocity can be obtained with good precision with spectroscopic measurements in the nearby galaxy clusters and therefore they represent a useful alternative to study the halo of galaxies where it is unfeasible to obtain kinematic information from the underlying stellar population [Forbes et al., 2011, Foster et al., 2014, Longobardi et al., 2015, Napolitano et al., 2002, 2009, Pota et al., 2013, Pota et al., 2018, Romanowsky et al., 2003, 2012, Schuberth et al., 2010, Spiniello et al., 2018]. The combined information of position and velocity of the discrete tracers in the intra-cluster regions allows us to analyse the phase-space (projected positions and line-of-sight velocities) to look for the typical signatures expected in the galaxy-galaxy interactions [Johnston et al., 2008, Romanowsky et al., 2012].

1.3.3 The Fornax cluster

The Fornax cluster is the closest galaxy cluster of the Southern hemisphere, located at a distance of $d = 20.0 \pm 1.4$ Mpc [i.e., $DM = 31.51 \pm 0.15$ mag Blakeslee et al., 2009]. Figure 1.10 shows a composite image of the Fornax galaxy cluster. After the Virgo cluster, in the Northern hemisphere, it is the second closest galaxy cluster to the MW, therefore it is also one of the most studied galaxy clusters. Fornax has a mass of $(7 \pm 2) \times 10^{13} M_{\odot}$ [Drinkwater et al., 2001] measured within a radius of 1.4 Mpc, Akin to the majority of the dynamically evolved galaxy clusters, most of the major galaxies within the Fornax cluster core are early-type galaxies, of which NGC 1399 is the BCG. Late-type galaxies are instead more common in its outermost regions [Drinkwater et al., 2001].

Recently, many surveys were devoted to the study of the Fornax cluster, such as the Fornax

[7] Planetary nebulae are evolved stars with an initial mass between $0.8 \leq M_{\odot} \leq 8$. Approximating the end of their life, these stars expel their outermost envelopes which are then ionised by the ultraviolet radiation emitted by the hot core, and afterwards re-emit almost 15% of the absorbed light at the specific frequency of the green OIII at 5007 Å [Dopita et al., 1992, Schönberner et al., 2010].

Figure 1.10: Color composite mosaic in the u, g and i bands, of the central $2° \times 1°$ of the Fornax cluster. The brightest galaxy on the left side of the image is the BCG NGC 1399. North is up and East is on the left. Image taken from [Iodice et al., 2016].

Deep Survey [FDS, Iodice et al., 2017, 2016, Raj et al., 2020, Venhola et al., 2017], and the Next Generation Fornax Survey [NGFS, Eigenthaler et al., 2018, Munoz et al., 2015]. Thanks to the deep photometry and the careful analysis achieved by the above quoted surveys, it was discovered that besides the main galaxy component, Fornax also hosts a conspicuous sub-population of ultra-diffuse galaxies [UDG, Munoz et al., 2015, Venhola et al., 2017] and an intracluster population of GCs [Bassino et al., 2006, Cantiello et al., 2020, Schuberth et al., 2010] and PNe [e.g., Napolitano et al., 2003].

Many recent works demonstrated that the mass assembly of Fornax is still ongoing at the present epoch [e.g., Cantiello et al., 2020, D'Abrusco et al., 2016, Iodice et al., 2017, 2016]. For example, Iodice et al. [2017] disclosed a very faint and diffuse intra-cluster light connecting the BCG NGC 1399 with other main galaxies within the cluster core, namely NGC 1387, NGC 1379 and NGC 1381. This ICL, depicted in Fig. 1.11 has been revealed at distances between $10'$ and $40'$ (i.e., $\sim 58 - 230$ kpc) from NGC 1399, and supports the scenario of a tidal stripping of stars and GCs of the above quoted galaxies by part of the Fornax BCG. Further evidence about recent galaxy-galaxy interactions was collected from the analysis of the intra-cluster population of GCs. For instance, D'Abrusco et al. [2016] revealed that the GCs spatial distribution is asymmetric (blue contours in Fig. 1.11), extending to the W-E, and in particular connecting the BCG NGC 1399 with other luminous galaxies in the Fornax core, namely NGC 1387, NGC 1404,

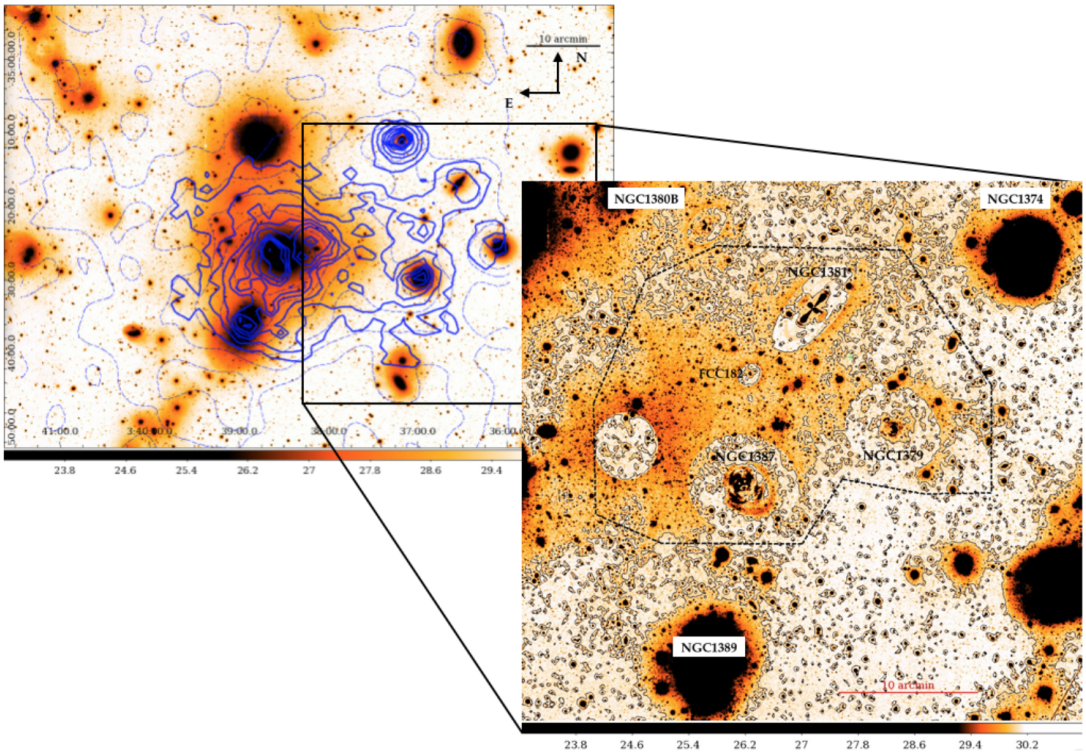

Figure 1.11: *Left:* Central regions ($2° \times 1°$) of the Fornax cluster in the r-band surface brightness levels. The spatial distribution of the GCs derived by D'Abrusco et al. [2016] (in blue) is superimposed on the image. *Left:* Zoom of the regions on the west side ($40.9' \times 42.7'$, $\sim 237 \times 248$ kpc), after a subtraction of the bright galaxies. The black contours mark the surface brightness levels ($\mu_r = 29.8 - 30.2$ mag/arcsec^2.

NGC 1380. Its distribution mirrors the ICL discovered by Iodice et al. [2017] (see Fig. 1.11) and therefore confirms the hypothesis of a sub-population of intra-cluster objects composed of tidally stripped material from the outermost regions of the galaxies around the BCG.

In this thesis we develop an ad hoc procedure, which exploits the kinematics of the intra-cluster objects, to bring to light the faint debris originated by the minor tidal interaction between a dwarf and a massive galaxy to constrain the recent mass assembly of the BCG and the origin of the ICL.

1.4 Main objectives of this thesis

In the previous sections, we presented the state-of-the-art knowledge of the MS. We underlined as, notwithstanding the huge efforts of so many researchers, there are still numerous open questions about the formation and evolution of the MC system. The main goal of this thesis is to investigate the past evolution and interaction history of the MCs, especially at look-back times greater than 3 Gyrs ago, as they are still poorly constrained. As described throughout this Chapter two complementary strategies can be adopted to get insights into the evolutionary history of a stellar system: (1) using the SC system as a proxy of the hosting galaxy evolution; (2) studying the tidal streams originated by the totality of the gravitational forces experienced by the galaxy. In this thesis, I combine both above quoted approaches to infer the past evolution of the MCs. To reach the proposed goals I exploited two recent and modern surveys (STEP and YMCA, see next chapter) whose deep photometry is able to resolve the MC stars down to the faint MS, in particular 1.5-2 mag below the MSTO of the oldest stellar population (see Chapter 2 for the description of the surveys). Even more valuable, many of the fields observed by these surveys reside in the outermost regions of the MCs, which were barely explored with the modern ground-based telescopes and hence have been poorly investigated. Overall, the combined wide spatial coverage and the achieved accuracy of the photometry make STEP and YMCA the deepest surveys ever carried out in the MS that homogeneously probed more than 150 square degrees around the MCs.

On these bases, I took advantage of one of the widest and deepest MC catalogue of stars to develop or improve different algorithms specifically designed at:

- Discovering and characterising still unknown SCs in the MCs. In this way, we will be able to build for the first time a catalogue of SCs complete down to the faint-end of the SC luminosity function.

In particular, we focused on the LMC outskirts as these regions have not been investigated yet with deep and homogeneous photometry.

- Estimating the main structural parameters of the MC SCs such as age, spatial distribution, size, mass, luminosity. To this aim, we have exploited both the SC CMDs after a careful decontamination by non-member stars, and the SBPs, which were analysed by fitting proper analytical functions to the data.

The STEP and YMCA data were complemented with the multi-dimensional data provided by the *Gaia* mission to search for still unknown tidal stellar sub-structures which represent pivotal witnesses of the past MC interactions.

Even if the reconstruction of the MCs evolutionary history is the main goal of this thesis, we also propose to analyze a very different environment, such as the Fornax cluster. In particular, we developed an algorithm with the aim of discovering cold kinematical substructures in the phase-space of the intra-cluster kinematic tracers, such as GCs and PNe, originated from the interaction of the very abundant dwarf galaxies with the cluster environment.

Finally, it is worth pointing out that the techniques developed in this thesis are very general and can be adapted to a wide range of stellar systems, environments and physical distances.

Chapter 2

Data

The majority of the results obtained in this thesis come from observations carried out with the Very Large Survey Telescope (VST). In particular, I used data from the optical surveys "SMC in Time: Evolution of a Prototype interacting late-type galaxy" (STEP; PI: V.Ripepi) and "Yes, Magellanic Clouds Again" (YMCA; PI: V.Ripepi). In this chapter I describe the main characteristics of the telescope, the surveys and data processing procedures.

2.1 The VST

The Very Large Survey Telescope (VST), displayed within its dome in Fig. 2.1, is a wide-field optical telescope with a primary mirror of 2.6 m, built by the INAF–Osservatorio Astronomico di Capodimonte, Naples, Italy [Capaccioli and Schipani, 2011]. It operates from the ultraviolet (u-band) to the near-infrared (z-band). The VST is located at Cerro Paranal, in the Atacama desert to the North of Chile, at an altitude of $\sim$ 2600 metres above the sea level, and is adjacent to the four VLT Unit Telescopes. The VST is equipped with the OmegaCAM instrument which consists in a mosaic of 32-CCD, 16k X 16k pixels each, with a resolution of 0.214 arcsec per pixel for a total field of view (FoV) of $1^\circ \times 1^\circ$ [Kuijken, 2011]. The camera also mounts 4 additional CCDs to enable image analysis, real-time active optics corrections, and guiding. OmegaCam is equipped with both intermediate and broad band filters. In particular it mounts the u,g,r,i,z set which closely resemble the Sloan Digital Sky Survey (SDSS) filters[1]. The wide FoV of

[1]see user manual at https://www.eso.org/sci/facilities/paranal/instruments/omegacam/doc/VST-MAN-OCM-23100-3110_p109_v1.pdf

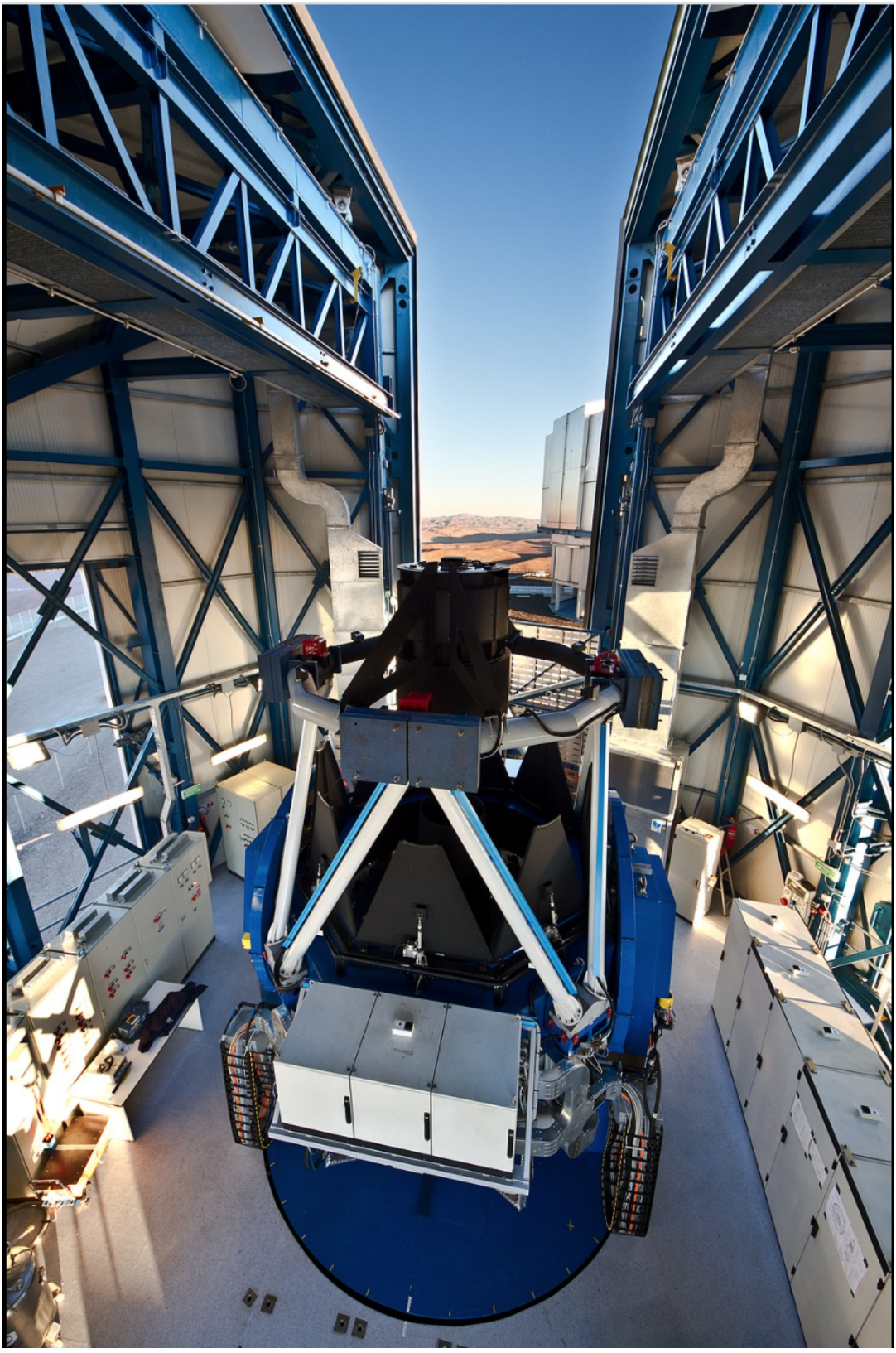

Figure 2.1: The VLT Survey Telescope (VST) within its dome in the Atacama desert of Northern Chile. On the background it is visible one of the adjacent VLT Unit Telescopes.

OmegaCAM@VST which covers an area as large as four times the full moon, makes it an ideal instrument to carry out homogeneous surveys devoted to the exploration of large portions of the sky, such as that covered by the MCs in the Southern hemisphere. Moreover the high spatial resolution and the excellent seeing secured by the location at Cerro Paranal, allows us to study also crowded regions such as the central regions of the MCs.

2.2 The STEP survey

The "SMC in Time: Evolution of a Prototype interacting late-type dwarf galaxy" [STEP, Ripepi et al., 2014] is a survey lead by the PI: V. Ripepi based on the VST Guaranteed Time Observations (GTO) allocated by ESO to Istituto Nazionale di Astrofisica (INAF) in exchange of the acquirement of the telescope. The survey has been designed to obtain the first homogeneous and deep optical photometic observations of the whole SMC main body, the Wing, its outskirts and the Bridge. The survey was designed to reach at least two magnitudes below the MSTO of the oldest stellar population, in order to study the SMC and Bridge SFH over the whole Hubble time. The STEP survey was originally conceived to cover 74 square degrees in the $g-r-i-H_\alpha$ bands, but at the end of the observations only 53 square degrees were obtained, so divided: 36 square degrees in the main body of the SMC and 17 square degrees in the Bridge. A footprint of the survey is illustrated in Fig. 2.2. Each tile is 1 square degree and the different tiles have a significant overlap each other in order to secure a homogeneous calibration. The limiting magnitude was $g \sim 24$ mag with S/N = 10 (AB system) and r(H_α) ~ 22.5 mag with S/N = 5. The STEP survey was proposed to achieve three main goals: (1) derivation of the spatially-resolved SFH throughout the SMC and in its outskirts; (2) mapping the three dimensional structure of the SMC by using variable stars as tracers; (3) identification and analysis of the SC system of the SMC and in the Bridge to reconstruct its evolutionary history. To reach the magnitude limit necessary for attaining the goals proposed by the survey even in the more crowded areas, such as the central bar of the SMC, "deep" images consisting in 5 or 10 exposures of 520s or 300s were carried out. Moreover, to prevent the saturation of bright SMC stars, also "shallow" images consisting of 5 exposures of 25s each one were obtained. The observations started in Dec. 2011 (ESO Period 88) and ended in Aug. 2017 (ESO Period 99). A detailed description of the STEP survey is in Ripepi et al. [2014]. In the following we only summarize briefly the main steps of reduction and analysis of the data.

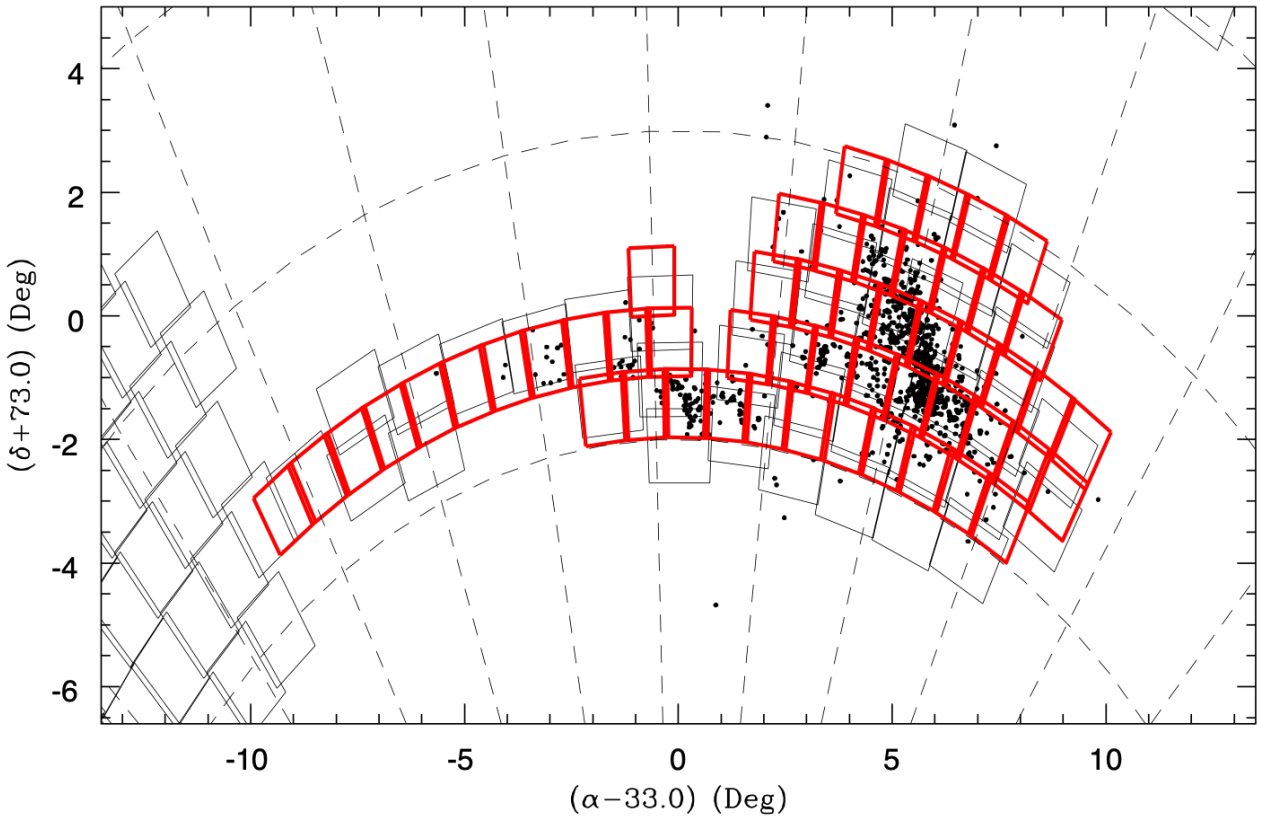

Figure 2.2: Footprint of the STEP survey. Black dots indicate the position of SCs and associations reported in the catalog of Bica et al. [2008]. Each red box corresponds to a tile whose FoV is 1 square degree.

2.2.1 Data reduction

The pre-reduction of the raw images was performed through the VST-TUBE imaging pipeline [Grado et al., 2012]. This pipeline was specifically designed for the VST and it is installed on the computers of the INAF-VST Center (VSTCeN6 hosted by the INAF Osservatorio Astronomico di Capodimonte, Naples). The VST-TUBE pipeline removes bias, perform flat-field correction, applies CCD gain equalization and apply an illumination correction.

Once the pre-reduction procedure was completed, it returned two images in both the g and i filters, one corresponding to the stack of the "shallow" and the other to the "deep" observations. To carry out the photometry in crowded regions such as the body of the SMC it is necessary to adopt the point spread function (PSF) photometry. This technique foresee different steps: 1) several potentially isolated stars are preliminary selected; 2) the bi-dimensional shape of these

stars is approximated with an analytical or empirical-analytical function (i.e. the PSF) and the residuals are analysed, removing the non-isolated objects or those with bad residuals; 3) the previous operation is iterated until a sample of stars with good residuals is obtained; 4) different models are tried, including PSF radially varying from the center of the detector, and the model that provides the overall best residuals (i.e. the best χ^2) is chosen; 5) this model is used to fit the shape of all the stars on the detector, including the crowded ones. All the previous steps have been carried out with the `DAOPHOT IV/ALLSTAR` [Stetson, 1987, 1992] packages. Having obtained the photometry for each shallow and deep image in both filters (the ".als" files from `ALLSTAR`), the following task was to homogenise and merge the shallow and deep catalogues, averaging the magnitudes of the stars in common. This was achieved by means of an ad-hoc procedure, which first performs a cross-match between the shallow and deep catalogues with the `STILTS` package [Taylor, 2006], setting a tolerance of $0.25''$ (slightly more than 1 pixel) in both RA and Dec coordinates. Then, the average of the magnitude of the stars in common is calculated to correct for the residual photometric zero-point difference (which is generally of the order of 0.01–0.015 mag). As a final step, the files are merged keeping the stars in common and those that appears only in one of the two catalogues. This procedure leaves us with two merged catalogues, one in g and the other in i. We then cross-match these two files to obtain the final photometric catalogue.

The calibration to obtain the absolute photometry of the sources was calculated whenever possible by means of local standard stars provided by The AAVSO Photometric All-Sky Survey (APASS). However, the spatial resolution of APASS is $2.57''$, preventing a reliable calibration in the crowded SMC regions, such as its main body, Wing and the tile hosting the SC 47 Tucanae. Thus, we adopted the photometry from the SkyMapper survey [Data Release 1; Wolf et al., 2018] which has a spatial resolution of $\sim 0.5''$, recalibrated into the APASS system, in the most crowded tiles. Finally, we adopted the following procedure to obtain the absolute calibration:

- We performed a cross-match of the STEP PSF photometric catalog with the APASS data, or in the crowded regions with the SkyMapper data (recalibrated into the APASS system). We used a cross-match radius of $0.5''$.
- We discarded APASS sources with uncertainties in magnitude larger than 0.1 mag.
- We also made use of the sources in the STEP PSF photometry with DAOPHOT $CHI \leq 10$ and $-1.0 \leq SHARPNESS \leq 1$ to reject objects with bad photometry.
- We looked for and eventually corrected any possible spatial residual of the photometric zero points, namely trends with RA or Dec, in each tile.

- We corrected the colour $(g-i)$ dependence of the zero points in g and i.

At the end of this process, we obtained an average accuracy of $\sim$0.02 and $\sim$0.03 mag in g and i, respectively.

Figure 2.3 depicts the errors provided by `ALLSTAR` package in the g and i bands as a function of the magnitude for two representative tiles. As visible in the figure, a relative error of 10% is reached at $g \sim 24$ mag and $i \sim 23$ mag, showing the goodness of the STEP survey photometry.

2.2.2 Completeness

To obtain a realistic estimate of the photometric error as a function of the magnitude we performed completeness experiments. This task is achieved by adding artificial stars to the stacked images and carrying out the photometry in the same way as described in §2.2.1. Then we count the number of artificial stars recovered and their magnitude, so that it is possible to estimate the fraction of the stars recovered at different magnitude bins. In particular, to obtain the completeness in the STEP survey the following steps were performed:

- A synthetic CMD roughly representing the population of stars located in the SMC and in the Bridge was generated to constrain colour and magnitude of the stars to be added to the images. About 2 million of stars were inserted in each tile, selected within the magnitude interval of $14 < g < 26.5$ mag.

- Each tile was sub-divided in boxes of 70 pixels per side. To avoid self-crowding issues, in each box is inserted only one artificial star at a random position.

- An artificial star is recovered if in both g and i bands its position is recovered within $0.25''$ from its original position, and its magnitude is returned within 0.75 mag from its input value.

Figure 2.4 illustrates the result of the completeness task in the g and i bands, performed on two representative tiles of the STEP survey. The tile 4_6 is one of the most crowded of the survey and the 50% of completeness is achieved at $g \sim 23.5$ mag and $i \sim 23$ mag, respectively. Instead, for the tile 3_7 the level corresponding to the 50% of recovered stars is at 0.5-1 mag fainter, i.e. $g \sim 24; 24.5$ mag, namely about 1.5 magnitudes below the MSTO of the oldest stellar population within the SMC.

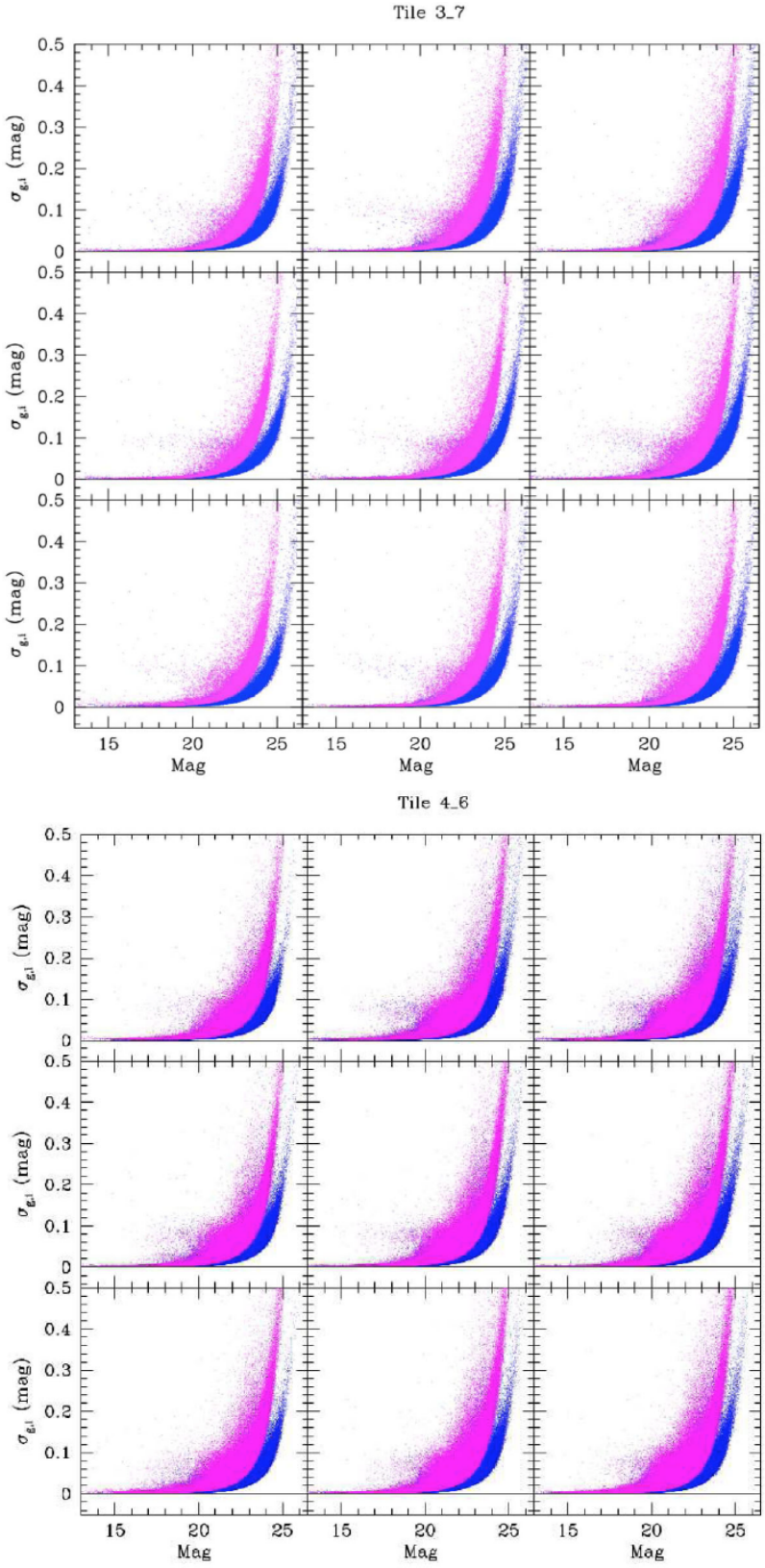

Figure 2.3: Photometric errors in g (blue) and i (magenta) filters for tiles 3_7 (*top panel*) and 4_6 (*bottom panel*). To verify the presence of possible differences within each image, the tiles were divided into nine sub-frames $20' \times 21'$ each. North is up and east is to the left. Image taken from Ripepi et al. [2014].

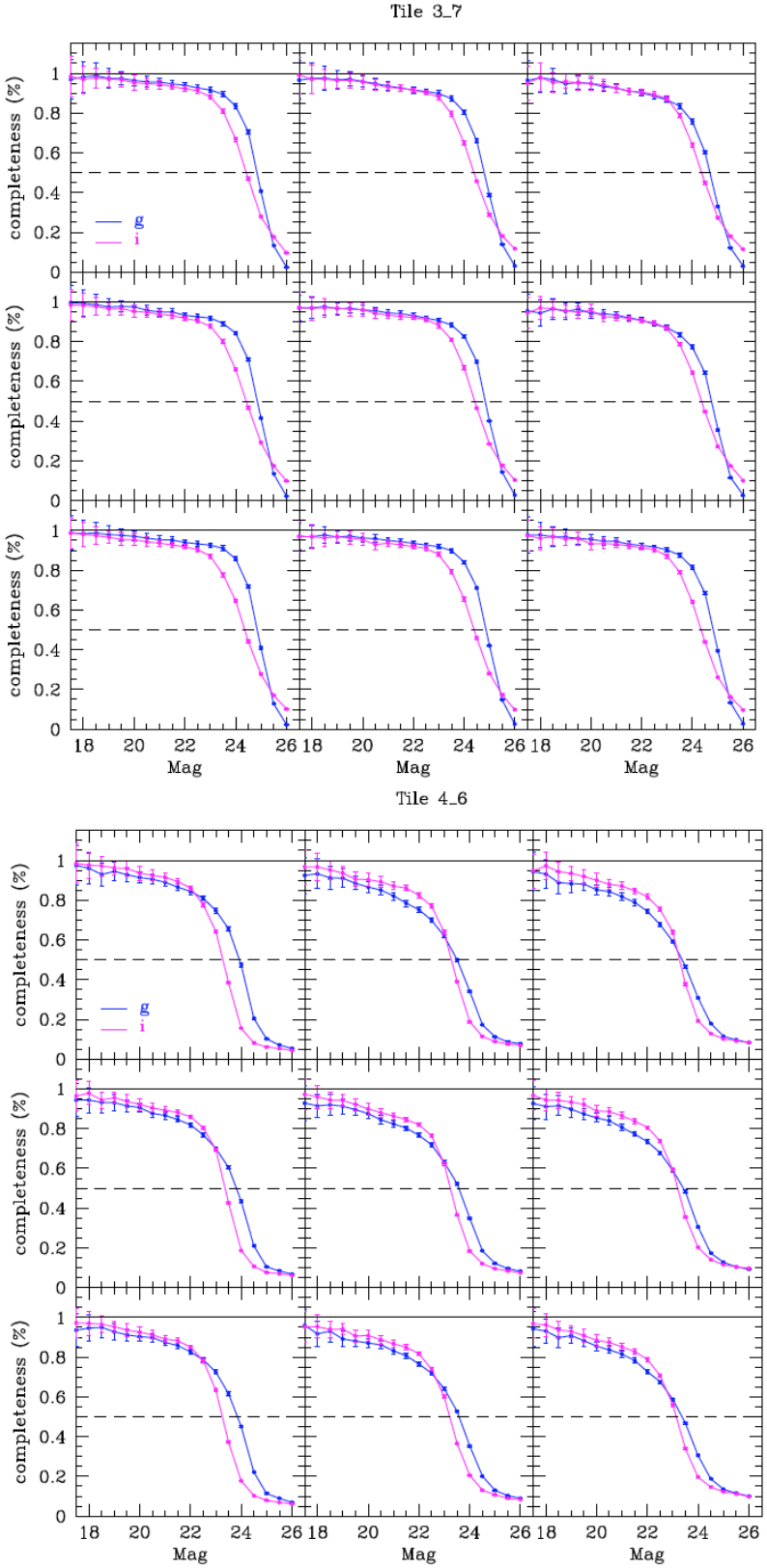

Figure 2.4: Completeness for the tiles 3_7 (*top panel*) and 4_6 (*bottom panel*). Blue and magenta solid lines refer to g and i bands, respectively. Similarly to what done in Fig. 2.3, the tiles were divided into nine sub-frames of $20' \times 21'$ each to check the presence of possible differences in completeness within each image. North is up and east is to the left. The 100 and 50 per cent levels of completeness are shown with black solid and dashed lines, respectively. Image taken from Ripepi et al. [2014].

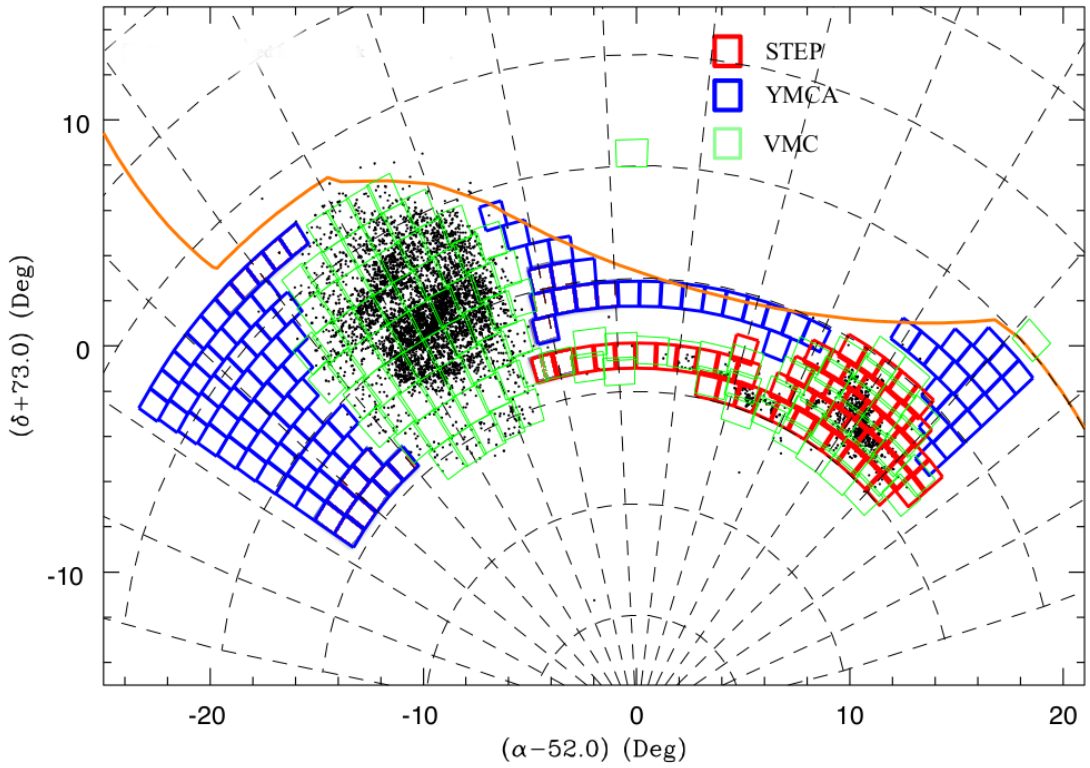

Figure 2.5: Footprint of the YMCA survey (blue boxes) in a zenithal equidistant projection. As comparison we also drew the footprint of the STEP survey (red boxes) and that of the VMC [Cioni et al., 2011, green boxes]. The red solid line indicates the border of the DES survey. Black points mark the position of all objects present in Bica et al. [2008].

2.3 The YMCA survey

The optical survey "Yes: Magellanic Cloud Again" (YMCA, PI: V.Ripepi) is a project based on the GTO allocated time and carried out with the VST telescope which was described above. The YMCA survey can be seen as complementary to the STEP survey, as it explores the outskirts of the SMC and LMC, as well as a strip above the Bridge connecting them. Fig. 2.5 shows the footprint of the survey, compared with that of the STEP project. YMCA aims at probing a total 110 square degrees with a deep and homogeneous optical photometry in the g and i filters. In particular, many of the YMCA tiles probe regions which was not yet investigated with deep and homogeneous photometry, therefore it will provide the first catalog of such kind in the peripheries of the LMC and SMC. Similarly to the STEP survey, it has the main goal of unveiling the evolutionary history of the LMC and more general of the MS, but also to better constrain in

time the moment of their past interactions. The completed survey will make feasible to derive the first SFH of the LMC since the moment of its formation in its periphery, which is still fair unexplored. Therefore achieving with a high accuracy the 1-2 magnitudes below the MSTO of the oldest LMC stellar population is a necessary ingredient to reach the purpose for which the survey was designed to. The photometric depth of the survey is also ideal to look for unknown low-massive and faint SCs that could represent a considerable population of undiscovered LMC SCs and which can be used as proxy of the MCs physical evolution. Moreover, the outermost regions of the LMC might also hide faint dwarf galaxies member of the MS [Bechtol et al., 2015, Drlica-Wagner et al., 2015, Kim and Jerjen, 2015, Koposov et al., 2015, Torrealba et al., 2018], augmenting the number of satellites possibly associated to the LMC. A further goal of the survey includes the research of low-surface brightness structures in the LMC periphery, as proxies of tidal induced disturbances.

The observations started during the Period 98 and ended during Period 108 with the observation of the last tile. Similarly to the STEP survey, each tile has been observed in a "deep" mode which consists 10 long exposures of 180 s and 140 s (in g and i, respectively) and in a "shallow" mode or namely 5 exposures of 25 s (both in g and i) each in order to do not saturate bright stars.

2.3.1 Data reduction and photometry

Many steps requested to obtain the catalog of stars within the YMCA tiles are identical to those described in §2.2 for the STEP survey. The first 21 observed YMCA tiles were pre-processed with the VST-TUBE imaging pipeline [Grado et al., 2012] which also performed the pre-processing of the images of the STEP survey (see §2.2.1 for a detailed description of the pipeline). For the remaining tiles, collected from the Period 103, these tasks have been performed with the ASTROWISE pipeline [McFarland et al., 2013]. The following steps were carried out by myself for the remaining 75 YMCA tiles as part of my PhD project. Also to YMCA we made use of the standard DAOPHOT IV/ALLSTAR [Stetson, 1987, 1992] packages to get the PSF photometry with a procedure identical to that described in §2.2.1.

2.3.2 Absolute photometric calibration

Similarly to the STEP survey, the absolute photometric calibration was obtained by means of the local standard stars provided by the AAVSO Photometric All-Sky Survey (APASS). For each

tile, we carried out the following steps:

- We cross-matched the PSF photometric catalog with the APASS data release 10 database by adopting a search radius of $0.5''$ to mitigate the number of wrong matches (the APASS instrument's pixel-size is $2.57''$), and retaining only APASS observations with signal-to-noise (S/N) ratio larger than 10.
- We checked for and eventually corrected any residual spatial variation of the photometric zero points (i.e. we searched for correlations of the photometry as a function of the RA and Dec).
- We corrected for the colour dependence of the zero points in g and i filters.

At the end of this procedure, we achieved an average accuracy of the order of 0.02 and 0.03 mag in g and i bands, respectively. Figure 2.6 illustrates the typical plots employed to verify the absolute photometric calibration for the cases of the South-East tiles 1_27 and 2_33. No spatial trends are visible and moreover the dispersion of the residuals are quite low. Similar plots have been drawn for the other tiles with an analogous level of crowding. Finally, we used the *SHARPNESS* output parameter of the DAOPHOT tool to filter out the extended sources or spurious detection due to bad pixels. In particular, the *SHARPNESS* cut has been made on a tile-by-tile basis, even if on average we retain sources within the interval -0.7$\leq SHARPNESS \leq$0.7. No further cuts have been applied to the CHI parameter to prevent removing bright stars.

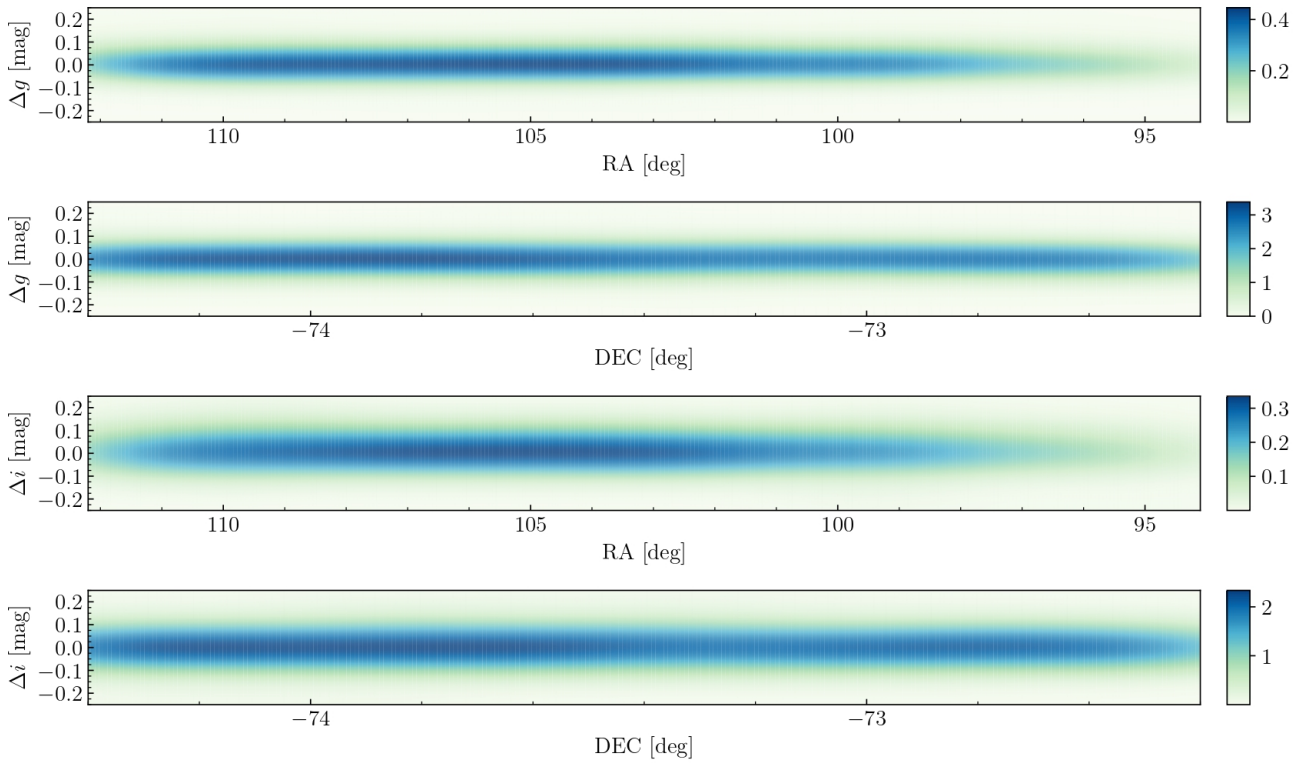

Figure 2.6: Comparison of the absolute calibrated photometry and the APASS one vs R.A. and Dec. Δg and Δi are in the direction "this work"-APASS. The data has been smoothed by means of a KDE. The colorbars report the density of data points. Image taken from Gatto et al. [2020].

Chapter 3

Search over-densities in the sky

This chapter is based on some sections of the paper published on the Volume 499 of the Monthly Notices of the Royal Astronomy Society (MNRAS), Gatto et al., 2020, MNRAS, Vol. 499, p. 4114-4139. The results of that paper are instead argument of the next Chapter.

One of the primary goal of this thesis is to build for the first time a complete census of SCs in the outskirts of the LMC and then to homogeneously estimate SCs main parameters. These information can be used to investigate, in particular, the LMC singularly and its interaction history with the SMC and the MW. To this aim, we used the YMCA and STEP catalogues[1] constructed as described in §2.2 and §2.3.

We limited our analysis to the periphery of the LMC for three main reasons: (i) these regions are still quite unexplored with deep homogeneous photometric data, thus they are ideal to look for low-luminous and faint SCs missed from previous photometric surveys; (ii) the longer dynamical time and in turn the low disruption rate of the SCs in the galaxy outskirts might permit also to the old and less populous SCs to survive, hence allowing us to probe even the earliest evolutionary stages of the LMC; (iii) the presence of the age gap in the LMC makes this galaxy an interesting and peculiar stellar system to analyze. In particular, investigating the real existence of the age gap is extremely valuable for the understanding of the LMC past evolution (see the detailed discussion in §1.2.4.2).

In this chapter we describe the algorithm thoroughly implemented in the `python` language to look for over-densities (agglomeration of stars) in the sky such as the SCs but it can also be

[1]Regarding the STEP tiles, we only made use of the tiles 3_21 and 3_20 as they only are located in the surrounding of the LMC (see Fig.2.2).

suitable to detect other stellar systems, such as dwarf galaxies. More generally this algorithm is able to spot any stellar system that in a given area present a rise of the number of its members with respect to the local average. In addition we also discuss the test of the algorithm on a suite of Montecarlo simulations generated ad hoc to properly set the parameters of the algorithm and to obtain a measure of its effectiveness.

In principle, a visual identification of agglomeration of stars in the deepest images of a survey can still be used to identify unknown stellar systems [e.g., Pieres et al., 2016]. Nonetheless, to achieve the goal of building a SC sample as complete as possible, we needed to go beyond the simple eye-inspection of the images. Indeed, visual methods are not very effective in detecting the less luminous and less dense SCs, that constitute a significant fraction of a galaxy's SC population, as the SC luminosity function steeply increases towards the faint end [e.g., de Grijs et al., 2003]. Furthermore, using an automated method allows us to also measure the completeness of the procedure on more objective grounds. It is worth underlining that, as this technique needs as input parameters only the sky coordinates of an object (i.e. RA and Dec), it can be easily generalized to other over-density finding problems, provided that a catalogue of coordinates is available.

3.1 Construction of density maps through a Kernel Density Estimation

The first step of the procedure is to find regions in the sky where the local density is significantly above the average one. This is done by counting the number of stars in a small region and comparing it with the locally mean estimated number of stars of the field stellar population. Thus, we adopted a two dimensional kernel density estimator (KDE)[2] applied to the R.A., Dec coordinates of the stars to create a surface density map in every tile and then look for spatial over-densities in the sky. The KDE is a non-parametric technique employed to estimate the probability density function of a random variable by smoothing data through a kernel function. The main advantage with respect to the classic two dimensional histogram is that the KDE gets rid of some histogram issues like the choice of the bin size or of the bin phase [Rosenblatt, 1956]. The bandwidth of the kernel function is the only parameter that must be set in a KDE, and it should be of the same size of the smallest objects that need to be detected [Piatti et al., 2018].

[2]We used the version available in the scikit-learn package [Pedregosa et al., 2011].

On this basis, to detect even the tiniest SC that could be present in the field explored, we run the KDE with a bandwidth of $0.2'$, comparable with the size of the smallest SCs around the LMC [Bica et al., 2008]. To augment the chance of detecting over-densities, we carried out the KDE analysis by adopting two different kernel functions, namely the Gaussian and tophat functions.

The KDE analysis was performed on a tile by tile basis, sub-dividing the catalog of stars in squares (pixels) of $4''$ per side[3], and successively calculating the star density value in every single pixel through the KDE (we indicate it as $d_{\rm pix}$ hereafter). $d_{\rm pix}$ must be compared with an average local density ($d_{\rm bkg}$ hereafter) to find pixels which show up a significant higher number of stars with respect to the expected density stellar background. Fig. 3.1 shows an example of the procedure outlined above, illustrating the density surface map build with the KDE in the STEP tile 3_21 (Southwest direction of the LMC). In the figure the density increases from lighter to darker colours, disclosing, as expected, the presence of a stellar density gradient towards the LMC centre, whose direction is indicated by the black arrow. The existence of such a remarkable gradient in the stellar background (also detected in several other tiles) led us to adopt as $d_{\rm bkg}$ a measure of the field stellar density obtained locally, rather than an average value measured over the whole tile. Indeed, the second approach would underestimate the mean background density in the tile regions closer to the LMC centre, and would overestimate it farther away. This would of course affect the detection of the over-densities.

Therefore, to obtain $d_{\rm bkg}$ within each pixel, we averaged the density values derived through the KDE in a box window having inner and outer sides of $1.5'$ and $2.5'$, respectively. The size of the inner box prevents that the presence of a SC could raise and in turn overestimate $d_{\rm bkg}$, thus decreasing the possibility of detecting over-densities. The outer box is large enough to ensure a statistically significant sampling and is small enough to guarantee that we were probing a local density. The derived $d_{\rm pix}$ and $d_{\rm bkg}$ allows us to measure the signal-to-noise ratio, or significance of each pixel, defined as:

$$S = \frac{d_{\rm pix} - d_{\rm bkg}}{\sigma_{\rm bkg}} \tag{3.1}$$

$\sigma_{\rm bkg}$ is the standard deviation of the $d_{\rm bkg}$.

Once we obtained the significance for each pixel within the tile, we must define a significance threshold ($S_{\rm th}$)[4] in order to select all pixels satisfying $S \geq S_{\rm th}$, as they represent the hunted over-densities. This is an important step since the $S_{\rm th}$ value determines either the lowest cluster

[3] As already mentioned, the size of the smallest SCs around the LMC is $\sim 0.2'$; hence such a choice of pixel size allows us to sample the candidate over-densities with at least three pixels.

[4] $S_{\rm th}$ represents the number of σ above the average background level to consider a pixel as an over-density.

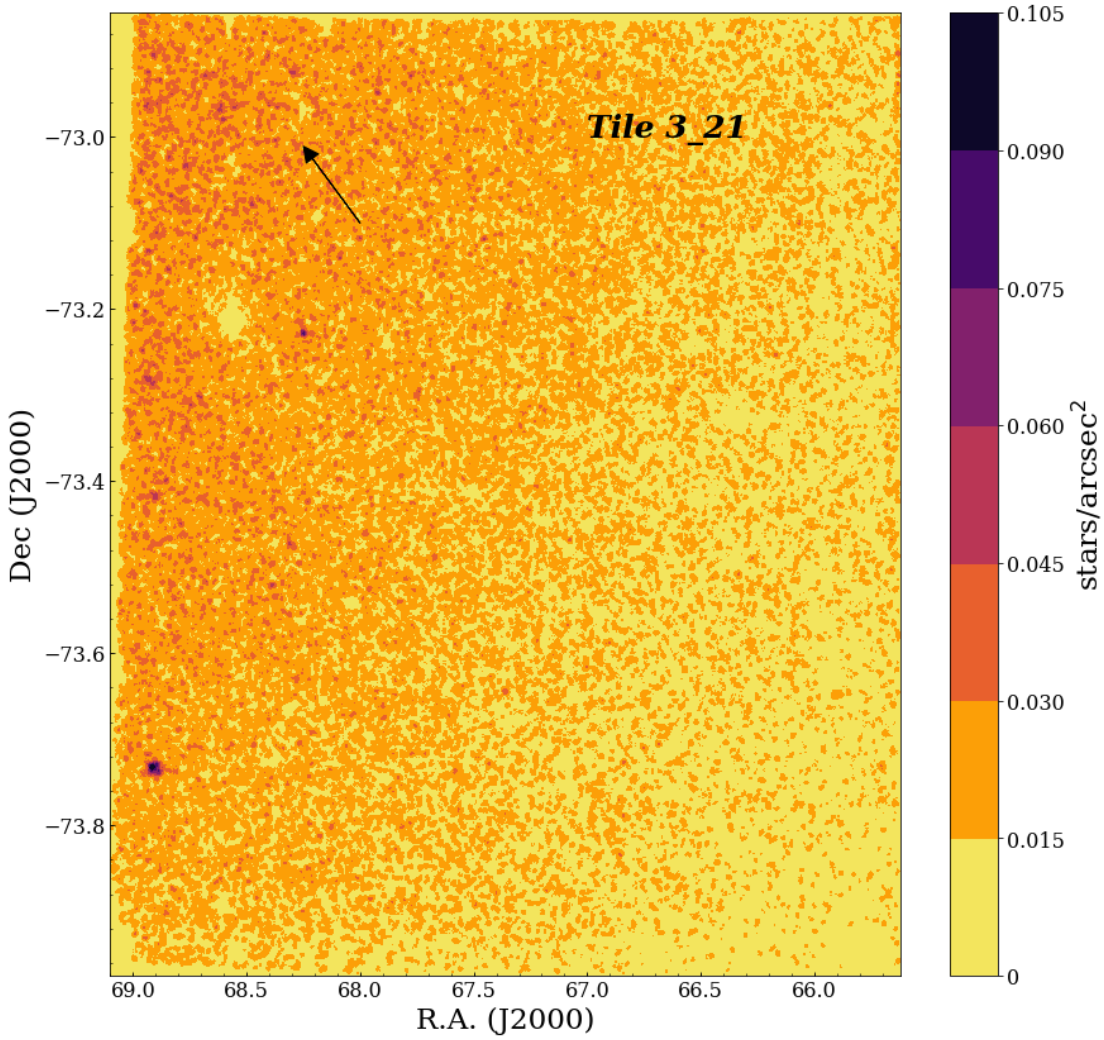

Figure 3.1: Example of the density surface map generated by the KDE, with density increasing from lighter to darker colors. This image corresponds to the tile 3_21 of the STEP survey. The black arrow indicates the direction of the LMC centre. The dark spot at the bottom left of the figure corresponds to the known cluster SL63.

density that the algorithm is able to detect than the number of false positives that it could yield. We availed on Montecarlo simulations to better constrain its value, finding in particular that it is crucial to adopt a threshold dependent on the local field stellar density (full details in the next section).

In the next step we joined all adjacent pixels that are above the the $S_{\rm th}$, discarding all groups with a number of pixels lower than four (corresponding to a dimension of $8'' \times 8''$) to remove likely false positives originated from stochastic fluctuations of the stellar field. The Montecarlo simulations described in the next section allowed us to estimate that such a choice would decrease the spurious over-densities by about 70%.

Finally, at the end of the procedure we have a list of over-densities per each tile, that need to be further inspected as an agglomerate of stars is not sufficient to claim the presence of a real SC. Before to go ahead in the description of the following steps of the algorithm, namely the estimation of the centre and radius for each over-density, it is important to introduce and describe the Montecarlo simulations which allowed us to better set-up the parameters of the algorithm, such as the $S_{\rm th}$.

3.1.1 Definition of the threshold through a suite of Montecarlo simulations

The threshold value of the significance ($S_{\rm th}$) has a great impact on the efficiency and reliability of the SC detection algorithm. It is therefore crucial to properly set this value. In fact, a low value of $S_{\rm th}$ is effective to discover sparse, faint structures composed by a handful of stars, but at the same time, it might augment the number of false positives, especially in low background density fields. On the contrary, a high threshold value would produce a more pure catalog, but at sample completeness' expenses. Moreover, as we already commented in §3.1, the density is not constant and increases towards the centre of the LMC in most of the YMCA and STEP analyzed tiles. Therefore it discouraged us to use a fixed threshold along the whole tile, thus complicating the choice of the proper $S_{\rm th}$ value.

To face this problem, we opted to carry out a suite of ad hoc Montecarlo simulations in order test the behaviour of the cluster finder algorithm at different field stellar densities. More in detail, we generated 2000 mock stellar fields with size $30' \times 30'$, placing the stars at a random position (uniform distribution). With the aim of simulating a range of field densities, we adopt as total

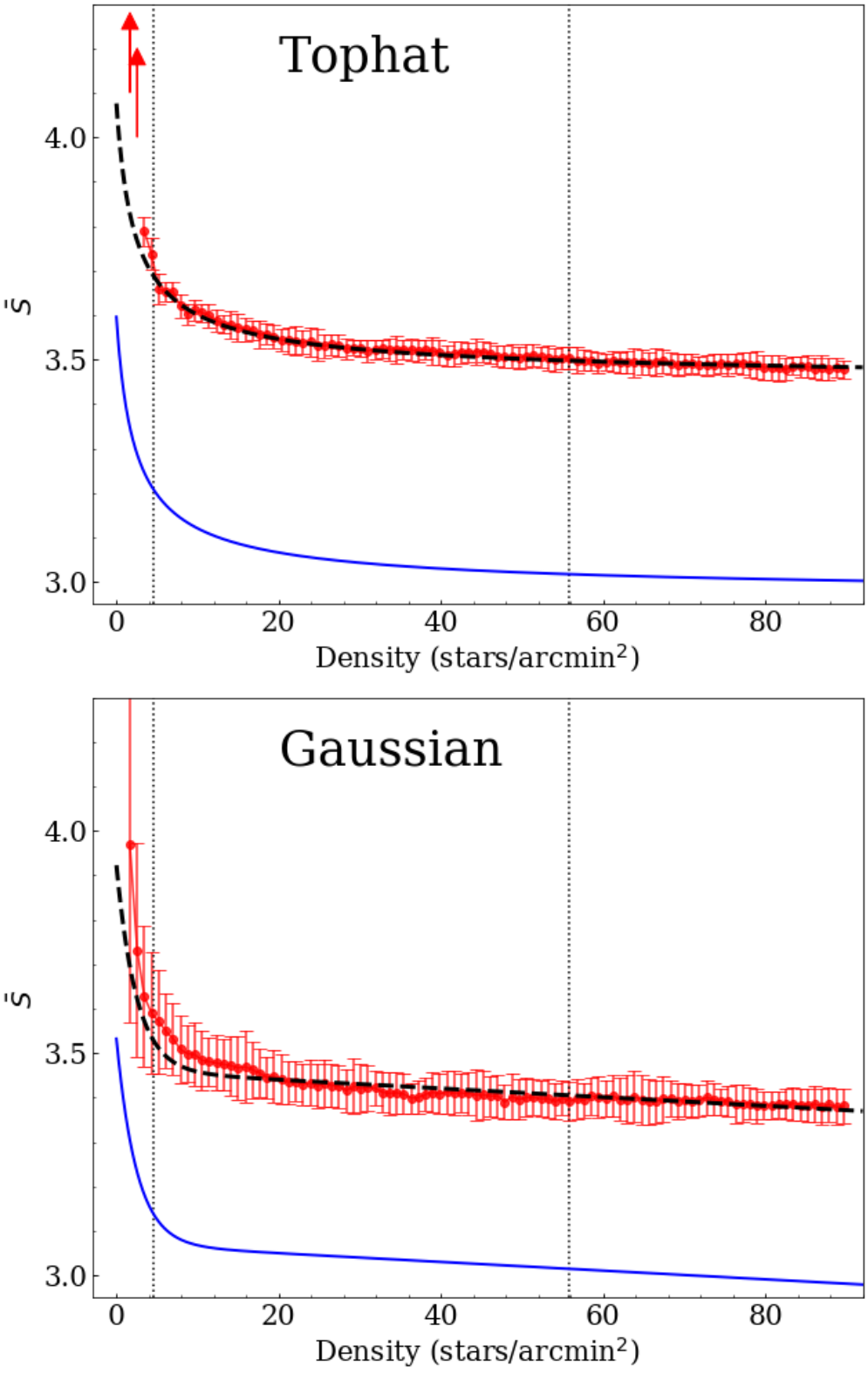

Figure 3.2: Mean of the significance (red points) with their standard deviation (red lines) of the false positives as a function of the stellar field density. Dashed lines represent the fit of these curves for the tophat kernel (*top panel*) and the Gaussian one (*bottom panel*)). In both panels, the blue lines represent a rescaling to a threshold=3 of the best-fitting lines. Dotted vertical lines define the lowest and highest density value of our observed fields.

number of stars 100 different amounts[5], ranging from 1500 ($\sim$ 1.7 stars/arcmin^2) up to 80700 stars ($\sim$ 89.7 stars/arcmin^2). These values encompass the lowest and highest density values measured in the investigated tiles (i.e. YMCA and STEP tiles in the outskirts of the LMC). Subsequently, we carried out the over-density search procedure on these mock fields exactly as they were real catalogues (see the detailed description of the algorithm in §3.1). We set by hand an initial threshold value of $S_{\rm th} = 3$. This value usually represents a reasonable compromise in maximizing the discovery of faint and sparse SCs while minimizing at the same time the spurious detection. We recall that no artificial SC has been added in these Montecarlo simulations, and therefore, every detection must be regarded as a false positive.

Figure 3.2 shows the outcomes of these tests for the two kernel functions used in this work, the tophat (top panel) and Gaussian (bottom panel) function. Both panels display the significance S of the spurious over-densities (averaged over each density bin) as a function of the star field density. For both kernel functions, we notice that the average significance of the false positives is fairly constant up to stellar field densities as low as 20 stars/arcmin^2. Below this value, this quantity begins to exponentially rise, especially for the tophat function, revealing that it is not suitable to adopt the same $S_{\rm th}$ also at low stellar density values. We modelled the trend with a simple curve (indicated with black dashed lines in Fig. 3.2) to derive the proper $S_{\rm th}$ value for each measured background stellar field density. It is important to note that the final $S_{\rm th}$ value was obtained by re-scaling down the black dashed curves in Fig. 3.2) in order to have a threshold equal to three at high densities (solid blue lines in the figure). With this choice, we are confident that at low densities a higher $S_{\rm th}$ is able to discard most false detections. Nonetheless, setting $S_{\rm th} = 3$ at higher density values ensures a great level of completeness, as we demonstrate in §3.4.2 through further tests about the ability of the algorithm in recovering artificial SCs.

To further support the usefulness of adopting a variable threshold depending on the background stellar field density, we display in Fig. 3.3 the average number of spurious detections at varying densities for the tophat (top panel) and Gaussian (bottom panel) kernel functions. We plotted the different outcomes of using a fixed (red dots) or variable (blue dots) threshold. An inspection of the figure reveals that the Gaussian function is more stable against density variations. In this case, the variable threshold removes a maximum of $\sim$ 15-20% of false positives at very low densities. On the contrary, when adopting a tophat kernel, there is an exponential increase of spurious detections at low field densities. The choice of a variable threshold, in this case, allows us to decrease the false positives by 30%. As a final consideration, the number of

[5]Thus for each value of the stellar density we ran 20 mock simulations.

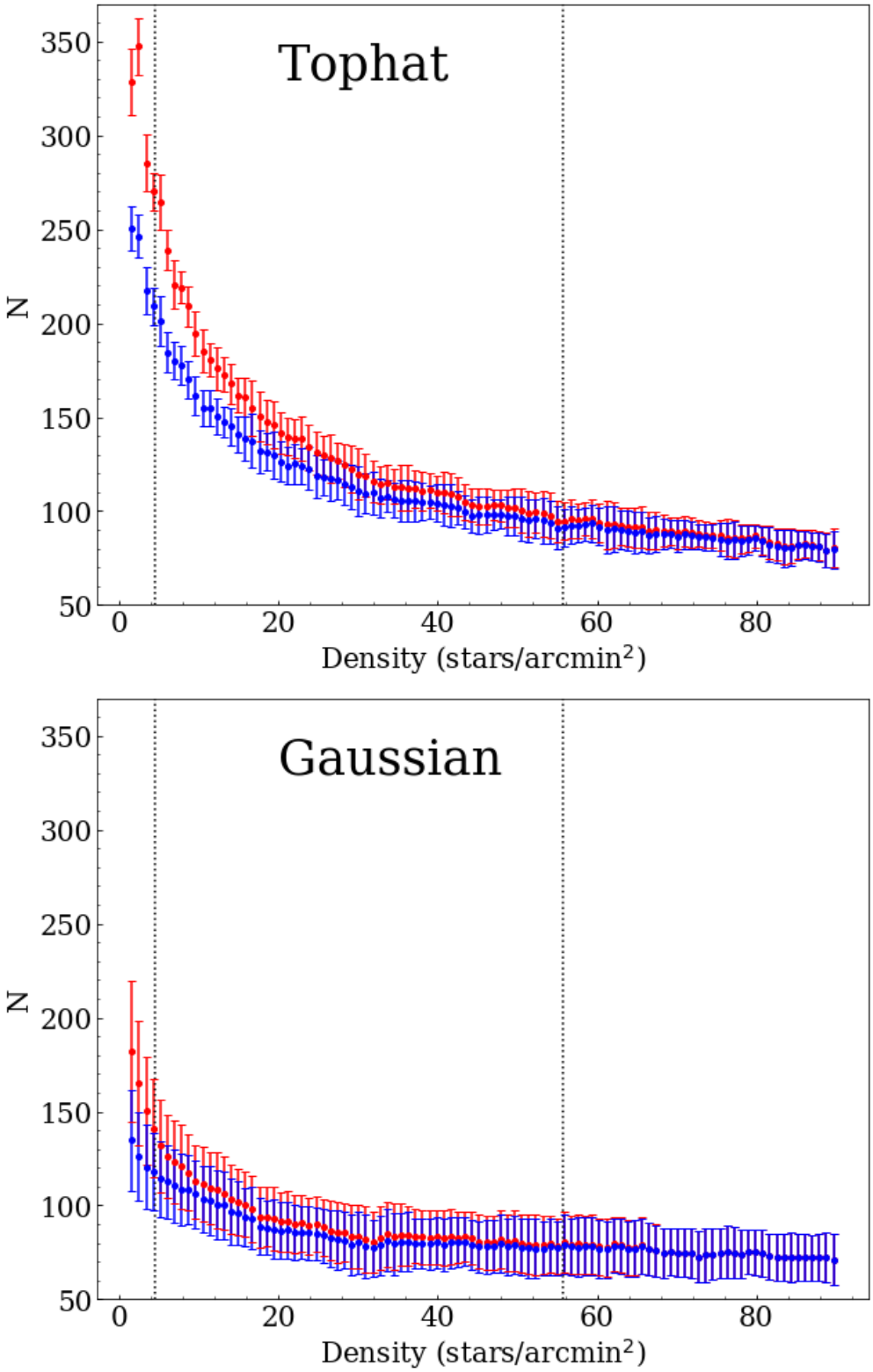

Figure 3.3: Total number of spurious over-densities, averaged in each density bin, as function of the stellar density field. The red and blue dots represent the number of false positives retrieved by using a fixed and a variable threshold, respectively. *Top:* Tophat function. *Bottom:* Gaussian function.

false detections expected in each tile goes from ~ 300 up to ~ 800. However, it is worth to point out that to assert that a star agglomeration is a real SC we need to exploit further physical information, such as the position of its stars on the CMD (as we see in §4.1) Therefore, we are confident that even if the false over-densities represent a significant amount of the total, with the complementary support of the photometric details, we are able to obtain a pure catalog of SCs as well as a very complete one.

3.2 Derivation of the over-density centre

Once the algorithm provided a list of over-densities, the next critical step is the properly estimate its centre. This is crucial as it could have a not negligible effect on the estimation of other SC properties, such as its radius or its radial density profile (RDP). We opted again to use an automated method to infer the coordinates of the over-density centre, that consists in executing another KDE limited in the region defined by the over-density. In particular, we picked up as trial centre the pixel with the highest value from the previous KDE run, and we performed another KDE in an region defined by a circle with radius twice as long as the maximum distance among all pixels belonging to the same over-density. We then looked for the pixel with the highest measured stellar density value, iterating the procedure until convergence is obtained. In particular, we repeated this process until two subsequent centres are separated less than $1.5''$. If the previous condition never happens, we stop the procedure after ten steps, accepting as centre the last pair of coordinates. However, we checked than more than 90% of the over-densities converged before the last step was reached. Figure 3.4 displays two examples of centre determination in the region of a typical over-density (candidate SC STEP-0025 and YMCA-0032).

The automated procedure described above is very effective but sometimes can mislead the determination of the centre. Indeed, in a very few cases a visual inspection of the results revealed a clear offset of the estimated centre with respect to the real one. For example, this could happen if another agglomerate of stars is located nearby the over-density, or because of border effects when the over-density is very close to the tile edge, or of course in the case of binary SCs. In all the circumstances quoted above, we manually corrected the centre values.

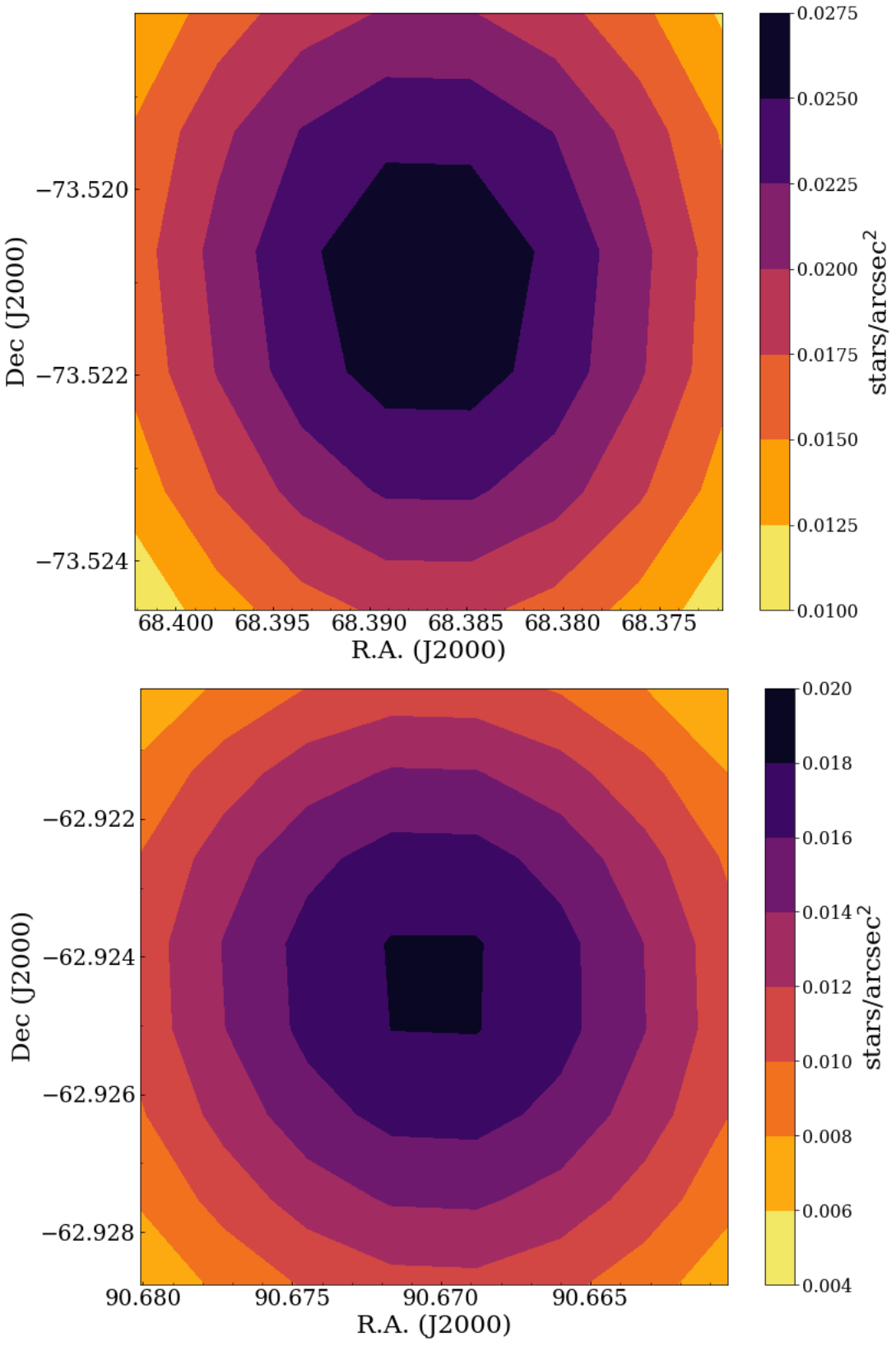

Figure 3.4: Example of the two dimensional KDE in the region of the two newly discovered SCs: STEP-0025 (top) and YMCA-0032 (bottom).

3.3 Estimation of the over-density radius

One of the method to determine the radius of a SC is to measure the distance from its centre at which the RDP, (i.e. number of stars per unit area) settles around the background density level [Bonatto and Bica, 2009, Pavani et al., 2011, Perren et al., 2015]. To obtain a RDP for each over-density, we calculated the number of stars located in concentric shells around the SC centre, separated in bins of $0.05'$, starting from the center up to a distance of $2.0'$. We then divided this value for the area of each shell. We did not apply any magnitude cut as most of our SC candidates represent sparse and poorly populated objects, which do not show a significant crowding level[6]. An estimation of the background density level, i.e. the expected number density of field stars, is obtained by calculating the number of stars within a shell of inner and outer radii of $2'$ and $4'$, respectively, from the candidate SC centre. We then divided this value by the area of the shell[7]. Fig. 3.5 displays the RDP of the candidate SCs STEP-0025 and YMCA-0032 (red dots/solid red line) to better illustrate the procedure. As expected, the RDP steadily decreases from the centre until it reaches and settles around the estimated background density of field stars (dashed line). The errors on the RDP (red vertical lines) and on the background density (solid black lines/grey area) are calculated assuming a Poissonian noise (the square root of the value). To estimate the proper radius, we availed of both the SC RDP and of the background density (with their errors), comparing at each distance bin from the SC centre the quantities $N_{\rm RDP} \pm \sqrt{N_{\rm RDP}}$ and $\mu_{bkg} \pm \sqrt{\mu_{bkg}}$, where $N_{\rm RDP}$ is the value of the RDP at a given distance from the SC centre, and μ_{bkg} is the background density value. Because of the fluctuations of the RDP when it approaches the background density value, it is not straightforward identify which is the distance select tat which the two above quantities are congruent. To overcome this problem we tested several criteria to define a condition of "stabilization", making the radius evaluation more robust against stochastic fluctuations of the RDP. In particular, we considered the RDP and the background level congruent if $N_{\rm RDP} - \sqrt{N_{\rm RDP}} \leq \mu_{bkg}$ is satisfied two consecutive times or if $N_{\rm RDP} - \sqrt{N_{\rm RDP}} \leq \mu_{bkg} + \sqrt{\mu_{bkg}}$ is reached three times on four adjacent concentric shells.

[6]Some exceptions are of course the already known SCs falling in our analyzed tiles. They suffer of a noticeable crowding effect. Nonetheless, this effect is strongly dependent on the distance from the SC centre. It rapidly diminishes at larger distances, and in particular becomes negligible in its outer regions, where the SC density reaches the field value, allowing a proper estimation of its radius anyhow.

[7]In Bica et al. [2008]'s catalogue only ∼3% of the SCs have a radius ≥ 2 arcmin, and they are also easily detectable by eye. We are therefore pretty confident that such SCs are not present in the analysed tiles.

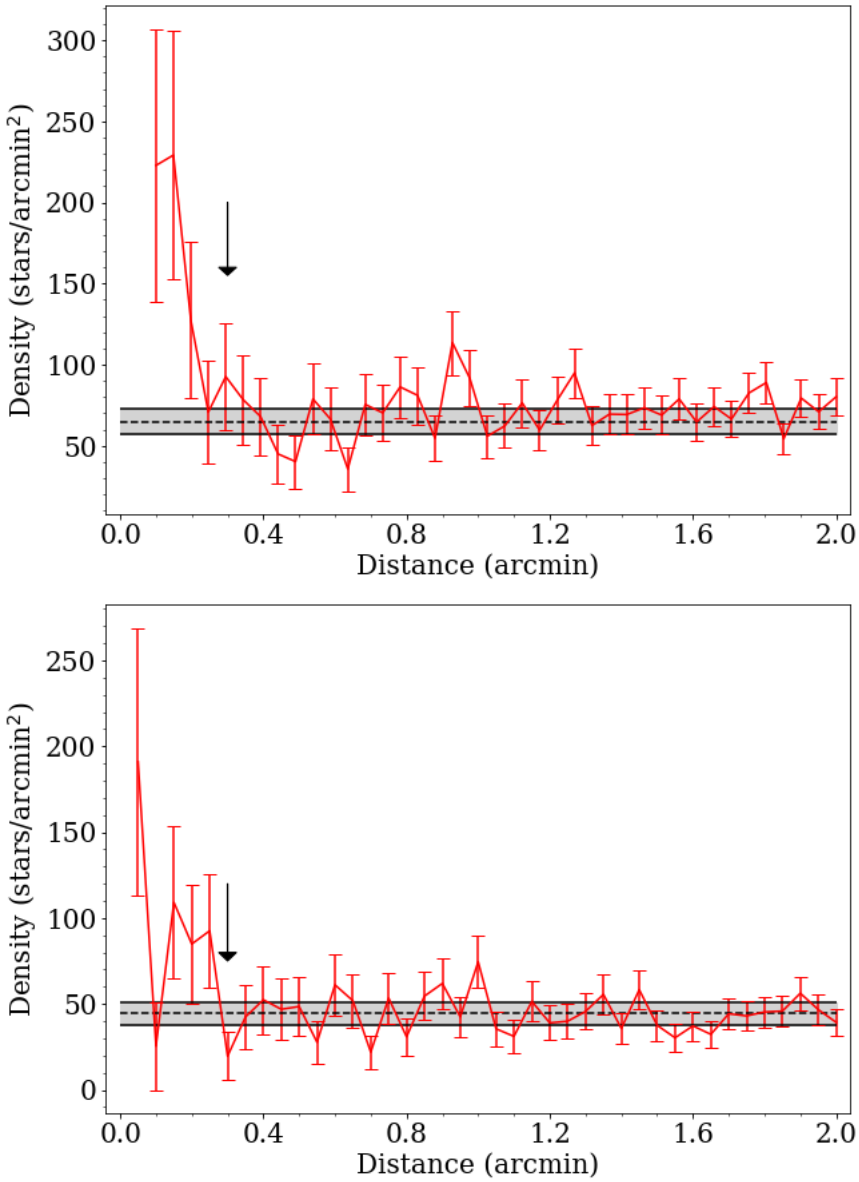

Figure 3.5: Radial density profile of the SCs STEP-0025 (top) and YMCA-0032 (bottom). The dashed line is the estimated background mean, and the two black solid lines represent the 1σ deviation. The red solid line sets the density of stars of the SC as a function of the distance to its centre. All errors are Poissonian. The black arrow indicates the estimated radius.

3.4 Testing the SC detection method with artificial clusters

The adoption of an automated procedure to detect unknown SCs has the advantage that it allows us to objectively determine the errors over the SC parameters and the efficiency of the algorithm. To quantify the completeness of the catalog, or the fraction of objects recovered, it is important to evaluate the accuracy of the cluster searching algorithm in finding targets and also to measure the detection limit of the procedure.

As the cluster finding algorithm measures the significance of each pixel within a tile, which basically is a measure of a signal-to-noise ratio, and a "good" pixel exceeds a given threshold ($S \geq S_{\rm th}$), it turns out that every parameter which plays a role in the measure of S, also affects the detection of a SC. In particular, both the concentration of the SC and the stellar field density could strongly influence the outcome of the SC detection algorithm, as altering the former changes the signal, while the latter represents the noise. For example, a decrease of the compactness of a SC or an increase of the background field star density, or both, makes it harder to reveal a SC, since the final outcome is a reduction of the S/N ratio. Consequently, if the pixel significance (S) drops below our selected threshold ($S_{\rm th}$), the SC will be lost, as could happen for sparse SCs embedded in dense fields. Therefore, a quantitative measure of the efficiency of the algorithm in detecting SCs as a function of different SC compactness (signal) and different background densities (noise) is required to estimate the completeness.

In the next sections I describe in detail the procedure used to perform a quantitative test of the effectiveness of the algorithm.

3.4.1 Generation of artificial star clusters

To measure the completeness of the algorithm, we generated artificial SCs with different values of density, and we overlaid them on the set of Montecarlo simulations described in §3.1.1 that represent artificial background stellar field populations with a different density as well. Following this procedure, we were able to test the sensitivity of the algorithm as a function of the SCs and stellar field densities. We remind that the mock simulations introduced in §3.1.1 are 2000 stellar fields with 100 distinct density values (20 for each field density value) ranging from 1.7 to 89.7 stars/arcmin^2, encompassing the actual stellar density values observed in the analyzed tiles. In addition, in each simulated field we inserted four artificial SCs with different values of density, namely $\rho_{\rm cl} = 30, 50, 70, 90$ stars/arcmin^2, therefore we totally place 8000 artificial SCs.

To generate the simulated SCs, we first randomly selected the coordinates of the centre of each

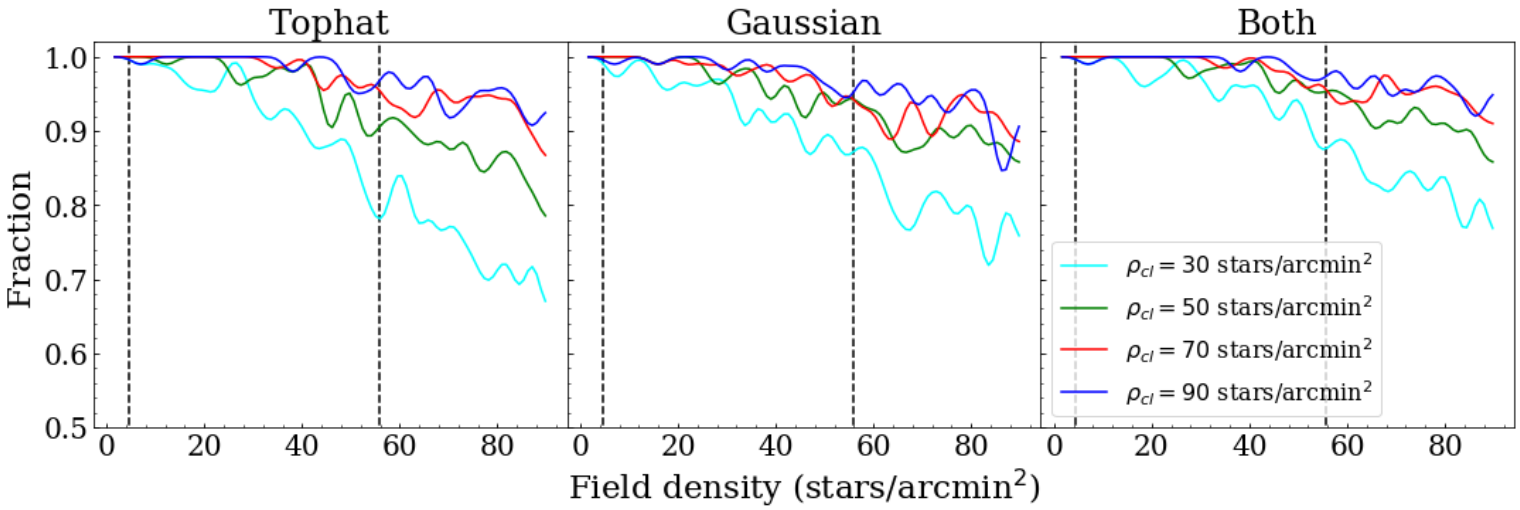

Figure 3.6: Recovery fraction of the four artificial SCs as a function of the stellar field density. Vertical dashed lines represent limits of field density in our tiles, estimated by dividing the number of stars within a tile by its area. Fractional values have been smoothed with a gaussian filter with $\sigma = 2$ stars/arcmin^2 to make less noisy images.

of the four SCs within the artificial fields. To prevent any overlap among two or more different SCs, we imposed that each centre must at least be placed more than $5'$ from all the other ones. We then randomly extracted the number of stars belonging to the SC, using a Gaussian with $\mu = 30$ and $\sigma = 20$. In this way we also sample a diverse degree of compactness along different SC densities, as the SC radius was adjusted to match the $\rho_{\rm cl}$ value. Finally, we also randomly place the single star members of the SC by using a Gaussian distribution having as a mean the position of the SC centre and as standard deviation the half of its radius. In the last step we removed all simulated stars closer than $0.8''$ to each other in order to reduce crowding. At this point, we run the algorithm over the 2000 stellar fields containing the 8000 artificial SCs. In particular, we carried out the procedures described in §3.1, §3.2 and §3.3. The results of this test are presented in the next section.

3.4.2 Efficiency of the algorithm

Figure 3.6 displays the recovery fraction, i.e. the ratio between the number of times the algorithm detected an artificial SCs, for each of the 100 field density steps, and the number of times that SCs was generated, as a function of the field densities. We also plotted with different colours the recovering fraction of each different SC density. In the left and centre panels of the same figure, the recovery fraction is displayed for the two different kernels (tophat and Gaussian functions,

respectively), giving insights on how the algorithm works in the two cases. In the right panel the contribute of both kernel functions are considered. As a reference, the vertical dashed lines indicate the lowest and highest density values measured on the tiles analyzed .

An inspection of the figure reveals that, regardless the kernel functions adopted, at any SC density the fraction of positive detections decreases towards higher field stellar density values, as expected. Similarly, less concentrate SCs have a lower recovery fraction and therefore they are harder to reveal. Looking more closer the outcomes of the different kernel functions, we noticed that the tophat function has a slightly higher recovery fraction at lower stellar field densities and for denser SCs ($\rho_{\rm cl} = 70 - 90$ stars/arcmin^2) while the gaussian kernel performs better on sparse SCs and in more crowded stellar fields. Therefore, despite of an increase of the computational time, running the algorithm by adopting the two different kernel functions provides a great gain in the SC detection. Indeed, as evident in the right panel of Figure 3.6, the recovery fraction when both kernel functions are used, settles above 90% even for the sparser SCs embedded in the highest observed field densities (right panel).

We also noticed that the impact of the stellar field density on the recovery fraction of the densest generated artificial SCs (i.e. $\rho_{\rm cl} = 70 - 90$ stars/arcmin^2, red and blue lines in the figure) is minimal, as the recovery rate is $\sim$100% till $\sim$50 stars/arcmin^2, and remains above $\geq 95\%$ even at the highest field densities present in our images. In artificial SCs with $\rho = 50$ stars/arcmin^2 (green line) the recovery fraction stays close to 100% up to ~ 40 stars/arcmin^2 and $\sim 90\%$ at the highest field observed density limit. Finally, the artificial SCs with $\rho = 30$ stars/arcmin^2 (cyan line), follow a similar trend, but the recovery fraction drops at $\sim$90% at high stellar field density. These encouraging results suggest that the cluster finder algorithm likely provides a catalog of SCs with a very high level of completeness, indeed all of the artificial SCs simulated have more than 90% probability of detection in the observed tiles.

Once we assessed the effectiveness of the algorithm in detecting over-densities in the sky in the observed tiles around the LMC, we also may wonder which is the error it commits in estimating the over-density parameters, such as their centres and radii. To this aim we repeated the same procedure described above, generating and inserting in each simulated stellar field four artificial SCs with four different $\rho_{\rm cl}$ values, but this time keeping constant also their radii and their total number of stars. In this way, we are able to calculate how the stellar background densities affect the measure of the SC estimated parameters. Summarizing, we artificially simulated the same set of four SCs and we randomly placed them on each simulated stellar field.

Figure 3.7 displays the estimated mean radius (top panel) and its standard deviation (centre

panel) for the artificial SCs generated with four different densities, as a function of stellar field density. The measured radius becomes smaller for all artificial SCs when the stellar field density increases. However, this difference is within the uncertainties in the stellar field density interval observed (vertical dashed lines). Indeed, the standard deviation settles around $0.1'$, thus defining our error on the estimated radius. The bottom panel of Fig. 3.7 shows the distance separation between the position of the artificial SC centre and the position of the centre estimated through the procedure described in §3.2, averaged over the 20 simulations per each stellar field density, as a function of the stellar field density. This figure reveals that the measurement of SC centres depends on both the background field density and SC density, improving towards SCs with high $\rho_{\rm cl}$, and less populate stellar fields, even if this effect is barely visible for SCs with $\rho_{\rm cl} = 70 - 90$ stars/arcmin^2.

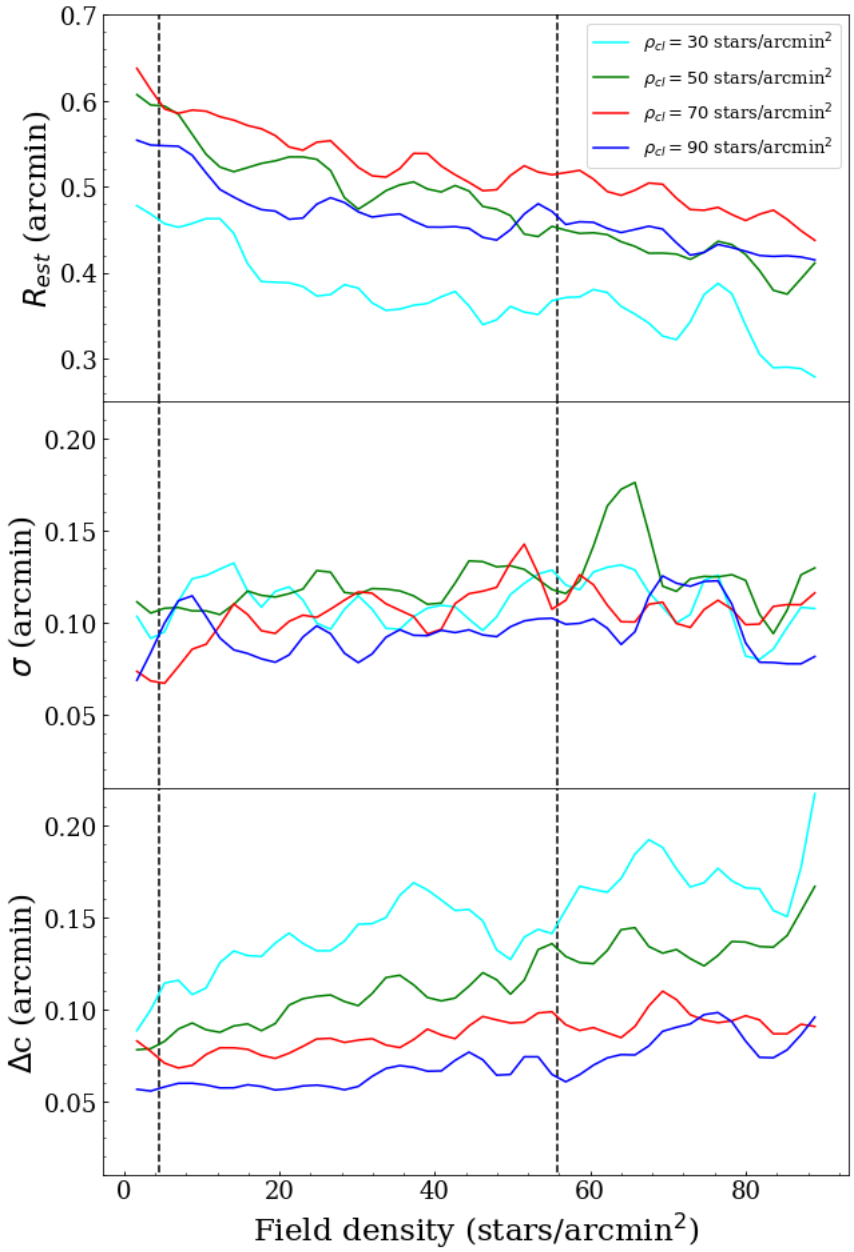

Figure 3.7: *Top:* Radius ($R_{\rm est}$) resulting from the average of 20 simulations per stellar field density vs stellar field density. Different colours identify simulated SCs with different $\rho_{\rm cl}$. *Centre:* Standard deviation of the estimated radii. *Bottom:* As above but for the distance separation between the position of the input simulated SC centre and the position of the centre estimated through the procedure described in §3.2. All values have been smoothed with a Gaussian filter having σ = 2 stars/arcmin^2 to make less noisy images.

Chapter 4

Application of the cluster finder algorithm to the LMC - Part I: overview and first results

This chapter is based on some sections of the paper published on the Volume 499 of the Monthly Notices of the Royal Astronomy Society (MNRAS), Gatto et al., 2020, MNRAS, Vol. 499, p. 4114-4139.

In this chapter we present the results of a pilot work which tested the potentiality of the cluster finder algorithm described in the previous Chapter on a real catalog of sources. In particular, we discuss the results obtained from the analysis of the first 21 YMCA available tiles and 2 STEP tiles, for a total of 23 square degrees investigated in the periphery of the LMC. In addition, we also describe the methods employed to estimate the main parameters of the newly discovered SCs.

As already anticipated in §2.2 and §2.3 both surveys reach about 1.5–2 mag [$\sim$24 mag in the g-band; Ripepi et al., 2014] below the MSTO of the oldest stellar population ($\geq$ 10 Gyrs, which in the LMC is at $\sim$ 22.5 mag in the g-filter). Therefore the noticeable high completeness achieved by the searching algorithm (see §3.4.2 and in particular Fig. 3.6) implemented on a deep photometric catalog of stars should ensure us the discovery of even the oldest and faint LMC SCs, allowing us to probe a still poorly constrained periods of the LMC. For example, the almost total absence of SCs in the so called “age gap", namely an interval of ages ranging from

~ 4 to ~ 10 Gyrs, has not been clearly explained yet (see §1.2.4.2 and §1.2.4.3 for the discussion about the age gap and the issues related to it). It is worth pointing out that the majority of the previous woks devoted to the research of unknown SCs focused mostly into the main body of the LMC, leaving the area beyond $\sim 4°$ from the centre almost unexplored. In fact, the quest for SCs in the outskirts of the LMC is limited to few works. For example, Pieres et al. [2016] used DES data to perform a visually search of SCs to the North of the LMC. They identified 255 clusters, among which 109 are new candidates, out to a distance of about 10 kpc from the LMC centre, in cylindrical coordinates. Sitek et al. [2016] discovered 226 new SC candidates in the outer disk of the LMC by exploiting OGLE IV [Udalski et al., 2015] data, and more recently, Piatti [2017a] found 24 newly SCs in the MCs periphery through the SMASH survey [SMASH; Nidever et al., 2017]. Therefore we opted to analyze regions of the LMC outskirts that have never been observed to this depth, and indeed, just a few of our candidate SCs were previously known (see next sections).

Figure 4.1 displays the position of the YMCA and STEP analyzed tiles (red filled boxes), while their features are provided in Tab. 4.1. These tiles are located at three different regions around the LMC, at North-East, South-East, and West-Southwest, and span a range of projected distances between 4.4 and 10.4 kpc from the LMC centre. The inspection of fields located in opposite directions with respect to the LMC centre allowed us to understand if the whole galaxy, at least in its outskirts, shares the same evolutionary history.

4.1 Cluster identification through the colour-magnitude diagram

Once the algorithm looked for SCs in the 23 probed tiles, it yielded a list of over-densities and their parameters (i.e. centre and radius). This list also contains a fraction of spurious objects, namely group of stars clumping due to projection effects (asterisms), which could also be not negligible at all. Piatti [2017b] in their paper devoted to the study of SCs located along the minor axis of the LMC, concluded that about 30% of the SCs belonging to Bica et al. [2008]'s catalog in their surveyed regions are not real physical stellar systems, thus demonstrating that in the absence of a rigorous procedure for removing false SCs, the degree of contamination can be significantly high. Therefore it is necessary to recognize and in turn discard the contaminants from the list of over-densities, in order to statistically sample the properties of a pure population

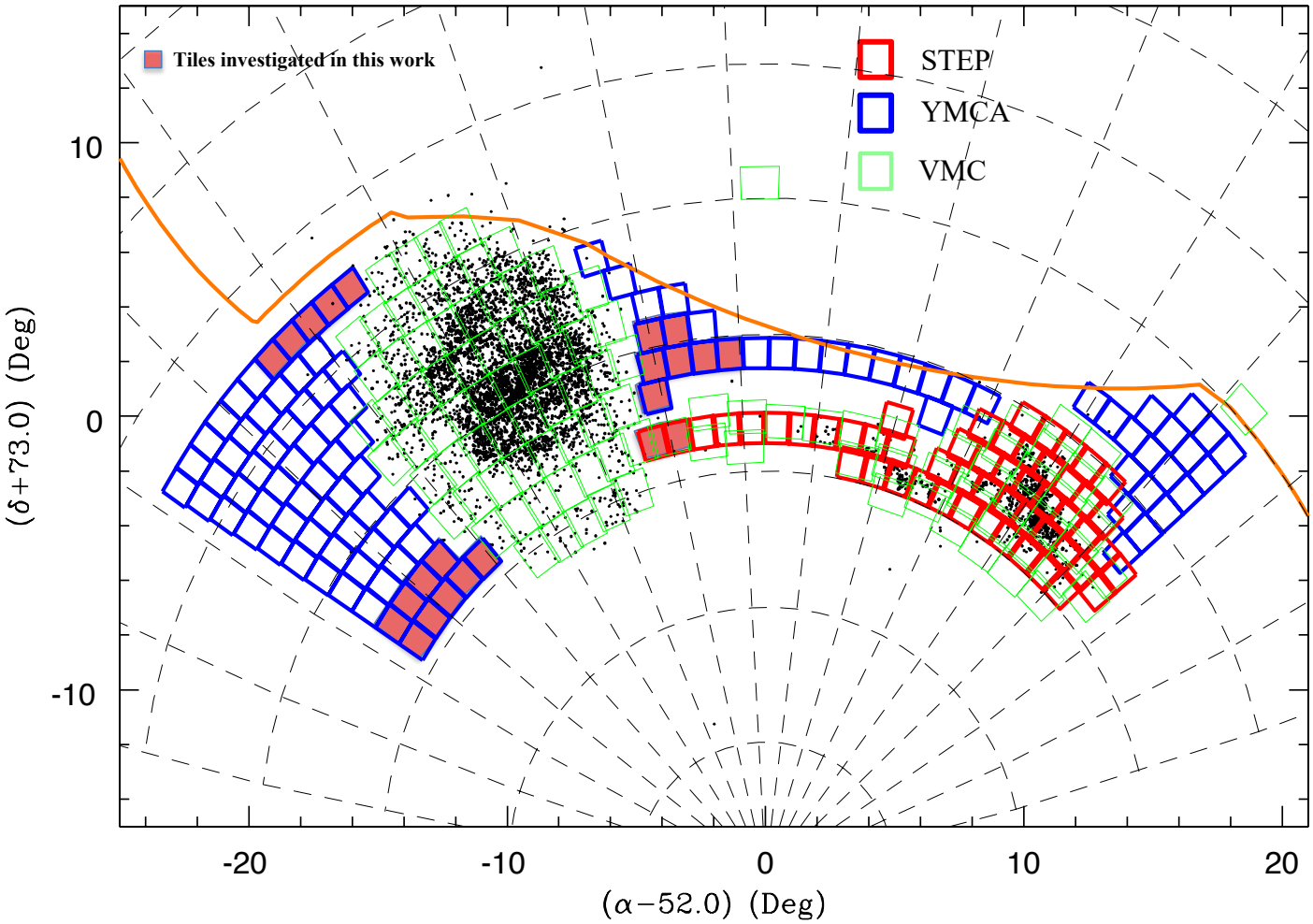

Figure 4.1: Footprint of the STEP and YMCA surveys (see labels) in a zenithal equidistant projection along with all objects present in Bica et al. [2008] (black dots). For comparison, we overdraw the VMC [Cioni et al., 2011] regions in green, whereas the DES surveyed area lays northwards of the orange line. The 23 tiles analysed in this work are filled in red.

Table 4.1: Log of Observations. The different columns show: name of the tile, its centre, date of observation, average FWHM over the images (S_g and S_i)

Tile	R.A. hms	Dec dms	Date	S_g $''$	S_i $''$
1_27	06:23:43.30	-73:59:14.1	2016-10-11	1.24	1.01
1_28	06:38:11.88	-73:59:14.1	2016-10-12	1.34	1.00
1_29	06:52:40.49	-73:59:14.1	2016-10-12	1.51	0.96
1_30	07:07:09.10	-73:59:14.1	2016-10-23	1.30	0.87
1_31	07:21:37.68	-73:59:14.1	2016-11-19	1.34	0.82
2_30	06:41:10.37	-72:53:04.1	2017-10-12	1.30	1.06
2_31	06:54:46.16	-72:53:04.1	2017-10-13	1.17	1.17
2_32	07:08:21.96	-72:53:04.1	2017-10-12	1.30	1.01
2_33	07:21:57.77	-72:53:04.1	2016-12-18	1.05	0.73
3_21	04:22:54.42	-71:46:54.4	2017-10-12	1.09	1.09
4_19	03:50:36.64	-70:40:44.2	2017-10-12	1.19	0.98
4_20	03:50:36.64	-70:40:44.2	2017-10-13	1.13	0.99
4_21	04:14:52.86	-70:40:44.2	2017-12-23	1.08	0.97
4_22	04:14:52.86	-70:40:44.2	2017-12-25	1.12	0.99
5_22	04:13:31.25	-69:34:33.9	2017-12-26	1.13	1.08
5_23	04:13:31.25	-69:34:33.9	2018-01-11	1.25	1.09
11_41	06:00:26.98	-62:57:31.7	2017-12-09	0.98	0.96
11_42	06:13:47.98	-62:57:31.7	2018-01-08	1.15	0.77
11_43	06:13:47.98	-62:57:31.7	2018-01-14	1.05	0.72
11_44	06:31:35.99	-62:57:31.7	2018-01-19	0.93	0.85
11_45	06:31:35.99	-62:57:31.7	2018-01-19	0.97	0.82

of LMC SCs.

Ideally, accurate kinematics of the stars could be one of the best solution to disentangle a group of isolated stars spatially close because of some projection effect from a stellar system whose moving as its own. Despite of several studies obtained the PMs of MC stars and satellites [e.g., Kallivayalil et al., 2018, Zivick et al., 2019], accurate PMs and radial velocities of the MC stars within the 23 square degrees explored in this work, down to the faint magnitudes of the MSTO of the oldest stellar population, are not available yet[1]. Therefore, the only additional information available beside the sky positions are the magnitudes and colors of the stars belonging to the candidate SC.

We can exploit the fact that, contrary to asterisms, stars belonging to real SCs follow precise sequences in the CMD. Indeed, stellar evolution theories predict that the members of a coeval system, like a SC, evolve along the evolutionary phases in the CMD defined by a SSP. Therefore, once corrected for the distance modulus (DM) and the reddening, they are expected to mirror an isochrone of a given age and metallicity. Thus the analysis of the over-density CMDs allows us not only to identify and rule out asterisms, but also to directly estimate the main parameters of the stellar population of the SC, namely its reddening, age and metallicity. However, disentangling false from true SCs on the basis of the CMD is not a straightforward task. For instance, due to the three dimensional geometry of the investigated galaxy, also field stars can be projected in the region occupied by genuine cluster stars. Therefore, a cleaning procedure of the SC CMD is necessary to assess the SC nature of the over-density and to properly estimate the main SC parameters.

4.1.1 Cleaning procedure of the CMD

We availed of the procedure developed by [Piatti and Bica, 2012] and commonly used in the literature [e.g., Ivanov et al., 2017, Piatti et al., 2014, 2015b, 2016] to clean the CMD from not SC member stars. In the following, we briefly report only the main steps of this method and the interested reader can refer to the original paper for a full description. In a nutshell, the procedure consists in adopting four distinct CMDs as representative of the stellar field to clean the SC candidate CMD. These four CMDs are located along four different directions (North, South, East and West) with respect to the SC centre. The distance between the comparison fields and the SC is chosen to be short enough to sample the local stellar properties, i.e. stellar

[1]The Gaia space satellite provides PMs of stars down to $g \sim 21$ mag, well above the expected MSTO of the oldest SCs.

density, luminosity and colour distribution but it is also large enough to avoid the inclusion of SC members. Following Piatti et al. [2014], to avail of a larger statistics, the cluster region to be cleaned spans an area described by a radius $R_{\rm ca}$=3$R_{\rm cl}$, where $R_{\rm cl}$ is the estimated SC radius (see §3.3 for the determination of the radius). Moreover, each of the four fields used as comparison also describes a circle with a radius $R_{\rm field}$=$R_{\rm ca}$ and the coordinates of their centres are positioned at a distance calculated as follows:

$$d = 2R_{\rm ca} + R_{\rm cl} \tag{4.1}$$

To sample the position of the stars in the CMD of each of the four stellar fields, the procedure avails of cells with different sizes: smaller boxes being generated in denser CMD areas, and larger ones in less dense CMD regions. In this way, the method is able to model the local CMD density, taking into account that distinct evolutionary stellar phases have a different degree of crowding. For example, being the lifetime of any stars in the main sequence phase at least ten times longer than in any other evolutionary phase, the the main sequence (MS) is much more populated than other CMD regions, like the sub-giant branch (SGB) or the RGB. Therefore, we started to generate a a box centred on each of the star belonging to the field, with sides (mag, col) = (2.0, 0.5). Then the shape of the box is adjusted according to the local CMD density, by reducing it until it reaches the closest star in magnitude and colour, separately. At the end of the first step of the procedure, each field star is surrounded by a box, whose shape depends on the local crowding in the CMD [see Piatti and Bica, 2012, their Figure 12].

The representative field CMD is then overlapped to the candidate SC CMD, and for each of the boxes we subtract the SC star closest to its centre, considering just the stars within the box. This operation is repeated four times, one for each field. Finally, we are able to assign a membership probability P for all stars within the candidate SC, depending on the number of times a star has been subtracted in the procedure. A membership probability to belong to the cluster $P \geq 75\%$ is assigned to stars that have been eliminated once or never, a $P = 50\%$ (same probability to belong to the cluster or to the field stellar population) for stars with two subtractions, while stars with $P \leq 25\%$ (three or four subtractions) are likely field stars. We considered as not actual SC members all stars with $P < 50\%$, allowing us to rule out all over-densities whose residual stars do not follow a SC isochrone on the CMD. Fig. 4.2 shows an example of such a procedure for the candidate cluster STEP-0018. In the top panels it is evident the noticeable difference between the CMD of the candidate SC (*left side*) with that one of a nearby stellar field with an area as large as the SC one (*right side*). The bottom-left panel of

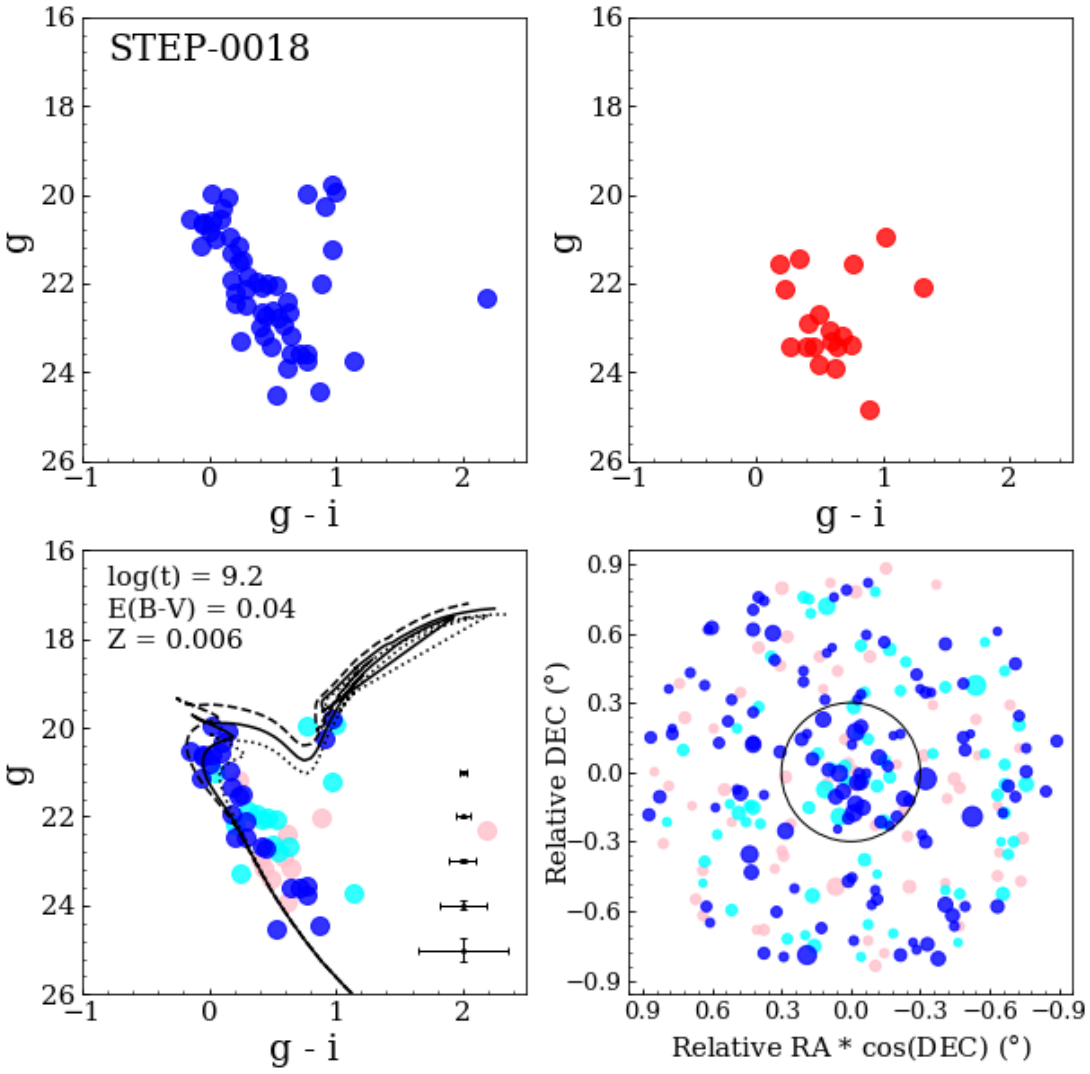

Figure 4.2: Example of the cleaning procedure for the SC STEP-0018. *Top:* SC CMD (*left side*) and CMD of a field (*right side*) taken at $7\times R_{\rm cl}$ and with an area equal to the cluster one. *Bottom left:* Cluster CMD after the cleaning procedure with stars colored by their membership probability. Blue, cyan and pink points are stars with $P \geq 75\%$, $P \geq 50\%$, $P \leq 25\%$, respectively. The black solid line marks the best fitting isochrone, obtained with the values listed in the top left corner of the figure, while dashed and dotted lines show isochrones with ages ± 0.1 in $\log(t)$ with respect to the best fitting one. The photometric errors are also displayed. *Bottom right:* Relative positions for all stars within $3\times R_{\rm cl}$, with the origin at the SC center, and the size proportional to their luminosity. The black circle indicates the cluster radius.

the figure illustrates how the SC CMD appears after the cleaning procedure, with stars color-coded according their membership probability (blue, cyan and pink for $P \geq 75\%$, $P = 50\%$ and $P \leq 25\%$, respectively) superimposed by the best fitting isochrone (solid line).

It is worth pointing out that following the original procedure outlined byPiatti and Bica [2012], an area as large as nine times that of the SC is chosen to augment the statistics and thus to improve the performance of the cleaning process. This procedure does not take into account the spatial distance from a star to the SC centre, but only its position on the CMD. This is useful in the case of poorly populated objects as the candidate SCs observed in the periphery of the LMC. Bearing in mind all these considerations, the presence of some residuals (stars with P $\geq$ 75%) beyond the cluster radius it is expected, actually.

We produced figures like Fig. 4.2 for all the over-densities detected with the searching algorithm (more than 3000 candidates in the 23 tiles analyzed in this work). A visual inspection of the residuals of the CMDs allowed us to recognize the asterisms, that resulted to be the large majority of the candidate over-densities. Indeed, at the end of the cleaning procedure, after a careful analysis we built a list composed by 85 candidate SCs. Identification, centre coordinates and radii of these candidate SCs are listed in the first four columns of Tab. 4.4. As the procedure outlined above still contains a certain degree of subjectivity, we also provide a statistical parameter to quantitatively assess the goodness of each SC. Thus, we define

$$G = \frac{N_{\rm cl} - N_{\rm bkg}}{\sqrt{N_{\rm bkg}}} \tag{4.2}$$

where $N_{\rm cl}$ is the number of stars within the SC radius and $N_{\rm bkg}$ is the average number of field stars within an area equal to that defined by the radius of the SC. We obtained $N_{\rm bkg}$ by counting the number of stars contained in shell of inner and outer radius $2'$ and $4'$ from the SC centre, and then by normalizing this value to the SC area. The G value ranges from 1.32 to 48.75 and it has a median of 3.48. It is listed in the tenth column of Table 4.4, along with the total number of stars within the SC radius (column 11).

4.2 Estimation of the SC main parameters

4.2.1 Isochrone fitting

The SC age can be estimated through the identification of the isochrone of a SSP that best matches the residual CMD SC stars. The isochrone fit can be either carried out visually or than by availed of an automated method. Both procedures have been used in the literature, and each

of them has its pros and cons. Automated methods used to estimate age, reddening, distance modulus and metallicity of the SCs are definitely more efficient on a large SC sample and they also enable to objectively quantify the uncertainties on the SC parameters [e.g., Nayak et al., 2016, Nayak et al., 2018]. At the opposite the visual fitting might suffer from systematic errors because it is more subjective. Furthermore it is less efficient since it requires to carefully analyze each SC singularly and often it is also necessary to "a priori" fix some physical quantities, such as the DM or the metallicity, in order to reduce the parameter space [Glatt et al., 2010, Piatti et al., 2014, 2015a,b, 2016]. Nonetheless, this procedure has to be preferred in case of poorly populated and sparse SCs, where significant statistical fluctuations could be present, and the decision of the inclusion or exclusion of a few stars can make a remarkable difference [Lançon and Mouhcine, 2000]. For example, some residual field stars with high membership probability could still be present in the CMD, even after the cleaning procedure described in §4.1.1. Therefore, in these cases a visual fitting avoids that residuals may considerably affect the estimation of the SCs parameters.

On these bases, we opted to carry out a visual isochrone matching, adopting the PARSEC models [Bressan et al., 2012]. This procedure allowed us to estimate the SCs ages by identifying the magnitude of the MSTO as well as to gauge their reddening and metal content through the position and inclination of the RGB stars, and red clump (RC) stars. However, it is tricky to disentangle the effect of reddening and metal content when comparing isochrones with observed RGB and RC stars because of their degeneracy. This occurrence makes the uncertainties associated to these two parameters to increase. We estimated the errors by varying the parameters until the isochrones no longer fit the RGB/RC stars and taking into account the above quoted degeneration. The resulting errors are ΔE(B - V) = 0.04 mag and ΔZ = 0.002. We corrected the isochrones for the distance and the extinction through the relations: $g = g_{\rm iso} + (m - M)_0 + R_{\rm g} \times E(B - V)$ and $E(g - i) = (R_{\rm g} - R_{\rm i}) \times E(B - V)$ with $R_{\rm g} = 3.303$ and $R_{\rm i} = 1.698$ [Schlafly and Finkbeiner, 2011].

We chose to fix the distance modulus to $(m - M)_{\rm o} = 18.49 \pm 0.09$ mag ($49.90^{+2.10}_{-2.04}$ kpc) [de Grijs et al., 2014] to reduce the number of possible combinations of isochrones to fit the CMD of each SC. This value is very close to the very accurate recent measurement of the LMC distance obtained by Pietrzyński et al. [2019] from a sample of eclipsing binaries. We took into account also the three-dimensional structure of the LMC, which has a non-negligible depth along the line of sight, namely 3.14 ± 1.16 kpc measured by Subramanian and Subramaniam [2009], and about ~ 7 kpc, due to a recent measure made by Choi et al. [2018b]. Therefore we considered

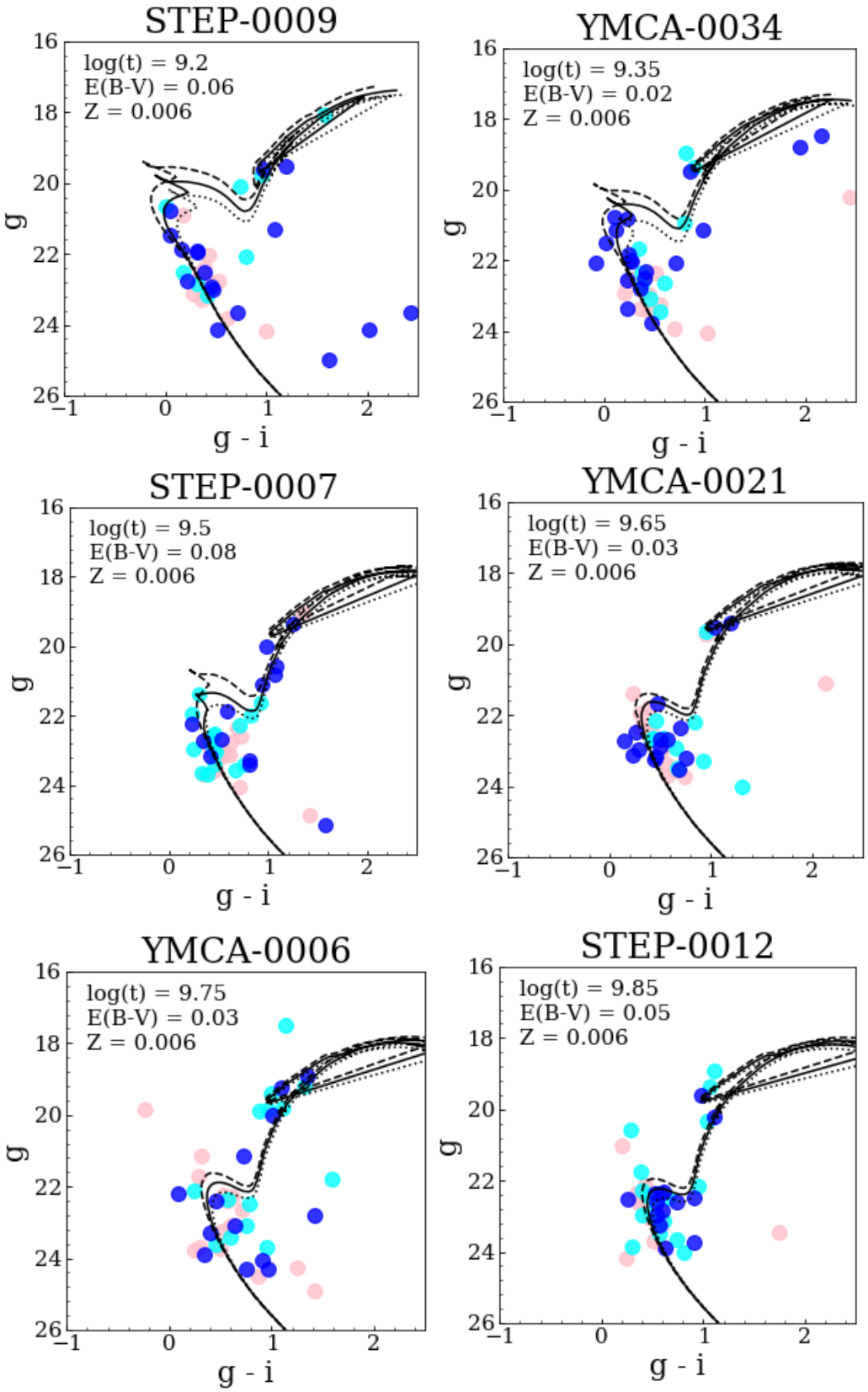

Figure 4.3: Isochrone fitting for six SCs. Solid lines represent the best fit isochrones obtained fixing the distance modulus (m - M = 18.49 mag), while dashed and dotted lines are isochrones with $\log(t) = \pm 0.1$ dex with respect to the best one. Stars are color-coded according by their membership probability, following the procedure described in §4.1.1.

a maximum error budget on the DM to be $\Delta(m-M) \sim 0.2$ mag. This uncertainty could seem significant, but our errors on the age, estimated by observing the overall dispersion obtained using the visual fitting procedure on the CMD, are typically $\sigma \log(t) \sim 0.1$ dex, that is equivalent to about 0.4 mag in the DM, at the LMC distance. Therefore we are confident that assuming a constant DM in the isochrone fitting procedure in all the tiles analyzed is acceptable. It is worth underlying that σlog(t) ~ 0.1 dex is an upper limit on the age estimate errors, since younger SCs could have even a smaller error (i.e σlog(t) = 0.05 dex). To adopt a more conservative approach, we decided to set all errors to this upper limit.

Finally, we performed the isochrone matching by varying the age, reddening, and metallicity to seek the qualitatively best match between isochrones and SC stars. We took into account only stars with membership probability $P \geq 50\%$. In particular, we focused on some more populated evolutionary phases to aid the visual identification of the best isochrone, such the main sequence, the RGB and RC stars. The SC parameters estimated in this way are listed in Table 4.4 (from the fifth to the seventh column), while Fig. 4.3 shows an example of the fitting procedure for six (typical) SCs detected in this work. The CMDs for all the 85 candidate clusters are shown in Figure A.1.

4.2.2 Absolute magnitudes

We obtained the absolute magnitudes of each candidate SC in the g-band by using the open source *photutils* `python` package [Bradley et al., 2019]. This software includes, amongst the others, tools to perform aperture photometry on astronomical images and, we applied it on the stacked image built as described in §2.2 and §2.3.

As a first step, we measured, for each SC, the total flux in a circular aperture defined by SC centre and by its estimated radius. Obviously, this flux includes a background that must be removed. We, therefore, also obtained the flux in eight circular apertures surrounding the SC, having a radius equal to 50 pixels (i.e. $10''$), and their centres placed at $2 \times R_{\rm cl}$ from the SC centre. Within each aperture we derived the median flux per pixel. We considered the median of the eight estimates as a measure of the mean background to be subtracted from the SC aperture photometry. Then, we obtained the instrumental magnitude in g-band of a given SC as $m_{\rm instr} = -2.5 * \log_{10}(flux)$. These magnitudes were then calibrated into the APASS system, by evaluating, for each tile, the zero point between the instrumental and the APASS magnitudes. To reach this scope, we calculated the instrumental magnitudes of all stars in each tile using the aperture photometry tool available in *photutils*. We then calculated the difference between

the star instrumental magnitudes and their calibrated PSF photometry. The zero point is then simply the mean of these differences, obtained adopting only sources in the limited magnitude interval $15 < g < 20$ mag to exclude bright saturated stars and faint, low S/N objects. We repeated this procedure for every tile in which a SC has been detected, obtaining a calibrated apparent magnitude in the g-band for each of the 85 SCs. Finally, the absolute magnitude in g-band was derived as $M_g = m_g + DM_{\rm LMC} - A_g$, where m_g is the apparent magnitude, A_g is the extinction in the g-band, and $DM_{\rm LMC}$ is the LMC DM adopted. The estimated g-band apparent and absolute magnitudes are listed in the eighth and ninth column of Table 4.4.

4.2.3 Radial density profiles

The RDP of the SCs is a useful tool to better assess the physical reality of our sample of newly detected objects. Indeed, SCs follow analytical functions, which usually can be approximated with a flat core close to the centre regions, and a power-law at higher distances from the SC centre. The two most employed analytical functions for the SCs in the MCs are the King's family of curves [King, 1962] and the Elson, Fall & Freeman profile [EFF; Elson et al., 1987]. The EFF profile is identical to the King's one when the parameter indicating the slope of the curve γ is 2 and the tidal radius goes to infinite. These analytical formulations are also useful to get insights into the SC dynamical evolution (see §7 where we use them to derive structural parameters of 170 SMC SCs). However, in this case we only avail of them as tools to substantiate the physical reality of the newly discovered SCs. Elson et al. [1987] concluded that the majority of the LMC SCs do not seem to have a tidally truncated radius, therefore the following analysis is carried out by considering a EFF profile, described by:

$$n(r) = n_0 \times \{1 + (\frac{r}{\alpha})^2\}^{-\gamma/2} + \phi \tag{4.3}$$

where $n(r)$ is the number of stars per squared arcminutes as a function of the distance from the cluster centre, n_0 is the central surface density, α and γ are the core and the slope parameter, respectively, and ϕ is the background value, considered here as a free parameter of the fit.

We considered only stars with $P \geq 75\%$ in the whole cleaned area (i.e. a circle of radius $R_{ca} = 3R_{cl}$, see §4.1.1) to build the RDPs. This choice allows us to: (i) assess the SC's existence, since the SC reliability increases if a central over-density persists after the cleaning procedure and the RDP is well reproduced by the EFF profile; and (ii) check the residuals of Piatti and Bica [2012]'s procedure (i.e. stars with P $\geq$ 75% beyond the SC radius). Indeed, if significant residuals are present after the cleaning procedure we should obtain a nearly flat RDP.

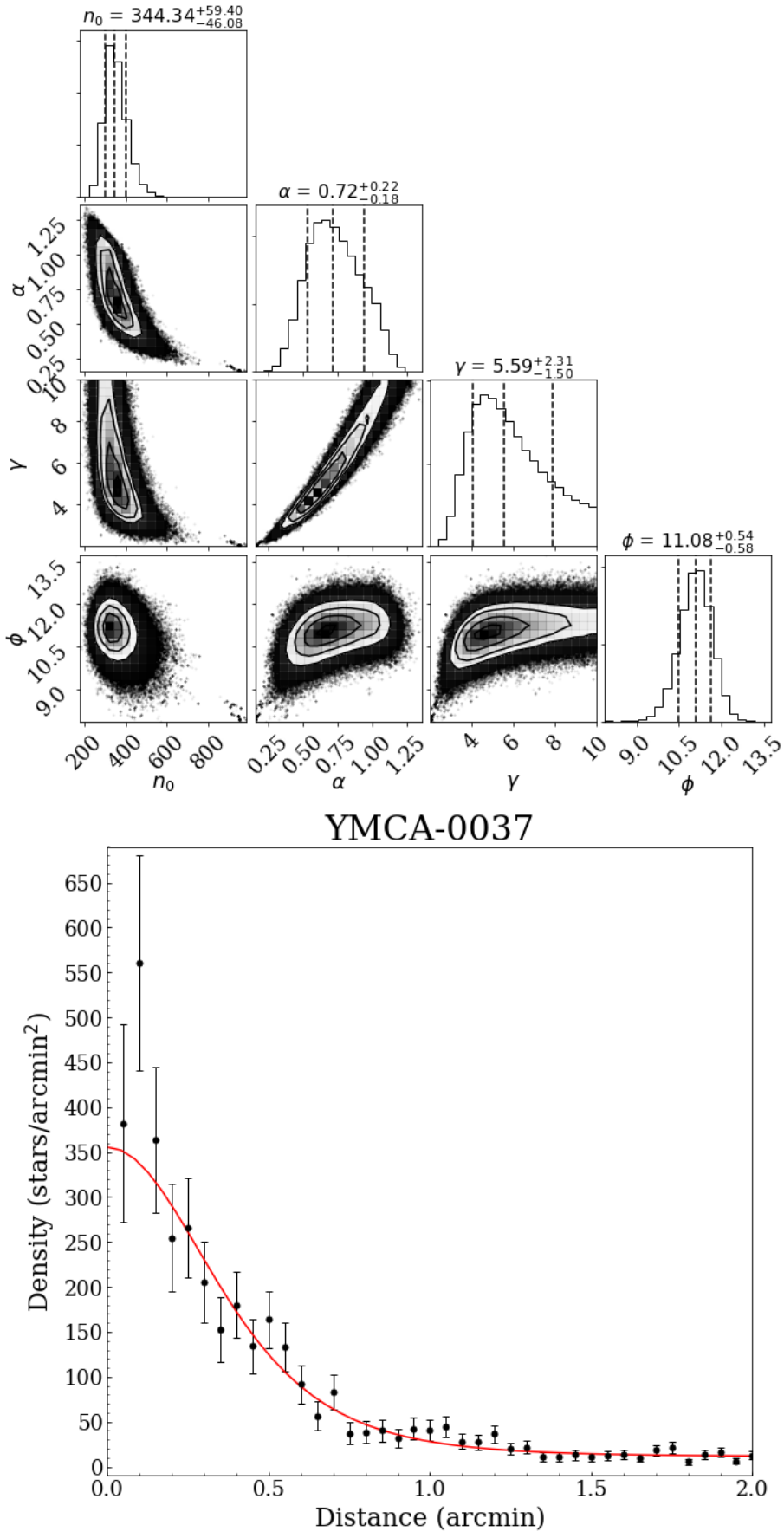

Figure 4.4: *Top:* Contour plots and marginalized histogram of all the four parameters for the SC YMCA-0037. The estimated values and their errors are also indicated. *Bottom:* RDP with overlapped an EFF profile for the same SC.

SCs whose RDPs derived with only $P \geq 75\%$ membership stars fit with a EFF profile ensure a high reliability of their physical real nature. This is the most conservative approach to exploit the SC RDP in order to determine its authenticity. However, the majority of the SC candidates is very sparse and composed by a handful of stars, making it harder to build reliable RDPs availing of only the most likely SC members. Moreover, as already mentioned, Piatti and Bica [2012]'s cleaning procedure does not take into account the cluster-centric distance of the stars, which might affect the shape of the RDP (see the detailed discussion below). On these bases, we opted to make use also of the stars with $P \geq 50\%$ to derive RDPs for all SCs where a reliable fit was not achieved with the former procedure. We already anticipated before that the purpose of this analysis is not to probe the internal structure of the SCs, but to statistically assess the goodness of our sample, and thus to provide further statistical parameters complementary to the G parameter defined by the eq. 4.2. In particular, we supply as a further statistic parameter representative of the reliability of each SC he ratio between the estimated central surface density (background subtracted) and the estimated background (i.e. the ratio between the estimated n_0 and ϕ parameters of the EFF profile).

To derive the four free parameters of the EFF profile we adopted a Markov Chain Monte Carlo technique (MCMC) available with the `emcee python` package[2]. The MCMC approach is a widely used technique to sample probability distributions in high dimensions of the parameter space. It is based on the idea that by using random sampling in a probabilistic space, after a number of steps (i.e. the length of the Markov chain) the chain will be made of points that follow the target distribution. Figure 4.4 shows a contour plot of the parameters along with their marginalized histograms (top panel), and the RDP with overlapped the best fit obtained with the MCMC method (red line in the bottom panel) for the SC YMCA-0037. Table 4.2 lists the parameters estimated with the MCMC approach and their uncertainties for 67 SCs (79% of the sample) with a RDP built adopting only stars with $P \geq 75\%$. More than half (precisely $\sim 65\%$) of the SCs have a ratio between the estimated central and the background density higher than 5, and all of them, except one, above 3. The mean of this ratio is 11.50 while its median is 10.44. The RDPs of these 67 SCs with the fit of the best EFF profile are in Fig. A.2. Table 4.3 lists the EFF parameters and the n_0 and ϕ ratio for those SCs whose RDP were derived by using all stars with $P \geq 50\%$, meaning that for them a reliable fit by employing the most likely members has not been obtained. In this case the ratio between the estimated central and background density has a mean of 3.95 and a median of 4.04. Figure A.3 shows the corresponding RDPs.

[2]https://emcee.readthedocs.io/en/stable/

Table 4.2: Elson, Fall & Freeman's fitting parameters obtained by using all stars with P≥75%. In the first and fourth column are listed the ID of the SCs, while the core parameter is in the second and fifth column and the slope parameter in the third and seventh column. The fourth and last column indicates the ratio between the estimated central density and the estimated background.

ID	α (arcmin)	γ	n_0/ϕ	ID	α (arcmin)	γ	n_0/ϕ
step-0001	$0.09^{+0.04}_{-0.04}$	$3.64^{+0.92}_{-1.01}$	14.41	step-0002	$0.06^{+0.02}_{-0.03}$	$3.49^{+1.01}_{-0.99}$	9.83
step-0004	$0.10^{+0.03}_{-0.04}$	$3.60^{+0.94}_{-0.99}$	18.30	step-0006	$0.08^{+0.04}_{-0.03}$	$3.39^{+1.08}_{-0.96}$	12.96
step-0008	$0.13^{+0.06}_{-0.02}$	$3.28^{+0.51}_{-0.73}$	4.39	step-0009	$0.25^{+0.06}_{-0.06}$	$3.01^{+0.66}_{-0.67}$	4.49
step-0010	$0.25^{+0.07}_{-0.07}$	$2.90^{+0.71}_{-0.63}$	3.26	step-0011	$0.15^{+0.07}_{-0.04}$	$3.28^{+0.51}_{-0.72}$	4.03
step-0012	$0.15^{+0.01}_{-0.00}$	$3.85^{+0.11}_{-0.23}$	7.04	step-0013	$0.11^{+0.01}_{-0.01}$	$3.70^{+0.22}_{-0.39}$	7.59
step-0014	$0.44^{+0.15}_{-0.14}$	$14.51^{+3.87}_{-5.28}$	3.70	step-0015	$0.09^{+0.04}_{-0.04}$	$3.36^{+1.07}_{-0.93}$	11.70
step-0016	$0.06^{+0.03}_{-0.03}$	$3.63^{+0.93}_{-1.03}$	4.08	step-0017	$0.24^{+0.04}_{-0.03}$	$8.39^{+1.15}_{-1.76}$	6.87
step-0018	$0.11^{+0.03}_{-0.03}$	$3.50^{+0.95}_{-0.91}$	6.25	step-0023	$0.10^{+0.04}_{-0.04}$	$2.88^{+1.26}_{-0.67}$	11.16
step-0024	$0.10^{+0.04}_{-0.03}$	$3.39^{+1.03}_{-0.90}$	10.82	step-0025	$0.10^{+0.03}_{-0.04}$	$3.46^{+1.01}_{-0.93}$	8.04
step-0026	$0.15^{+0.07}_{-0.06}$	$3.80^{+0.84}_{-1.05}$	4.31	step-0030	$0.13^{+0.03}_{-0.02}$	$4.26^{+0.53}_{-0.81}$	5.70
step-0031	$0.08^{+0.04}_{-0.03}$	$3.41^{+1.07}_{-1.00}$	10.69	step-0032	$0.12^{+0.02}_{-0.04}$	$2.81^{+1.27}_{-0.62}$	6.07
step-0033	$0.12^{+0.02}_{-0.03}$	$2.89^{+1.02}_{-0.62}$	5.81	step-0034	$0.27^{+0.05}_{-0.07}$	$3.44^{+0.77}_{-0.79}$	12.40
step-0035	$0.21^{+0.02}_{-0.01}$	$4.61^{+0.29}_{-0.55}$	4.06	step-0036	$0.08^{+0.04}_{-0.02}$	$3.81^{+0.82}_{-1.01}$	6.15
step-0037	$0.19^{+0.04}_{-0.03}$	$3.77^{+0.85}_{-1.03}$	3.12	ymca-0001	$0.16^{+0.07}_{-0.04}$	$3.92^{+0.76}_{-1.01}$	7.13
ymca-0002	$0.22^{+0.03}_{-0.02}$	$4.48^{+0.37}_{-0.65}$	16.36	ymca-0003	$0.08^{+0.04}_{-0.04}$	$3.62^{+0.94}_{-1.04}$	17.39
ymca-0004	$0.20^{+0.06}_{-0.06}$	$3.64^{+0.92}_{-1.00}$	13.92	ymca-0005	$0.35^{+0.07}_{-0.04}$	$12.26^{+1.96}_{-2.99}$	6.50
ymca-0007	$0.37^{+0.07}_{-0.05}$	$11.83^{+2.21}_{-3.04}$	5.48	ymca-0008	$0.08^{+0.04}_{-0.04}$	$3.32^{+1.11}_{-0.93}$	26.83
ymca-0009	$0.10^{+0.03}_{-0.04}$	$3.53^{+0.97}_{-0.98}$	16.19	ymca-0010	$0.10^{+0.03}_{-0.04}$	$3.35^{+1.03}_{-0.89}$	18.34
ymca-0012	$0.11^{+0.03}_{-0.04}$	$3.28^{+1.07}_{-0.86}$	24.48	ymca-0013	$0.09^{+0.03}_{-0.02}$	$3.86^{+0.79}_{-1.03}$	8.91
ymca-0014	$0.40^{+0.07}_{-0.07}$	$9.74^{+3.37}_{-2.97}$	9.37	ymca-0015	$0.18^{+0.04}_{-0.02}$	$3.95^{+0.73}_{-1.01}$	7.06
ymca-0018	$0.11^{+0.03}_{-0.03}$	$3.27^{+1.07}_{-0.86}$	13.58	ymca-0019	$0.10^{+0.03}_{-0.04}$	$3.10^{+1.13}_{-0.79}$	16.04
ymca-0020	$0.09^{+0.04}_{-0.04}$	$3.49^{+1.01}_{-0.98}$	13.15	ymca-0021	$0.08^{+0.04}_{-0.04}$	$3.47^{+1.04}_{-1.01}$	13.75
ymca-0023	$0.27^{+0.09}_{-0.11}$	$5.43^{+3.01}_{-2.05}$	1.50	ymca-0024	$0.09^{+0.03}_{-0.03}$	$3.66^{+0.91}_{-1.01}$	7.68
ymca-0025	$0.24^{+0.09}_{-0.07}$	$2.86^{+0.94}_{-0.59}$	56.85	ymca-0026	$0.07^{+0.04}_{-0.04}$	$3.65^{+0.93}_{-1.07}$	5.87
ymca-0028	$0.10^{+0.03}_{-0.04}$	$3.10^{+1.16}_{-0.79}$	10.44	ymca-0029	$0.09^{+0.03}_{-0.03}$	$3.54^{+0.98}_{-0.98}$	11.16
ymca-0030	$0.10^{+0.03}_{-0.04}$	$3.22^{+1.13}_{-0.87}$	11.36	ymca-0031	$0.11^{+0.03}_{-0.04}$	$3.12^{+1.10}_{-0.79}$	14.71
ymca-0034	$0.09^{+0.04}_{-0.04}$	$3.21^{+1.14}_{-0.88}$	15.75	ymca-0035	$0.22^{+0.04}_{-0.02}$	$8.67^{+0.96}_{-1.66}$	13.63
ymca-0036	$0.08^{+0.04}_{-0.04}$	$3.43^{+1.05}_{-0.98}$	19.52	ymca-0037	$0.72^{+0.22}_{-0.18}$	$5.59^{+2.31}_{-1.50}$	31.1
ymca-0038	$0.07^{+0.04}_{-0.04}$	$3.58^{+0.96}_{-1.02}$	19.87	ymca-0039	$0.09^{+0.04}_{-0.04}$	$3.47^{+1.01}_{-0.97}$	17.23
ymca-0040	$0.08^{+0.04}_{-0.04}$	$3.64^{+0.93}_{-1.02}$	14.27	ymca-0041	$0.11^{+0.03}_{-0.04}$	$3.49^{+0.94}_{-0.89}$	10.85
ymca-0042	$0.08^{+0.03}_{-0.02}$	$3.87^{+0.79}_{-1.04}$	4.76	ymca-0043	$0.08^{+0.04}_{-0.04}$	$3.68^{+0.92}_{-1.04}$	10.20
ymca-0044	$0.10^{+0.03}_{-0.04}$	$3.51^{+0.99}_{-0.99}$	9.99	ymca-0045	$0.20^{+0.07}_{-0.07}$	$5.91^{+2.73}_{-2.53}$	3.33
ymca-0046	$0.12^{+0.02}_{-0.03}$	$3.25^{+0.87}_{-0.72}$	14.75	ymca-0047	$0.07^{+0.04}_{-0.04}$	$3.71^{+0.89}_{-1.05}$	6.57
ymca-0048	$0.08^{+0.03}_{-0.02}$	$3.92^{+0.75}_{-1.00}$	6.57				

Table 4.3: Same of Tab4.2 but with EFF fitting parameters obtained by using all stars with P≥50%.

ID	α (arcmin)	γ	n_0/ϕ	ID	α (arcmin)	γ	n_0/ϕ
step-0003	$0.17^{+0.05}_{-0.04}$	$3.12^{+0.59}_{-0.67}$	4.55	step-0005	$0.21^{+0.05}_{-0.06}$	$3.00^{+0.67}_{-0.66}$	3.63
step-0007	$0.06^{+0.03}_{-0.03}$	$3.52^{+0.99}_{-0.97}$	5.02	step-0019	$0.14^{+0.04}_{-0.04}$	$2.65^{+0.54}_{-0.45}$	4.73
step-0020	$0.05^{+0.03}_{-0.03}$	$3.63^{+0.93}_{-1.05}$	2.43	step-0021	$0.11^{+0.03}_{-0.03}$	$3.26^{+1.08}_{-0.86}$	4.03
step-0022	$0.06^{+0.03}_{-0.03}$	$3.60^{+0.95}_{-1.02}$	2.89	step-0027	$0.77^{+0.15}_{-0.17}$	$3.39^{+1.04}_{-0.93}$	2.63
step-0028	$0.10^{+0.03}_{-0.03}$	$3.52^{+1.00}_{-1.02}$	4.03	step-0029	$0.08^{+0.04}_{-0.03}$	$3.71^{+0.88}_{-1.04}$	3.91
ymca-0006	$0.57^{+0.09}_{-0.05}$	$8.71^{+0.93}_{-1.39}$	2.20	ymca-0011	$0.14^{+0.04}_{-0.03}$	$3.24^{+0.53}_{-0.71}$	5.45
ymca-0016	$0.54^{+0.08}_{-0.03}$	$8.90^{+0.82}_{-1.57}$	1.66	ymca-0017	$0.16^{+0.05}_{-0.04}$	$2.81^{+0.47}_{-0.51}$	4.99
ymca-0022	$0.13^{+0.04}_{-0.02}$	$3.10^{+0.29}_{-0.46}$	4.04	ymca-0027	$0.14^{+0.05}_{-0.03}$	$2.90^{+0.42}_{-0.54}$	4.04
ymca-0032	$0.06^{+0.03}_{-0.03}$	$3.57^{+0.97}_{-1.03}$	4.07	ymca-0033	$0.06^{+0.03}_{-0.03}$	$3.63^{+0.93}_{-0.99}$	4.56

This test allows us to state that a great fraction of the candidate SCs looks like to follow a EFF profile very well, strengthen their authenticity, despite of most of them are very small and poorly populated. Nonetheless, a few SCs have a profile that does not seem consistent with an EFF profile, likely because of the very low number of stars which makes unfeasible to derive a robust RDP. These cases suggest us that a deeper investigation is needed to assess whether or not they are genuine physical stellar systems. We want to stress out that all 85 SCs are over-densities in the sky and each cleaned CMD is reasonably well fitted by a single isochrone. Both circumstances suggest that they could be actual clusters. Moreover, as discussed in §4.1.1, Piatti and Bica [2012]'s cleaning procedure subtracts stars considering only their position on the CMD, regardless the distance between the star and the SC centre. This approach should be preferred in the case of very small, sparse and scarcely populated objects as our candidate SCs [Piatti and Bica, 2012], but on the other hand it has the effect that the cleaning procedure in some cases could be more severe in the inner regions with respect to the outer ones. When this happens the central density surface decreases, thus hampering a reliable fit.

Finally, in the last column of Tab 4.4 we reported a flag which indicates the statistical reliability of each SC. A SC has flag = 3 if it has $G \geq 3$ and $n_0/\phi \geq 5$; flag = 2 and flag = 1 if only the latter or the former condition is satisfied, and flag = 0 if both conditions are false. It is important to notice that the flag does not take into account the SC CMDs, which also represent a valuable tool to discern whether or not a group of stars is a genuine SC. To conclude, 65% of

the SCs have a central to background ratio above 5 even considering only the most likely star members.

4.3 Results

The cluster finder algorithm and the analysis of the over-density CMDs returned 85 SCs in 23 square degrees in the periphery of the LMC. 78 of these SCs are newly discoveries, while the other 7 SCs were already known in the literature. Actually, within the probed tiles there were eight already known SCs; although the algorithm detected all of them, we concluded that the catalogued OGLE-LMC-CL-0757 object is not a real SC as its CMD did not match any isochrone. Table 4.4 lists the estimated parameters and other information about the 85 candidate SCs identified in this work.

In Fig. 4.5 we show the sky images of the six SCs whose CMD has been presented in Fig. 4.3. In the following section we discuss in some detail the characteristics of the 85 SCs.

4.3.1 Comparison with literature

As the already known SCs within the analyzed fields are limited, it is unsuitable to make a statistically significant comparison with the literature in order to test our parameter estimates. Indeed, only two of the seven already detected SCs have a reddening and age estimates in the literature. As for the ages we obtained $\log(t) = 9.4$ dex vs $\log(t) = 9.35$ dex for OGLE-LMC-CL-1133 and the same $\log(t) = 9.3$ dex value for SL842 (see also Tab 4.4). For the reddening we also attained reasonable values, namely $E(B-V) = 0.08$ mag vs $E(B-V) = 0.06$ mag for OGLE-LMC-CL-1133 and the same $E(B-V) = 0.03$ mag for SL842. Finally, we found the literature metallicity estimate only for the SC SL842, finding that its value Z$\sim$0.005 is consistent within the uncertainties with our measure Z = 0.006. Overall, our SCs have a radius smaller with respect to the literature ones. We argued that this difference is due to the different methods adopted to derive such a measure. We discuss this point more in detail in §4.4.

4.3.2 Spatial distribution

Figure 4.6 shows the position of all 85 SCs disclosed in this work. The majority (62 objects) is located to the West-South-West region (37 and 25 objects in STEP and YMCA tiles, respectively). Among the remaining SCs, 15 and 8 were detected to the North-East and to South-East

Table 4.4: Estimated parameters of all the 85 SCs identified in this work. The columns in the table indicate: 1) name of the cluster; 2-3) R.A. and Dec; 4) estimated cluster radius; 5) age; 6) reddening; 7) metallicity; 8) apparent magnitude in g-band 9) absolute magnitude in g-band; 10) G as defined by the eq. 4.2; 11) number of stars within the SC radius; 12) the tile name where the cluster lie; 13) flag to assess the statistical reliability of a SC: 0 is minimum, 3 is maximum (see §4.2.3 for details)

ID	R.A. (J2000)	Dec (J2000)	R ($'$)	log(t)	E(B-V) (mag)	Z	m_g (mag)	M_g (mag)	G	N. stars	Tile	Flag
ymca-0001	63.8302	-70.7697	0.35	9.75	0.04	0.006	17.79	-0.83	2.72	14	4_22	2
ymca-0002	63.8712	-71.1712	0.25	9.65	0.18	0.004	18.78	-0.31	5.77	14	4_22	3
ymca-0003	64.3757	-69.3018	0.25	9.5	0.03	0.006	18.27	-0.32	4.11	10	5_23	3
ymca-0004	64.4336	-70.2989	0.25	9.6	0.03	0.006	18.81	0.22	4.36	13	4_22	3
ymca-0005	64.991	-71.9376	0.4	9.25	0.06	0.008	17.69	-1.00	3.84	30	3_21	3
ymca-0006	65.1621	-71.5519	0.55	9.75	0.03	0.006	16.24	-2.35	2.84	42	3_21	0
step-0001	65.2362	-73.4328	0.3	9.75	0.04	0.006	18.21	-0.41	4.82	22	3_20	3
ymca-0007	65.3561	-70.5944	0.5	9.7	0.02	0.006	17.00	-1.56	3.46	42	4_22	3
ymca-0008	65.4038	-70.5862	0.25	9.6	0.03	0.008	18.10	-0.49	4.07	16	4_22	3
ymca-0009	65.4748	-71.1374	0.35	9.05	0.15	0.008	17.84	-1.15	5.12	29	4_22	3
step-0002	65.4784	-73.5847	0.3	9.55	0.03	0.006	18.29	-0.30	3.56	18	3_20	3
ymca-0010	65.5203	-70.232	0.5	9.4	0.03	0.006	17.38	-1.21	2.94	37	4_22	2
step-0003	65.6166	-72.9424	0.55	9.5	0.05	0.008	17.33	-1.33	6.36	76	3_21	1
ymca-0011	65.6829	-71.4134	0.3	9.5	0.03	0.006	18.05	-0.54	4.44	26	3_21	1
step-0004	65.885	-73.798	0.35	9.95	0.06	0.006	18.14	-0.54	3.37	23	3_21	3
ymca-0012	66.0329	-71.2766	0.2	9.95	0.03	0.006	18.58	-0.01	4.58	16	3_21	3
ymca-0013	66.1188	-70.7725	0.25	9.8	0.07	0.006	18.15	-0.57	3.03	16	4_22	3
ymca-0014	66.1419	-70.4832	0.45	9.35	0.06	0.008	15.70	-2.99	3.13	38	4_22	3
step-0005	66.1542	-73.4368	0.4	9.8	0.03	0.006	17.93	-0.65	2.90	31	3_21	0
ymca-0015	66.1664	-70.3033	0.5	9.25	0.06	0.006	16.73	-1.96	4.21	52	4_22	3
step-0006	66.2021	-73.5264	0.3	9.55	0.05	0.004	18.17	-0.48	4.09	23	3_21	3
ymca-0016	66.2049	-69.1095	0.4	9.55	0.02	0.006	17.90	-0.66	3.39	23	5_23	1
ymca-0017	66.4461	-71.1112	0.4	9.7	0.02	0.006	16.18	-2.38	3.37	34	4_22	1
ymca-0018	66.6028	-70.218	0.4	9.55	0.01	0.006	16.96	-1.56	4.13	38	4_22	3
ymca-0019	66.6152	-72.0306	0.5	9.5	0.03	0.006	17.33	-1.25	3.18	55	3_21	3
ymca-0020	66.6736	-70.6311	0.45	9.45	0.06	0.006	17.07	-1.62	3.14	42	4_22	3
ymca-0021	66.7019	-70.3302	0.45	9.65	0.03	0.006	17.00	-1.58	2.85	39	4_22	2
ymca-0022	66.8356	-71.9218	0.45	9.45	0.1	0.006	17.11	-1.71	2.54	47	3_21	0
step-0007	66.8558	-73.8335	0.5	9.5	0.08	0.006	17.50	-1.25	2.50	45	3_21	0
ymca-0023	67.0673	-71.62	0.45	9.7	0.05	0.006	16.39	-2.26	2.21	46	3_21	0
ymca-0024	67.1417	-71.7341	0.35	9.0	0.1	0.02	17.76	-1.06	1.32	27	3_21	2

ID	R.A. (J2000)	Dec (J2000)	R (′)	log(t)	E(B-V) (mag)	Z	m_g (mag)	M_g (mag)	G	N. stars	Tile	Flag
step-0008	67.1827	-73.3176	0.25	9.25	0.06	0.006	17.90	-0.79	1.94	16	3_21	0
step-0009	67.2051	-73.3117	0.4	9.2	0.06	0.006	16.95	-1.73	1.87	35	3_21	0
ymca-0025[a]	67.395	-71.8408	0.8	9.35	0.05	0.006	14.11	-4.55	18.98	302	3_21	3
step-0010	67.6849	-73.4533	0.45	9.45	0.08	0.006	16.93	-1.82	3.98	56	3_21	1
step-0011	67.8165	-73.8014	0.3	9.5	0.06	0.006	18.11	-0.58	4.29	29	3_21	1
step-0012	67.9018	-73.6612	0.4	9.85	0.05	0.006	17.21	-1.45	3.50	45	3_21	3
step-0013	67.9237	-72.9487	0.3	9.5	0.03	0.006	18.06	-0.53	3.59	36	3_21	3
step-0014	67.9965	-73.5009	0.4	9.4	0.05	0.006	17.87	-0.79	2.94	45	3_21	0
step-0015[b]	68.0319	-73.6709	0.4	9.1	0.02	0.006	17.41	-1.15	2.98	43	3_21	2
step-0016	68.0349	-73.345	0.25	9.4	0.05	0.006	18.24	-0.41	3.19	23	3_21	1
step-0017	68.153	-73.43	0.2	9.5	0.07	0.006	18.12	-0.60	4.34	20	3_21	3
step-0018[c]	68.2506	-73.2275	0.3	9.2	0.04	0.006	16.67	-1.95	7.56	54	3_21	3
step-0019	68.2628	-73.7053	0.35	9.4	0.02	0.006	17.58	-0.97	4.12	39	3_21	1
step-0020	68.2673	-73.2126	0.55	9.3	0.08	0.008	16.81	-1.94	3.02	88	3_21	1
step-0021	68.2948	-72.9248	0.45	9.45	0.02	0.006	16.16	-2.40	3.69	74	3_21	1
step-0022	68.3022	-73.1334	0.25	9.45	0.05	0.006	17.71	-0.94	4.02	29	3_21	1
step-0023	68.3077	-73.4732	0.45	9.45	0.08	0.006	17.14	-1.61	4.65	74	3_21	3
step-0024	68.319	-73.1468	0.4	9.6	0.08	0.004	17.34	-1.42	2.27	49	3_21	2
step-0025	68.386	-73.5211	0.3	9.35	0.07	0.006	17.55	-1.17	4.13	36	3_21	3
step-0026	68.4947	-73.3416	0.4	9.35	0.02	0.006	17.40	-1.15	3.13	55	3_21	1
step-0027	68.5198	-73.8413	0.35	9.5	0.06	0.006	18.35	-0.34	3.37	36	3_21	1
step-0028	68.6028	-72.98	0.25	9.5	0.03	0.006	17.22	-1.37	2.85	27	3_21	0
step-0029	68.7477	-73.3113	0.25	9.85	0.02	0.006	18.23	-0.33	3.20	28	3_21	1
step-0030	68.845	-73.1543	0.35	9.55	0.05	0.008	16.77	-1.88	4.17	49	3_21	3
step-0031	68.855	-73.9019	0.3	9.45	0.03	0.006	18.06	-0.52	3.14	26	3_21	3
step-0032	68.8971	-73.4728	0.45	9.5	0.03	0.006	16.75	-1.84	2.64	64	3_21	2
step-0033[d]	68.8974	-73.4169	0.35	9.45	0.02	0.006	17.32	-1.24	4.80	54	3_21	3
step-0034[e]	68.9113	-73.7331	1.05	9.35	0.06	0.006	14.43	-4.26	18.02	450	3_21	3
step-0035	68.9257	-73.6976	0.35	9.6	0.06	0.004	17.11	-1.58	2.04	32	3_21	0
step-0036	68.9323	-73.1327	0.35	9.0	0.12	0.008	18.10	-0.78	3.78	47	3_21	3
step-0037	68.9358	-73.2805	0.5	9.4	0.04	0.006	16.18	-2.44	6.70	104	3_21	1
ymca-0026	89.2224	-63.3843	0.2	9.4	0.02	0.004	18.48	-0.07	1.89	15	11_41	2
ymca-0027	89.3118	-62.7561	0.25	9.35	0.02	0.004	17.85	-0.70	2.74	19	11_41	0
ymca-0028	89.3897	-63.3484	0.3	9.1	0.08	0.008	17.58	-1.17	3.19	37	11_41	3
ymca-0029	89.5528	-62.4595	0.4	9.45	0.02	0.004	17.17	-1.38	3.97	42	11_41	3

ID	R.A. (J2000)	Dec (J2000)	R (′)	log(t)	E(B-V) (mag)	Z	m_g (mag)	M_g (mag)	G	N. stars	Tile	Flag
ymca-0030	89.5887	-62.7257	0.35	9.55	0.04	0.004	16.42	-2.20	5.31	41	11_41	3
ymca-0031	90.4314	-62.957	0.35	9.65	0.03	0.006	17.27	-1.32	4.07	35	11_41	3
ymca-0032	90.6697	-62.9244	0.3	9.2	0.03	0.006	17.31	-1.28	4.07	27	11_41	1
ymca-0033	90.9858	-63.3337	0.5	9.7	0.03	0.004	15.18	-3.41	3.68	60	11_41	1
ymca-0034	91.1703	-63.1483	0.4	9.35	0.02	0.006	16.75	-1.80	3.09	40	11_41	3
ymca-0035	91.4224	-62.7954	0.2	9.55	0.02	0.006	18.10	-0.46	4.55	13	11_42	3
ymca-0036	91.5201	-62.569	0.5	9.5	0.02	0.006	16.76	-1.79	3.36	35	11_42	3
ymca-0037[f]	92.0658	-62.9875	1.4	9.3	0.03	0.006	12.70	-5.89	48.75	847	11_42	3
ymca-0038	92.8553	-63.2278	0.45	9.25	0.03	0.006	17.46	-1.13	3.42	34	11_42	3
ymca-0039	93.0118	-63.2107	0.3	9.45	0.06	0.006	16.14	-2.55	4.04	20	11_42	3
ymca-0040	94.0711	-63.3558	0.45	9.5	0.02	0.004	17.19	-1.36	3.06	32	11_43	3
ymca-0041	94.2216	-73.6311	0.5	9.55	0.02	0.006	16.70	-1.86	2.93	75	1_27	2
ymca-0042	94.297	-73.5258	0.4	8.95	0.1	0.01	17.09	-1.73	2.13	46	1_27	0
ymca-0043	94.3731	-74.0865	0.35	9.15	0.07	0.01	17.69	-1.03	2.23	31	1_27	2
ymca-0044	94.4404	-73.773	0.2	8.8	0.2	0.02	16.81	-2.34	3.48	18	1_27	3
ymca-0045	94.8468	-74.214	0.45	9.45	0.08	0.008	17.77	-0.98	4.02	44	1_27	1
ymca-0046[g]	95.8541	-73.8284	0.5	9.4	0.05	0.006	16.02	-2.63	12.00	106	1_27	3
ymca-0047	96.1662	-73.8367	0.3	8.8	0.2	0.02	18.23	-0.92	4.01	24	1_27	3
ymca-0048	97.3995	-73.5321	0.35	9.45	0.02	0.006	17.67	-0.89	2.93	22	1_27	2

Reference names.

a: NGC1629,SL3,LW3,KMHK4

b: OGLE-LMC-CL-0824

c: OGLE-LMC-CL-0827

d: OGLE-LMC-CL-0826

e: OGLE-LMC-CL-1133,SL5,LW8,KMHK14

f: SL842,LW399,KMHK1652,ESO86SC61

g: OGLE-LMC-CL-0849

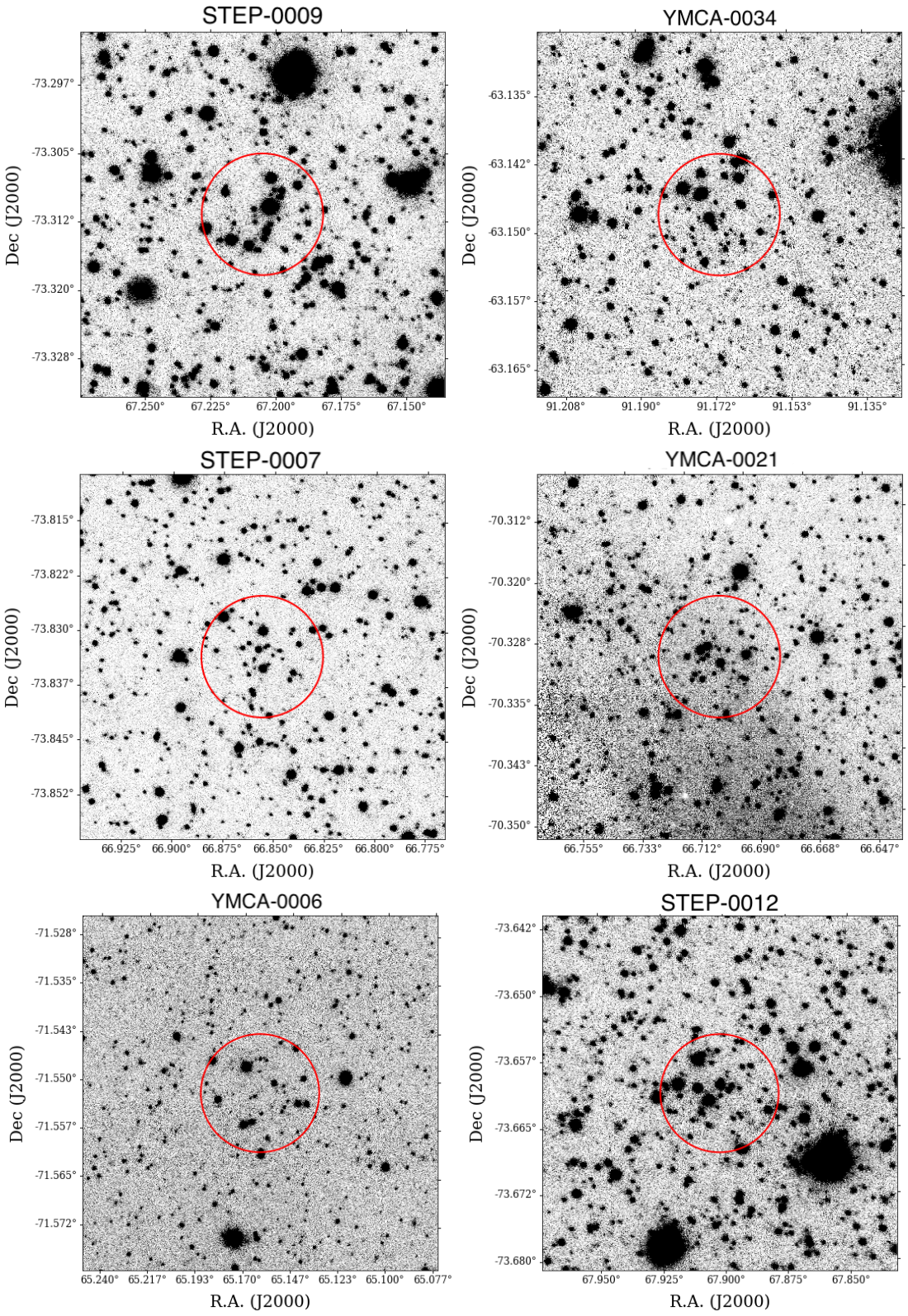

Figure 4.5: Sky images of the same SCs whose CMDs are displayed in Fig. 4.3. Each panel has a size three times as large as the SC radius, which is represented by a red circle.

of the LMC, respectively. The high number of SCs revealed in the STEP 3_21 tile (N. SCs = 35) with respect to the nearby tiles at a similar R.A. (9 SCs in the tile YMCA 3_21 and 14 SCs in the tile YMCA 4_22) is noticeable. A natural explanation is that the STEP 3_21 tile probes a region of higher star density with respect to the other two tiles ($\sim$ 30% and 70% more stars than YMCA 3_21 and YMCA 4_22, respectively). However, such discrepancy alone does not justify a number of SCs 4 and 2.5 times larger than YMCA 3_21 and YMCA 4_22 tiles, respectively. It is important to underline that the STEP 3_21 tile probes the end of the Bridge connecting the LMC with the SMC, where some substructures were unveiled likely due to the repeated interaction between the MCs [e.g., Belokurov and Erkal, 2019, Mackey et al., 2018]. We may therefore argue that the overhead number of SCs detected within the STEP 3_21 tile can be due to these interactions.

We measured the angular distance of the SCs from the LMC centre by adopting Eq. 1 from-Clariá et al. [2005]:

$$d = d_0\{1 + [sin(p - p_n)^2][tan(i)]^2\}^{0.5} \tag{4.4}$$

Despite of our tiles covered the LMC outskirts up to $\sim$ 12 degrees, we did not detect any SC beyond $\sim$ 9 degrees from the LMC centre ($\sim$7.7 kpc), even though previous works showed up that the disk of the LMC extends up to about 15 kpc [Balbinot et al., 2015, Saha et al., 2010]. This outcome is in agreement with the works by Piatti [2017b] and Pieres et al. [2016].

It is known that both MCs host a numerous population of binary clusters [e.g., Pietrzyński and Udalski, 1999], therefore we performed an internal research to look for those candidate SCs that are closer than one arcminute. We found three pairs that satisfied the previous condition. The first couple of candidate SCs, namely STEP-0008 and STEP-0009, has a high probability to be a real physical binary SC system. Indeed, their centres are separated, in projection, by $\sim 0.5'$, and their estimated ages are very similar ($\log(t) = 9.2$ dex and $\log(t) = 9.25$ dex, respectively). The other two couples have a lower chance to be binary SCs, and we report them here for completeness: the centres of STEP-0018 and STEP-0020 are separated by $0.94'$ and have a slightly different estimated age ($\log(t) = 9.2$ dex and $\log(t) = 9.3$ dex, respectively); STEP-0022 and STEP-0024 are separated by $0.86'$ with estimated ages of $\log(t) = 9.45$ dex and $\log(t) = 9.6$ dex, respectively.

The detection of numerous uncatalogued SCs in all three regions explored with the cluster finder algorithm suggest us that there could be stil many other SCs undiscovered in the unexplored regions of the LMC, periphery, at least within 9° . In particular, excluding the STEP

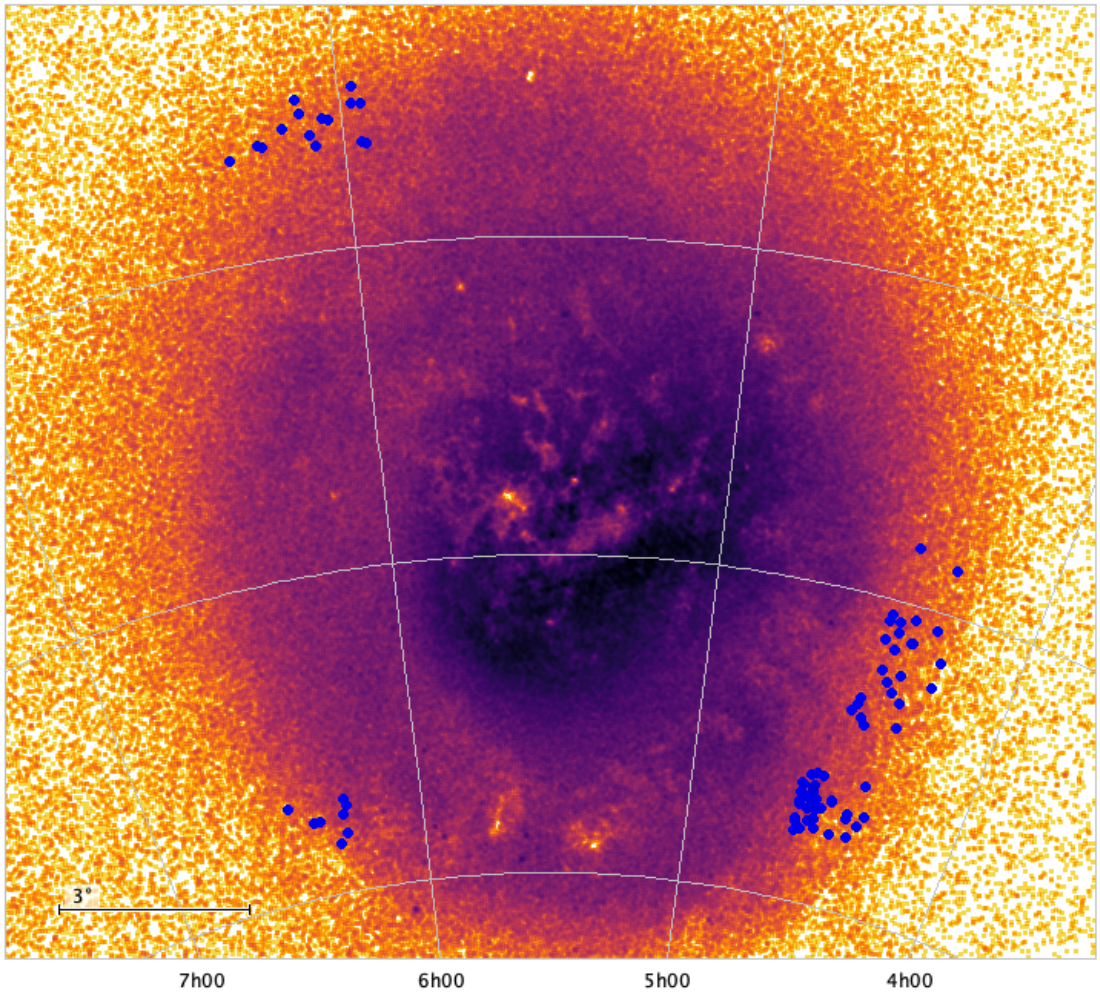

Figure 4.6: Position of the 85 clusters in the sky showed as blue points. The LMC galaxy is depicted using RC stars taken from *Gaia* DR2 [Gaia Collaboration et al., 2018a].

tiles[3], we disclosed 42 new SCs in the six innermost YMCA tiles (a range of distances of 4.8° - 9.0° from the LMC centre). Hence, the expected number of SCs in the same distance interval is of the order of ~ 7 SCs per square degree. This implies that roughly ~ 70 unknown SCs in the LMC outskirts are still awaiting to be detected in the remaining YMCA tiles.

4.3.3 Age distribution: first evidence of clusters in the age gap

Figure 4.7 shows the age distribution of all the 85 SCs detected in this work (black contours). As the visual inspection of the cleaned CMD suffers from an unavoidable degree of subjectivity, we also plot in the same figure the age distribution of the 64 SCs having $G \geq 3$ (red contours), as they are statistically more robust. The ages range from $\log(t) = 8.80$ dex to $\log(t) = 10.05$ dex, but with the exception of three SCs, the remaining ones are older than 1 Gyr. This outcome suggests that in the LMC periphery there was no SC formation activity in the last Gyr, at least in the 23 probed tiles. A result which, on the one side, is in agreement with the existing literature about the SFH and AMR in the LMC outer disc, which showed up that it is primarily composed by an old (and metal-poor) stellar population [e.g., Piatti and Geisler, 2013, Saha et al., 2010]. On the other side, however, this occurrence is at odds with what is known for the inner part of the LMC, where the SC distribution shows an increase of formation activity at about $\sim 100-300$ Myrs ago [Glatt et al., 2010, Nayak et al., 2016, Pietrzyński and Udalski, 2000]. These authors proposed the last close passage between the MCs to be the main cause that of such enhancement in the SC formation rate, the same encounter which led to the formation of the connecting bridge, as confirmed by Montecarlo simulations [Besla et al., 2012, Diaz and Bekki, 2012, Kallivayalil et al., 2013, Zivick et al., 2018]. Fig. 4.7 reveals that the age distribution of SCs has a peak at ~ 3 Gyrs, very close to the secondary peak at 2.7 Gyrs found by Pieres et al. [2016] in their work devoted to the investigation of the Northern regions of the LMC through the public DES data. A possible explanation for this enhancement implies a previous close encounter between the LMC and SMC. Indeed, it is difficult to invoke a tidal interaction with the MW to justify this peak, as the MCs should be on their first infall onto the Galaxy halo [Besla et al., 2007, Kallivayalil et al., 2013]. In addition, current simulations of the Magellanic System, taking into account the recent accurate PM measurements of the MCs [Kallivayalil et al., 2013, Zivick et al., 2018], agree that they became an interacting pair just a few Gyrs ago [see Besla et al., 2012, Diaz and Bekki, 2012, Pardy et al., 2018, Tepper-García et al., 2019]. Such models, depending on the assumed initial conditions on the parameters, support the occurrence of a first close encounter

[3]The over-density of SCs found in the tile STEP 3_21 would influence the following considerations.

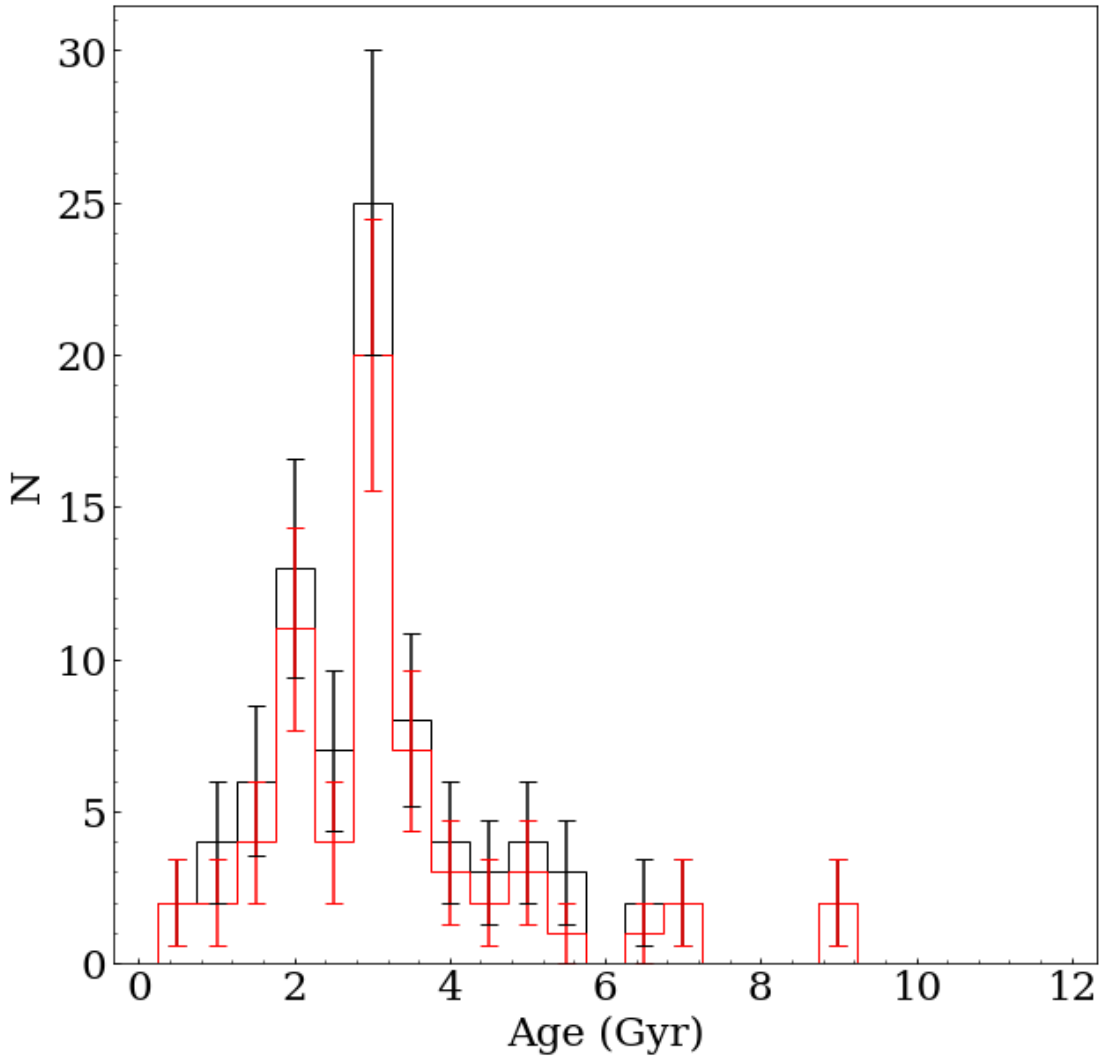

Figure 4.7: Age distribution of the whole cluster sample (black histogram) and of the 64 SCs with a $G \geq 3$ (red histogram). Errors are poissonian.

2 - 3 Gyrs ago consistent with the peak visible in the Figure 4.7. It is worth pointing out that also the LMC field stars present an increase of star formation at about 2-3 Gyrs [Harris and Zaritsky, 2009, Rubele et al., 2012, Tosi, 2004, Weisz et al., 2013]. A LMC-SMC close passage is expected to also rise the formation activity of the SMC. Unfortunately, most of the literature works devoted to the analysis of SMC SCs did not have a sufficient deep photometry to estimate the age of SCs older than 1 Gyr. However, concerning the works about SFH of the stellar field, several literature studies reported peaks in the SFH, some of which are consistent with our main peak [e.g., Harris and Zaritsky, 2004, Weisz et al., 2013, ho revealed a peak at 2-3 Gyr and 3.5 Gyr, respectively], others not [e.g., Rubele et al., 2015, 2018, who found a peak at 1.5 Gyr]. This argument deserves further investigations that will be possible when a complete and homogeneous characterization of the SCs belonging to both MCs will be available.

In Fig. 4.7 it is also discernible a likely secondary peak at 2 Gyr. As $\sigma \log(t) = 0.1$ dex at 2 Gyrs corresponds to $\sim$ 500 Myrs of uncertainty, there is a chance that such a minor peak might represents the tail of the main peak. A definitive answer is only possible when all YMCA tiles will be explored. Interestingly, Pieres et al. [2016] found a main peak at $\sim$1.2 Gyrs. Even considering SC age uncertainties, our secondary and their main peak are very unlikely to be associated. This difference is very interesting and might suggest a different SC formation history in different LMC regions due to a past interaction between the MCs. Indeed, fields analyzed by Pieres et al. [2016] are very far away from the majority of our tiles (with the exception of the very few tiles to the North-East side). Anyway, a definitive answer could be achieved only with the analysis of the remaining YMCA tiles all around the LMC.

An additional interesting aspect of Fig. 4.7 is the presence of a not negligible number of SCs in the discussed LMC age gap (see §1.2.4.2). In particular, we detected 16 SCs (corresponding to 19% of the total sample) with estimated ages in the interval $9.6 < \log(t) \leq 10.0$ ($\sim 4 \leq$ t (Gyrs) ≤ 10), although only four SCs have ages between 7 and 10 Gyrs. Until few years ago, only one age gap SC was known in the literature [e.g., ESO121-03 Mackey et al., 2006, Mateo et al., 1986]. Recently, Pieres et al. [2016] re-estimated the age of NGC 1997 to be $\sim 4.5 \pm 0.1$ Gyrs, inside the age gap, although it is close to its edge. The absence of SCs in this broad interval of the LMC life has been a debated question for about 30 years, suggesting different formation and evolution paths for the SCs and the stellar field, since in the latter a similar gap is not observed [Piatti and Geisler, 2013, Tosi, 2004, see also the detailed discussion in §1.2.4.2]. Moreover, the SMC does not present a similar gap in the SC age distribution, despite of as already discussed in §1.2.4.1 the SMC and LMC share a similar evolution in more recent periods, as witnessed by

the common enhanced periods of SC formation [e.g., Glatt et al., 2010, Nayak et al., 2018]. We wonder if this gap might have been an observational bias. As already mentioned, most surveys focused on the inner LMC, leaving the periphery almost unexplored. As central areas might have stronger disruption effects because of a shorter evaporation time at smaller galactocentric distances [Baumgardt and Makino, 2003], a lower number of old SCs with respect to young ones is expected in the central parts of the LMC. Indeed, the LMC bar and inner disc host a very high number of young SCs [Glatt et al., 2010, Nayak et al., 2016, Piatti et al., 2015a, 2018, Pietrzyński and Udalski, 2000]. Furthermore, the SC luminosity function decreases with age [e.g., de Grijs et al., 2003, Hunter et al., 2003], making it harder to detect old SCs (including SCs in the age gap) without a very deep photometry. It is worth mentioning again that most surveys had not enough depth to reveal such clusters, being limited to the analysis of SCs younger than 1-1.5 Gyrs [Glatt et al., 2010, Nayak et al., 2016, Pietrzyński and Udalski, 2000]. The presence of a subsample of SCs belonging to the age gap represents an important opportunity to disclose the past LMC evolution, hence such objects may be the follow-ups target for a deeper photometry in order to better assess their physical properties. As the age distribution of the SCs with $G \geq 3$ looks similar to that of the entire sample (it is just shifted down), all the above considerations still hold even if some candidate SCs turn out to be not actual SCs. In particular, the SCs falling in the age gap with $G \geq 3$ are 11.

To be more confident with our results, we tested the reality of our detection of SCs in the age gap against the possibility that we underestimated the uncertainties on the age for the SCs with $\log(t) \geq 9.5$ dex[4]. As a matter of fact, if such SCs had a larger age uncertainty, i.e. $\sigma \log(t) = 0.2$ dex with respect to our estimate $\sigma \log(t) = 0.1$ dex, it could happen that some SCs falling in the age gap could actually be younger. We basically aim at verifying whether it is statically possible to observe a consistent number of SCs in the age gap from a parent distribution with no SCs at all in this age interval, if age uncertainties are greater with respect our evaluation. To check this hypothesis, we random generated three distributions: the first one is a Gaussian peaked at ~ 3 Gyrs, with standard deviation equal to $\sigma = 0.1$ dex and with no SCs in the age gap, called $D0$ hereafter. We generated other two distributions ($D1$ and $D2$) that differ from the former in having 8 and 16 SCs in the age gap, i.e. half and the total number of SCs detected in the age gap in this work, respectively. We added Gaussian errors to the objects in the three distributions with σ=0.1 dex or 0.2 dex based on whether their estimated ages are

[4]It is very unlikely that for SCs younger that 3 Gyrs our errors are underestimated (see also discussion at §4.2.1).

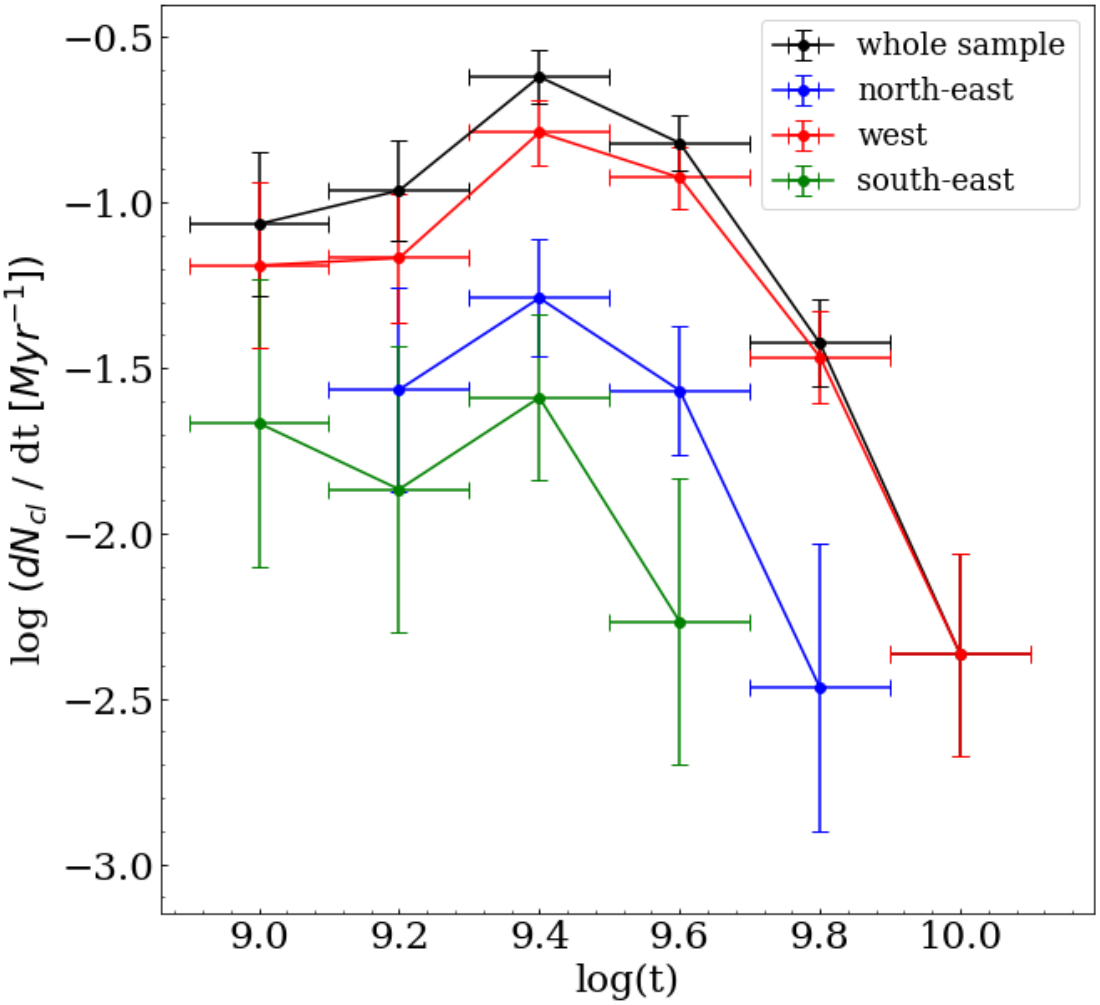

Figure 4.8: Number of SCs per bin of age as a function of age. The black solid line corresponds to the whole cluster sample, while coloured solid lines represent clusters in different regions of the LMC.

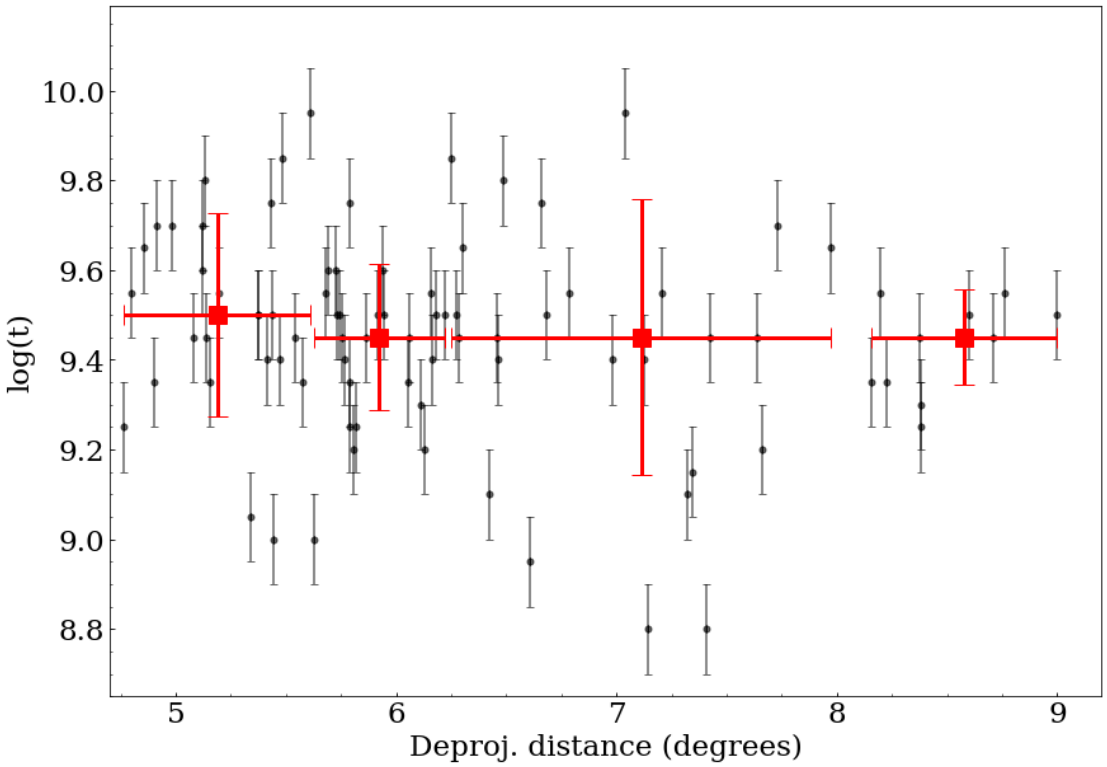

Figure 4.9: Estimated SC ages as a function of the deprojected distance from the LMC center (black points). Red squares indicate the median of the $\log(t)$ per distance bin calculated in order to have 25 SCs in each bin.

below or above $\log(t) = 9.5$ dex, respectively. We then performed a Kolmogorov-Smirnov test to identify the parent distribution that better approximate our data. We repeated the same procedure 1000 times and in more than 88% of the cases we obtained that the distributions that best approximate the observed one were those with age gap SCs (445 and 440 cases for $D1$ and $D2$, respectively). On these bases, we can confidently discard the hyphotesis that our subsample of SCs in the age gap is artificially generated by an underestimation of their age uncertainties with a ∼90% confidence. In addition, the distribution $D0$ returned a mean number of SCs in the age gap (after we added the errors), of 8.7 ± 2.9, i.e. at $\sim 2.5\ \sigma$ from the actual value. In principle, $D0$ could explain about half of the SCs discovered within the age gap, but not all of them, confirming that it is very unlikely that $D0$ is the parent distribution of our data. For completeness, $D1$ and $D2$ had a mean number of age gap SCs of 13.0 ± 3.0 and 13.1 ± 3.1, well consistent within the errors with the actual number of identified age gap SCs. Concluding, this test further strengthen our results, supporting the reality of the presence of a consistent number of SCs in the age gap.

Fig. 4.8 displays the number of SCs per Myr (SC frequency) as a function of the age. Because of the very low number of SCs younger than 1 Gyr, we set $\log(t) = 9.0$ dex as the minimum value on the x-axis. The figure shows the SC frequency for the entire sample (black solid line) as well as that for the three different analysed regions, namely North-East, West and South-East of the LMC (blue, red and green lines, respectively). The peak of the SC formation, already visible in Fig. 4.7, is clearly evident in all three regions at ∼2-3 Gyrs[5]. Concerning the age gap interval ($9.65 \leq \log(t) \leq 10.0$), focusing on the whole sample (black solid line), the SC frequency seems to be consistent with the one measured at more recent epochs ($9.0 \leq \log(t) \leq 9.3$). Instead, beyond $\log(t) \sim 9.8$ dex the SC frequency has a sharp decrease, as expected from the fact that we detected only a few SCs in the 7-10 Gyr age range. However, it is important to emphasize that the SC frequency also depends on disruption effects, such as two-body relaxation or disc and bar shocking [Baumgardt and Makino, 2003, Baumgardt et al., 2002, Spitzer, 1987, Zhang and Fall, 1999]. Even if the LMC periphery is a low-density environment, such effects could be present [e.g., Lamers et al., 2005], driving to the dissolution of low-mass SCs. On this basis, the outcomes reported in this work suggest that the SC frequency in the age gap does not reflect an epoch of quenched SC formation as it is commonly assumed, but more likely is the result of an observational bias (at least in the outskirt of the LMC).

Finally, we did not reveal any correlation between SC ages and deprojected distance from the LMC centre, as shown in Fig. 4.9, where we plotted the estimated SC age as a function of the galactocentric deprojected distance. The median of the age in each distance bin, calculated in order to have 25 SCs in each interval, clearly indicates that the age is fair constant in the LMC periphery. This outcome is in agreement to what obtained by Pieres et al. [2016] in the Northern side of the LMC.

4.3.4 Star cluster metallicity

The metallicity estimated for the SCs from the isochrone fitting described in §4.2.1 ranges from Z = 0.004 up to 0.02. The youngest SCs show a solar metallicity, whereas the metallicity of the majority of the newly discovered SCs is Z = 0.006, corresponding to the mean LMC metallicity value for the last 2-3 Gyrs [Piatti and Geisler, 2013]. As it is shown in the right panel of Fig. 4.10, there is apparently no correlation between the SC metal content and the corresponding deprojected distance from the LMC centre, even if any SC is more metal rich than

[5]Considering our uncertainties of $\sigma \log(t) = 0.1$ dex on the estimated SC ages and the bin interval of $\log(t) = 0.2$ dex, the actual position of the peak could be at slightly lower or higher values.

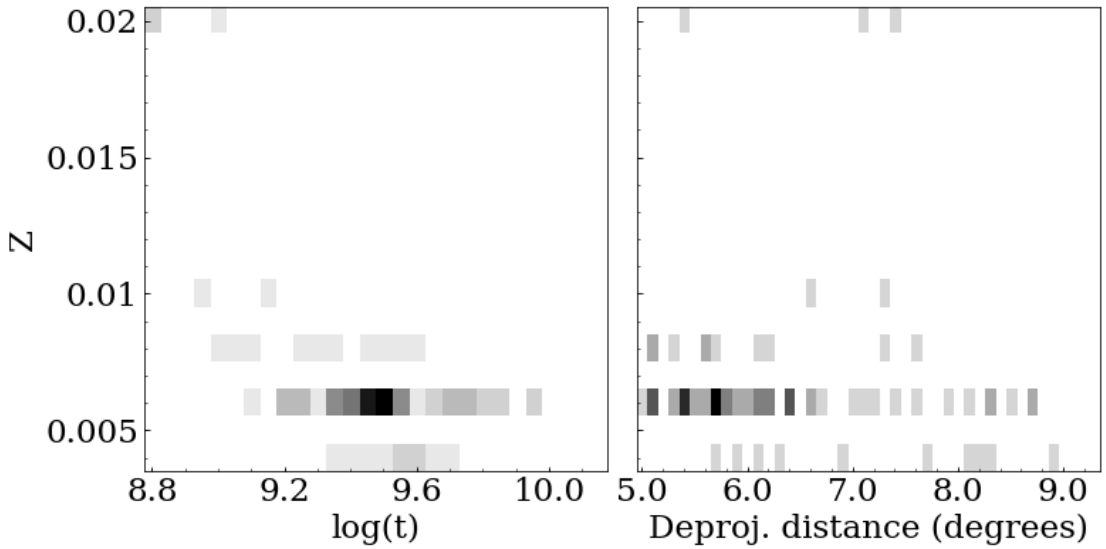

Figure 4.10: *Left:* Density plot of the metal content as a function of the age. The map is 28×17 pixels. *Right:* Density plot of the metal content as function of the deprojected distance from the LMC centre. The map is 44×17 pixels.

Z = 0.006 beyond 8°.

Concerning the AMR displayed in the left panel of Fig. 4.10, we did not note any clear correlation for SCs older than ∼1.5 Gyrs (i.e., $\log(t) \sim 9.2$ dex). A few SCs younger than $\log(t) \sim 9.2$ dex have Z $\geq$ 0.006, but the statistics is too poor to devise any possible AMR.

4.3.5 Absolute magnitudes

Fig. 4.11 displays the absolute magnitude distribution of the 85 detected SCs (black histogram) and that of the SCs with $G \geq 3$ (red histogram). As the two distributions have similar shapes, the following considerations holds for both cases. Most of the SCs have a M_g in the range between -3 and 0 mag. This interval of magnitudes is well below the magnitude limit reported by previous works present in the literature [e.g., Hunter et al., 2003, see their fig. 4], suggesting that we are sampling the low end of the SC luminosity function. Indeed, the distribution has a peak around $M_g = -1$ mag, then it sharply decreases. This value might reflects our observational limit or could have a physical origin, i.e. can be regarded as the lower limit absolute magnitude (mass) for bound objects, and/or as the limiting mass needed by a SC to survive destruction for at least 1 Gyr.

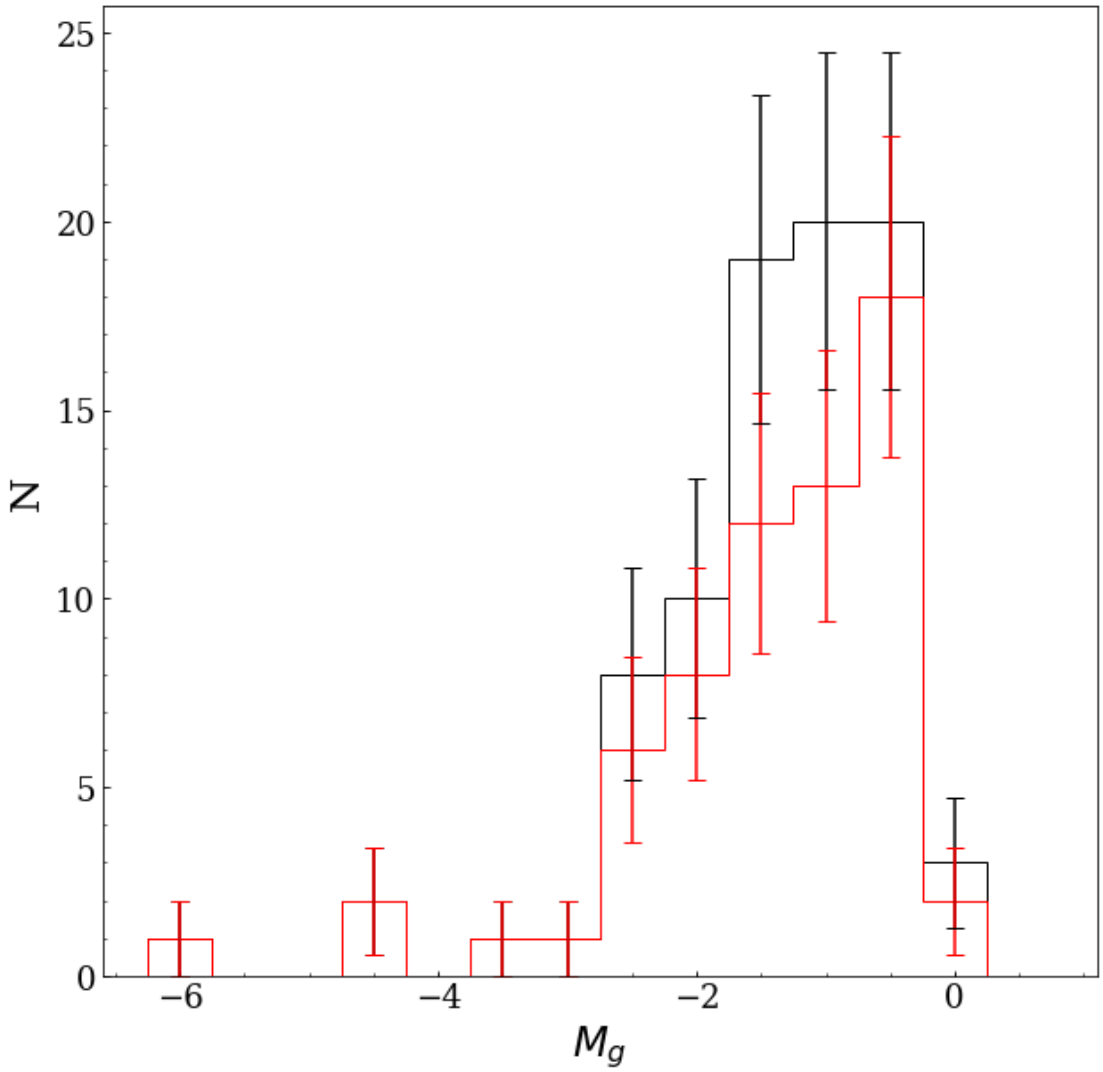

Figure 4.11: Distribution of the absolute magnitudes of the entire SC sample (black histogram) along with SCs having $G \geq 3$ (red histogram). Errors are poissonians.

4.4 Discussion and conclusion

To get some insight into the global evolution of the LMC it is necessary to combine our SC sample with the others available in the literature. To this aim and to produce a rather homogeneous sample, we selected only SCs whose ages were estimated through isochrone fitting. In particular, we adopted the catalogues by Bonatto and Bica [2010]; Glatt et al. [2010]; Popescu et al. [2012]; Baumgardt et al. [2013]; Piatti [2017b], Piatti et al. [2015a, 2018]; Nayak et al. [2016]; Pieres et al. [2016]. To avoid duplicates, we identified all SC pairs whose centres were closer than $20''$ to each other, retaining only the SC belonging to the most recent work. At the end of this procedure, we collected 2610 SCs (including the sample build in this work), whose spatial position with respect to the LMC centre is displayed in Fig. 4.12. In this figure, each sub-panel shows the position with respect to the LMC centre of SCs belonging to a given age interval. In particular, black points represent SCs taken from the literature while red points are our new SC candidates. It can be seen that the youngest SCs displayed in the top three panels of Fig. 4.12 are mainly located along the bar of the LMC, or along the LMC arms, contrarily to SCs older than 1 Gyr, that are more evenly distributed. Interestingly, such SCs are completely absent in some regions of the LMC, despite we doubled the number of known SCs with t $\geq$ 2 Gyrs (see bottom central and bottom right panels of the figure). This is a clear observational bias, as most of the surveys devoted to the analysis of LMC SCs were not deep enough to discover SCs older than $\sim$ 1-1.5 Gyr [Glatt et al., 2010, Nayak et al., 2016, Pietrzyński and Udalski, 2000], unless their post-main sequence evolutionary phases are very populous, like the old known LMC GCs. Furthermore, the majority of the surveys explored the inner regions of the LMC, as it is evident from the figure (bottom left panel). The solely exception is the work by Pieres et al. [2016] who exploited the deep DES photometry to investigate the Northern part of the LMC (see the bottom left and bottom central panels of the figure). Therefore, we can conclude that the census of SCs in the LMC is still quite incomplete, not only in the outskirts, but also in more central regions of the galaxy, were SCs surveys were shallower.

Figure 4.13 shows the number density profile of all 2610 SCs (red points) along with that of LMC field stars (black points) in order to infer analogies and/or differences between these two populations. LMC stars were taken from the *Gaia* DR2 Gaia Collaboration et al. [2016, 2018a], and were selected according to their PMs to remove likely MW stars. In particular, as we were more interested in having a clean sample rather than a complete one, we estimated the peak of LMC's stars PMs and retained only the stars whose PMs are within a rectangular box with size

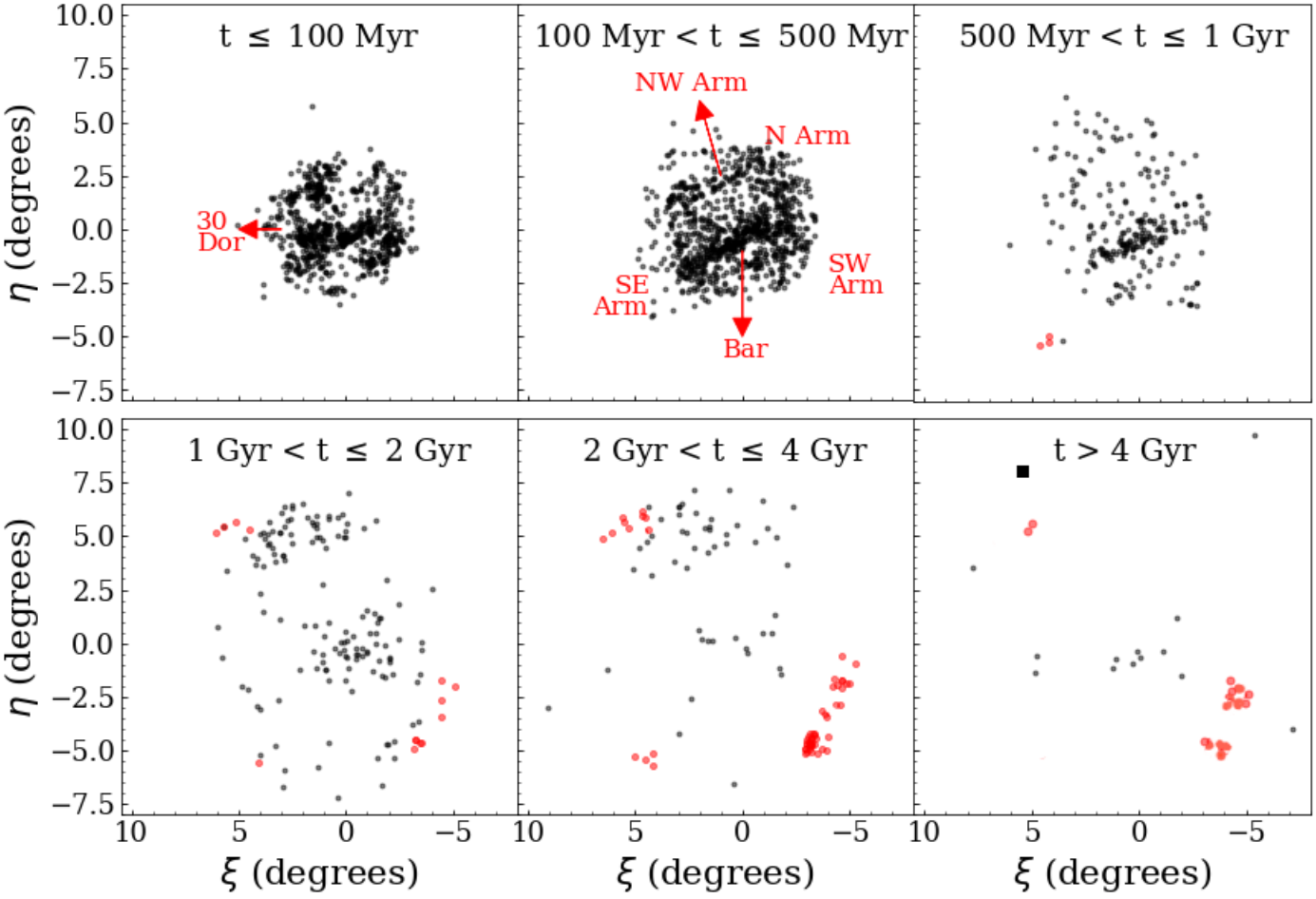

Figure 4.12: SCs relative position, with respect to the LMC centre, detected in this work (red points) and present in the literature (black points), divided per age bins. Black square in the bottom right panel marks the position of ESO121-SC03, the first known SC of the age gap. Besides ESO121-SC03, the only other previously known clusters in the > 4 Gyr age range are the old GCs.

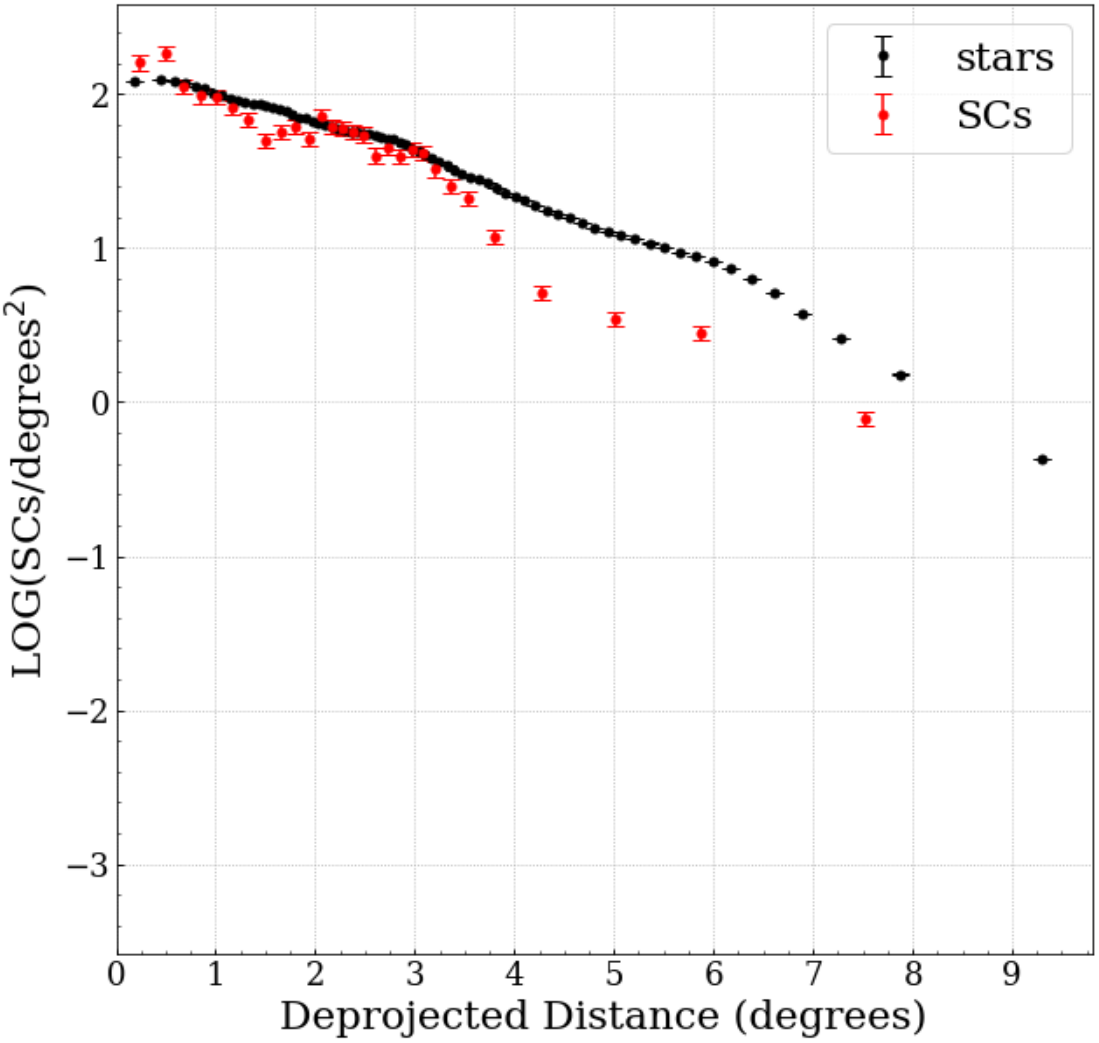

Figure 4.13: Number density profile of SCs (red points) and field stars (black points) taken from the Gaia DR2.

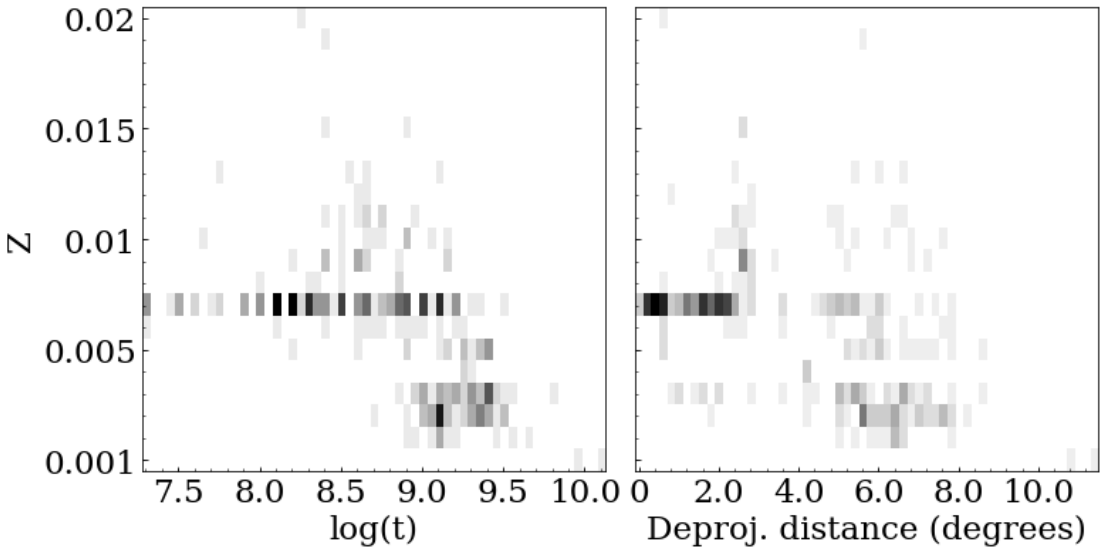

Figure 4.14: *Left:* Density plot of the metal content as a function of the age. The map is 57×21 pixels. *Right:* Density plot of the metal content as function of the deprojected distance from the LMC centre. The map is 58×21 pixels.

(μ_{α^*}, μ_δ) = (1.8, 1.2) mas yr^{-1} centred around the quoted peak.

The star number density profile was scaled in order to overlap with the radial profile of the SCs, thus the values on the y-axis refer to the SCs. The figure reveals that in the LMC innermost 3°, the slope of the SC and star distributions agree very well, with two exceptions: i) there is a central peak in the SC number density profile, likely due to the very high number of young SCs located in the LMC bar, while the star distribution is flat, likely a consequence of lower completeness of the *Gaia* dataset at the LMC centre; ii) the SC number density drops at about 1.5°, indicating perhaps the low density regions between the LMC bar and the spiral arms, in corresponding of which the SC surface density quickly increases again. However, as previous literature works aiming at SC detection were mainly devoted to the regions of the bar and spiral arms, the SC low density at ∼1.5° could be an observational bias.

An interesting feature in Fig. 4.13 is a slope change in both SC and star distributions (although the SC profile becomes steeper with respect to the stellar counterpart), at ∼3° from the LMC centre, indicating the distance from the LMC centre where the spiral arms are no longer visible. All these similarities could be a signature of a common evolutionary path between SCs and stellar field population. Even though the two distributions look different beyond ∼3-4° , we cannot compare them anymore, due to the already mentioned high SC incompleteness in the LMC periphery (clearly visible also in Fig.4.12). Interestingly enough, Fig. 4.13 shows a flattening of

the SC number density profile beyond 5°, an obvious result of the newly SCs discovered in this work and by Pieres et al. [2016], suggesting again that many SCs are still missing.

In Fig. 4.14 we investigated the AMR and the metallicity-LMC distance correlation by including SCs studied in the literature. To obtain a catalog as homogeneous as possible, we selected only SCs from works that published metallicities for a large number of objects. Therefore, we collected data from Piatti et al. [2014], Palma et al. [2016], Pieres et al. [2016], obtaining a sample of 328 SCs, which span a range of ages from ∼10 Myrs to > 10 Gyrs and cover all distances from the LMC centre up to ∼11°. All metallicities retrieved from the above cited works have been estimated through isochrone fitting of the SC CMDs, whose results were given in [Fe/H]. Therefore, we converted them using the relation $Z = 10^{[Fe/H]} * Z_{\odot}$ where $Z_{\odot} = 0.02$. Fig. 4.14 clearly reveals a trend between metallicities, age, and distances, with the more metal-poor SCs being also the oldest ones and are located at larger galactocentric distances with respect to the metal-rich counterpart. This is more evident in the plot metallicities vs. age (left panel), as almost all SCs younger than 1 Gyr have Z $\geq$ 0.006 and all those older than 1 Gyr have Z lower than that. The correlation between metal content and galactocentric distance is less evident (right panel), but again most of the SCs with Z $\geq$ 0.006 are concentrated in the inner 5° , whereas those more metal poor are beyond that radius. This outcome is also confirmed by the AMR in the stellar field population. In particular, Carrera et al. [2011] concluded that metal-poor stars have mostly been formed in the outer disc, while the more metal-rich ones preferentially formed in the inner disc. This scenario have been confirmed by Piatti and Geisler [2013] using 5.5 million stars belonging to LMC main body. The figure also shows many SCs having Z = 0.007, i.e. a value very close to the LMC metallicity value for the last 2-3 Gyr [Z = 0.006 Piatti and Geisler, 2013]. A comparison with the SCs detected in this work is not immediate since our sample is mainly composed by old SCs that are all located farther than 5° from the LMC centre. Anyway, the majority of the 85 SCs studied here have a metallicity of Z = 0.006, consistent with many SCs distributed throughout the LMC, although at a first glance our SCs appear more metal-rich compared to the SCs with the same estimated ages present in the literature, i.e. Z $\sim$ 0.006 vs Z $\sim$ 0.003. However, considering the uncertainties on metallicities in our and in the cited works, the above quoted difference is consistent within the errors. Indeed, we estimated an error of ΔZ = 0.002, while literature SCs have a mean uncertainty of ΔZ $\sim$ 0.001 - 0.002. Furthermore, we cannot discard the possibility that the reddening-metallicity degeneracy could enhance this disagreement. For example, if we underestimated the reddening while previous authors overestimated it, the difference in metallicity naturally arises.

Finally, it is instructive to compare the SC radii calculated in this work with those in the literature. However, defining the edge of a SC (the distance from the SC centre beyond which no star belongs to the SC anymore) is not a trivial task. In fact, there are many different definitions of a SC radius, depending on how it is estimated. Hence, comparing radii measured by different authors means to deal with possible diverse definitions. Bearing this in mind, we tried to build a sample of literature SCs as large as possible, but avoiding to mix catalogs built adopting very different ways to measure the radii. To this aim, we checked the average difference between the estimated radii of SCs in common in each pairs of investigations. At the end of the procedure, we remained with 2315 SC radii, including the works by Glatt et al. [2010], Bonatto and Bica [2010], Nayak et al. [2016], whose radii are consistent or homogeneizable within less than $0.1'$. Instead, we excluded the catalogs by Palma et al. [2016], Pieres et al. [2016], Sitek et al. [2016]; because the spread around the mean of the radii differences was considerably high ($\sim 0.3'$). Figure 4.15 displays the radius distribution (up to $2'$) of our 85 SCs (red filled histogram) along with the literature SCs sample (black histogram). Both histograms are normalized to their maximum to facilitate the comparison. An inspection of the figure reveals that most of the SCs in the LMC have $0.2' \leq \mathrm{R} \leq 1.0'$, being the mode of the distribution placed at $\sim 0.2 - 0.3'$. Our SCs have radii in the same range of those taken from literature, as the bulk of them have a size comprised between $0.2'$ and $0.6'$, with a peak at $\sim$0.2-0.3$'$, in agreement with the literature.

In this work we explored 23 square degrees in the outskirt of the LMC, using data from the YMCA and STEP surveys, to detect new SCs and thus constrain the LMC evolutionary history. To this purpose, we developed a procedure that we can basically resume in two steps. The first step is to search for over-densities in the sky (pixels with a S/N ratio above a given threshold), through a density map built with a KDE, and then derive their centers and radii. We exploited Montecarlo simulations to both define a threshold depending on the field densities and simulate artificial SCs to quantify the efficiency of the adopted method. As a result, a detection percentage around 90% was obtained even in the worst case, e.g. high stellar field density and sparse SCs. The second step consisted in using the cleaning CMD procedure developed by Piatti and Bica [2012], in order to recognize real physical systems from false positives. In the end, we were left with 85 candidate SCs, among which 78 were not catalogued in the literature. We estimated age, reddening, metallicity of each cluster through an isochrone fitting technique, keeping the distance modulus constant to 18.49 mag [de Grijs et al., 2014]. We also measured the integrated absolute magnitudes for each SCs. Finally, we fitted their RDP built by using only stars with P$\geq$75% with an EFF profile to adduce further robustness to their physical reality. About 70%

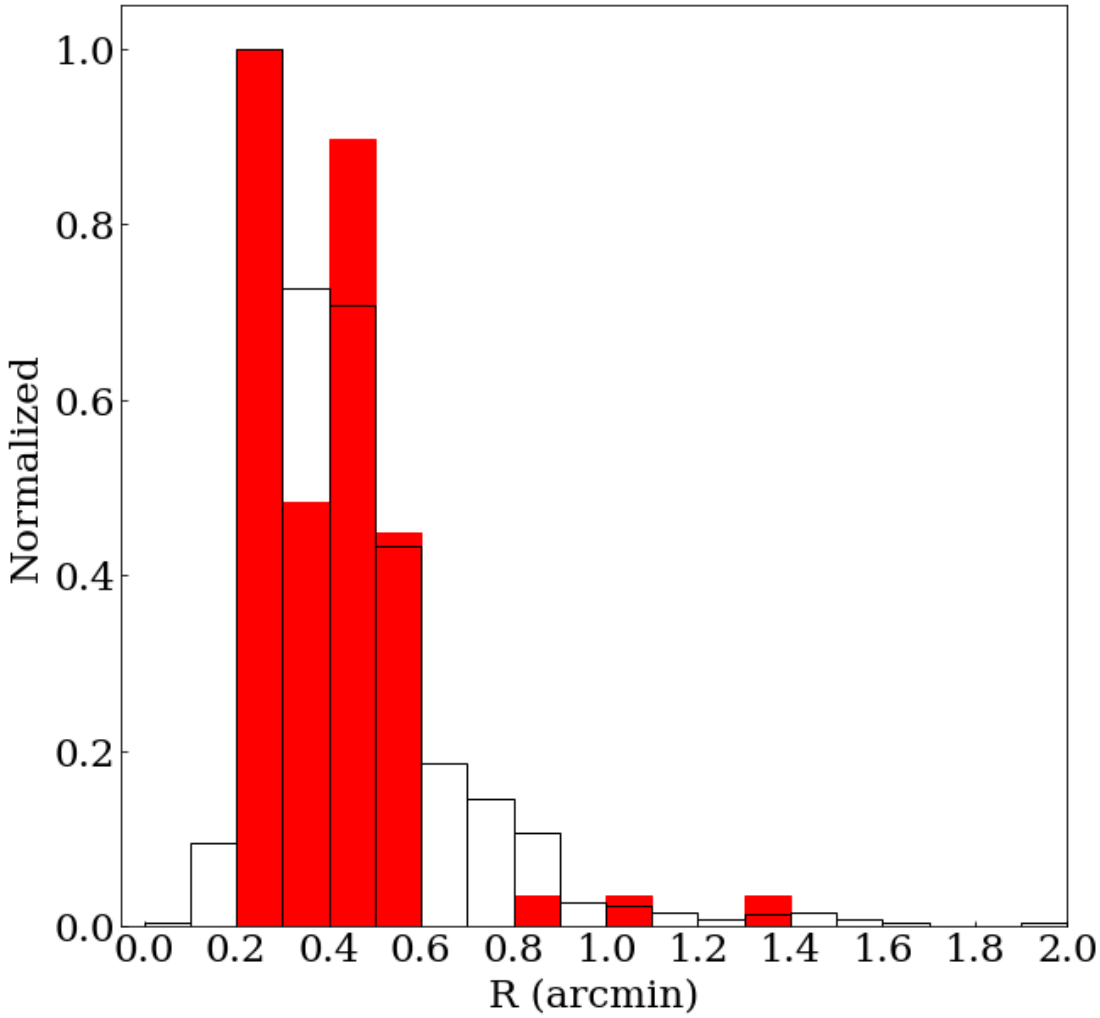

Figure 4.15: Radius distribution of all SCs from literature (black histogram) along with our sample (red filled histogram), normalized at maximum.

of the SC RDPs are well fitted with an EFF profile. The remaining SCs have been fitted by employing stars with P≥50%.

From the SC parameters we derived the following results:

- The age distribution has a sharp peak at ∼ 3 Gyrs, likely due to a close encounter between the MCs, that might have enhanced the SC formation activity. Such interaction is expected from simulations [Besla et al., 2012, Diaz and Bekki, 2012, Pardy et al., 2018, Tepper-García et al., 2019], which take into account the recent PM measurements of the MCs. Furthermore, an increase in the star formation rate ∼ 2-3 Gyr ago has been observed also in the stellar field [Harris and Zaritsky, 2009, Rubele et al., 2012, Weisz et al., 2013].

- For the first time, we detected a consistent number of candidate SCs in the age gap, a period ranging from 4 to 10 Gyrs lacking of SCs [Da Costa, 1991]. Given the high number of SCs in the age gap (19% of our sample) and from the analysis of the SC frequency, the natural outcome is that the age gap is not an interval of minimal SCs formation as it has been believed so far. On the contrary, the age gap is likely the product of an observational bias, due to surveys using too shallow photometry and unable to detect clusters older than 1-1.5 Gyr [Glatt et al., 2010, Nayak et al., 2016, Pietrzyński and Udalski, 2000]. Moreover most observations up-to-date were focused on the LMC centre/bar where the extremely high stellar field density makes it harder to detect old and faint SCs. A more accurate analyses of these SCs through follow-ups will provide a relevant opportunity to shed light on this evolutionary period of the LMC, and even on the whole MC system.

- There is no trend either between the age and the distance from the LMC centre, or between the galactocentric distance and the cluster metallicity. Indeed, even though young clusters have a higher metal content with respect to old ones, the very few young clusters detected do not allow us to establish any correlation between cluster ages and their metallicities.

This work is the first of a series aiming at completing the census of SCs around MCs. As demonstrated here, many SCs are still undetected but their census and the estimation of their parameters are vital to get insights into the recent and past evolution of the MCs. As the YMCA survey is complete, we will be able, along with data from STEP, to explore the surroundings of the LMC, the SMC and their connecting bridge and thus to trace the evolutionary history of the entire Magellanic system.

Chapter 5

Application of the cluster finder algorithm to the LMC - Part II: the complete census of SCs in the LMC outskirts

In the previous chapter we presented the discovery of 78 new candidate SCs in the outskirts of the LMC, 16 of which with estimated ages evenly distributed within the gap. We adopted an ad hoc algorithm, tested on a suite of Monte Carlo simulations, aiming at detecting even faint and sparse SCs, and reaching a very high level of completeness (see §3.4.2 and Fig. 3.6). We exploited the algorithm in 23 YMCA and STEP tiles located in the periphery of the LMC and we found that the age gap might be an observational bias, originated by the combination of the shallow photometry of past surveys with the lack of systematic studies in the periphery of the LMC, where field contamination is considerably lower, and the SC mortality due to strong dynamical perturbations in the LMC interiors should be mitigated [Lamers et al., 2005]. However, Piatti [2021b] re-analyzed a sub-sample of age gap SC candidates reported in §4, using data from the SMASH survey [Nidever et al., 2017]. They concluded that some of the candidate SCs may not be real physical systems, but rather field star density fluctuations. Albeit the SMASH data has poorer quality (worse spatial resolution and photometric deepness), with respect to the STEP and YMCA photometry, we decided to refine further the analysis of SC candidates in our next

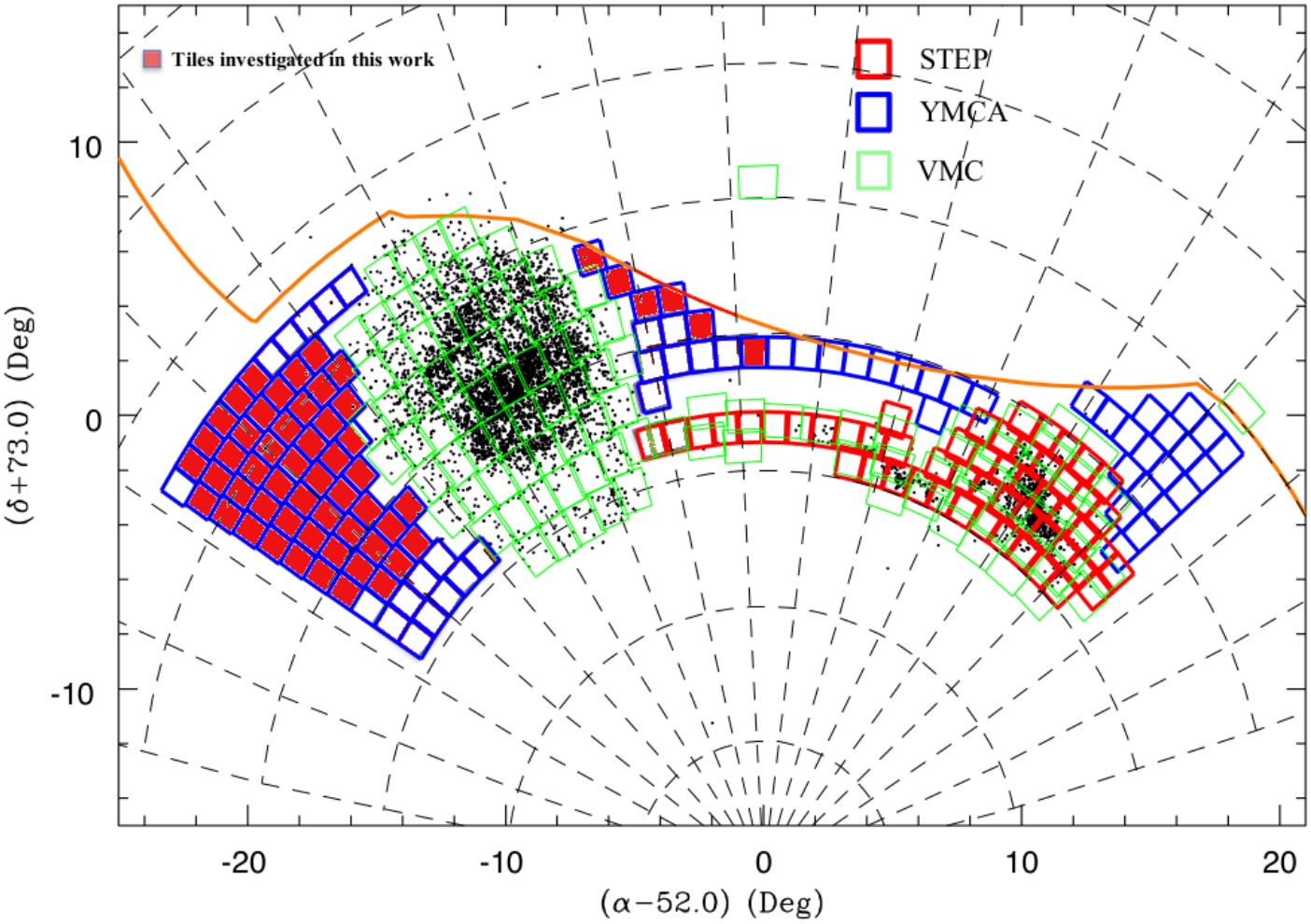

Figure 5.1: Footprint of the STEP and YMCA surveys (see labels) in a zenithal equidistant projection along with all objects present in Bica et al. [2008] (black dots). For comparison, we overdraw the VMC [Cioni et al., 2011] regions in green, whereas the DES surveyed area lays northwards of the orange line. The 56 tiles analysed in this work are filled in red.

work.

Indeed, motivated by the very positive results achieved in the analysis of the 23 YMCA and STEP tiles presented in §4 and also by the recent newly debating issues about the age gap real existence, we exploited the cluster searching algorithms over the remaining 56 YMCA tiles in the LMC periphery, displayed in the Figure 5.1, and whose features are reported in Table 5.1. In this chapter we describe the results of the algorithm and present one of the most complete and homogeneous SC catalog in the LMC periphery, composed by the candidate SCs discovered in this work and in §4 in a total area of 79 square degrees barely explored with the modern panoramic deep surveys, as attested by the only 21 already known SCs in these regions. As done also in §4 [Gatto et al., 2020, hereafter], we also homogeneously estimate the age of each SC through a visual isochrone fitting procedure over a de-contaminated CMD, and use their properties to reliable constrain the past LMC and more generally MC evolutionary history.

5.1 Cleaning the colour-magnitude diagram from field star contamination

The cluster-finder algorithm provided a list of over-densities which also contains asterisms which are not real physical systems and thus must be removed. As SCs can be approximately treated as SSPs, the distribution of their stars in the CMD should resemble isochrones of a given age and metallicity. We use this property to remove asterisms from our original list. The first step consist in decontaminating the SC CMD from field stars which can affect the isochrone matching procedure. Also in this work we adopted the method developed by Piatti and Bica [2012] to clean the CMDs as it was conceived to face with sparse SCs made by handful of stars such as those found in this work. Nonetheless, there are some little variations with respect to the procedure adopted in Gatto et al. [2020] and therefore we present below a quick recap of the entire method. The procedure basically consists in comparing the candidate SC (overdensity) CMD with those of six fields surrounding the overdensity, with the scope of probing the local properties of the stellar field and identifying likely star field members in order to remove them from the candidate SC CMD. Each field is a circular region with a radius as large as three times the over-density one, thus enclosing an area nine times greater than the candidate SC. In this manner we avoid poor sampling of the local stellar background and we ensure that the procedure operates with a sufficient statistics even in low-density environments. For each of the six CMD fields, we built

Table 5.1: Log of Observations. The different columns show: name of the tile, its centre, average FWHM over the images (S_g and S_i)

Tile	RA (hms)	Dec (dms)	S_g $''$	S_i $''$
3_32	06:43:59.688	-71:46:52.680	1.16	1.07
3_33	06:56:49.032	-71:46:52.680	1.03	0.80
3_34	07:09:38.352	-71:46:52.680	0.92	0.86
4_18	03:32:27.048	-70:40:41.520	1.04	0.97
4_33	06:34:28.728	-70:40:41.520	1.23	1.09
4_34	06:46:36.840	-70:40:41.520	1.02	1.08
4_35	06:58:44.952	-70:40:41.520	0.96	0.77
4_36	07:10:53.064	-70:40:41.520	0.92	0.82
5_21	03:56:16.680	-69:34:30.360	1.38	1.07
5_36	06:49:06.720	-69:34:30.360	1.05	1.17
5_37	07:00:38.040	-69:34:30.360	0.93	1.04
5_38	07:12:09.384	-69:34:30.360	1.46	1.13
5_39	07:23:40.728	-69:34:30.360	1.44	1.14
6_23	04:06:56.040	-68:28:19.560	1.19	0.90
6_24	04:17:54.360	-68:28:19.560	0.99	0.81
6_37	06:40:32.616	-68:28:19.560	1.22	1.27
6_38	06:51:30.960	-68:28:19.560	1.31	0.97
6_39	07:02:29.280	-68:28:19.560	1.00	0.95
6_40	07:13:27.600	-68:28:19.560	0.87	1.16
6_41	07:24:25.944	-68:28:19.560	1.12	0.86
7_26	04:27:11.160	-67:22:08.400	1.14	1.10
7_27	04:37:39.720	-67:22:08.400	1.45	1.11
7_38	06:32:53.784	-67:22:08.400	1.22	1.08
7_39	06:43:22.320	-67:22:08.400	1.23	0.98
7_40	06:53:50.880	-67:22:08.400	1.14	0.97
7_41	07:04:19.416	-67:22:08.400	1.04	1.50
7_42	07:14:47.976	-67:22:08.400	1.38	1.06
7_43	07:25:16.536	-67:22:08.400	1.03	0.95
8_28	04 35:45.696	-66:15:57.600	1.20	0.89
8_39	06:26:02.880	-66:15:57.600	1.22	1.03
8_40	06:36:04.464	-66:15:57.600	0.95	1.11
8_41	06:46:06.024	-66:15:57.600	0.96	0.76
8_42	06:56:07.584	-66:15:57.600	0.92	0.71
8_43	07:06:09.144	-66:15:57.600	0.86	0.88
8_44	07:16:10.704	-66:15:57.600	1.02	0.96
8_45	07:26:12.288	-66:15:57.600	0.94	0.93
9_40	06:19:53.976	-65:09:46.440	1.17	0.99
9_41	06:29:30.984	-65:09:46.440	1.00	0.93
9_42	06:39:07.992	-65:09:46.440	0.76	1.08
9_43	06:48:45.000	-65:09:46.440	0.97	1.00
9_44	06:58:21.984	-65:09:46.440	0.92	0.79
9_45	07:07:58.992	-65:09:46.440	0.84	0.82
9_46	07:17:36.000	-65:09:46.440	0.98	0.83
9_47	07:27:13.008	-65:09:46.440	0.90	1.00
10_42	06:23:36.600	-64:03:35.640	0.75	0.62
10_43	06:32:51.168	-64:03:35.640	1.01	1.16
10_44	06:42:05.736	-64:03:35.640	1.06	1.18
10_45	06:51:20.304	-64:03:35.640	0.97	1.03
10_46	07:00:34.872	-64:03:35.640	1.20	1.14
10_47	07:09:49.440	-64:03:35.640	1.16	0.85
10_48	07:19:04.008	-64:03:35.640	1.08	1.00
10_49	07:28:18.576	-64:03:35.640	1.08	0.81
11_46	06:44:58.872	-62:57:24.480	1.02	0.87
11_47	06:53:52.872	-62:57:24.480	1.20	1.26
11_48	07:02:46.872	-62:57:24.480	1.20	1.27
11_49	07:11:40.896	-62:57:24.480	1.16	0.74
11_50	07:20:34.896	-62:57:24.480	0.96	0.71

boxes centred on every star, with sides varying according to the local density of the CMD stars. In particular, small boxes are constructed in denser areas and vice-versa [see figure 12 in Piatti and Bica, 2012, as explanatory of the procedure]. Then, we estimate the median of the stars located in the six field regions and normalized it at the cluster area, in order to have the number of expected contaminant stars ($N_{\rm bkg}$) within the candidate SC area. Finally, for each field we randomly extracted $N_{\rm bkg}$ stars and use them to identify probably star field contaminants within the SC CMD. In particular, we look for the $N_{\rm bkg}$ stars in the SC candidate closest in the CMD to the extracted $N_{\rm bkg}$ ones. We repeated the same procedure for all six fields and finally measure the probability of a star to belong to the cluster as $P = 1-(N_{\rm subt})/6$, where $N_{\rm subt}$ is the number of times a star was subtracted. The position of the stars with high membership probability on the CMD was used to discern between real physical system and asterisms as well as to estimate the age of the SCs via an isochrone fitting procedure (see §5.2). Figure 5.2 illustrates an example of the cleaning procedure over the candidate SC YMCA-0051, showing in the bottom panels the position of the stars on the CMD and with respect to the SC centre colour-coded according to their membership probability.

As done in Gatto et al. [2020], to quantitatively gauge the goodness of each SC we also estimates how many stars the SC contains in terms of standard deviations above the local average mean. Hence, we define

$$G = (N_{\rm cl} - N_{\rm bkg})/N_{\rm bkg} \tag{5.1}$$

where $N_{\rm cl}$ is the number of stars within the SC radius. With respect to Gatto et al. [2020] and at the light of the considerations raised in Piatti [2021b], we preferred a more conservative approach by taking into consideration only candidate SCs with $G > 4.5$. It is worthwhile to highlight that this is a very conservative threshold value, as one of the already known SC OGLE-LMC-CL-0824 has $G = 2.98$.

5.2 Determine SC age through isochrone fitting

We determined age and reddening of each SC via visual isochrone matching procedure. To this aim we adopted the PARSEC isochrones [Bressan et al., 2012] and fixed the distance modulus to DM = 18.49 mag in order to reduce the number of parameters of which the isochrone fitting procedure depends on. Despite the LMC has a not negligible depth in the line of sight [e.g., Choi et al., 2018b, Subramanian and Subramaniam, 2009], in Gatto et al. [2020], we calculated that the error committed on the ages considering a constant DM is $\sigma \log t \sim 0.1$ dex. To break the

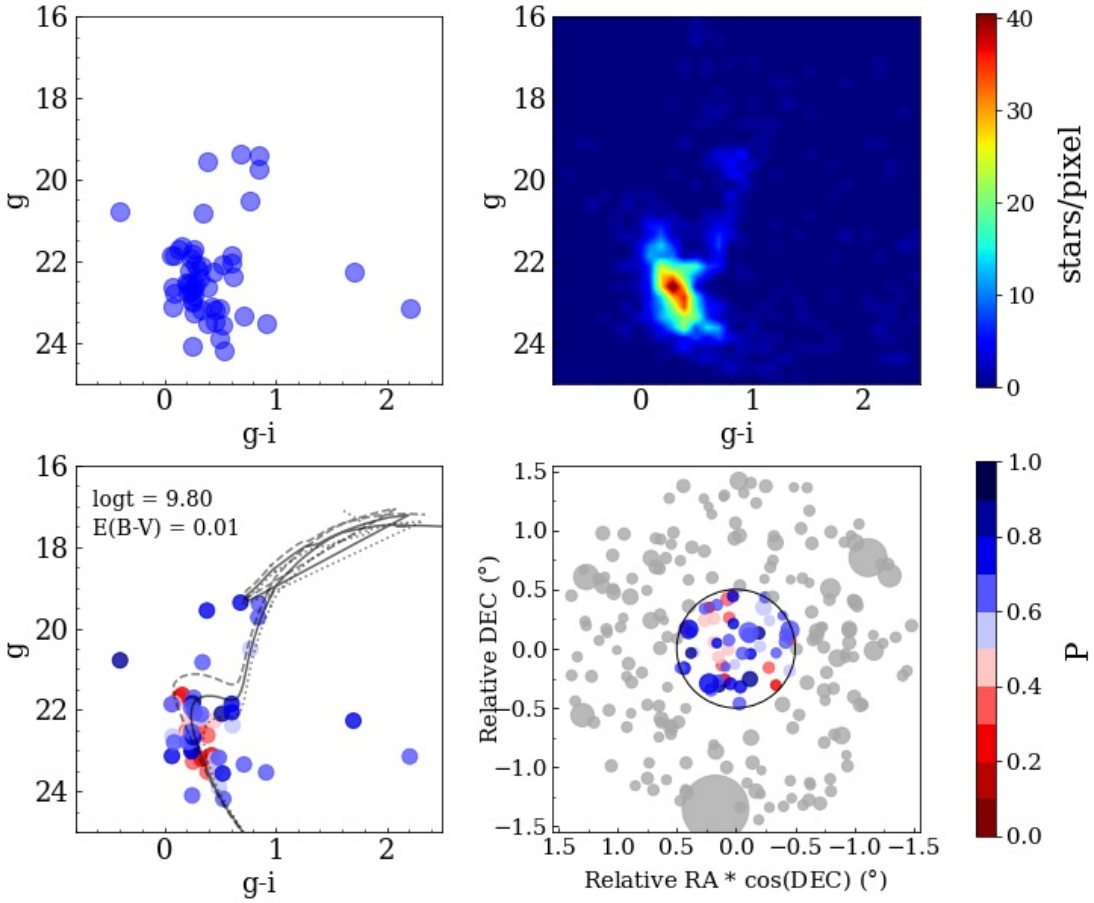

Figure 5.2: *Top left:* CMD of the stars belonging to the candidate SC YMCA-0051; *Top right:* Hess diagram of the 6 regions as representative of the local stellar field. *Bottom left:* SC candidate stars colour-coded according to their membership probability, with the best isochrone drawn as a solid line and the two isochrones at $\log t \pm 0.2$ dex with respect to the best solution as dotted and dashed lines, respectively. Age and reddening adopted for the best isochrone are indicated in the top left corner; *Bottom right:* Relative spatial position of stars with respect to the candidate SC centre. The circle indicates the SC estimated radius.

reddening-metallicity degeneracy we also fixed the metal content according to the age-metallicity relation (AMR) derived by Piatti and Geisler [2013]. In particular, we adopted Z = 0.004 for SCs with $\log t \leq 9.65$ and Z = 0.002 for SCs having $\log t > 9.65$.

We varied age and reddening of the isochrones to seek for the best one who match the positions of the stars with high membership values (i.e. $P \geq 50\%$) on the CMD. In particular, we focus on the following evolutionary phases to aid the matching procedure: MS, RC, RGB, sub-giant branch (SGB). To be conservative, we considered an age uncertainty of $\sigma \log t = 0.2$ dex, that takes into account either the statistical error based on the visual procedure and the systematic one due to the elongation of the LMC along the line of sight. Fig. 5.2 (bottom left panel) shows an example of the fitting isochrone procedure for the candidate SC YMCA-0051. It displays the best isochrone (solid line) and the two isochrones at $\log t \pm 0.2$ dex (dotted and dashed lines) superposed to the position of stars on the CMD, colour-coded according to their membership probability.

5.3 Results

After a careful analysis of the cleaned CMDs, we selected a total of 40 candidate SCs, 27 of which were not present in literature. Table 5.2 lists the main parameters of the SCs derived in this work, while Fig. B.1 shows the cleaned CMDs of all SCs detected in this work. In order to have an overall view of the SC census in the LMC outskirts, we joined the list of candidate SCs derived in this work and the previous one §4. In doing this operation, to obtain a homogeneous sample, we kept from our first work only SCs with $G > 4.5$, namely 15 SCs, as done here. The combined list is therefore made by a total of 55 SCs, 35 of which (63% of the sample) are new discoveries.

5.3.1 Spatial distribution

To investigate the spatial distribution of the SC in the LMC periphery we made use of the Eq. 1 from Clariá et al. [2005] to measure the angular distance of the SCs from the LMC centre:

$$d = d_0\{1 + [sin(p - p_n)]^2[tan(i)]^2\}^{0.5} \tag{5.2}$$

where d is the angular de-projected distance from the LMC optical centre at $(\alpha, \rho) = (79.91^\circ, -69.45^\circ)$ [de Vaucouleurs and Freeman, 1972a], d_0 is the angular distance on the plane of the sky, p and p_n are the position angle of the SC and of the line of nodes, respectively and finally i is the

ID	RA (J2000)	Dec (J2000)	R (')	$\log t$	E(B-V) mag	G	N_{stars}	Tile
YMCA-0049	66.1961	-67.4452	0.30	9.45	0.02	5.6	20	7_26
YMCA-0050	66.6824	-67.1022	0.25	10.00	0.02	7.1	21	7_26
YMCA-0051	66.7169	-67.2573	0.50	9.80	0.01	6.8	53	7_26
YMCA-0052	66.7251	-67.2559	0.40	9.50	0.03	6.8	37	7_26
YMCA-0053[a]	67.3577	-67.4462	0.25	9.35	0.04	8.0	36	7_26
YMCA-0054	67.6154	-67.7678	0.20	9.45	0.04	5.6	21	7_26
YMCA-0055[b]	67.6588	-66.9543	0.35	9.25	0.05	14.7	72	7_26
YMCA-0056[c]	67.8233	-67.7799	0.20	9.40	0.02	5.5	21	7_26
YMCA-0057	68.6103	-66.9525	0.40	9.40	0.06	5.3	42	7_27
YMCA-0058	68.6162	-66.6513	0.35	9.45	0.07	6.1	40	8_28
YMCA-0059	68.6283	-67.2077	0.40	9.40	0.02	6.0	43	7_27
YMCA-0060	68.6398	-67.2396	0.35	9.50	0.03	5.0	33	7_27
YMCA-0061[d]	68.8659	-67.7115	0.50	9.35	0.04	8.5	85	7_27
YMCA-0062	69.1369	-67.2015	0.25	9.40	0.03	7.8	29	7_27
YMCA-0063	69.1724	-66.0549	0.30	9.45	0.06	4.9	26	8_28
YMCA-0064[e]	69.4153	-66.1983	1.30	9.15	0.15	29.2	686	8_28
YMCA-0065	69.5140	-67.7983	0.40	9.00	0.03	4.8	54	7_27
YMCA-0066	69.7150	-67.4736	0.20	9.90	0.03	4.9	19	7_27
YMCA-0067	69.7896	-67.4994	0.25	10.05	0.07	5.2	27	7_27
YMCA-0068	69.8615	-67.5558	0.20	9.65	0.02	5.5	21	7_27
YMCA-0069	69.9975	-67.3837	0.25	9.80	0.10	5.2	29	7_27
YMCA-0070	70.0166	-66.5335	0.40	9.50	0.05	6.1	62	8_28
YMCA-0071	70.3150	-67.6319	0.25	9.50	0.10	5.9	37	7_27
YMCA-0072[f]	70.4281	-66.8496	0.35	9.50	0.03	7.3	43	7_27
YMCA-0073	70.4646	-67.4433	0.20	9.20	0.02	4.6	23	7_27
YMCA-0074[g]	93.9911	-64.9727	0.65	9.25	0.04	15.0	176	9_40
YMCA-0075[h]	94.4244	-65.5472	0.45	9.45	0.05	10.8	94	9_40
YMCA-0076	95.8344	-66.5836	0.35	9.40	0.04	5.2	38	8_39
YMCA-0077[i]	96.1210	-66.5061	0.55	9.25	0.07	12.1	117	8_39
YMCA-0078	96.2493	-66.5820	0.40	9.40	0.04	7.1	54	8_39

Table 5.2: Main parameters of the SCs investigated in this work in the following order: the ID and the coordinates of the SCs; their estimated radius, age and reddening; the value of the G parameter defined in 5.1; the number of stars within the SC radius and finally the tile in which each SC resides.

ID	RA (J2000)	Dec (J2000)	R (')	$\log t$	E(B-V) mag	G	N_{stars}	Tile
YMCA-0079	97.0177	-65.5068	0.40	9.60	0.04	5.3	34	9_41
YMCA-0080	97.0752	-67.3376	0.25	9.45	0.02	5.5	20	7_38
YMCA-0081	97.1357	-70.8255	0.25	9.55	0.02	5.6	24	4_33
YMCA-0082	97.3765	-70.6610	0.25	9.30	0.01	5.0	22	4_33
YMCA-0083[l]	97.4261	-70.5884	0.75	9.30	0.05	13.3	192	4_33
YMCA-0084[m]	97.5510	-64.3280	2.05	10.05	0.02	179.6	2604	10_43
YMCA-0085	97.9656	-70.3349	0.30	9.45	0.04	5.1	26	4_33
YMCA-0086[n]	98.2584	-71.1257	0.95	9.10	0.05	27.9	336	4_33
YMCA-0087	98.7479	-70.9206	0.35	9.50	0.03	5.0	24	4_33
YMCA-0088[o]	106.9143	-69.9840	0.30	9.70	0.13	23.5	32	5_38

Reference names.

a: OGLE-LMC-CL-0841

b: HS8; KMHK5

c: OGLE-LMC-CL-0834

d: HS13; KMHK11

e: NGC1644; SL9; LW11; ESO84SC30

f: OGLE-LMC-CL-0836

g: LW444; KMHK1710

h: OGLE-LMC-CL-0758

i: OHSC34; KMHK1751

l: OHSC36; KMHK1757

m: NGC2257; SL895; LW481; ESO87SC24

n: SL897; LW483; KMHK1760

o: OHSC37; KMHK1762

inclination of the LMC disk with respect to the plane of the sky. We adopted $p_n = 149.23$ and $i = 25.86$ recently estimated by Choi et al. [2018b].

Fig. 5.3 illustrates the spatial position of all SCs superposed on the distribution of a sample of RGB stars selected from the *Gaia* EDR3 [Gaia Collaboration et al., 2021b] to guide the eye about the LMC morphology. This figure depicts a patchy distribution of the SCs around the LMC, strongly depending of the position angle, as different tiles/regions at the same radial distance from the LMC show up significant differences regarding the number of detected SCs. Indeed, clumps of SCs are separated by extended gaps (up to 2°) where no SC has been detected. Interestingly, two regions to the West side of the LMC exhibit a remarkable average higher number of SCs. In Gatto et al. [2020] we already discussed the fact that the over-density of SCs present at the conjunction between the Bridge and the LMC (tile 3_21 of the STEP survey) should be regarded as a real physical increase in the SC average density based on simple statistical arguments, after excluding any bias originated by different observational conditions among distinct tiles. In Fig. 5.3 we notice a further SC clump at (RA, Dec) $\simeq$ (65°,-67°), corresponding to the tiles $7\_26 - 7\_27 - 8\_28$. These tiles are amongst the ones with the highest number of stars, and are also amongst the closest with respect to the LMC centre. Thus, in principle, we could hypothesize that such a SC over-density is related to the highest number of stars located in these regions. Nonetheless, this argument is at odds with the detection of a very fewer SCs in some tiles with a similar number of stars (e.g. tile $8\_39 - 9\_40$) or with the total absence of SC in tiles at a similar radial distance (e.g. tile 6_24). More likely, as the SC agglomeration is located at the edge of the LMC bar, it might be connected to the highest star formation occurred in this region in the last Gyrs [Mazzi et al., 2021].

Finally, all SCs hosted by the LMC reside within 10° from the LMC centre, similar to what found previously in other works [Gatto et al., 2020, Pieres et al., 2016], although the disc extension is larger, namely 16° to the North [Saha et al., 2010], and up to $\sim$ 10° -14° to the South [Mackey et al., 2018, see also §1.2.1].

5.3.2 Discussion: the age distribution of the SCs in the LMC outskirts

Figure 5.4 shows the age distribution of the final list of candidate SCs. In agreement with what already discussed in Gatto et al. [2020], the age distribution displays a remarkable peak at about 3 Gyrs, whose tails are clearly asymmetric. The number of SCs steadily decreases towards younger ages ($t \leq 3$ Gyr), while at the opposite side, within the age gap, it sharply drops down. The sudden SC formation enhancement at $\sim$ 3 Gyr could reveal a past close

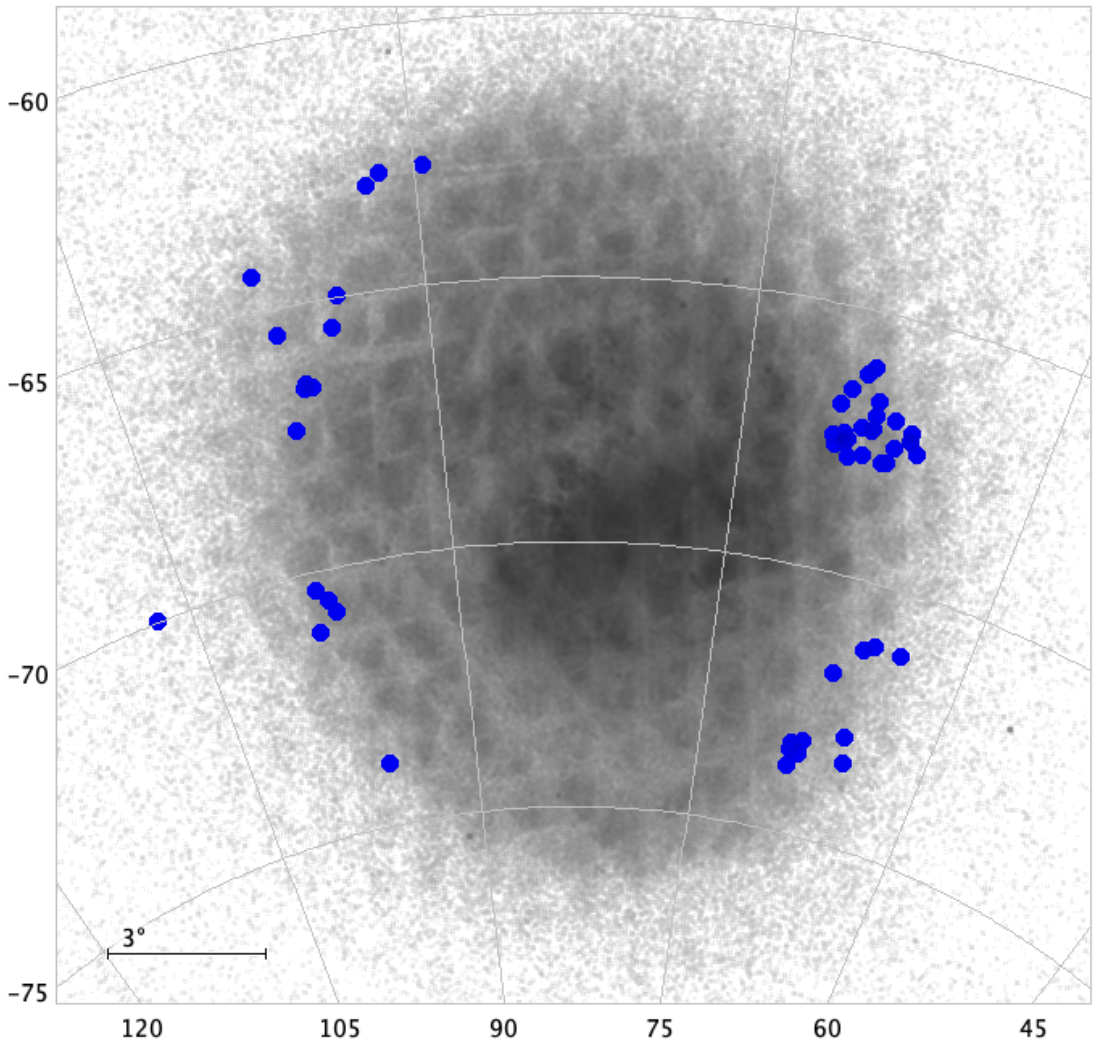

Figure 5.3: Position of the 55 SCs belonging to our combined final list, superposed to RGB stars selected from the *Gaia* EDR3 database.

encounter between the MCs, which triggered a new episode of massive SC formation. This is independently confirmed by different authors who tried to reconstruct the history of the orbital path of the MCs, and most of them agree that a past pericentric passage between the LMC-SMC happened about 2-3 Gyr ago [Bekki and Chiba, 2005, Patel et al., 2020, and references therein]. Interestingly, Pieres et al. [2016] found a similar peak at $\sim$ 2.7 Gyr by analysing the CMD of 109 SCs to the Northern side of the LMC, but they also evidenced a major peak at $\sim$ 1.2 Gyr which is absent in our SC sample. Indeed, we detected a few object as young as 1-2 Gyrs and none of them is younger than 1 Gyr, suggesting that no recent SC formation events occurred in the LMC outskirts, at least in our analyzed tiles, and in agreement with the general consensus that LMC peripheries are inhabited by an old population [Mazzi et al., 2021, Piatti and Geisler, 2013, Saha et al., 2010]. Alternatively, these results may indicate that an episodic increase in the SC formation $\sim 1-2$ Gyrs ago interested the Northern region of the LMC, investigated by Pieres et al. [2016], leaving quite unaltered the fields investigated in this work. To confirm this hypothesis, we took advantage of Mazzi et al. [2021]'s work that exploited the near-infrared VMC [Cioni et al., 2011] to derive the spatial-resolved LMC SFH in 96 deg^2, down to sub-spatial regions of 0.125 deg^2. Looking at their Figure 5, we noticed that in the 1-1.58 Gyr interval (left-lower panel in their figure), the LMC star formation was more intense within the central bar and in a morphological feature which resembles a spiral arm that departs from the West edge of the bar and wraps to the North, covering the regions investigated by Pieres et al. [2016], in a counter-clock wise. At greater look-back time, the SF is more evenly distributed around the LMC, with only the bar showing a significant SF activity. On this basis, it seems plausible to speculate that Pieres et al. [2016] explored a region where the peak in the SC formation happened about 1.2 Gyrs ago, while the LMC outskirts in the other directions, including the fields analyzed in this work, reached their maximum SF activity about 2-3 Gyrs ago, after a close passage between the MCs [as revealed also by the secondary peak at 2.7 Gyrs by Pieres et al., 2016].

Even more importantly, as shown in Fig. 5.4, we confirm the presence of several SCs in the age gap. Indeed, we detected highly reliable SCs candidates (we recall that we only included SCs with high G values, see Eq. 5.1) which fill the period between 4-7 Gyr. In particular, we also re-estimated the age of the already known SC KMHK 1762 based on the much more accurate YMCA photometry to be about 5 Gyrs old, making it a further genuine age gap SC, besides ESO121-03 and KMHK 1592 (see §6.1 where we describe in detail the analysis performed on KMHK 1762). Only 2 candidate SCs have an estimated age between 7-10 Gyr. As they have

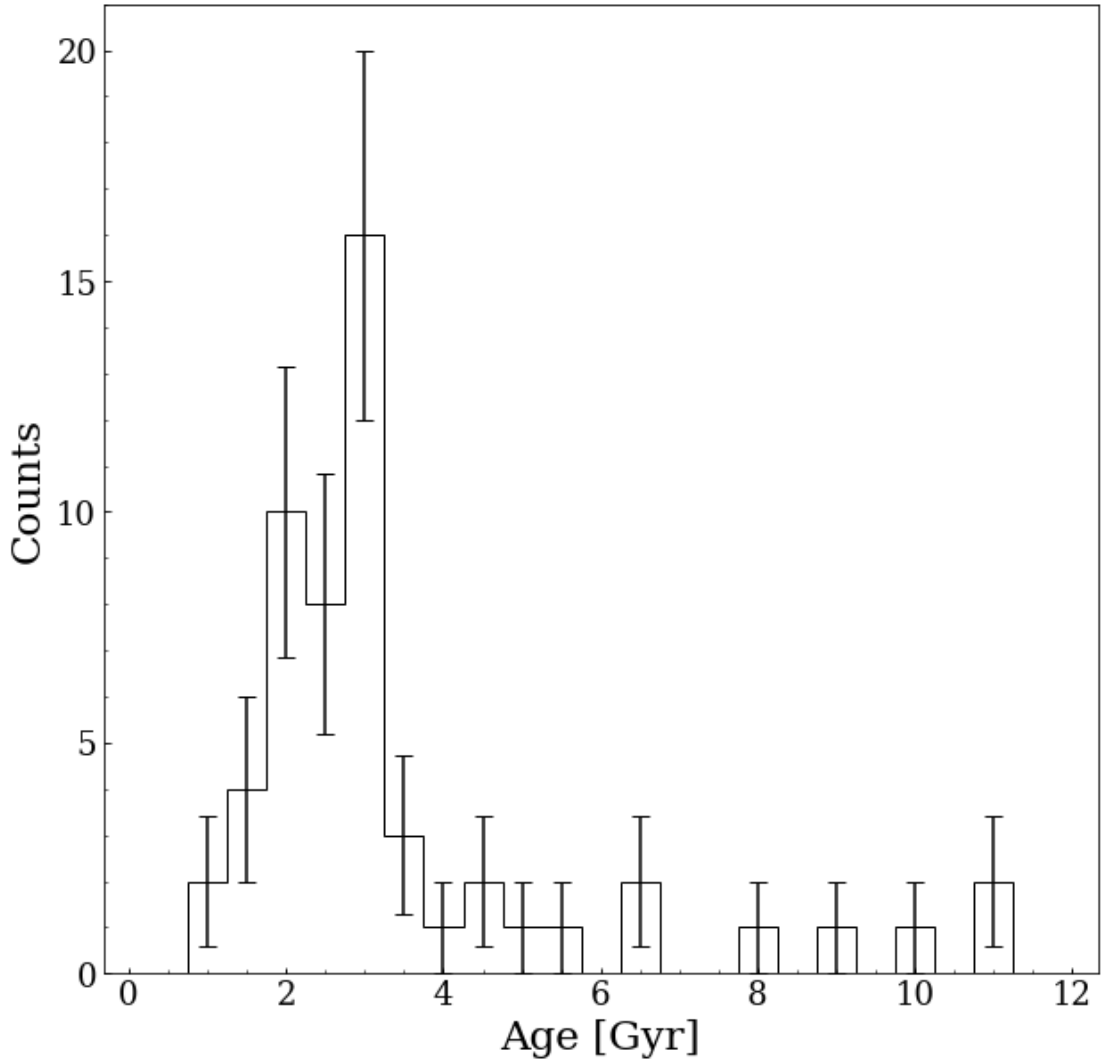

Figure 5.4: Age distribution of the 55 SCs belonging to the final combined list.

$G < 5$, deep follow up photometry is mandatory to establish definitely their reliability. On these bases, we shall conclude that the age gap is either significantly narrower than previously thought, lasting no more than 3 Gyr (e.g. between 7 - 10 Gyr), or it is only the consequence of the photometric and spatial limitations attained by the previous surveys. If confirmed, our results would fix the long-lasting debated issue about a different evolutionary path between SC and stellar field components in the LMC. A step further in this subject is thus a photometric follow-up to definitely confirm the reality of the SC candidates found in this work, especially those in the age gap. Indeed, given that the new SC candidates are generally old and faint, very deep photometry, up to four magnitudes below the MSTO (i.e. $V \sim 26.5$ mag) obtained in condition of very good seeing (to reduce confusion) would be valuable to confirm them as real physical systems. However, it is difficult to obtain such deep and spatially resolved photometry, as it can only be obtained with 8m-class telescopes in perfect weather conditions or from the HST, instruments where the competition on the observing time is extremely high. However, a great help in this direction has to be expected by the advent of the Rubin-LSST telescope which promise to deliver very deep photometry over all the southern sky, and has a special observational program devoted to the MCs [Olsen et al., 2018].

5.4 Conclusions

In this work we employed the searching algorithm described in Chapter 3 to detect undiscovered SCs in 56 YMCA tiles in the LMC periphery. Using the CMD cleaning procedure developed by Piatti and Bica [2012], we were able to identify 40 LMC candidate SCs, 27 of which represent new discoveries. We joined the candidate SCs of this work with those presented in Gatto et al. [2020], keeping only the most reliable of them, based on the condition that $G > 4.5$ (see Eq. 4.2), in order to perform a statistical analysis on a purer sample, and in turn to achieve more robust physical conclusions. From the combined list composed by 55 total SCs, among which 35 ($\sim 60\%$ of the sample) were discovered by our algorithm, we derived the following results:

- The spatial distribution of the SCs is not homogeneously distributed around the LMC. In particular, we detected an accumulation of SCs at the Western edge of the bar and a further smaller clump at the edge of the Magellanic Bridge. We suggest that the over-density at the edge of the bar reflects the higher SFR observed in the last Gyrs in the LMC bar [e.g., Mazzi et al., 2021].

- The age distribution shows a clear peak at about 2-3 Gyrs, that we suggest being the outcome of a past close encounter between the LMC and the SMC. The presence of this enhancement in the SCF is a valuable tool to constrain the N-body models carried out to recover the orbital history of the MCs.

- In agreement with Gatto et al. [2020], we identified a sub-sample of SCs within the well known age gap. Although we stress that they are candidates and a follow-up with more powerful telescopes is needed to assess their physical nature, it is also worthwhile to underline that the final list presented in this work relies on bona-fide SCs, as all of them satisfy the condition $G > 4.5$. Even if a small number of these age gap SCs were confirmed to be a real physical system, it would be a breakthrough in the knowledge of the LMC past evolution, as it will clarify a debated issue lasting for more than 30 years.

This work evidences the importance of obtaining a complete catalog of SCs to use them as a proxy of LMC SFH, as age-biased sample towards young and/or more luminous objects might strongly affect the comprehension of the dynamical evolution of a galaxy.

Chapter 6

Two outstanding SCs in the LMC - YMCA 1 and KMHK 1762.

This chapter is based on the published work on the Research Notes of the American Astronomical Society: Gatto M. et al., RNAAS, Vol.5, p.159 (2021), and on the paper submitted on the Astrophysical Journal Letters: Gatto et al., 2022b, "Deep VLT photometry of the faint stellar system in the Large Magellanic Cloud periphery YMCA-1.".

This chapter is devoted to the discussion of two particular SCs within the LMC which revealed to be very rare stellar system with respect to the ensemble of known LMC SCs, and thus such a results represent a breakthrough for the understanding of the LMC past evolution through the analysis of its SC system.

6.1 KMHK 1762: a confirmed age gap SC

In the previous Chapter we presented the discovery of several SCs in the LMC periphery through the analysis of all the YMCA tiles around the LMC with the algorithm described in Chapter 3. The catalog, which is one of the most complete in the LMC periphery, includes many age gap SC candidates, whose reliability is also sufficiently high to indicate they are actual SCs rather than randomly association of stars. However, to be more conservative, we strongly suggest that for most of them deeper photometric images, down to about 3-4 magnitudes below the MSTO are needed to prove or disprove their nature as genuine SCs. Nonetheless, among the 10 candidate

age gap SCs, the already known SC KMHK 1762[1] is different. Indeed, its reality as a bound physical system is out of question given that it has an extremely significant G value, that is $G = 23.5$, hence much higher than other already known and confirmed LMC SCs in our sample. Previous photometric observations of KMHK 1762 were carried out at the Cerro Tololo Inter-American Observatory (CTIO) with the 0.9 m telescope [Geisler et al., 1997]. They adopted the magnitude difference in the Washington T_1 filter between the giant branch clump and the MSTO (δT_1) to derive the age of KMHK 1762, obtaining $t \sim 2.7$ Gyrs. Combined with a metal content estimate of [Fe/H] $= -0.91$, based on the spectroscopic measurements of the CaII triplet for one spectroscopically confirmed member star [Olszewski et al., 1991]. This metallicity evaluation placed KMKH 1762 at a fairly lower metallicity level with respect to other SCs with similar ages [Geisler et al., 1997].

In this section we report the result of our new study of KMHK 1762 SC, based on the YMCA deep and accurate photometry, complemented with parallaxes and PMs from the *Gaia* EDR3 [Gaia Collaboration et al., 2021a].

6.1.1 Analysis

A sky map of KMHK 1762 is displayed in Fig. 6.1 (left panel). The cluster is located at about 9.8° towards the East of the LMC, making it one of the farthest SC of the galaxy, as shown in Fig. 6.1 (right panel). The centre and the radius of the cluster were determined through the technique developed and described in detail in §4.1, obtaining $(\alpha, \delta) \simeq (106.9143°, -69.984°)$ (J2000) and r$\sim$0.5'. We expect that LMC and MW field stars fall in front or in the back of KMHK 1762, thus to exploit its CMD with isochrone fitting, we must first apply a cleaning procedure to mitigate the impact of the contaminant stars. This task appear to be not straightforward in the case of KMKH 1762, as it is placed in a relatively poorly populated region of the LMC and it is thus difficult to apply the usual procedure to remove contaminants by using the CMD of representative fields around the SC (see for example the procedure described in §4.1). Therefore, to mitigate the stellar field contamination, we took advantage of the recent *Gaia* EDR3 data, with the purpose of removing likely MW foreground or LMC field stars based on their parallaxes and PMs. To this aim, we first performed a cross-match of the positions of all YMCA stars within 0.5' from the KMHK 1762 centre, with the *Gaia* EDR3 catalogue, by adopting a maximum tolerance of 1". We obtained 15 common stars[2]. Following the criterion

[1] YMCA-0088 in Table 5.2, also referred to as OHSC 37 in the Bica et al. [2008]'s catalog

[2] The small number of matches is due to the shallow limiting magnitude of *Gaia* which is $g \simeq 21$ mag.

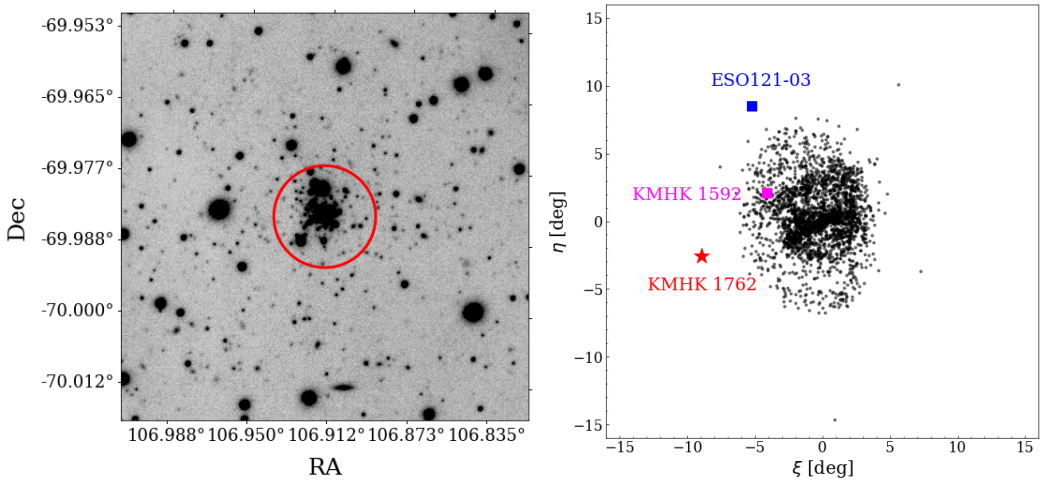

Figure 6.1: *Left:* Image of 4' in diameter in the g-band centred on KMHK 1762. The red circle indicates the SC radius of 0.5':*Right:* Relative positions of SCs collected in the Bica et al. [2008]'s catalogue with respect to the LMC centre. The red star indicates the position of KMHK 1762, whereas the blue and magenta squares mark the position of ESO121-03 and KMHK 1592, the two only genuine age gap SCs known hitherto.

described in Gaia Collaboration et al. [2021b] we looked for stars not compatible with the LMC distance by checking if $\varpi > 5\ \sigma_{\varpi}$, where ϖ and σ_{ϖ} are the *Gaia* EDR3 parallaxes and parallaxes uncertainties. Three stars satisfy the previous condition, thus they are likely Galactic foreground stars. The PMs of the remaining 12 common stars are displayed in Fig. 6.2. We clipped out stars with PMs beyond 5σ from the weighted mean (see figure) as they do not likely represent actual SC members. The agglomerate of stars which, based on their kinematics, might belong to the SC possess an average PM of $(\mu_\alpha, \mu_\delta) = (1.42 \pm 0.04), (1.31 \pm 0.04)$ mas yr^{-1}. Among them, the star with $(\mu_\alpha, \mu_\delta) = (1.09, 2.92)$ mas yr^{-1} is barely consistent with the clump of objects closely piling up around the average KMHK 1762 PM values, and only in virtue of the large uncertainties of its PMs. As it is unlikely that this object belongs to the cluster, we mark it with a different symbol in Fig. 6.2. Figure 6.3 (left panel) shows the CMD of KMHK 1762 where the stars that have parallaxes or PMs incompatible with those of the cluster are highlighted with different symbols. In the right panel of the same Figure, we displayed the CMD of a field used as a comparison, by taking all stars within an annulus of inner radius $r_{\rm in} = 1.0'$ (i.e. two times the KMHK 1762 estimated radius) having the same area of the SC. The handful of stars present in the surrounding of KMHK 1762 prevented any effort to remove contamination from field and foreground stars through the CMD, as discussed above. The left panel of Fig. 6.3 shows the CMD of KMHK 1762 with overimposed an isochrone calculated with the age and metallicity

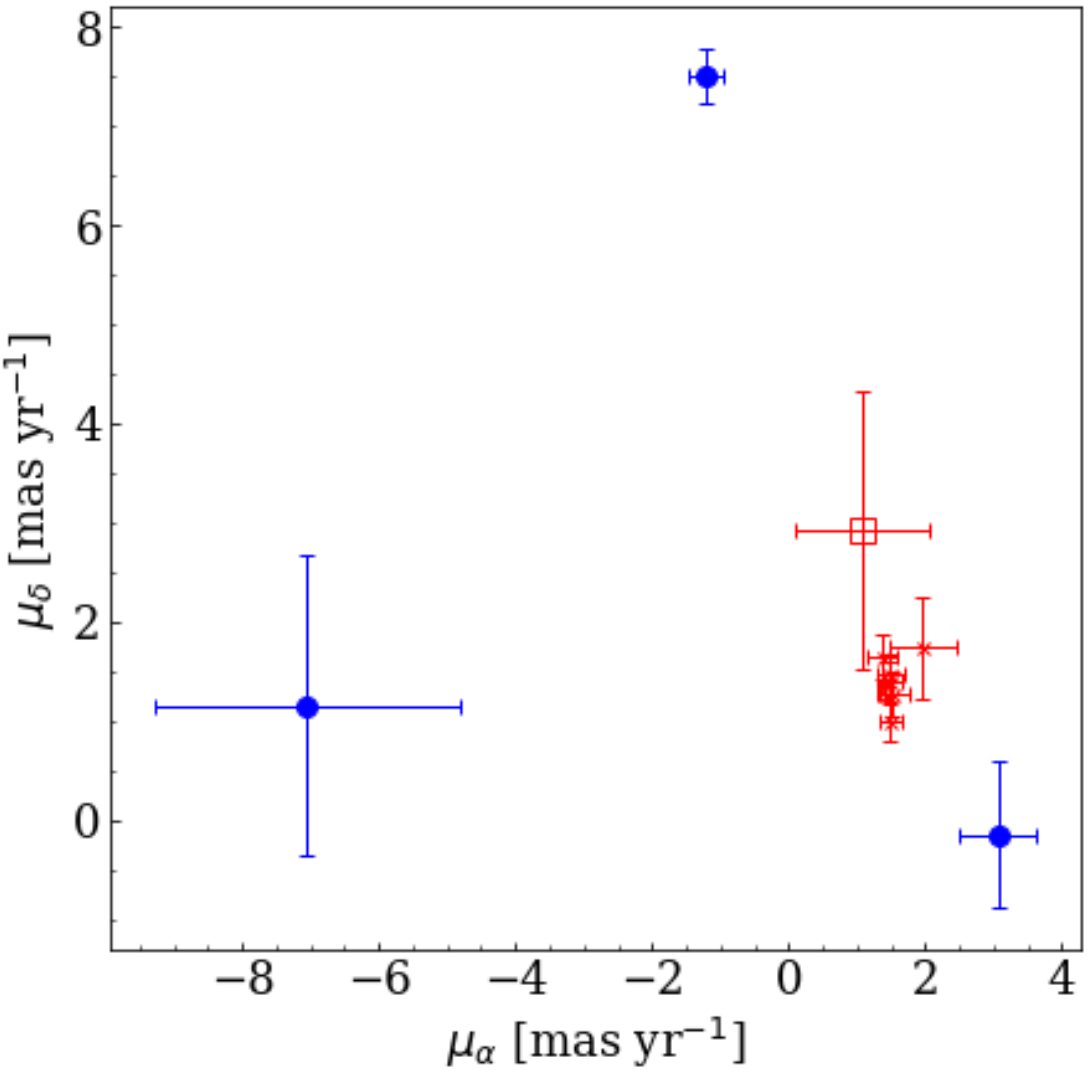

Figure 6.2: PMs of the 12 stars of KMHK 1762 having astrometric data from *Gaia* EDR3. The red crosses are the stars with PMs compatible with the cluster within their uncertainties. The empty red square indicates a star likely non-member of the cluster but with statistically compatible PMs. Blue circles are stars with measured PMs beyond 5σ from the average SC PM.

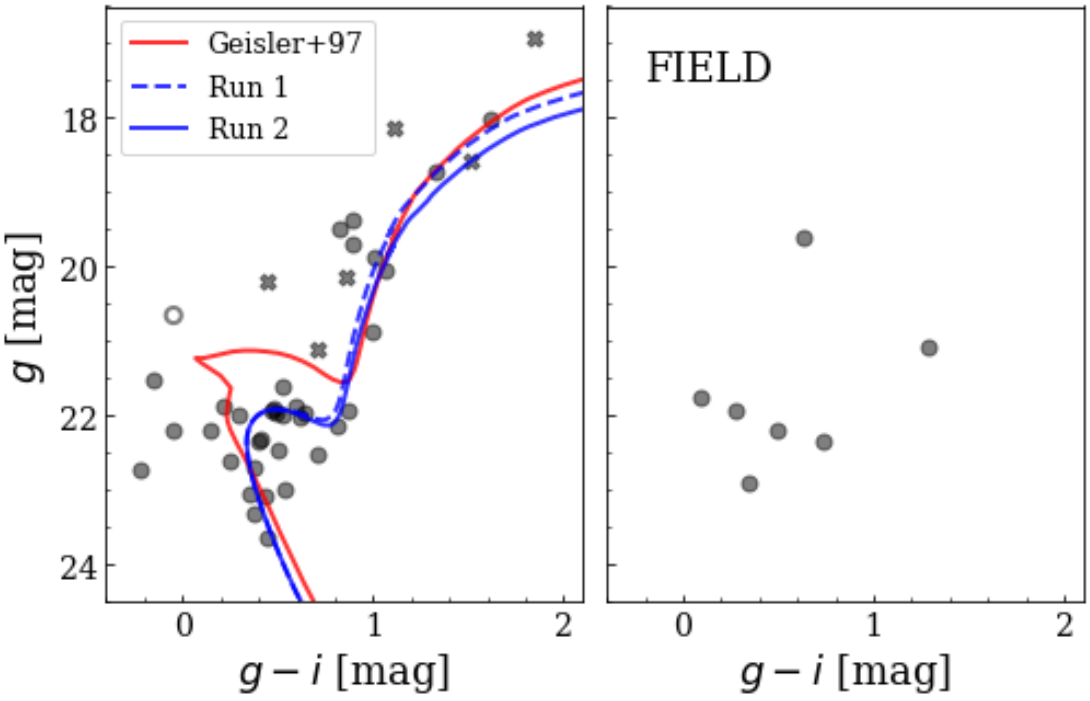

Figure 6.3: CMD of KMHK 1762. Crosses indicate stars that should not be SC members based on their parallaxes and/or PMs estimates. The empty circle indicates the star likely non-member of the cluster but with statistically compatible PMs (see text). Note that the cross-match with the *Gaia* dataset was able to clean the CMD only for stars more luminous than $g \sim 21$ mag. The red and blue lines represent the isochrone of a SSP with parameters adopted by Geisler et al. [1997], and those estimated in this work, respectively.

estimated by Geisler et al. [1997] (red solid line), that is $t \simeq 2.7$ Gyrs and [Fe/H] $= -0.91$ dex (in addition they used $E(B-V) = 0.15$ mag, and $m - M = 18.49$ mag)[3]. The isochrone does not match the SC stars on the CMD. In particular, the isochrone's sub-giant branch (SGB) is about 1 mag more luminous than the stars piled up at $g \sim 22$ mag and in the colour interval $g - i = [0.2, 1]$ which we assume to be the actual SGB of the SC. On this basis, the proper SC age should be much older than previous estimated.

We thus carried out an objective isochrone matching procedure through the Automated Stellar Cluster Analysis package [`ASteCA, Perren et al., 2015`]. `ASteCA` adopts synthetic generated single stellar populations coupled with a genetic algorithm to find the isochrone that best matches the observed CMD[4]. We performed two runs with `ASteCA` adopting two different choices for the priors. In particular, in *Run 1* we fixed the metallicity to the value [Fe/H] =

[3]We used the PARSEC isochrones [Bressan et al., 2012] which adopt $Z_{\odot} = 0.0152$

[4]Note that the `ASteCA` package at moment can only use the PARSEC isochrones [Bressan et al., 2012]

Table 6.1: Properties of KMHK 1762.

Property	Run 1	Run 2
$\log(t)$	9.74 ± 0.15 dex	9.69 ± 0.14 dex
μ_0	$18.62^{+0.24}_{-0.29}$ mag	$18.68^{+0.19}_{-0.27}$ mag
[Fe/H]	-0.91 dex (fixed)	$-0.65^{+0.27}_{-0.41}$ dex
E(B-V)	$0.09^{+0.06}_{-0.05}$ mag	$0.08^{+0.07}_{-0.05}$ mag
Mass	$1215^{+536}_{-497} M_{\odot}$	$1347^{+694}_{-523} M_{\odot}$

-0.91 dex estimated by Olszewski et al. [1991], while in *Run 2* we let it free to vary in the $-3 \leq$ [Fe/H] ≤ 0 dex interval. In both runs we restricted the distance modulus between 18 and 19 mag. In Table 6.1 we listed the output of `ASteCA` in the two configurations, while the best isochrones from each of the two runs are overlaid to the KMHK 1762 CMD in Fig. 6.3 (left panel). The isochrone calculated with *Run 1* (i.e. with fixed metallicity) better approximates the bright end of the RGB compared with that from *Run 2*, which shows a too steep RGB at $g \leq 19.5$ mag, as a consequence of the larger estimated metallicity (i.e. [Fe/H]$=-0.65^{+0.27}_{-0.41}$ dex). We therefore judge that the solution provided by *Run 1* is the best one, even if, from the purely statistical point of view the two runs provide parameters in agreement each other within the uncertainties. Obviously, a further refinement of the isochrone matching would be possible if a more accurate estimate of the KMKH 1762 metallicity were available, as the presently available empirical value is based on only one star.

6.1.2 Discussion

The age of KMHK 1762 estimated as discussed in the previous section is t$=5.5^{+2.3}_{-1.6}$ Gyr. This mean that it is the third genuine age gap SC, in addition to ESO121-03 and KMHK 1592, as mentioned in the introduction. The actual presence of an age gap among the LMC SC system is an open question, considering that both old and recent studies devoted to the reconstruction of the LMC SFH in the stellar field do not show an absence of star formation in the 4-10 Gyr interval [see e.g. Mazzi et al., 2021, Piatti and Geisler, 2013, Rubele et al., 2012, Tosi, 2004, and references therein]. Therefore, the hypothesis of a quiescent period of SC formation in the LMC during the age gap interval contradicts one of the paradigms of star formation, which foresee that a great fraction of stars is formed within SCs [Lada and Lada, 2003]. Hence, we should

conclude that we do not observe SCs in the age gap because they could have been destroyed by the tidal forces of the LMC, but this hypothesis is at odds with the steep increase of the SC age distribution at $\sim$ 3 Gyr [see e.g. Gatto et al., 2020, Pieres et al., 2016, and references therein]. Even assuming that this sharp increase in SC formation at about 3 Gyr ago is due to a close encounter with the SMC, it is however difficult to imagine an ad hoc disruption mechanisms which only act in the age interval 4–10 Gyr and becomes suddenly inefficient at an age of 3 Gyr [Da Costa, 2002].

The presence of the age gap also prevents the derivation of the age-metallicity relation (AMR) by means of the LMC SC system, as the gap is mirrored by a similar gap in the metallicity [Rich et al., 2001]. The AMR for a subsample of LMC SCs is shown in Fig. 6.4. In particular, we adopted the samples recently analysed through spectroscopic observations by Song et al. [2021] and Mucciarelli et al. [2021]. While the old LMC GCs are on average all metal-poor (the majority has [Fe/H ≤ -1.3 dex), the younger SCs have on average [Fe/H $\simeq -0.7$ dex, thus they are separated by a considerable gap in the metal content.

In between the two sup-populations stands out the presence of ESO121-03, KMHK 1592, and now KMHK 1762, thanks to its newly estimated age.

The case of KMHK 1762 appears emblematic: SC ages estimated on the basis of too shallow photometry or not correctly de-contaminated CMDs can result significantly younger than the true value. It is worth noticing that also in the case of NGC 1997, the analysis of deeper data led to an age estimate 2 Gyr older than past investigations, shifting this SC slighly into the age gap, even if it is very close to the gap younger edge [Pieres et al., 2016]. These results cast even more doubt on the physical origin of the age gap, supporting instead its explanation as an observational bias. Indeed, in §4.4 we showed that, while the spatial distribution of young SCs traces the main features of the LMC, such as the central bar or the spiral arms, that traced by SCs older than 1 Gyr is rather clumpy (see Fig.4.12), generally mimicking the regions explored with modern deep photometric observations. In fact, most of the works devoted to the research of undiscovered SCs were conducted on the basis of photometrically shallow surveys, allowing the researchers to detect only SCs younger than $\sim$ 1–1.5 Gyrs [Glatt et al., 2010, Nayak et al., 2016, Pietrzyński and Udalski, 2000]. It is therefore reasonable to assume that a consistent fraction of the LMC intermediate-age old SCs is still missing. Concluding, if the LMC SC age gap puzzle is a simple observational bias, this can be verified following two lines of action: 1) complete the census of the LMC SCs on the basis of deep and high spatial resolution photometry as we did in its outskirts (see Chapter 4 and Chapter 5); 2) re-analise the sample of known SCs in the

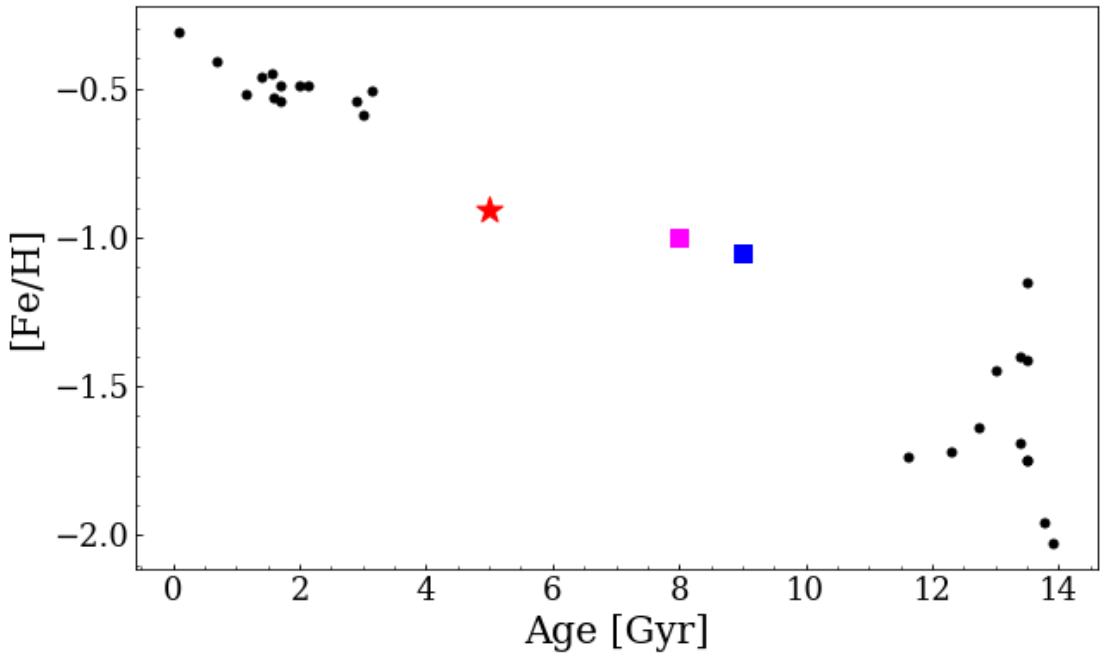

Figure 6.4: Metallicity as a function of the age for the LMC analyzed by Song et al. [2021] and Mucciarelli et al. [2021]. The red star marks the position in the plot of KMHK 1762, while blue and magenta squares indicate the SC ESO121-03 and KMHK 1592.

LMC whose ages have been estimated on the basis of too shallow photometry, as in the case of NGC 1997 and in the case of the object of present work, KMHK 1762. Both actions will certainly be possible in the near future, once the Rubin-LSST survey will enter into operation and provide the first results.

6.1.3 Summary

In this work we presented a study of the known SC KMHK 1762 based on the deep photometry provided by the YMCA survey which allowed us to construct a CMD in the g and i bands reaching at least 1.5-2 mag below the MSTO, that is significantly deeper than the previous works in the literature.

We took advantage of the PMs and parallaxes provided by the *Gaia* EDR3 to mitigate the contamination of the KMHK 1762 CMD due to LMC and MW foreground/background stars. The bright limiting magnitude of the *Gaia* mission (i.e. $g \simeq 21$ mag) allowed us to clean the CMD from non-cluster members only in the post-main sequence evolutionary phases, that are however crucial to constrain the metal-content of the SC based on the inclination of the RGB.

The SGB clearly visible at $g \sim 22$ mag indicates that KMHK 1762 is older than previously estimated based on shallower photometry. Indeed, the automatic isochrone fitting procedure performed with the `ASteCA` package yielded an age of $t = 5.5^{+2.3}_{-1.6}$ Gyr, making it the third genuine age gap SC ever discovered, after ESO121-03 and KMHK 1592. We speculate that other intermediate-age SCs analysed with shallow photometry could actually be older and thus potentially formed during the age gap period. In addition, as recently shown by Gatto et al. [2020], several age gap SCs could be hidden in the outskirts of the LMC, and due to their intrinsic faintness, can only be revealed on the basis of deep photometry. On these bases, the increased the number of confirmed or suspected SCs formed in the age gap period, suggests that the age gap may be an observational bias rather than a true quiescent period of SC formation in the LMC.

6.2 YMCA-1: a peculiar faint old LMC Globular Cluster

As already discussed in §1.2 it is largely accepted that the LMC entered into the MW halo with its own system of dwarf galaxy satellites [Kallivayalil et al., 2018]. The LMC is also known to possess at least 15 globular clusters (GCs), as old as its oldest stars (i.e. 12-13 Gyrs), which can be used to probe the earliest phases of its evolution. Indeed, a complete census of the objects orbiting a galaxy and a characterization of their chemo-physical properties represent an invaluable source of information to unveil the evolutionary history of their parent galaxy.

For example, based on accurate spectroscopic analysis, Mucciarelli et al. [2021] discovered that the old cluster NGC 2005 has been captured by the LMC from a smaller satellite galaxy now completely dissolved.

In recent years, thanks to the advent of deep panoramic surveys probing large portions of the sky, the number of faint stellar systems discovered in the vicinity of the Magellanic Clouds (MCs) has dramatically increased [Bechtol et al., 2015, Bellazzini et al., 2019, Drlica-Wagner et al., 2015, Kim and Jerjen, 2015, Koposov et al., 2015, Martin et al., 2016b, Torrealba et al., 2018], bringing new puzzle pieces to the reconstruction of the MCs evolutionary history. For example, Martin et al. [2016b] reported the discovery of SMASH-1, a faint stellar system at 11.3° in projection from the LMC centre, whose properties place it in between the classical GCs and the ultra-faint dwarf galaxies (UFDs). The compactness of SMASH-1 led the authors to suggest that it likely is an old star cluster (SC) fundamentally different from UFDs which are heavily dark-matter dominated [see e.g., Simon, 2019, and references therein]. Nonetheless, the

properties of SMASH-1 are very different from those shown by the historically known LMC old GCs. Indeed, unlike these objects, it is faint ($L_V = 10^{2.3} L_\odot$), compact ($r_h = 9.1$ pc), and highly elliptical in shape. Detecting these old stellar systems and unveiling their origin is of primary importance to understanding how the MCs and galaxies in general form and evolve. In this context, one of the main goals of the YMCA survey, discussed in §2.3 is the search of low surface brightness satellites or clusters in the outskirts of the MCs. The extensive analysis of the YMCA photometry led us to discover an uncatalogued stellar system, which we dubbed YMCA-1, placed at about 13° to the East of the LMC centre. In the following, we derive and discuss the properties of this uncommon stellar system.

6.2.1 Observations and discovery of YMCA-1

This work is based on the observations obtained with VST telescope [Capaccioli and Schipani, 2011] in the context of the YMCA survey (see §2.3 for a description of the survey and data reduction). As one of the goals of this survey is the discovery of low brightness stellar systems satellite of the MCs, streams or SCs, we run the algorithm constructed to search for over-densities in the sky (see Chapter 3 for a detailed description) on all the YMCA tiles. Besides the discovery of several new SCs described in Chapters 4 and Chapter 5, this search allowed us to identify an uncatalogued stellar system which soon appeared to have different characteristics with respect to the other SCs discovered on the YMCA tiles. Indeed, this object is placed about 13° to the East of the LMC centre within the YMCA tile 9_47, isolated and much farther from the LMC centre than the other new SCs. This over-density, which we called YMCA-1, has a significance of 12.2 sigma over the local background and is easily visible as an agglomerate of stars centred at (RA, Dec) = (110.8369°,-64.8313°), in the image shown in the left panel of Fig. 6.5.

6.2.2 Analysis

The corresponding CMD is displayed in the right panel of the same figure. Stars within 0.3′ from the system center are plotted as red filled circles, over the grey-scale Hess diagram of the population of the entire 1.0 deg^2 YMCA tile. While the number of measured stars within the selected area is very small (15 stars), their distribution in the CMD is markedly different than that of the surrounding field. In particular, none of the candidate YMCA-1 members matches the most densely populated feature of the CMD attributable to the LMC, i.e. the Main Sequence (MS) Turn Off region in the range $22.2 \leq g \leq 24.0$ mag, around $g - i = 0.6$ mag, with the

SGB at $g \simeq 22.3$ mag. The two reddest putative YMCA-1 stars, at $g - i > 2.0$ mag, are nearby interlopers according to their proper motions, as measured by the ESA/Gaia mission [EDR3, Gaia Collaboration et al., 2021a]. Most of the remaining stars seem to be aligned along a steep Red Giant Branch (RGB), typical of old and metal poor stellar systems. The CMD of YMCA-1 can be fitted with an old (age=12.6 Gyr) and metal-poor ([Fe/H]=-2.0 dex) isochrone of the PARSEC set [Bressan et al., 2012], shifted to the distance of $\simeq 105$ kpc and corrected for $E(B-V) = 0.13$ (from the Schlegel et al. 1998 maps, recalibrated after Schlafly and Finkbeiner 2011). In this solution, the distance estimate is mainly anchored to the interpretation of the faintest stars at $g \simeq 23.8$ mag as belonging to the system Sub Giant Branch (SGB). Adopting this set of parameters, we estimate $M_g \simeq -2.3$ mag (corresponding to $M_V \simeq -2.8$ mag) and $r_h \simeq 4.8$ pc, from a surface brightness profile obtained by integrated aperture photometry on concentric annuli, and fitted with a Plummer [1911] model, as displayed in Fig. 6.6. The integrated color of YMCA-1 was derived through circular aperture photometry on both the g and i images, adopting a radius equal to $0.3'$, obtaining $g - i = 1.1$ mag. The luminosity and color we estimated for YMCA-1 were used to estimate the total mass by means of the mass/luminosity - integrated color relationship available in Roediger and Courteau [2015], finding a value of $\log M/M_\odot = 3.44$ dex. As a sanity check for the mass estimate, we used a synthetic CMD, with appropriate age and metallicity, built from the PARSEC isochrones [Bressan et al., 2012], to derive the total mass of a stellar system with a similar number of RGB stars ($6 \leq N \leq 9$) as observed in YMCA-1. The estimated mass after 1000 random extractions is $\log M/M_\odot = 3.28 \pm 0.15$ dex, consistent with the value obtained through integrated properties. In this scenario, YMCA-1 would thus be a remote Milky Way star cluster, with unusual properties compared to other star clusters at similar galactocentric distances. The uncertainty is admittedly very high, but alternative interpretations provide significantly worse fits to the observed CMD. For instance, assuming the system to be at the same distance of the LMC (D = 50 kpc), and letting the isochrone best fitting YMCA-1 fit also the LMC CMD would require assuming a reddening value much larger than that provided by the Schlegel et al. [1998] reddening maps, i.e. E(B-V)=0.25 mag, as well as an isochrone with larger metallicity ([Fe/H]~ -1.3, see right panel of Fig. 6.5).

The luminosity - half-light radius diagram is shown in the top panel of Fig. 6.7, while the luminosity - galactocentric radius is shown in the bottom panel of the same figure. YMCA-1 is plotted along with 161 Galactic globular clusters taken from the Baumgardt and Hilker [2018] catalog. We retrieved reddening values from Harris [1996, 2010 version], with some exceptions as listed in Tab. 6.2. YMCA-1 could be one of the faintest star clusters ever discovered hitherto

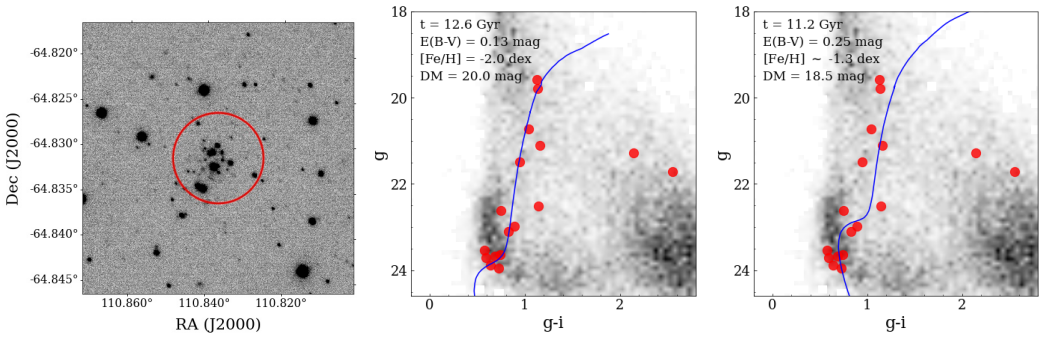

Figure 6.5: *Left:* $g-$band sky image of $1.5' \times 1.5'$ in size centred on YMCA-1. The seeing is $0.9''$ FWHM. The red circle has a radius of $0.3'$. *Centre and Right:* CMD of a $1° \times 1°$ region around YMCA-1 (gray shaded) with stars within $0.3'$ from the YMCA-1 centre, shown as red filled circles, and best fitting isochrones, assuming two different distance modulus, of the YMCA-1 CMD (blue solid lines), whose parameters are reported in the top left corner of the panels.

and definitely the most compact beyond 50 kpc. The Baumgardt and Hilker [2018] catalog lists only nine globular clusters (GCs) beyond a galactocentric distance of R_{GC}=50 kpc, three of them discovered in the last decade thanks to deep multi-band photometric surveys. With the remarkable exception of NGC 2419 ($M_V = -9.4$ mag), they are all relatively sparse clusters. Still, seven of them are significantly more luminous ($-4.7 \leq M_V \leq -5.8$ mag) and more extended (13.7 pc$\leq r_h \leq$29.0 pc) than YMCA-1, in the hypothesis that it is a distant star cluster of the MW. On the other hand, Laevens 3 [Longeard et al., 2019], at $R_{GC} = 58.8$ kpc, has structural properties quite similar to YMCA-1, i.e. $M_V = -3.1$ mag and $r_h = 7.1$ pc. Such relatively compact but very faint star clusters are very difficult to spot at such large distances from us, suggesting that several more may be still lurking in the remotest region of the Galactic halo [see also Webb and Carlberg, 2021].

However, before any firm conclusion can be drawn, follow-up with deeper photometry is required to unambiguously detect the MS of YMCA-1, to confirm its nature and reliably estimate its distance.

6.2.3 Follow-up with the VLT

As we have seen in the previous section, tthe available VST data, which revealed only a few stars in the red-giant branch (RGB) and in the top main sequence (MS), were not sufficiently deep to unambiguously establish its real physical nature, mainly because we could not obtain a robust distance for the target. Indeed, given the lack of evolved distance indicators such as Horizontal Branch (HB) or Red Clump (RC) stars, the distance can only be constrained by a clear

Cluster	Reference
BH 140	Schlegel et al. [1998]
Crater	Weisz et al. [2016]
FSR 1716	Minniti et al. [2017]
FSR 1758	Schlegel et al. [1998]
Leavens 3	Laevens et al. [2015]
RLGC 1	Ryu and Lee [2018]
RLGC 2	Ryu and Lee [2018]
Sagittarius II	Laevens et al. [2015]
VVV-CL001	Fernández-Trincado et al. [2021]

Table 6.2: List of the GCs whose extinction values were not present in Harris [1996], and their references. Reddening values taken from Schlegel et al. [1998] have been re-calibrated by Schlafly and Finkbeiner [2011].

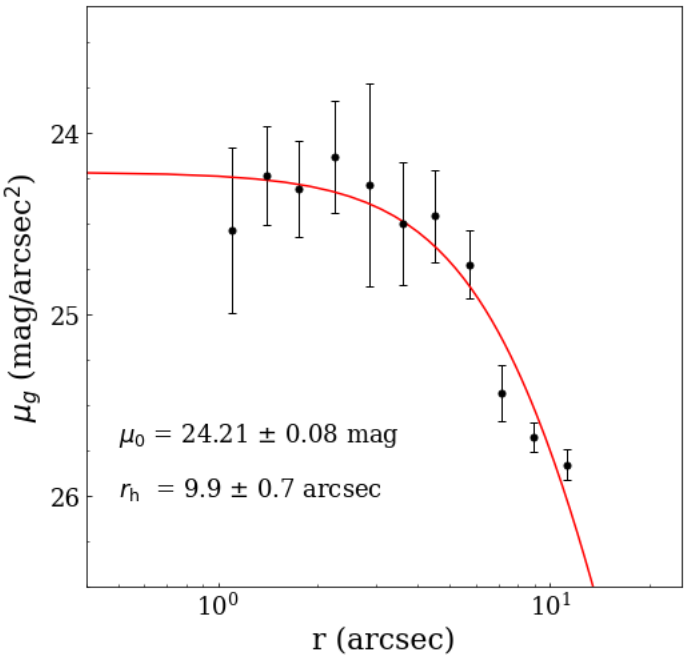

Figure 6.6: Surface brightness profile of YMCA-1. The red solid line represents the best-fit of a Plummer profile, whose parameters are displayed in the left lower corner of the figure.

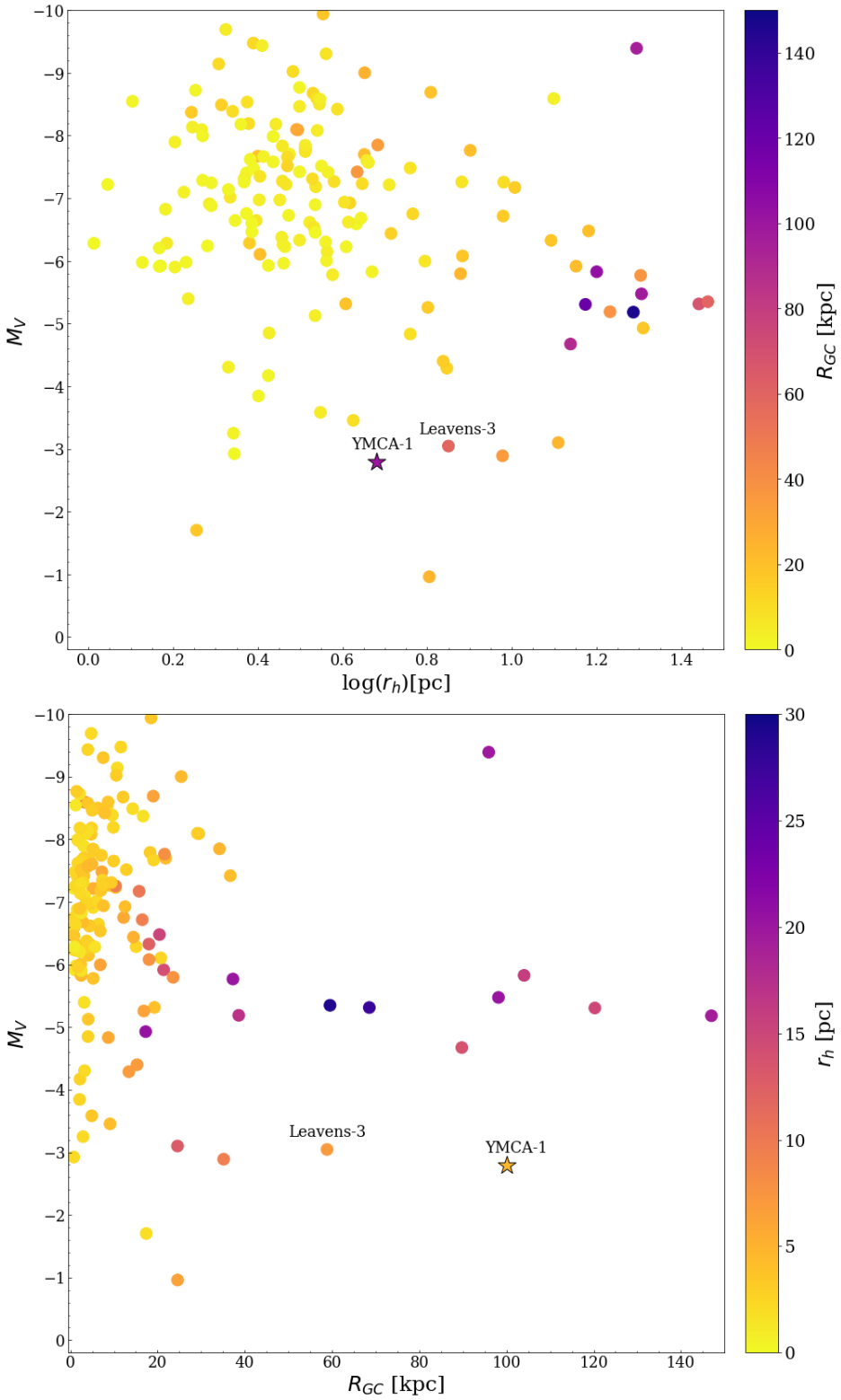

Figure 6.7: *Top:* luminosity - half-light radius diagram, with points color-coded according their galactocentric distances. *Bottom:* luminosity - galactocentric distances diagram, with points color-coded according their half-light radius. YMCA-1 is shown as a star in both panels.

identification of the MS of the system. This can only be achieved with deep follow-up photometry. Hence, to unveil the real nature of this very interesting stellar system, we submitted a proposal to the Director Discretionary Time (DDT) program of the European Southern Observatory (ESO), proposing to obtain deep photometry of YMCA-1 with the FORS2 imager which operates at the Unit Telescope 1 (UT1) of the Very Large Telescope (VLT), placed at Cerro Paranal in Chile. The proposal was accepted and the observations were carried out during the nights of November 2 and 29, 2021, for the $g_{\rm HIGH}$ and $I_{\rm BESSEL}$ filters, respectively. The observations were divided into 5 sub-exposures 480s each in the $g_{\rm HIGH}$ filter and 13 sub-exposures of 240s each in the $I_{\rm BESSEL}$-band, to reach faint magnitudes without saturating the bright members of YMCA-1. The typical seeing was of $0.51''$ and $0.72''$ in g and I respectively. For the setup of FORS2, we chose a pixel scale of 0.25 arcsec/pixel with a field of view $6.8' \times 6.8'$. FORS2 is equipped with a mosaic of two 2k×4k MIT CCDs[5]. As the dimension of YMCA-1 is much smaller than the FoV of each of the two CCDs of FORS2, we decided to place the target only on the top CCD which has a larger FoV than the bottom one. We adopted a dithering procedure between the different sub-exposures to eliminate cosmic rays and bad pixels. The images were pre-reduced (de-biasing and flat-fielding) using the standard procedures with the `IRAF` package [Tody, 1986, 1993]. To obtain the photometry, we adopted the DAOPHOT/ALLFRAME packages [Stetson, 1987, 1994] which are best suited to reach faint magnitudes in a relatively crowded field such as YMCA-1. In brief, the different steps of the procedure were the following:

- A quadratically varying PSF was modelled, by letting the code free to adopt the function which minimized the χ^2 of the fit. The most used function was the Moffat25, while in some cases the alogorithm choosed the Penny1 or the Penny2 functions. A WCS plate solution was computed for each individual image by querying the astroquery.astrometry_net python module. Then, stars' XY position were converted to WCS coordinates by using the WCSCTRAN command, available under IRAF.

- A stack of all the sub-exposures was created with MONTAGE2 [Stetson, 1987, 1994] to obtain a master list of sources on the image as deep as possible.

- ALLFRAME was run on all the sub-exposures using the derived master list as input for the stars' position

[5]see the manual at http://www.eso.org/sci/facilities/paranal/ instruments/fors/doc/VLT-MAN-ESO-13100-1543_P01.pdf

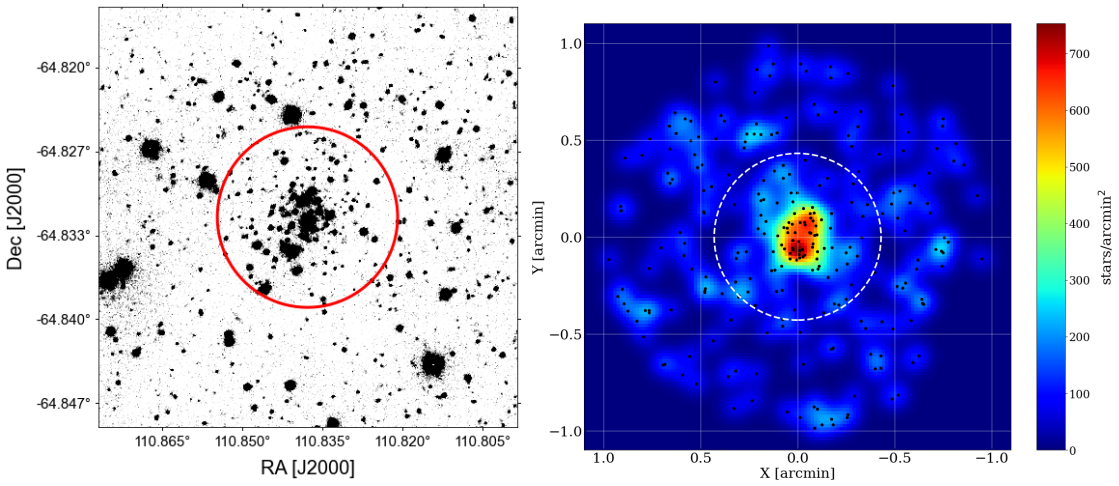

Figure 6.8: *Left:* Sky image of a region of radius r = 1' around the YMCA-1 centre. The red circle indicates the area defined by $2r_{\rm h} = 0.43'$. *Right:* Density map of stars' relative positions with respect to the YMCA-1 centre in a circular region of 1' in radius. We used a Gaussian function with $\sigma = 0.05'$ to smooth the map. Black points indicate the position of the stars, while the white dashed circle marks a radius r = 0.43', namely twice the estimated half-light radius.

- DAOMATCH/DAOMASTER [Stetson, 1987, 1994] were used to match the 5 and 13 different photometric catalogues obtained for each exposure of the $g_{\rm HIGH}$ and $I_{\rm BESSEL}$ filters. Finally, the catalogue in the two bands was put together.

To calibrate the stars we followed the same procedure described in §2.3.2 with the main difference that we adopt the VST catalogue of the tile YMCA 9_47 instead of the APASS one. In the end we obtained the following calibration equations: $g = 9.6558 - 0.0325 * (g - i)$ with $rms = 0.044$ and $i = 8.6749 + 0.0946 * (g - i)$ with $rms = 0.055$.

Before exploiting the YMCA-1 photometric catalogue obtained as described above, we applied a cleaning procedure to remove undesired extended sources and the remaining few spurious detections. To this aim, we used the SHARPNESS parameter of the *DAOPHOT* package, retaining only sources having $-0.15 < SHARPNESS < 0.15$.

6.2.4 Analysis of VLT data

The first step of the analysis consisted in estimating the centre of YMCA-1 by means of a technique based on a KDE algorithm (see §7.2.1). As a result, the coordinates (J2000) of YMCA-1 centre are (RA, Dec) = (110.8378°, -64.8319°). The left panel of Fig. 6.8 shows a sky map of the region (radius = 1') around the YMCA-1 centre, while the right panel displays a density map of the same region, smoothed by means of a Gaussian function with bandwidth = 0.05'. There is

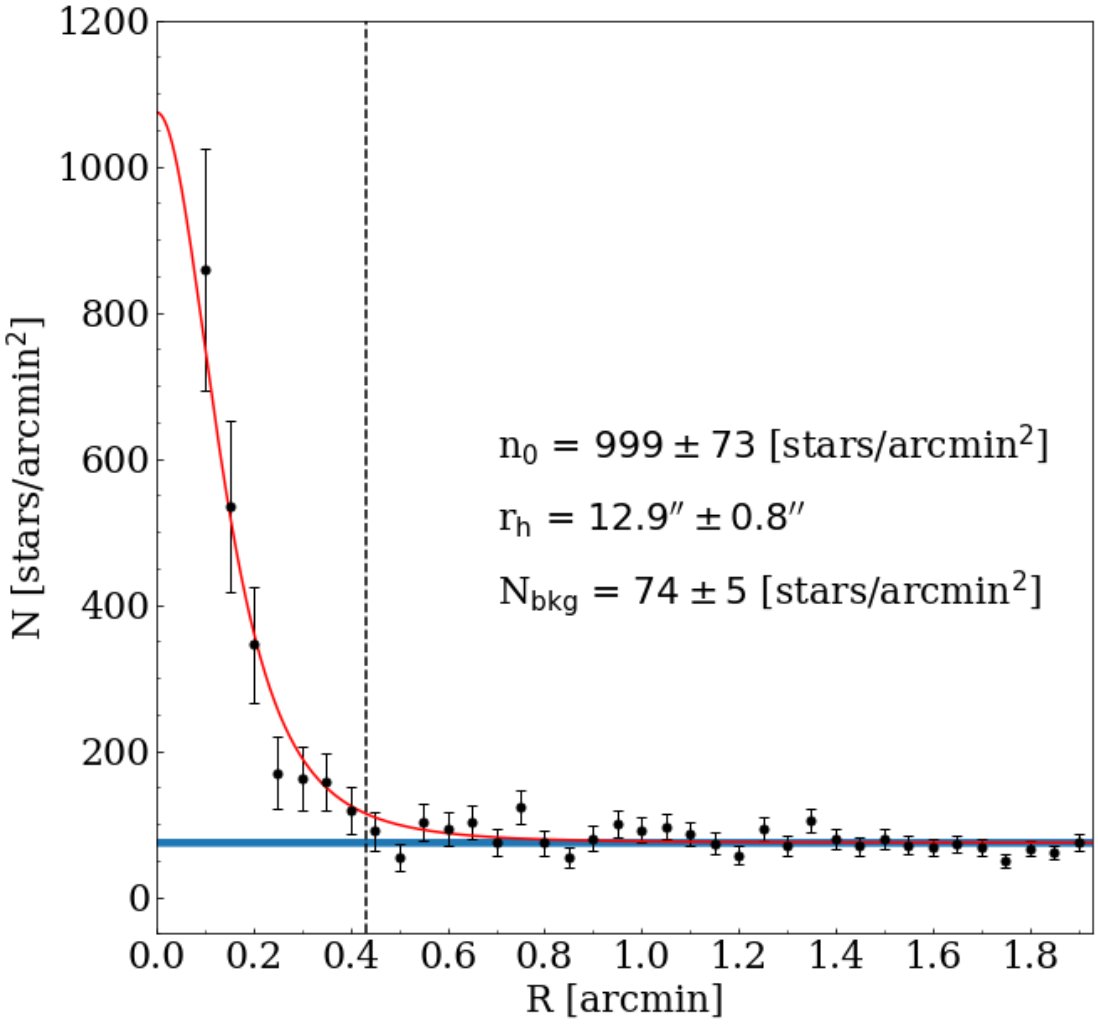

Figure 6.9: Radial density profile of YMCA-1. Each point represents the density of stars in shells having a radius of 0.05'. Errors are Poissonian. The red solid line is a best fit of a Plummer model as indicated in the text, whose parameters are indicated at the centre of the figure. The horizontal blue strip region marks the $N_{bkg} \pm 1\sigma$ estimated values. The vertical dashed line is at r = 0.43', namely $2r_h$.

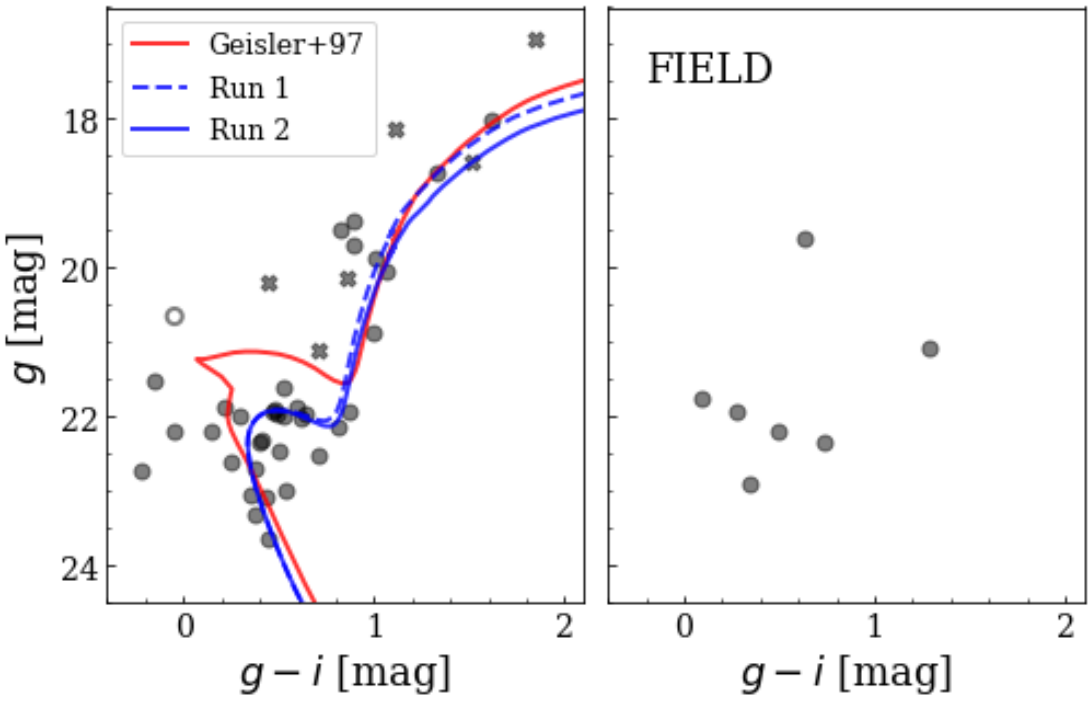

Figure 6.10: *Left:* Stars whose photometry was obtained with the VLT (red points) within $r_h = 0.43'$ from YMCA-1 centre. In the background, as grey points, the stars whose photometry was obtained with the VST and within 30' from YMCA-1 centre. The blue solid line represents the best isochrone found with the ASteCA python package matching YMCA-1 stars, whose parameters are reported in the left top corner. *Right:* Same as the left panel, but the red points are stars of a representative local field, which is a shell having an inner radius of 1' and outer radius set in order to have the same area adopted in the left panel.

a remarkable over-density of stars with respect to the YMCA-1's surroundings, clearly asserting the presence of a stellar system. These maps also suggest that YMCA-1 might be slight elongated in the North-West South-East direction. To explore this possibility, we adopted the same method used by Martin et al. [2016a] to estimate (among the other parameters) the ellipticity and position angle of SMASH-1 [Martin et al., 2016b]. However, the result was inconclusive and therefore in the following we employ a conservative approach, neglecting any possible elongation in the analysis of YMCA-1. Fig. 6.9 displays the radial density profile (RDP, number of stars per squared arcmin) of YMCA-1 built by using concentric shells of 0.05' size. We modeled the RDP with a Plummer [1911]'s profile, whose analytic form is the following:

$$n(r) = \frac{n_0 \cdot r_{\rm h}^4}{(r_{\rm h}^2 + r^2)^2} + N_{\rm bkg} \tag{6.1}$$

where n_0 is the central surface density, r_h is the half-light radius, and N_{bkg} is the estimated level of the background density. The free parameters of the model are n_0, r_h and N_{bkg}. To fit the model to the data we adopted the `curve_fit` routine of the `scipy` python library, which allows us to estimate the best parameters of the Plummer's model through a non-linear least-squares method. The outcomes of the fit are labeled in Fig. 6.8 (right panel). In particular, the half-light radius r_h is an important parameter to select in an objective way stars likely members of YMCA-1.

In Fig. 6.10 (left panel) we display the CMD of YMCA-1 within a radius R=0.43′ around its centre, corresponding to twice the half-light radius r_h. The right panel of Fig. 6.10 displays the CMD of a representative local field, taken at 1′ from YMCA-1 centre and having an area as large as the area adopted in the left panel. In the background of both panels of the same figure, we show the stars observed with the VST in a region of 30′ around YMCA-1. The CMD of YMCA-1 shows a well-defined MS, which extends below g=26 mag, that is at least 2.5 mag below the Turn-Off (TO), while the morphology for g <24 mag is similar to that depicted by the VST data. The comparison with the field provides further confirmation about the physical reality of YMCA-1. To exploit our deep CMD we adopted the Automated Stellar Cluster Analysis package [`ASteCA, Perren et al., 2015`] which allows us to perform an automated search of the best isochrone model which matches the data. In particular, `ASteCA` compares the position of the stars in the CMD with those of synthetic generated single stellar populations (SSP), adopting a genetic algorithm to find the best solution [see Perren et al., 2015, for full details]. We ran `ASteCA` on a set of PARSEC isochrone models [Bressan et al., 2012] to estimate age, reddening, metallicity, distance modulus and mass values of YMCA-1 and their uncertainties. To speed up

the operations with the `ASteCA` package, we feed it with realistic priors, namely: t $\geq$ 10 Gyrs, E(B-V) $\leq$ 0.3 mag, $10^{-3} \leq$ Z $\leq 10^{-1}$ and 18.0 $\leq$ (m - M) $\leq$ 19.50 mag. The results of the application of `ASteCA`, are listed in Table 6.3. The isochrone with the best fitting parameters is overlaid on the data in the left panel of Fig. 6.10. The `ASteCA` fit provides a distance modulus $\mu_0 = 18.72^{+0.15}_{-0.17}$ mag which corresponds to about 55 kpc, which is a significantly smaller value compared to the ∼100 kpc estimated with the shallower VST photometry [Gatto et al., 2021]. Similarly to the analysis with VST data, we find that the age of YMCA-1 is $t \sim 11.7^{+1.7}_{-1.3}$ Gyr, but with a higher metallicity ([Fe/H] $\simeq -1.12^{+0.21}_{-0.13}$ dex)[6]. It is confirmed that YMCA-1 is a low-mass (M $\simeq 10^{3.03} M_{\odot}$) and compact ($r_h = 3.5 \pm 0.3$ pc) stellar system.

Figure 6.10 also shows that the average main-sequence turn-off (MSTO) of the LMC field seems to be brighter compared to that of YMCA-1. As the LMC stellar population at the outer rim of the LMC disc should also be old and metal-poor [Mazzi et al., 2021], we speculate that the magnitude difference between the LMC and YMCA-1 MSTOs raises from a different distance modulus. The currently adopted distance for the LMC centre is $\sim$ 49.6 kpc [e.g. Pietrzyński et al., 2019], which corresponds to a distance modulus of DM $\sim$ 18.49 mag, but the LMC disc is inclined in such a way that the North-East side (i.e. where YMCA-1 resides) is closer to us [e.g., Choi et al., 2018b][7]. Therefore, YMCA-1 should be placed well behind the LMC main disc.

6.2.5 Discussion

The estimated distance of YMCA-1 suggests that it is likely associated to the LMC. Indeed, its three-dimensional distance from the LMC is $\sim$ 13 kpc, well within the LMC tidal radius [i.e. ∼16 kpc measured by van der Marel and Kallivayalil, 2014]. However, the possibility that YMCA-1 is incidentally projected beyond the LMC but not physically associated to this galaxy cannot be ruled out yet, as we still lack radial velocity measurements of its member stars.

To further investigate the YMCA-1 properties, it is useful to compare them with those of SMASH-1, which appears to have close similarities with YMCA-1. To this aim, we first estimate the total luminosity of YMCA-1 with a technique similar to that described in §6.2.2. In brief, we adopted a synthetic SSP with $t \simeq 11.7$ Gyr and [Fe/H] $\simeq -1.12$ dex (corresponding to the best isochrone found with `ASteCA`) constructed by means of the PARSEC isochrones[8]. Then, we measure the total luminosity of the synthetic SSP with a comparable number of MS stars

[6] We adopted the PARSEC $Z_{\odot} = 0.0152$ value.

[7] There is any definitive evaluation of how closer to us the LMC is at YMCA-1 distance.

[8] http://stev.oapd.inaf.it/cgi-bin/cmd

Table 6.3: Properties of YMCA-1.

Property	Value
RA (J2000)	110.8378°
Dec (J2000)	-64.8319°
Age	$11.7^{+1.7}_{-1.3}$ Gyr
μ_0	$18.72^{+0.15}_{-0.17}$ mag
[Fe/H]	$-1.12^{+0.21}_{-0.13}$ dex
E(B-V)	$0.19^{+0.04}_{-0.02}$ mag
Mass	$1080^{+366}_{-300} M_\odot$
r_h	3.5 ± 0.3 pc
L_g	$10^{2.1\pm0.3} L_\odot$
L_i	$10^{2.1\pm0.4} L_\odot$
M_g	-0.18 ± 0.50 mag
M_i	-0.83 ± 0.55 mag
M_V	-0.47 ± 0.57 mag

as observed in YMCA-1. In particular, we consider only YMCA-1 MS stars in the magnitude interval $23.5 \leq g \leq 25$ and with a maximum colour distance of 0.2 mag from the best isochrone (i.e. 24 ± 5 YMCA-1 stars by adopting the estimated $\mathrm{r_h} = 0.43'$). The bright limit was set to select only MS stars, avoiding the use of the much less populated sub-giant branch (SGB) and RGB phases. The faint magnitude limit, instead, was chosen to take into account that at a fainter level the completeness problems could become significant. After 500 random extractions we estimated a total luminosity for YMCA-1 equal to $L_g = 10^{2.1\pm0.3} L_\odot$ and $L_i = 10^{2.1\pm0.4} L_\odot$.

In Fig. 6.11 we display the luminosity (M_V[9]) and half-light radius of YMCA-1 and SMASH-1, in comparison with those of old LMC GCs for which structural parameters were available in literature, and dwarf spheroidal galaxies (dSph) as well as UFDs from Simon [2019]. The figure

[9]To estimate M_V of YMCA-1 we first transformed L_g and L_i into M_g and M_i. Then we used the following color transformation: $V = g - (0.361 \pm 0.002)[(g-i) - 1.0] - (0.423 \pm 0.001)$ with rms=0.024 mag. This equation was derived using several thousands of stars in the outskirts of the MCs having $V\,g\,i$ data from the APASS (The AAVSO Photometric All-Sky Survey) survey (https://www.aavso.org/apass).

also shows the position of the old MW GCs whose parameters were taken from Baumgardt and Hilker [2018] and Harris [1996] (see also caption of Fig. 6.11). The proximity of YMCA-1 and SMASH-1 in this diagram is noticeable. Both stellar systems lie in the region of the M_V vs r_h space occupied by some peculiar faint MW GCs, such as AMR 4, Palomar 1, Koposov 1 and Koposov 2, and also near to objects with difficult classification but suspected to be at the faint end of the UFDs distribution. Even more interesting is the difference between YMCA-1 and the known old LMC GCs, which are located in a completely different locus of the M_V vs r_h plane. They are several orders of magnitude more luminous and reside in the same parameter region occupied by the majority of the MW GCs. Therefore, YMCA-1 and SMASH-1 might belong to a peculiar sub-class of stellar systems within the LMC whose properties are in between the classical GCs and the UFDs. Unlike the more massive GCs, these low-dense objects are more sensitive to the external tidal fields and hence can be subject to complete disruption, which might explain the scarcity of these stellar systems in the LMC. Indeed, Martin et al. [2016b] concluded that SMASH-1 is experiencing an ongoing tidal disruption, based on its strong ellipticity and its estimated tidal radius. Of course, other faint LMC-bound systems could still lay undiscovered in the outermost regions of the LMC. Finally, Fig. 6.12 shows the relative position of the LMC SCs with respect to the LMC centre. The picture reveals that YMCA-1 and SMASH-1 are among the farthest SCs ever detected around the LMC, but they are not spatially close, as the former is found to the East of the LMC, while the latter is in the South. Moreover, YMCA-1 is superimposed (but not necessarily associated) to a substructure recently discovered in the north-est of the LMC (i.e. the North-East Structure, see §8).

To summarize, YMCA-1 is likely an LMC old GC with features very similar to SMASH-1. Spectroscopic follow-up of both these interesting stellar systems can be very valuable to confirm their association with the LMC. Until such spectroscopic confirmation is obtained, we cannot discard the less likely hypothesis that YMCA-1 (and possibly SMASH-1) is instead a MW remote GC.

6.2.6 Summary

In this work we exploited the FORS2@VLT follow-up of YMCA-1, a new stellar system discovered within the context of the YMCA survey, placed at about 13° from the LMC centre. The deep catalogue obtained in this work ($g \sim 26.5$ mag) allowed us to definitely confirm that YMCA-1 is a real physical stellar system. The exploitation of its CMD by means of the automatic isochrone fitting package `ASteCA` [Perren et al., 2015] and the analysis of its radial density profile, reveals

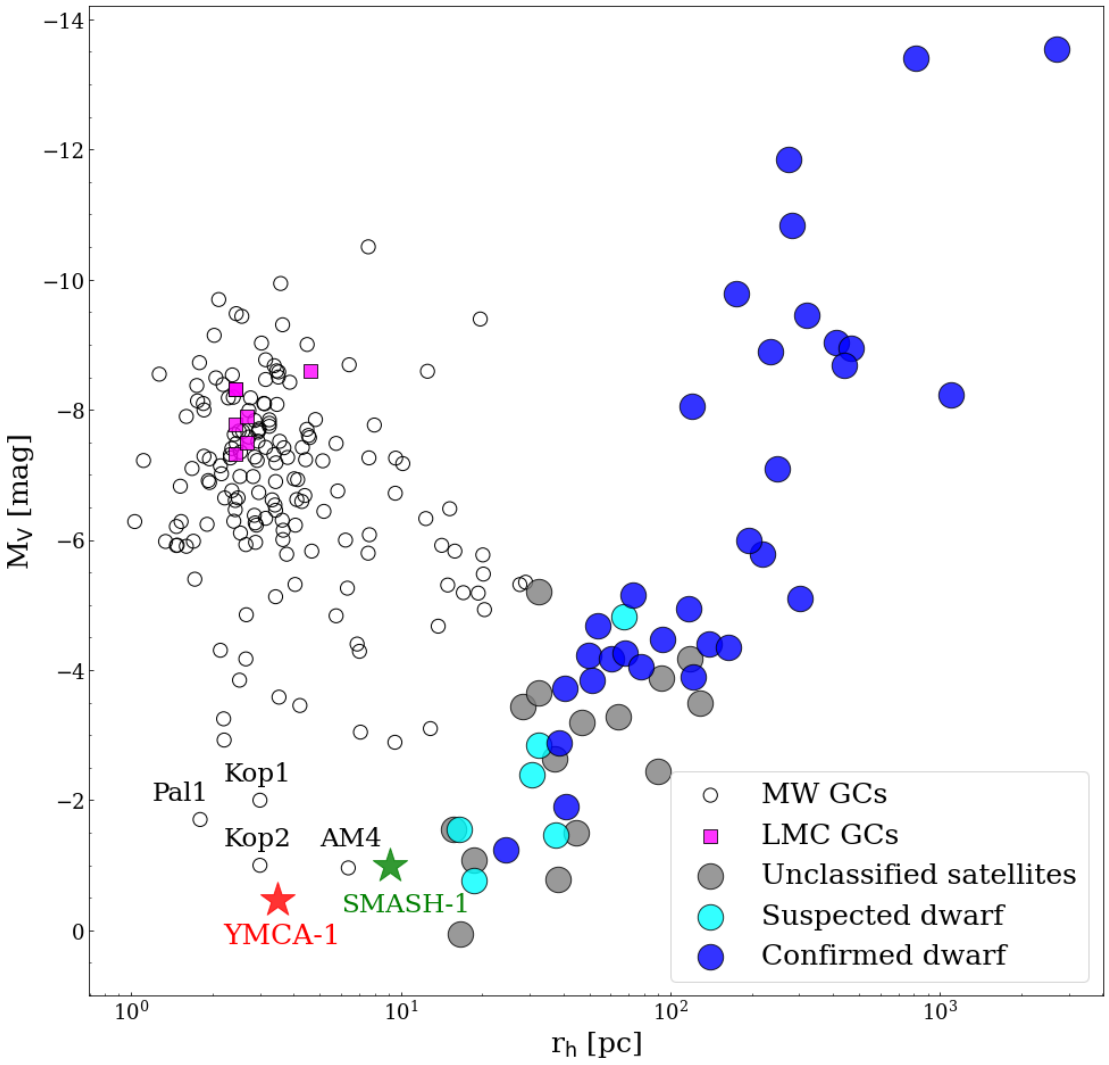

Figure 6.11: M_V versus r_h in which we depict the position in this plane of YMCA-1 and SMASH-1 (coloured stars), of some old LMC GCs (magenta squares; r_h taken from Piatti and Mackey 2018 and M_V taken from Mackey and Gilmore 2003a) and MW GCs (empty circles; taken from the Baumgardt and Hilker [2018] catalog and from Koposov et al. 2007). We retrieved reddening values from Harris 1996, 2010 version, with some exceptions as listed in Tab.1 in Gatto et al. 2021). Finally, we also indicate the position of some confirmed and probable dwarfs (coloured circles) reported in the Supplementary Table 1 in Simon 2019.

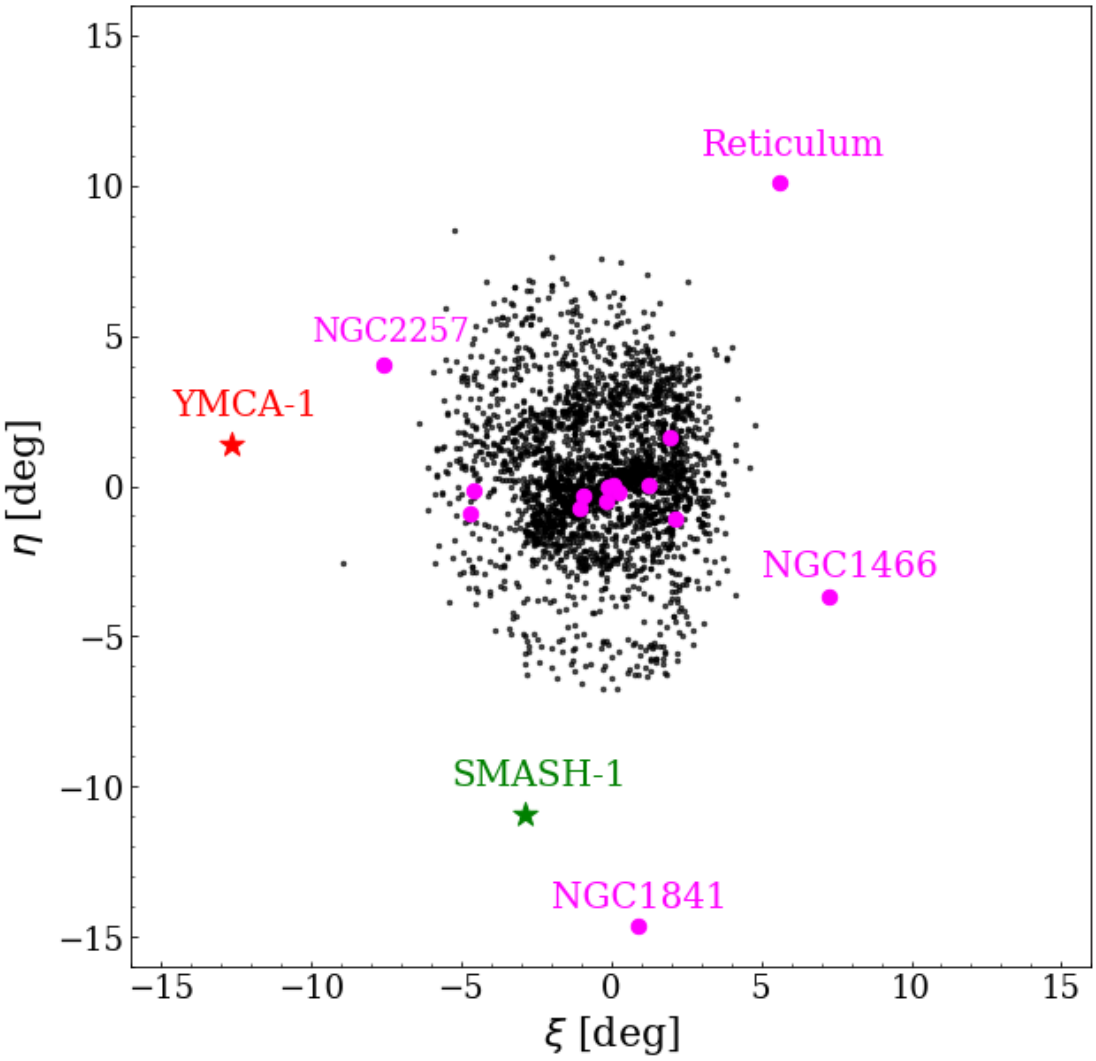

Figure 6.12: Relative position with respect to the LMC centre of the SCs present in the Bica et al. [2008]'s catalog (black dots), old GCs (magenta points) and YMCA-1 and SMASH-1. Names of the outermost old GCs are also reported in the figure.

that YMCA-1 is an old ($t = 11.7^{+1.7}_{-1.3}$ Gyrs), metal-intermediate ([Fe/H] $\simeq -1.12^{+0.21}_{-0.13}$ dex), low-mass (M $\simeq 10^{3.03} M_{\odot}$) and compact ($r_h \sim 3.5 \pm 0.3$ pc) stellar system. The new estimate of YMCA-1 distance modulus suggests that it could belong to the LMC rather than to the MW halo as supposed on the basis of previous shallower VST data [Gatto et al., 2021]. Nonetheless, the uncertainties on its distance do not allow us to definitely rule out the possibility that YMCA-1 is indeed a satellite of the MW. YMCA-1 properties are remarkably different from the ones of the 15 known old LMC GCs, as they are all very massive. As far as we are aware, only SMASH-1 [Martin et al., 2016b] exhibits properties similar to that of YMCA-1, an occurrence that might indicate they have a common origin. Spectroscopic measurements of the brightest stars belonging to YMCA-1 (and SMASH-1) with the aim of obtaining their radial velocities and evaluating their metal abundances are pivotal to assess their LMC membership and to unveil the origin of these very interesting and rare stellar systems.

Chapter 7

Dynamical study of the SMC SCs through their surface brightness profile

This chapter is based on the work published on the Monthly Notices of the Royal Astronomy Society (MNRAS), Gatto et al., 2021, MNRAS, Vol. 507, p. 3312-3330, devoted to the analysis of a subsample of 170 SMC SCs with the purpose of deriving insights on their inner evolution.

The MCs represent an ideal test-bed to probe the main physical mechanisms driving the evolution of the SCs during their lifetime (see the detailed discussion in §1.2.5). A key ingredient for the study of the dynamical evolution of SCs is the availability of accurate and homogeneously derived SBPs, extending as far as possible from the cluster centre. Here we focus on the SMC, which contains a large sample of SCs and for which we can exploit the deep and accurate photometry provided by the STEP survey. The most complete and recent catalog by Bica et al. [2020] reports about 850 SMC objects classified as SCs. Historically, the SPB shapes Galactic globular clusters (GGC) are approximated with the so called King profiles [e.g., King, 1962, see also §C.1]. However, Elson et al. [1987] pointed out that a different kind of analytical function, nowadays called Elson, Fall and Freeman (EFF) profile, better describes the SBP of the LMC SCs. The main difference between the two quoted profiles is that the latter does not present a "truncation" at large radii that separates the SC from the field. Which of the two profiles better represent the SBP shape of the MCs SCs is still debated. Hill and Zaritsky [2006] and afterwards

Werchan and Zaritsky [2011] analyzed structural parameters of 204 SMC and 1066 LMC SCs, respectively, fitting the SBP with both the above mentioned profiles. Despite the significant statistical sample of analysed SCs these authors did not find any favored profile, both of them were satisfactory for the majority of the SCs, with King profiles performing slightly better. Very recently, Santos et al. [2020] carried out a detailed analysis of 83 SCs located at the periphery of both the MCs in the context of the VIsible Soar photometry of star Clusters in tApii and Coxi HuguA [VISCACHA Maia et al., 2019] survey, with the SOuthern Astrophysical Research (SOAR) telescope. The analysis of the SBPs of these 83 SCs, fitted with both King and EFF profiles, allowed these authors to confirm that the SPBs can be matched almost equally well by both EFF and King models. At the same time, they assessed the presence of an evolution of $r_{\rm c}$ for older SCs in both the LMC and SMC, as already suggested in the literature (see the detailed discussion in §1.2.5).

In this chapter we take advantage of the STEP photometry in the SMC (see §2.2) to carry out a detailed analysis of the dynamical evolution of a conspicuous sample of SMC SCs, deriving their main properties through the analysis of their SBPs in the g band and CMDs in the g and i bands. Our aim is to provide the scientific community with new accurate structural parameters like sizes, luminosities and masses, derived via fitting of both King and EFF profiles. We also supply age estimates for a subsample of SCs. Our sample consists of 170 SMC SCs which are already listed in the catalogue by Bica et al. [2020], located throughout the inner parts (most of them reside within $\sim$ 2-3 deg) of the SMC, and spanning a wide range of ages and masses. Of these 170 SCs, 62 have never been examined before. Our sample extends the range of masses towards values lower than those already present in the literature. As far as we are aware, it is the first time that a wide-range of structural parameters, from sizes to masses, have been derived homogeneously in the SMC. Moreover, these features are used to study the dynamical phase of SCs, probing the age of the SMC SC system, from the dynamical point of view. Finally, SC properties are also used as a tool to gain hints on the SMC environment by inspecting how they depend on the distance from the SMC centre. As already described in (see §2.2) the STEP survey reaches $g\sim$25 mag (in non-heavily crowded regions), well below the MSTO of the oldest stellar population, allowing us to investigate accurately even SCs with very low surface brightness. The high resolution of STEP even at faint magnitudes makes it feasible to achieve a reliable accuracy even for SCs of $\sim$ 100 solar masses, probing in detail a locus of the parameter space barely explored with a conspicuous number of SCs.

7.1 Construction of the SC sample

To achieve the proposed goals, we built a statistically significant sample of SCs, covering as much as possible different regions of the SMC. We focused our research on all objects classified as star clusters (i.e., those indicated with the letter *C* in the column TYPE of the catalogue) by Bica et al. [2020]. Then, we restricted the list to those SCs whose spatial positions overlapped with tiles 3_3, 3_4, 3_5, 3_6, 3_7, 3_8, 4_4, 4_5, 4_6, 5_5, 5_6 [see Ripepi et al., 2014, their Fig. 2 and Table 2 for the definition of the tiles].

Despite our efforts, we could not analyse all the 404 SCs present in Bica et al. [2020]'s catalogue and falling on the above quoted tiles. In fact, we had to discard almost all the SCs with a minor axis smaller than $\sim 0.5'$, corresponding to about 40% of the starting list, because they showed too noisy SBPs. Moreover, we had to reject also those SCs whose centres were too close to the edges of the tile ($\sim$10%) or which on the images did not appear as real SCs ($\sim$10%). At the end, we were left with 170 usable SCs. Figure 7.1 shows the SC relative positions with respect to the SMC centre defined by classical Cepheids variables: (α_0, δ_0) = (12.54°, -73.11°), [Ripepi et al., 2017]. This centre is very similar to the one adopted by Gonidakis et al. [2009] based on K and M giants, i.e. (α_0, δ_0) = (12.75°, -73.10°).

7.2 Method

For each SC we derived the SBP (i.e. mag/arcsec^2 as a function of the cluster-centric distance) by means of integrated aperture photometry. After a careful analysis of SPBs in both the g and i bands, we choose to work with the $g-$band, since the data in this filter provide significantly less noisy SPBs for the large majority of the SCs in our sample. Detection of individual stars in such distant and crowded clusters is biased by significant incompleteness, with strong variation with distance from the cluster center. Integrated photometry overcomes this problem, allowing a safe tracing of the light density distribution.

7.2.1 Star cluster centre estimation

The key to compute accurately the SBP of a SC is to carefully determine its centre. This sample contains many SCs that are very patchy and irregular, making the centre estimation procedure rather tricky. Since the majority is also asymmetric, it is unsuitable to make use of algorithms, such as the mirror-autocorrelation method described by Djorgovski [1988] which takes advantage

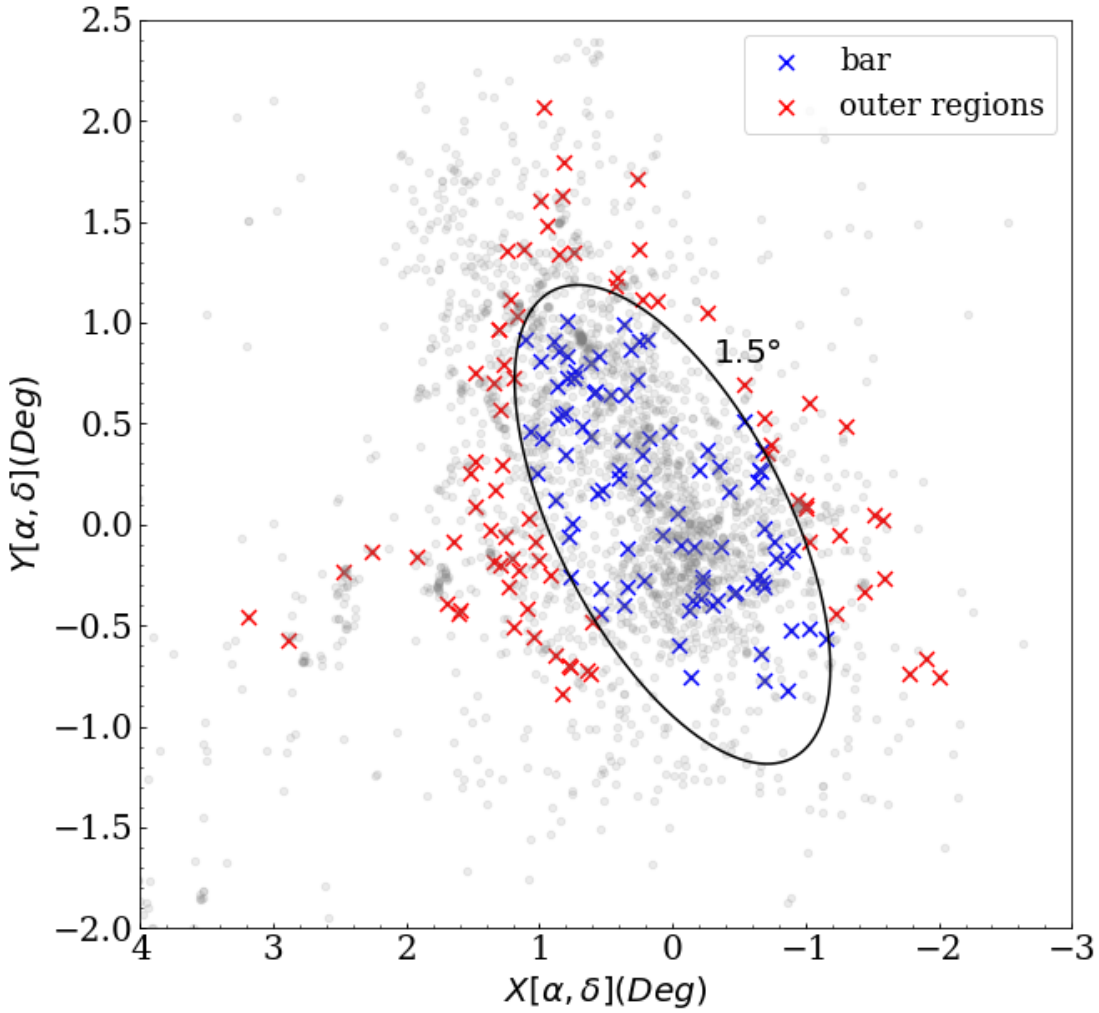

Figure 7.1: Positions of all 170 SCs studied in this paper, in a zenithal equidistant projection, with respect to the SMC centre reported by Ripepi et al. [2017]. Small grey dots show the whole SC catalogue by Bica et al. [2020]. Blue crosses represent SCs within an ellipse with its semimajor axis $a = 1.5°$ and ellipticity $e = 0.5$, whereas red crosses are the SCs outside the ellipse (see §C.2).

of the symmetry to properly determine the centre of an object [Mackey and Gilmore, 2003a]. Therefore, we preferred to use individual star positions to locate the “centroid" of the cluster and define it as SC centre. To this aim, we employed an iterated two dimensional KDE by using the star coordinates R.A. and Dec as inputs to find the SC centre, with a technique similar to that described in §3.2. As a starting point, we used the SC centres and major axes by Bica et al. [2020] to build surface density maps via KDE, obtained by calculating its value in a circular region centred on the SC with a radius twice its major axis. For each SC, we updated the SC centre by assigning it the coordinates where the surface density map has its maximum, and we repeated the same procedure until two successive estimated centres differ by less than $1''$. To better assess the SC centre, we ran the KDE many times by varying the bandwidth of the kernel function in the range $0.01'$-$0.4'$. Finally, we took the mean of all centroids as our best estimate for each SC centre.

To check the validity of this procedure, we compared our SC centres with those derived by Carvalho et al. [2008], who have 19 SCs in common with our sample. The mean difference between the two centre evaluations is below $2''$. In the second and third column of Tab. C.1 we listed all SC centres determined with the described procedure.

7.2.2 Surface brightness determination.

We followed the procedure developed by [Djorgovski, 1988], which consists of dividing the entire annulus in eight sectors of equal area and evaluating the flux in each of them. The flux in each annulus was obtained through the open source PHOTUTILS package [Bradley et al., 2019], written in PYTHON. The SB of an annulus is then the median of the eight fluxes, and we adopted $\Delta_\mu = 1.4826 \cdot MAD$, where MAD is the median absolute deviation, as their estimated uncertainty. This technique mitigates the impact of very bright or foreground stars on the SBP. Indeed, bright stars will increase the SB, and might generate artificial bumps in its shape, leading to wrong physical interpretations. This effect could be dramatic in our selected sample of SCs, since many of them have a low SB. The median ensures that sectors with such stars do not dominate the budget of the estimated SB.

In order to evenly sample inner and outer regions, many authors [e.g., Carvalho et al., 2008, Mackey and Gilmore, 2003a,b] utilized four sets of annuli of different thickness. Since many SCs in our sample have a SB only marginally above the background level, in order to better assess the SB value at a given radius we preferred to deal with 16 sets of annuli, having widths between $1.0''$ and $4.0''$ with a step size of $0.2''$. Since smaller annuli aim to sample the inner regions, we

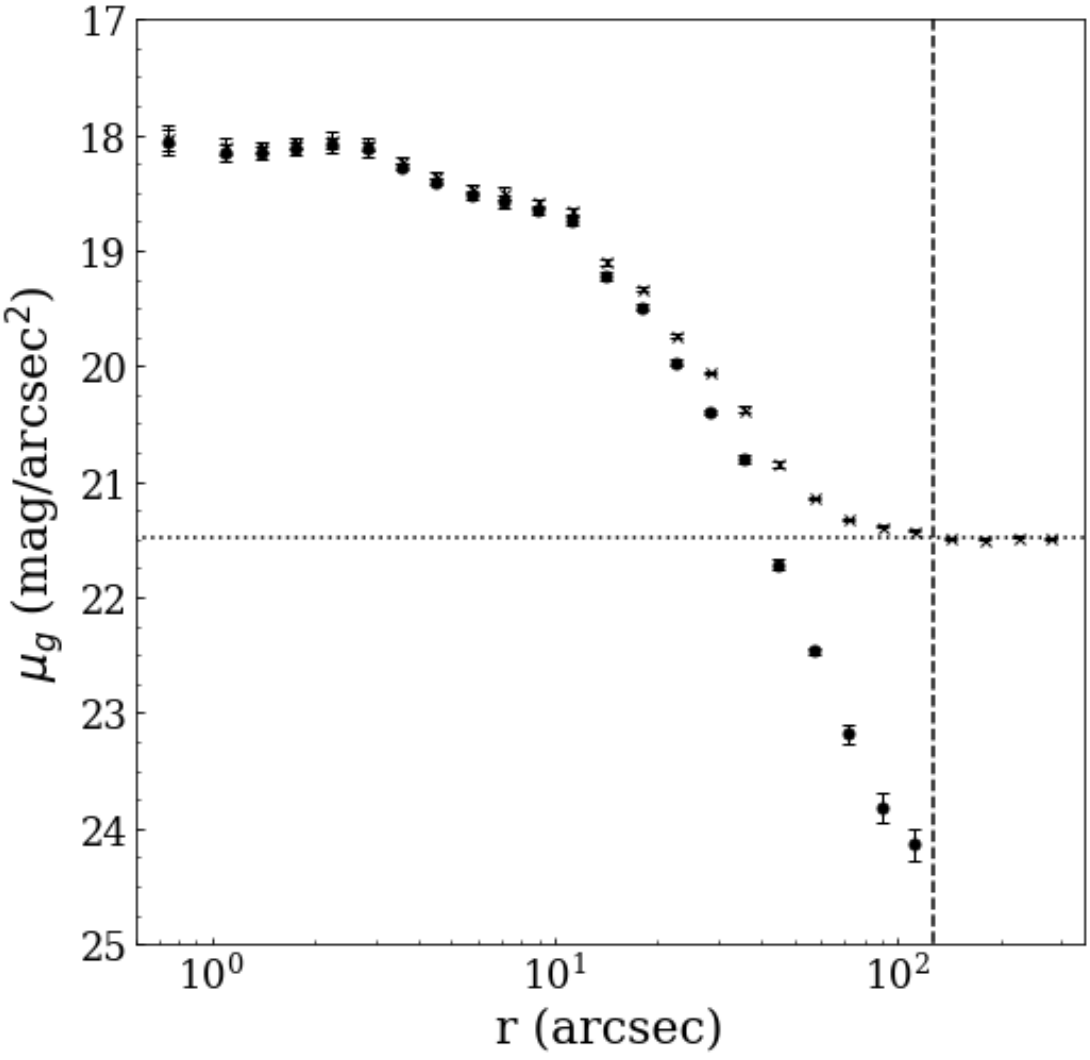

Figure 7.2: Example of the background subtraction procedure for NGC 419. The SBP calculated with the background contribution is displayed with crosses, while the decontaminated one is in black dots. Errorbars mark the uncertainties on the SBP as defined in the text. The horizontal line represents the estimated background as described in the text. The vertical line shows the cluster-centric distance where the contaminated SBP intersects the background level.

used those with sizes between 1.0″-1.5″ and 1.5″-2.0″ up to 20″ and to 30″ from the centre, respectively. The remaining sets of annuli, i.e. those with sizes between 2.2″ up to 4.0″, need to probe the outer regions, hence we constructed them up to 5′ from the centre of the cluster. Once all annuli were produced, and SB was derived in each of them, we averaged all the values in regular intervals of $\log_{10}(r/arcsec) = 0.1$. We performed a weighted mean to obtain our best estimate of the SB and its error. Similarly, we used as cluster-centric radius the mean of all radii within each interval of the binning procedure.

The SBP derived as described above is still affected by background contamination from field stars and sky background that needs to be corrected before proceeding with the analysis. The background level needs to be determined in a region well away from the cluster, and the VST data are suitable for such requirements due to the large field of view. To this purpose, we extended the annuli construction up to 300″ for every SC and adopted as local background the average flux measured between 150″ and 300″. This range of values is large enough to be both statistically significant and robust against fluctuations (i.e. a rich SC located within the background estimation area would have increased the sky level if the sampling regions were smaller). Finally, the background level was subtracted from each annulus in order to get a decontaminated SBP. Figure 7.2 shows an example of the background subtraction in the case of NGC419. In detail, the figure shows the SBPs before (crosses) and after (filled circles) the background subtraction, while the horizontal line shows the estimated background level.

Even though the procedure applied to obtain the SBP prevents saturated stars from dominating the luminosity budget, their effect must be carefully investigated. Shallow images provided by the STEP survey (see §2.2) allow us the opportunity to evaluate the impact of their presence in 11 SCs containing more than 5 saturated stars in the deep images, but not in the shallow ones. Figure 7.3 shows the SBP derived with either shallow (red points) or deep (blue squares) images for the SC NGC 376, and, apart from some barely visible differences, the overall SBP shape is unchanged. We inspected shallow and deep images for all the 11 SCs with more than 5 saturated stars, not finding any remarkable difference, which led us to conclude that, with our methodology, saturated stars do not alter our SBP shapes.

7.3 Fitting procedure

We adopted both EFF and King profiles to fit SBPs and to derive the SC structural parameters. As the results obtained with the two different profiles are very close to each other, in the following

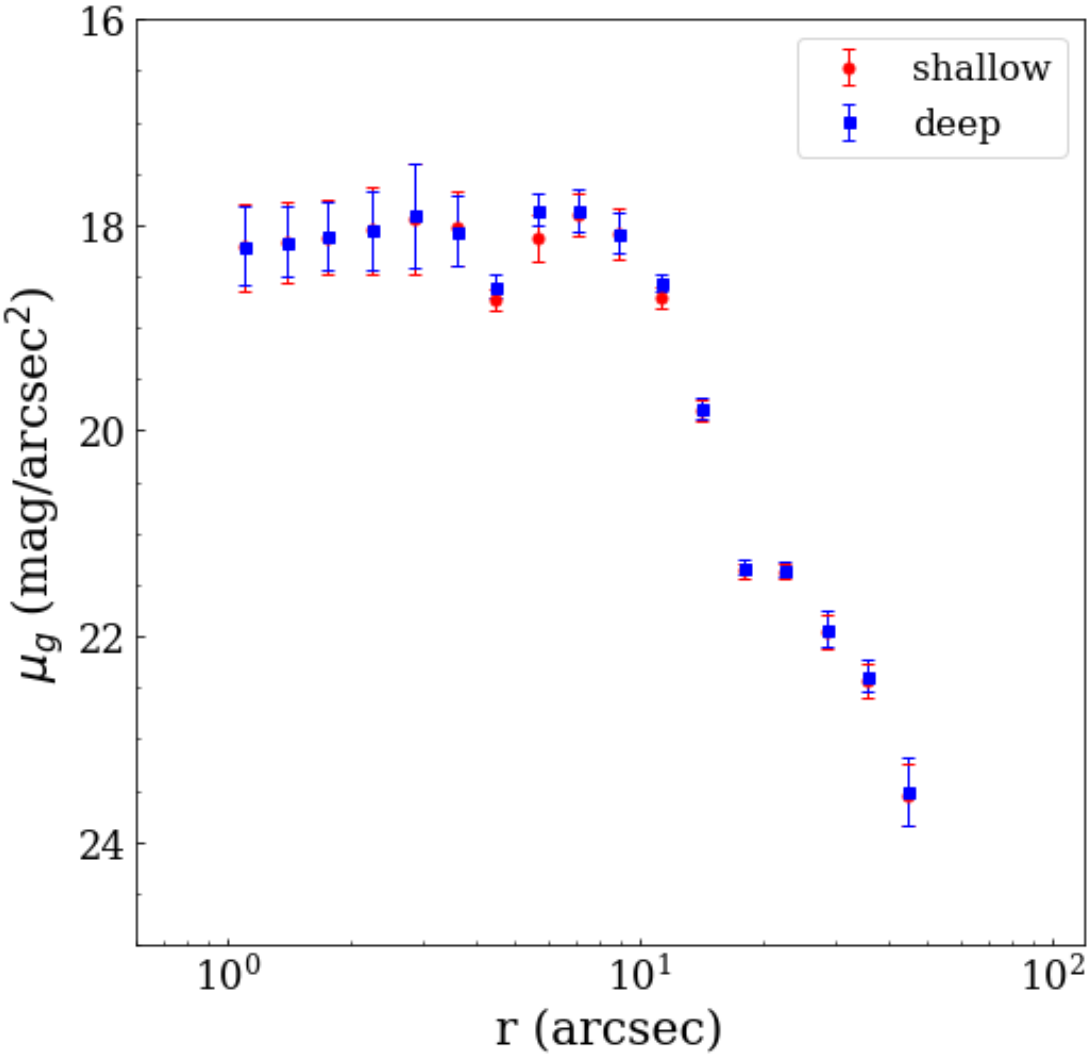

Figure 7.3: SBPs derived with shallow (red points) and deep (blue squares) images for NGC376.

we focus the discussion on the EFF profile in order to be consistent with previous works, since most of them adopted only the EFF profile. A detailed report about the King profile is in §C.1.

7.3.1 EFF model

The EFF formulation is the following:

$$\mu(r) = \mu_0 + 1.25\gamma \log\left(1 + \frac{r^2}{\alpha^2}\right) \tag{7.1}$$

where $\mu(r)$ is the SB expressed in mag/arcsec^2 at a given distance r from the cluster centre. μ_0, γ and α are, respectively, the central SB, the dimensionless slope of the power-law and a parameter (expressed in arcsec) related to the core radius r_c, which is the cluster-centric distance where the surface brightness has half of its central value, through the relation

$$r_c = \alpha\sqrt{2^{2/\gamma} - 1} \tag{7.2}$$

These three parameters have been derived via a non-linear least squares method through a χ^2 minimization. As it would not be appropriate to perform the fit all along the SBP, since it extends well beyond the cluster limit, we set a limiting radius, hereafter called fitting radius (r_f), within which we executed the fit. To estimate its value we adopted the local background estimated for each cluster, and set as r_f the distance from the cluster centre where the original SBP (i.e. not subtracted) reaches it or when $\mu(r) - \Delta_\mu(r)$ is smaller than the background level in two consecutive bins. These requirements may fail when two SCs are too close in projection: the SBP increases again at the distance where the annuli begin to incorporate stars belonging to the nearby cluster. Overall, the net effect is an unrealistically large r_f, thus forcing us to set the fitting radius by hand for these SCs. The SC luminosity comes from the integration of eq. 7.1, at the limit of r_f to infinity and yields:

$$L_\infty = \frac{2\pi 10^{-0.4\mu}\alpha^2}{\gamma - 2} \tag{7.3}$$

provided that $\gamma > 2$, otherwise the luminosity becomes infinite.[1] To calculate the extinction-corrected total luminosity, we adopted the extinction values obtained through the procedure described in §7.4.2 when available, or the extinction maps provided by Schlegel et al. [1998], re-calibrated by Schlafly and Finkbeiner [2011], otherwise.

To convert r_c from arcseconds to a real physical size expressed in parsec (pc), we needed the distance modulus (DM) of the cluster. As a first approximation, we adopted the same DM for

[1] We set $\gamma = 2$ as lowest bound limit in the curve fitting to avoid negative luminosities.

all SCs, i.e. $DM = 18.98$ mag, corresponding to the SMC centre distance, recently estimated by Graczyk et al. [2020] (see also discussion in §7.4). To be conservative, we considered an error on the DM of $\Delta DM = 0.4$ mag, corresponding to about 25 kpc at the SMC distance, in order to take into account also the depth of the SMC along the line of sight. The derived values of $\mu_0,\ \alpha,\ \gamma$ for the EFF models are listed in Table C.1, while r_c and L_∞ are reported in the first columns of Table 7.1.

We pointed out that for H86-6 and H86-11 we were not able to perform the fit of the g SBP because it was too noisy. For these SCs, we adopted the i-band SBP to derive their structural parameters.

7.3.2 Comparison with literature

We compared the results on the main properties of SCs with those existing in the literature for SCs in common with our sample. Since 62 SCs were analyzed for the first time in this work, the comparison was carried out with the remaining $\sim$ 100. The literature studies considered here include Mackey and Gilmore [2003b]; Hill and Zaritsky [2006]; Carvalho et al. [2008]; Glatt et al. [2009]; Santos et al. [2020], who derived the main structural parameters in a homogeneous way for several SMC SCs using EFF profiles. The top panel of Fig. 7.4 displays the comparison between our r_c obtained via the EFF profile and the literature ones, with the exception of Hill and Zaritsky [2006], which will be discussed separately. To make the comparison with previous works meaningful, we homogenized the core radii, recalculating the literature values for the SMC distance modulus we have adopted. [2] An inspection of Fig. 7.4 reveals that our core radii are nicely consistent within the errors with those estimated in the literature. Indeed, the average residual between our and the literature values is 0.01 ± 0.52 pc, corresponding to less than 2% in terms of fractional residuals.

The bottom panel of Fig. 7.4 shows the comparison between our and Hill and Zaritsky [2006]'s core radii values. In this case, we were not able to adjust their core radii to our SMC distance, since they did not give information on their adopted distance. The figure shows that our r_c are systematically lower (-1.05 ± 3.86 pc). Although the large uncertainties prevent us from determining whether the offset is real or not, we speculate that this systematic difference might originate from the different assumption of the SMC DM by Hill and Zaritsky [2006]. Furthermore,

[2] Mackey and Gilmore [2003b]; Glatt et al. [2009] and Santos et al. [2020] set the SMC distance modulus to $DM = 18.88 - 18.9 - 18.96$ mag, respectively. Carvalho et al. [2008] did not provide information on their adopted SC distances.

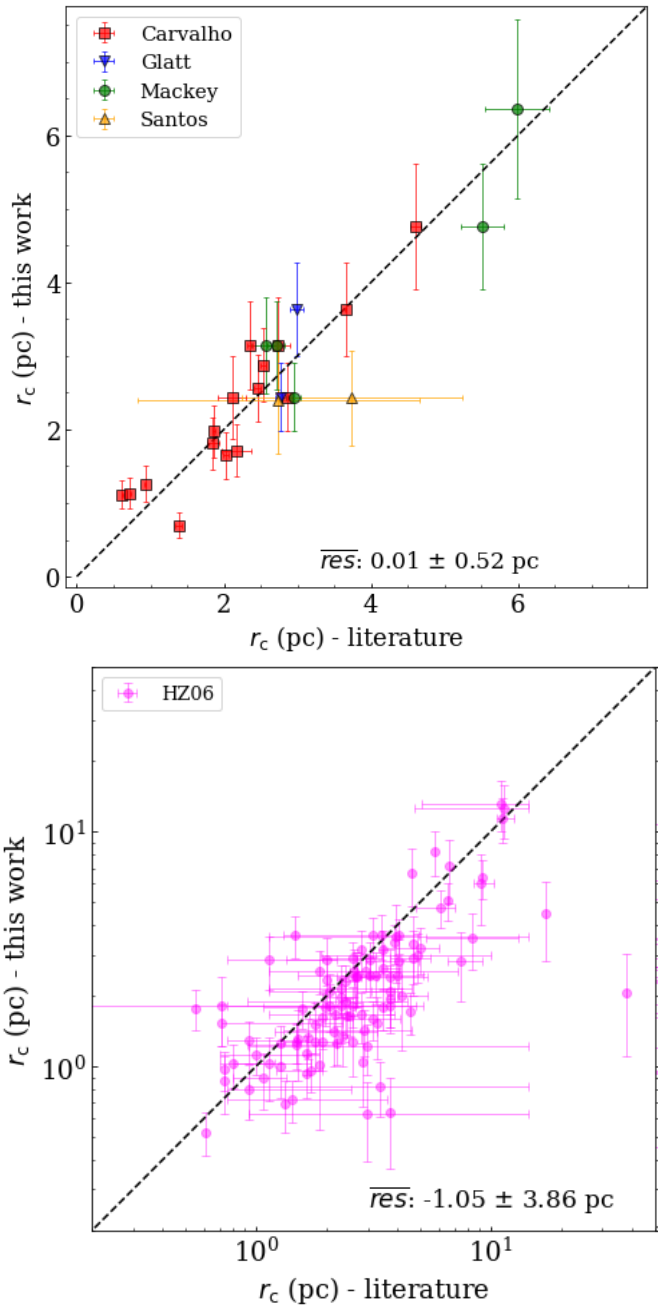

Figure 7.4: *Top:* Comparison of our core radii (y-axis) with values in the literature (x-axis). Different works are marked with different colours. *Bottom:* Comparison of our core radii with those taken from Hill and Zaritsky [2006]. Note that this panel is in logarithmic scale.

their work is based on the Magellanic Clouds Photometric Survey (MCPS), which is significantly shallower than the STEP survey[3]. This occurrence might be responsible for the large scatter observed between the results based on the two surveys. Indeed, also Santos et al. [2020], using data from the VISCACHA survey, found significant residuals (1.1 ± 2.7 pc, see their Fig.6), with respect to Hill and Zaritsky [2006].

7.4 Analysis of the CMD

We exploited the SC CMDs to extract additional fundamental physical parameters, such as the age and the mass. To this aim, the common procedure is to use the CMD to estimate the SC age from isochrone fitting and then to convert the integrated SC luminosity into total mass by adopting a mass-to-light ratio (MLR)-age-metallicity relation [e.g., Santos et al., 2020] or alternatively to use integrated colors [e.g., Roediger and Courteau, 2015]. However, these procedures are not usable for SCs with masses lower than $\sim$5000 $M_{\odot}$ as the stochasticity in the stellar luminosity function can produce substantial systematics in the inferred SC mass [Fouesneau and Lançon, 2010, Fouesneau et al., 2014, Krumholz et al., 2015, Silva-Villa and Larsen, 2011]. Since our sample includes many low mass SCs, we decided to follow a different procedure, adopting the Automated Stellar Cluster Analysis (ASteCA) open source python package [Perren et al., 2015]. This tool generates synthetic SCs from a set of theoretical isochrones and performs an automatic isochrone fitting procedure. A genetic algorithm is used to find the best solution [see Perren et al., 2015, for full details]. The great advantage of using ASteCA is that in practice it provides simultaneously an estimate of the age, reddening, mass and their uncertainties by taking into account the inherently stochastic process of the isochrone fitting procedure, as a synthetic cluster is generated from a stochastically sampled initial mass function (IMF)[4] [see Sect. 2.9.1 in Perren et al., 2015]. In the following two sections we describe the procedure employed to derive SC ages and masses.

7.4.1 Visual isochrone fitting

We carefully examined the CMD of each SC in our sample before running ASteCA, with the aim of performing in advance a visual isochrone fitting procedure. Such results have been used as priors for ASteCA in order to make it quicker, and to avoid that the software could catch in a

[3]The MCPS has a completeness at $\sim$50% for V$\sim$21 mag [Zaritsky et al., 1997]

[4]We adopted a Kroupa [2001] IMF.

local minimum, far away from the actual solution. This section describes the steps we performed to get SC ages from a visual ischrone fitting.

The CMD of a SC is contaminated by background/foreground stars belonging to the field of the host galaxy (the SMC in our case). In order to obtain reliable ages, non-cluster members should be statistically removed, especially for less populous SCs where the expected fraction of field stars is relatively high. To this aim we adopted the procedure developed by Piatti and Bica [2012] (already described in §4.1.1), which allows us to estimate the membership probability P of each SC star, permitting us to carry out the isochrone comparison procedure using only stars with the highest membership probability. We made use of the PARSEC models [Bressan et al., 2012][5] to visually identify the isochrone of a given age and metallicity[6] that best fits the distribution of SC stars with $P > 60\%$, in the CMD. To reduce the wide space of parameters affecting the shape of an isochrone, we fixed the DM for all SCs to $DM = 18.98$ mag [Graczyk et al., 2020], and we made use of an AMR derived for the SMC SCs [Parisi et al., 2015] to fix the metal-content of the SCs, as well. Although the SMC has a considerable extension along the line of sight [see e.g., Haschke et al., 2012, Jacyszyn-Dobrzeniecka et al., 2016, Ripepi et al., 2017, Subramanian and Subramaniam, 2012, and references therein], we estimated the total age uncertainty of the visual fitting procedure to be $\Delta \log(t) = 0.2$ dex, which comprises both a statistical error of 0.1 dex originating from the method, and a further 0.1 dex to take into account the fixed DM for the galaxy.[7] We varied the age and reddening of the isochrones looking for the one best matching the following key evolutionary sequences: main sequence (MS), turn-off (TO) point, subgiant branch, blue loop (BL) and red clump (RC). These sequences have been used to aid the visual fitting procedure, which was performed by the authors independently, in order to check the resulting reliability/uncertainty. For 36 SCs we were not able to derive even a rough estimate of the age, as their CMDs present none or too few stars on the above quoted key evolutionary stellar phases. Therefore, we conservatively decided to exclude them from the analysis with ASteCA. For these 36 clusters we only provide the structural parameters derived through the study of their SBPs.

[5] http://stev.oapd.inaf.it/cgi-bin/cmd

[6] We corrected the isochrones for the adopted distance and the colour excess through the relations $g = g_{\rm iso} + DM + R_{\rm g} \times E(B-V)$ and $E(g-i) = (R_{\rm g} - R_{\rm i}) \times E(B-V)$ with $R_{\rm g} = 3.303$ and $R_{\rm i} = 1.698$ [Schlafly and Finkbeiner, 2011].

[7] An error of 0.1 dex in the age estimate is the result of a ΔDM$\sim$0.4 mag at the SMC distance.

7.4.2 Analysis of the CMD with ASteCA

The 134 SCs with an age estimate from visual isochrone fitting of their CMD have been further analyzed with ASteCA with the main scope of deriving their ages and masses as well as the proper uncertainties by means of an objective methodology.[8] To use the ASteCA package we have first to define a list of priors for the relevant SCs quantities to be estimated. In more detail, we fixed the metallicity as already done in §7.4.1 but we let the DM vary in the $18.6 \leq DM \leq 19.2$ mag interval[9], in order to correct any bias we introduced in the visual fitting procedure by fixing it. The reddening values were allowed to vary in the range $0 \leq E(B-V) \leq 0.3$ mag. Priors on the SC ages were of $\log(t) \pm 0.6$ dex, (i.e. 3σ), around the age estimated in the previous section through the visual fitting procedure. Finally, we allowed the SC total mass to vary over a large interval, i.e. $10 \leq (M/M_{\odot}) \leq 10^6$.[10] Results from the CMD fitting by means of the ASteCA package are listed in Table 7.1.

7.4.3 Comparison with previous studies

We compared the ages derived from our CMDs with those present in the literature. To this aim we selected the works by Chiosi et al. [2006]; Glatt et al. [2010]; Perren et al. [2017] and Nayak et al. [2018] who presented ages for a significant number of SCs using the isochrone fitting procedure (visual or automatic). We note that Nayak et al. [2018]'s errors are between 0.24 and 0.26 dex in $\log(t)$, hence we adopted a mean of 0.25 dex for all their SCs, while for Glatt et al. [2010]'s SCs we adopted a mean error of 0.3 dex, i.e. their lowest error. The left panel of Fig. 7.5 shows the comparison between our results and those by Chiosi et al. [2006]; Glatt et al. [2010] and Nayak et al. [2018]. It can be clearly seen that, except for a few cases, our age estimates are in very good agreement with those from the literature up to 1 Gyr, whereas for older ages, the difference becomes noticeable. This discrepancy is likely due to the too shallow photometry analysed in the quoted works, which makes it unfeasible to correctly detect the MSTO for SCs older than 1 Gyr. Indeed, Glatt et al. [2010] pointed out the difficulty to derive ages of intermediate-age clusters with their MCPS data (see their Sect. 2). In contrast, the comparison with Perren et al. [2017],[11] displayed in the right panel of Fig. 7.5, shows very good agreement for the whole range of ages derived in this work. Concerning the estimated total masses, Fig. 7.6 (left panel)

[8] We adopted the same set of PARSEC isochrones utilized in §7.4.1.

[9] All priors indicated in the text are flat.

[10] We checked that estimated masses did not change within uncertainties with a different prior selection.

[11] Their data set consists of CT_1 Washington photometry, compiled on the basis of 19 previous works.

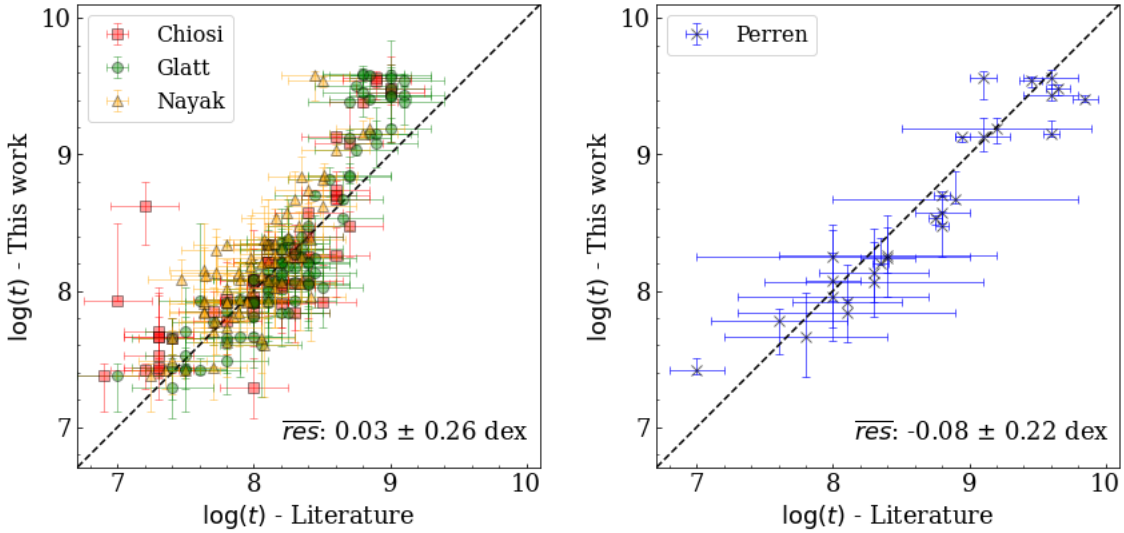

Figure 7.5: Comparison between our age estimates (y-axis) with those taken from the literature (x-axis). Different works are marked with different colours. The black dashed line indicates the one-to-one relationship. Residuals are to be read as our work minus literature. Note that residuals in the left panel have been calculated using only SCs younger than 1 Gyr.

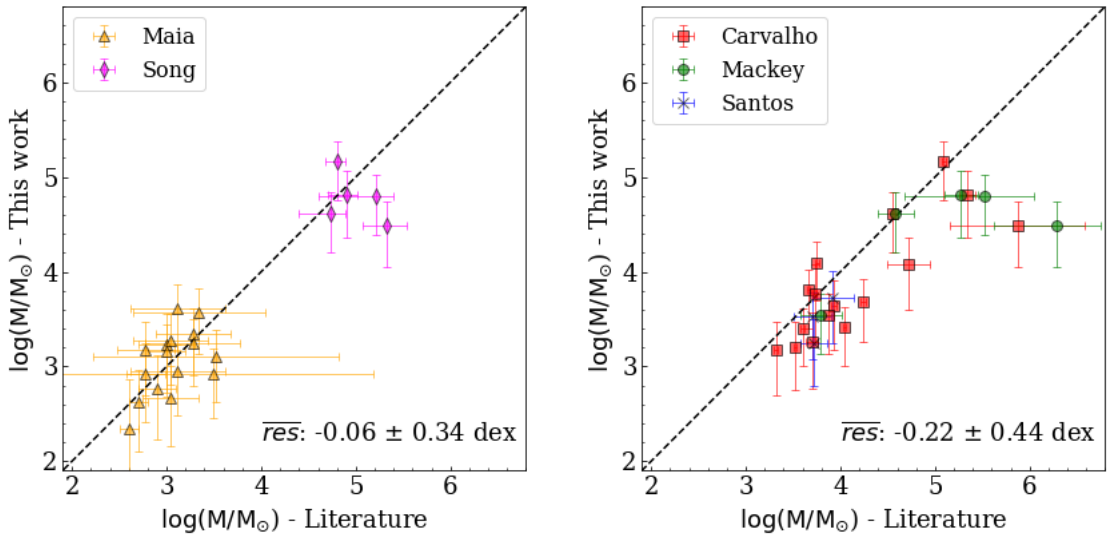

Figure 7.6: Comparison between our mass estimates (y-axis) with those taken from the literature (x-axis). Different works are marked with different colours. The black dashed line indicates the one-to-one relationship. Residuals are to be read as our work minus literature.

shows the comparison between our results and those by Maia et al. [2014] and Song et al. [2021] for the samples of SCs in common. Maia et al. [2014] provided SC masses derived through star counts integrated down to 0.1 $M_{\odot}$, while Song et al. [2021] obtained dynamical masses through spectroscopic measurements of radial velocities of the individual member stars. The figure shows a very good agreement between this work and the two quoted investigations, with an average of the residuals (our work minus literature) equal to -0.06±0.34 dex, i.e. without any systematic difference over a very broad range of masses, down to few hundreds of solar masses. In addition, we also considered the works by Mackey and Gilmore [2003b], Carvalho et al. [2008] and Santos et al. [2020], which provided mass estimates trough a MLR by using the total cluster luminosity estimated from the EFF model fitting. The result of this comparison is presented in the right panel of Fig. 7.6, which shows an overall overestimate of the masses in the aforementioned investigations with respect to this work, even if a relatively high scatter is present. The comparison of the masses with 4 SCs in common between Song et al. [2021], Mackey and Gilmore [2003b] and Carvalho et al. [2008], revealed that the latter two works derived larger masses also with respect to the dynamical estimates, i.e. $\Delta \log M = 0.37$ dex for Mackey and Gilmore [2003b] and $\Delta \log M = 0.27$ dex for Carvalho et al. [2008]. As dynamical masses are more reliable than those derived through integrated properties, the good agreement displayed in the left panel of the figure makes us confident about our mass assessment.

7.5 Results

The SC parameters derived from the SBP fitting are shown in Table C.1, along with the radius fitting, the coordinates and the tile hosting the SC. The physical SC parameters, like their sizes, luminosities and masses are, instead, listed in Table 7.1. The best fit profiles for all SCs are depicted in Fig.C.2 for both EFF and King models. Again, throughout this section we provide results obtained with the EFF profiles. For completeness, a discussion about quantities obtained with the King profile is presented in §C.1.

7.5.1 Core radius evolution with age: is it mass dependent?

An expansion of the core radius is expected to take place after a few hundreds of Myr. Besides the MCs, Ryon et al. [2015] analyzed a large sample of young ($\log(t) \leq 8.5$ dex) and massive ($\log(M/M_{\odot}) \geq 10^4$) SCs in M83, and found evidence of an increasing trend between core radius and age. Ryon et al. [2017] noticed a similar trend in NGC 628 and NGC 1313 again with

	EFF		KING				CMD					
ID	r_c (pc)	$\log(L/L_\odot)$	r_c (pc)	c	r_h (pc)	$\log(L/L_\odot)$	log (t)	E(B-V) (mag)	Z	$\log(M/M_\odot)$	$\log(M/L)$	$\log(t_{rh})$
B10	0.2 ± 0.2	3.95 ± 0.59	0.2 ± 0.2	1.6 ± 0.8	0.7 ± 0.3	3.87 ± 0.30	$9.48^{+0.17}_{-0.39}$	0.11	0.002	$3.03^{+0.39}_{-0.58}$	-0.92	6.86
B100	0.7 ± 0.1	4.18 ± 0.34	0.6 ± 0.1	1.0 ± 0.1	1.1 ± 0.2	4.16 ± 0.18	$8.00^{+0.15}_{-0.20}$	0.09	0.004	$3.12^{+0.23}_{-0.42}$	-1.06	7.05
B103	0.9 ± 0.2	-	1.4 ± 0.5	0.8 ± 0.3	1.8 ± 0.5	3.87 ± 0.28	$8.24^{+0.32}_{-0.10}$	0.20	0.004	$2.95^{+0.28}_{-0.46}$	-0.92	7.33
B105	0.8 ± 0.2	4.11 ± 0.88	0.9 ± 0.2	1.1 ± 0.2	1.6 ± 0.4	3.83 ± 0.20	$7.67^{+0.31}_{-0.23}$	0.05	0.004	$3.03^{+0.26}_{-0.44}$	-1.08	7.26
B108	1.3 ± 0.4	-	2.0 ± 1.0	0.7 ± 0.6	2.1 ± 0.7	3.42 ± 0.34	$9.39^{+0.01}_{-0.04}$	0.06	0.002	$3.62^{+0.21}_{-0.40}$	0.20	7.79
B111	0.8 ± 0.2	-	1.2 ± 0.4	0.9 ± 0.4	1.5 ± 0.4	3.00 ± 0.25	$9.13^{+0.13}_{-0.11}$	0.12	0.002	$2.62^{+0.34}_{-0.52}$	-0.38	7.19
B113	1.0 ± 0.3	3.52 ± 0.39	1.2 ± 0.4	0.7 ± 0.2	1.3 ± 0.3	3.47 ± 0.27	$9.04^{+0.04}_{-0.05}$	0.05	0.002	$3.29^{+0.25}_{-0.43}$	-0.22	7.35
B115	1.0 ± 0.4	-	1.6 ± 0.8	0.8 ± 0.6	2.0 ± 0.7	4.11 ± 0.35	-	-	-	-	-	-
B117	1.0 ± 0.2	4.19 ± 0.75	1.3 ± 0.3	0.9 ± 0.2	1.8 ± 0.4	3.94 ± 0.20	$8.17^{+0.15}_{-0.24}$	0.09	0.004	$3.08^{+0.40}_{-0.59}$	-1.11	7.37
B119	-	-	2.9 ± 2.4	0.1 ± 0.4	1.4 ± 0.4	2.95 ± 5.09	-	-	-	-	-	-
B12	-	-	2.4 ± 2.0	0.3 ± 0.6	1.7 ± 0.6	3.20 ± 0.88	$9.46^{+0.26}_{-0.09}$	0.14	0.002	$3.13^{+0.46}_{-0.64}$	-0.07	7.49
B121	1.3 ± 0.4	4.33 ± 0.66	2.7 ± 0.8	0.3 ± 0.1	1.9 ± 0.4	4.16 ± 0.60	$7.92^{+0.18}_{-0.13}$	0.11	0.004	$2.93^{+0.28}_{-0.47}$	-1.40	7.36
B122	2.1 ± 1.0	-	6.2 ± 4.7	0.4 ± 0.7	4.8 ± 1.7	3.83 ± 0.50	$8.21^{+0.32}_{-0.34}$	0.07	0.004	$3.30^{+0.24}_{-0.43}$	-0.52	8.11
B124	1.2 ± 0.3	3.63 ± 0.37	2.0 ± 0.6	0.4 ± 0.2	1.6 ± 0.3	3.57 ± 0.46	$8.08^{+0.20}_{-0.35}$	0.10	0.004	$2.35^{+0.51}_{-0.70}$	-1.29	7.06
B128	-	-	2.9 ± 1.9	0.3 ± 0.4	2.0 ± 0.6	3.52 ± 0.98	$8.02^{+0.15}_{-0.29}$	0.12	0.004	$2.71^{+0.33}_{-0.52}$	-0.81	7.33
B137	0.8 ± 0.2	-	1.2 ± 0.3	1.0 ± 0.3	1.8 ± 0.4	3.65 ± 0.21	-	-	-	-	-	-
B165	1.1 ± 0.3	3.09 ± 0.32	1.5 ± 0.5	0.6 ± 0.2	1.5 ± 0.3	3.08 ± 0.32	-	-	-	-	-	-
B18	0.7 ± 0.2	3.29 ± 0.43	0.8 ± 0.2	0.7 ± 0.3	0.8 ± 0.2	3.20 ± 0.23	$9.72^{+0.27}_{-0.65}$	0.10	0.002	$2.93^{+0.67}_{-0.86}$	-0.36	6.97
B21	0.8 ± 0.4	3.39 ± 2.32	2.5 ± 1.2	0.0 ± 0.2	1.1 ± 0.2	2.85 ± 6.51	$9.49^{+0.11}_{-0.49}$	0.05	0.002	$2.81^{+0.45}_{-0.63}$	-0.57	7.05
B22	0.2 ± 0.1	-	0.3 ± 0.1	1.2 ± 0.3	0.6 ± 0.1	3.27 ± 0.21	$9.97^{+0.09}_{-0.24}$	0.12	0.002	$3.42^{+0.53}_{-0.71}$	0.16	6.95
B26	0.6 ± 0.2	2.98 ± 0.87	1.5 ± 0.5	0.2 ± 0.2	0.9 ± 0.2	2.67 ± 1.09	-	-	-	-	-	-
B34A	0.8 ± 0.3	3.55 ± 0.30	1.7 ± 0.9	0.3 ± 0.3	1.1 ± 0.3	3.55 ± 1.29	-	-	-	-	-	-
B39	1.5 ± 0.3	-	2.2 ± 0.6	0.9 ± 0.3	2.9 ± 0.6	4.09 ± 0.22	$8.67^{+0.20}_{-0.04}$	0.13	0.004	$3.39^{+0.26}_{-0.45}$	-0.70	7.85
B52	4.1 ± 1.3	-	10.6 ± 8.1	0.3 ± 0.6	6.3 ± 2.1	4.40 ± 1.15	-	-	-	-	-	-
B65	1.3 ± 0.2	4.49 ± 0.26	1.4 ± 0.3	0.6 ± 0.1	1.5 ± 0.3	4.48 ± 0.22	-	-	-	-	-	-
B70	0.5 ± 0.1	3.74 ± 1.01	0.5 ± 0.1	1.7 ± 0.1	1.4 ± 0.2	3.45 ± 0.15	$9.64^{+0.14}_{-0.19}$	0.07	0.002	$2.97^{+0.42}_{-0.61}$	-0.77	7.30
B71	1.8 ± 0.4	4.65 ± 0.24	2.8 ± 0.7	0.4 ± 0.1	2.2 ± 0.4	4.66 ± 0.51	$7.53^{+0.28}_{-0.18}$	0.13	0.004	$3.01^{+0.25}_{-0.44}$	-1.63	7.45
B79	1.3 ± 0.3	4.56 ± 0.60	1.3 ± 0.4	1.1 ± 0.3	2.3 ± 0.5	4.45 ± 0.22	$7.70^{+0.32}_{-0.25}$	0.05	0.004	$2.98^{+0.25}_{-0.43}$	-1.57	7.49
B80	0.6 ± 0.3	-	0.9 ± 0.4	1.0 ± 0.6	1.4 ± 0.5	3.52 ± 0.32	$9.08^{+0.27}_{-0.18}$	0.14	0.002	$2.84^{+0.44}_{-0.62}$	-0.68	7.20
B9	1.0 ± 0.5	3.73 ± 1.56	2.7 ± 1.1	0.3 ± 0.2	1.8 ± 0.4	3.36 ± 0.92	-	-	-	-	-	-
B96	2.6 ± 0.5	4.24 ± 0.28	4.2 ± 1.0	0.4 ± 0.1	3.1 ± 0.6	4.21 ± 0.51	$8.27^{+0.00}_{-0.16}$	0.18	0.004	$3.26^{+0.26}_{-0.44}$	-0.98	7.82
B97	1.4 ± 0.5	-	3.1 ± 2.1	0.3 ± 0.5	1.9 ± 0.6	3.14 ± 1.05	-	-	-	-	-	-
B99	1.4 ± 0.4	4.43 ± 0.99	1.8 ± 0.6	0.8 ± 0.3	2.3 ± 0.6	4.11 ± 0.26	$8.25^{+0.24}_{-0.32}$	0.19	0.004	$3.23^{+0.32}_{-0.51}$	-1.20	7.62
BS102	1.2 ± 0.4	3.73 ± 2.07	1.7 ± 0.7	0.7 ± 0.5	1.7 ± 0.4	3.17 ± 0.29	$8.37^{+0.28}_{-0.32}$	0.06	0.004	$2.56^{+0.35}_{-0.53}$	-1.17	7.18
BS128	-	-	1.1 ± 0.7	0.8 ± 1.3	1.0 ± 0.2	3.11 ± 0.37	$8.35^{+0.32}_{-0.36}$	0.10	0.004	$2.23^{+0.44}_{-0.62}$	-0.89	6.73
BS131	1.3 ± 0.3	4.04 ± 0.62	2.3 ± 1.1	0.3 ± 0.3	1.5 ± 0.3	3.83 ± 0.84	-	-	-	-	-	-
BS138	3.5 ± 0.9	-	6.0 ± 4.8	0.4 ± 0.8	4.1 ± 1.2	3.85 ± 0.55	$9.53^{+0.03}_{-0.04}$	0.12	0.002	$3.68^{+0.22}_{-0.41}$	-0.17	8.26
BS2	1.1 ± 0.3	2.94 ± 0.43	1.1 ± 0.4	0.9 ± 0.4	1.6 ± 0.4	2.89 ± 0.27	-	-	-	-	-	-
BS276	0.5 ± 0.1	4.19 ± 0.50	0.5 ± 0.1	1.2 ± 0.1	1.0 ± 0.2	4.15 ± 0.17	$8.38^{+0.24}_{-0.32}$	0.10	0.004	$3.01^{+0.28}_{-0.47}$	-1.18	6.99
BS76	1.7 ± 0.4	3.78 ± 0.48	1.9 ± 0.5	0.8 ± 0.3	2.4 ± 0.6	3.69 ± 0.22	$8.15^{+0.17}_{-0.27}$	0.05	0.004	$2.95^{+0.30}_{-0.49}$	-0.83	7.53
BS88	1.2 ± 0.4	-	2.3 ± 1.7	0.3 ± 0.6	1.3 ± 0.4	3.13 ± 0.85	$9.56^{+0.05}_{-0.16}$	0.12	0.002	$3.20^{+0.37}_{-0.55}$	0.07	7.35
H86-11	0.5 ± 0.3	-	0.9 ± 0.5	0.9 ± 0.5	1.3 ± 0.5	2.80 ± 0.37	-	-	-	-	-	-
H86-114	1.4 ± 0.3	-	2.2 ± 0.6	0.7 ± 0.3	2.5 ± 0.6	4.05 ± 0.25	$8.34^{+0.26}_{-0.37}$	0.06	0.004	$2.79^{+0.24}_{-0.42}$	-1.26	7.50
H86-137	0.8 ± 0.2	4.28 ± 1.05	0.9 ± 0.2	1.3 ± 0.2	1.5 ± 0.3	3.87 ± 0.16	$9.14^{+0.02}_{-0.01}$	0.13	0.002	$3.52^{+0.28}_{-0.47}$	-0.76	7.50
H86-146	0.4 ± 0.2	-	0.6 ± 0.3	1.3 ± 0.4	1.4 ± 0.4	4.11 ± 0.26	-	-	-	-	-	-
H86-150	0.9 ± 0.3	-	1.5 ± 0.6	0.8 ± 0.4	1.8 ± 0.5	3.91 ± 0.31	$7.62^{+0.16}_{-0.09}$	0.12	0.004	$2.92^{+0.26}_{-0.44}$	-0.99	7.31
H86-159	1.6 ± 0.4	3.60 ± 0.43	2.0 ± 0.7	0.6 ± 0.3	2.0 ± 0.6	3.51 ± 0.30	-	-	-	-	-	-
H86-165	1.7 ± 0.7	-	2.5 ± 1.4	0.6 ± 0.6	2.6 ± 0.9	3.79 ± 0.39	$8.08^{+0.23}_{-0.26}$	0.10	0.004	$2.94^{+0.27}_{-0.46}$	-0.85	7.57
H86-174	1.3 ± 0.3	4.64 ± 2.49	1.8 ± 0.6	0.7 ± 0.3	2.0 ± 0.5	3.85 ± 0.25	$8.58^{+0.13}_{-0.08}$	0.19	0.002	$2.92^{+0.32}_{-0.51}$	-1.73	7.44
H86-175	0.9 ± 0.2	3.56 ± 0.19	1.3 ± 0.3	0.4 ± 0.1	0.9 ± 0.2	3.55 ± 0.51	-	-	-	-	-	-
H86-179	1.2 ± 0.5	3.72 ± 0.81	2.6 ± 1.9	0.2 ± 0.4	1.6 ± 0.4	3.53 ± 1.73	-	-	-	-	-	-
H86-181	0.5 ± 0.2	4.23 ± 0.81	0.6 ± 0.2	1.2 ± 0.3	1.1 ± 0.3	4.01 ± 0.22	-	-	-	-	-	-
H86-182	2.3 ± 0.6	4.44 ± 0.71	3.1 ± 1.1	0.6 ± 0.3	3.2 ± 0.7	4.22 ± 0.29	-	-	-	-	-	-
H86-186	1.1 ± 0.2	4.11 ± 0.33	1.2 ± 0.2	0.8 ± 0.1	1.5 ± 0.3	4.08 ± 0.19	$8.21^{+0.28}_{-0.18}$	0.11	0.004	$3.15^{+0.28}_{-0.46}$	-0.96	7.30
H86-190	0.6 ± 0.2	-	1.0 ± 0.5	0.7 ± 0.5	1.1 ± 0.3	3.54 ± 0.32	$7.66^{+0.32}_{-0.29}$	0.05	0.004	$2.30^{+0.38}_{-0.56}$	-1.24	6.75
H86-191	-	-	2.0 ± 1.5	0.3 ± 0.5	1.3 ± 0.4	3.28 ± 1.16	$8.04^{+0.44}_{-0.31}$	0.08	0.004	$2.53^{+0.24}_{-0.43}$	-0.75	7.00
H86-193	1.8 ± 0.4	3.75 ± 0.49	2.3 ± 0.7	0.6 ± 0.3	1.9 ± 0.4	3.62 ± 0.25	$8.06^{+0.31}_{-0.34}$	0.14	0.004	$2.78^{+0.27}_{-0.45}$	-0.98	7.31
H86-194	0.7 ± 0.4	-	2.3 ± 1.1	0.1 ± 0.2	1.1 ± 0.2	3.27 ± 2.82	$8.07^{+0.32}_{-0.27}$	0.07	0.004	$2.36^{+0.42}_{-0.60}$	-0.92	6.85
H86-213	0.3 ± 0.1	-	0.5 ± 0.2	1.3 ± 0.3	1.0 ± 0.2	2.99 ± 0.20	$8.40^{+0.20}_{-0.28}$	0.12	0.004	$2.74^{+0.26}_{-0.45}$	-0.25	6.92
H86-6	1.2 ± 0.3	2.57 ± 0.37	2.4 ± 0.9	0.2 ± 0.2	1.4 ± 0.3	2.48 ± 1.43	$9.44^{+0.07}_{-0.22}$	0.08	0.002	$2.86^{+0.34}_{-0.52}$	0.29	7.24
H86-60	-	-	1.5 ± 1.1	0.3 ± 0.5	0.9 ± 0.3	2.84 ± 1.24	-	-	-	-	-	-
H86-74	0.9 ± 0.2	4.77 ± 0.82	1.0 ± 0.2	1.1 ± 0.2	1.7 ± 0.3	4.51 ± 0.18	$7.92^{+0.12}_{-0.14}$	0.14	0.004	$2.66^{+0.37}_{-0.56}$	-2.10	7.20
H86-86	0.3 ± 0.1	2.83 ± 0.62	0.4 ± 0.2	0.9 ± 0.4	0.6 ± 0.1	2.68 ± 0.26	-	-	-	-	-	-
H86-87	1.7 ± 0.6	-	4.1 ± 3.5	0.3 ± 0.6	2.5 ± 0.8	3.81 ± 1.07	$8.26^{+0.21}_{-0.30}$	0.15	0.004	$2.92^{+0.27}_{-0.46}$	-0.89	7.54
H86-97	1.5 ± 0.4	-	2.7 ± 0.9	0.5 ± 0.2	2.2 ± 0.5	4.39 ± 0.35	$7.92^{+0.27}_{-0.00}$	0.22	0.004	$3.10^{+0.29}_{-0.47}$	-1.29	7.52

Table 7.1: In the first column we report the SC ID as taken from Bica et al. [2020]. SC properties derived through EFF models: core radius and total luminosity are in the second and third column, respectively. SC properties obtained through King's profile are listed in the fourth to the seventh column, i.e., the core radius, concentration parameter, the half-light radius and luminosity, respectively. Then we list parameters derived through ASteCA, namely, age, reddening, metallicity and mass. Mass-to-light ratio was derived by using the total luminosity derived from the EFF model when available, or through the King model, otherwise. Finally, in the last columns, we indicate the relaxation time.

	EFF		KING				CMD					
ID	r_c (pc)	$\log(L/L_\odot)$	r_c (pc)	c	r_h (pc)	$\log(L/L_\odot)$	log (t)	E(B-V) (mag)	Z	$\log(M/M_\odot)$	log (M/L)	$\log(t_{rh})$
HW10	3.0 ± 0.7	-	4.4 ± 1.4	0.8 ± 0.3	5.7 ± 1.4	3.92 ± 0.26	$9.59^{+0.25}_{-0.09}$	0.09	0.002	$4.29^{+0.37}_{-0.56}$	0.38	8.72
HW11	3.6 ± 1.3	-	5.4 ± 2.5	0.9 ± 0.6	7.1 ± 2.3	4.22 ± 0.36	-	-	-	-	-	-
HW14	7.1 ± 2.2	-	13.6 ± 10.0	0.4 ± 0.7	9.6 ± 2.7	4.27 ± 0.52	$9.50^{+0.01}_{-0.02}$	0.12	0.002	$4.23^{+0.24}_{-0.43}$	-0.04	9.03
HW18	0.5 ± 0.1	-	0.8 ± 0.3	0.8 ± 0.3	1.0 ± 0.3	2.72 ± 0.27	-	-	-	-	-	-
HW22	1.0 ± 0.2	3.86 ± 0.58	0.9 ± 0.2	1.3 ± 0.1	1.9 ± 0.4	3.78 ± 0.17	$9.41^{+0.03}_{-0.03}$	0.02	0.002	$3.59^{+0.26}_{-0.45}$	-0.27	7.73
HW26	0.2 ± 0.0	4.11 ± 0.49	-	-	-	-	-	-	-	-	-	-
HW34	-	-	1.9 ± 1.4	0.2 ± 0.5	1.0 ± 0.3	2.90 ± 2.17	$9.58^{+0.07}_{-0.09}$	0.06	0.002	$3.35^{+0.38}_{-0.56}$	0.45	7.20
HW35	0.9 ± 0.2	3.61 ± 0.62	0.9 ± 0.2	1.1 ± 0.2	1.4 ± 0.3	3.47 ± 0.17	$8.18^{+0.31}_{-0.33}$	0.12	0.004	$2.81^{+0.29}_{-0.48}$	-0.81	7.14
HW36	0.9 ± 0.2	3.12 ± 0.29	1.2 ± 0.5	0.5 ± 0.2	1.1 ± 0.3	3.09 ± 0.40	$9.12^{+0.19}_{-0.11}$	0.09	0.002	$2.74^{+0.48}_{-0.67}$	-0.37	7.04
HW37	-	-	3.4 ± 2.7	0.2 ± 0.4	2.1 ± 0.6	4.15 ± 2.30	$7.60^{+0.28}_{-0.38}$	0.11	0.004	$2.30^{+0.38}_{-0.56}$	-1.84	7.21
HW38	2.4 ± 0.7	3.64 ± 0.99	3.3 ± 1.8	0.6 ± 0.6	2.9 ± 0.9	3.38 ± 0.33	$9.59^{+0.03}_{-0.31}$	0.06	0.002	$3.72^{+0.29}_{-0.48}$	0.07	8.06
HW40	1.6 ± 0.3	3.59 ± 0.53	1.7 ± 0.3	1.1 ± 0.1	2.9 ± 0.5	3.51 ± 0.17	$9.43^{+0.08}_{-0.04}$	0.04	0.002	$3.53^{+0.24}_{-0.43}$	-0.06	7.96
HW41	2.8 ± 0.9	-	5.6 ± 2.3	0.8 ± 0.5	6.4 ± 1.7	3.89 ± 0.31	$9.56^{+0.06}_{-0.08}$	0.08	0.002	$3.85^{+0.24}_{-0.43}$	-0.04	8.63
HW43	1.6 ± 0.4	-	2.6 ± 0.9	0.6 ± 0.3	2.6 ± 0.7	3.71 ± 0.29	$8.08^{+0.19}_{-0.09}$	0.06	0.004	$3.11^{+0.26}_{-0.45}$	-0.60	7.63
HW44	1.4 ± 0.6	-	4.3 ± 3.5	0.2 ± 0.6	2.5 ± 0.8	3.57 ± 1.22	$8.63^{+0.14}_{-0.36}$	0.11	0.004	$2.71^{+0.35}_{-0.53}$	-0.87	7.51
HW48	1.0 ± 0.2	4.06 ± 0.74	0.9 ± 0.2	1.4 ± 0.2	1.9 ± 0.4	3.90 ± 0.16	$8.11^{+0.07}_{-0.23}$	0.10	0.004	$3.01^{+0.30}_{-0.48}$	-1.05	7.40
HW50	1.1 ± 0.7	-	3.6 ± 3.4	0.5 ± 1.0	3.0 ± 1.0	3.46 ± 0.49	$8.14^{+0.07}_{-0.26}$	0.11	0.004	$2.65^{+0.25}_{-0.44}$	-0.81	7.57
HW52	1.9 ± 0.5	3.98 ± 0.64	4.3 ± 1.6	0.2 ± 0.2	2.6 ± 0.5	3.80 ± 1.19	$8.14^{+0.32}_{-0.22}$	0.04	0.004	$2.77^{+0.35}_{-0.54}$	-1.21	7.52
HW53	1.3 ± 0.3	3.19 ± 0.74	2.2 ± 0.9	0.3 ± 0.3	1.3 ± 0.3	2.88 ± 0.70	$9.58^{+0.03}_{-0.19}$	0.03	0.002	$3.27^{+0.38}_{-0.57}$	0.08	7.37
HW54	1.9 ± 0.8	-	-	-	-	-	$9.43^{+0.24}_{-0.01}$	0.11	0.002	$3.35^{+0.25}_{-0.43}$	-2.03	8.13
HW55	2.1 ± 0.6	-	5.3 ± 2.8	0.2 ± 0.4	3.1 ± 0.8	3.50 ± 1.07	$9.19^{+0.07}_{-0.11}$	0.08	0.002	$2.86^{+0.28}_{-0.47}$	-0.64	7.75
HW59	-	-	0.6 ± 0.2	0.2 ± 0.1	0.4 ± 0.1	2.57 ± 1.60	-	-	-	-	-	-
HW61	1.8 ± 0.6	4.36 ± 2.27	3.7 ± 1.6	0.2 ± 0.3	2.3 ± 0.5	3.76 ± 1.10	$7.93^{+0.24}_{-0.00}$	0.11	0.004	$3.02^{+0.31}_{-0.49}$	-1.35	7.50
HW68	0.7 ± 0.3	-	1.2 ± 0.7	0.8 ± 0.6	1.5 ± 0.5	3.06 ± 0.42	-	-	-	-	-	-
HW74	2.3 ± 0.8	4.08 ± 1.81	3.7 ± 1.8	0.5 ± 0.4	3.3 ± 0.9	3.61 ± 0.42	$7.43^{+0.16}_{-0.32}$	0.09	0.004	$2.67^{+0.32}_{-0.51}$	-1.41	7.59
HW78	0.8 ± 0.2	3.66 ± 0.32	0.8 ± 0.3	0.9 ± 0.2	1.2 ± 0.2	3.64 ± 0.24	$7.13^{+0.45}_{-0.11}$	0.09	0.004	$2.31^{+0.38}_{-0.57}$	-1.35	6.79
HW8	1.0 ± 0.3	-	1.4 ± 0.4	1.4 ± 0.3	3.3 ± 0.8	4.24 ± 0.22	$7.81^{+0.18}_{-0.03}$	0.07	0.004	$3.49^{+0.24}_{-0.43}$	-0.75	7.90
HW82	0.6 ± 0.2	-	0.8 ± 0.2	1.3 ± 0.3	1.9 ± 0.4	3.83 ± 0.20	$7.73^{+0.30}_{-0.36}$	0.07	0.004	$2.10^{+0.36}_{-0.55}$	-1.72	7.06
HW9	1.2 ± 0.3	-	2.1 ± 0.8	0.6 ± 0.4	2.1 ± 0.6	3.18 ± 0.30	$9.52^{+0.08}_{-0.04}$	0.12	0.002	$3.48^{+0.30}_{-0.49}$	0.29	7.74
IC1611	1.8 ± 0.4	5.28 ± 0.98	1.9 ± 0.4	1.5 ± 0.3	4.4 ± 0.9	4.97 ± 0.17	$8.21^{+0.22}_{-0.28}$	0.10	0.004	$4.07^{+0.29}_{-0.47}$	-1.21	8.34
IC1612	3.3 ± 1.1	-	8.5 ± 6.1	0.4 ± 0.7	6.2 ± 1.9	4.65 ± 0.50	$8.08^{+0.15}_{-0.17}$	0.08	0.004	$3.25^{+0.31}_{-0.49}$	-1.39	8.25
IC1624	2.6 ± 0.5	4.86 ± 0.43	2.7 ± 0.5	0.9 ± 0.1	3.9 ± 0.7	4.81 ± 0.18	$8.31^{+0.05}_{-0.26}$	0.10	0.004	$3.80^{+0.22}_{-0.40}$	-1.06	8.17
IC1662	2.6 ± 0.6	4.22 ± 0.46	2.7 ± 0.7	0.9 ± 0.2	4.0 ± 1.0	4.16 ± 0.23	$8.01^{+0.22}_{-0.24}$	0.10	0.004	$3.22^{+0.41}_{-0.59}$	-1.00	7.94
K1	7.8 ± 1.6	4.44 ± 0.42	9.1 ± 2.4	0.7 ± 0.3	10.2 ± 2.0	4.37 ± 0.23	$9.84^{+0.03}_{-0.20}$	0.10	0.001	$4.44^{+0.23}_{-0.42}$	-0.00	9.19
K11	3.2 ± 0.6	3.87 ± 0.31	3.5 ± 0.8	0.7 ± 0.1	4.1 ± 0.8	3.85 ± 0.23	$9.32^{+0.09}_{-0.04}$	0.16	0.002	$3.54^{+0.26}_{-0.44}$	-0.33	8.19
K13	6.0 ± 2.0	-	19.1 ± 15.5	0.2 ± 0.5	9.8 ± 3.1	4.28 ± 2.74	$9.54^{+0.05}_{-0.04}$	0.05	0.002	$4.63^{+0.24}_{-0.43}$	0.35	9.21
K15	1.8 ± 0.3	4.76 ± 0.98	1.8 ± 0.3	1.6 ± 0.2	4.0 ± 0.7	4.46 ± 0.16	$8.84^{+0.15}_{-0.39}$	0.14	0.002	$3.43^{+0.31}_{-0.49}$	-1.33	8.08
K16	2.1 ± 0.4	3.46 ± 0.31	2.9 ± 0.8	0.5 ± 0.2	2.3 ± 0.5	3.40 ± 0.35	$9.46^{+0.08}_{-0.02}$	0.05	0.002	$3.55^{+0.28}_{-0.47}$	0.08	7.83
K17	2.0 ± 0.4	4.78 ± 0.69	1.9 ± 0.3	1.4 ± 0.1	4.6 ± 0.8	4.66 ± 0.16	$8.82^{+0.08}_{-0.13}$	0.11	0.002	$3.64^{+0.27}_{-0.46}$	-1.15	8.26
K21	8.3 ± 1.7	-	10.7 ± 2.7	0.9 ± 0.3	14.8 ± 3.1	4.91 ± 0.22	$9.48^{+0.02}_{-0.31}$	0.05	0.002	$4.96^{+0.20}_{-0.39}$	0.05	9.61
K25	1.8 ± 0.6	-	2.8 ± 1.2	0.8 ± 0.5	3.5 ± 1.2	4.38 ± 0.33	$8.25^{+0.22}_{-0.32}$	0.15	0.004	$3.40^{+0.25}_{-0.43}$	-0.97	7.96
K27	3.6 ± 0.7	-	5.2 ± 1.4	0.9 ± 0.3	7.1 ± 1.6	4.56 ± 0.23	$9.13^{+0.06}_{-0.07}$	0.11	0.002	$4.03^{+0.27}_{-0.45}$	-0.53	8.72
K28	5.1 ± 0.9	4.99 ± 0.68	5.2 ± 1.0	1.2 ± 0.2	8.9 ± 1.6	4.83 ± 0.17	$9.57^{+0.03}_{-0.04}$	0.08	0.002	$4.70^{+0.23}_{-0.41}$	-0.28	9.18
K30	6.6 ± 1.8	-	10.0 ± 3.6	0.7 ± 0.4	11.7 ± 3.2	4.89 ± 0.30	$8.30^{+0.09}_{-0.30}$	0.09	0.004	$3.87^{+0.27}_{-0.45}$	-1.02	8.91
K31	13.2 ± 3.2	-	20.8 ± 8.8	0.5 ± 0.4	18.1 ± 5.7	5.28 ± 0.32	$8.63^{+0.17}_{-0.29}$	0.06	0.004	$4.24^{+0.26}_{-0.44}$	-1.05	9.37
K34	2.9 ± 0.5	4.80 ± 0.31	3.4 ± 0.6	0.6 ± 0.1	3.6 ± 0.6	4.77 ± 0.22	$8.74^{+0.06}_{-0.10}$	0.11	0.002	$3.69^{+0.24}_{-0.42}$	-1.12	8.11
K38	12.6 ± 3.2	-	19.7 ± 8.1	0.5 ± 0.4	17.7 ± 4.8	4.92 ± 0.32	$9.48^{+0.03}_{-0.05}$	0.05	0.002	$4.69^{+0.24}_{-0.43}$	-0.23	9.61
K4	4.3 ± 0.9	-	5.3 ± 1.2	1.0 ± 0.3	7.7 ± 1.5	4.17 ± 0.19	$9.70^{+0.01}_{-0.01}$	0.14	0.002	$4.11^{+0.26}_{-0.45}$	-0.06	8.86
K42	0.7 ± 0.1	4.85 ± 0.91	0.7 ± 0.1	1.5 ± 0.2	1.7 ± 0.3	4.61 ± 0.16	$7.85^{+0.14}_{-0.12}$	0.13	0.002	$2.83^{+0.30}_{-0.48}$	-2.02	7.25
K43	2.3 ± 0.5	-	3.5 ± 1.1	0.8 ± 0.3	4.5 ± 1.1	4.40 ± 0.26	$8.21^{+0.18}_{-0.02}$	0.16	0.004	$3.61^{+0.25}_{-0.43}$	-0.79	8.19
K44	11.4 ± 2.5	4.77 ± 0.48	13.3 ± 3.9	0.8 ± 0.3	15.7 ± 3.7	4.68 ± 0.24	$9.57^{+0.08}_{-0.06}$	0.09	0.002	$5.09^{+0.29}_{-0.47}$	0.32	9.71
K45w	1.6 ± 0.4	3.82 ± 0.37	2.2 ± 0.6	0.6 ± 0.2	2.2 ± 0.5	3.78 ± 0.31	$8.20^{+0.17}_{-0.41}$	0.08	0.004	$2.72^{+0.29}_{-0.47}$	-1.10	7.39
K47	1.7 ± 0.4	4.47 ± 0.33	1.8 ± 0.5	0.8 ± 0.2	2.4 ± 0.5	4.44 ± 0.23	$7.42^{+0.09}_{-0.03}$	0.03	0.004	$3.17^{+0.29}_{-0.48}$	-1.29	7.55
K5	3.6 ± 0.7	4.83 ± 0.69	3.7 ± 0.7	1.2 ± 0.2	6.6 ± 1.2	4.67 ± 0.17	$9.14^{+0.03}_{-0.01}$	0.15	0.002	$4.18^{+0.23}_{-0.42}$	-0.65	8.73
K50	2.6 ± 0.5	4.74 ± 0.60	3.4 ± 1.1	0.6 ± 0.3	3.0 ± 0.7	4.54 ± 0.27	$7.38^{+0.09}_{-0.26}$	0.09	0.004	$3.36^{+0.23}_{-0.41}$	-1.38	7.77
K53	2.3 ± 0.8	-	8.3 ± 2.5	0.1 ± 0.1	4.0 ± 0.7	4.28 ± 2.83	$8.07^{+0.09}_{-0.09}$	0.07	0.004	$2.93^{+0.25}_{-0.43}$	-1.35	7.85
K54	2.9 ± 0.7	4.58 ± 0.31	3.1 ± 0.9	0.7 ± 0.2	3.8 ± 1.0	4.56 ± 0.26	-	-	-	-	-	-
K55	2.4 ± 0.6	4.67 ± 1.03	2.9 ± 0.8	1.1 ± 0.3	4.9 ± 1.1	4.32 ± 0.22	$8.48^{+0.11}_{-0.23}$	0.13	0.004	$3.35^{+0.26}_{-0.45}$	-1.32	8.16
K56	2.2 ± 0.5	-	3.1 ± 0.9	0.8 ± 0.3	3.8 ± 0.8	4.26 ± 0.24	$7.90^{+0.23}_{-0.21}$	0.11	0.004	$3.33^{+0.24}_{-0.43}$	-0.93	7.95
K57	2.4 ± 0.6	-	4.2 ± 2.2	0.5 ± 0.5	3.1 ± 0.8	3.89 ± 0.38	$8.53^{+0.02}_{-0.05}$	0.09	0.004	$3.24^{+0.26}_{-0.45}$	-0.65	7.84
K61	2.0 ± 0.6	-	5.0 ± 2.3	0.3 ± 0.3	3.4 ± 0.8	4.10 ± 0.81	$7.96^{+0.49}_{-0.33}$	0.13	0.004	$2.67^{+0.33}_{-0.52}$	-1.43	7.64
K63	1.5 ± 0.5	-	2.4 ± 0.9	0.8 ± 0.3	2.9 ± 0.8	4.06 ± 0.29	$8.07^{+0.29}_{-0.26}$	0.08	0.004	$3.16^{+0.29}_{-0.47}$	-0.90	7.72
K8	2.4 ± 0.5	-	3.4 ± 1.0	0.9 ± 0.3	4.6 ± 1.1	3.89 ± 0.24	$9.45^{+0.02}_{-0.00}$	0.12	0.002	$3.65^{+0.25}_{-0.43}$	-0.24	8.32
K9	2.9 ± 0.9	-	6.3 ± 2.3	0.6 ± 0.4	6.5 ± 1.7	3.91 ± 0.29	$8.85^{+0.09}_{-0.06}$	0.09	0.002	$3.52^{+0.26}_{-0.45}$	-0.39	8.44
L14	2.8 ± 0.7	4.20 ± 1.18	3.7 ± 1.1	0.8 ± 0.3	4.7 ± 1.1	3.76 ± 0.25	$9.38^{+0.11}_{-0.03}$	0.13	0.002	$3.65^{+0.24}_{-0.42}$	-0.55	8.32
L19	4.5 ± 1.7	-	-	-	-	-	$9.55^{+0.03}_{-0.05}$	0.19	0.002	$3.85^{+0.32}_{-0.50}$	-2.08	8.67

	EFF		KING				CMD					
ID	r_c (pc)	$\log(L/L_\odot)$	r_c (pc)	c	r_h (pc)	$\log(L/L_\odot)$	log (t)	E(B-V) (mag)	Z	$\log(M/M_\odot)$	log (M/L)	$\log(t_{rh})$
L28	1.3 ± 0.3	4.38 ± 0.62	1.3 ± 0.3	1.2 ± 0.1	2.8 ± 0.5	4.28 ± 0.17	-	-	-	-	-	-
L31	1.6 ± 0.3	4.49 ± 1.03	1.7 ± 0.3	1.3 ± 0.2	3.3 ± 0.6	4.12 ± 0.17	-	-	-	-	-	-
L33	1.7 ± 0.4	4.28 ± 0.71	1.9 ± 0.5	1.0 ± 0.3	3.1 ± 0.7	4.10 ± 0.23	-	-	-	-	-	-
L48	1.6 ± 0.3	4.48 ± 0.31	1.6 ± 0.4	0.9 ± 0.1	2.3 ± 0.4	4.46 ± 0.20	$7.63^{+0.20}_{-0.05}$	0.09	0.004	$3.40^{+0.21}_{-0.40}$	-1.08	7.63
L51	1.3 ± 0.3	4.93 ± 1.29	1.7 ± 0.5	1.0 ± 0.3	2.6 ± 0.7	4.45 ± 0.23	$7.48^{+0.23}_{-0.24}$	0.02	0.004	$3.21^{+0.25}_{-0.44}$	-1.72	7.64
L52	1.1 ± 0.2	4.15 ± 0.61	1.1 ± 0.2	1.2 ± 0.2	2.0 ± 0.4	4.04 ± 0.17	$8.31^{+0.08}_{-0.10}$	0.02	0.004	$3.23^{+0.30}_{-0.48}$	-0.92	7.52
L56	1.1 ± 0.2	5.10 ± 0.38	1.0 ± 0.2	1.1 ± 0.1	1.9 ± 0.4	5.07 ± 0.18	$7.65^{+0.15}_{-0.25}$	0.05	0.004	$3.41^{+0.22}_{-0.41}$	-1.69	7.50
L65	2.0 ± 0.8	-	4.6 ± 2.9	0.7 ± 0.7	5.0 ± 2.2	4.37 ± 0.44	$7.84^{+0.18}_{-0.24}$	0.11	0.004	$3.24^{+0.23}_{-0.42}$	-1.13	8.09
L66	1.3 ± 0.2	4.85 ± 0.33	1.3 ± 0.3	0.8 ± 0.1	1.7 ± 0.3	4.82 ± 0.19	$7.44^{+0.25}_{-0.23}$	0.05	0.004	$3.21^{+0.27}_{-0.45}$	-1.64	7.36
L80	3.2 ± 0.7	-	4.7 ± 1.4	0.8 ± 0.3	5.8 ± 1.3	4.45 ± 0.24	$8.34^{+0.04}_{-0.01}$	0.05	0.004	$3.57^{+0.23}_{-0.41}$	-0.88	8.34
L91	3.6 ± 0.8	4.37 ± 0.69	5.2 ± 1.8	0.5 ± 0.3	4.5 ± 1.0	4.12 ± 0.30	$9.15^{+0.10}_{-0.02}$	0.19	0.002	$3.60^{+0.26}_{-0.44}$	-0.77	8.26
L93	3.4 ± 0.6	3.93 ± 0.47	3.8 ± 0.9	0.8 ± 0.2	4.3 ± 0.8	3.83 ± 0.20	$9.43^{+0.22}_{-0.21}$	0.06	0.002	$3.32^{+0.26}_{-0.45}$	-0.60	8.16
NGC152	6.4 ± 1.2	5.20 ± 0.74	6.7 ± 1.4	1.2 ± 0.3	11.2 ± 2.1	4.99 ± 0.18	$9.15^{+0.03}_{-0.02}$	0.13	0.002	$4.80^{+0.23}_{-0.41}$	-0.40	9.32
NGC176	3.1 ± 0.7	4.56 ± 0.37	3.5 ± 0.9	0.8 ± 0.2	4.3 ± 0.9	4.52 ± 0.23	$8.11^{+0.01}_{-0.04}$	0.07	0.004	$3.54^{+0.22}_{-0.41}$	-1.02	8.12
NGC220	2.9 ± 0.6	5.11 ± 0.72	2.9 ± 0.6	1.3 ± 0.3	6.2 ± 1.3	4.95 ± 0.18	$8.08^{+0.13}_{-0.26}$	0.08	0.004	$3.90^{+0.24}_{-0.43}$	-1.21	8.49
NGC222	2.4 ± 0.6	-	3.2 ± 0.9	1.1 ± 0.3	5.8 ± 1.5	4.90 ± 0.22	$7.92^{+0.20}_{-0.24}$	0.09	0.004	$3.79^{+0.24}_{-0.42}$	-1.12	8.40
NGC231	2.9 ± 0.7	-	4.3 ± 1.3	1.0 ± 0.3	7.2 ± 2.2	4.82 ± 0.25	$7.94^{+0.27}_{-0.15}$	0.06	0.004	$3.84^{+0.23}_{-0.41}$	-0.99	8.55
NGC241	1.8 ± 0.4	4.71 ± 0.62	1.8 ± 0.4	1.2 ± 0.3	3.5 ± 0.8	4.60 ± 0.20	$7.84^{+0.09}_{-0.21}$	0.07	0.004	$3.57^{+0.25}_{-0.43}$	-1.14	7.98
NGC242	1.4 ± 0.4	-	1.9 ± 0.5	1.1 ± 0.3	3.5 ± 0.9	4.59 ± 0.22	$7.78^{+0.10}_{-0.24}$	0.07	0.004	$3.27^{+0.28}_{-0.46}$	-1.31	7.87
NGC256	1.8 ± 0.4	4.72 ± 0.23	3.0 ± 0.7	0.3 ± 0.1	2.2 ± 0.4	4.74 ± 0.56	$7.92^{+0.00}_{-0.01}$	0.13	0.004	$3.13^{+0.29}_{-0.47}$	-1.59	7.52
NGC265	2.9 ± 0.5	5.11 ± 0.49	3.0 ± 0.6	1.0 ± 0.1	4.7 ± 0.9	5.04 ± 0.18	$8.40^{+0.05}_{-0.13}$	0.16	0.004	$3.85^{+0.25}_{-0.43}$	-1.26	8.32
NGC269	1.8 ± 0.3	4.80 ± 0.70	1.8 ± 0.3	1.3 ± 0.1	3.7 ± 0.6	4.66 ± 0.16	-	-	-	-	-	-
NGC290	0.7 ± 0.2	-	0.9 ± 0.3	1.4 ± 0.3	2.3 ± 0.5	4.96 ± 0.20	$7.93^{+0.56}_{-0.00}$	0.19	0.004	$3.76^{+0.32}_{-0.50}$	-1.20	7.78
NGC294	2.3 ± 0.4	4.92 ± 0.40	2.4 ± 0.4	0.9 ± 0.1	3.5 ± 0.6	4.88 ± 0.17	$8.70^{+0.03}_{-0.01}$	0.08	0.004	$3.81^{+0.25}_{-0.44}$	-1.10	8.14
NGC299	1.3 ± 0.3	4.98 ± 0.38	1.3 ± 0.3	0.8 ± 0.1	1.8 ± 0.4	4.94 ± 0.19	$7.65^{+0.15}_{-0.12}$	0.04	0.004	$3.05^{+0.24}_{-0.43}$	-1.93	7.36
NGC306	1.7 ± 0.4	4.71 ± 0.41	2.9 ± 0.9	0.4 ± 0.2	2.3 ± 0.5	4.66 ± 0.46	$7.77^{+0.13}_{-0.17}$	0.10	0.004	$3.27^{+0.24}_{-0.43}$	-1.44	7.60
NGC330	3.1 ± 0.6	6.08 ± 0.55	3.0 ± 0.6	1.3 ± 0.1	6.6 ± 1.2	6.01 ± 0.17	$7.29^{+0.22}_{-0.23}$	0.14	0.004	$4.61^{+0.23}_{-0.41}$	-1.46	8.77
NGC361	4.8 ± 0.9	5.09 ± 0.62	5.0 ± 0.9	1.1 ± 0.1	8.3 ± 1.5	4.95 ± 0.17	$9.49^{+0.02}_{-0.01}$	0.07	0.002	$4.49^{+0.25}_{-0.44}$	-0.60	9.03
NGC376	2.4 ± 0.6	5.32 ± 0.37	2.4 ± 0.7	0.9 ± 0.2	3.8 ± 0.8	5.29 ± 0.22	$7.42^{+0.05}_{-0.13}$	0.11	0.004	$4.10^{+0.21}_{-0.40}$	-1.22	8.21
NGC416	2.4 ± 0.5	5.45 ± 0.78	2.3 ± 0.5	1.6 ± 0.3	6.1 ± 1.2	5.30 ± 0.17	$9.79^{+0.03}_{-0.04}$	0.12	0.002	$4.81^{+0.26}_{-0.44}$	-0.64	9.00
NGC419	3.6 ± 0.6	5.72 ± 0.57	3.3 ± 0.6	1.3 ± 0.1	7.9 ± 1.4	5.65 ± 0.16	$9.13^{+0.00}_{-0.04}$	0.09	0.002	$5.16^{+0.22}_{-0.40}$	-0.56	9.25
OGLE132	-	-	2.5 ± 1.9	0.4 ± 0.6	1.8 ± 0.6	3.55 ± 0.59	$9.09^{+0.21}_{-0.09}$	0.14	0.002	$2.95^{+0.40}_{-0.58}$	-0.60	7.42
OGLE172	0.5 ± 0.2	2.66 ± 0.31	1.7 ± 0.5	0.0 ± 0.1	0.7 ± 0.1	2.60 ± 5.67	-	-	-	-	-	-
OGLE28	0.6 ± 0.2	-	1.1 ± 0.6	0.6 ± 0.5	1.1 ± 0.3	2.94 ± 0.39	-	-	-	-	-	-
OGLE5	0.6 ± 0.2	2.31 ± 0.39	1.7 ± 0.7	0.0 ± 0.2	0.7 ± 0.1	2.20 ± 4.91	-	-	-	-	-	-
OGLE53	0.9 ± 0.3	-	2.4 ± 1.9	0.1 ± 0.5	1.0 ± 0.3	3.39 ± 3.54	-	-	-	-	-	-
OGLE6	0.2 ± 0.1	-	0.3 ± 0.1	1.1 ± 0.3	0.6 ± 0.2	2.67 ± 0.22	$9.59^{+0.14}_{-0.40}$	0.08	0.002	$2.86^{+0.57}_{-0.75}$	0.19	6.71
RZ140	1.3 ± 0.4	-	2.0 ± 0.8	0.7 ± 0.4	2.3 ± 0.7	3.21 ± 0.32	$9.13^{+0.05}_{-0.04}$	0.09	0.002	$3.15^{+0.25}_{-0.44}$	-0.06	7.66
RZ82	1.1 ± 0.2	3.24 ± 0.69	1.3 ± 0.4	0.8 ± 0.3	1.6 ± 0.3	3.02 ± 0.22	-	-	-	-	-	-

a sample of young massive SCs (i.e. $\log(M/M_{\odot}) \geq 5 * 10^3$ and $t \leq 200$Myr). Both works indicated the mass-loss by stellar evolution as the candidate physical mechanism responsible for the presence of such core radius-age relationship. Chandar et al. [2016] studied 3816 SCs in M51, finding again an expansion during their early life. San Roman et al. [2012], on the basis of the study of 161 SCs in M33 depicted a trend quite similar to the one observed in the LMC [Elson, 1991, 1992, Elson et al., 1989, Mackey and Gilmore, 2003a], namely an increasing core radius spread with age [see e.g., Fig. 14 in Mackey and Gilmore, 2003a]. A hint for a similar behaviour was found for the first time in the SMC by Mackey and Gilmore [2003b] based on a sample of 10 SCs. More recently, Carvalho et al. [2008] and Santos et al. [2020] investigated a larger but still rather small sample of 23 and 25 SMC SCs, respectively, observing a larger spread of the core radius for SCs older than $\log(t) \sim$8.5 dex with respect to young SCs [e.g., Fig. 14 in Santos et al., 2020]. The current scenario assumes that, besides an expansion in the early SC life likely due to mass-loss from stellar evolution, another inner physical process triggers some SCs to increase their core radius as they get older than $\log(t) = 8.0 - 8.5$ dex, but what the actual mechanism is and why it affects only a fraction of the SCs is still an open question. In Fig. 7.7 we showed the $r_{\rm c}$ as a function of the SC ages, colour coded according to their estimated mass for the sample of 134 SCs investigated in this work. To widen the sample and to augment the probed age interval, we also plotted in the same figure LMC and SMC SCs analyzed by Mackey and Gilmore [2003a] and Mackey and Gilmore [2003b], so that the total sample of SCs displayed in the figure is 185 objects. An inspection of Fig. 7.7 confirms that SCs younger than $\sim$ 200-300 Myr ($\log(t) \sim 8.3 - 8.5$ dex) are all compact with no exception.[12] More precisely, an early expansion in the first 10-20 Myr seems to be present. This early expansion has been detected also in stellar systems beyond the MCs [e.g., Chandar et al., 2016, Ryon et al., 2015, 2017], and is thought to be caused by mass-loss from stellar evolution.

After this rapid phase of expansion, for the next 200-300 Myr the core radius does not seem to experience any further alteration. Beyond $t \sim$200 Myr a few SCs with $r_{\rm c} > 3.5$ pc appear, while at $t \geq 1$ Gyr the fraction of SCs with $r_{\rm c} > 3.5$ pc becomes significant. Hence, a different process with respect to that responsible for the early expansion must be invoked to explain the core radius expansion at ages later than $t \sim$200 Myr. In the following we refer to this feature as core radius-age relationship, as done in previous works. This behaviour has been explained by Elson et al. [1989] and Mackey and Gilmore [2003a] as a real evolution during the SCs lifetime. Taking advantage of the larger number and wider range in mass of our SC sample we may put

[12] Actually, three SCs reach 3.5 pc at 1σ.

constraints on the physics behind the core radius expansion. First of all, the fraction of SCs having $\log(t) \geq 8.25$ and $r_c \geq 3.5$ pc is ~ 0.28. If this fraction were constant all along the SC lifetime we would expect about 22 young SCs with a large core radius, hence the complete lack of them is significant at more than the 4σ level.

A closer inspection of Fig. 7.7 also suggests that the majority of the SCs with large core radii are also very massive. We wonder whether the mass could be, in first approximation, the physical parameter that drives intermediate-age SCs to expand their inner regions. To better investigate this hypothesis, in Fig. 7.8 we split up the r_c-age plot into two different mass intervals. The difference between the two panels is remarkable: in the high mass range (i.e. $M \geq 10^{3.5} M_\odot$, bottom panel) 40% of the SCs older than $\log(t) \geq 8.25$ have experienced an inner expansion. Keeping the same percentage also in the low mass interval (i.e. $M < 10^{3.5} M_\odot$, top panel) I would expect to find that 13 intermediate-age SCs have $r_c \geq 3.5$ pc, while, in practice, none are observed, a result that is significant at more than the 3σ level. Another interesting feature visible in the same figure is that SCs older than 10-20 Myr in the high-mass regime seem to have, on average, a larger core radius with respect to those in the low-mass regime. This might indicate that the early expansion could be more severe for massive SCs, or perhaps that low-mass SCs that experience a great expansion do not survive. To summarize, after a rapid expansion during the first 10-20 Myr, all SCs younger than about 200-300 Myr are compact regardless of their mass, while the subsequent evolutionary path appears to be very different for low/high mass SCs as they get older.

In principle, we cannot exclude the possibility that only massive clusters are able to survive to old ages even if they are not very compact. However, in our sample a non-negligible number of old and low mass SCs is present. In particular, in the low-mass regime, 18 SCs are older than 1 Gyr. This confirms the hypothesis that the SC mass is crucial to drive the core expansion.[13]

The fact that the core radius-age relationship likely originates from a physical process that begins when the SC is already a few hundred Myr old, and that affects only massive SCs, suggests that gas expulsion or mass loss due to stellar evolution are not the favourite mechanisms responsible for the expansion, as they are only effective in the early phases of a SC's life. Mackey et al. [2008] discussed the possibility that a consistent population of retained stellar mass black holes could lead to an expansion of the cluster core. Such a process starts after a few hundreds of Myr and causes a sustained increase of the cluster core, lasting for many Gyrs. They tested

[13] One potential selection effect is that low mass SCs, especially with large radii (and/or old ages) are unlikely to end up in cluster catalogues in the first place.

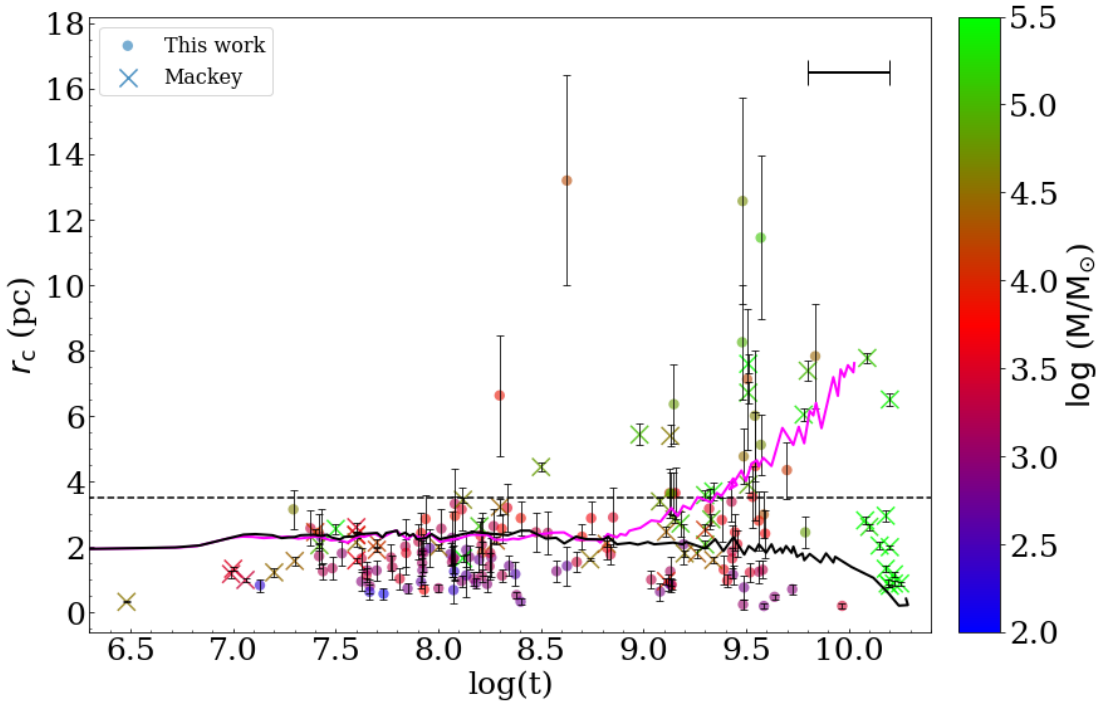

Figure 7.7: Core radius, estimated via an EFF profile, versus the SC age. Filled circles indicate SCs analyzed in this work while crosses represent SCs studied by Mackey and Gilmore [2003a] and Mackey and Gilmore [2003b]. All SCs are colour coded according to their mass. In order to keep the figure readable, we do not draw the errors on the x-axis. A typical age errorbar of $\Delta \log(t) = 0.2$ dex is shown in the upper-right corner. The horizontal dashed line is at 3.5 pc. The two solid lines represent the results of N-body simulations extrapolated from Mackey et al. [2008]; for a case with no primordial mass segregation and a fraction of retained BH $f_{\rm BH} = 1$ (magenta line) and $f_{\rm BH} = 0$ (black line), respectively.

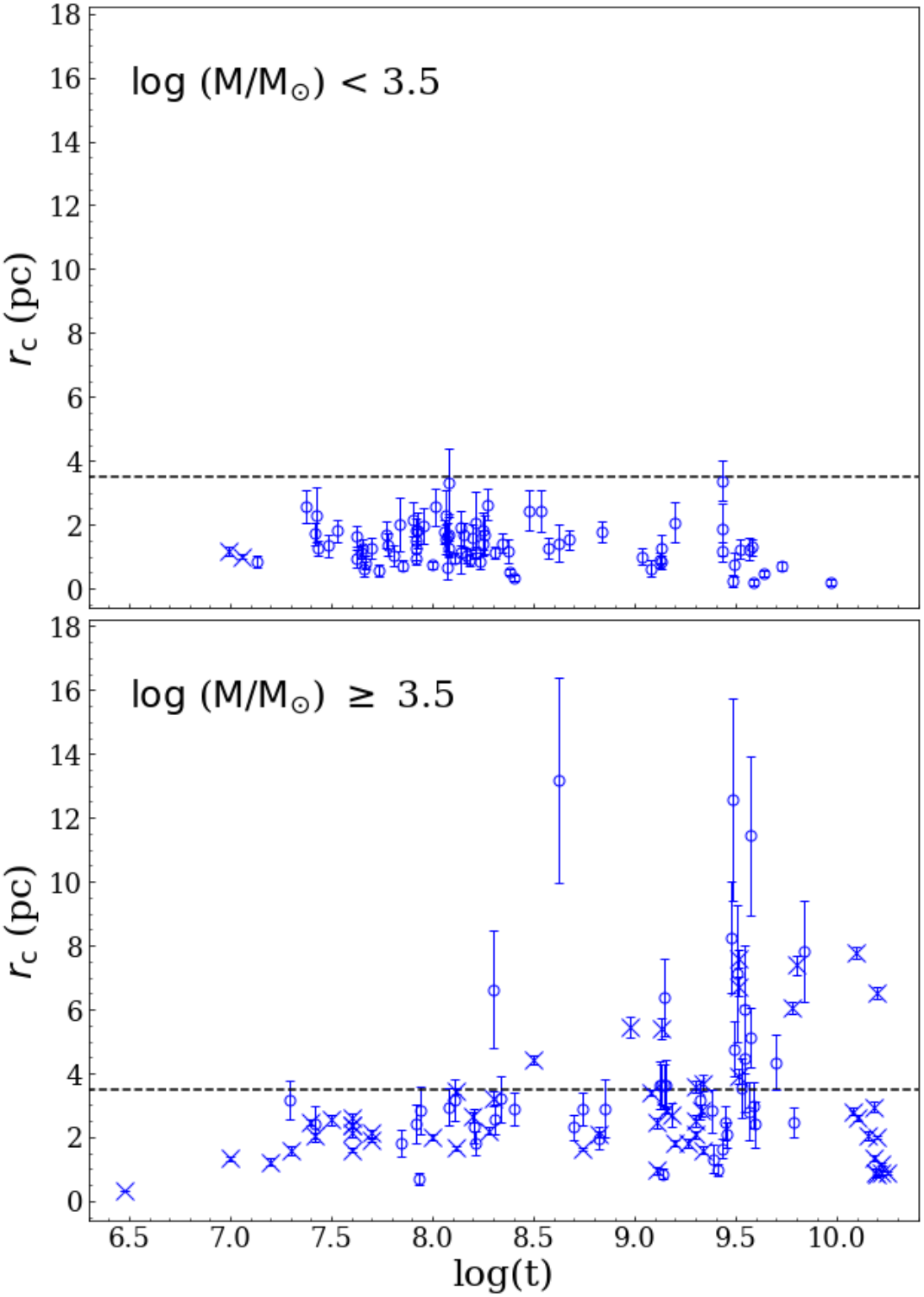

Figure 7.8: Same as figure 7.7 but with SCs splitted into different mass ranges. *Top*: SCs with $M < 10^{3.5} M_{\odot}$. *Bottom*: SCs with $M \geq 10^{3.5} M_{\odot}$.

this process through N-body simulations of massive clusters (i.e. initial total cluster masses of $\log M_{\rm tot} \sim 10^{4.75}$). By varying the fraction of retained stellar BHs at a fixed SC mass, they found that the expansion rate is strongly dependent on this fraction, and that if it is not large enough, the expansion would not begin at all. In Fig. 7.7 we reported two runs of the N-body simulations performed by Mackey et al. [2008], extrapolated from their Fig. 5. The two lines represent two extreme cases: i) with no primordial mass segregation and a fraction of retained BH $f_{\rm BH} = 1$ and ii) with a fraction $f_{\rm BH} = 0$. The former predicts an expansion of the core radius, which never ends, after about 1 Gyr. Mackey et al. [2008] tested also other possibilities (not displayed in the figure to preserve readability), that foresee different evolutionary paths. For example, by imposing also a primordial mass segregation, the inner expansion starts when a SC has about 10 Myr (see their Fig. 15), and this occurrence might explain the few SCs younger than 1 Gyr observed to have a larger core radius. As the potential well of low mass SCs is shallower, it would be possible that a large fraction of BHs is able to escape from their parent SC. This hypothesis might explain why we do not observe a core radius growth for low mass SCs. Nevertheless, N-body simulations with a finer mass resolution are crucial to shed light on this matter. For example, it could clarify whether or not a small fraction of retained BHs in low mass SCs could trigger the inner expansion. Even the presence of a IMBH could drive a prolonged expansion of the SC radius, although Baumgardt et al. [2004b] showed that this effect is anti-correlated with the number of stars belonging to the SC, hence this outcome is at odds with our result. Nevertheless, we cannot exclude the possibility that also less massive SCs undergo an increase of their $r_{\rm c}$, but due to their low mass (i.e. low gravitational potential) this process ends up with the evaporation of the SC. Therefore we do not observe such kind of SCs, since they dissolve faster with respect to the more massive ones.

Unfortunately, all previous investigations based on N-body simulations studied only the evolution of SCs with $M \sim 10^4 - 10^5 M_{\odot}$ or larger. N-body studies probing lower mass SCs (down to hundreds of solar masses as in the present study) are urgently needed to understand how the different physical mechanisms affect differentially low and high mass SCs.

7.5.2 Mass-radius relationship

Figure 7.9 depicts the estimated SC mass as a function of the core radius derived through the EFF profile. We notice a tight linear trend in the $\log - \log$ space along almost the whole range of core radii, even if we can recognise a few very compact but massive SCs. A weighted linear

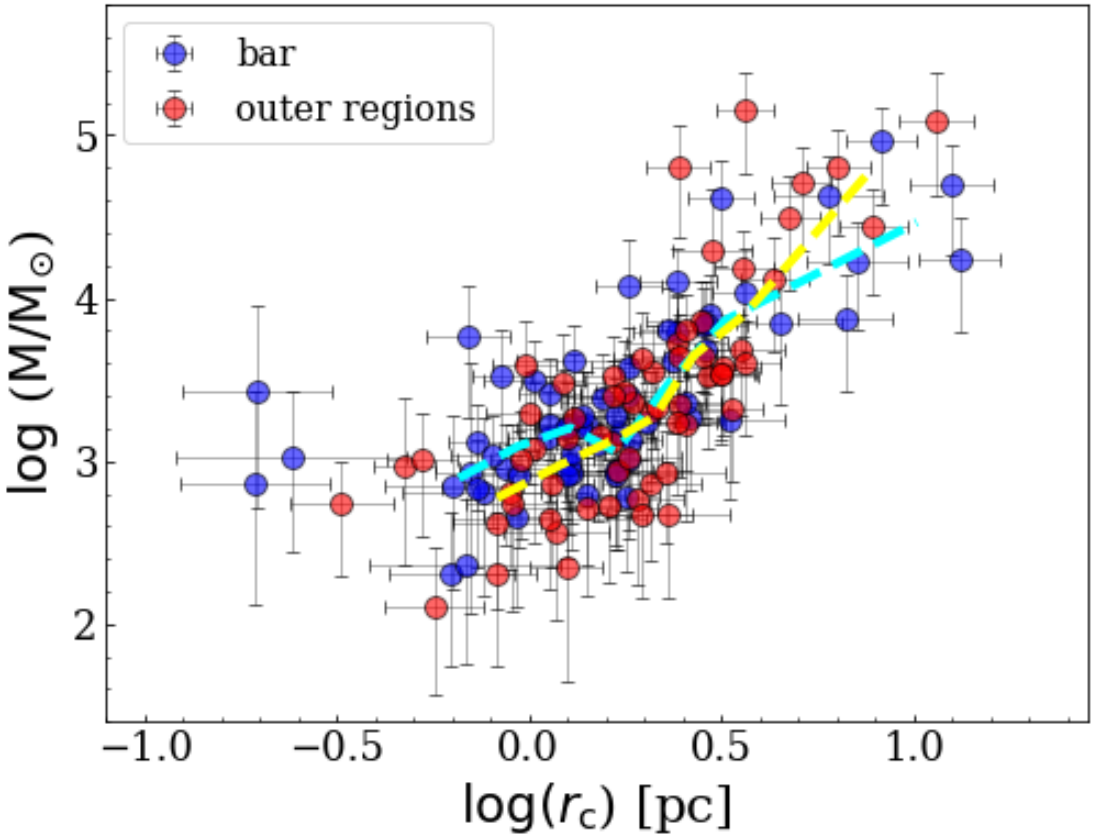

Figure 7.9: Mass-size relationship. The core radius was derived with an EFF profile. Blue and red points define the SCs belonging to the SMC bar and to the outer regions, respectively. Cyan and yellow dashed lines indicate the median of the SC mass calculated in bin intervals built in order to have a minimum number of 10 objects for the bar and outer SCs, respectively.

fit (i.e. $\log M = a + b \cdot \log r_c$) [14] yielded a = 2.91 ± 0.08 and b = 1.54 ± 0.30. We derived a Spearman rank of 0.43, with a significance larger than 99%. This outcome is at odds with Mackey and Gilmore [2003b] and their sample of 10 SMC SCs, while a linear trend has been found by Carvalho et al. [2008], although their range of masses was considerably smaller than ours. In fact, it is the first time that such a trend is observed in the SMC for a conspicuous number of SCs spanning an interval of masses of ~ 4 order of magnitudes, down to hundreds of solar masses.

In Figure 7.9 we also analyzed separately the behaviour of the SCs located within the SMC bar and in the outer regions (see also Fig. 7.1). An inspection of this figure suggests that the most compact objects are in the bar. Looking at the median masses that are outlined with dashed lines in Fig. 7.9 for both inner and outer SCs, we observed, on average, a similar mass at any given radius between the two sub-populations, indicating that the bar, despite being a denser environment, might not have a primary role in the evolutionary path of the SCs in the SMC.

7.5.3 SC parameters as function of their spatial positions

We investigated the distribution of the SC main parameters as a function of their galactocentric distance. Figure 7.10 shows the distribution of the age (top panel), core radius (middle panel) and mass (bottom panel) with the distance. Regarding the age, the majority of SCs younger than $\sim \log(t) = 8.5$ dex is placed in the bar. Vice versa, beyond $\sim 1.5°$ the SC population is preferentially composed by intermediate-age objects. This result is consistent with the literature [Bica et al., 2020, Dias et al., 2016, Maia et al., 2014, Piatti, 2021c]. No apparent trend stands out clearly in the last two panels, as is evident also by the medians of these physical quantities. The SCs located beyond 3° belong to the SMC Bridge and are younger than 1 Gyr. Moreover, their size and mass are smaller than the averages estimated within 3° (i.e. ~ 1 pc and ≤ 1000 solar masses, respectively). We can speculate that this reflects their birth in a low-density region.

7.6 Discussion

A mass-radius relation is expected to be present since the early stages of SC formation. Indeed, a relation of the form $R \propto M^{\alpha}$ has been found in the MW's SC forming regions, where they

[14] We adopted the RANSAC (RANdom SAmple Consensus) algorithm implemented by the SCIKIT-LEARN python package [Pedregosa et al., 2011], in conjunction with a bootstrap procedure

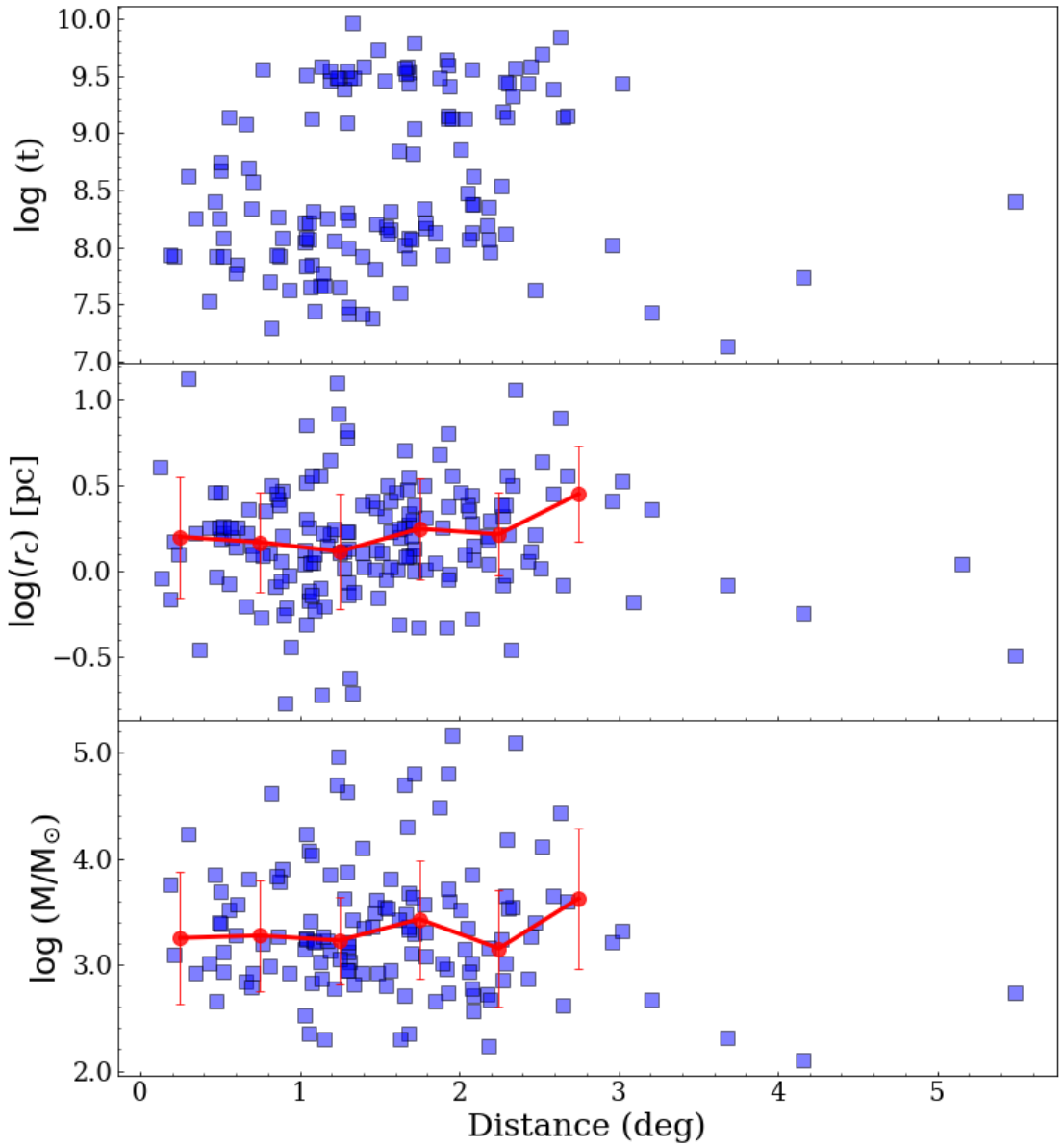

Figure 7.10: Age (top), core radius (middle) and mass (bottom) as a function of galactocentric distance, expressed in degrees. Red circles mark the medians estimated in bins of 0.5 degrees.

are present as dense clumps within giant molecular clouds (GMCs). The same kind of relation was found very recently also in the LMC [see Mok et al., 2021, and references therein]. The exponent of this power-law estimated from the proto-clusters is in the range $0.3 \leq \alpha \leq 0.6$. A mass-radius direct proportionality holds also in the already formed SCs, and it has been observed in other environments beside the MW, such as nearby galaxies [e.g. M31, M51, M82, etc., see the detailed review by Krumholz et al., 2019, and references therein]. In figure 9 in Krumholz et al. [2019], the authors drew on the same plot the half-light radius as a function of the mass for SCs belonging to many different galaxies in the Local Group, concluding that the relation seems to have the general form $r_{\rm h} \propto M^{1/3}$[15]. Nevertheless, the authors also pointed out that the scatter is too broad to devise a linear fit, either by considering only SCs hosted by the same galaxy or all SCs belonging to different systems. As a cluster grows older, new physical mechanisms become dominant and the mass-radius trend could change or even reverse its sign.

We can take advantage of our large sample of SCs to investigate the dynamical status of our SCs. Mass segregation and core collapse may be signs of an advanced evolutionary phase. A good proxy for the dynamical evolutionary status of a SC is represented by the ratio between the age and the relaxation time of the SC, i.e. $age/t_{\rm rh}$. According to Spitzer [1987], $t_{\rm rh}$ is expressed as:

$$t_{\rm rh} = 8.933 \times 10^5 yr \times \frac{1}{\ln(0.4N_*)} < m_* >^{-1} M^{1/2} r_{\rm h}^{3/2} \tag{7.4}$$

where $N_* = M/ < m_* >$ is the estimated number of stars belonging to the SC and $< m_* >$ is the average stellar mass in solar units. To get an appropriate $< m_* >$, I integrated IMF models of different ages, in order to derive a very tight $< m_* >$-age relationship. Glatt et al. [2011] determined the present day mass function of six intermediate-age SMC SCs (in the age interval between 6 and 10.5 Gyr) using deep data from the HST, finding that all six SCs show signs of mass segregation to different degrees, suggesting that they are dynamically evolved and/or had primordial mass segregation. They also estimated the present day relaxation time for the six SCs to be a few Gyrs, i.e comparable to their ages, with the exception of one object. In Fig. 7.11 we plotted the estimated half-light radius as a function of the core radius, with SCs painted with different colours according to their evolutionary age for the SMC SCs investigated in this work (left panel). The six SCs studied by Glatt et al. [2011] are also overplotted in Fig 7.11[16] and their dynamical ages are very similar to most SCs investigated in this work, hence we expect that also other SMC SCs might show signs of mass segregation.

[15] In this work (see also figure 7.9) we obtained a relation of $r_{\rm c} \propto M^{0.34}$.

[16] Their sizes have been taken from Glatt et al. [2009].

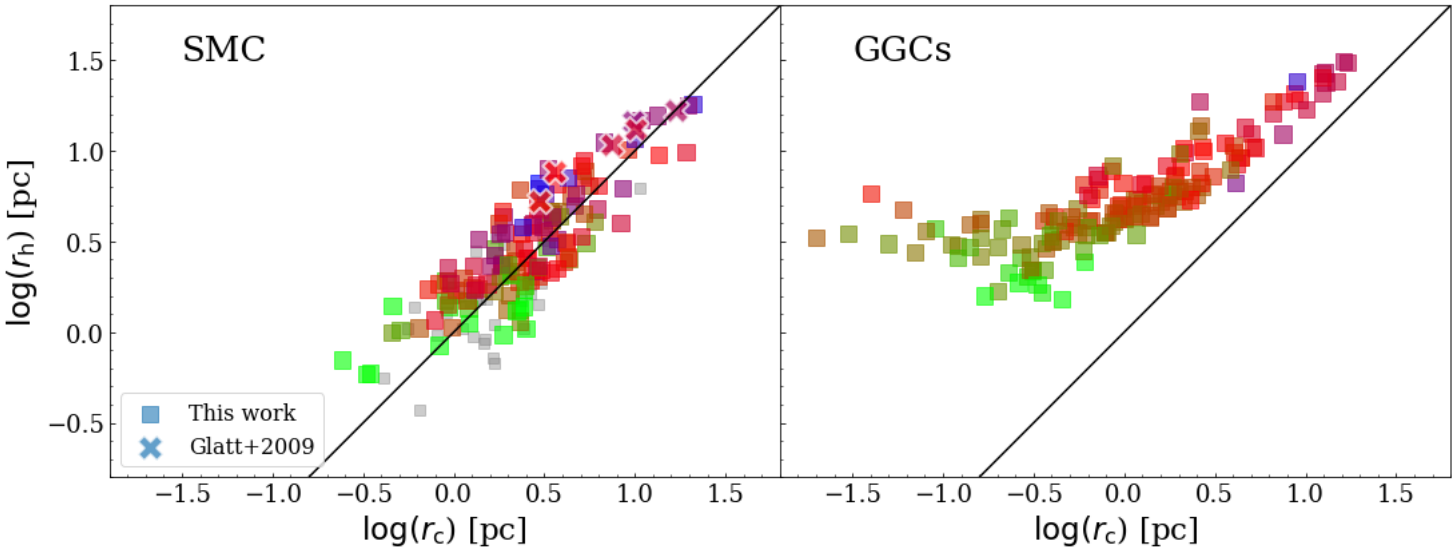

Figure 7.11: *Left:* Half-light radius as a function of core radius, estimated in this work using King profiles. *Right:* Same plot for GGCs taken from Baumgardt's GGC database. Crosses indicate six SCs analysed by Glatt et al. [2009]. The black solid line indicates the one-to-one relationship. SCs are colour-coded according their dynamical age (see definition in the text). SCs with no estimated age are plotted in gray

In the right panel of the same figure, we also plotted the GGCs.[17] The GGC population is quite different with respect to the SMC SC system, as it contains much more massive and much older objects. In particular, the SMC contains only one GC (i.e. NGC 121), while the MW does not have populous intermediate-age and young SCs as the SMC. Also, GGCs are objects typically older than 10 Gyr. Nevertheless, it would be instructive comparing the two systems. In addition, the MW is also representative of a very different environment with respect to the SMC (i.e. stronger tidal fields, the presence of a bulge and a thick and thin discs where the GGCs pass through, etc.). A remarkable feature visible in Figure 7.11 for the GGCs is a noteworthy deviation from the identity relationship for $r_c \leq 5$ pc ($\log r_c \sim 0.7$). While going towards lower r_c values the trend flattens out, settling around $r_h \sim 1-3$ pc ($\log r_h \sim 0.0-0.5$) at the lowest end of the relation. As suggested by Djorgovski [1996], r_c and r_h are fairly similar as long as $t_{rc} \gg$ SC age, after which the core collapses with little changes in the half-light radius. A completely different behaviour is visible for the SMC clusters studied here. Indeed, a linear trend emerges for the entire range of observed radii. This reveals that, unlike SMC SCs, the GGCs have entered a core collapse phase despite a similar age/t_{rh} ratio. suggesting that the SC evolutionary path

[17] Here we exploited data from Baumgardt's GGC database (https://people.smp.uq.edu.au/HolgerBaumgardt/globular/) which contains an up-to-date compilation of 158 GGCs fundamental parameters.

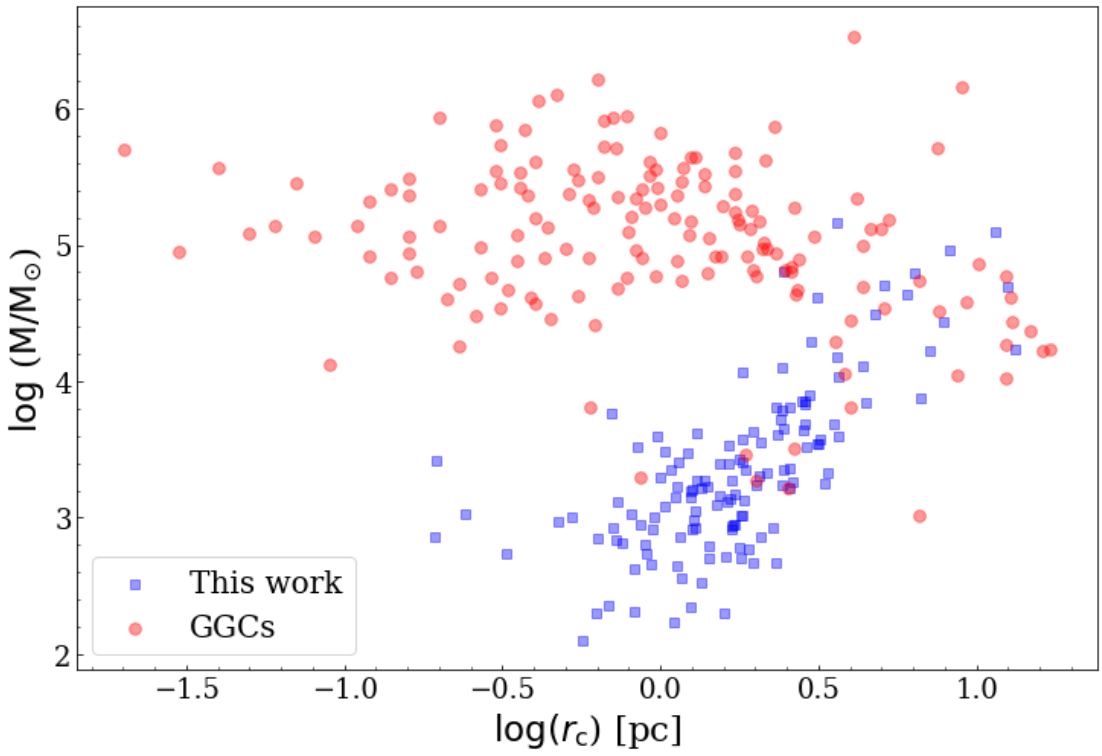

Figure 7.12: Core radius - mass relationship with GGCs (red points) and our SMC sample (blue squares).

in the two systems is noticeable different.

In order to better investigate how a different evolutionary status leads to different mass-size trends, in Fig. 7.12 we compare mass vs core radius for our sample of SCs with those of GGCs. This plot shows that, in contrast to the SMC case, the average mass of GGCs is quite constant (i.e. $\log(M/M_\odot \sim 10^5 - 10^{5.5}$ dex) up to $r_c \leq 1$ pc, then it begins to decrease at larger core radii. As anticipated, the break of the mass-size relationship, or even the reverse sign at the upper end, reveals that the dynamical state of GGCs entered the so-called core collapse phase [Harris, 1996, McLaughlin and van der Marel, 2005]. Additionally, the mass spectrum of the two galaxies is remarkably different. The SCs analyzed in this work cover a broad range of masses, from hundreds up to a million of solar masses, while the majority of the GGCs have $M \geq 10^4 M_\odot$ [e.g., Baumgardt and Hilker, 2018, Harris, 1996]. It is evident that tidal effects of the MW had a great impact on the survival of the low mass GGCs, as expected, while this effect is not visible in the SMC, at least in our sample. In their landmark paper, Gnedin and Ostriker [1997] investigated the destruction of the GGCs and showed that in the inner regions, only fairly massive and compact clusters can survive. This is largely due to external effects

such as tides, disk shocks, etc., which should be largely absent in the SMC. Thus, environment can play a considerable role, but is probably much less important in a dwarf irregular like the SMC. Another key difference is the age: with the exception of NGC 121, the SMC SCs are much younger than the GGCs and hence had less time to evolve dynamically. To summarize, although the SMC SCs seem dynamically evolved, showing in a few cases signs of mass segregation Glatt et al. [2011], they are not in a core-collapse phase yet.

7.7 Conclusions

We provide SBPs from homogeneous g band integrated photometry for 170 SMC star clusters. For 62 of them this is the first SBP appearing in the literature. The derived profiles were fitted with EFF and King models. We list for all the clusters the structural parameters obtained from the SBP fits (core and half-light radii, total luminosity, etc.). We estimated ages and masses for 134 SCs by means of the open source python package ASteCA. Finally, we derived the projected distances of all SCs with respect to the SMC centre to investigate if/how their properties vary with galactocentric distance. The main results of this study are the following: disclose the following outcomes:

- We find that young SCs are compact, while clusters older than $\log(t) \sim 8.3$ dex show a wide range of r_c values. This occurrence has been already noted and discussed in the literature, here we confirm and strengthen it on the basis of a much larger SC sample. The quoted feature has been observed also in other galaxies (see discussion in the Introduction), suggesting that the evolutionary path of SCs is the same regardless of the hosting galaxy. However, the physical mechanism responsible for this phenomenon is still unclear. We speculate that the SC mass is the main parameter driving the inner expansion, as none of the SCs with $\log(M/M_{\odot}) < 3.5$ dex have been observed to go through such an expansion.

- A mass-size relation clearly stands out over almost the entire range of radii covered in this work. Analysing this relationship separately for SCs placed in the bar (i.e. with distance $d \leq 1.5°$ from the SMC centre) and those outside, we did not find any remarkable difference.

- We do not find any trend of the relevant SC parameters with distance from the SMC centre, except that young SCs are mainly concentrated in the bar and vice-versa. We caution that projection effects may play a role given the large depth extent of the SMC.

- We derived the dynamical age of our sample and we excluded that any of the studied SCs is in a core collapse phase. However, we cannot rule out that some of them present mass segregation to different degrees, as observed by Glatt et al. [2011], in a sub-sample of six old ($t > 6$ Gyrs) SMC SCs.

Chapter 8

Research of ongoing tidal stripping structures around the LMC

This chapter is based on the manuscript submitted to the Astrophysical Journal, Gatto et al., 2022a: "Discovery of NES, an extended tidal structure in the North-East of the Large Magellanic Cloud".

As extensively discussed in §1.2, due to their proximity, the MCs offer a unique opportunity to investigate in great detail the physical effects of a three-body encounter, among the LMC, SMC, and the MW. According to N-body simulations, the expected outcome of these interactions is a wealth of complex and extended tidal features, that may be very difficult to detect because of their very low surface brightness [e.g., Bullock and Johnston, 2005, Cooper et al., 2010]. Moreover, the origin and the present-day shape of these features require not just tidal effects, but also hydro-dynamical effects of interaction between the MCs [e.g. Wang et al., 2019, and references therein].

In the last decade, several of these structures have been discovered, thanks to modern deep panoramic surveys [e.g, Belokurov and Koposov, 2016, Choi et al., 2018b, El Youssoufi et al., 2021, Mackey et al., 2016, 2018, Massana et al., 2020, Pieres et al., 2017]. These discoveries aided to decipher the interaction history of the MCs, whose morphology and kinematics have been shaped in the last Gyrs by their mutual attraction and by the gravitational interference induced by the MW [e.g., Belokurov and Erkal, 2019, Besla et al., 2012]. Even more valuable, the Early Data Release 3 (EDR3) of the *Gaia* mission [Gaia Collaboration et al., 2016, 2021a] made it possible to kinematically characterize the already known tidal substructures [e.g., Cullinane

et al., 2022, James et al., 2021, Omkumar et al., 2021, Piatti, 2022a, Schmidt et al., 2020, Zivick et al., 2019], to unveil the response of the MW halo to the LMC [e.g., Belokurov et al., 2019, Conroy et al., 2021, Garavito-Camargo et al., 2019, Vasiliev et al., 2021], and also to discover new stellar streams [Belokurov and Erkal, 2019, De Leo et al., 2020, Grady et al., 2021, Petersen et al., 2021].

Amongst the numerous sub-structures revealed in the last years, the arm-like stellar over-density to the North of the LMC, currently known as Northern Tidal Arm (NTA), discovered by Mackey et al. [2016] thanks to the analysis of the public Dark Energy Survey (DES), is particularly prominent. This sub-structure was traced in all its extension by Belokurov and Erkal [2019] using red giant branch (RGB) stars selected by means of *Gaia* DR2 [Gaia Collaboration et al., 2018a]. Different authors ran N-body simulations of a MW-LMC interaction to explain the origin of this feature [Belokurov and Erkal, 2019, Cullinane et al., 2022, Mackey et al., 2016]. For example, Belokurov and Erkal [2019] simulated the evolution of the LMC particles in the last 1 Gyr in the presence of the only MW or SMC, and also under the influence of both galaxies. They also sampled the simulation outcomes with different LMC and SMC mass values. They concluded that the MW is the main actor producing the bending of the Northern part of the LMC disc, but a combination of both the MW and the SMC is needed to originate the ensemble of tidal substructures observed around the LMC. Cullinane et al. [2022] also produced a suite of dynamical simulations of MW-LMC or MW-LMC-SMC interactions, letting them evolve during the last 1 Gyr, and treating each system as a particle sourcing potential in order to consider the response of the MW motion to the LMC. Similarly to Belokurov and Erkal [2019], they inferred that the tidal force of the MW is the primary responsible of the LMC Northern bending. It is worth noticing that all these simulations predict a more diffuse twisted stream, located towards the North-East of the LMC, rather than a thin and horizontal arm as observed so-far.

In this paper, we use *Gaia* EDR3 results to select stars belonging to the intermediate and old population of the LMC to trace the very low-surface brightness regions in the outskirts of the LMC. This procedure allows us to discover a more diffuse stellar structure protruding from the outer disk of the LMC in the North-East direction, right below the NTA and in the same position predicted by existing dynamical models [Belokurov and Erkal, 2019, Cullinane et al., 2022, Mackey et al., 2016].

In this chapter we discuss the discovery of the observational counterpart of the stellar sub-structure predicted by the above mentioned simulations and protruding for $> 5^{\circ}$ from the North-Eastern rim of the LMC disc. Differently to the works described in the previous chapters,

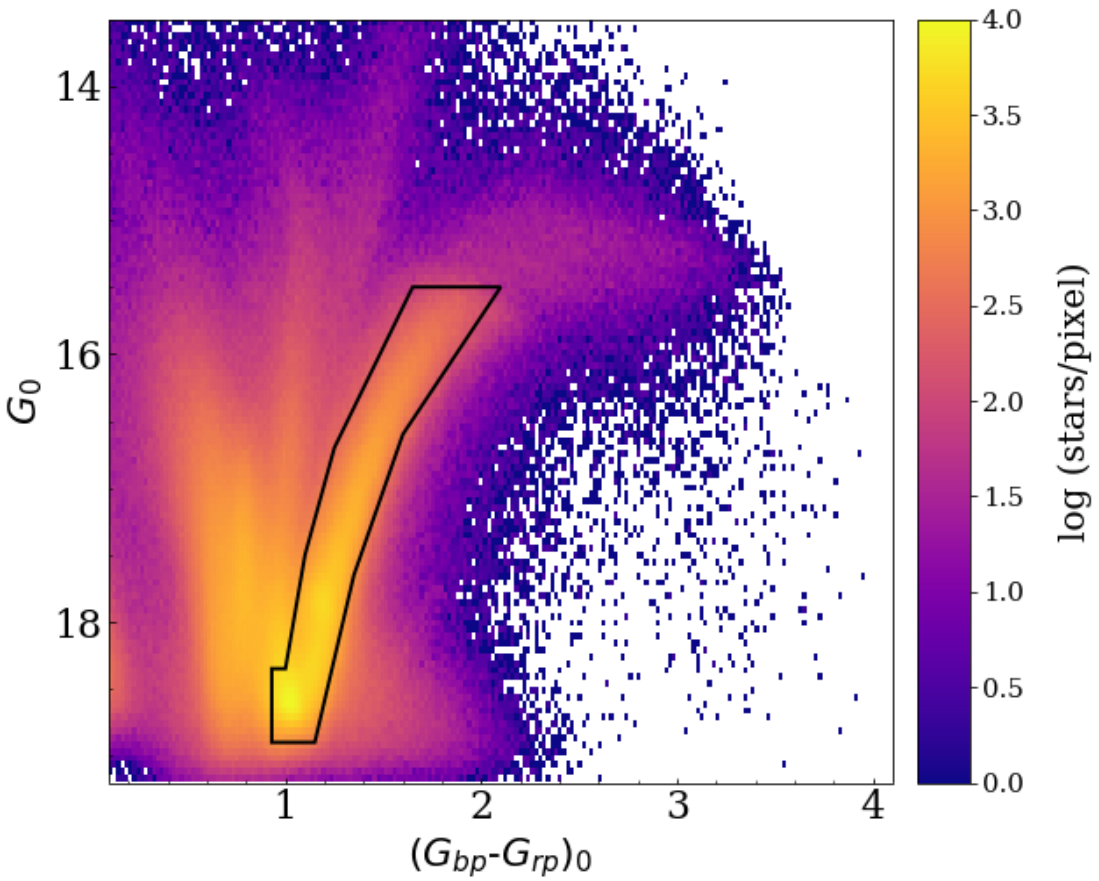

Figure 8.1: CMD of all stars retrieved with the *Gaia* query, corrected for reddening. The black polygon defines the RGB+RC star selection.

which are based on the YMCA and STEP surveys deep photometry, here we adopted the multi-dimensional data retrieved from the *Gaia* EDR3. Indeed, the proper motions conjugated with the accurate and homogeneous photometry provided by *Gaia* allowed us to select stars belonging to the intermediate and old population of the LMC, removing the contamination from the MW and permitting us to trace the very low-surface brightness regions in the outskirts of the LMC.

8.1 Sample selection

To carry on a preliminary selection of stars potentially belonging to the LMC, we performed a query to the Gaia database[1] to retrieve astrometric and photometric information from *Gaia*

[1]https://gea.esac.esa.int/archive/

EDR3 [Gaia Collaboration et al., 2021a]. In particular, we confined our research in a sky region defined by the Galactic longitude $200 \leq l \leq 360$ and Galactic latitude $-90 \leq b \leq -10$, in order to avoid likely MW disc stars which can cause significant contamination to the sample. Moreover, we restricted the query to objects whose PMs are within 3σ from the mean LMC and SMC PMs as measured by Gaia Collaboration et al. [2021b]. Following a procedure similar to that described by Gaia Collaboration et al. [2021b], we minimized contamination from MW foreground stars, by requiring that $\varpi \leq 3\ \sigma_{\varpi}$, where ϖ and σ_{ϖ} are the parallax and the parallax uncertainties, respectively. The latter selection allowed us to exclude sources not compatible with the LMC distance. In addition, we filtered out the stars having errors larger than 0.2 mas yr^{-1} in each of the two PM components and the sources with $\mathrm{RUWE}^2 > 1.3$ astrometric_excess_noise_sig > 2 to limit our sample to objects with good PMs accuracy and reliable astrometric solutions (see App. **??** for a reproduction of the query). This query yielded a total of $4,363,722$ stars.

We used the photometry provided by *Gaia* to select both RGB and red clump (RC) stars in the colour-magnitude diagram (CMD), using G, G_{BP}, G_{RP} *Gaia* filters. We focused only on the stars belonging to the intermediate-old populations, because they are known to be distributed at large distances from the LMC centre [e.g., El Youssoufi et al., 2021, Gaia Collaboration et al., 2021b]. As a first step, we corrected the photometry for the reddening, to avoid that highly extincted MW disk stars could contaminate our sample. To this end, we adopted the reddening maps by Skowron et al. [2021] that provided extinction values in the inner regions of the LMC and SMC, i.e. $\sim 6^{\circ}$ and $\sim 5^{\circ}$ from the LMC and SMC centre, respectively. Outside these regions, we sampled the reddening maps by Schlegel et al. [1998] by means of the python package `DUSTMAPS` [Green, 2018]. We calculated the extinction in the *Gaia* filters through the relations provided by Wang and Chen [2019]. Using the dereddened photometry, we finally selected bona-fide RGB and RC stars by including in our sample all the stars inscribed within the polygon shown in Fig. 8.1 (see also App. **??**). This procedure yielded a total of $1,759,796$ stars, that after a quick visual investigation about their sky positions we deduced are a mix of LMC and SMC stars, with a still not negligible contamination by MW stars (see next section). To further remove the MW noise, it is useful to adopt a new reference frame centred on the LMC, in which the new PMs represent the motion of a star in the plane of the LMC disc. To this aim, we took advantage of the transformation laws reported in Gaia Collaboration et al. [2021b] (see their Eqs. 5 and 6) to define the new coordinates ξ, η, the new PMs $\dot{\xi}, \dot{\eta}$, which represent the

[2]Re-normalised unit weight error, see Sect. 14.1.2 of "Gaia Data Release 2 Documentation release 1.2"; https://gea.esac.esa.int/archive/documentation/GDR2/

coordinates and PMs of a star moving on the flat disc defined by the plane of the LMC[3]. In this new reference system we also calculated the radial and tangential velocities v_R, v_ϕ, and the third component of the angular momentum L_z. The quantity L_z is particularly useful to further clean our sample. In particular, we estimated the average LMC $L_{z,LMC}$ by using all the stars within 8° from the LMC centre and filtered out all the stars that did not satisfy the condition $L_{z,LMC} - 5\sigma_{L_{z,LMC}} < L_z < L_{z,LMC} + 5\sigma_{L_{z,LMC}}$, where $\sigma_{L_{z,LMC}}$ is the standard deviation of $L_{z,LMC}$. This cut yielded a total of $1,452,155$ stars.

8.2 Selection of LMC stars through machine learning techniques

To discern stars belonging to different stellar sub-components we used a Gaussian Mixture Modelling (GMM)[4], which estimates the statistics of the Gaussians of each underlying single stellar sub-population and, in turn, evaluates for each star the probability of belonging to these sub-populations. The GMM is an unsupervised clustering technique which needs only one parameter, i.e the number N of finite Gaussian functions that describes the N sub-populations within an overall population. We run the GMM with $N = 3$ Gaussian to model the three stellar components of our sample: the LMC, the SMC and the MW. As input for the GMM we adopted six parameters[5]: the classical PMs (μ_α, μ_δ); the parallax ϖ, the radial and tangential velocities defined in the new reference frame v_R, v_ϕ; and the de-reddened colour of the stars $(G_{BP}-G_{RP})_0$. Finally, we assigned to each stellar sub-component, i.e. LMC, SMC and MW, only stars having at least 99% of probability to belong to one of the three galaxies, while the remaining objects are filtered out. After this step our total sample is reduced to $1,290,166$ stars.

8.3 Results

Table 8.1 lists the statistics of the three Gaussians derived for each sub-population by the GMM, as well as the number of stars assigned to each component. It can be seen that the MW star residuals were $\sim 1.3\%$, while the percentage of SMC stars raises to more than 5%, as expected

[3]We adopted the inclination and position angle values reported in Gaia Collaboration et al. [2021b] to correct for the orientation effects.

[4]We used the library available within scikit-learn python package [Pedregosa et al., 2011]

[5]This set of parameters ensures a better separation of the three stellar components. The stellar structures we discuss in this work are clearly visible also with any other choice of input parameters anyhow.

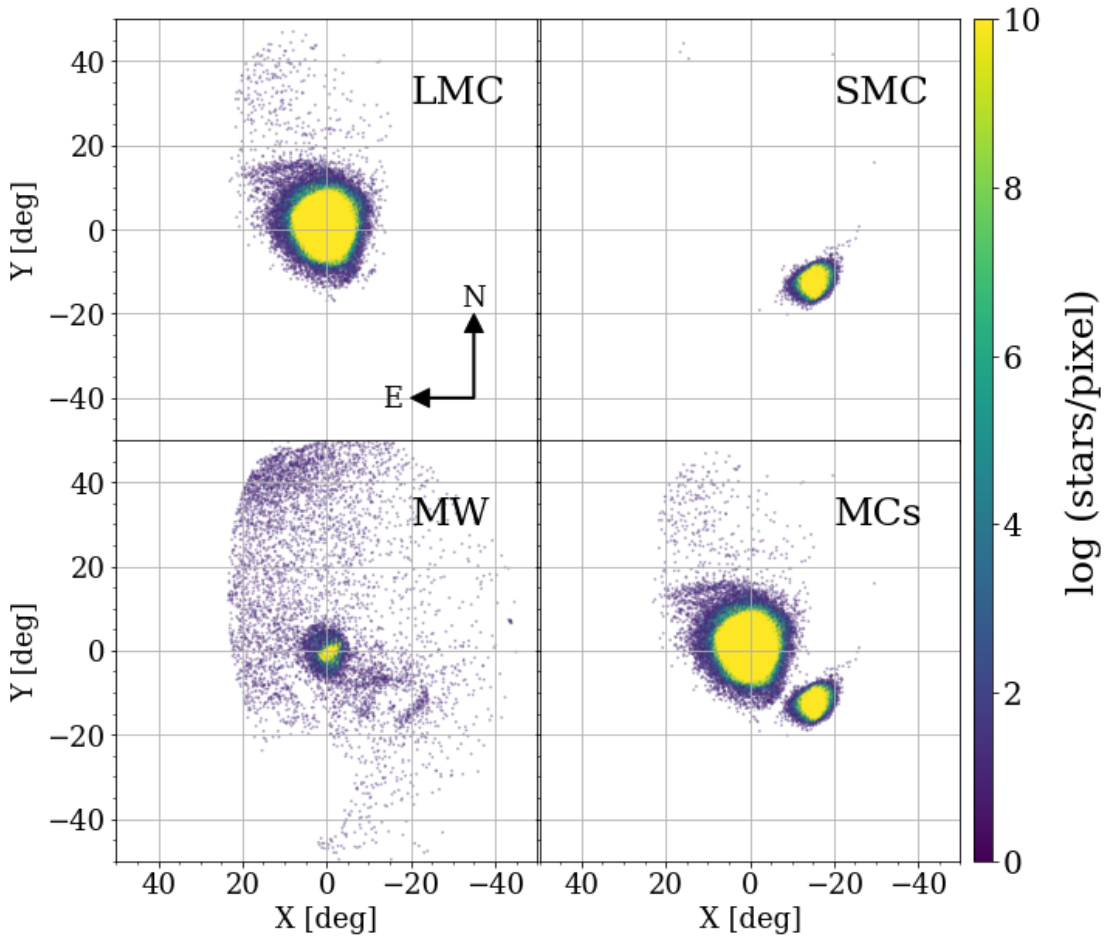

Figure 8.2: Spatial density of the stars belonging to the LMC, SMC, MW and MCs together, respectively, in an orthographic projection centred on the LMC. Each pixel has a resolution of $0.2° \times 0.2°$.

Pop.	N	μ_α	μ_δ	v_r	v_t	ω	$(G_{BP} - G_{RP})_0$
LMC	1202727	1.79 ± 0.26	0.39 ± 0.45	0.26 ± 0.22	-0.01 ± 0.22	-0.003 ± 0.110	1.2 ± 0.2
SMC	70856	0.80 ± 0.24	-1.10 ± 0.10	0.09 ± 0.09	0.50 ± 0.50	-0.024 ± 0.113	1.2 ± 0.2
MW	16583	1.85 ± 0.62	0.30 ± 0.80	0.25 ± 0.56	-0.01 ± 3.64	0.040 ± 0.199	1.1 ± 0.1

Table 8.1: Mean and standard deviations of the Gaussians estimated through the GMM.

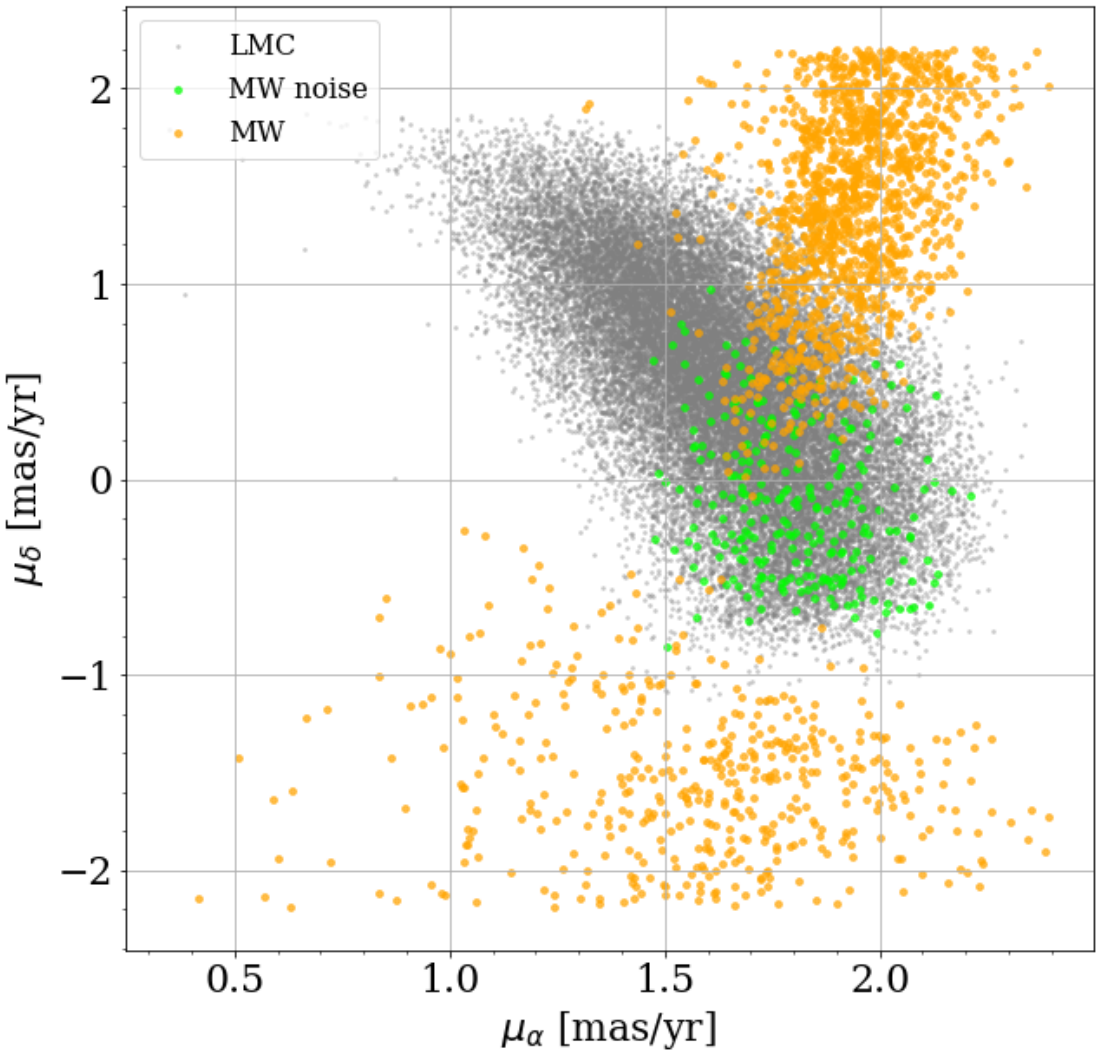

Figure 8.3: PM space of LMC disc stars beyond 8° (gray points) along with the MW noise (green points) and MW stars in the same region of the MW noise (orange points).

because of the large overlapping of their stars on the CMD. The average PMs of the MCs are in very good agreement with those estimated by Gaia Collaboration et al. [2021b] using a selection of RGB stars, e.g. $\mu_\alpha = 1.77 \pm 0.44$ mas yr^{-1}; $\mu_\delta = 0.33 \pm 0.63$ mas yr^{-1} for the LMC and $\mu_\alpha = 0.71 \pm 0.36$ mas yr^{-1}; $\mu_\delta = -1.22 \pm 0.29$ mas yr^{-1} for the SMC, making us confident about the reliability of the GMM technique.

Figure 8.2 shows the allocation of each star to one of the three components, displayed through an orthographic projection centred on the LMC [we used Eq. 1 of Gaia Collaboration et al., 2021b]. An inspection of the figure reveals that the GMM technique was able to properly separate the LMC from the MW and the SMC, with two exceptions. The first is the wrong assignment of LMC stars to the MW. These stars are mainly located within the LMC bar and we speculate that the more chaotic kinematics [see e.g. Gaia Collaboration et al., 2021b] of the central bar misleads the GMM so that it incorrectly associates these stars to the MW. Furthermore, the v_ϕ values within $4^\circ - 5^\circ$ to the LMC centre is different with respect to those measured in the outer regions [see e.g., Gaia Collaboration et al., 2021b, their Fig. 14]. The second is a cloud of stars ($\simeq 0.02\%$ of the stars assigned to the LMC), that we call "MW noise" hereafter, located between $20 - 50^\circ$ North of the LMC (top-left panel) which we speculate are MW misclassified stars. To confirm this hypothesis, we plotted in Fig. 8.3 the PMs of LMC stars placed beyond 8° from the LMC centre (gray points), of the MW noise (green points) and the stars assigned by the GMM to the MW situated in the same position of the MW noise (yellow points). The position and PM distribution of the latter population suggest that the MW noise is likely a tail of the MW sample that is being misclassified because of a significant overlap with the corresponding distributions of genuine LMC stars.

Regarding the stars assigned to the SMC (top right sub-panel in Fig. 8.2), besides its main body it is also visible the Small Magellanic Cloud Northern Over-Density (SMCNOD) discovered by Pieres et al. [2017], which attests the ability of the GMM at revealing also very low-surface brightness structures [Pieres et al., 2017, estimated $\mu_V = 31.2$ mag arcsec^{-2} for the SMCNOD]

8.4 Discussion

In this section we discuss separately the morphology and velocity fields of the outer LMC substructures unveiled by the GMM algorithm.

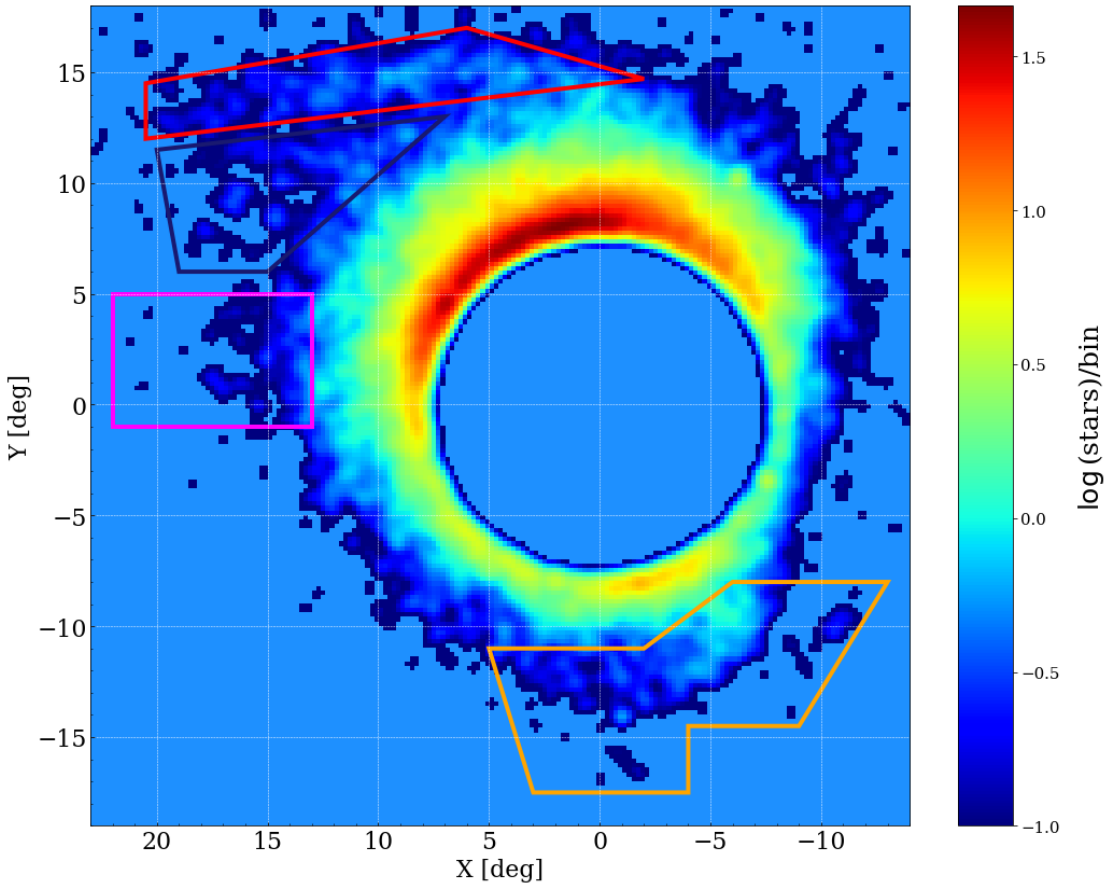

Figure 8.4: Zoom-in of the stars assigned to the LMC by the GMM in a density plot with a bin size of 0.2°× 0.2°, smoothed with a Gaussian function with $\sigma = 0.3°$. We masked the central 8°regions to enhance the distribution of stars in the outer regions.

8.4.1 Morphology

The spatial distribution of the stars selected as LMC members by the GMM is shown in Fig. 8.4. We only displayed objects located beyond 8° from the LMC centre to better visualize the outer regions (similar density plots with different choices of the bin size and/or smoothing width are displayed in Fig. D.1). The morphology of the LMC towards the Galactic disk (i.e., North-East direction) is strongly disturbed as witnessed by several sub-structures emanating from the disc edge. The most noticeable one is the already introduced NTA which is identified by a red polygon in the figure. It is also possible to discern some elongated features towards the East, up to $(X, Y) \simeq (20°, 0)$, that we dubbed Eastern Substructure (ES hereafter, highlighted with a magenta rectangle in Fig. 8.4, which represent the Eastern substructure I [de Vaucouleurs, 1955] and the recently unveiled Eastern substructure II [El Youssoufi et al., 2021]. In addition, the GMM-selected sample of very likely LMC stars also reveals the ensemble of Southern sub-structures already discovered by Belokurov and Erkal [2019] and Mackey et al. [2018] that we collectively call S-Sub and highlight with an orange polygon.

The figure also reveals a diffuse sub-structure protruding from the outer LMC disc and extending at more than 20 deg from the LMC centre and placed in between the NTA and the ES. This feature, indicated with a blue polygon in Fig. 8.4, represents, as far as we know, a still undiscovered tidal feature, which we call North-Eastern Structure (NES). The NES presents a horizontal over-density of stars ("Finger" hereafter) at $Y \simeq 11° - 12°$ which mimics the NTA at about 5° South of this feature and a more diffuse component which departs from the outer disk at $Y \simeq 5° - 7°$ deg and connects itself with the Finger at about $(X, Y) \simeq (15° - 20°, 10°)$.

Figure 8.5 shows the CMD of the stars belonging to the NTA, the NES, the ES and the MW noise (highlighted with different colours), superposed with the CMD of LMC stars at its North-East side and beyond 9°. The NTA (top-left panel) and the NES (top-right panel) have an RC-RGB similar to the underlying population of the outer LMC disc. This occurrence strengthens the hypothesis that the NES is composed by stars tidally stripped from the outer LMC disc, as the NTA. To be more quantitative, the ratio (f) between the number of RC (indicated with the black polygon in the figure) and RGB stars for the LMC outer disc, the NES and the NTA are very similar, being $f = 0.34 \pm 0.01$, $f = 0.29 \pm 0.05$ and $f = 0.28 \pm 0.05$, respectively. The ES, instead, shows an almost total lack of RC stars. Such lower fraction for the ES might be due to issues with the completeness and/or reddening estimates, however investigating this occurrence is beyond the purpose of this work. Finally, the MW noise (bottom right panel) contains stars

mostly having $G_0 > 18$, reinforcing the hypothesis that they are MW misclassified stars.

To further strengthen the reality of the NES, we point out that some hints of its presence were already visible in other works that exploited the *Gaia* catalogue. For example, the Finger is barely visible in the density maps constructed with *Gaia* EDR3 in Gaia Collaboration et al. [2021b] (their fig. 17), but the NES is more visible in fig. 2 of Grady et al. [2021], which shows a selection of 226,119 RGB stars in both the LMC and SMC from the *Gaia* DR2. The main scope of their work was to obtain photometric metallicity estimations and an overall picture of the PMs of their sample of stars rather than discover new undetected substructures in the faint outer regions of the LMC, therefore they also did not need to remove the minor MW component from their sample. The GMM adopted in this work cleaned the RGB stars from the MW contamination, yielding an almost pure catalogue of LMC stars, hence particularly enhancing the NES visibility.

To investigate the origin of the NES we inspected the recent results obtained using N-body simulations of the interaction between the LMC, SMC and MW. Mackey et al. [2016] ran N-body MW-LMC simulations to understand the physical origin of the NTA. They demonstrated that the tidal interaction with the MW can warp and distort the outer LMC disk, generating two spiral-like patterns, one twisted towards the North-East and the other towards the South-West direction. Their results strongly indicate that the NTA originated by the tidal interaction of the LMC with the MW. Similar structures have been predicted by Belokurov and Erkal [2019] N-body models. In particular, simulations of the LMC-SMC-MW or of the MW-LMC interactions, under some initial conditions[6] foresee both a leading and trailing spirals, stretched in the Southwest-Northeast direction (see their Fig. 4). They speculated that the NTA originated from the gravitational interaction with the MW, but a combined influence of the MW and SMC is necessary to explain all the features observed in the South of the LMC. Interestingly, these models also forecast, as a distinct and separated feature from the NTA, the bending of the entire Northern outer disc of the LMC caused by the MW gravitational pulling. Therefore, besides a thin horizontal stellar over-density, one should observe a more diffuse and wide stellar structure which should represent the distorted Northern LMC disk. However, observational works until now did not disclose any diffuse stellar over-density in the North, but only the thin NTA. Morphologically, the NES is in the position expected from the quoted dynamical models and we can hypothesize that it might have had the same origin of the NTA. In this scenario it would represent the tidal distortion induced by the MW to the outer North-East of the LMC

[6] Of course, N-body simulations are strongly dependent on the initial conditions, in particular the galaxy masses involved, which are not known accurately yet.

disk.

To be complete it is worthwhile to underline that some models of the LMC interacting with the SMC and the MW do not expect the presence of a diffuse bended outer structure. For example, Besla et al. [2016] brought to light the existence of stellar arcs and multiple stellar arms to the North of the LMC. From hydrodynamical simulations of the MCs either when evolved in isolation or under the gravitational influence of the MW, they concluded that repeated close interactions with the SMC are the main cause of the many stellar substructures observed in the Northern periphery, included the NTA. However, their models were based on the observations that a Southern counterpart of the features revealed to the North does not exist. These Southern substructures (S-SUB in Fig. 8.4) were disclosed afterwards by Mackey et al. [2018] and Belokurov and Erkal [2019]. Therefore, because of the asymmetric features revealed only to the North, Besla et al. [2016] disfavor a formation scenario driven by global Milky Way tides. This is at odds with the more recent models carried out by Belokurov and Erkal [2019] and Cullinane et al. [2022] which are based on more recent and complete data on the features unveiled around the LMC.

8.4.2 Velocity field

If the NES and NTA had the same origin, they should also show a coherent velocity field. In the context of the *MagEs* survey, Cullinane et al. [2022] analyzed the kinematics of the NTA through spectroscopic measurements of different fields centred along the arm, in conjunction with *Gaia* EDR3 PMs. From a combined study of NTA metallicity and overall kinematics, they definitely confirmed that the NTA is made of LMC outer disc material tidally distorted by an external gravitational potential. They also carried out a suite of N-body simulations, obtaining that the LMC embedded in a heavy-MW potential (mass MW $\sim 10^{12}$) represents the best qualitative match between models and observations. However, their best model shows a diffuse stellar component connecting the LMC disc with the NTA, which resembles the NES. From the dynamical point of view, the Cullinane et al. [2022] simulations are not able to reproduce the measured kinematics of the NTA. Indeed, while the measured tangential velocity is quite well replicated by the best model, the radial and vertical velocities are inconsistent with stars in an equilibrium disc and very different from what is expected by a solely LMC-MW interaction.

To further investigate this point, Fig. 8.6 (top row) shows the LMC v_ϕ (left panel) and v_R (right panel), calculated as median of the velocity of the stars within pixels of $0.7^\circ \times 0.7^\circ$, and their dispersions (bottom row). Both these diagrams seem to suggest a similar velocity pattern for the NTA and the NES, constituted by strong velocity gradients, with their velocity

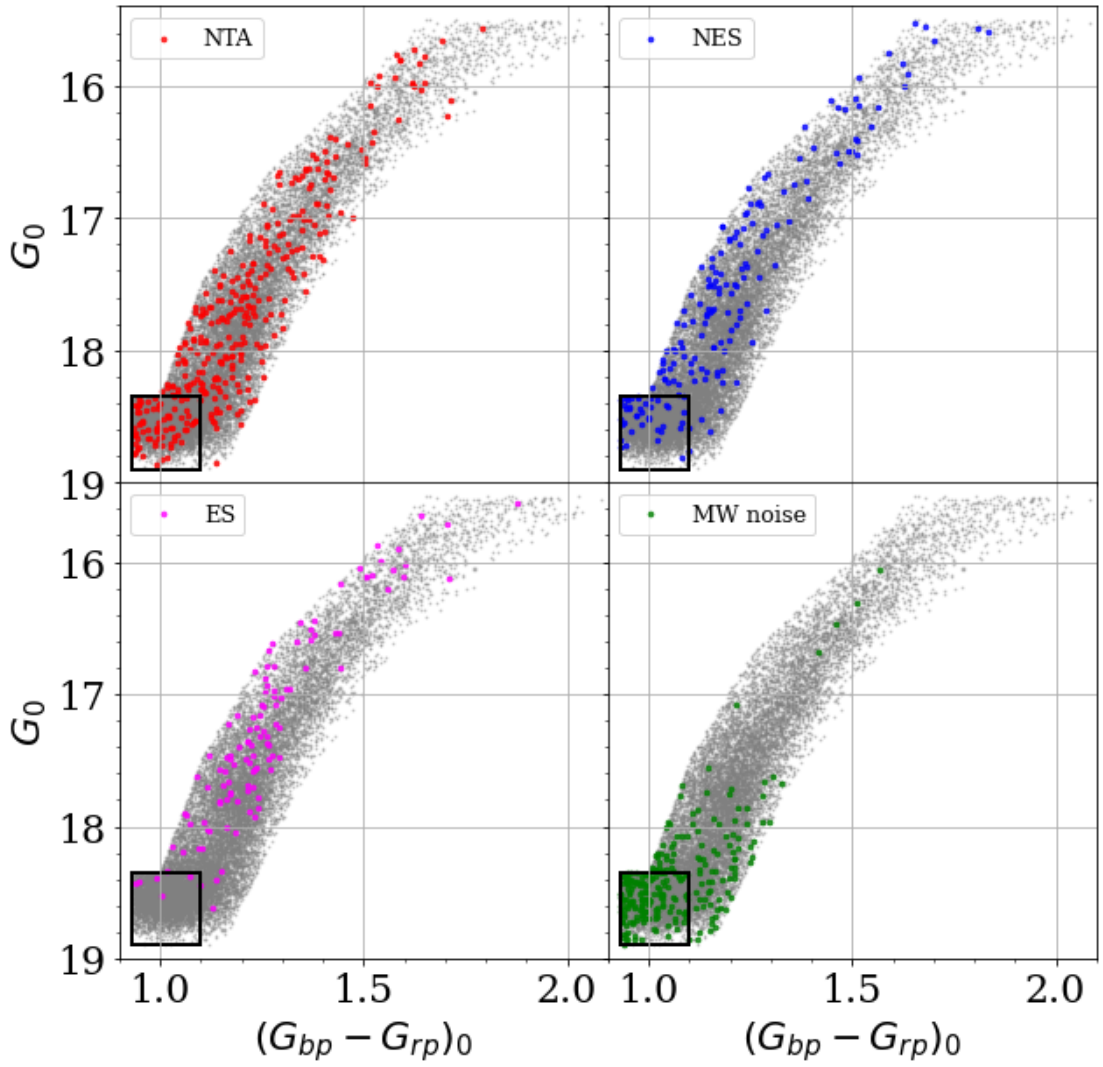

Figure 8.5: CMD of stellar sub-structures described in the text (labeled in the top left corner of each sub-panel), superimposed with an LMC outer disc stellar population located in the North-East side. The black square defines the RC.

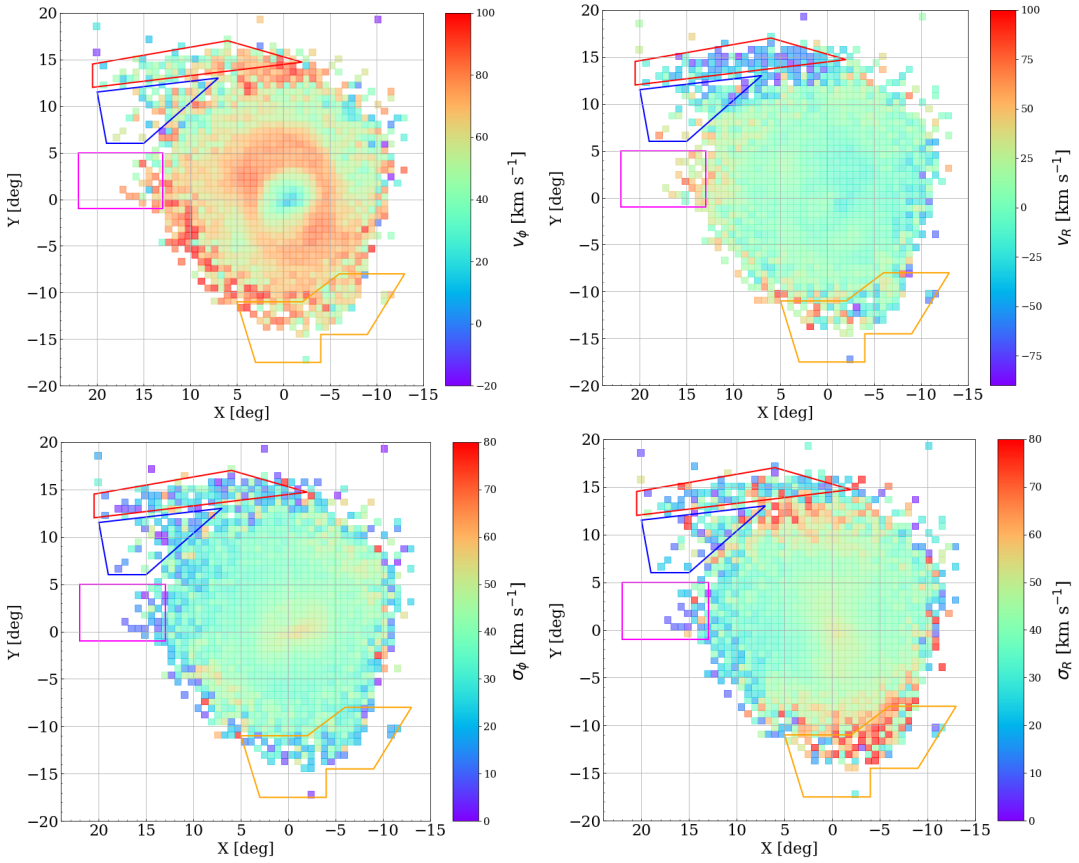

Figure 8.6: *Top:* Median velocity of the LMC tangential velocity v_ϕ (left panel) and LMC radial velocity v_R (right panel). *Bottom:* Velocity dispersion of v_ϕ (left panel) and v_R (right panel). Each pixel is 0.7° × 0.7° in size. The coloured polygons are the same as in the right panel of Fig. 8.4

decreasing either going from the ES towards the NTA or moving along the NTA towards the West direction. According to the velocity dispersion maps in the lower panels of Fig. 8.6 (the one in σ_R, in particular), NES and NTA appear dynamically colder than the adjacent edge of the LMC disc (around $(X, Y) \simeq (5°, 12°)$ or than other tidal structures, such as S-SUB, which is very hot (i.e. $\sigma_R \geq 70$ km s^{-1}). However, some of the pixels beyond $10° - 15°$ include few stars, causing the outer velocity map of the LMC to be noisier and more scattered. It is also visible from the v_R plot that the NTA and the Finger present negative radial velocities (top right panel) of the order of $\simeq -50$ km s^{-1}, similar to those estimated by Cullinane et al. [2022], with peaks of $\simeq -80$ km s^{-1}.

To explain the origin of the peculiar observed radial velocities of NTA's stars Cullinane et al. [2022] speculated that they could have been caused by recurring close passages of the SMC, happened more than 1 Gyr ago, beyond the time span of their models, which cover only the last Gyr. According to their simulations, any close passage of the SMC in this period was not able to alter significantly the kinematics of the NTA. In this context, the Finger might have been affected by past nearby passages of the SMC as well, hence it might be connected to the NTA and physically distinct from the rest of the NES. However, the velocity maps of the NTA and NES displayed in Fig. 8.6 do not allow us to establish whether the NES-NTA is a single highly disturbed sub-structure or is made by two uncorrelated physical sub-structures originated at different times. An additional characteristic visible in Fig. 8.6 is the large positive radial velocity shown by ES stars, with peaks of $v_R \simeq 80$ km s^{-1}, possibly indicating that the ES is in an ongoing stripping process.

An overall picture of the bulk motion of the outer regions, corrected for the solar reflex motion, is depicted in Fig. 8.7. At first glance the plot suggests that the NTA is being pulled back by the gravitational potential of the LMC towards equilibrium, as already visible in Fig. 8.6. The overall kinematics of the ES, and more generally of the outer East-North-East side of the LMC, indicates that this side is strongly moving away from the LMC. The NES, instead, shows a more chaotic kinematics, as some regions have a motion more similar to the ES while others have an opposite velocity direction. In the same figure the highly disturbed kinematics in the S-SUB is also visible. The high perturbations induced by the MW is testified by the strong deviations from the rotational motion of the East LMC side with respect to its West side. However, we caution the reader that the LMC inclination may affect the velocities discussed above and the consequent results. A quantitative discussion of this scenario could be provided only when the velocity field is drawn also with spectroscopically inferred radial velocities. Recently, also Choi

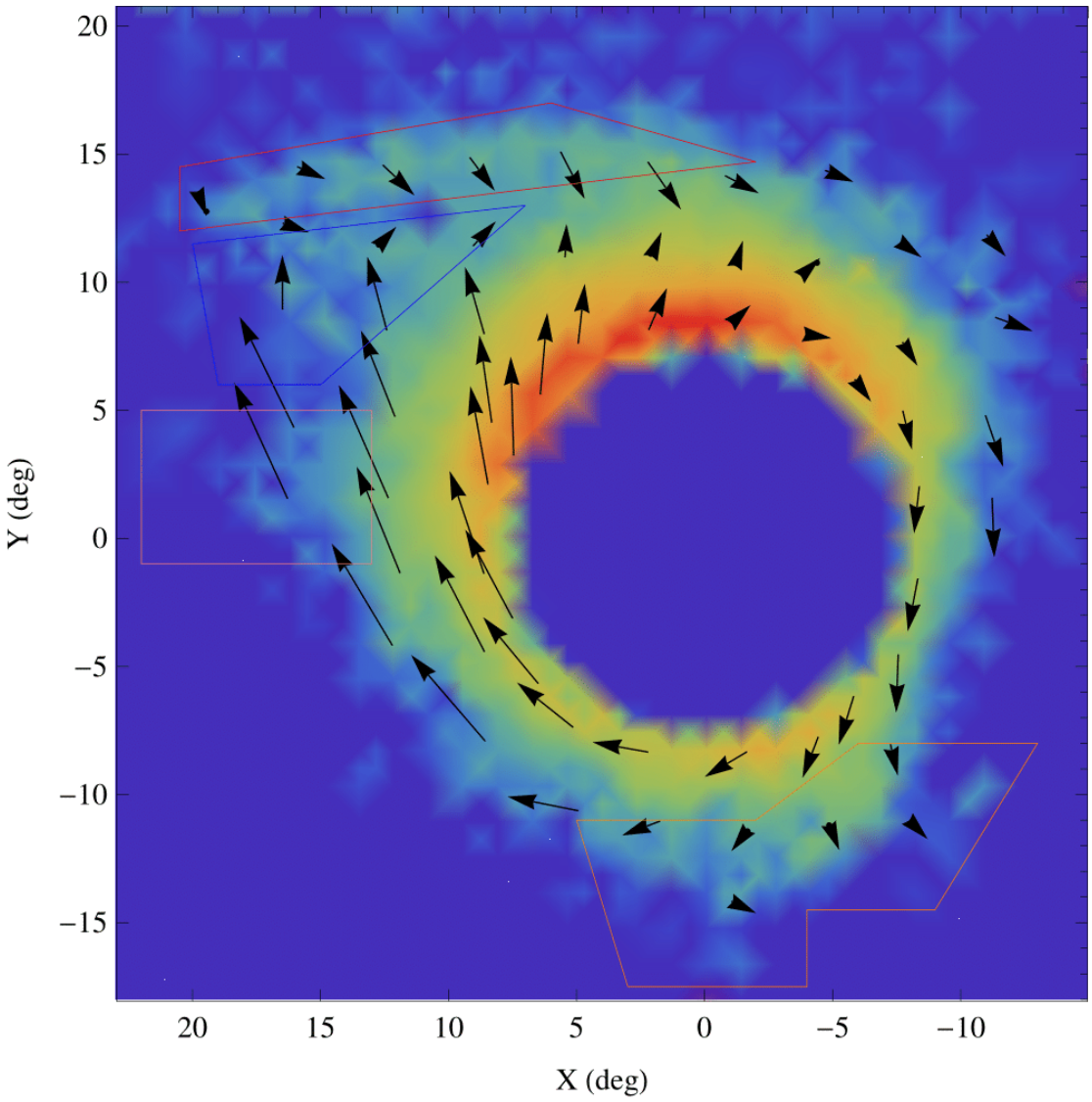

Figure 8.7: Velocity map (arrows) of the LMC overlaid on a star density map of the regions beyond 9° from the LMC centre. Bin size is 0.7°× 0.7°. The length of the arrows is proportional to the velocity vector's module.

et al. [2022] revealed large PM residuals in the Southern disc with a sample of RC and RGB stars collected from Gaia EDR3, even though their analysis was limited to the inner 6° from the LMC centre. They compared the observed LMC PMs with the outcome of numerical simulations of a LMC in interaction with the MW and SMC, putting constraints on the lookback time the last close encounter between the MCs happened (i.e., $t < 250$ Myrs ago) and on its impact parameter (i.e., ≤ 10 kpc.)[7].

An additional interesting feature in the North-East side of the LMC was recently discovered by Petersen et al. [2021] using the RR Lyrae variables as kinematics tracers. Indeed, they detected a tidally stripped stream, expected to be the outcome of the MW tidal force, in the same direction of the features we have discussed in the North-East side of the LMC. Petersen et al. [2021] probed only regions beyond $20 - 25°$ from the LMC centre, and revealed the stream signal up to $\sim 30°$ (see their fig. 1), finding also likely stream members in the Northern hemisphere at about 70° from the LMC centre. In this context, we speculate that the ensemble of stellar streams in the North-East outer disc could represent the inner part of the outer stream disclosed by Petersen et al. [2021], which extends up to the Galactic disc.

Dynamical simulations of LMC-SMC-MW interactions, going back to at least 2-3 Gyr, are essential to explain the peculiar kinematic features observed in the North-East LMC, such as the strong velocity gradients along the NES-NTA sub-structures.

8.5 Summary

In this work we exploited the exquisite multi-dimensional data provided by *Gaia* EDR3 to investigate the outer low surface brightness substructures of the LMC. We selected LMC RGB and RC stars based on their position on the CMD and filtered out all the stars having angular momentum beyond 5 σ that of the average LMC disc. We run the unsupervised clustering technique GMM with 6 input parameters to separate the remaining stars into the three main stellar components, the MW, LMC and SMC, and we limited our analysis to highly-likely LMC members ($P > 99\%$).

The GMM was able to recover the outer sub-structures discovered in the last years in the LMC, such as the NTA, the S-SUB or the ES. In addition, this procedure allowed us to detect an unknown diffuse tidal structure at its North-East side extending up to $\sim 20°$ from the LMC centre, the North-East Structure (NES). The NES fills the gap between the outer LMC disk

[7]These constraints are very similar to those inferred by Zivick et al. [2018]

and the other known structures in the North-East of the LMC, namely the ES and the NTA. The presence of tidally distorted LMC stars at the location of the NES was expected based on N-body simulations of a MW-LMC interaction [Belokurov and Erkal, 2019, Cullinane et al., 2022] as a consequence of the tidal stress induced by the MW on the LMC. This occurrence might induce us to think that the NES has the same origin as the NTA. From the kinematic analysis based on the Gaia EDR3 PMs, these tidal stellar components reveal a strong velocity gradient towards the outer LMC, but the present dataset is not sufficient to assess whether or not the NES is physically correlated to the NTA. Overall, the North-East side of the LMC displays radial velocities not consistent with a disc in equilibrium, showing large negative velocities for the NTA-Finger and positive for the ES. This occurrence indicates that the outer LMC disc has been strongly disturbed in the past few Gyrs. Spectroscopic follow-up to measure accurate radial velocities and more detailed and extended in time N-body simulations are requested to assess the origin of the NES and of the other sub-structures in the North-East side of the LMC.

Chapter 9

The COld STream finder Algorithm: Searching for kinematical substructures in the phase space of discrete tracers

This chapter is based on the paper published on Astronomy & Astrophysics: Gatto et al., 2020, A&A, Vol.644, p.A134.

The final part of this thesis is devoted to the development of new methods for the detection of signatures of past merger events in distant systems, such as the streams of stars and GCs tidally stripped from the outer regions of a galaxy, far enough that the stars are not resolved singularly any longer. In particular, we applied this method to the Fornax cluster, one of nearby galaxy clusters, whose photometric deep data have already demonstrated that the mass assembly within the core of the cluster is still ongoing [e.g., Cantiello et al., 2020, D'Abrusco et al., 2016, Iodice et al., 2017, 2016]. Nonetheless, the algorithm presented in this chapter is more general as it is suitable for any kind of stellar system with available kinematic information of the objects adopted as tracers. As already described in §1.3.2, outside the Local Group, stars cannot be resolved and other kinematic tracers have to be used. PNe[1] and GCs are suitable tracers of

[1]PNe are actually evolved stars, but they are easily observable also at large distances as they emit at the green OIII at 5007 Å [Dopita et al., 1992, Schönberner et al., 2010].

this kind as they are observable at large distances from the galaxy centers Cortesi et al. [2011], Douglas et al. [2007], Durrell et al. [2003], Merrett et al. [2003], Richtler et al. [2011], Shih and Méndez [2010] and their velocities can be measured with good precision in nearby galaxies and galaxy clusters. The combined information of position and velocity of tracers in the halo regions of galaxies allows us to study substructures in the tracer phase space, where they have not yet fully mixed due to the long dynamical times [Arnaboldi et al., 2004, 2012, Bullock and Johnston, 2005, Longobardi et al., 2015, Napolitano et al., 2003].

Historically, the methods adopted to search for streams were based on an empirical approach and were lacking of objective criteria to systematize the search for streams in the full phase space. Only recently, a big effort has been done to develop stream-locator algorithms suitable for different datasets. For the Milky Way, [Malhan and Ibata, 2018] implemented STREAMFINDER, with the aim of unveiling dynamically cold structures in the 6D phase space, by taking advantage of the *Gaia* space mission data. This code looks for a handful of particles (as few as 15 members) that lie along a similar orbit, allowing them to detect tiny and ultra-faint streams in the Galactic Halo. Other algorithms have been focused on the automatic search for tidal structures, like shells or ridges, in deep images [e.g., Hendel et al., 2019, Kado-Fong et al., 2018]. Such approaches are more directed toward large samples of galaxies to build statistically significant samples of stream features, but they do not rely on kinematics. As stated before, this is not ideal when looking for low-surface-brightness tidal features, which we expect to be those originating from minor mergers [see Cooper et al., 2010].

In this context, we developed the COld STream finder Algorithm (COSTA), a new method used to search for candidate cold substructures that can be interpreted as signatures of recent or past interaction between a main galaxy and the dwarf galaxies surrounding it. COSTA aims at filling the gap left by the above algorithms, introducing a method that relies on kinematics (namely a reduced 3D phase space of projected positions and LOS velocities), which can reveal streams even beyond the Local Group and can still be applied to large galaxy samples but below the detection limits imposed by the photometry. We introduce the basic statistical methods that allow the identification of cold kinematical substructures made of a few tens of particles, compatible with what is expected for faint streams around galaxies. The method is based on a k-nearest neighbors (KNN) approach, which groups nearby particles in 2D positions and in velocity to find coherent kinematic substructures. The algorithm is general and can be applied to any nearby stellar system, either galaxies or galaxy clusters cores (where large galaxy haloes and intracluster light concentration reside). As a template of this latter example to show the potential

Table 9.1: Parameters of the selected galaxies in the galmer simulation. The values of the velocity dispersion $\sigma_{\rm v}$, listed in the last column, have been measured in the configuration $N_{\rm giant}$ = 2000 - $N_{\rm dwarf}$ = 150

	M_B $[2.3 \times 10^9 M_\odot]$	M_H $[2.3 \times 10^9 M_\odot]$	M_{disk} $[2.3 \times 10^9 M_\odot]$	r_B [Kpc]	r_H [Kpc]	N_{stars}	N_{DM}	N_{gas}	σ_v $[kms^{-1}]$
gE0	70	30	0	4	7	320000	160000	0	145
dE0	7	3	0	1.3	2.2	32000	16000	0	77
gSa	10	50	40	2	10	240000	160000	80000	162
dS0	1	5	4	0.6	3.2	32000	16000	0	149

of the method, we discuss here the specific case of the Fornax cluster core. The Fornax cluster is particularly suitable for such a test as different studies have provided evidence of recent galaxy interactions [e.g., D'Abrusco et al., 2016, Iodice et al., 2017, Sheardown et al., 2018, Spiniello et al., 2018]. This complexity represents a challenging test bench for the algorithm. We used a mock observation of the Fornax cluster to assess the reliability of the method and to demonstrate how to set up the best parameters in a real case. We then apply COSTA to identify real streams of GCs and PNe from the Fornax VST Spectroscopic Survey [FVSS Pota et al., 2018, Spiniello et al., 2018].

9.1 The COld STream finder Algorithm

In this section, we introduce COSTA, which is intended to detect cold substructures in the reduced phase space (position on the sky and radial velocity) of discrete tracers. In order to find cold substructures that are correlated both in position and in velocity, we implemented an algorithm that looks for points close both in the RA/Dec position space and in the reduced phase space (velocity vs. radius). The method relies on a pseudo-KNN method based on a deep friend-of-friend algorithm that isolates groups of N particles with a small velocity dispersion (σ_{cut}, chosen between 10 km s^{-1} and 100 km s^{-1}). The main difficulty lies in efficiently detecting particles belonging to the stream, which should preserve the low velocity dispersion of the dwarf progenitor while they are moving in regions where the potential of the cluster rules, and the local velocity dispersion is that of the cluster (i.e., up to 50 times larger than typical dwarf-like velocity dispersions).

To do that, for each particle, the algorithm starts performing an iterated sigma clipping on a number k of neighbors. In particular, it removes all the particles with a velocity outside the

interval $[\bar{v} - n \times \sigma, \bar{v} - n \times \sigma]$, where $\bar{v}$ and σ are the mean velocity and the velocity dispersion of the k particles, and n is the sigma clipping value. As a proxy for the velocity dispersion, we used the standard deviation of the individual velocities (see §9.2.2). The algorithm iterates the procedure, with the mean velocity and velocity dispersion of the remaining particles, until there are no outliers to be clipped. Once the procedure is over, the algorithm selects all structures in the position and velocity space with a minimal number ($N_{\rm min}$) of particles. To define the maximum velocity dispersion acceptable for a given substructure to be considered cold, COSTA uses another parameter: the cut-off velocity dispersion, $\sigma_{\rm cut}$. We fine-tuned our algorithm to locate cold streams originating from the interaction of dwarf galaxies with the cluster. In fact, we expect that dwarf disruption is the main mechanism contributing to the later formed intracluster stellar population and the assembly of large stellar halos around galaxies. Hence, we allow for $\sigma_{\rm cut}$ values ranging from 10 to $\sim$ 100 kms^{-1}, based on the typical dwarf-like dispersion values found in the Coma cluster [Kourkchi et al., 2012]. The final COSTA output is a list of substructures with low velocity dispersion, below the fixed threshold, $\sigma_{\rm cut}$.

We note here that more massive galaxies would produce more diffuse substructures, due to a higher velocity dispersion and larger sizes. These would be harder to "filter" in the phase space, as they would be more mixed in the warm halo environment. Thus, to summarize, the COSTA algorithm has a total of three parameters (k, n, and $N_{\rm min}$) for any given (upper) dispersion threshold, $\sigma_{\rm cut}$, which needs to be properly chosen to maximize the number of real cold substructures (completeness) and minimize the number of spurious detections (purity), caused by the intrinsic stochastic nature of the velocity field of hot systems. For this purpose, one can use Monte Carlo realizations of the specific sample under examination.

Our approach has the advantage of being able to refine the selection of coherent spatial and velocity substructures, but it has the disadvantage of being biased toward round geometries. In fact, the algorithm is based on a simple metric that uses the distances from every single particle. This reduces the chance of identifying chain-like structures, which are expected in elongated streams. To remove this bias, we added a second stage to COSTA, at which we verify if some of the groups belong to a single structure. In particular, we define two or more groups belonging to a single structure if they show at least one common particle and their velocity dispersion values differ by less than their uncertainties. To demonstrate that it is possible to identify regions in this parameter space that can reliably detect streams with an acceptable fraction of false positives, we first tested the algorithm on a simulated sample from the publicly available hydrodynamical GalMer simulations [Chilingarian et al., 2010], and then train the algorithm to search for stellar

streams in the Fornax cluster core. The results of these tests are presented in the next sections.

9.2 Testing COSTA on hydrodynamical simulations

We used a suite of publicly available simulations, the GalMer database [Chilingarian et al., 2010], to test the ability of our algorithm to recover streams originating from a dwarf when passing close to a giant galaxy. The simulated data cubes are needed to test the algorithm self-consistently. We first defined the series of (*k, n,* $N_{\rm min}$,and $\sigma_{\rm cut}$) setups that minimize false detections, and then applied them to find the stream. Finally, we checked how meaningful the recovered properties (e.g., mean velocity, local velocity dispersion, and fraction of particles) were with respect to the intrinsic property of the stream. At this point, we were interested in verifying whether for a given stream a series of parameter setups would allow COSTA to find it and how these might change as a function of the observational conditions (i.e., measurement errors and total number of particles).

9.2.1 The GalMer Simulations

The GalMer simulations are based on a tree-smoothed particle hydrodynamics (SPH) code, in which gravitational forces are calculated using a hierarchical tree method [Barnes and Hut, 1986] and gas evolution is followed by means of SPH [Gingold and Monaghan, 1982, Lucy, 1977]. Dark matter particles and baryon particles both have masses of $\sim 10^5 M_{\odot}$, while the softening lengths are $\epsilon = 280$ pc for giant-giant interactions, and $\epsilon = 200$ pc for giant-intermediate and giant-dwarf runs. This gives an appropriate mass and spatial resolution to trace low-mass and low-surface-brightness substructures. The typical mass residing in stellar streams stripped by the dwarf during its interaction with the large galaxy is of the order of 10% of its mass; thus, given the typical GC- and PN-specific number densities (the number of particles per unit of luminosity), the stream is fairly sampled with a few tens of and up to a hundred tracers (e.g., GCs and PNe together). We simulated different depths of our observational setup by assuming different numbers of stellar particles expected to populate the stream. The advantage of testing the algorithm on simulations is that we can separate the particles belonging to the dwarf galaxy from the ones belonging to the target system. We can, therefore, characterize the phase space of both the galaxy target and streams produced in the fly-by of the dwarf galaxy through the central galaxy halo.

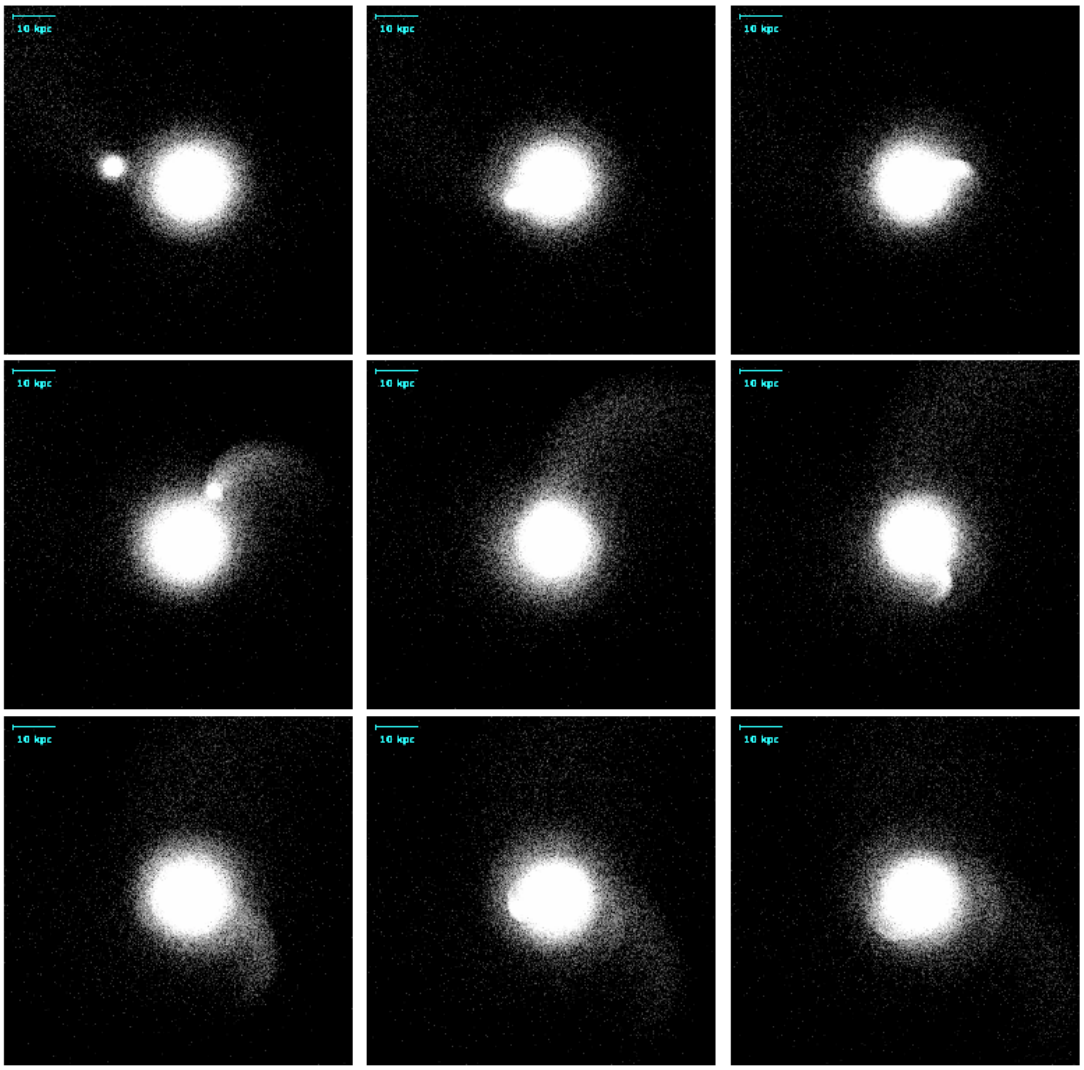

Figure 9.1: Snapshots of gE0-dE0 encounter, from 1850 Myr (top left) up to 2250 Myr (bottom right) after the beginning of the simulation, and separated by steps of 50 Myr. To test COSTA, we use the configuration at the center of the image, which is temporarily located at 2050 Myr after the start of the encounter.

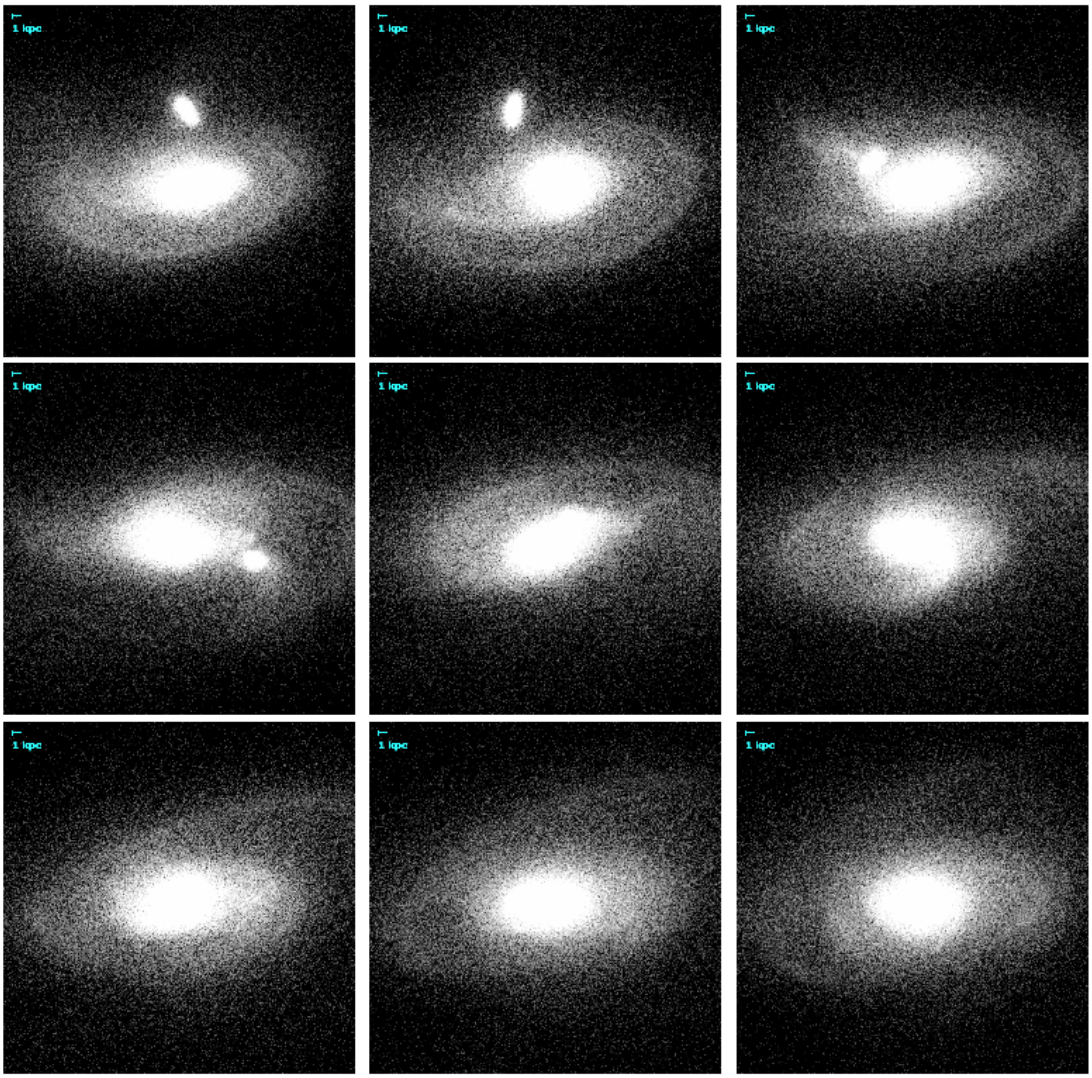

Figure 9.2: Same as Fig. 9.1 but for gSa-dS0 interaction. These snapshots correspond to a time interval between 1650 Myr and 2050 Myr after the beginning of the simulation, with our test configuration (1850 Myr) at the center of the image.

The GalMer database[2] provides about 1019 simulations of colliding galaxies and more than 70 000 snapshots showing the development of these interactions up to 3 Gyr from the beginning of the encounter with a bin interval, for each snapshot, of 50 Myr. From the whole database, we focused on two encounter configurations: 1) the one between a giant elliptical galaxy, gE0, and a dwarf E0 galaxy, dE0, with a mass ratio of 1:10 (the minimum found in the database for all simulations); and 2) the one between a giant Sa galaxy, gSa, and a dwarf S0 galaxy, dS0, also with a mass ratio 1:10. Table 9.1 shows the parameters of the four galaxies. We need to point out that a mass ratio of 1:10 is not optimal for generalizing the results because a wider population of systems, also with lower mass ratios, exist in real cases. As we show later, however, this is a conservative starting point as our algorithm is more efficient in detecting groups in phase spaces, which are generally much colder than the surrounding environment. Hence, the differences in velocity dispersion, which characterize the GalMer systems, are representative of extreme cases: if COSTA is able to detect substructures in these systems, then it will be even more successful in cases involving lower mass satellites.

We selected the gE0-dE0 and gSa-dS0 cases as realistic representations of the dynamics of a giant-dwarf encounter. In particular, the case of the gE0-dE0 is fairly representative of a typical encounter between a hot, high-dispersion system and a colder satellite, like the one happening in large galactic halos [see e.g., Cooper et al., 2010, Iodice et al., 2016]. In both configurations, we chose an encounter with the satellite starting 100 kpc away, and falling toward the larger galaxy in a prograde orbit with an inclination of 33 degrees and a pericentral distance of 16 kpc. We initially used a prograde orbit because this is expected to exchange a lower amount of energy and therefore to minimize the scatter of dwarf particles into warmer tails. However, since in the case of the gSa-dS0 encounter the dwarf and the giant stars were too mixed, for this latter case we also considered a retrograde encounter. In Fig. 9.1 and Fig. 9.2, we show a few snapshots of the gE0-dE0 and gSa-dS0 encounters, respectively. The final configuration we adopt for our tests is shown in the central panel (encounter), while the other panels show different time snaps, each one spaced in time by 50 Myr, with the top-left corner temporarily located 200 Myr before the chosen configuration. The choice of the central configurations is motivated by the fact that the distance between the intruder and the giant galaxy is the shortest (as is evident from Figs. 9.1 and 9.2). This allows us to have a sufficient spatial mix of the two systems, and thus stress as much as possible the ability of COSTA to recover stream particles well embedded in high-density regions. From the figures, it is also clear that the encounters start producing a stream-like

[2] http://galmer.obspm.fr

structure from the first passage at a few tens of kpc. Particles belonging to the original stream become mixed after a few hundred Myr, but subsequent close passages produce even brighter streams. These latter ones remain visible and well separated from the background galaxy for hundreds of Myr. They later diffuse and mix with galaxy halo particles. This timescale is set by the specific dynamical time of the system in question, and this can be larger for hotter central systems and lower mass ratios. Unfortunately, the GalMer database does not provide lower mass ratios than the ones adopted here. Nevertheless, these examples allow us to test the ability of COSTA to find such cold streams as a function of a few observational parameters.

9.2.2 Running COSTA on GalMer simulations

In order to apply COSTA to GalMer simulations, we first needed to extract simulated 6D data cubes from the velocity field (i.e., RA, DEC, and a radial velocity) that mimics a typical observational situation. Then, COSTA can be applied to the mock velocity field to recover the cold substructures, together with their intrinsic kinematical parameters. We intended to test the possibility of identifying streams made of a few particles in velocity fields of different sizes. In particular, we tested the case of $N_{\rm part} = 2000, 1000, 500$ extracted from the giant galaxy. These are typical numbers of test particles found in external galaxies, like PNe (Fornax cluster: ~ 1000, ~ 1500 PNe: Spiniello et al. 2018; and references therein; M31, $\sim$2000 PNe: Merrett et al. 2006; NGC 5128, ~ 1100 PNe: Peng et al. 2004; NGC 4374, ~ 500 PNe: Napolitano et al. 2011; or globular clusters (Fornax cluster: ~ 1000 GCs: Pota et al. 2018; and references therein; M87, ~ 500: Romanowsky et al. 2012). For the dwarfs, we instead considered $N_{\rm part} = 150, 75, 38$, respectively [e.g., Fahrion et al., 2020]. These numbers of particles were chosen to match with the expected particles observable from streams of surface brightness of the order of 28-30 mag arcsec^{-2} (see discussion below). Finally, to test different observational conditions, we adopted three orders of measurement errors, $\Delta_v = 10,\ 20,\ 40$ km s^{-1} ,for each of the three different selected encounters (i.e., gE0-dE0 and gSa-dS0 prograde/retrograde) by re-sampling the particle velocities with a Gaussian distribution centered on the particle velocity and with $\sigma = \Delta_v$ ($v_{\rm obs}$ hereafter). These values are comparable to what is typically reached with mid and low spectral resolution. Measurement errors have the effect of diluting the observed velocity distribution of the cold substructure by increasing the observed squared velocity dispersion, that is, $\sigma^2_{\rm obs}$=σ^2_I+Δ^2_v, where σ_I indicates the intrinsic velocity dispersion of the stream and $sigma_{\rm obs}$ the observed velocity dispersion. In the following, we define the mean velocity and velocity dispersion

of the detected substructures using a standard statistical definition [see also Pota et al., 2018]:

$$v_{\rm mean} = \frac{1}{N}\sum v_{\rm obs,i}, \quad \sigma_I^2 = \frac{1}{N-1}\sum (v_{\rm obs,i} - v_{\rm mean})^2 - (\Delta_v)^2. \tag{9.1}$$

Hence, the larger the Δ_v, the greater the chance that a cold structure will become warm enough to skip the cold criterion on $\sigma_{\rm cut}$, or that some of the particles are discarded by the sigma-clipping part of the algorithm. This would then leave too few particles to meet the minimum particle number ($N_{\rm min}$) limit, hence making COSTA lose good candidate streams.

9.2.3 Setting the reliability of COSTA

Before running COSTA to search for streams, we need to check whether and how often COSTA returns spurious detections. In the case of simulations, this is easily performed by running COSTA on the central galaxy particles only; these represent the smooth warm background in which streams must be found when the intruder is added. For our analysis, we defined the following datasets: the white noise sample (WNS) includes RA, DEC, and $v_{\rm obs}$ of the giant galaxy or cluster regions without any artificial stream added and the detection sample (DS) includes RA, DEC, and $v_{\rm obs}$ of the full system including the WNS and the particles of the stream. We used the WNS to select those setups (i.e., combination of *k, n,* $N_{\rm min,}$ and σ_{cut}) that have a reasonably low probability to find artificial detection and to be used to look for streams in the DS. A given setup that finds no spurious streams in the WNS has maximum "reliability," which means that if it detects a stream in the DS then this is likely to be real. On the other hand, a setup that finds many spurious detections is highly unreliable and has to be discarded. In order to have a statistical definition of the reliability of the setups in the *k, n,* $N_{\rm min,}$ and $\sigma_{\rm cut}$ space, we used 100 different mock datasets randomly extracted from all particles in the simulations. We used different combinations of number of particles $N_{\rm part}$ and velocity errors Δ_v for each of the three encounters, and we present some representative cases here. Specifically, we discuss the cases where we randomly extracted 2000 particles with errors Δ_v =10 and 40 km s^{-1}; 1000 particles with Δ_v =40 and 500 particles with Δ_v = 20 km s^{-1}. For each case, we uniformly sampled the *k, n,* $N_{\rm min}$ parameters' space, for different $\sigma_{\rm cut}$ and ran COSTA with all the possible combinations of the free parameters selected in the following ranges:

- k: from 10 to 30 with steps of 5.
- n: from 1.3 to 3 with steps of 0.2-0.3.
- $N_{\rm min}$: all values from 5 up to k.

- $\sigma_{\rm cut}$: from 10 to 80 km s^{-1}with steps of 5 km s^{-1}.

For each combination of these parameters, we defined the reliability of the 100 random extractions as

$$\texttt{Rel} = 100 - N_{\rm spu}\ \%, \tag{9.2}$$

where $N_{\rm spu}$ is the number of times we obtain at least one spurious detection from COSTA. We use 70% as the threshold for defining a reliable setup. This threshold is somehow arbitrary, as it might depend on the risk one is willing to take in considering a group of particles as a stream. In principle, one should set the reliability toward 100%, to be sure that none of the detection is spurious. However, this could result in a too conservative choice that might cut all streams statistically closer to the white noise given by the background particles. For instance, the properties of streams with a low number of particles and/or too close to the $\sigma_{\rm cut}$ may be very close to the properties of the spurious detections, and thus would be filtered out by too-conservative thresholds. For this reason, we were motivated to choose a lower threshold that might provide greater completeness but less purity, due to the increased chance of finding spurious detections. Since the main scope of COSTA is to provide stream candidates that will then be confirmed with deeper observations, a fair amount of false detections are acceptable. We discuss the impact of the threshold in §9.2.6. Here we discuss the results for the gE0-dE0 and the gSa-dS0 encounters separately and in detail.

9.2.4 The case of the gE0-dE0 encounter

We first tested COSTA parameter combinations on the WNS to check which configurations produced spurious detections over 100 re-extractions of the same catalog, re-sampling the velocity errors for each particle. We excluded the particles in the central 1 kpc of the main galaxy, since these regions are usually highly incomplete in discrete tracer detection [see e.g., Napolitano et al., 2001] and any attempt to look for streams would produce very uncertain results. Then, we collected all configurations that returned at least 70% of the re-simulated field COSTA analysis with no spurious detection (e.g., $\texttt{Rel} \geq 70$).

9.2.4.1 Reliability as a function of the COSTA parameters

In Fig. 9.3, for the four different combinations of $N_{\rm part} - \Delta_v$, we show the scatter plot between all the possible free parameter pairs. This is color-coded according to the fraction of times a given pair overcame the chosen reliability threshold, and it is marginalized over the other two

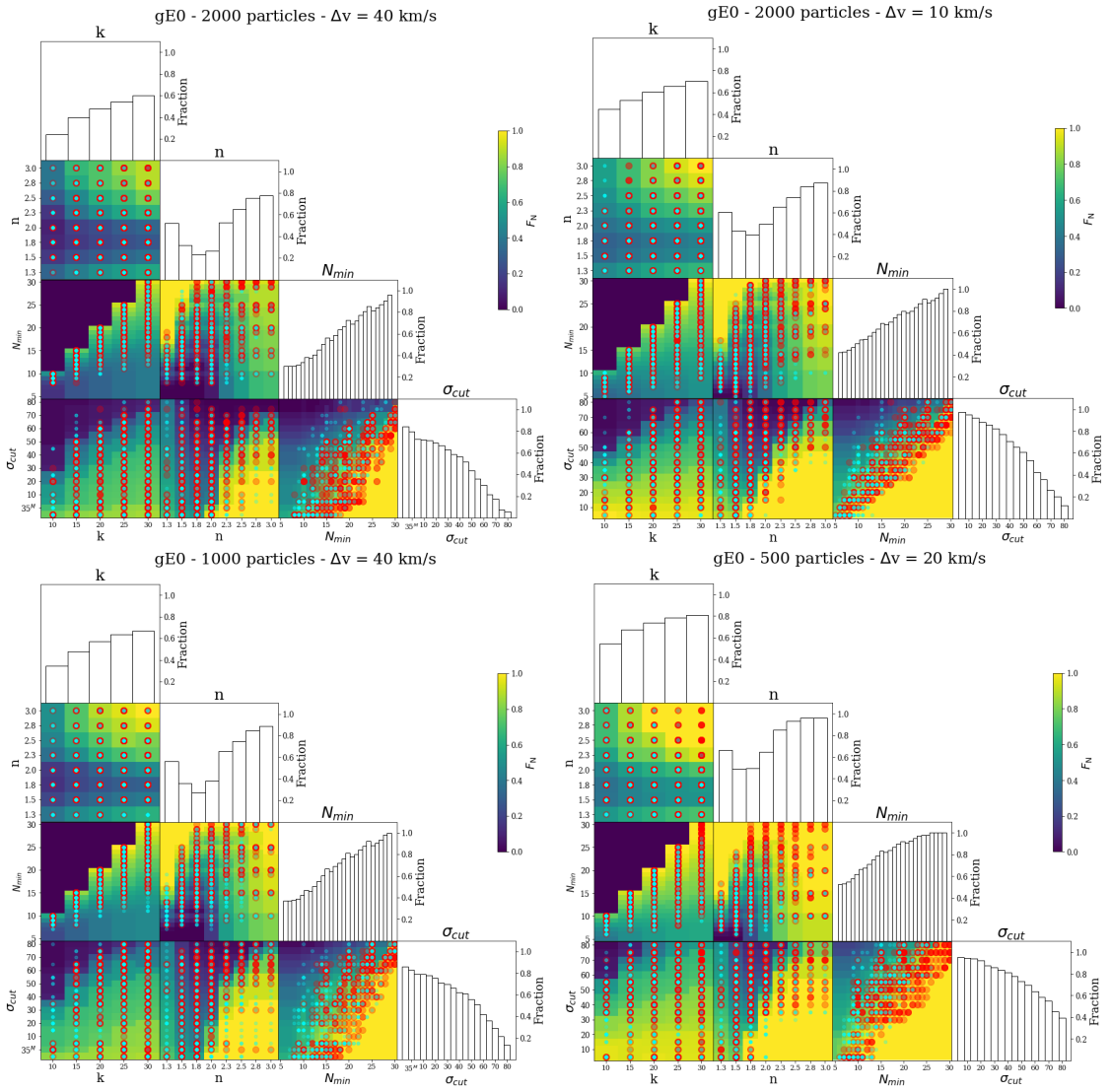

Figure 9.3: Scatter plot between all possible free parameter pairs, color-coded by the fraction of times (F_N) a given pair of parameters has a reliability greater than 70% over the total number of possible configurations, along with the distribution of each parameter. Red points (cyan points) indicate the combination of parameters where COSTA detected a real (spurious) stream in ten random extractions of the giant+dwarf

free parameters. This cumulative fraction, related to each parameter pair, is hence defined as

$$F_{\rm N} = \frac{\texttt{\# parameter-pair with Rel.} \quad \geq 70\%}{\texttt{\# total tests for a fixed parameter-pair}}.$$

The latter quantity is expected to be higher for the combinations of parameters that have a lower chance of producing spurious detection for any other choice of the other parameters, and, as such, it represents a quality flag for a given configuration. Indeed, when a parameter configuration with a low $F_{\rm N}$ finds a stream, the chance that this is a spurious one is higher. In the following, we use the high-$F_{\rm N}$ regions in the parameter space to label the detection as higher quality (see also below), as they represent the regions where all parameters show high reliability.

In Fig. 9.3, the regions of the parameter space that reach the maximum level of reliability ($> 70\%$ for all possible parameter configurations) are shown in yellow, while the quality of the configuration degrades toward the blue as the fraction of $>70\%$ reliability decreases over the total combination including that particular pair. For the yellow area, this means that, having fixed two of the four free parameters, the reliability threshold is reached regardless of the values of the other two. Looking at the results for the different $N_{\rm part} - \Delta_v$ cases, we can see that regions with $F_{\rm N} \sim 1$ are located in the upper-right corner of the $k - n$ panel, on the diagonal of the $k - N_{\rm min}$ projection, at the bottom right corner of the $k - \sigma_{\rm cut}$, $n - \sigma_{\rm cut}$ and of the $N_{\rm min} - \sigma_{\rm cut}$ panels, in the upper-left corner and right side of the $n - N_{\rm min}$ projection. This is valid for all $N_{\rm part} - \Delta_v$, but with different extensions. Moreover, many other regions in the parameter space have an $F_{\rm N} > 70\%$ (light green color), indicating that there are numerous highly reliable combinations of the four parameters, which hence produce very reliable streams with little or no chance of being spurious. The same figure also shows the 1D distribution of all four COSTA parameters, corresponding to `Rel`$> 70\%$, highlighting the peak values in the parameter space that allow the greatest chance of producing little or no spurious streams. In particular, the distribution of $N_{\rm min}$ shows that this is a critical parameter to avoid spurious detections, as the probability of finding spurious structures (i.e., groups of particles with similar velocities) is larger for small $N_{\rm min}$ and monotonically decreases as $N_{\rm min}$ increases, producing a higher overall reliability at larger $N_{\rm min}$. Indeed, too-small $N_{\rm min}$ would increase the chance of a group of particles in k neighbors having close velocities, thus returning a spurious detection. On the other hand, as $N_{\rm min}$ defines the minimal mass of the stream that COSTA would detect, too large an $N_{\rm min}$ will produce high reliability but also high incompleteness in the final list of stream candidates (as small streams would be filtered out). The distribution of $\sigma_{\rm cut}$, instead, justifies our choice to employ many cut-offs, as larger values allow us to find warmer streams

with larger $N_{\rm min}$ ($F_{\rm N}$ is close to 1 in the bottom right of the $N_{\rm min} - \sigma_{\rm cut}$ panel), while lower $\sigma_{\rm cut}$ minimizes the number of spurious structures (from the 1D distribution of the $\sigma_{\rm cut}$ fraction). Concerning the $\sigma_{\rm cut}$ parameter, it is worth mentioning that in some cases we adopted cut-offs lower than the nominal instrumental errors. This is because a stream with an intrinsic velocity dispersion smaller than the instrumental error would give an observed value that can be any random number lower than Δ_v. Hence, using $\sigma_{\rm cut} \geq \Delta_v$ would exclude any real stream colder than Δ_v. Using smaller cuts, we expect to detect such streams, although we cannot evaluate their intrinsic kinematics. In these cases, we consider the $\sigma_{\rm mea} \sim \sigma_{\rm obs}$, that is, without subtracting Δ_v in quadrature, and we mark the latter with an apex. Looking at the n distribution, the setups with the highest reliability fractions are located at high n, since a shallow sigma clipping removes fewer outliers. Hence, only structures with an initial low-velocity-dispersion value fall below a given threshold, unless one sets a higher $N_{\rm min}$, in which case there is little chance of finding a spurious structure with small n (see e.g., the central panel in the top left of Fig. 9.3). Finally, the k distribution increases monotonically. Since the higher k is, the larger the possible values of $N_{\rm min}$ ($N_{\rm min}$ is varied from 5 up to k) are, it is expected that this distribution mimics the trend of the $N_{\rm min}$ one.

As all the previous considerations may be dataset dependent, it is crucial to explore the behavior of the reliability in the parameter space as a function of the number of particles, the velocity errors, and also the minimal reliability threshold (e.g., changing this to a lower or higher threshold than 70%). In this section, we consider the first two quantities (number of particles and the velocity errors), while we discuss the reliability threshold in §9.2.6. By comparing the top-right panel of Fig. 9.3, which shows the case of a lower $\Delta_v = 10$ km s^{-1} with the top-left panel, which shows $\Delta_v = 40$ km s^{-1} , the number of possible combinations that have `Rel` $\geq$70% increases by more than 10% when considering smaller errors. In fact, the smaller velocity error values allow COSTA to more efficiently recognize the absence of streams without spurious detections. This is quite encouraging, as it shows that there is little room for spurious cold structures to be produced by the white noise of the background velocity field. Also, this shows that the velocity measurements are crucial to increasing the purity of stream detection. The bottom-left and bottom-right panels of Fig. 9.3 show the configurations with 1000 and 500 particles with $\Delta_v = 40$ km s^{-1}and $\Delta_v = 20$ km s^{-1}, respectively. These situations exhibit a wider parameter space with high $F_{\rm N}$ (i.e. high reliable setups), similarly to the case of 2000 particles and $\Delta_v = 10$ km s^{-1}. This is likely because the smaller number of particles further reduces the effect of the noise for a given Δ_v, and consequently the probability of COSTA finding a spurious

Table 9.2: *Column 1*: adopted configuration. *Column 2*: percentage of setups where the stream has been recovered with respect to the total setups in which COSTA detected at least a cold substructure averaged on ten simulations. *Column 3*: the contaminant fraction (`CF`: see definition in the text).

gE0 - dE0	f	`CF`
2000 part - 40 km s^{-1}	0.54 ± 0.18	0.71 ± 0.12
[a]2000 part - 40 km s^{-1}	0.59 ± 0.24	0.73 ± 0.11
2000 part - 10 km s^{-1}	0.54 ± 0.08	0.67 ± 0.13
[a]2000 part - 10 km s^{-1}	0.67 ± 0.10	0.71 ± 0.12
1000 part - 40 km s^{-1}	0.40 ± 0.22	0.70 ± 0.13
[a]1000 part - 40 km s^{-1}	0.47 ± 0.25	0.71 ± 0.12
500 part - 20 km s^{-1}	0.51 ± 0.20	0.64 ± 0.17
[a]500 part - 20 km s^{-1}	0.56 ± 0.21	0.66 ± 0.17

a: in these configurations, we ruled out setups with $F_{\rm N} < 50\%$ in the $n - N_{\rm min}$ space as described in the text.

structure becomes lower. However, the smaller number of particles also decreases the sampling of the stream and its signal, overall decreasing the signal-to-noise ratio by roughly $\sqrt{\rm N_{part}}$. The consequence here is that COSTA might not detect the stream with the same efficiency as it would for higher numbers of particles. Thus, it is essential to also test the detection ability of COSTA as a function of $N_{\rm part}$ when a stream is present in the detection sample.

9.2.4.2 Stream detection

We then ran COSTA using all setup configurations with `Rel`$\geq$70% over the DS made of the gE0 and dwarf/stream particles, to test the algorithm's ability to detect cold structures embedded in the hot environment of the central galaxy. We repeated this procedure ten times in order to take into account statistical fluctuations due to a random extraction of the detection sample particles. Furthermore, in order to reproduce a lower limit for the surface brightness of the extracted stream, we imposed a minimum number of ten particles to be picked up in an area of about 40 kpc located in the tail of the dwarf. These numbers correspond to a stream with a surface brightness of the order of 28-30 mag arcsec^2 (see discussion in §9.3.3).[3] We note that

[3]We stress here that this condition has been imposed regardless of the $N_{\rm part}$, which might bias the detection toward intrinsically denser streams for lower $N_{\rm part}$, and, as such, increase the detection power of COSTA for these cases. As we are interested in covering a variety of observational conditions, we kept this condition; however, we take into account the detection efficiency as a function of $N_{\rm part}$ when drawing conclusions.

COSTA does not only detect streams in the proximity of the dwarf, but it also correctly identifies other groups of stream particles, including portions of the stream that are far from the dwarf body. However, these latter detections are fairly occasional because particles that are far from the dwarf have spent more time in the halo of the host galaxies and have started to mix in the phase space of the host halos to be detected as part of a decoupled stream (see discussion in §9.2.4.4). It is likely that streams detected from COSTA contain, along with the actual dwarf particles, also some contaminants, meaning particles close to the stream that accidentally also have similar velocities to those of the dwarf's particles. This "contamination" is a critical parameter to evaluate because contaminants alter the inferred stream properties. Since we know from the simulation which of the systems the particles belong to, we used this information to estimate the contamination fraction (see §9.2.4.3). Regardless of the mix of the dwarf/stream particles with the background main galaxy particles, we expect that the stream particles closer to the dwarf body are the ones that most keep their kinematics clearly decoupled by the hot background (see also §9.2.4.4). Among all candidate streams that COSTA recognizes on the DS, we consider the ones where COSTA correctly identifies at least four particles of the stream/dwarf, or where at least one third of the total particles (dwarf + contaminants from the main galaxy) is from the stream/dwarf, as true detections. The final results of COSTA true positive detections are shown also in Fig. 9.3. Here, we overplot the combination of parameters where COSTA found the stream (i.e., true positives, red points) and spurious groups (i.e., false positives, cyan points), in the ten repeated DS extractions, on the density plots. In many panels, real (red points) and spurious (cyan) streams are clustered in different regions, even though it is not always simple to see this. The most evident case is the $N_{\rm min} - \sigma_{\rm cut}$ plot, where red points are slightly shifted toward the right corner, where $F_{\rm N}$ is higher. More quantitatively, in the $N_{\rm min} - \sigma_{\rm cut}$ projection of the case with 2000 particles and $\Delta_v = 40$ km s^{-1}, the median $F_{\rm N}$ for true positive equals 0.88, while that of spurious streams is only 0.73.

Another useful projection that slightly separates real streams from spurious ones is the $n - N_{\rm min}$ in the middle of each corner plot. This panel shows the compromise between how strong the sigma clipping can be depending on the minimal number of particles expected in the stream. Indeed, a closer inspection of the $n - N_{\rm min}$ plot reveals that many spurious structures have been detected in the bottom-left region, while red points tend to cluster in the upper right. Being more quantitative, the median $F_{\rm N}$ of red and cyan points in the $n - N_{\rm min}$ panel are 0.58 and 0.49, respectively. Thus, in order to minimize the chance of over-collecting spurious streams, we adopted a threshold on the $F_{\rm N}$ in the $n - N_{\rm min}$ panel. In particular, setting a minimum value of

$F_{\rm N} = 0.5$, we removed about 50% of the spurious structures. We note that, despite the separation being clearer in the $\sigma_{\rm cut} - N_{\rm min}$ panel, we prefer to set a threshold in a perpendicular direction of the parameter space, with respect to $\sigma_{\rm cut,}$ in order to reduce the chances of biasing the final selection in a projection that is strictly related to a stream's physical properties. In fact, a further clean involving $\sigma_{\rm cut}$ might alter the estimated stream kinematics. Since some of the very low $F_{\rm N}$ regions lie at high $\sigma_{\rm cut}$ values, removing such regions would rule out all the combination of parameters with $\sigma_{\rm cut}$ close to the actual dwarf velocity dispersion (77 km s^{-1}, see also Table 9.1). In the following, we use this threshold as a further condition on the detected structures to clean out our list of candidate streams. The effectiveness of this choice becomes clearer in §9.2.4.4. In Table 9.2, we report the fractions of setups that reveal the stream tail without any false positive (called f hereafter), averaged over ten simulations returning at least one detection (i.e., either a true or false positive), with and without applying the threshold of $F_{\rm N} = 0.5$. We also report the contaminant fraction, which is defined in §9.2.4.3. Generally, the threshold in $n - N_{\rm min}$ increases the number of setups where the stream is recovered. This is particularly evident for the best case with $N_{\rm part} = 2000$ and $\Delta_v = 10$ km s^{-1}, where the fraction of setups returning streams with no spurious is $\sim 67\%$ when applying the threshold of $F_{\rm N} = 0.5$ in the $n - N_{\rm min}$ plane, while it is $\sim 54\%$ withouth any threshold in $F_{\rm N}$. Given the uncertainties, however, this makes very little difference. The same can be said for the impact of changing the number of particles and adopting different velocity uncertainties. Going from 2000 to 1000, keeping Δ_v fixed to 40 km s^{-1}, f goes down from 0.54 to 0.40, but it is always consistent within one-σ errors. Lower velocity errors tend to shift detected streams toward "more reliable" regions of the parameter space. This is also visible directly from Fig. 9.3, comparing the top-left and top-right panels and again using the the $n - N_{\rm min}-$ and the $N_{\rm min} - \sigma_{\rm cut}$ panels to discriminate between real streams and spurious ones. Yellow regions are more extended in all panels for $\Delta_v = 10$ km s^{-1}. The bottom-left panel of Fig. 9.3 shows the results of the case of 1000-75 giant-dwarf particles and $\Delta_v = 40$ km s^{-1}. Here, COSTA is still able to detect the stream, even though the ratio of the number of setups where the stream was recovered over the total number of setups is the lowest (see column 2 of Table 9.2), with and without the threshold. Finally, we consider the case with 500-38 giant-dwarf particles. Here, we show the result for $\Delta_v = 20$ km s^{-1}in the bottom-right plot of the same figure. This is in fact the precision one can obtain with typical mid-resolution spectroscopy. In this case, COSTA is also well able to catch the stream in a quite ample range of configurations in the parameter space ($\sim 50\%$).

In conclusion, for all the different configurations we tested, when changing the number of

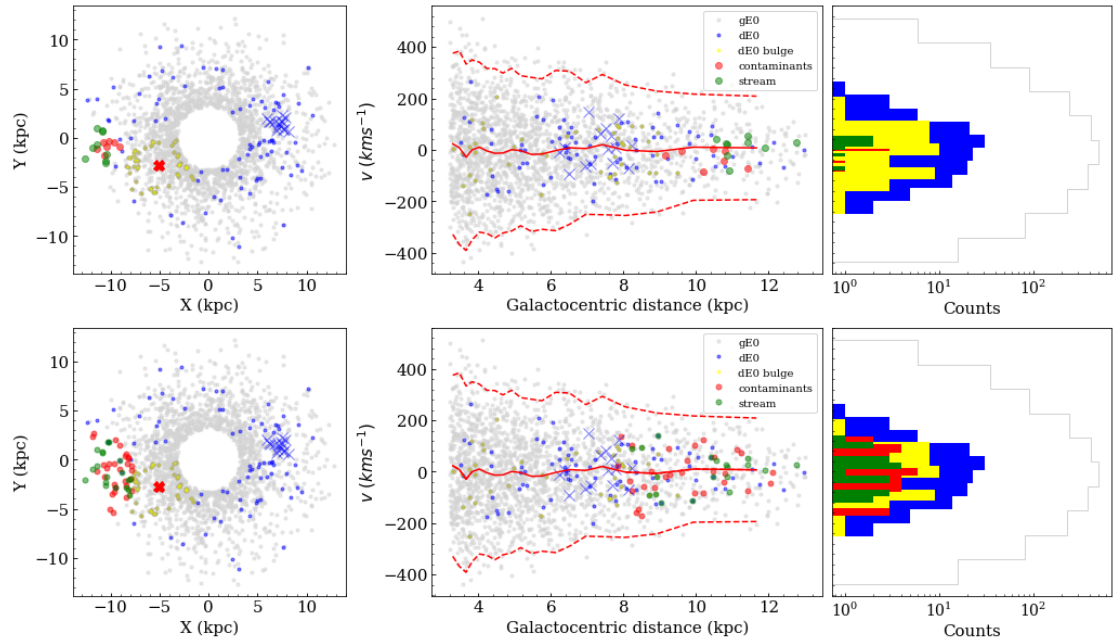

Figure 9.4: *Top:* relative positions (left panel) and reduced phase space (right panel) in the case of the stream recovered with $N_{min} = 15$. *Bottom:* same as above but with the stream recovered with $N_{min} = 30$. Light gray points are gE0 particles, while blue ones are those belonging to the dE0. Yellow points represent dwarf particles within three effective radii from the dwarf center, while the recovered stream is colored in green (real stream particles) and in red (contaminants).

particles and the velocity accuracy, COSTA is able to recover the stream in a relatively broad space of parameters (ranging between 40% and 67%). We note that a 50% success rate is acceptable in blind stream searches if one wants to find a list of candidates to follow up on, and if they represent a fair compromise between purity (no false positives) and completeness (i.e., find as many real streams as possible; see also §9.2.4.3).

9.2.4.3 Completeness and contamination

We can now better describe and quantify the stream properties as returned by the different setups. So far, we have identified the setups that give the true positives, but every setup produces different groups of particles, including real stream particles. In particular, we can check the degree of contamination introduced by the different setups with the aim of finding a method to define the best setup (e.g., the one optimizing the ratio between the number of real particles and contaminators). To do that, we defined the observed completeness (`OC`) as

$$\texttt{OC} = \frac{\texttt{\# recovered stream particles}}{\texttt{total recovered (stream and non-stream)}}.$$

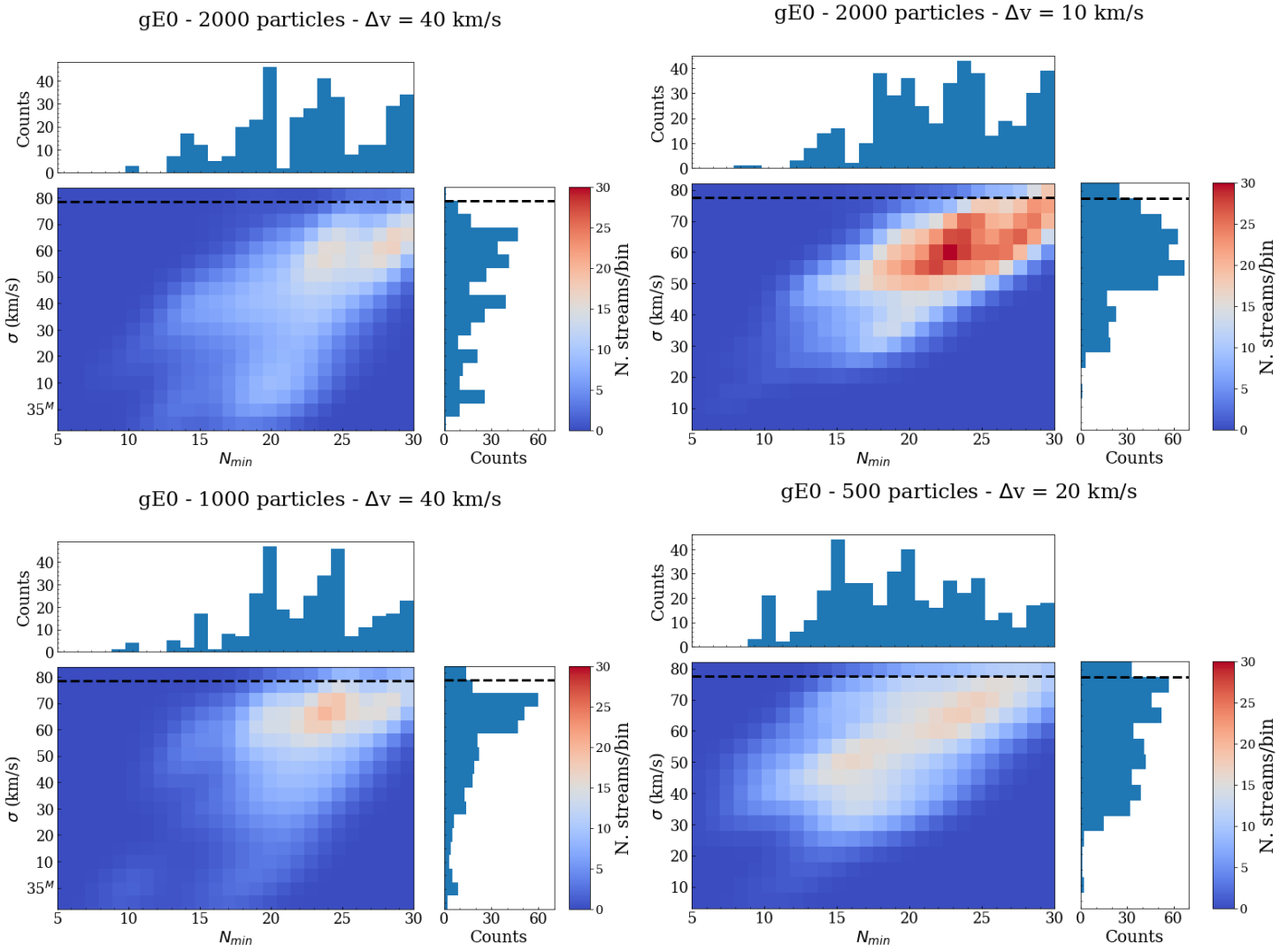

Figure 9.5: Density plot of number of setups with a reliability above the selected threshold and with $F_{\rm N}$ (≥ 0.5) in the $n - N_{\rm min}$ space. Data were smoothed with a Gaussian kernel with a bandwidth equal to three bins.

This parameter is clearly complementary to the contaminant fraction (CF) of the stream (i.e., CF = 1 - OC):

$$\texttt{CF} = \frac{\texttt{\# recovered non-stream particles}}{\texttt{total recovered (stream and non-stream).}}$$

The mean CF derived over all of the setups producing no false positive (column 3 of Table 9.2) are always $\sim 65-70\%$, almost independently of the sample size and velocity accuracy, which, by definition correspond to $\sim 35-30\%$ of OC. This high fraction of contaminants can significantly affect the conclusion about physical properties of the stream (see e.g., §9.2.4.4). However, we stress that these quantities are an average over many setups, and, in principle, one can define the optimal setup that maximizes the OC. We consider this optimization in more detail in §9.3.5. We also remark here that the contaminant fraction does not impact the detection of the stream that remains a good candidate for subsequent follow ups. These are needed in any case to obtain the physical properties of the stream (luminosity, colors, surface brightness, kinematics, etc.).

9.2.4.4 Stream kinematics

After having demonstrated that COSTA is able to detect a stream, we are interested in extracting physical properties from the recovered stream. In particular, we are interested in deriving kinematical information concerning the stream from the velocities of the tracers collected as part of it. Hence, we want to find a rule of thumb to apply to the many configurations that find the stream and identify the setups that better characterize its kinematical properties (e.g., its velocity dispersion). Sadly, a dynamical definition of the stream velocity dispersion is not straightforward, even in simulated samples like GalMer. Technically, the stream is made of all the particles left behind by the disrupting dwarf, which have a different degree of mixing depending on the time at which they became unbound. In Fig. 9.4, we compare the position and velocity distribution of particles belonging to the galaxy background (in gray), the ones belonging to the outskirts of the dwarf galaxy (in yellow, of which the center is shown as a red cross), and the stream particles (in blue) for one of the runs discussed in §9.2.4 and two different $N_{\rm min}$ values ($N_{\rm min}$=15 top, $N_{\rm min}$=30 bottom). In the same figure, we also plot the true stream particles detected by COSTA in this run (in green), and contaminants that COSTA selected but are instead not part of the true streams (in red). From this figure, we can see that the stream particles (blue) overall have a wider distribution with respect to both the dwarf body particles (yellow) and the ones that COSTA detects in the proximity of the dwarf (red and green), while they are not as dispersed as the gray particles of the central galaxy halo. As such, they are both unbound from the parent dwarf and unmixed with the host halo, hence

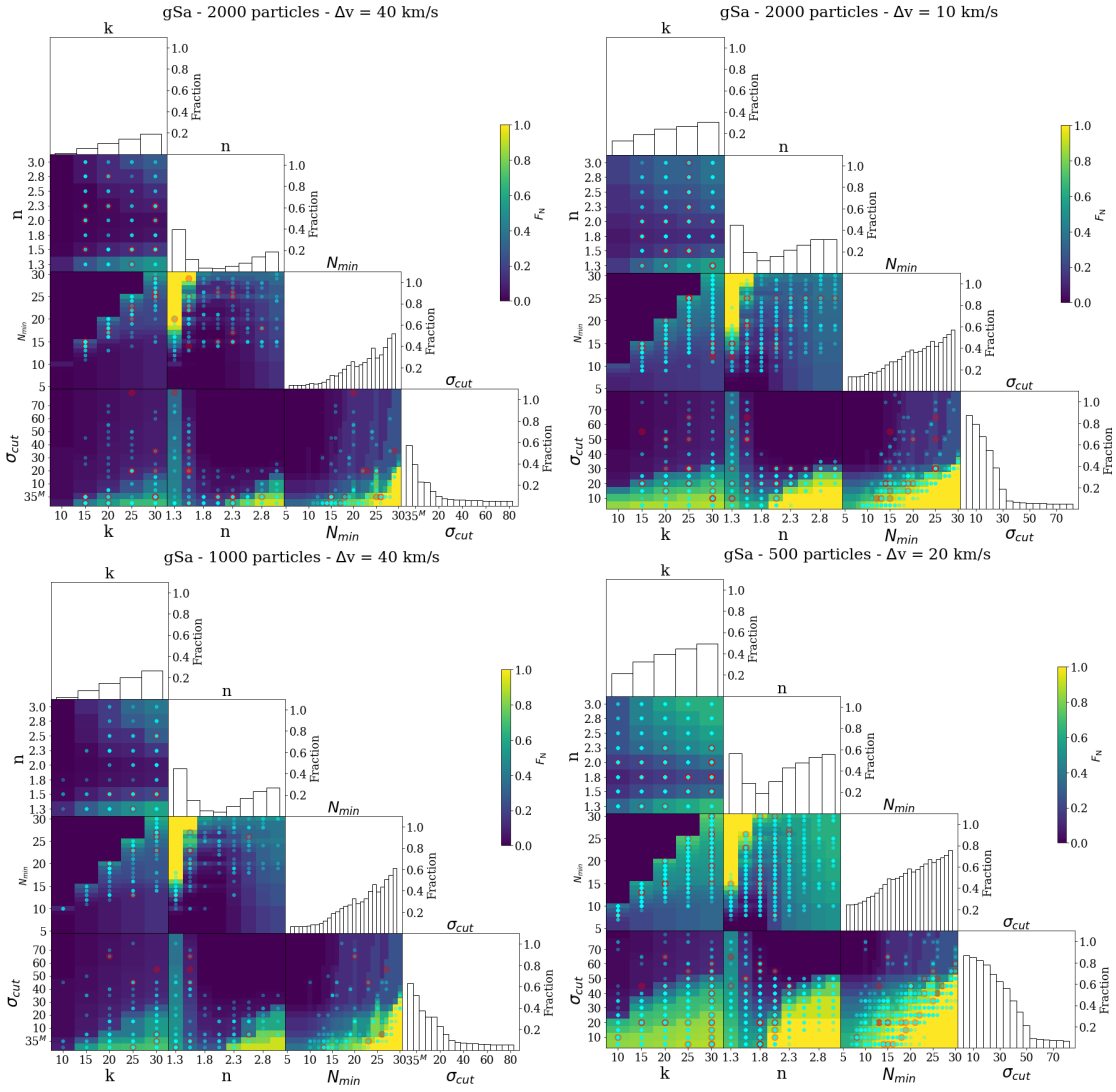

Figure 9.6: Same as Fig. 9.3 but for the gSa in the prograde encounter.

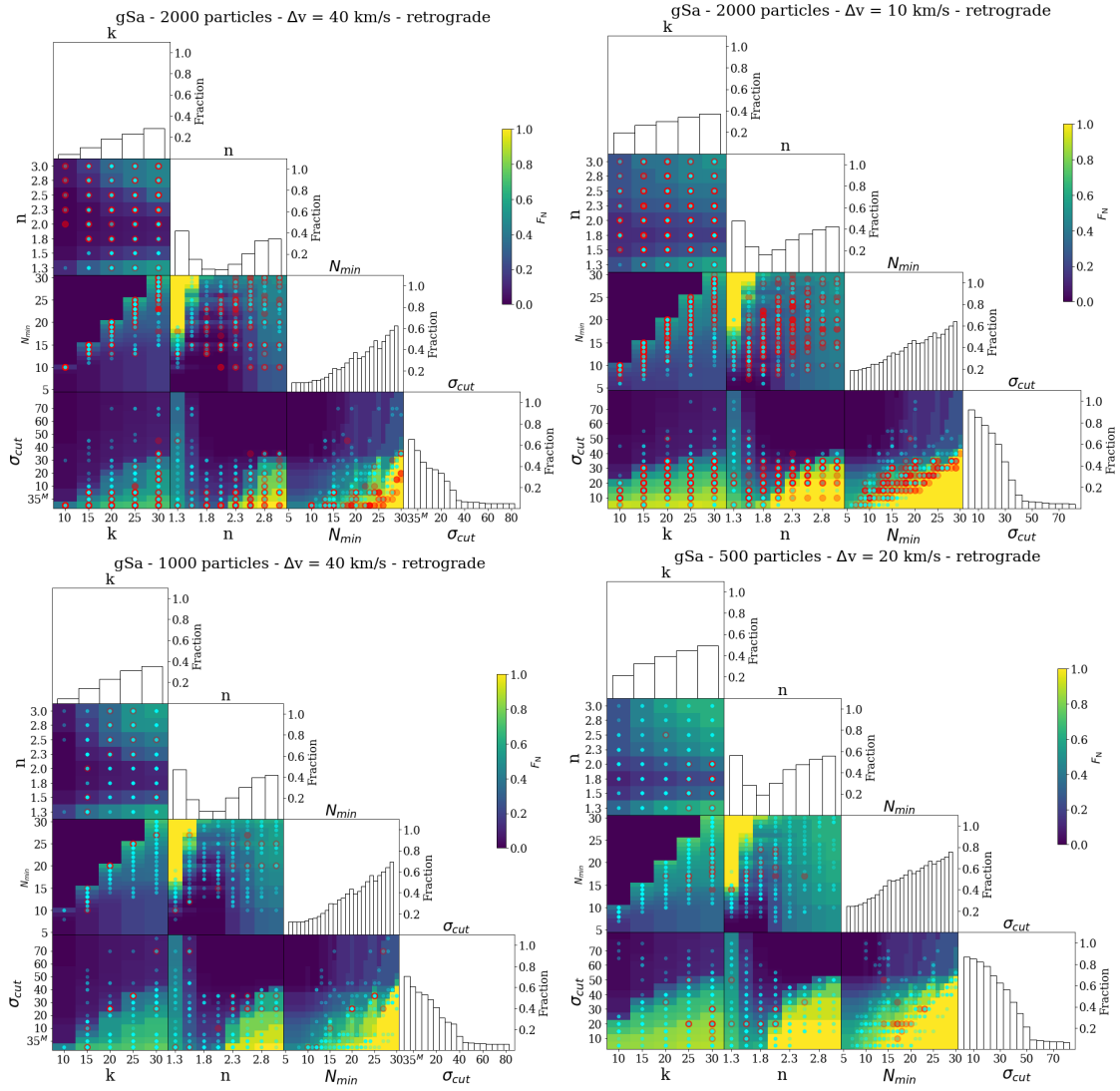

Figure 9.7: Same as Fig. 9.3 but for the gSa in the retrograde encounter.

their velocity dispersion does not have a dynamical meaning because hydrostatic equilibrium does not hold. On the other hand, the "youngest" regions of the stream (green particles) show a distribution that is similar to the ones of the dwarf particles (yellow) at the equilibrium. Thus, the particles recently lost in the tail (and more likely detected with COSTA) keep the record of the kinematics of the parent galaxy[4]. This means that these latter particles have not yet fully dynamically decoupled from their progenitor, and we are motivated to compare their velocity dispersion with the dwarf velocity dispersion (i.e., 77 km s^{-1}; see Table 9.1). This is useful for two main reasons: 1) algorithm-wise, this is the best way to identify setups that better describe (dynamically motivated) kinematical properties of a detected stream; and 2) dynamically, we postulate that the stream velocity dispersion should follow the Faber-Jackson relation [Faber and Jackson, 1976] of the parent dwarfs (i.e., the velocity dispersion should correlate with the luminosity of the progenitor, if any). To illustrate how this works via data, looking at Fig. 9.4 again we clearly see a typical situation of a stream detection where stream particles (including some contaminants) are close to the bulk of the parent galaxy. For both the case with $N_{\rm min}$=15 and that with $N_{\rm min}$=30, COSTA selects only a limited fraction of particles, and it selects them very close to the dwarf (tail). The ratio of the red particles over all particles (i.e. red+green colors in Fig. 9.4) gives the `OC`, which decreases toward higher $N_{\rm min}$ (e.g., 0.56 vs 0.40). On the contrary, the overall velocity dispersion increases from the $N_{\rm min} = 15$ to 30 (as seen in both the phase-space diagram, the velocity-radius plot in the middle panels, and the velocity histogram in the right panels), and, in the latter case, it becomes closer to the one of the dwarf (i.e., 77 km s^{-1}). Green and red particles have rather similar velocity dispersion values both in the case with $N_{\rm min} = 15$ (top row in the figure): $\sigma_{\rm green,15} = 40$km s^{-1}, $\sigma_{\rm red,15} = 35$km s^{-1}, and the case with $N_{\rm min} = 30$ (bottom row in the figure): $\sigma_{\rm green,30} = 74$km s^{-1}, $\sigma_{\rm red,30} = 83$km s^{-1}. This suggests that the contaminants only slightly alter the true velocity dispersion of the stream. Only in very few runs does COSTA also detect groups of particles in the tail of the stream that are further away from the dwarf main body, on the opposite side of the central galaxy (see e.g., blue crosses in Fig. 9.4). This shows that COSTA can, in principle, also identify portions of the debris of a stream in absence of a close dwarf (e.g., at the pericenter/apocenter of stream orbits where lost particles tend to accumulate around zero systemic velocity in the reference frame of the

[4]Dynamically speaking, this means that both the energy transfer from orbital momentum to the dwarf GCs [e.g., via tidal approximation; Napolitano et al., 2002] and the dynamical friction ($\propto \rho/\sigma^2_{\rm env}$, where the density, ρ and the inverse of the velocity dispersion $1/\sigma^2_{\rm env}$ of the environment are small) have a minor impact on the stripped particles.

central galaxy). This is due to the fact that, being stream (blue) particles still unmixed with the halo, they are also recognized as cold substructures. The fact that the majority of the detections occur in the regions close to the galaxy depends strongly on the fact that these particles are fully unmixed. For a detection to occur at greater distances, one needs an ad-hoc combination of poor mixing and occasional overdensity, which is more unusual. It remains that the velocity dispersion of these latter detections cannot be dynamically connected to the parent dwarf (e.g., via a Faber-Jackson relation). The only case in which one is motivated to dynamically interpret the velocity dispersion of an isolated group of particles that has no clear dwarf association is in the one with evidence that the parent dwarf has recently been disrupted and the remaining particles are the latest lost. Finally, since we postulate a connection between the kinematics of the stream and the one of the parent dwarf (e.g., a sort of Faber-Jackson stream), and given that COSTA can detect the same stream with different configurations, we wish to check whether we can identify configurations that reproduce, as close as possible, the real internal dispersion of the dwarf. In Fig. 9.5, we show the density plot of the velocity dispersion estimates of the selected stream particles as a function of the most sensitive parameter discussed in this paragraph, $N_{\rm min}$. In particular, we show the values obtained using a threshold on $F_{\rm N} = 0.5$ in the $n - N_{\rm min}$ space as described in §9.2.4.2. The four plots correspond to the measured velocity dispersion, $\sigma_{\rm mea}$, from the streams selected according to the four different cases as in Fig. 9.3. Overall, we notice that the velocity dispersion estimates tend to cluster around the true value of the dwarf (77 km s^{-1}), with the tails toward lower values. This happens regardless of the sample size and velocity errors, although higher velocity accuracy (e.g., $\Delta_v \leq 10$ km s^{-1}, top right panel, and $\Delta_v \leq 20$ km s^{-1}, bottom left panel) gives less pronounced tails toward low $\sigma_{\rm mea}$ in the velocity distribution. This is particularly evident when comparing the 2000-particle cases (top row of Fig. 9.5). Being more quantitative and using the median of the distribution as a probe of the peak, we obtain the following stream velocity dispersion: 43 $\pm$ 23 km s^{-1}, 57 $\pm$ 12 km s^{-1}, 57 $\pm$ 15 km s^{-1}, and 57 $\pm$ 18 km s^{-1}for the 2000 (40), 2000 (10), 1000 (40), and 500 (20) cases, respectively. Of course, the final dispersion of the stream is in all cases affected by the contaminants from the main galaxy, but overall the median values are always consistent within 1-σ uncertainties and are all close, although slightly lower, to the true velocity dispersion of the dwarf. This implies that the contaminants selected by COSTA as part of the stream are almost statistically indistinguishable from the stream particles, as they hold similar overall kinematics (see Fig. 9.4).

9.2.5 The case of the gSa-dS0 encounter: Testing COSTA on a cold system

Having demonstrated that COSTA is able to find cold streams embedded in the halo of hot early-type systems, we now need to test the case of late-type galaxies. We selected a gSa-dS0 encounter, and tested both a prograde and a retrograde motion for the dwarf, because the stronger rotation of the galaxy disk might have a different impact in the two cases. We followed the same steps as in the gE0-dE0 case, and we highlight the results in the following sections.

9.2.5.1 Reliability

First, we ran COSTA over the WNS using all parameter combinations to determine the reliability distribution in the parameter space. In Figs. 9.6-9.7, we show the reliability maps for the prograde and retrograde cases on two separate rows. Also in this case, we show the density plot obtained with different numbers of particles for the giant and the dwarf and different values of Δv. Since the gSa is colder than the gE0, it is much easier for COSTA to find combinations of galaxy particles with a local velocity dispersion close to that of the $\sigma_{\rm cut}$ (i.e., there is a smaller contrast). It is much easier for COSTA to find spurious substructures, and consequently it is harder to find setups with high reliabilities (i.e., with more than 70% of detections being non-spurious). As a result, the regions of the parameter space with high $F_{\rm N}$ (yellow) are considerably reduced with respect to the gE0 case, and there is generally a higher chance of finding some false positives. As for gE0, the adoption of smaller velocity errors produces a slightly higher number of good setups, especially in the retrograde case, and the $F_{\rm N}$ also increases over a relatively wider area for the smallest number of tracers tested in our simulations (fourth panel). The results for the prograde (top) and retrograde (bottom) cases are very similar because in the two cases the WNS does not change dynamically in a significant way, despite the fact that the different interaction with the intruder might have introduced different perturbations.

9.2.5.2 Stream detection

The second step is to run COSTA on the DS, which is made by the main galaxy and dwarf particles, to recover the stream particles. As with the gE0+dE0 encounter, we performed ten random extractions of the giant+dwarf system, imposing a limit on the lower surface brightness of the stream. The results of this test are listed in Table 9.3, both for the prograde and the retrogade encounters. In general, COSTA only detects the stream in few setups (with reliability `Rel`$\geq$70%$\geq$

Table 9.3: Same as Table 9.2 but in the case of the spirals.

gSa-dS0 Prograde	f	CF
2000 part - 40 km s^{-1}	0.10 ± 0.13	0.61 ± 0.14
[a]2000 part - 40 km s^{-1}	0.14 ± 0.20	0.74 ± 0.15
2000 part - 10 km s^{-1}	0.08 ± 0.15	0.57 ± 0.15
[a]2000 part - 10 km s^{-1}	0.11 ± 0.19	0.67 ± 0.19
1000 part - 40 km s^{-1}	0.04 ± 0.06	0.73 ± 0.13
[a]1000 part - 40 km s^{-1}	0.04 ± 0.12	0.89 ± 0.11
500 part - 20 km s^{-1}	0.03 ± 0.04	0.71 ± 0.12
[a]500 part - 20 km s^{-1}	0.04 ± 0.05	0.73 ± 0.16
gSa-dS0 Retrograde	f	CF
2000 part - 40 km s^{-1}	0.14 ± 0.22	0.13 ± 0.14
[a]2000 part - 40 km s^{-1}	0.11 ± 0.19	0.26 ± 0.17
2000 part - 10 km s^{-1}	0.29 ± 0.34	0.16 ± 0.15
[a]2000 part - 10 km s^{-1}	0.14 ± 0.21	0.26 ± 0.12
1000 part - 40 km s^{-1}	0.04 ± 0.12	0.36 ± 0.14
[a]1000 part - 40 km s^{-1}	0.03 ± 0.09	0.44 ± 0.19
500 part - 20 km s^{-1}	0.04 ± 0.05	0.57 ± 0.10
[a]500 part - 20 km s^{-1}	0.03 ± 0.04	0.50 ± 0.13

a: in these configurations, we ruled out setups with $F_{\rm N} < 50\%$ in the $n - N_{\rm min}$ space as described in the text.

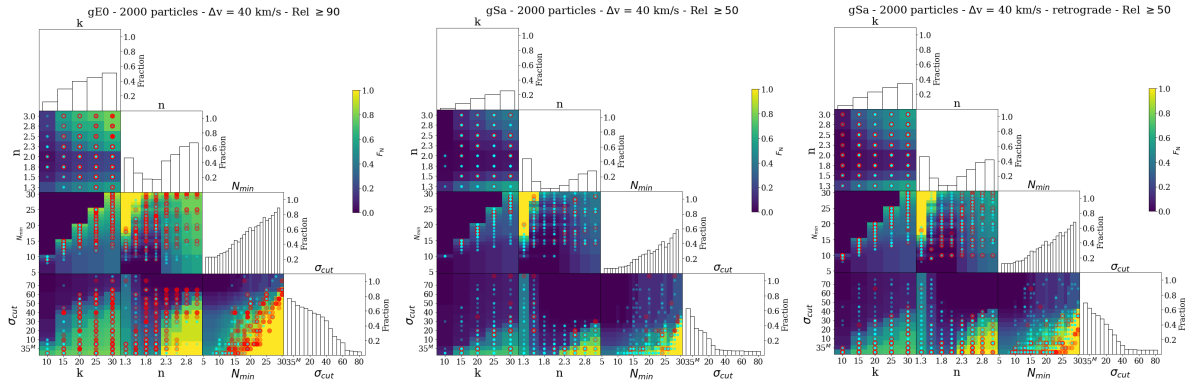

Figure 9.8: Parameter space overlapped with true and false streams detected by COSTA for both early- and late-type galaxies, in the standard configurations (2000 particles and Δ_v= 40 km s^{-1}) for three cases (gE0, gSa prograde, and gSa retrograde), but using different reliability thresholds.

70% both for the prograde and retrograde motions). Furthermore, in the gSa-dSO case, most of the setups that correctly found the stream particles also detected spurious substructures (see bottom-left panel of Figure 9.7 or Table 9.3). Overall, for the retrograde encounter, COSTA performs better, with a much lower `CF` (e.g., $\sim$ 15% versus $\sim$ 60% for the 2000 particles case with $\Delta_v = 40$ km s^{-1}). The number of setups in which COSTA detects a stream is also higher in the retrograde case, at least for the best possible configuration, that is, 2000 parts - 10 km s^{-1}(11% for the prograde and 29% for the retrograde, assuming a threshold of 50% in the $n - N_{\rm min}$ panel, although with a large uncertainty). In this configuration, and partially also in that with 2000 particles and a larger velocity error, the stream has been detected in regions that tend to accumulate toward the highly reliable $F_{\rm N}$ (yellow areas) regions in the parameter space. This is especially visible in the $N_{\rm min} - \sigma_{\rm cut}$ plot, as we see for the gE0 system. In particular, high-reliability configurations favor a smaller $\sigma_{\rm cut}$ ($\leq$ 40 km s^{-1}). However, this is not always true for the prograde and retrograde cases with a smaller number of particles, at least not for all the projections. In these cases, the stream was detected only a few times, and they are very sparse in the region of the single plots of the parameter pairs. Finally, as seen in Fig. 9.7 (at least for the retrograde case), COSTA performs generally better when the velocity errors are smaller. Here, the algorithm reveals the stream in more setups. An interesting contrast between the gE0-dE0 and gSa-dS0 cases is that, for the latter, the number of particles produces a very different number of setups with high reliability. This is valid both for the prograde and for the retrograde case. Going from 2000 particles to 500, the f is between three and five times smaller, while the CF increases. We also note that, for the gSa-dS0 cases, and in particular for the prograde encounters, the configurations for which we correctly detect the streams are often embedded in low-$F_{\rm N}$ areas. This is different from what happens in the gE0-dE0 interaction and it is due to the fact that, since COSTA finds more spurious stream, the configurations that allow us to find the stream also find some of them that are spurious, at least with the change of other parameters. This means that, even if the stream is found, this has a generally lower reliability in cold systems. We need to stress here that this conclusion is not general, as this applies to the case of a mass ratio 10:1, that is, with a small contrast between the dispersion of the stream and the dispersion of the background velocity field (see below).

9.2.5.3 Stream kinematics

The $\sigma_{\rm cut}$ ($\leq$ 40km s^{-1}) is an upper limit, beyond which COSTA no longer detects the stream. The median of the velocity dispersion, using only setups with $F_{\rm N} > 0.5$ in the $n - N_{\rm min}$ plot

in the retrograde encounter, gives a velocity dispersion lower than the one of the parent dwarf galaxy ($\sigma_{\rm dwarf} = 74$ km s^{-1}). In fact, we obtain the following medians of the velocity dispersion distributions: 24 ± 13km s^{-1}, 31 ± 7km s^{-1}, 33 ± 2km s^{-1}, and 37 ± 6km s^{-1}for the 2000(40), 2000(10), 1000(40), and 500(20) cases. Here, the worse performance of COSTA with respect to the gE0-dE0 is due to little contrast between the dwarf velocity field (which is rather hot in the specific GalMer simulation; i.e., $\sigma_{\rm dwarf} \sim 74$ km s^{-1}) and the gSa ($\sigma_{\rm giant} \sim 81$ km s^{-1}). Thus, the exercise we carried out here has to be interpreted as an "extreme case" to set a guideline for the methodology to follow in "real" cases, where the difference between the velocity dispersion of the dwarf and that of the giant is larger.

9.2.6 The dependence of COSTA's performance on the reliability threshold

In this section, we explore how different reliability thresholds can affect the completeness and purity of COSTA. Overall, logically, a lower threshold allows us to increase the probability of finding a stream (at the expense of a greater contamination), while a higher limit has the opposite effect. In the case of the gE0-dE0 interaction, we increased the lower limit of the reliability and we only used combinations of free parameters above 90%. We only ran COSTA on the $N_{\rm giant} = 2000$, $N_{\rm dwarf} = 150$, and Δv $= 40$ km s^{-1} configurations. Of course, the number of parameter combinations overcoming the threshold is reduced with respect to the previously used threshold of 90%. This can be seen in the left panel of Fig. 9.8 (left panel). However, the stream is still detected in many setups, and they show almost the same distribution in the parameter space as for the lower threshold. For the gSa-dSa interaction, the situation is reversed, as we lowered the acceptable value of reliability to 50%. Indeed, in both the prograde and retrograde encounters, COSTA could not find streams using a higher threshold, so we checked a lower one. In both encounters we used $N_{\rm giant} = 2000$, $N_{\rm dwarf} = 150$, and Δv $= 40$ km s^{-1}. In the prograde case (central panel of Fig. 9.8), COSTA finds the stream in a slightly higher number of setups, with respect to the very few that have a reliability cut-off of 70%. In the retrograde case (right panel of the same figure), the improvement is even higher as the number of setups where COSTA detects the stream increases by 50% with respect to the previous case. Thus, we conclude that for the late-type case, the 70% reliability threshold is too conservative, and a lower reliability threshold would give more opportunities to identify streams.

9.3 The case of the Fornax cluster core

We tested COSTA on a cluster environment where streams are produced in a more complex situation with many large coexisting galaxies. In such environments, multiple low-surface-brightness streams from a larger population of dwarf galaxies and with a given luminosity function and different kinematics can be produced. In particular, we present here the case of the Fornax cluster, for which there are GCs [from Pota et al., 2018] and PNe [from Spiniello et al., 2018] available for stream search, which we will present in forthcoming analyses. The aim of this section is to show that for a more complex case, such as the Fornax cluster core, COSTA can also be set to detect cold streams of small numbers of particles, as was done for the GalMer simulations. For the Fornax cluster, unfortunately, we do not possess a simulation realistic enough to produce an equally large structure distribution of particles as the one reported in GC and PNe studies. We thus decided to build up Monte Carlo realizations of the kinematical tracer distribution in the 3D phase space (i.e., 2D positions and radial velocity) over which we we were able to obtain a reliability map for COSTA and test its stream detection performances. Indeed, following the approach adopted for the GalMer simulations, we first require the Monte Carlo realizations of the Fornax core in order to have a smooth cluster background with no streams (i.e., the WNS). This allows us to explore the parameter space and assess the reliability function of COSTA as a function of the different parameters. Secondly, we added a number of artificial streams (hence generating different DSs) and ran COSTA to recover them and to calculate the `OC` and `CF`.

9.3.1 Monte Carlo simulations of the Fornax cluster core

To produce COSTA reliability maps, we performed a suite of Monte Carlo simulations resembling the Fornax core as closely as possible in terms of spatial distribution, local density, and radial velocity distribution of the kinematical tracers (WNS). We only simulated the region covered by the current discrete tracer surveys [FVSS Pota et al., 2018, Spiniello et al., 2018], covering about 1.8 $\deg^2$ around the cD, NGC 1399. In this area, there are two other bright early-type galaxies: NGC 1404, located just below the cD in the south-east direction at about $9'$; and NGC 1387, at a distance of $\sim 19'$ to the west of NGC 1399. A third relatively massive galaxy, NGC 1379, located at $\sim 60'$ toward West, was observed with one FORS2 pointing in S+18. However, this system is excluded from this analysis because we do not have continuity with the rest of the Fornax core area, hence it is useless with regard to stream finding. We generated simulated GCs and PNe in a total number that is as close as possible to what has been observed in Spiniello et al. [2018] and

Pota et al. [2018]. In the following, we assume that both GCs and PNe trace the same underlying population of old stars[5], at the equilibrium in the gravitational potential of these three galaxies, assumed to be the superposition of the individual galaxy potentials with spherical symmetry. Following Napolitano et al. [2001], we produced the 3D position starting from a 3D spherical density profile and projected them on the 2D sky plane (X-Y in our case). For each particle, we determined the 3D velocity vector according to the hydrostatic equilibrium equations (see below), which we projected along the line of sight to derive the intrinsic radial velocity. We finally simulated a radial velocity measurement by randomly extracting the measured velocity from a Gaussian having the intrinsic radial velocity as mean and standard deviation equal to the measurement errors. In order to produce these Monte Carlo realizations of particles sampling the total potential in the Fornax core, we assumed a total mass of about 10^{14} $M_{\odot}$ and a Hernquist [Hernquist, 1990] density distribution of the stellar-like tracers for the cluster. This is a good approximation for elliptical galaxies following a de Vaucouleurs [1948] law. For NGC 1399, which gathers most of the light in the cluster core, Iodice et al. [2016] found a Sersic index $n = 4.5$, which is very close to the $n = 4$ that describes the de Vaucouleurs law. The luminous mass density is expressed by the formula

$$\rho(r) = C\frac{M_{\rm l}a}{2\pi}\frac{1}{r(r+a)^3}, \tag{9.3}$$

where $M_{\rm l}$ is the total luminous mass, a is a distance scale ($R_{\rm e} = 1.81534\ a$) and C is a normalization constant. We made the same assumption for all other galaxies in the area, with the adopted parameters as in Table 9.4. In addition to the stellar mass density, we also considered a dark halo following a Navarro-Frenk-White (NFW) [Navarro et al., 1997] profile, to define realistic internal kinematics for the simulated particles. Hence, the potential of the system at equilibrium is provided by the total mass:

$$M_{\rm tot} = M_{\rm l} + M_{\rm dm}. \tag{9.4}$$

We assumed non-rotation[6] and an isotropic velocity dispersion tensor, and we solved the radial Jeans equation,

$$\frac{d(\rho\sigma^2)}{dr} = -G\frac{M_{\rm tot}(r)\rho(r)}{r^2}, \tag{9.5}$$

to derive the 3D velocity dispersion σ^2 in the three directions of the velocity space, and we generated a full 3D phase space. As briefly anticipated above, we simulated an observed phase

[5]For a discussion about the statistical similarity between the two tracers, see Napolitano et al. [2022]

[6]Although some rotation of blue GCs in the radial range between 4 and 8 arcminutes was measured, the kinematics of the outskirt of NGC 1399 is dominated by the random motion [Coccato et al., 2013, Schuberth et al., 2010]

Table 9.4: Parameters of the simulated galaxies. The effective radii were taken from the literature, unless specified otherwise. The velocity and velocity dispersion values were retrieved from the Nasa Extragalactic Database (NED), unless specified otherwise.

Galaxy	Number of points	R_e (arcsec)	Vel. (kms^{-1})	σ_p (kms^{-1})
NGC 1399	1855	138	1425	320
NGC 1387	90	42	1302^a	160
NGC 1404	40	100^a	1947	247

a: Values adopted to obtain a more realistic reproduction (see text).

space by projecting the tracer distribution on the sky plane, and we derived the LOS velocity of the individual particles. In particular, we used the X-Y plane as the sky plane and the z-axis as the LOS. However, due to the full spherical symmetry of the model, the particular projection is irrelevant. Finally, in order to simulate a velocity measurement, we used the same approach as for the GalMer simulations: we adopted a Gaussian error distribution and re-sampled the radial velocities produced by the Monte Carlo simulations with a $\Delta_v = 37$ km s^{-1}, which is consistent with typical measurement errors from P+18 and S+18. In this case, we do not vary the errors, as this test is meant to demonstrate that COSTA can be applied to a real dataset and provide a series of reliable setups for finding stream candidates from real datasets. We included 1985 particles in the simulation to reproduce the number of observed PNe and GCs selected in the area as accurately as possible. The number of points for each satellite galaxy was then obtained with a cross-match with the real data, counting the number of plausible PNe and GCs bound to the galaxies, while both effective radii and velocity dispersions are taken from the literature (see Table 9.4). To obtain a realistic reproduction of the PN and GC systems around NGC 1404 (in terms of number and radial abundance), we need to adopt an effective radius (i.e., the radius enclosing half of the total light of the galaxy), $R_e \sim 100''$, slightly larger than the one estimated by Corwin et al. (1985, $R_e \sim 80''$). For NGC 1387, we took into account the velocity offset of PNe reported by Spiniello et al. [2018] (i.e., a mean velocity higher than the systemic velocity of the galaxy reported in literature by ~ 100 kms^{-1}). Indeed in this area, we have a larger number of PNe than GCs, respectively 117 (88%) and 16 (12%), within three effective radii from NGC 1387; thus the offset of the PN velocities might generate an overall velocity excess of 100 kms^{-1}, that we thus artificially added to all simulated points around NGC 1387 in order to

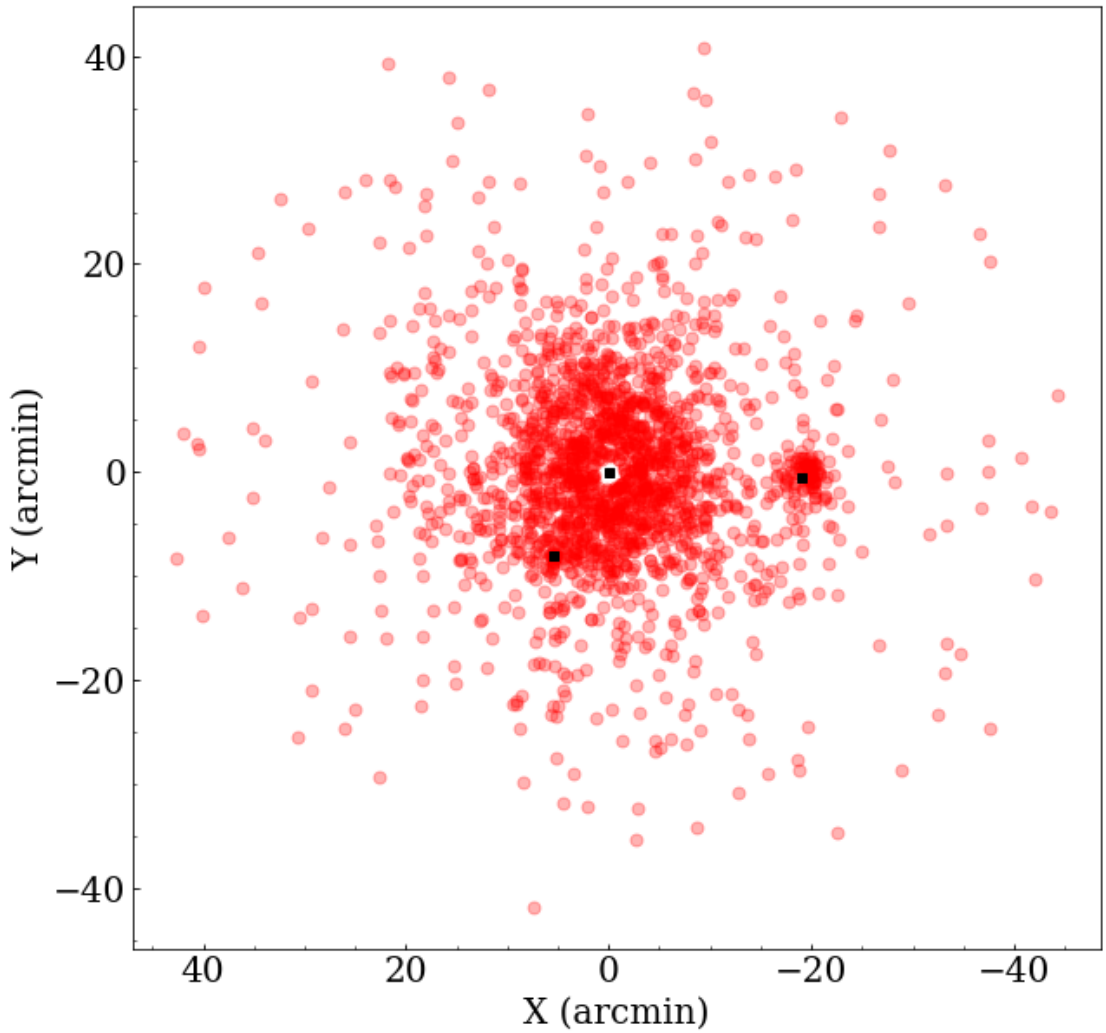

Figure 9.9: Simulated data points for one Monte Carlo realization, with NGC 1399 at the origin of coordinates. NGC 1404 is just below the cD ($X \sim -5$, $Y \sim -5$), and NGC 1387 is at $X \sim -20$ arcmin. The positions of the three galaxies are indicated by black squares.

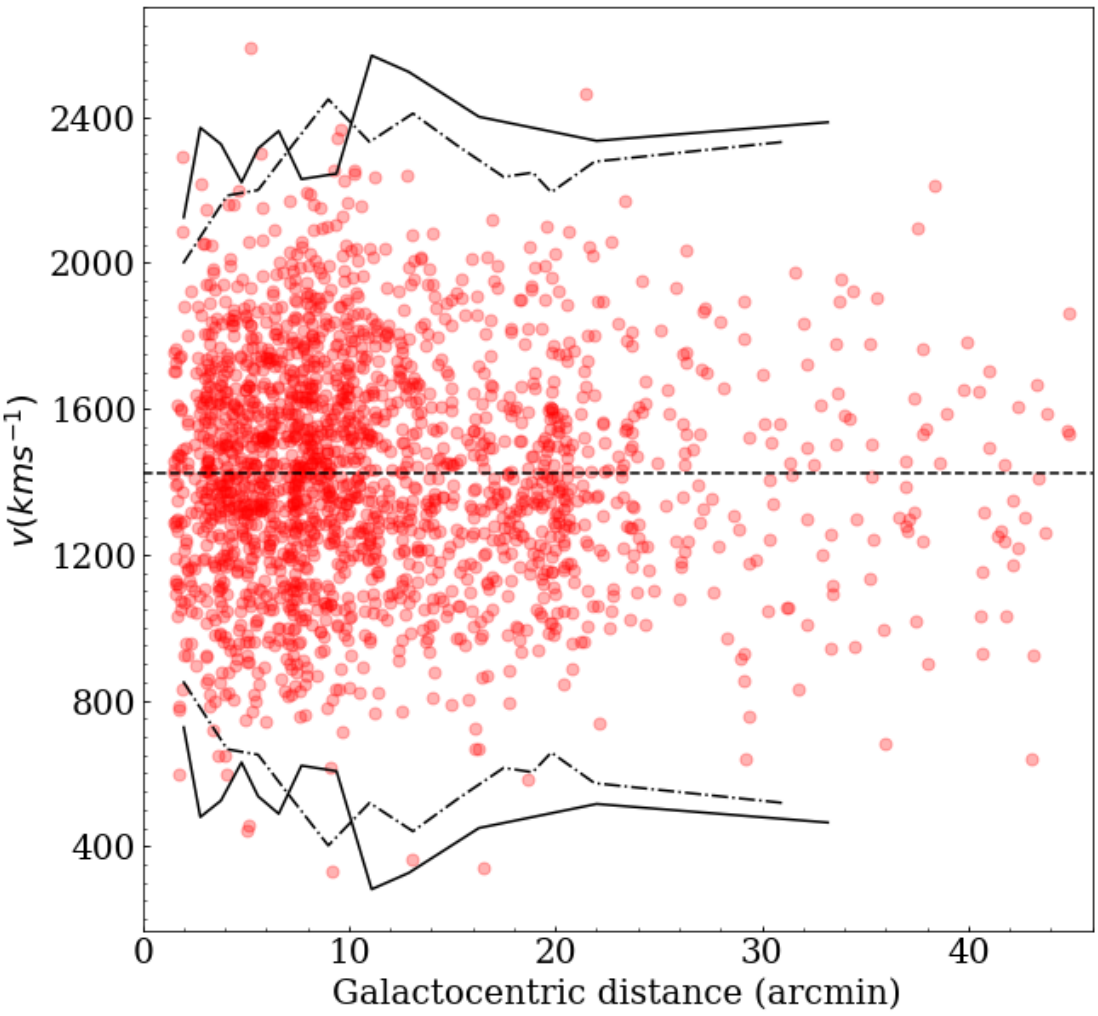

Figure 9.10: Phase space of one Monte Carlo simulation. On the x-axis, we plot the distance from NGC 1399 in arcminutes, and on the y-axis we plot the velocities of the points in km s^{-1}. The continuous solid and dashed-dotted lines represent the $\pm 3\sigma_P$ profiles of the GCs and PNe, respectively, extracted from Pota et al. [2018] (their Fig. 9). The dashed black horizontal line represents the systemic velocity of NGC1399 (1425 km s^{-1}).

.

match the real objects (see also Table 9.4). The final result of all these fine-tuning calibrations for the simulated sample gives the distribution of the simulated particle, as shown in Fig. 9.9. Here, we plot the simulated points for one of the mock realizations using positions computed with respect to the simulated cluster center. We observe a fair spatial correspondence between the main galaxies in the field of view (whose positions are highlighted as black squares) and the simulated particles (red points). In Fig. 9.10, we show the phase-space distribution of the same simulated particles together with the $\pm 3\sigma_p$ profiles (where σ_p is obtained as in Eq. 9.1) of the GCs from Pota et al. [2018] and the PNe from Spiniello et al. [2018] (curves are extracted from Fig. 9 in Pota et al. 2018). Once again, the similarities are quite evident between the overall kinematics of the simulated particles and of the observed ones. Once we had optimized the Monte Carlo simulation setups to best reproduce the observed GC+PN dataset, we finally produced 100 realizations of the system, which represent the WNS from which we obtained the reliability maps for COSTA. Differently from the GalMer simulations, where the statistical variation of the parameters were obtained only by perturbing the velocities of the particles, for the Fornax-like case we re-sampled the full parameter space. Hence, we added more statistical noise to the simulated sample, coming from different spatial configurations of the same physical streams.

9.3.2 COSTA setup and reliability map

To obtain the reliability map, we followed the same steps as in the GalMer simulations (§9.2.4 and §9.2.5). To begin with, we ran COSTA for each parameter combination over the 100 Monte Carlo realizations of the WNS and counted the number of configurations for which COSTA finds no spurious streams. In this case, we uniformly sampled the *k, n,* $N_{\rm min}$ parameters' space for a different $\sigma_{\rm cut}$ and ran COSTA with all the possible combinations of the free parameters selected in the following ranges:

- k: from 10 to 50 with steps of 5.
- n: from 1.3 to 3 with steps of 0.2-0.3.
- $N_{\rm min}$: all values from 5 up to k.
- $\sigma_{\rm cut}$: from 10 to 120 km s^{-1}with steps of 5 km s^{-1}.

The difference with respect to the gE0-dE0 case (i.e., the case of another hot systems) is the adoption of a larger $\sigma_{\rm cut}$, k, and a larger $N_{\rm min}$ range. This is motivated by the fact that, as the Fornax environment is hotter than the GalMer gE0, we can detect higher velocity substructures

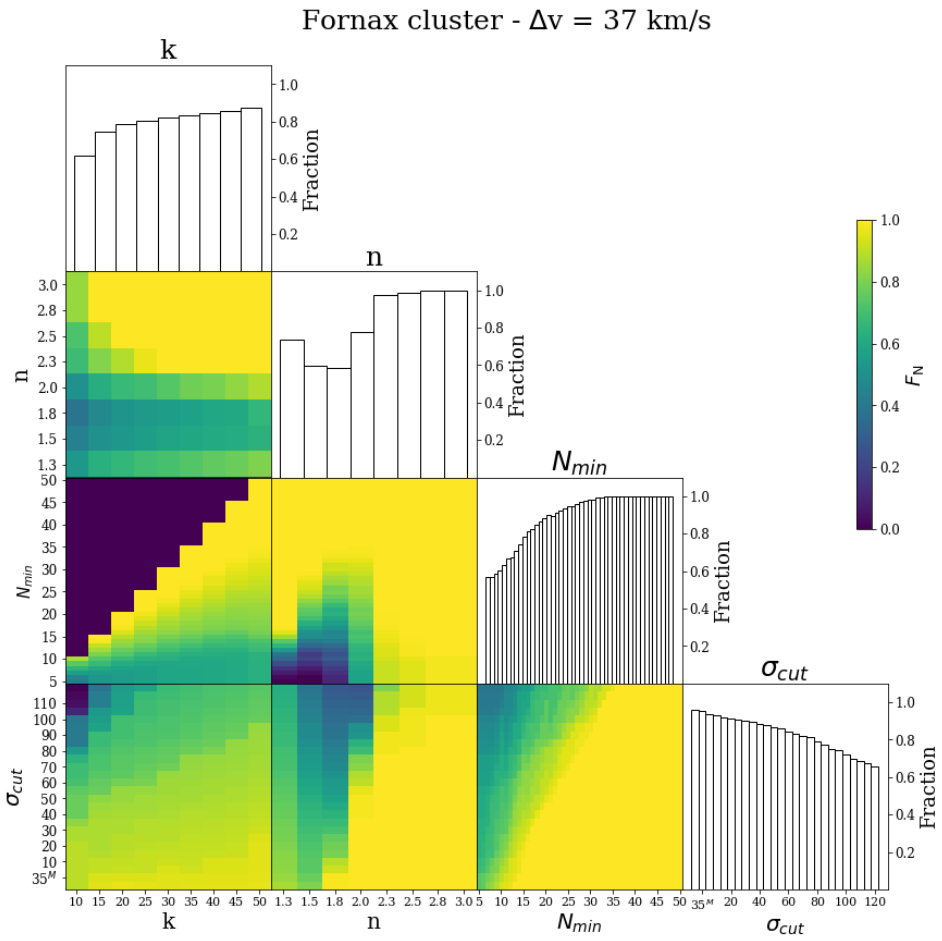

Figure 9.11: Reliability map for Fornax cluster obtained with a reliability threshold of 70%.

(if any). Similarly to the GalMer simulations, we also used $\sigma_{\rm cut}$ values below the instrumental errors, considering in these cases $\sigma_{\rm mea} \sim \sigma_{\rm obs}$ (see discussion in §9.2.4). Figure 9.11 shows the reliability map, color-coded by the fraction of the number of setups with a reliability $\geq 70\%$. The case of the Fornax-like system is fairly different with respect to the configurations tested with the GalMer simulation. Indeed, the intrinsically higher velocity dispersion provides a much smaller chance of obtaining a correlated group of particles characterized by a small dispersion; this is due to statistical fluctuation in the parameter space. For this reason, COSTA has a quite large range of parameters that find a spurious stream in less than 30% of the extractions. One may argue that in this case 70% is a too-loose threshold, and higher values might be used too. However, the Monte Carlo simulations only partially catch the full statistical fluctuations, and

they might be too smooth with respect to the real data. In a second step, we ran COSTA on the DS where the artificial streams were added to assess the effectiveness of COSTA detection.

9.3.3 Recovering simulated substructures

When applying COSTA to real cases, detection is the minimum we want to achieve (completeness), while we can compromise on the full recovery of stream particles vs. contaminants (purity), as we correctly expected that we would lose some particles and also obtain some contaminants (non-stream particle) as part of a correctly detected stream (see also discussions in §9.2.4 and §9.2.5). To check COSTA's ability to recover known streams in the Fornax-like environment and to assess completeness and purity, we added three artificial streams to our Monte Carlo simulations. Since we cannot reproduce the full dynamics of a stream in our Monte Carlo simulations, and we wanted to test COSTA in more observational situations, we chose typical stream sizes and kinematics that can be realistically found in real data. As shown in the case of the GalMer simulations (see e.g., Fig. 9.4), despite the fact that a dwarf galaxy spreads a large number of particles along its encounter orbit, COSTA can identify only the closer ones, which were the last to be stripped (of the order of a few tens, depending on the surface brightness of a stream), spread over ∼5–15 kpc, that is, $1' - 3'$ at the distance of Fornax. The first stream (stream 1, hereafter) is made of 20 particles, measures $1' \times 2'$, and has an intrinsic velocity dispersion of $\sigma = 35$ kms^{-1}. Two other streams were extracted by randomly sampling particles from the tail of the GalMer gE0-dE0 case discussed in §9.2.4. We isolated a group of 30 particles, distributed over an area of about $3' \times 1.5$' in one case (GalMer 1 hereafter) and $6' \times 3'$ in a second case (GalMer 2), with an intrinsic velocity dispersions of $\sigma = 45$ kms^{-1} and $\sigma = 62$ kms^{-1}, respectively. These two streams have the advantage of being more realistic (in shape and density) as they are based on a simulated encounter, although the dynamics of the GalMer simulation adopted is not really close to the one of the Fornax core, in particular because of the lower mass of the main galaxy as compared to NGC 1399. We also took larger streams ($3'$ roughly corresponds to 30 kpc) in order to explore the ability of COSTA to find larger and more diffuse streams. The final properties of the artificial streams are summarized in Table 9.5. In order to simulate a real measurement of the particle redshift, we randomly re-extracted their "measured" velocities from a Gaussian with a central velocity equal to the intrinsic radial velocity, and standard deviation of 37 kms^{-1}. We stress here that the three streams have a velocity dispersion within the range expected for dwarf galaxies [Kourkchi et al., 2012]. Also, the number of particles is not arbitrary: indeed, assuming that we split the particles in the same number of PNe and GCs, and assuming a typical

Table 9.5: Properties of the simulated streams

	N	Size (arcmin)	σ_I (kms^{-1})	σ_M (kms^{-1})
stream 1	20	2 X 1	35	42
GalMer 1	30	3 X 1.5	45	58
GalMer 2	30	6 X 3	62	69

(bolometric) PN-specific number density of 50×10^{-9} PN/$L_\odot$ [see e.g., Feldmeier et al., 2004], the luminosity in the g-band corresponding to 10-15 PN-like particles is of the order of $10^8 L_\odot$. The corresponding surface brightness of streams, with sizes as in Table 9.5, is of the order of 28-29 mag/arcsec^2, which is close to the typical low-surface-brightness levels expected for these substructures [see e.g., Cooper et al., 2010]. At this point, we built a set of Monte Carlo simulations to which we added the particles of the three simulated streams each time randomly varying their mean velocity using a Gaussian with a 0 kms^{-1} mean, assuming the cD at rest in the cluster center, and with a standard deviation of 300 kms^{-1}, which is similar to the velocity dispersion of the Fornax cluster (see Pota et al. 2018 and Spiniello et al. 2018 for a discussion). We also systematically randomized their positions to recover them in three different ranges of cluster-centric radii, in order to verify a dependence of the recovery rate with the distance (and hence the local particle density). We chose three shells: $R = 5' - 7'$, $R = 7' - 12'$, and $R = 12' - 18'$, while we excluded the region within $5'$. Here, the light is too dominated by the cD and it would be very hard to detect low-surface-brightness structures. We did not place the streams at distances larger than $18'$ in order to be conservative, as in less dense regions the frequency at which the stream is recovered could be overestimated because of a lower background. Furthermore, the stream GalMer 2 was only inserted in the two external shells because this diffuse stream is typical of longer lived passages happening far from the cluster center (see e.g., the tail of the encounter in Fig. 9.1). As for the GalMer systems, we ran COSTA on 10 out of 100 of the Monte Carlo simulations from the reliability run to evaluate the stream-detection performances. The results for the three streams at different radii and their reliability maps are displayed in Fig. 9.12 and listed in Tab. 9.6. The general result is that COSTA is able to recover all streams with a broad number of setup parameters. On average, recovery increases slightly for the GalMer streams at greater distances, mainly because the signal from the particles belonging to the stream is higher with respect to the noise of the hot environment (with lower local density). This does not happen for stream 1, which is smaller and more compact. Specularly, the contaminant fraction decreases

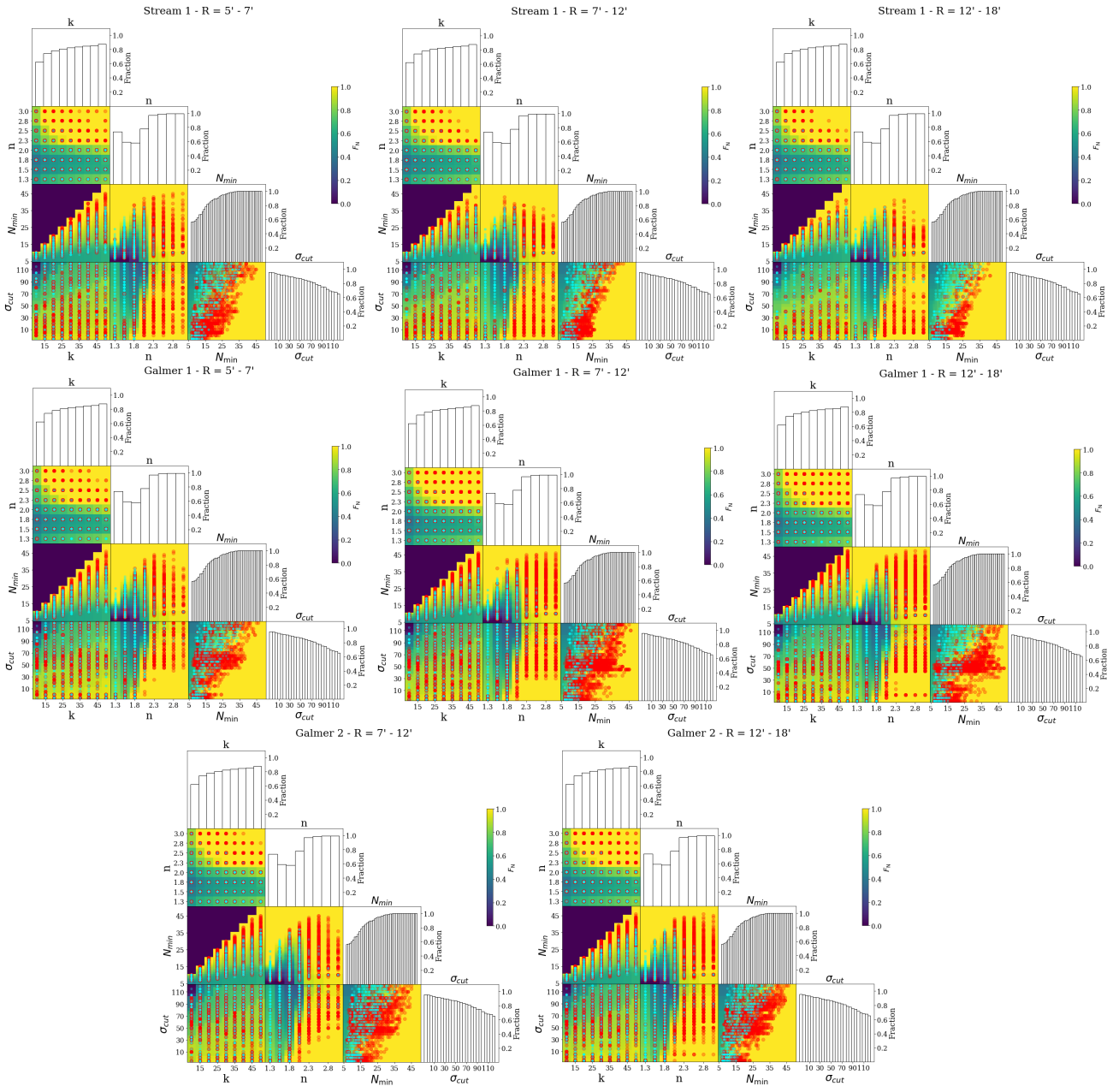

Figure 9.12: Stream (red points) and spurious structures (cyan points) overlapped on Fornax cluster reliability maps in the different shells (left column R = $5' - 7'$; middle columns R = $7' - 12'$; right column R = $12' - 18'$) and for the three different simulated streams (top: stream 1, middle: GalMer 1, and bottom GalMer 2).

Table 9.6: Same as Table 9.2 but in the case of artificial streams in a Fornax-like cluster.

Stream	**f**	**CF**
R = 5' - 7'		
stream 1	0.69 ± 0.07	0.26 ± 0.18
GalMer 1	0.66 ± 0.22	0.24 ± 0.12
R = 7' - 12'		
stream 1	0.69 ± 0.06	0.18 ± 0.15
GalMer 1	0.78 ± 0.09	0.22 ± 0.18
GalMer 2	0.68 ± 0.15	0.20 ± 0.15
R = 12' - 18'		
stream 1	0.60 ± 0.19	0.17 ± 0.15
GalMer 1	0.77 ± 0.08	0.18 ± 0.18
GalMer 2	0.74 ± 0.10	0.15 ± 0.14

with increasing radius, and this is true for all the streams.

9.3.4 Stream kinematics

The only aspect of the algorithm we wish to discuss in more detail at this level is how much (and what kind of) physical information COSTA can provide, besides the stream detection. In fact, despite the detection being important *p*er se, as it provides candidates for follow-up observations (e.g., deep imaging, higher resolution spectroscopy), having predictions about relevant intrinsic properties such as surface brightness, a reliable estimate of the velocity dispersion, and, possibly, the membership of particles, is fundamental to planning such follow-up programs. As introduced in §9.3.3, the estimation of the true kinematics of the stream is equivalent to estimating the real number of true particles belonging to the stream and the fraction of contaminants from the background system as a function of the setups. In principle, one may think that this should depend on the structure of the stream: compact, well-populated, and very cold streams should produce almost no contaminants, while very diffuse warmer streams would more easily be contaminated by particles of the galaxy halo, which have similar velocities to those of the central galaxy. However, as we discuss in §9.3.5, contaminants do not have a huge effect on the estimation of the velocity dispersion of the stream, since by construction COSTA picks up particles with similar velocities. In Fig. 9.13, we show the density plot of the recovered streams in the $N_{\rm min} - \sigma$ di-

agram, which were cleaned using a threshold of $F_{\rm N} = 0.5$ in the $n - N_{\rm min}$ panel, only for the $R = 7' - 12'$ shell, as indicative of the ability to recover the stream kinematics. The results for the other two annuli are similar to those obtained for the central one. We note that, differently from the GalMer simulations, we constructed the streams with a given velocity dispersion, and thus we can check if the real value is recovered. From the figure, it is evident that the setups via which the stream is detected accumulate around the true velocity dispersion of the streams (35 km s^{-1}, 45km s^{-1}, and 62km s^{-1}for stream 1, GalMer 1, and GalMer 2, respectively), indicated by the dashed black line. In particular, the median of the σ_{mea} distribution is found to be 16 $\pm$ 24 km s^{-1}, 52$\pm$ 15 km s^{-1}, 62 $\pm$ 28 km s^{-1}, which is consistent within 1σ uncertainties. We notice that the difference between the median values and the true velocity dispersion values are of the same orders of magnitude as normal measurement errors for mid-resolution spectroscopy. For stream 1, however, the mean value is below the accuracy allowed by the velocity, hence the median value just reveals that the assumed precision does not make it possible to recover the true kinematics, for which a higher velocity accuracy is required. We also estimated the median number of particles recovered for each stream so as to check whether COSTA allows us to infer the total "luminosity" associated with the stream, and we found a median of $N_{\rm recov} = 22, 31, 29$ for stream 1, GalMer 1, and GalMer 2, respectively. These median values are very similar to the true number of particles belonging to the stream (20, 30, 30; see Table 9.5), even if we do not expect that all of these particles truly belong to the stream (see discussion in the next session).

9.3.5 Contaminants and fraction of recovered particles

We evaluate here the fraction of contaminant (`CF`, defined in §9.2.4.2) particles within the different streams as a function of the different parameters. We used the Fornax simulations to decipher how the contamination can change depending on stream compactness (from the compact stream 1, to the very diffuse GalMer 2), internal velocity dispersion, and position within the central potential. We stress that this is a test that one can do only a-posteriori, by placing stream candidates in the Monte Carlo simulations at the right distance and with the right geometry to perform a "contamination run." Nevertheless, this is useful for assessing the realistic contamination of a given stream. Our main goal is to provide a general example of the impact contaminants have on the inference one can derive from COSTA candidates and on the intrinsic properties of the streams. We show in Fig. 9.14 the trend of `CF` as a function of the different setup parameters for every shell of the three streams. We see a clear dependence of the `CF` on $N_{\rm min}$ and on k: thus, the larger $N_{\rm min}$ and k are, the higher the number of contaminants is. This is valid for all the

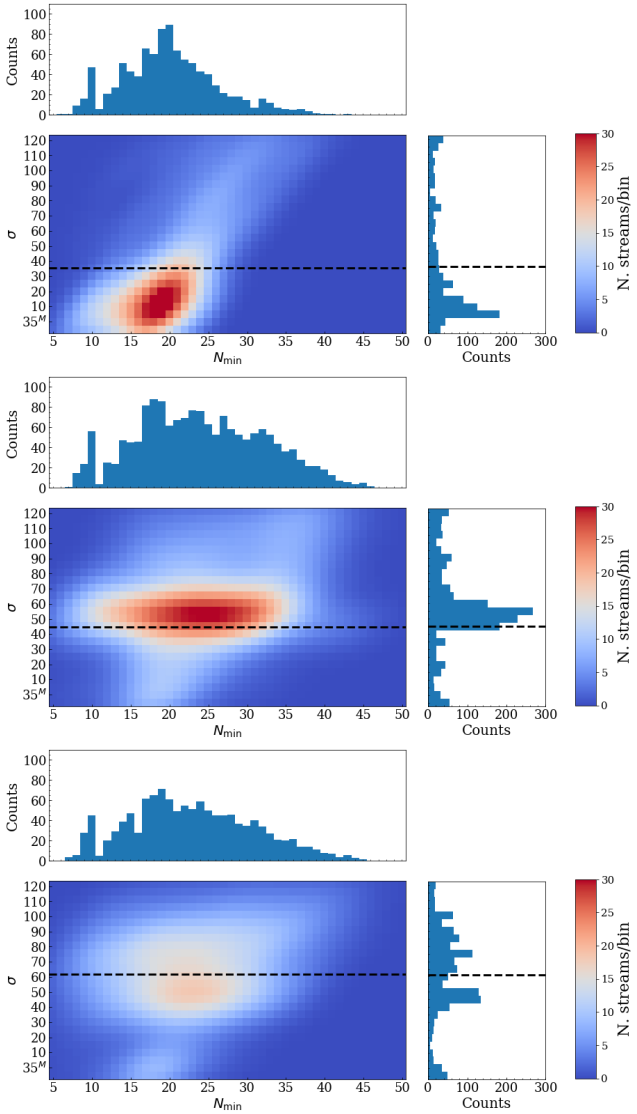

Figure 9.13: Density plot in $N_{\rm min} - \sigma$ diagram, and number counts of the recovered artificial streams for the middle shell (i.e., 7′-12′) for stream 1 (top), GalMer 1 (middle), and GalMer 2 (bottom). The horizontal dashed line shows the true velocity dispersion of each stream. The sample was cleaned by using $F_{\rm N} = 0.5$ as the threshold in the $n - N_{min}$ space. Data were smoothed using a Gaussian kernel with a bandwidth equal to 3.

streams, in all the shells, but the slope of stream 1 is steeper and reaches a larger CF, especially for $N_{\rm min}$. A similar trend is also present for the velocity dispersion cut-off, although it is more noisy and dependent on the shell one considers (more evident at lower radii; for n, instead, the CF is constant around $\texttt{CF} \sim 0.2 - 0.3$). In the worst cases, we see an increase up to 60% for stream 1 and $\sim$ 40% for the two GalMer streams, $\sigma_{\rm cut} > 100$ kms^{-1} , and $N_{\rm min} > 35$. The main reason for the greater contamination is that, while the number of recovered true particles remains almost constant, the larger $\sigma_{\rm cut}$ and $N_{\rm min}$ make COSTA select more particles that have compatible velocities, but that do not belong to the stream. For $k = 50$, the CF reaches the highest level of 50% for the inner radial bin, while it stays below 40% for the outer ones. For any value of n, the CF is always below 40%. In this case, it is also on average lower for the outer bins with respect to the inner one. The number of particles recovered has a strong dependence on the number of k (neighbors), as we can expect, and it also has a small dependence on the value n of the sigma clipping: higher values of n give better results. Completeness and contaminant fractions are very similar in the case of the two GalMer streams, even if they are different sizes. This suggests that COSTA is able to recover even diffuse streams; for example, the recovery frequency is independent of the dimension of the structure. However, we do speculate that it could be harder to detect these kinds of streams in the denser region, where the noise due to the hot component of the cluster increases. It is also instructive to verify the correlation between the number of the recovered particles and the setup parameters. To do that, we define the true completeness (TC) as

$$\texttt{TC} = \frac{\texttt{\# recovered stream particles}}{\texttt{\# true stream particles}},$$

where the true stream particle numbers are given in Table 9.5 for the three simulated streams. The TC is used here to decipher the range of parameter setups that maximize the number of recovered particles compared to the real ones, by contemporary imposing a low CF.

All quantities listed above are not known in observations and depend on the specific dataset and on the distance (i.e., the local particle density). To investigate the effect of distance, we plotted the values of the TC parameter (transparent triangles) and of the OC parameter (full dots), defined in §9.2.4.2, for the three simulated streams in the three different shells. Overall, the TC tends to rise with increasing values of all the setup parameters. This indicates that COSTA recovers more particles by using stronger constraints (i.e., greater numbers of neighbors and particles). However, this also causes a higher number of contaminants, as seen in Fig. 9.14. We also note that the behavior of the TC is more "extreme" in the cases of the GalMer streams (red and green points). We speculate that this may be due to the fact that stream 1 is much more

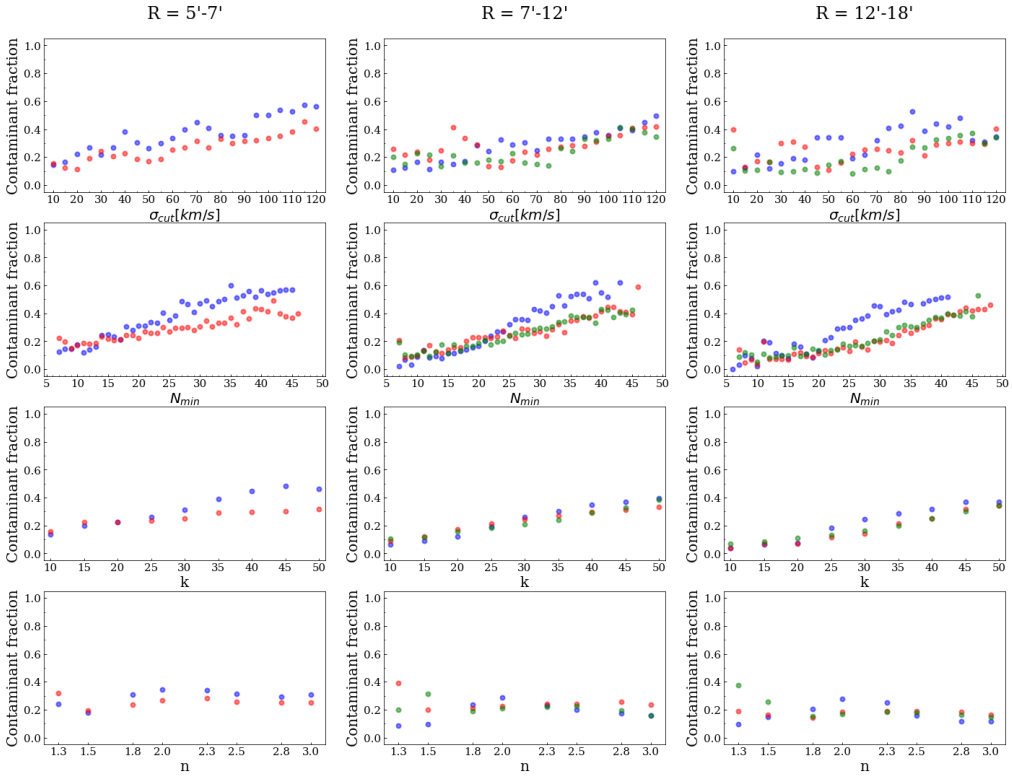

Figure 9.14: Contaminant Fraction as a function of setup parameters for $R = 5' - 7'$ shell (left column), $R = 7' - 12'$ shell (middle column), and $R = 12' - 18'$ shell (right column). Red points are for the GalMer 1 stream, green points for the GalMer 2 stream, and the blue points are for stream 1.

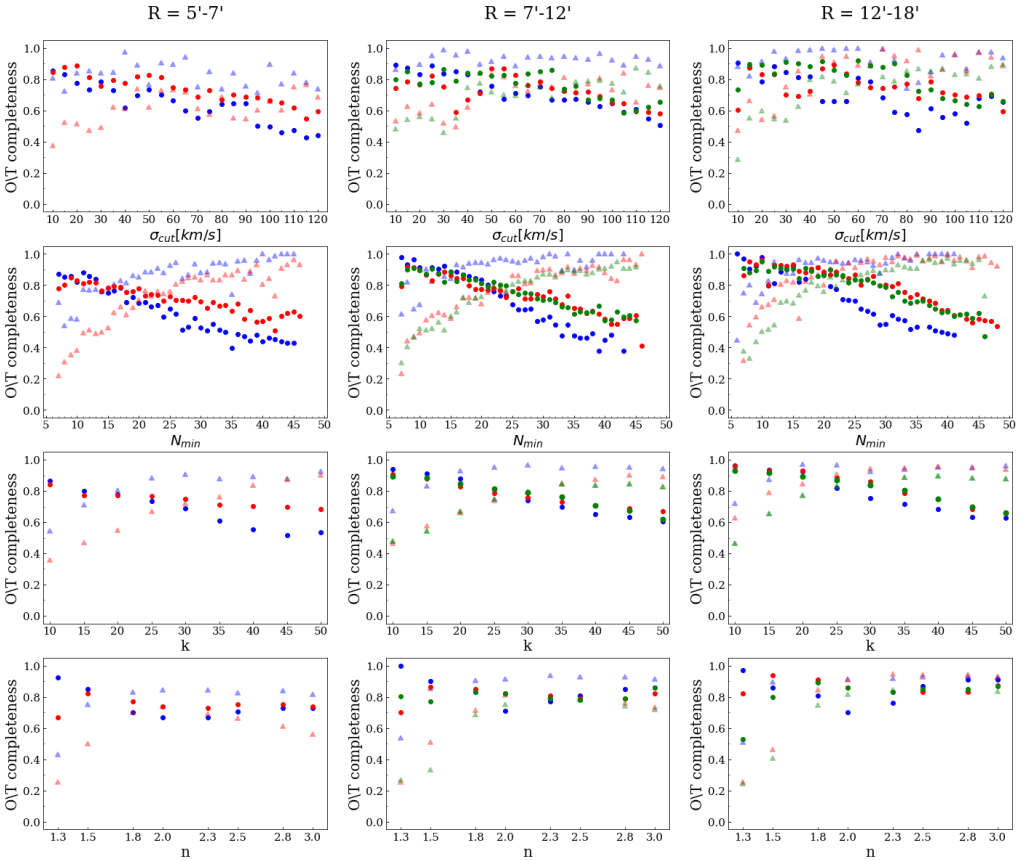

Figure 9.15: Observed completeness (full dots) and true completeness (transparent triangles) as a function of the setup parameters for $R = 5' - 7'$ shell (left column), $R = 7' - 12'$ shell (middle column), and $R = 12' - 18'$ shell (right column). The color-code is the same as in Fig. 9.14: red points for GalMer 1, green points for GalMer 2, and blue points for stream 1.

compact than the other two. The observed completeness (full dots) instead decreases for larger $\sigma_{\rm cut}$, $N_{min,}$ and k while it stays roughly constant all along n values. A compromising rule of thumb we derived when cross-checking Fig. 9.13, Fig. 9.14, and Fig. 9.15 is that if a stream is found with different setups with similar reliability, one should first select the parameters that better reproduce its kinematics: the median of the distributions shown in Fig. 9.13 for $N_{\rm min}$ and $\sigma_{\rm cut}$. Then, one should try to select values for n and k, for which the `OB` and `TC` are similar, while the `CF` is the minimum possible. For the streams simulated here, this region is around the following values: $k \sim 25 - 30$ and $n \geq 1.8$. This should allow for a reasonable level of completeness ($\sim$80%), with a contamination that is $\sim 50\%$ in the worst case (i.e., high $\sigma_{\rm cut}$), or lower than that. It is important to stress, however, that these numbers depend on the system one considers and on the morpho-kinematic characteristics of the streams one aims to recover. Thus, each run of COSTA needs to be properly trained with ad-hoc Monte Carlo simulations before the algorithm can be used with real data. Finally, we checked how accurately COSTA can reconstruct the intrinsic properties of the streams. The presence of contaminants (estimated to be of the order of 20% of the total number of particles for low $\sigma_{\rm cut}$, if the rule of thumb holds) is expected to alter the properties of the recovered stream. In fact, these should have hotter kinematics and be characterized by a higher velocity dispersion. However, to be selected as friend-of-friend particles, they likely have velocities reasonably compatible with the bulk of the stream, so the effect should not be dramatic. From Fig. 9.13, we see that the smaller the cut-off, the smaller the measured stream dispersion; although, if the adopted cut-off is larger than the real stream dispersion, the dispersion estimates tend to saturate around the true dispersion value. This implies that if using a too large a cut-off does not produce a dramatic overestimate of the true velocity dispersion, too small a cut-off might produce an underestimation of the stream's velocity dispersion. Thus, adopting a larger cut-off would be the safest choice. It would give a more realistic estimate of the stream dispersion, but, as discussed before, this is at the cost of a larger fraction of contaminants. Overall, both the number of particles of the stream and the stream velocity dispersion are underestimated by COSTA. These two quantities are the major parameters we want to retrieve for our stream candidates, because they can give information about the amount of dispersed stellar mass per event and the dispersion of the parent dwarf galaxy (and likely its virial mass). However, the optimization of the setup in view of recovering the best estimates is beyond the current goals of the preliminary test carried out in this work, as we are primarily interested in the detection of the streams. In conclusion, for what we have discussed in this section we are confident that COSTA is able to find real streams in our data, if

any.

9.4 Application of COSTA on a real datasets of Fornax discrete kinematical tracers

Once demonstrated the effectiveness of COSTA, here we describe the outcomes of the algorithm on a real sample GCs and PNe retrieved from the Fornax Cluster VLT Spectroscopic Survey (FVSS) in the inner ∼200 kpc of the Fornax cluster. In particular, the dataset is based on the GCs catalog collected by Pota et al. [2018] which counts 1183 GCs and ∼ 1452 PNe collected by Spiniello et al. [2018]. Here we discuss only the main results, reminding to the original paper, Napolitano N.R., Gatto M. et al., A&A, Vol. 657, p.A94 for more details.

COSTA detected 13 stream candidates in total. The positions of the particles composing each stream are plotted in different colors in Fig. 9.16 superposed on the deep $g-$band image of the core of Fornax cluster from FDS. To visualize the stream particles, we choose the closest configuration to the median parameter setup of each stream as representative of the "average stream". In the same figure, we also report dwarf galaxies from the literature [Eigenthaler et al., 2018, Munoz et al., 2015] that are in the vicinity of the streams. These are plotted as orange diamonds or squares (depending whether they have velocity measurements or not, respectively) and their sizes are proportional to the $i-$band total magnitude taken from Cantiello et al. [2020]. From this figure, we see that streams are either very close to some of the detected dwarf galaxies (e.g., FVSS-S1, FVSS-S2, FVSS-S5, FVSS-S7, FVSS-S12) or live in the halo or are associated to larger galaxies in the Fornax core (e.g., FVSS-S3, FVSS-S4, FVSS-S6, FVSS-S8, FVSS-S13). In Fig. 9.17 we show the candidate streams in the phase space of all GCs and PNe in the Fornax core. The locations of the major galaxies in the area are also reported in the same figure. Amongst the 13 candidate streams, we highlight the likely discovery of a giant, still unknown stream connecting NGC 1380, NGC 1381, and NGC 1382, suggesting that this stream might originate from one of these galaxies, and the first independent kinematical confirmation of a stream identified by Iodice et al. [2016] in the deep photometry of the Fornax cluster.

9.5 Conclusion

In this work, we introduced the COld STream finder Algorithm: a new tool used to detect cold kinematic substructures in the outer halos of massive galaxies, as a probe of their recent and past

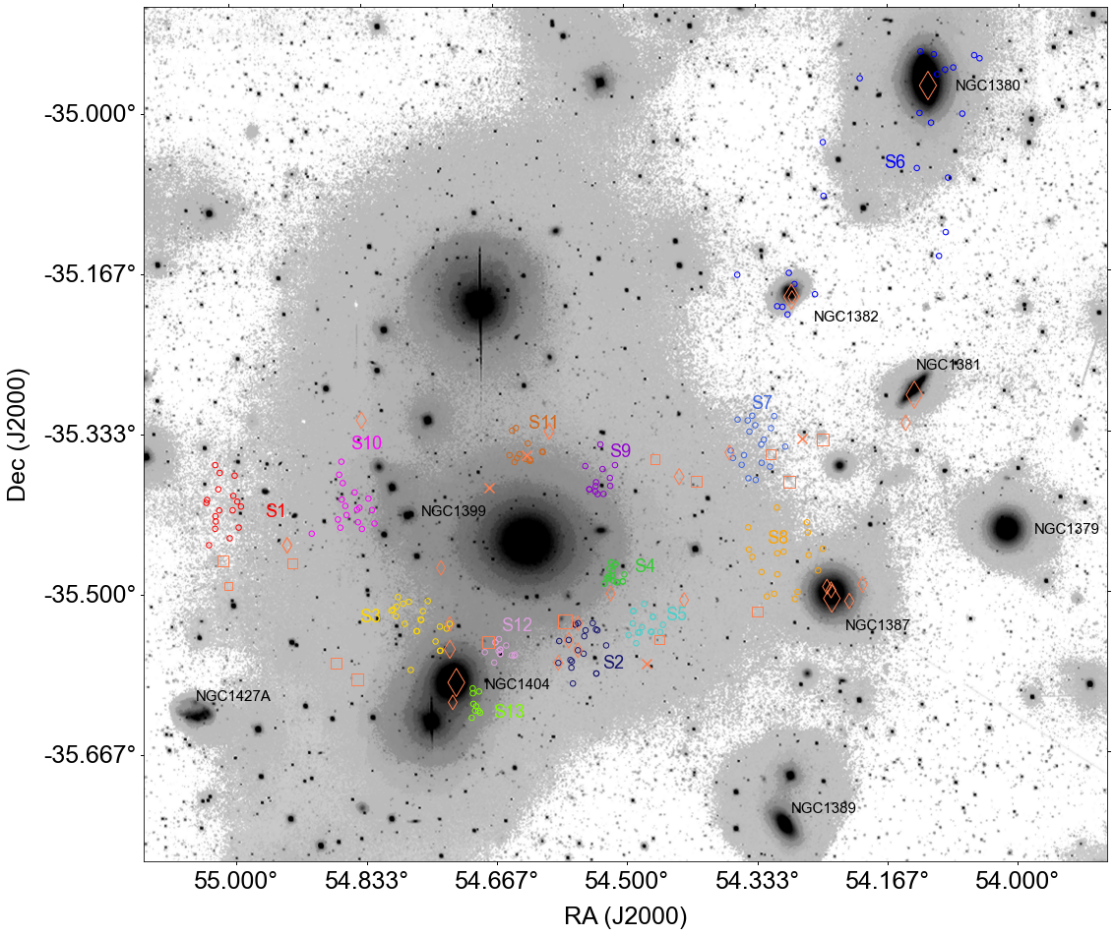

Figure 9.16: Image of the Fornax cluster core region. We show representative particles of each cold substructure found by COSTA in the closest configuration to the median setups; these are colored according to the associated stream. Orange squares and diamonds indicate some galaxies of the Fornax core taken from Munoz et al. [2015] and Eigenthaler et al. [2018], with symbol size proportional to their $i-$band luminosities. Orange crosses represent galaxies with no luminosity measurement.

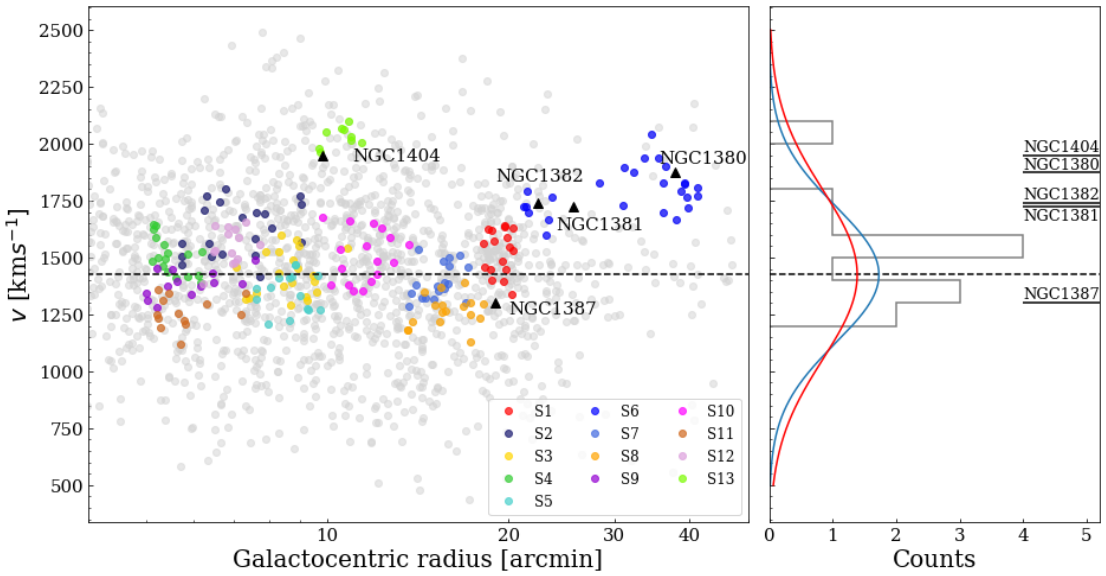

Figure 9.17: *Left:* Particles of each cold substructure in the phase space, with the same colors as in Fig. 9.16, superposed on all particles used in this work (light gray). *Right:* Gaussians with mean = 1425 km s^{-1}, i.e., the NGC 1399 systemic velocity, and standard deviation of 300 km s^{-1} (blue solid lines) and 374 km s^{-1} (red solid lines), namely the velocity dispersion of the Fornax cluster and of the Fornax members analyzed by Drinkwater et al. [2001].

merger history. As all massive galaxies build their halos through minor mergers [e.g., Amorisco, 2019], it is of great value to reveal such tidal debris and infer their intrinsic properties in order to unveil the mechanisms playing a role in the mass assembly history of massive galaxies. Since these structures have very low surface brightnesses, it is incredibly difficult to detect them by means of photometric observations alone. In the last years, thanks to new instrumentation that allowed for more accurate spectroscopy, the research of merger signatures shifted to the exploration of the phase space of kinematical tracers. So far (supported by numerical simulations and analytical models), the detection of streams has been limited to the search for shells and narrow diagonal tracks, which have a chevron-like shape in the position-velocity diagram [e.g., Longobardi et al., 2015, Romanowsky et al., 2012]. Unfortunately, these patterns are not produced by low dispersion streams made of a handful of particles (of the order of a few tens) and originated from dwarf galaxies in a recent encounter with a massive galaxy (see e.g., Fig. 9.4). COSTA allows us to search for these low-surface-brightness streams in the phase space in a systematic way. It also makes it possible to detect cold kinematic substructures moving in a warm/hot environment composed of relaxed particles. COSTA relies on a deep friend-of-friend algorithm that, through an iterative sigma clipping, detaches groups of neighbor particles with cold kinematics (with

velocity dispersions of the order of tens of km s^{-1}). The algorithm has four free parameters that have to be set with Montecarlo simulations, mimicking the real system under examination. The final aim of this work has been the detection of streams with COSTA in simulated systems, and we are fully confident that our algorithm is also able to detect them in real cases. In particular, in this work, we did the following:

- We discussed the ability of COSTA to recover cold substructures in different dynamical conditions, from cold giant spiral galaxies to giant ellipticals living in the core of large clusters of galaxies (§9.2 and §9.3). The general result is that COSTA is able to detect real substructures with a variety of combinations of the four free parameters, and with a limited number of spurious events, if one selects the regions in the parameter space that maximize the reliability of a stream detection and minimize the chance of false positive.

- We showed that the COSTA algorithm can find cold streams embedded in a hotter environment. The efficiency of COSTA in recovery streams heavily depends on the ratio between the velocity dispersion of the stream and that of the host galaxy, favoring cold streams embedded in a hot surrounding. In fact, the performance of COSTA is much worse when the difference between the velocity dispersion of the giant and that of the dwarf intruder is very small (see the case of a gSa-dSa interaction, §9.2.5, versus the case of a gE0-dE0 interaction, §9.2.4, and that of the Fornax core, §9.3). The algorithm also depends somewhat on the number of tracers of the stream (i.e., the mass ratio of the dwarf and the giant galaxy; see §9.3).

- We showed that the difference between the measured and the real velocity dispersion is similar to the uncertainties on velocities, hence the assessment of the stream kinematics would improve if higher spectroscopic resolution is available (section §9.2.4.4).

- We demonstrated that in order to best estimate the reliability of the COSTA setups, we have first to construct a realistic realization in the phase space of the system under analysis. This is not an easy task and it also requires customized Monte Carlo realizations (§9.3). Furthermore, the reliability map one can derive might depend on how accurate the description of the underlying "relaxed" system is with respect to the stream population. However, we note that an over-detailed dynamical description of a given system can also incorporate substructures as a part of the relaxed component, hence reducing the chance of being recognized as a true substructure. We believe that the Monte Carlo approach,

as in §9.3, is a reasonable start, but we cannot exclude that a more sophisticated relaxed model based on N-body codes will be used in the future to refine the predictions on real systems applying COSTA to real data.

- We derived a rule of thumb to unveil the real kinematics of a given stream, and hence to obtain insights on the properties of the parent galaxy from which these particles were stripped. We note, however, that COSTA generally underestimates the true velocity dispersion of the stream (§9.5).

To conclude, we prove here that COSTA is a useful tool in detecting stream candidates that originated from close galaxy encounters in a 3D phase space. It uses the right ascension, declination, and radial velocity of particles as input. Since its ability increases when the stream is considerably colder than the surrounding environment, its natural implementation concerns galaxy clusters in which the high velocity dispersion of the relaxed particles moving in the potential well of the cluster makes it easier to unveil a group of particles coherent both in position and in velocity. Nevertheless, we demonstrate that COSTA is also suitable for other situations, such as galaxy-galaxy encounters; hence, in principle it could be used wherever a sample of kinematic tracers is available.

Chapter 10

Conclusions and future perspectives

In this thesis, I exploited different kinds of data (photometry, proper motions, radial velocities) with the main goal of investigating the evolutionary and interaction history of the Magellanic Clouds. To this aim, I mainly used their vast sample of SC as tracers. Most of the results shown in this thesis are based on the deep and accurate photometry provided by the YMCA and STEP surveys, conducted during the past years with the VST telescope. These surveys secured deep and homogeneous photometry for more than 160 square degrees of the LMC, SMC and their peripheries. The very deep photometry achieved by these surveys allowed us to accurately resolve the MC stars singularly, down to about 1.5-2 mag below the MSTO of the oldest stellar population, which combined with the enormous spatial coverage ensured us to investigate the stellar population within the MCs with unprecedented detail. Finally, these surveys, and in particular YMCA, also targeted the outermost and up-to-date barely explored regions of the MCs, allowing us to probe for the first time the faint magnitudes of the MC outskirts.

While the photometry of the STEP data has been already carried out by other members of the STEP collaboration, the photometry for the 110 squared degrees of the YMCA survey was performed by the writer adopting the DAOPHOT/ALLSTAR [Stetson, 1987, 1992] together with customised procedures to obtain the absolute photometric calibration and to merge the catalogues of the single tiles. The resulting YMCA photometric catalogue, complemented with selected tiles of the STEP survey (in particular those close to the west of the LMC) was at the basis of the works described in Chapter 3, 4, 5 and 6. In the first work (Chapter 3 and 4), published on MNRAS (Gatto et al., MNRAS, Vol.499, p.4114-4139, 2020) we developed an "ad hoc" algorithm that was fine-tuned to detect the diffuse and poorly populated SCs in the

MCs that were missed by the previous shallower photometric surveys. The technique adopted in this thesis to discover new SCs is described in detail in Chapter 3. It is composed by two main steps: 1) the over-density finder algorithm: it builds a density map by means of a KDE algorithm, using the star coordinates as input parameters, and searches local over-densities in the sky. For each over-density the algorithm automatically derives its centre and radius. A suite of Montecarlo simulations was carried out to properly assess the goodness of the algorithm. As a result, we obtain completeness estimates better than 90% in all the cases, being the lowest value (i.e. 90%) achieved in the worst case, e.g. high stellar field densities and poor populated SCs. 2) cleaning of the sample from spurious objects: to this aim, the CMD of each over-density is constructed based on YMCA or STEP photometry. These CMDs were first cleaned from the field star contamination by adopting the cleaning CMD procedure by Piatti and Bica [2012] and then analysed visually with the aid of isochrone to separate true SCs from spurious objects.

As test-bed of the algorithm we ran it on a star catalog constructed on the basis of the photometry of 21 YMCA and 2 STEP tiles in the LMC outskirts (Chapter 4), regions almost unexplored with modern, deep and homogeneous photometry. As a result, we reported the discovery of 85 candidate SCs, among which 78 were unknown before. The age of these SCs was estimated by means of the isochrone fitting procedure, and we identified for the first time a not negligible sub-sample of candidate SCs within the well-known LMC age gap, a period ranging from 4 to 10 Gyrs almost lacking SCs [Da Costa, 1991]. Even though most of our SC candidates would need follow-up photometry to construct deeper CMDs and to confirm them as genuine SCs, the presence of many age gap SC candidates suggests that the age gap might be the product of an observational bias. Indeed, the shallow photometry employed in previous works did not allow them to detect SCs older than 1-1.5 Gyr [Glatt et al., 2010, Nayak et al., 2016, Pietrzyński and Udalski, 2000]. Moreover, previous studies did not investigate the peripheries of the MCs, where the low stellar field background makes it easier to detect old and faint SCs.

In the second study (Chapter 5, Gatto et al. 2022c in preparation) we have extended the search for new SCs on the 56 remaining YMCA tiles in the LMC periphery, covering a total of 79 square degrees in the LMC surrounding. We were thus able to obtain for the first time a very complete and homogeneous sample of SCs inhabiting the LMC outskirts, especially in the East and North-West directions. The final list, which contains only the most reliable candidate SCs, based on their statistical significance, contains 55 objects, 35 of which (60% of the sample) have been new discoveries made in this project. We found that 10 candidate SCs have estimated ages within the age gap, representing, if confirmed, a breakthrough in the understanding of the LMC

past evolution, as it would finally solve the puzzle represented by the age gap feature. Moreover, the age distribution of the SCs displayed a sharp peak at $\sim$ 3 Gyrs, which we suggested being the by-product of a past close encounter between the MCs, which may have enhanced the SC formation activity, in agreement with the increase in the SFR $\sim$ 2-3 Gyr ago observed in the stellar field in many previous articles [Harris and Zaritsky, 2009, Rubele et al., 2012, Weisz et al., 2013], strengthen the hypothesis of a nearby passage, which is also expected from simulations [Besla et al., 2012, Diaz and Bekki, 2012, Pardy et al., 2018, Tepper-García et al., 2019]

The third investigation based on the YMCA data is reported in chapter 6 and is composed by the study of two notable SCs (Gatto et al. 2022b, submitted to the Astrophysical Journal Letters, and Gatto et al. 2022d in preparation). The first SC is the already catalogued SC KMHK 1762. The adoption of the YMCA data allowed us to build a CMD for this SC which is significantly deeper and more accurate than that present in the literature. In addition, the adoption of *Gaia* astrometric observations permitted us to clean accurately the CMD of KMHK 1762, at least for what concerns the bright evolutionary phases. The isochrone fitting procedure, applied to this CMD showed that KMHK 1762 is much older than what was previously estimated, that is about 5.5 Gyr, an age that places this SC in the age gap. Therefore, KMHK 1762 is the third confirmed SC other than ESO121-03 and KMHK 1592 to fall in the age gap. This result suggests that other intermediate-old and poorly populated SCs analysed until now on the basis of too shallow photometry might result older than previously estimated and might therefore fall in the age gap, similarly to KMHK 1762. In turn, this occurrence would further corroborate the hypothesis that the age gap is not a physical feature, but rather an observational bias, as already suggested in Chapter 4 and Chapter 5.

The second remarkable cluster is YMCA-1, discovered via the cluster finder algorithm in one of the YMCA tiles farthest from the LMC centre. We obtained the first CMD of this object on the basis of the YMCA data, which allowed us to reach $g \sim$24 mag but not to detect stars significantly below what we supposed to be MSTO of the cluster. This first CMD allowed us to estimate SC's main parameters, such as distance, age, metallicity, reddening. These data suggested that YMCA-1 was a very peculiar, old, remote SC of the MW halo. This analysis was at the basis of the the paper Gatto et al., RNAAS, Vol.5, p.159, 2021. However, as the YMCA CMD was not deep enough to establish unambiguously the distance of the object, and hence it belonging to the LMC instead of the MW halo, we carried out a photometric follow-up with FORS2@VLT, obtaining a very deep CMD reaching $g \sim 27$ mag. On this basis, we re-estimated YMCA-1 main parameters, and especially the distance, equal to $\sim$55 kpc, hence compatible with the LMC. Our best estimate

for the age and metallicity of YMCA-1 is $t = 11.7^{+1.7}_{-1.3}$ Gyrs and [Fe/H] $\sim -1.12^{+0.21}_{-0.13}$ dex, hence we confirm that it is an old and metal-intermediate SC. We also measured the structural parameters of YMCA-1, finding $r_h = 3.5 \pm 0.3$ pc and $M_V = -0.47 \pm 0.57$ mag. These quantities place YMCA-1 at the border between very faint SCs and UFDs, making it practically the twin of another recently discovered remote and old SCs in the LMC, namely SMASH-1. Both SCs result to have completely different characteristics with respect to the other 15 old LMC GCs, making them very peculiar LMC likely associated stellar systems.Complementary to the YMCA survey, we also took advantage of the stellar catalog obtained by means of the STEP survey, which covers the entire main body of the SMC and the MB, to carry out an unprecedented thoroughly analysis of its SC system. In this work, reported in Chapter 7 and published on MNRAS (Gatto et al., MNRAS, Vol. 507, p.3312-3330, 2021), we derived the SBPs from homogeneous g-band integrated photometry, and then fitted them with EFF and King models, for 170 SMC SCs, aiming at understanding the physical mechanisms behind the dynamical evolution of the SCs. For each SC we provided structural parameters obtained from the SBP fits, such as core and half-light radii, total integrated luminosities, central surface brightness, etc. In addition, we estimated ages and masses for 134 SCs by means of the open source `python` package `ASteCA`. For the first time, we analyzed a sample of SCs spanning a very broad range of masses, from hundreds to 10^5 solar masses, allowing us to probe a wider region of the parameter space. We confirmed, with a much higher statistical significance than previous works, that while young SCs are compact, SCs older than $\log(t) \sim 8.3$ dex show a wide range of r_c values, as some of them undergo an expansion of their inner regions. Although the physical mechanism responsible for this phenomenon is unclear, thanks to our mass-unbiased sample, we suggest that the SC mass is the main parameter driving the inner expansion, as none of the SCs with $\log(M/M_\odot) < 3.5$ dex experienced such an expansion.

Besides analysing the SC system as a proxy of the MCs past evolution, in this thesis a complementary approach was adopted, namely the exploitation of the multi-dimensional data provided by the *Gaia* mission EDR3. Indeed, the availability of homogeneous photometric and astrometric data for all the stars in and around the MCs up to $G \sim 20$ mag, suggested us to try to detect and analyse the tidally streams originated by the manifold gravitational interactions experienced by the MCs and by the LMC in particular. In the work presented in Chapter 8, and submitted to the Astrophysical Journal (Gatto et al., "Discovery of NES, an extended tidal structure in the North-East of the Large Magellanic Cloud", 2022a), we adopted the multi-dimensional data provided by *Gaia* EDR3 (photometry, parallax and proper motions) to probe

the outermost and faint regions of the LMC. After applying a correction for the reddening, we performed a first selection of bona-fide RGB and RC LMC stars based on their position on the CMD build with the *Gaia* EDR3 photometric dataset. We then adopted an unsupervised clustering GMM technique in a six-dimensional parameter space to further filter-out the MW and SMC stellar component from the LMC stellar population, obtaining a pure LMC sample of RGB and RC stars. The spatial distribution of this sample revealed several sub-structures already reported in the literature such as the NTA and other less clear substructures towards the East [e.g., El Youssoufi et al., 2021] (ES) and the South [Belokurov and Erkal, 2019, Mackey et al., 2018], but it also shown for the first time the presence of a previously undetected diffuse tidal structure at its North-East side, extending up to $\sim 20°$ from the LMC centre, that we dubbed the North-East Structure (NES). The NES fills the gap between the outer LMC disk and the other known structures to the North-East of the LMC, namely the ES and the NTA. The existence of the NES was expected based on N-body simulations of a MW-LMC interaction [Belokurov and Erkal, 2019, Cullinane et al., 2022] as a consequence of the tidal stresses induced by the MW on the LMC. Hence, our work provides empirical confirmation of theoretical predictions. The availability of *Gaia* EDR3 PMs, allowed us to study the kinematics of the system. We find that the North-East side of the LMC displays radial velocities not consistent with a disc in equilibrium, indicating that the outer LMC disc has been strongly disturbed in the past few Gyrs.Furthermore, the NTA and NES seems to possess a similar velocity pattern, constituted by strong velocity gradients, and they also appear dynamically colder than the adjacent edge of the LMC disc or than other tidal structures which are very hot.

The last Chapter of this thesis (Chapter 9), published on A&A (Gatto et al., A&A, Vol.644, p.A134, 2020), was devoted to the development of new techniques for the detection of signatures of past merger events in distant systems, far enough that the stars are not resolved singularly any longer. In this context, we developed the COld STream finder Algorithm (COSTA), a new algorithm that search in a reduced 3D phase space (projected positions and radial velocities) cold kinematic substructures that are candidate debris of recent or past interaction between the main galaxy and the ensemble of dwarf galaxy satellites surrounding it. In this work we demonstrated that COSTA is able to reveal streams made of tens particles, even beyond the Local Group, allowing us to detect the remnants of galaxy interactions below the detection limits imposed by the photometry. As test-bed for the COSTA algorithm, we applied it to the Fornax cluster, one of the nearby galaxy clusters, whose high-density environment makes the number of galaxy encounters reach its maximum and whose photometric deep data have already demonstrated

that the mass assembly within the core of the cluster is still ongoing [e.g., D'Abrusco et al., 2016, Iodice et al., 2016].

As result, we identified 13 cold kinematic substructures candidates of past remnants originated by close encounters between dwarf or main galaxies with the BCG. Among them, we underline the detection for the first time of a very extended stream likely produced by the interaction of two giant early-type galaxies with the BCG and the confirmation of the kinematic signature of a stream already discovered on the basis of deep photometry of the Fornax cluster.

10.1 Future perspectives

The results presented in this thesis open a wide range of future projects that can be carried out in the next years and promise to shed light on different aspects of the MCs evolutionary history and, more generally, about the evolution of the galaxies in ongoing interaction.

The first subject which deserves further investigation is whether or not the age gap among the LMC SC is a real feature or an observational bias, as we have extensively discussed in this thesis. The definitive solution to this debated question would have important consequences for our understanding of the LMC past evolution. In this context, a final answer can only be achieved through deep photometric follow-up of the age gap cluster candidates presented in Chapter 4 and Chapter 5 by means of instruments such as 8m class telescopes placed at the Southern hemisphere. We have already presented several observational proposals in this direction at the ESO@VLT and will extend the request for observational time to other international facilities. An alternative is represented by the future advent of the Rubin-LSST instrument, whose observations promise to satisfy all our needs both in terms of the deepness of the photometry and precision PMs, allowing us to determine deep and clean CMDs for all known and candidate SCs in the MCs. I am personally involved in Rubin-LSST and at present, I am a data holder in the context of the Italian participation in the Rubin-LSST project. Similar to the previous point, our experience with the KMHK 1762 SC shows that a follow-up with deep photometry is needed also for other LMC SCs formerly classified as intermediate-age based on shallow photometry. This is especially true for the poorly populated SCs in which the identification of the MSTO is hampered by the scarcity of stars.

The discovery of YMCA-1 also brought up new questions that we aim to answer with a spectroscopic follow-up. Indeed, a measurement of the radial velocity of YMCA-1 (and SMASH-1) is crucial to finally assess the membership to the LMC or to the MW halo of one or both

of these systems. In addition, the determination of their chemical abundance would help in establishing if both YMCA-1 and/or SMASH-1 have an in-situ origin or have been accreted by the LMC together with a parent dwarf galaxy, now completely dissolved (see the work made by Mucciarelli et al. 2021 about NGC 2005). To this aim, we plan to submit a proposal to obtain medium-resolution spectroscopy of the brightest stars of both YMCA-1 and SMASH-1 with XSHOOTER@VLT.

The results presented in Chapter 7 demonstrated that the dynamical evolution of a SC is strongly mass-dependent and therefore we still do not have a clear picture of the main physical processes that shape the observables for SC with $M \leq 10^3 M_{\odot}$. Indeed, the current N-body simulations allow us to get insights about the inner evolution of massive SCs (i.e. $M \geq 10^4 M_{\odot}$), but are not suitable to investigate the inner properties of SCs with masses of the order of hundreds or a few thousands of solar masses such as that we investigated in Chapter 7 of this thesis. It is therefore necessary to construct improved models in order to probe even SCs with hundreds of solar masses and in turn finally obtain an exhaustive perspective about the inner dynamical evolution of less massive SCs.

The discovery of the NES to the North-East side of the LMC, carried out during this thesis, also requests spectroscopic follow-up to better constrain its kinematics. Indeed, radial velocity estimates through spectroscopic measurements of the stars associated with the NES are necessary to obtain the three-dimension velocity vector in that region and finally discern if it shares the same origin of the other Eastern substructures, like the NTA or the ES. A complete census and kinematics assessment of the complex substructures unveiled in the LMC periphery is crucial to compare the observations with the numerical models that aim at reconstructing the orbital pattern of the SMC around the LMC and more generally of the MCs in their first infall to the MW. More valuable, it could also better constrain the still fair uncertain LMC and MW masses, to understand the morphological evolution of the LMC because of the tidal forces induced by the MW and to evaluate the response of the Galaxy to the LMC infall. A great help in this context will be given during the next years by the advent of spectroscopic surveys of the MCs such as the ESO public surveys which will be carried out with the 4MOST@VISTA instrument. In particular, the "One Thousand and One Magellanic Fields (1001MC)" survey [Cioni et al., 2019] will target the MCs up to large radii from the galaxies centres and will therefore provide invaluable information in the context of LMC external structure formation and evolution.

The algorithm presented in Chapter 3 can be easily re-calibrated for the research of any over-density stellar system in the MW neighborhood, provided that a catalog relying on deep

photometry is available. For example, it could be adapted for the research of faint dwarf galaxy satellites of the MW and/or the LMC, of low-luminous GCs located in the outermost regions of the MW halo, or to proceed in the extensive research of small old LMC GCs similar to YMCA-1. Again, the obvious field of application of this algorithm is the deep photometric catalogue that will be released by the Rubin-LSST telescope.

Finally, when the cluster-finder algorithm becomes unfeasible because of the large distances of the systems involved, it can be relieved by the COSTA algorithm, as potentially it can be applied up to distances where a reliable radial velocity through spectroscopic measurements of some kinematic tracers can be attained (about 50 Mpc).

Acknowledgements

Dedicato a tutte le persone che mi hanno aiutato o mi sono state vicine in questi tre anni di percorso. Sono sempre stato una persona che difficilmente ha saputo esternare le proprie emozioni, ma cercherò di mettere da parte la mia timidezza in queste poche righe. Il primo pensiero va al mio supervisor Vincenzo che mi ha guidato e sostenuto in questo lungo cammino, non senza una buona dose di affetto. Ha reso il mio lavoro una passione, e i miei risultati li condivido con piacere con lui che mi ha guardato le spalle per tutti e tre gli anni. Insieme abbiamo osservato il cielo stellato ad occhi nudi in Cile, il sogno di tutti gli astronomi. Porterò sempre con me i suoi insegnamenti. Al Prof. Giuseppe Longo il merito di avermi sempre suggerito la strada giusta, dai tempi della magistrale fino alla fine del dottorato. Con Nicola abbiamo condiviso un intenso pezzetto di questo percorso: è grazie a lui la mia esperienza in Cina che rimarrà indimenticabile. A Marcella, un grazie di cuore per credere sempre nei giovani e aver dato anche a me un'opporutnità. Con Silvio, Roberto e Crescenzo abbiamo condiviso i momenti spensierati di questo percorso, il cui unico credo era la "pistacchina". L'edificio Coppola è stata la mia seconda casa in questi tre anni, e gli abitanti la mi seconda famiglia. Un sentito grazie ai due Referee, Prof.sa Eva Grebel e Dr. Enzo Brocato, che hanno dedicato il loro tempo al mio lavoro. Infine, ringrazio la mia famiglia che mi ha sempre supportato in tutte le mie scelte, fin da quando a 7 anni, nel lontano luglio del '94 avevo mostrato l'intenzione di intrapendere questo percorso dopo una serata di divulgazione tenutasi proprio all'osservatorio di Capodimonte per l'evento speciale della caduta della cometa Schomaker-Levy nell'atmosfera di Giove. Di questa famiglia fa ormai parte anche Rossella, la mia compagna di vita e la mia migliore amica, senza la quale probabilmente sarebbe stato molto più difficle raggiungere gli obiettivi che mi ero preposto. La sua vicininza nei periodi più stressanti e difficili è sempre stata la vera spinta che mi ha garantito il massimo impegno nel lavoro, nella vita e in qualsiasi attività quotidiana.

Appendix A

Supplementary material of the 85 LMC SCs presented in Chapter 4

A.1 Cleaned Colour-magnitude diagrams

Figure A.1 displays the same figure described in Fig.4.2 for the 85 candidate SCs.

A.2 Radial density profiles

Figures A.2 and A.3 show the RDPs with overlapped the EFF profile build by using only stars with $P \geq 75\%$ or $P \geq 50\%$, respectively, as described in 4.2.3.

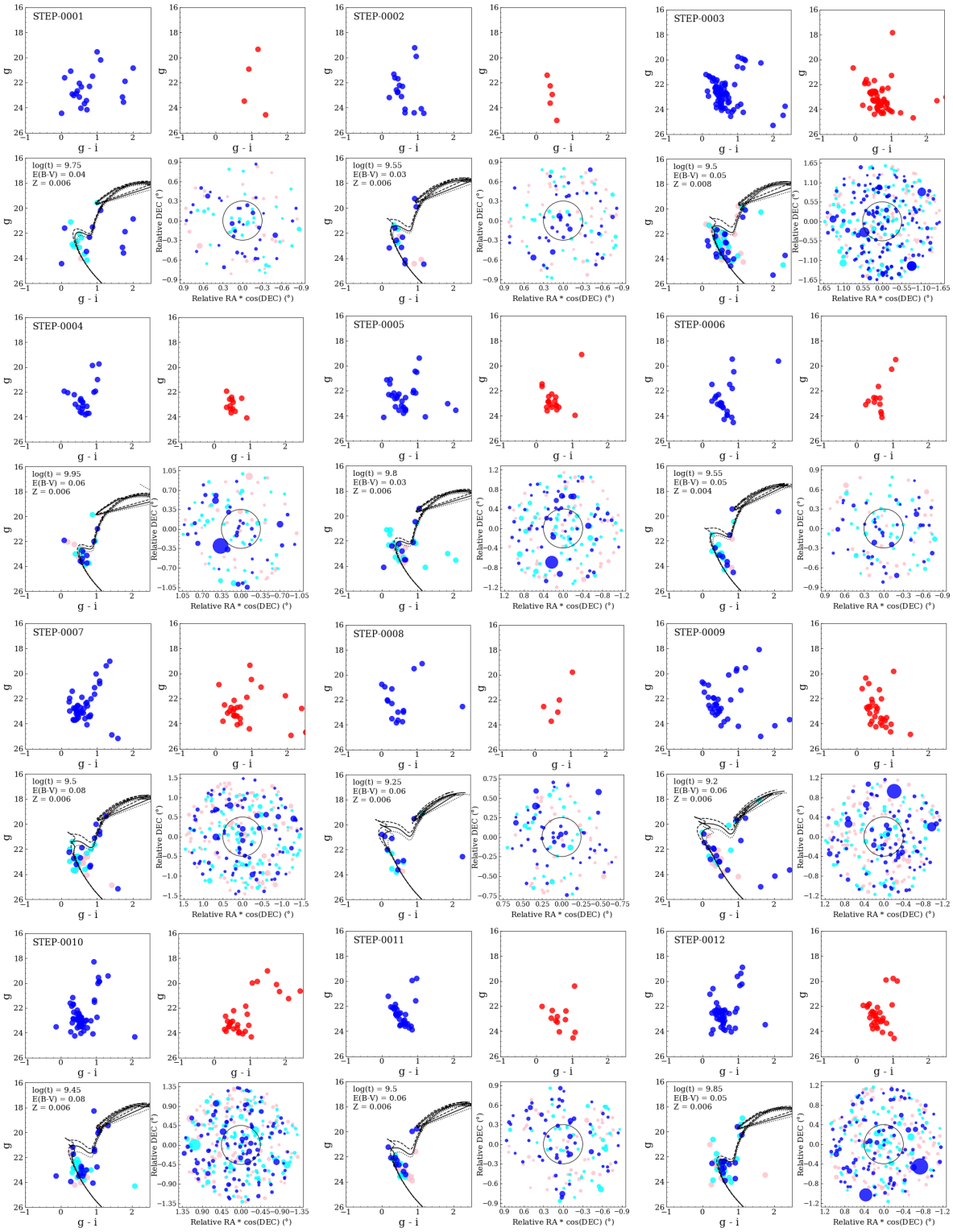

Figure A.1: Cleaning procedure for the 85 candidate SCs detected in this work (see Fig. 4.2 for the explanation of each figure). The stars are colored according to their probability to belong to the cluster. Blue points are stars with $P \geq 75\%$, cyan points have P = 50% while pink points indicate stars with $P \leq 25\%$. The solid line shows the best fitting isochrone, whereas dashed and dotted lines are the isochrones shifted by $\log(t) = \pm 0.1$ dex, respectively.

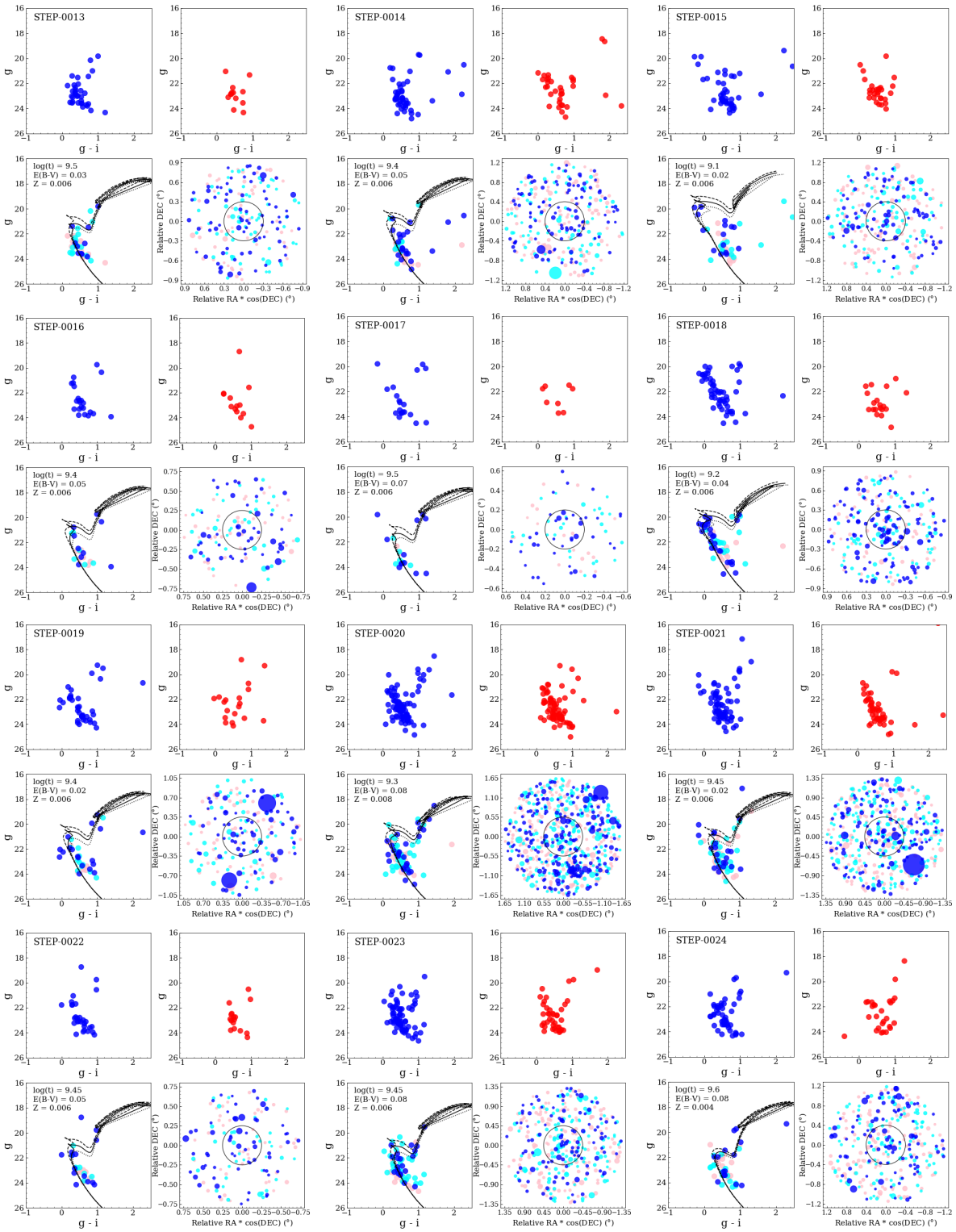
STEP-0013
log(t) = 9.5
E(B-V) = 0.03
Z = 0.006
STEP-0014
log(t) = 9.4
E(B-V) = 0.05
Z = 0.006
STEP-0015
log(t) = 9.1
E(B-V) = 0.02
Z = 0.006
STEP-0016
log(t) = 9.4
E(B-V) = 0.05
Z = 0.006
STEP-0017
log(t) = 9.5
E(B-V) = 0.07
Z = 0.006
STEP-0018
log(t) = 9.2
E(B-V) = 0.04
Z = 0.006
STEP-0019
log(t) = 9.4
E(B-V) = 0.02
Z = 0.006
STEP-0020
log(t) = 9.3
E(B-V) = 0.08
Z = 0.008
STEP-0021
log(t) = 9.45
E(B-V) = 0.02
Z = 0.006
STEP-0022
log(t) = 9.45
E(B-V) = 0.05
Z = 0.006
STEP-0023
log(t) = 9.45
E(B-V) = 0.08
Z = 0.006
STEP-0024
log(t) = 9.6
E(B-V) = 0.08
Z = 0.004
g - i
g
Relative DEC (°)
Relative RA * cos(DEC) (°)

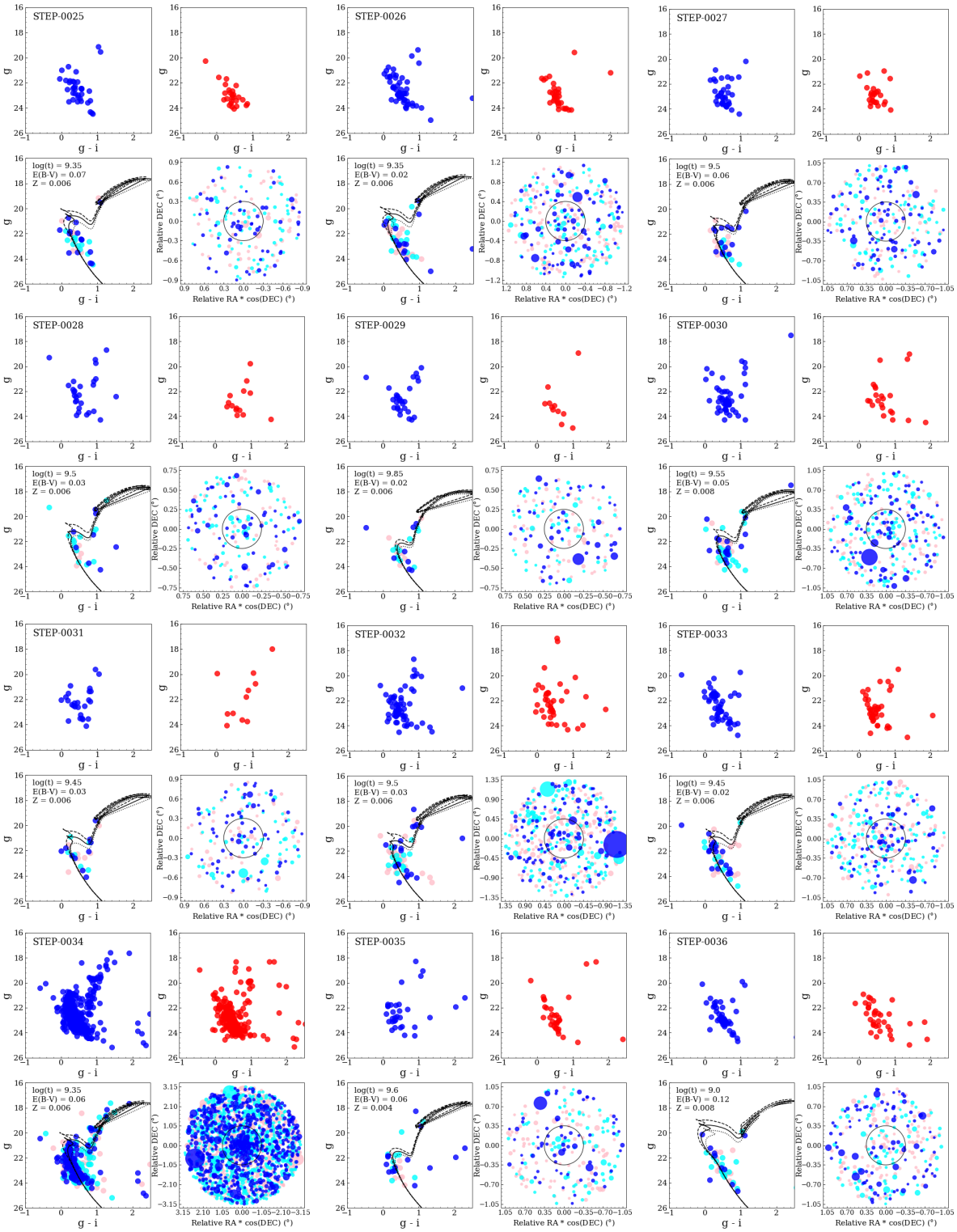
STEP-0025
log(t) = 9.35
E(B-V) = 0.07
Z = 0.006
STEP-0026
log(t) = 9.35
E(B-V) = 0.02
Z = 0.006
STEP-0027
log(t) = 9.5
E(B-V) = 0.06
Z = 0.006
STEP-0028
log(t) = 9.5
E(B-V) = 0.03
Z = 0.006
STEP-0029
log(t) = 9.85
E(B-V) = 0.02
Z = 0.006
STEP-0030
log(t) = 9.55
E(B-V) = 0.05
Z = 0.008
STEP-0031
log(t) = 9.45
E(B-V) = 0.03
Z = 0.006
STEP-0032
log(t) = 9.5
E(B-V) = 0.03
Z = 0.006
STEP-0033
log(t) = 9.45
E(B-V) = 0.02
Z = 0.006
STEP-0034
log(t) = 9.35
E(B-V) = 0.06
Z = 0.006
STEP-0035
log(t) = 9.6
E(B-V) = 0.06
Z = 0.004
STEP-0036
log(t) = 9.0
E(B-V) = 0.12
Z = 0.008
g - i
g
Relative RA * cos(DEC) (°)
Relative DEC (°)

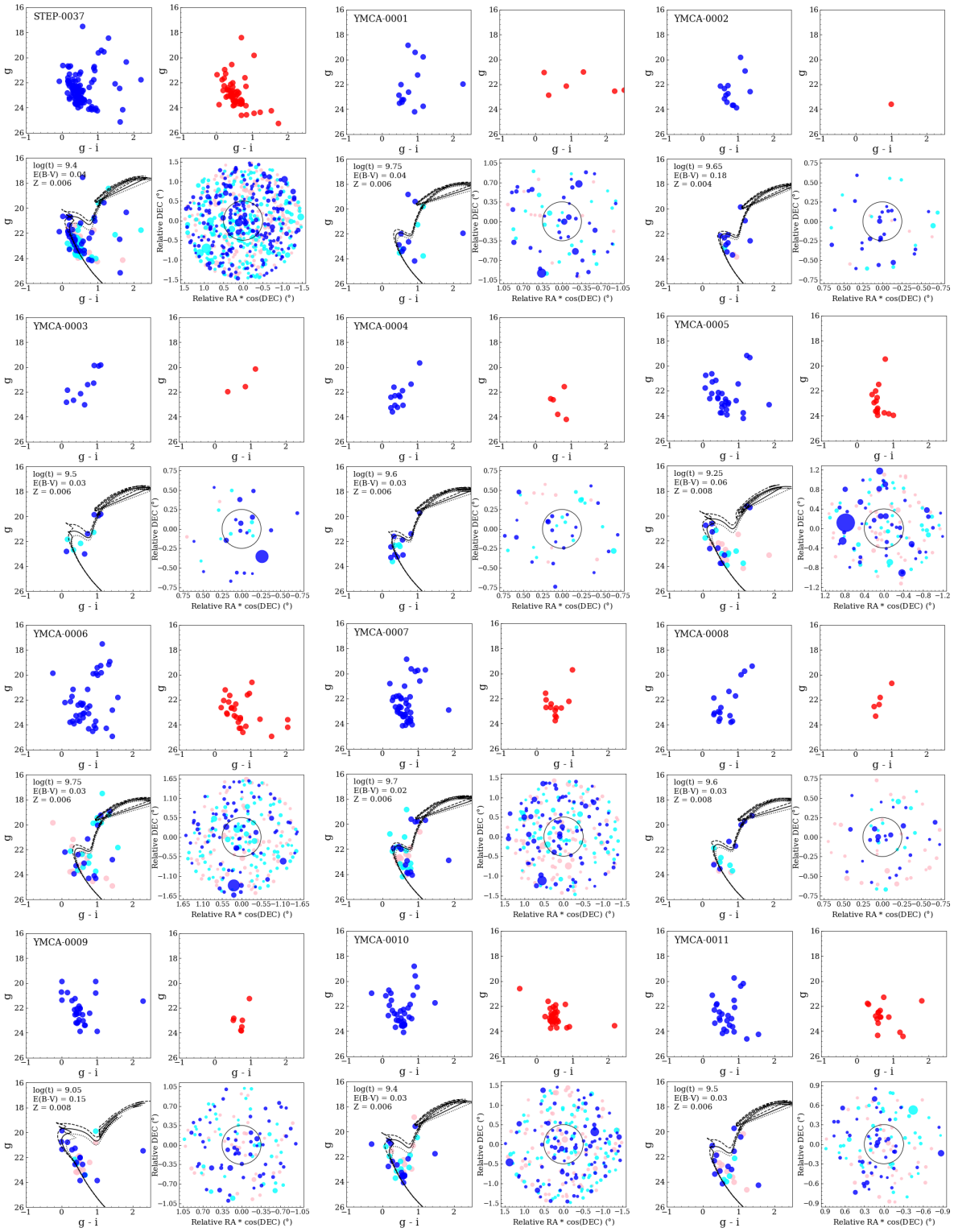
STEP-0037
YMCA-0001
YMCA-0002
log(t) = 9.4
E(B-V) = 0.04
Z = 0.006
log(t) = 9.75
E(B-V) = 0.04
Z = 0.006
log(t) = 9.65
E(B-V) = 0.18
Z = 0.004
YMCA-0003
YMCA-0004
YMCA-0005
log(t) = 9.5
E(B-V) = 0.03
Z = 0.006
log(t) = 9.6
E(B-V) = 0.03
Z = 0.006
log(t) = 9.25
E(B-V) = 0.06
Z = 0.008
YMCA-0006
YMCA-0007
YMCA-0008
log(t) = 9.75
E(B-V) = 0.03
Z = 0.006
log(t) = 9.7
E(B-V) = 0.02
Z = 0.006
log(t) = 9.6
E(B-V) = 0.03
Z = 0.008
YMCA-0009
YMCA-0010
YMCA-0011
log(t) = 9.05
E(B-V) = 0.15
Z = 0.008
log(t) = 9.4
E(B-V) = 0.03
Z = 0.006
log(t) = 9.5
E(B-V) = 0.03
Z = 0.006
g - i
g
Relative DEC (°)
Relative RA * cos(DEC) (°)

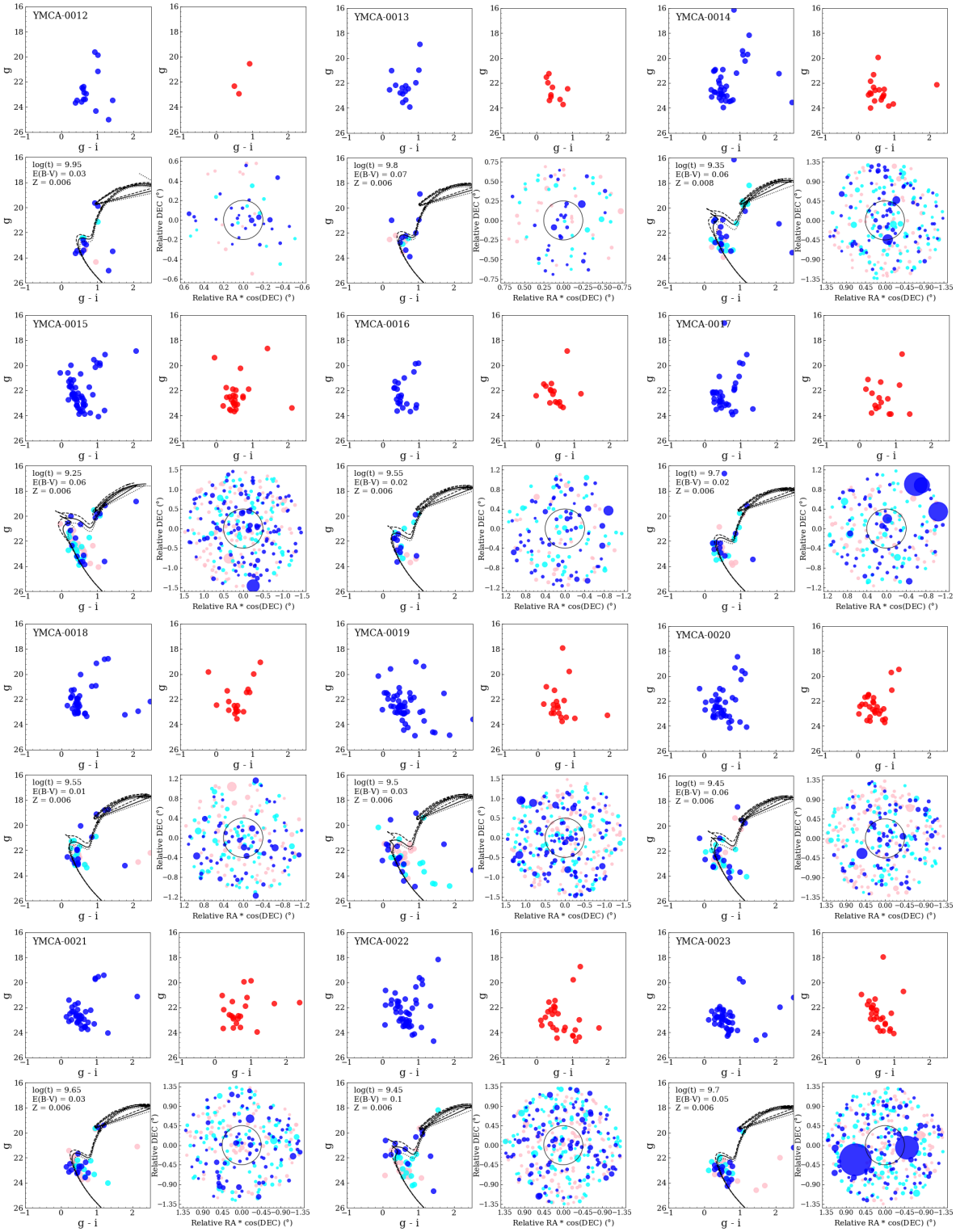
YMCA-0012
log(t) = 9.95
E(B-V) = 0.03
Z = 0.006
YMCA-0013
log(t) = 9.8
E(B-V) = 0.07
Z = 0.006
YMCA-0014
log(t) = 9.35
E(B-V) = 0.06
Z = 0.008
YMCA-0015
log(t) = 9.25
E(B-V) = 0.06
Z = 0.006
YMCA-0016
log(t) = 9.55
E(B-V) = 0.02
Z = 0.006
YMCA-0017
log(t) = 9.7
E(B-V) = 0.02
Z = 0.006
YMCA-0018
log(t) = 9.55
E(B-V) = 0.01
Z = 0.006
YMCA-0019
log(t) = 9.5
E(B-V) = 0.03
Z = 0.006
YMCA-0020
log(t) = 9.45
E(B-V) = 0.06
Z = 0.006
YMCA-0021
log(t) = 9.65
E(B-V) = 0.03
Z = 0.006
YMCA-0022
log(t) = 9.45
E(B-V) = 0.1
Z = 0.006
YMCA-0023
log(t) = 9.7
E(B-V) = 0.05
Z = 0.006
g - i
g
Relative DEC (°)
Relative RA * cos(DEC) (°)

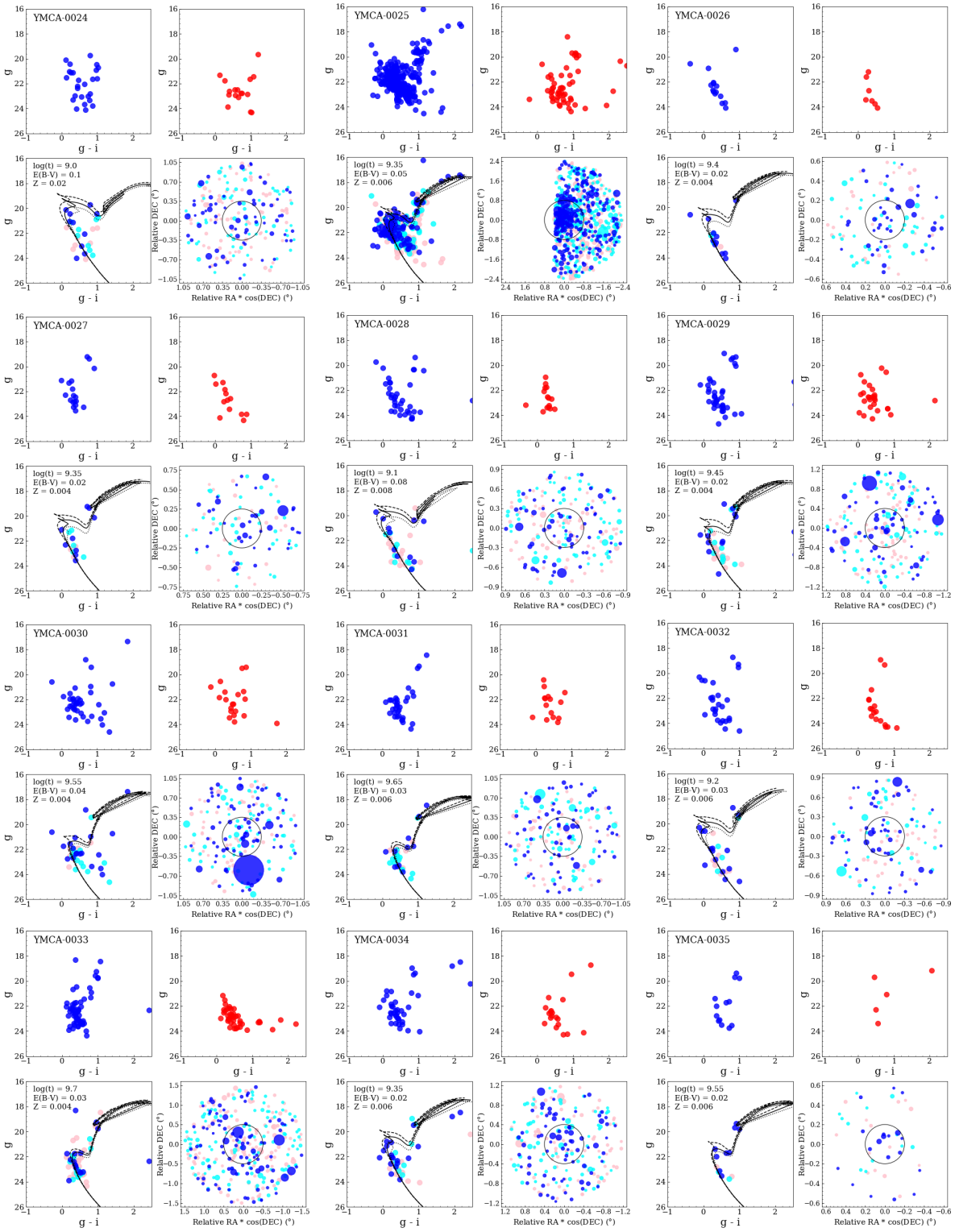
YMCA-0024
YMCA-0025
YMCA-0026
log(t) = 9.0
E(B-V) = 0.1
Z = 0.02
log(t) = 9.35
E(B-V) = 0.05
Z = 0.006
log(t) = 9.4
E(B-V) = 0.02
Z = 0.004
YMCA-0027
YMCA-0028
YMCA-0029
log(t) = 9.35
E(B-V) = 0.02
Z = 0.004
log(t) = 9.1
E(B-V) = 0.08
Z = 0.008
log(t) = 9.45
E(B-V) = 0.02
Z = 0.004
YMCA-0030
YMCA-0031
YMCA-0032
log(t) = 9.55
E(B-V) = 0.04
Z = 0.004
log(t) = 9.65
E(B-V) = 0.03
Z = 0.006
log(t) = 9.2
E(B-V) = 0.03
Z = 0.006
YMCA-0033
YMCA-0034
YMCA-0035
log(t) = 9.7
E(B-V) = 0.03
Z = 0.004
log(t) = 9.35
E(B-V) = 0.02
Z = 0.006
log(t) = 9.55
E(B-V) = 0.02
Z = 0.006
g - i
g
Relative DEC (°)
Relative RA * cos(DEC) (°)

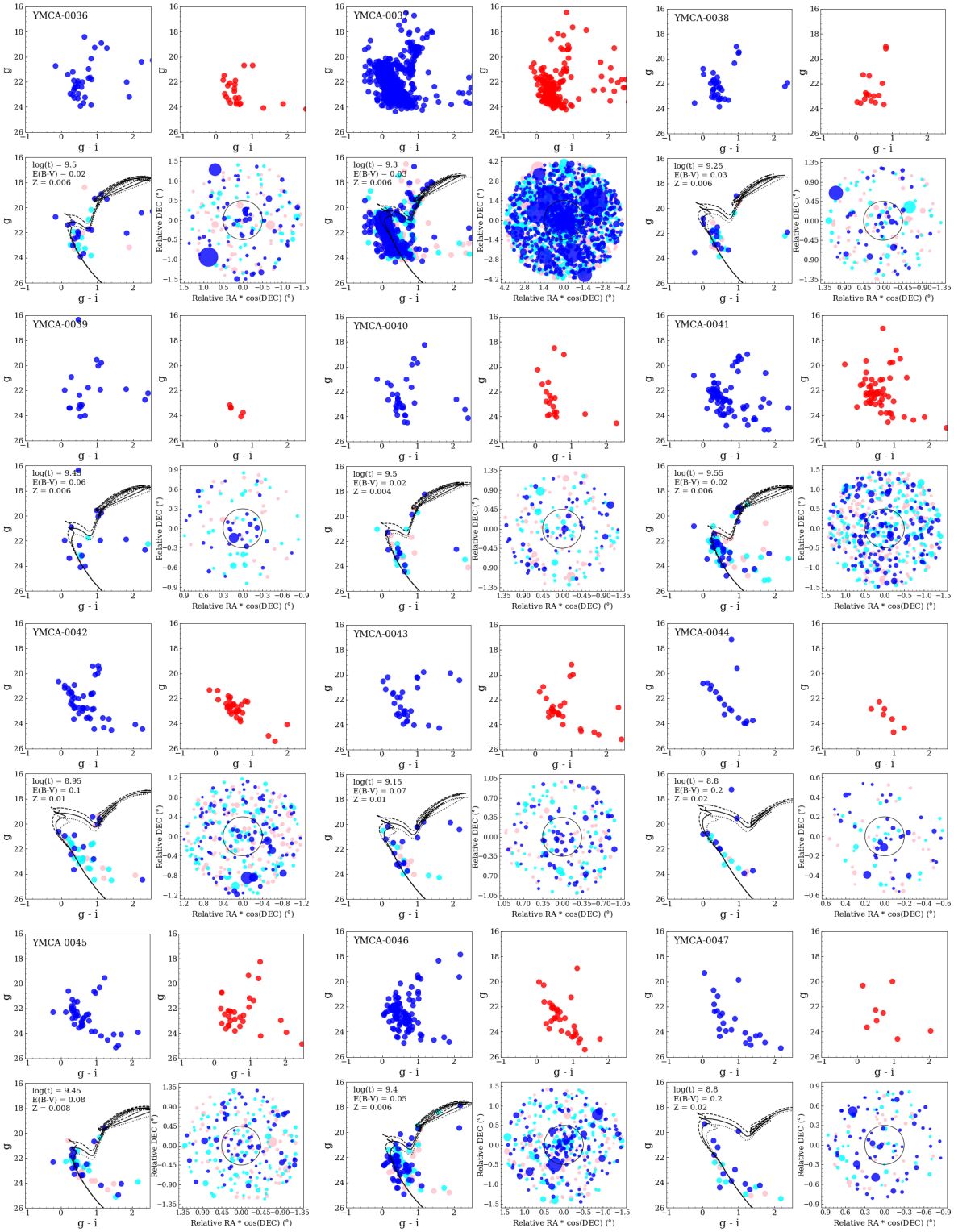
YMCA-0036
log(t) = 9.5
E(B-V) = 0.02
Z = 0.006
YMCA-0037
log(t) = 9.3
E(B-V) = 0.03
Z = 0.006
YMCA-0038
log(t) = 9.25
E(B-V) = 0.03
Z = 0.006
YMCA-0039
log(t) = 9.45
E(B-V) = 0.06
Z = 0.006
YMCA-0040
log(t) = 9.5
E(B-V) = 0.02
Z = 0.004
YMCA-0041
log(t) = 9.55
E(B-V) = 0.02
Z = 0.006
YMCA-0042
log(t) = 8.95
E(B-V) = 0.1
Z = 0.01
YMCA-0043
log(t) = 9.15
E(B-V) = 0.07
Z = 0.01
YMCA-0044
log(t) = 8.8
E(B-V) = 0.2
Z = 0.02
YMCA-0045
log(t) = 9.45
E(B-V) = 0.08
Z = 0.008
YMCA-0046
log(t) = 9.4
E(B-V) = 0.05
Z = 0.006
YMCA-0047
log(t) = 8.8
E(B-V) = 0.2
Z = 0.02
g
g - i
Relative DEC (°)
Relative RA * cos(DEC) (°)

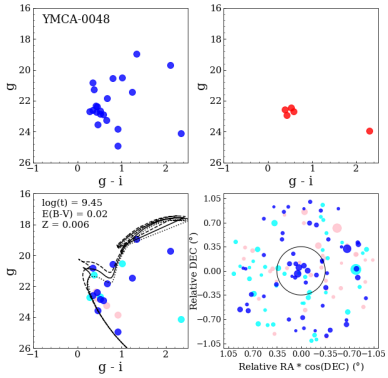
YMCA-0048
log(t) = 9.45
E(B-V) = 0.02
Z = 0.006
g
g - i
Relative DEC (°)
Relative RA * cos(DEC) (°)

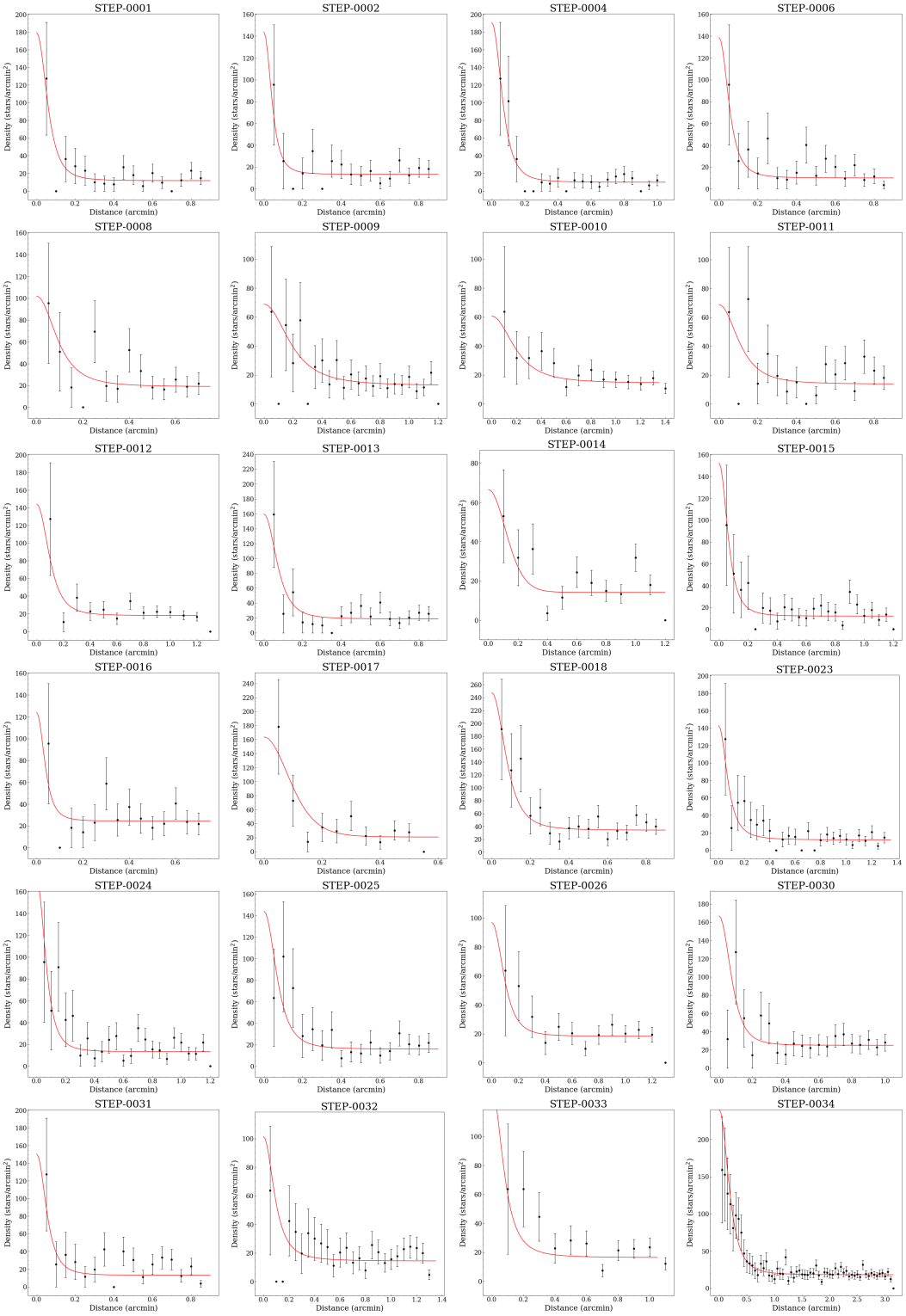

Figure A.2: RDP obtained using only stars with P $\geq$75%. The red line represents the best fit with an EFF profile.

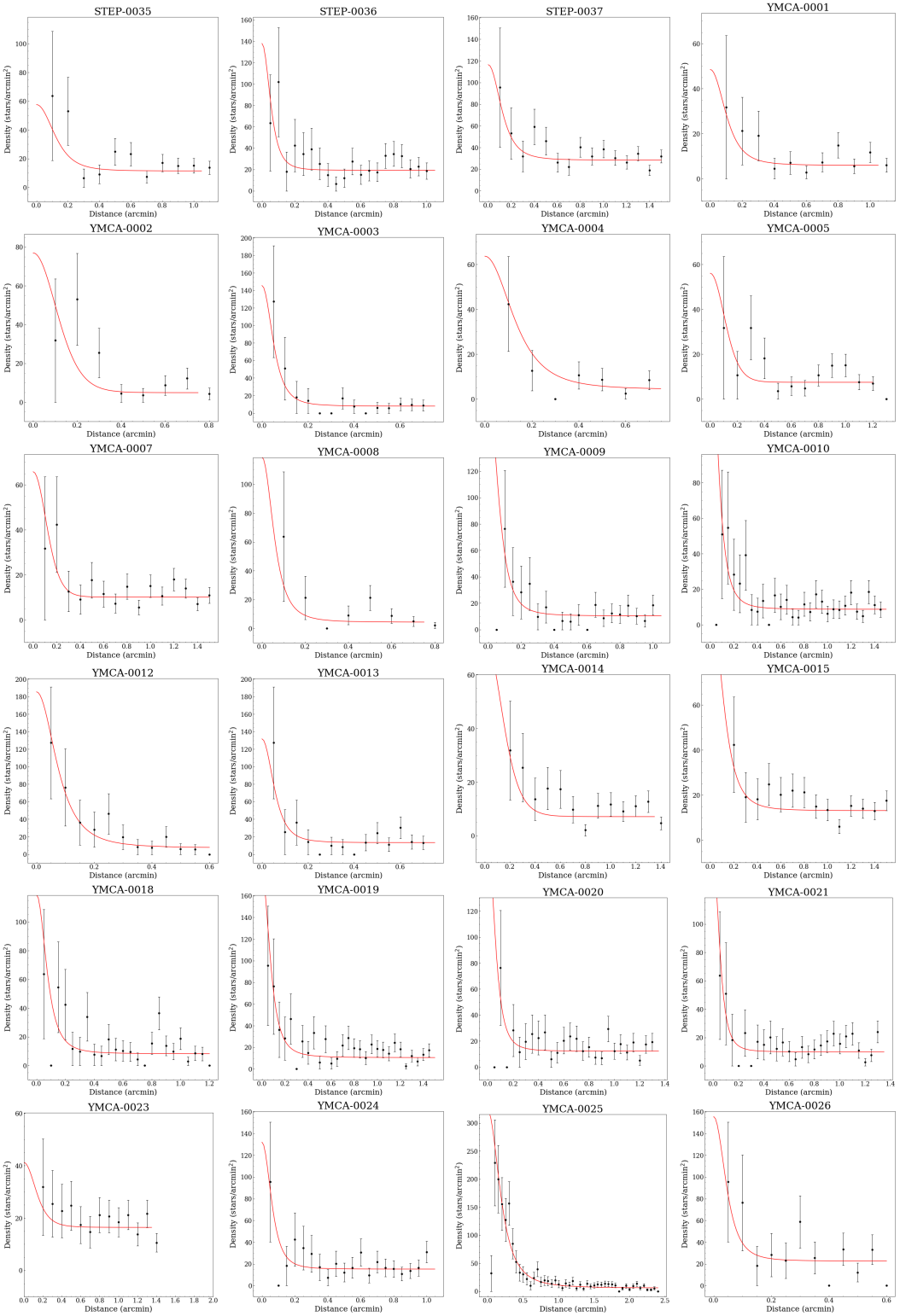
STEP-0035
STEP-0036
STEP-0037
YMCA-0001
YMCA-0002
YMCA-0003
YMCA-0004
YMCA-0005
YMCA-0007
YMCA-0008
YMCA-0009
YMCA-0010
YMCA-0012
YMCA-0013
YMCA-0014
YMCA-0015
YMCA-0018
YMCA-0019
YMCA-0020
YMCA-0021
YMCA-0023
YMCA-0024
YMCA-0025
YMCA-0026
Density (stars/arcmin²)
Distance (arcmin)

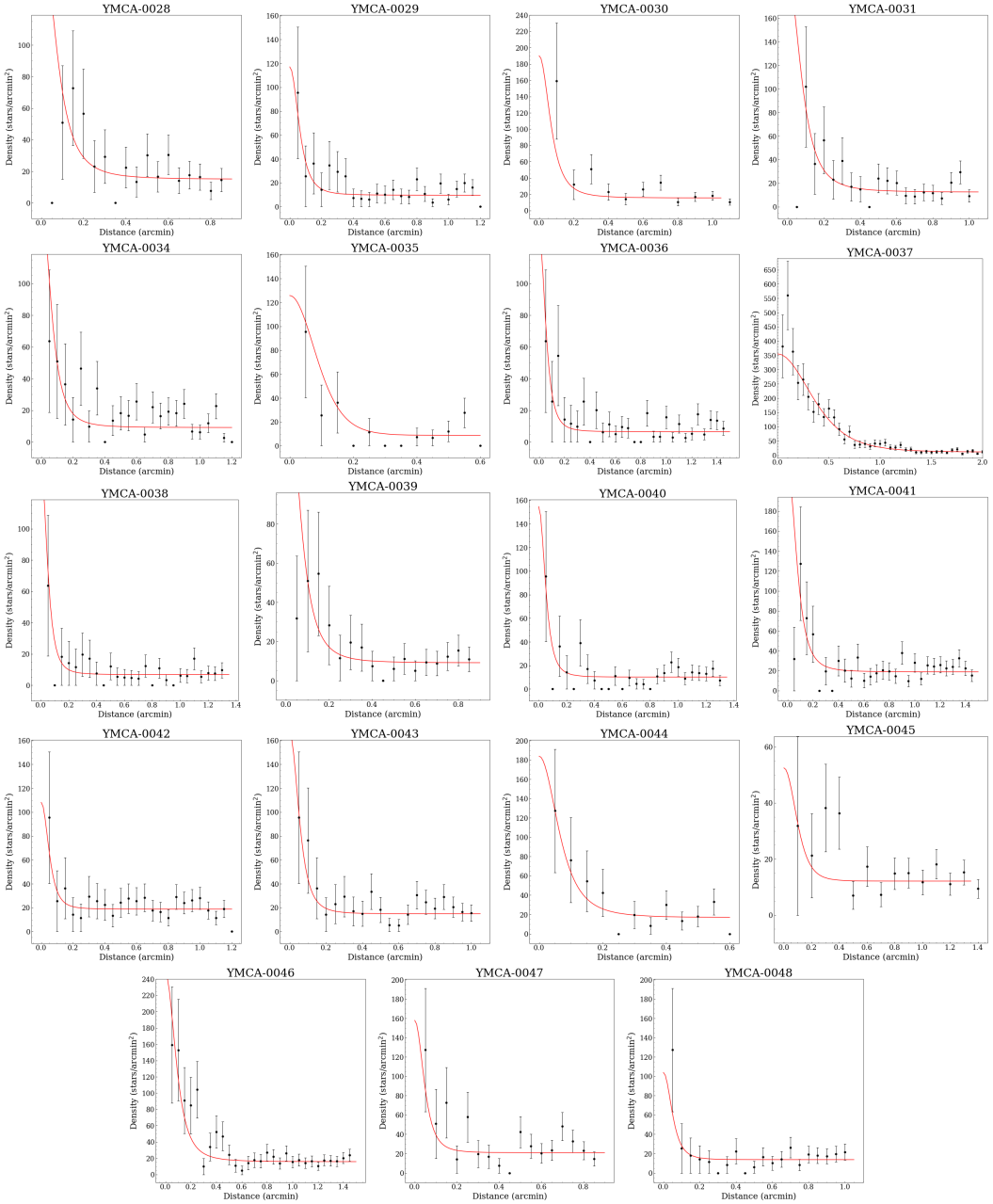
YMCA-0028
YMCA-0029
YMCA-0030
YMCA-0031
YMCA-0034
YMCA-0035
YMCA-0036
YMCA-0037
YMCA-0038
YMCA-0039
YMCA-0040
YMCA-0041
YMCA-0042
YMCA-0043
YMCA-0044
YMCA-0045
YMCA-0046
YMCA-0047
YMCA-0048
Density (stars/arcmin^2)
Distance (arcmin)

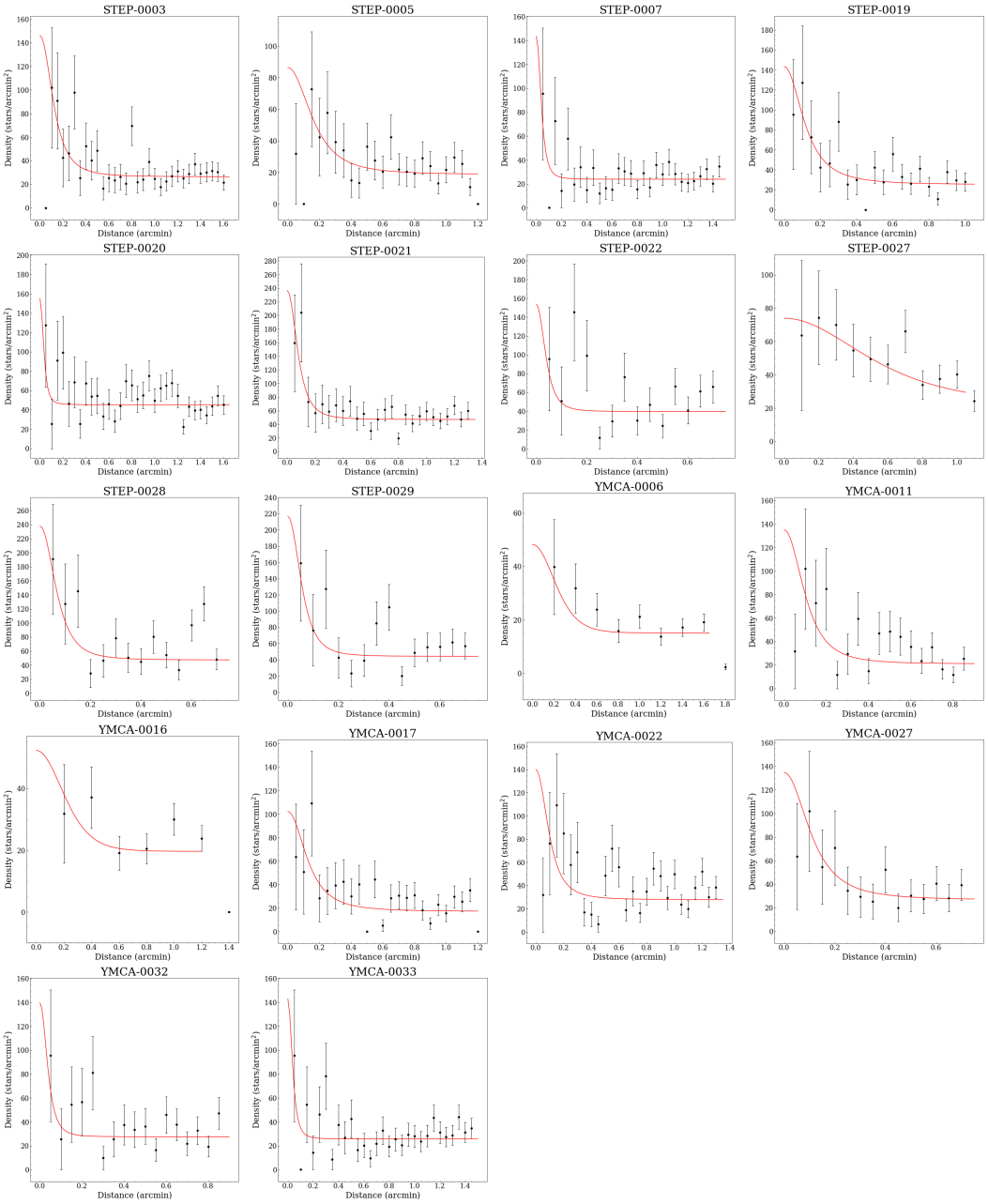

Figure A.3: RDP obtained using only stars with P $\geq$50%. The red line represents the best fit with an EFF profile.

Appendix B

Supplementary material to the 40 SCs detected in the LMC periphery and presented in Chapter 5

Figure B.1 displays the same of Fig.5.2 for the 40 candidate SCs.

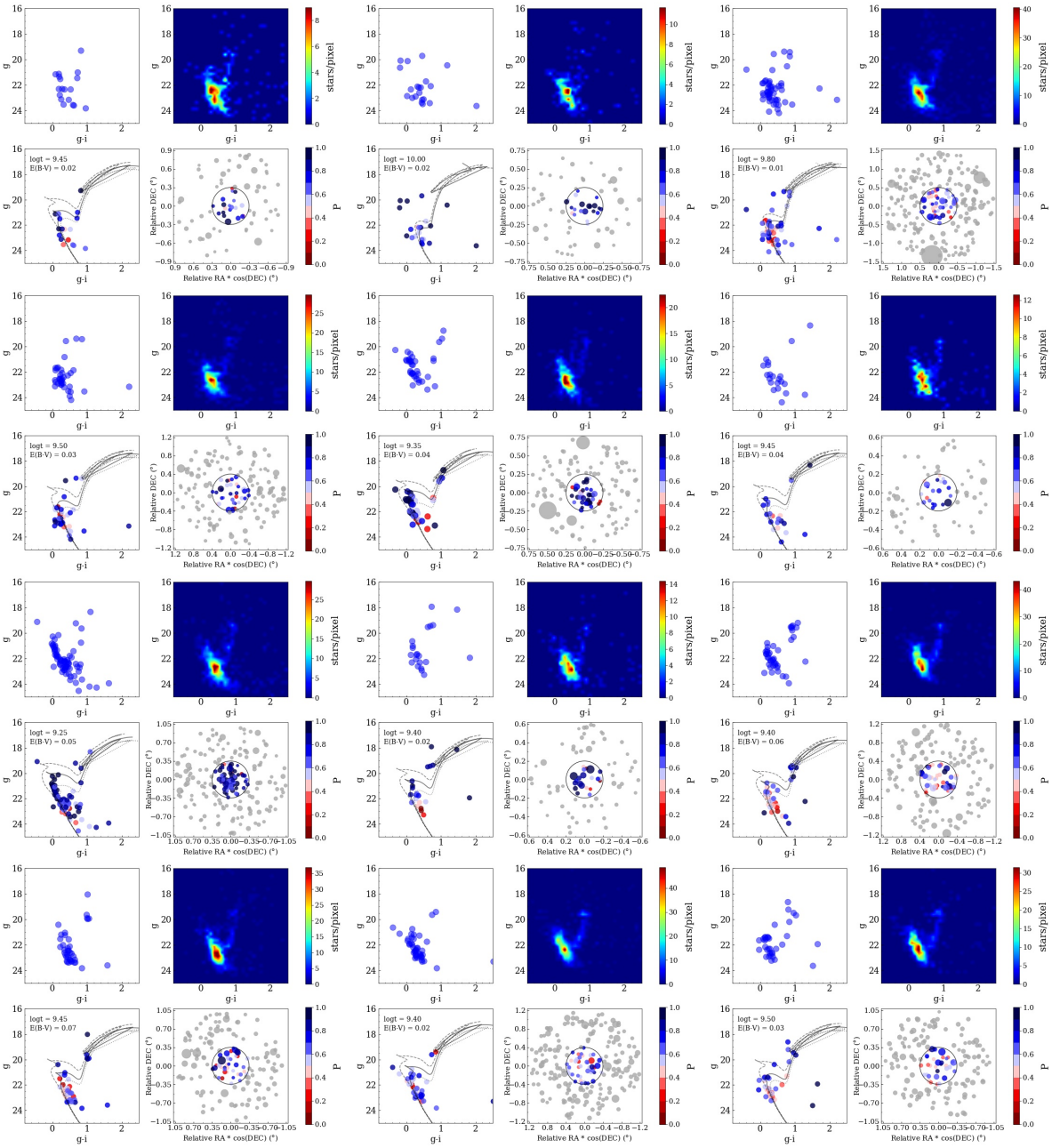

Figure B.1: Cleaning procedure for the 40 candidate SCs detected in this work (see Fig. 5.2 for the explanation of each figure). The stars are colored according to their probability to belong to the cluster. The solid line shows the best fitting isochrone, whereas dashed and dotted lines are the isochrones shifted by $\log(t) = \pm 0.2$ dex, respectively.

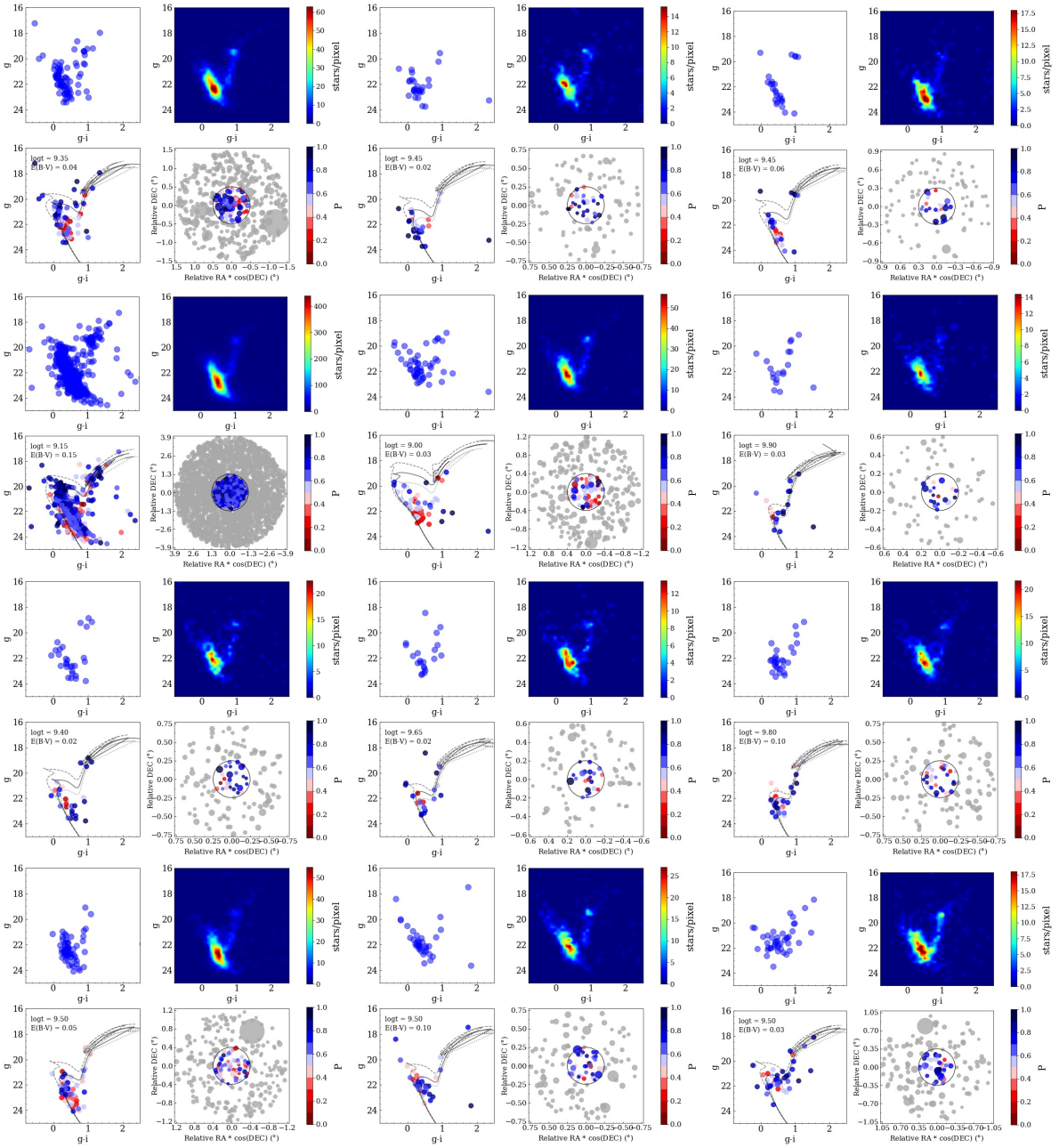
logt = 9.35
E(B-V) = 0.04
logt = 9.45
E(B-V) = 0.02
logt = 9.45
E(B-V) = 0.06
logt = 9.15
E(B-V) = 0.15
logt = 9.00
E(B-V) = 0.03
logt = 9.90
E(B-V) = 0.03
logt = 9.40
E(B-V) = 0.02
logt = 9.65
E(B-V) = 0.02
logt = 9.80
E(B-V) = 0.10
logt = 9.50
E(B-V) = 0.05
logt = 9.50
E(B-V) = 0.10
logt = 9.50
E(B-V) = 0.03
g
g-i
Relative DEC (°)
Relative RA * cos(DEC) (°)
stars/pixel
P

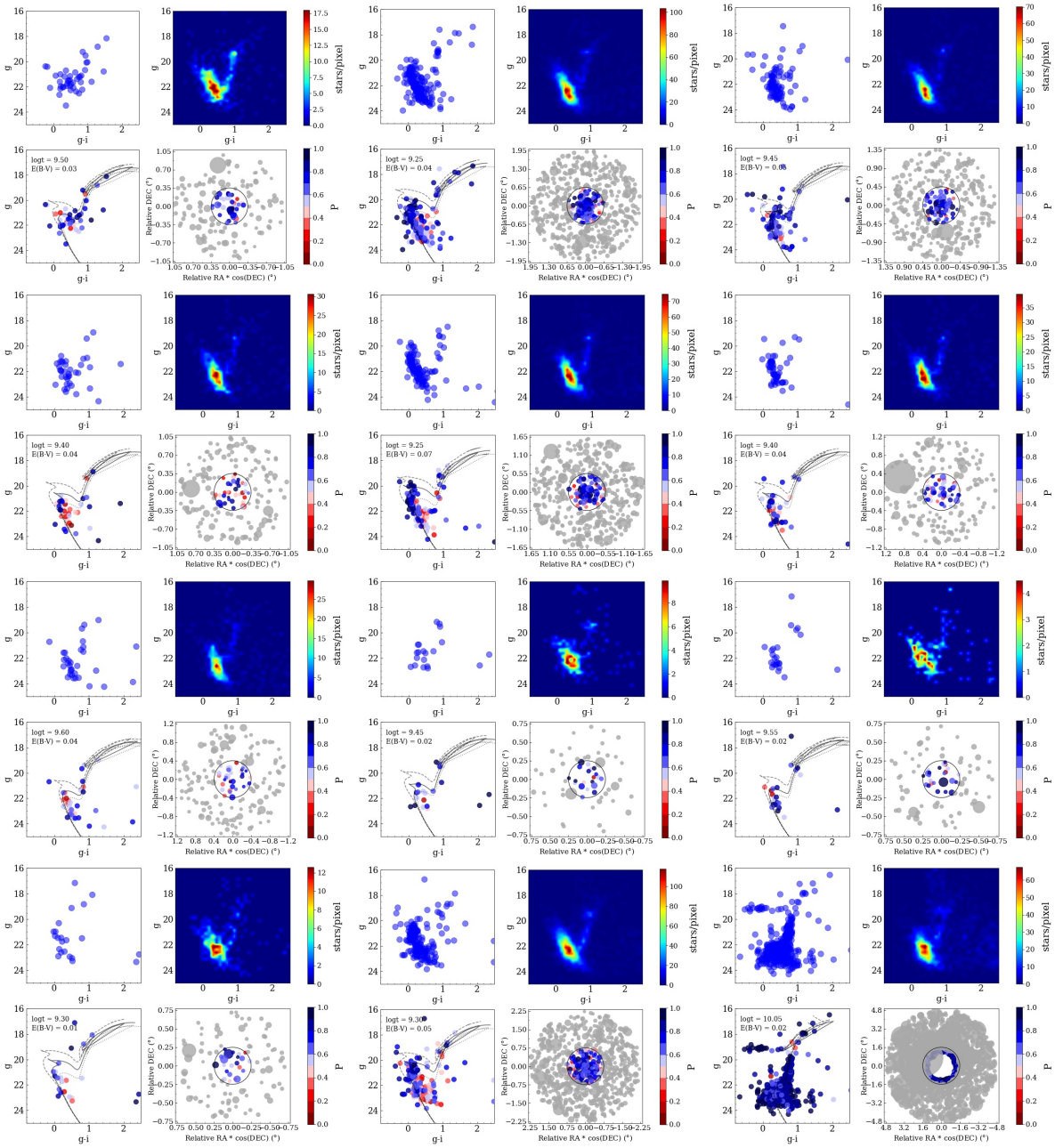
logt = 9.50
E(B-V) = 0.03
logt = 9.25
E(B-V) = 0.04
logt = 9.45
E(B-V) = 0.05
logt = 9.40
E(B-V) = 0.04
logt = 9.25
E(B-V) = 0.07
logt = 9.40
E(B-V) = 0.04
logt = 9.60
E(B-V) = 0.04
logt = 9.45
E(B-V) = 0.02
logt = 9.55
E(B-V) = 0.02
logt = 9.30
E(B-V) = 0.01
logt = 9.30
E(B-V) = 0.05
logt = 10.05
E(B-V) = 0.02
g
g-i
Relative DEC (°)
Relative RA * cos(DEC) (°)
stars/pixel
P

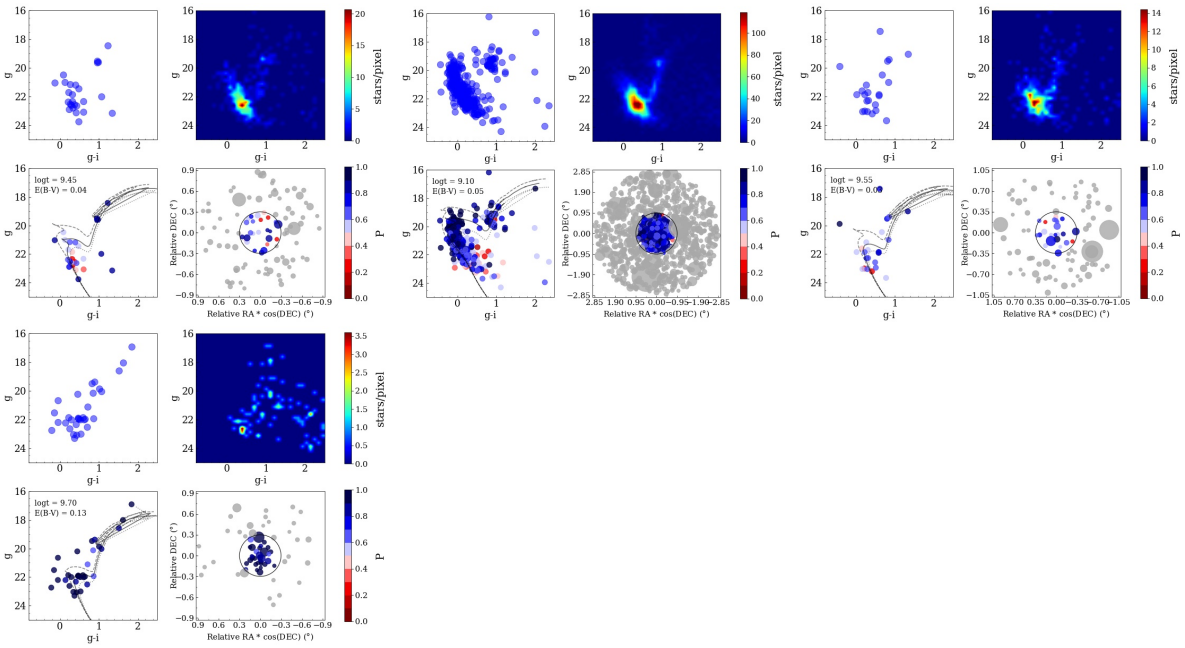
logt = 9.45
E(B-V) = 0.04
logt = 9.10
E(B-V) = 0.05
logt = 9.55
E(B-V) = 0.06
logt = 9.70
E(B-V) = 0.13
g
g-i
stars/pixel
P
Relative DEC (°)
Relative RA * cos(DEC) (°)

Appendix C

Supplementary material to the SMC SCs analysed in Chapter 7

C.1 King model

The empirical King's profile [King, 1962], expressed in mag/arcsec^2, is given by

$$\mu(r) = \mu' - 5\log_{10}\left(\frac{1}{\sqrt{1+\left(\frac{r}{r_\mathrm{c}}\right)^2}} - \frac{1}{\sqrt{1+\left(\frac{r_\mathrm{t}}{r_\mathrm{c}}\right)^2}}\right) \tag{C.1}$$

$$\mu' = \mu_0 + 5\log_{10}\left(1 - \frac{1}{\sqrt{1+\left(\frac{r_\mathrm{t}}{r_\mathrm{c}}\right)^2}}\right) \tag{C.2}$$

where μ_0 is the central SB, r_c is the core radius and r_t is the tidal radius. With these values, it is possible to calculate the SC concentration, defined as $c = \log(r_\mathrm{t}/r_\mathrm{c})$. It is worth to point out that r_c defined through eq. C.1 is similar (it indicates the distance at which the SB is half the central value) to r_c derived by means of eq. 7.1 only if $r_\mathrm{t} \gg r_\mathrm{c}$ (high concentration). For low concentrations, the r_c value obtained from the King profile is larger than its counterpart determined from the EFF function [see also Fig. 10 in Glatt et al., 2009].

Another useful parameter is the half-light radius (r_h), which is the radius enclosing half of the cluster total light. We derived it from the best model achieved through eq. 7.1. We calculated the projected luminosity as a function of radius (substantially the growth curve), normalized by

the total projected luminosity.The total projected luminosity is obtained by integrating up to the fitting radius. The errors are calculated with a Monte Carlo-like approach, perturbing each parameter with Gaussians with the best fitted value as mean, and the error on the parameter as sigma, and these are "propagated" in the calculation.
Regarding the fitting procedure, and the choice of $r_{\rm f}$ for the King's profiles, we proceeded as discussed in the previous section for the EFF models.

Again, an integration of the equation C.1 by using as extreme values of the integral 0 and $r_{\rm t}$ provides the total luminosity L of the SC.

$$L = \pi r_{\rm c}^2 k \{ \ln \left[1 + \left(\frac{r_{\rm t}}{r_{\rm c}} \right)^2 \right] + \frac{\left(\frac{r_{\rm t}}{r_{\rm c}} \right)^2 + 4\sqrt{1 + \left(\frac{r_{\rm t}}{r_{\rm c}} \right)^2} - 4 \left[1 + \left(\frac{r_{\rm t}}{r_{\rm c}} \right)^2 \right]}{1 + \left(\frac{r_{\rm t}}{r_{\rm c}} \right)^2} \} \tag{C.3}$$

$$k = 10^{-0.4\mu} \left(1 - \frac{1}{\sqrt{1 + \left(\frac{r_{\rm t}}{r_{\rm c}} \right)^2}} \right) \tag{C.4}$$

In Table C.1 we reported the values of μ_0, $r_{\rm c}$ and $r_{\rm t}$ (in arcsec), from fitting all SCs in our sample with King models. We listed luminosities, $r_{\rm c} - r_{\rm h}$ (in pc) and the concentration parameter in table 7.1.

We also briefly discuss the parameters derived through the King profile in order to show that they provide the same results achieved with the EFF model. In Fig. C.1 we display the half-light radius as a function of the age (top panel). Overall, $r_{\rm h}$ seems to show a trend with the SC age akin that observed in Fig. 7.7. In particular, all SCs younger than 100-300 Myr have $r_{\rm h} \leq 7.5$ pc. Then, some SCs undergo an increase of their inner regions while the majority remains compact. We find also in this case that the bulk of the SCs having large half-light radius are also the most massive. Figure C.1 (bottom panel) shows the concentration parameter as a function of the age. No particular trend can be detected in this case.

C.2 Deprojected distance from the SMC centre

To obtain the 2D distance from the SMC centre we followed the recipe developed by Piatti et al. [2005] and successively used in other works [e.g. Dias et al., 2014, 2016]. The core idea is to define the distance from the SMC through ellipses, as they better reproduce the SMC 2D geometry. Following Piatti et al. [2005], we draw ellipses with an ellipticity of $e = 0.5$, having the semi-major axis direction at 45°, starting from the north in a counterclockwise pattern. For

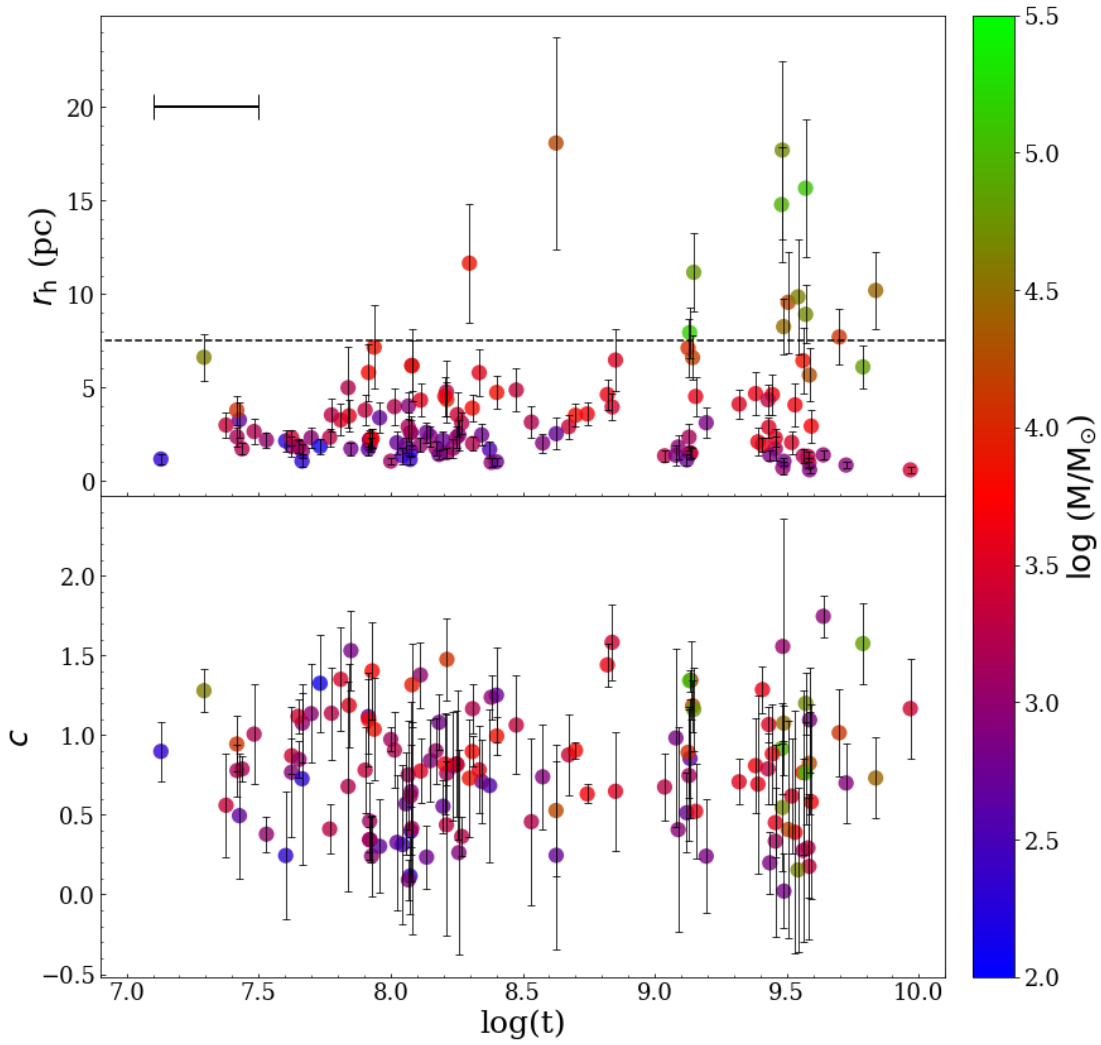

Figure C.1: *Top:* half-light radius, and *bottom:* concentration parameter as a function of the SC age. Points are colour coded according their mass. Diamonds are SCs flagged as OLD (see text for details). In the lower right cornel of the bottom panel we sketched the size of the age uncertainties, equal for all SCs.

each SC, we looked for the ellipse intersecting its position and we set the major-axis of the ellipse as the SC galactocentric distance. Moreover, following Dias et al. [2016] we also splitted our SC sample into subpopulations based on their 2D distance: i) the bar, constituted by SCs with a distance lower than 1.5° and (ii) the outer regions, made by the remaining objects. Note that while Dias et al. [2016] called bar those SCs within 2°, we utilized a separation of 1.5° in order to have a similar number of SCs in each of the two subpopulations.

C.3 Parameters of the fitting procedure

In Table C.1 we reported all the SC parameters derived by fitting the SBPs with EFF and King profiles. In the first column the SC's name is displayed, while in the second and third columns SCs' coordinates are reported. From the fourth to the sixth columns we inserted fitting parameters estimated through the EFF profile, namely $\mu_0 - \alpha - \gamma$ which are described in §7.3.1. From the seventh to the nineth columns we put parameters obtained via the King profile, or $\mu_0 - r_c - c$, described in Appendix C.1. The last two columns display the fitting radius (see discussion in §7.3.1) and the tile where SCs reside.

C.4 Surface Brightness Profiles of all 170 SCs

In Figure C.2 we display all SBPs with the best fit obtained through the EFF (red line) and King (blue line) profiles.

			EFF			KING				
ID	R.A. (J2000)	Dec (J2000)	μ_0 (mag/arcsec^2)	α (arcsec)	γ	μ_0 (mag/arcsec^2)	r_c (arcsec)	r_t (arcsec)	r_f (arcsec)	Tile
B10	9.4345	-73.2108	16.78 ± 1.33	1.0 ± 0.8	2.8 ± 0.6	17.19 ± 1.68	0.8 ± 0.8	28.8 ± 25.8	12.0	3_4
B100	15.0999	-72.0888	17.96 ± 0.10	4.0 ± 0.4	4.5 ± 0.4	17.79 ± 0.16	2.1 ± 0.2	19.9 ± 1.2	16.0	4_6
B103	15.2375	-73.1541	20.02 ± 0.21	2.9 ± 1.0	2.0 ± 0.4	20.24 ± 0.24	4.5 ± 1.4	28.8 ± 13.4	16.0	3_5
B105	15.4037	-72.4073	19.41 ± 0.23	3.0 ± 0.9	2.4 ± 0.4	19.49 ± 0.19	3.1 ± 0.6	37.3 ± 14.2	16.0	4_6
B108	15.4637	-72.1821	21.39 ± 0.23	4.3 ± 2.6	2.0 ± 1.0	21.51 ± 0.23	6.5 ± 3.0	31.7 ± 26.0	16.0	4_6
B111	15.5094	-71.0208	21.78 ± 0.18	2.7 ± 0.9	2.0 ± 0.5	21.95 ± 0.19	3.9 ± 1.1	28.1 ± 16.2	12.0	5_6
B113	15.7273	-73.3380	20.25 ± 0.22	5.1 ± 2.3	3.9 ± 1.7	20.25 ± 0.20	4.0 ± 1.0	18.8 ± 4.4	12.0	3_6
B115	15.8500	-72.6516	19.35 ± 0.27	3.4 ± 1.8	2.0 ± 0.7	19.57 ± 0.27	5.4 ± 2.5	33.6 ± 30.1	16.0	4_6
B117	16.0545	-73.2603	19.64 ± 0.12	4.0 ± 0.9	2.5 ± 0.4	19.69 ± 0.13	4.1 ± 0.7	33.0 ± 10.2	16.0	3_6
B119	16.0813	-73.1678	-	-	-	21.96 ± 0.19	9.7 ± 7.7	12.3 ± 2.9	10.0	3_6
B12	9.5871	-73.2707	-	-	-	21.96 ± 0.24	8.0 ± 6.5	17.4 ± 10.1	13.0	3_4
B121	16.1257	-72.6191	19.45 ± 0.21	5.3 ± 2.6	2.8 ± 1.3	19.65 ± 0.11	8.7 ± 2.0	19.3 ± 2.0	16.0	4_6
B122	16.1007	-71.7144	21.92 ± 0.35	6.8 ± 5.4	2.0 ± 1.1	22.47 ± 0.18	20.5 ± 15.1	56.1 ± 48.3	32.0	5_6
B124	16.2608	-73.0427	20.57 ± 0.13	6.5 ± 2.5	4.2 ± 1.8	20.66 ± 0.11	6.7 ± 1.5	16.8 ± 2.2	13.0	3_6
B128	16.4628	-71.9534	-	-	-	21.45 ± 0.26	9.6 ± 6.2	20.4 ± 6.9	16.0	4_6
B137	17.6174	-72.9574	20.18 ± 0.12	2.8 ± 0.5	2.0 ± 0.2	20.35 ± 0.16	3.8 ± 0.8	38.8 ± 18.6	16.0	3_6
B165	22.7115	-73.4340	21.46 ± 0.25	6.3 ± 2.5	4.8 ± 1.9	21.55 ± 0.23	5.0 ± 1.2	18.3 ± 1.8	16.0	3_8
B18	10.2765	-72.7259	20.35 ± 0.14	3.4 ± 1.2	3.6 ± 1.4	20.34 ± 0.13	2.7 ± 0.6	13.7 ± 4.9	6.0	4_4
B21	10.3142	-72.8316	21.29 ± 0.41	2.8 ± 2.7	2.3 ± 2.0	21.53 ± 0.11	8.2 ± 3.7	8.6 ± 0.7	8.0	4_4
B22	10.3361	-72.8244	18.32 ± 0.66	0.7 ± 0.3	2.0 ± 0.2	18.96 ± 0.39	1.1 ± 0.3	15.9 ± 6.8	6.0	4_4
B26	10.1890	-73.7390	21.23 ± 0.29	2.4 ± 1.5	2.6 ± 1.4	21.51 ± 0.10	4.8 ± 1.3	8.2 ± 0.9	6.0	3_4
B34A	11.1054	-72.9446	19.50 ± 0.43	5.0 ± 4.0	5.4 ± 4.8	19.77 ± 0.31	5.6 ± 2.7	10.5 ± 1.3	10.0	3_4
B39	11.3626	-73.4800	20.49 ± 0.09	5.1 ± 1.0	2.0 ± 0.3	20.61 ± 0.12	7.1 ± 1.4	53.8 ± 21.2	25.0	3_4
B52	12.4189	-73.0582	21.41 ± 0.16	13.5 ± 8.8	2.0 ± 1.2	21.65 ± 0.12	35.0 ± 25.9	62.5 ± 33.4	40.0	3_5
B65	13.1845	-72.9795	17.93 ± 0.08	8.6 ± 1.4	6.6 ± 1.3	17.88 ± 0.10	4.6 ± 0.5	20.0 ± 1.3	16.0	3_5
B70	13.3609	-71.7489	19.68 ± 0.11	1.7 ± 0.2	2.2 ± 0.1	19.64 ± 0.10	1.5 ± 0.1	84.2 ± 20.0	20.0	5_5
B71	13.3237	-72.7660	18.63 ± 0.13	13.2 ± 4.9	7.5 ± 3.7	18.71 ± 0.12	9.4 ± 1.8	22.4 ± 1.5	20.0	4_5
B79	13.6992	-72.4661	18.73 ± 0.20	5.3 ± 1.7	2.8 ± 0.6	18.69 ± 0.21	4.2 ± 0.9	57.7 ± 28.3	25.0	4_5
B80	13.7084	-73.2241	20.13 ± 0.40	2.1 ± 1.2	2.0 ± 0.6	20.39 ± 0.34	3.1 ± 1.3	29.8 ± 26.4	12.0	3_5
B9	9.3155	-72.9626	20.97 ± 0.42	3.7 ± 3.0	2.3 ± 1.3	21.30 ± 0.20	8.8 ± 3.4	17.8 ± 2.2	16.0	4_4
B96	14.8078	-72.6089	20.75 ± 0.08	16.7 ± 5.7	5.8 ± 2.7	20.79 ± 0.07	13.7 ± 2.5	31.7 ± 3.2	25.0	4_6
B97	14.9158	-71.7446	21.87 ± 0.26	4.5 ± 3.9	2.0 ± 1.6	22.08 ± 0.16	10.1 ± 6.8	18.9 ± 8.6	12.0	5_6
B99	15.1180	-73.0865	20.21 ± 0.20	5.3 ± 2.3	2.4 ± 0.8	20.27 ± 0.19	6.0 ± 1.7	39.8 ± 19.4	20.0	3_5
BS102	15.3120	-73.7949	21.64 ± 0.22	4.2 ± 2.5	2.2 ± 1.2	21.74 ± 0.18	5.5 ± 2.1	26.4 ± 18.9	12.0	3_6
BS128	16.3894	-73.4904	-	-	-	21.29 ± 0.22	3.5 ± 2.2	23.3 ± 54.7	6.0	3_6
BS131	16.4978	-72.3411	19.70 ± 0.14	5.6 ± 3.3	3.1 ± 2.2	19.79 ± 0.12	7.7 ± 3.4	14.9 ± 4.3	10.0	4_6
BS138	16.8159	-72.1005	22.30 ± 0.12	11.7 ± 8.5	2.0 ± 1.6	22.38 ± 0.13	19.8 ± 15.5	48.7 ± 47.6	25.0	4_6
BS2	7.1291	-73.0137	21.86 ± 0.26	5.0 ± 2.3	3.6 ± 1.4	21.82 ± 0.29	3.5 ± 1.1	29.9 ± 14.7	16.0	3_3
BS276	17.5233	-72.7370	17.63 ± 0.18	2.3 ± 0.4	3.1 ± 0.3	17.47 ± 0.26	1.5 ± 0.3	26.0 ± 3.8	16.0	4_6
BS76	13.9092	-71.9203	20.97 ± 0.12	7.7 ± 2.4	3.3 ± 1.0	20.96 ± 0.12	6.2 ± 1.2	42.7 ± 16.8	20.0	5_6
BS88	14.4583	-72.9444	21.69 ± 0.17	4.1 ± 3.4	2.0 ± 1.8	21.79 ± 0.11	7.6 ± 5.4	14.4 ± 9.0	8.0	4_6
H86-11	8.2348	-73.5038	20.48 ± 0.58	1.6 ± 1.1	2.0 ± 0.6	21.00 ± 0.44	3.0 ± 1.5	23.0 ± 16.8	12.0	3_3
H86-114	12.6414	-72.6520	20.08 ± 0.12	4.7 ± 1.3	2.0 ± 0.4	20.22 ± 0.13	7.2 ± 1.7	37.1 ± 13.5	20.0	4_5
H86-137	13.1392	-72.6804	19.85 ± 0.06	3.0 ± 0.3	2.2 ± 0.2	19.86 ± 0.06	3.0 ± 0.2	65.3 ± 32.2	12.0	4_5
H86-146	13.4132	-72.3935	17.61 ± 0.65	1.2 ± 0.7	2.0 ± 0.3	18.16 ± 0.56	2.0 ± 0.8	41.3 ± 25.4	20.0	4_5
H86-150	13.7475	-73.4191	19.83 ± 0.23	3.1 ± 1.3	2.0 ± 0.5	20.06 ± 0.25	5.0 ± 1.9	29.4 ± 16.7	16.0	3_5
H86-159	13.7995	-72.6830	21.15 ± 0.17	7.8 ± 4.1	3.7 ± 2.2	21.17 ± 0.17	6.6 ± 2.2	27.7 ± 12.1	16.0	4_5
H86-165	13.9242	-72.8798	21.07 ± 0.27	5.7 ± 4.3	2.1 ± 1.3	21.16 ± 0.25	8.3 ± 4.4	36.6 ± 28.0	20.0	4_5
H86-174	14.3251	-72.9343	20.63 ± 0.16	4.3 ± 1.6	2.1 ± 0.6	20.74 ± 0.15	5.9 ± 1.6	32.3 ± 15.6	16.0	4_6
H86-175	14.4596	-72.4401	19.57 ± 0.09	9.2 ± 3.6	14.4 ± 9.0	19.56 ± 0.10	4.2 ± 0.6	9.6 ± 0.5	8.0	4_6
H86-179	14.4882	-72.4456	20.72 ± 0.42	4.8 ± 4.7	2.9 ± 2.6	20.95 ± 0.28	8.7 ± 6.0	15.3 ± 4.0	12.0	4_6
H86-181	14.5811	-72.2996	17.97 ± 0.35	1.8 ± 0.7	2.4 ± 0.4	18.05 ± 0.35	1.8 ± 0.5	27.3 ± 12.2	12.0	4_6
H86-182	14.6073	-72.6656	20.42 ± 0.16	9.2 ± 4.4	2.7 ± 1.3	20.48 ± 0.15	10.2 ± 3.3	44.7 ± 20.1	25.0	4_6
H86-186	14.9814	-72.3719	19.11 ± 0.06	6.2 ± 0.7	4.7 ± 0.5	19.06 ± 0.08	3.9 ± 0.4	22.5 ± 1.7	16.0	4_6
H86-190	15.1377	-72.2581	19.50 ± 0.32	2.1 ± 1.2	2.0 ± 0.8	19.72 ± 0.26	3.2 ± 1.4	17.1 ± 13.6	8.0	4_6
H86-191	15.2430	-72.5398	-	-	-	21.03 ± 0.30	6.5 ± 4.9	13.3 ± 5.3	10.0	4_6
H86-193	15.3260	-72.2283	21.35 ± 0.08	8.4 ± 3.7	3.5 ± 2.0	21.36 ± 0.08	7.6 ± 2.0	28.0 ± 13.4	12.0	4_6
H86-194	15.3105	-72.5506	20.25 ± 0.54	2.3 ± 2.2	2.0 ± 1.4	20.74 ± 0.11	7.7 ± 3.2	10.0 ± 1.4	8.0	4_6
H86-213	23.6721	-73.2746	20.22 ± 0.36	1.1 ± 0.3	2.0 ± 0.2	20.68 ± 0.32	1.7 ± 0.4	29.7 ± 12.9	12.0	3_8
H86-6	7.3467	-72.9988	22.25 ± 0.19	6.2 ± 3.5	4.3 ± 2.9	22.42 ± 0.11	8.0 ± 2.6	12.7 ± 1.5	10.0	3_3
H86-60	10.1858	-73.1180	-	-	-	21.34 ± 0.24	4.9 ± 3.7	9.2 ± 4.0	6.0	3_4
H86-74	11.3058	-73.2199	18.31 ± 0.12	3.5 ± 0.7	2.4 ± 0.3	18.34 ± 0.12	3.4 ± 0.5	44.4 ± 17.9	16.0	3_4
H86-86	11.7602	-73.3945	20.27 ± 0.42	1.4 ± 0.7	2.8 ± 0.9	20.34 ± 0.41	1.4 ± 0.5	10.8 ± 5.2	5.0	3_4
H86-87	11.7713	-73.3706	21.07 ± 0.23	5.6 ± 4.4	2.0 ± 1.5	21.34 ± 0.15	13.4 ± 11.2	24.5 ± 15.8	16.0	3_4
H86-97	11.9695	-73.2217	19.64 ± 0.13	5.0 ± 2.0	2.0 ± 0.7	19.80 ± 0.09	8.9 ± 2.4	25.8 ± 7.5	16.0	3_4
HW10	9.1296	-72.9866	22.23 ± 0.12	9.9 ± 3.0	2.0 ± 0.4	22.34 ± 0.15	14.5 ± 3.8	96.4 ± 45.7	50.0	3_4

Table C.1: Parameters derived by fitting the EFF and King profiles.

			EFF			KING				
ID	R.A. (J2000)	Dec (J2000)	μ_0 (mag/arcsec^2)	α (arcsec)	γ	μ_0 (mag/arcsec^2)	r_c (arcsec)	r_t (arcsec)	r_f (arcsec)	Tile
HW11	9.3803	-73.6131	21.78 ± 0.23	11.9 ± 6.9	2.0 ± 0.8	21.91 ± 0.24	17.7 ± 7.6	126.4 ± 107.4	64.0	3_4
HW14	10.0640	-73.8710	23.00 ± 0.14	23.6 ± 16.8	2.0 ± 1.5	23.13 ± 0.13	44.7 ± 32.0	114.3 ± 97.1	60.0	3_4
HW18	10.7491	-72.4121	21.07 ± 0.24	1.6 ± 0.5	2.0 ± 0.4	21.42 ± 0.25	2.7 ± 0.9	15.6 ± 7.2	8.0	4_4
HW22	11.6878	-72.0632	19.74 ± 0.10	4.0 ± 0.5	2.8 ± 0.2	19.66 ± 0.13	3.0 ± 0.3	57.3 ± 12.8	25.0	4_5
HW26	12.3886	-73.7053	15.17 ± 0.39	0.8 ± 0.1	3.2 ± 0.2	-	-	-	8.0	3_5
HW34	14.4662	-73.5455	-	-	-	21.37 ± 0.15	6.2 ± 4.3	9.3 ± 3.2	6.0	3_5
HW35	14.6820	-73.5834	20.60 ± 0.08	3.6 ± 0.6	2.7 ± 0.3	20.58 ± 0.08	3.0 ± 0.3	36.7 ± 10.9	12.0	3_5
HW36	14.7667	-73.8414	20.95 ± 0.27	5.6 ± 3.1	5.5 ± 3.6	21.00 ± 0.29	4.0 ± 1.5	13.1 ± 2.7	10.0	3_5
HW37	13.8725	-71.8852	-	-	-	19.96 ± 0.42	11.3 ± 8.7	19.8 ± 3.0	20.0	5_6
HW38	14.8576	-73.8170	22.45 ± 0.18	9.8 ± 7.6	2.7 ± 2.4	22.48 ± 0.18	10.8 ± 5.7	41.0 ± 36.0	20.0	3_5
HW40	15.1060	-71.2949	21.50 ± 0.08	7.1 ± 0.9	3.0 ± 0.3	21.47 ± 0.08	5.5 ± 0.5	64.1 ± 10.6	32.0	5_6
HW41	15.1485	-71.4601	22.45 ± 0.21	9.3 ± 4.6	2.0 ± 0.7	22.80 ± 0.17	18.4 ± 7.1	107.1 ± 86.5	50.0	5_6
HW43	15.2849	-71.7537	21.10 ± 0.16	5.4 ± 2.3	2.0 ± 0.7	21.22 ± 0.15	8.5 ± 2.7	35.3 ± 15.0	20.0	5_6
HW44	15.3429	-73.7883	21.45 ± 0.30	4.7 ± 3.7	2.0 ± 1.3	21.91 ± 0.14	14.3 ± 11.4	25.3 ± 14.3	16.0	3_6
HW48	16.2437	-73.6375	19.85 ± 0.10	3.7 ± 0.5	2.5 ± 0.2	19.80 ± 0.11	3.1 ± 0.3	72.9 ± 27.3	20.0	3_6
HW50	16.5115	-71.7110	21.72 ± 0.53	3.7 ± 3.4	2.0 ± 1.1	-	-	-	20.0	5_6
HW52	16.7359	-73.2362	20.88 ± 0.18	8.1 ± 4.6	3.0 ± 1.7	21.03 ± 0.11	14.0 ± 4.7	24.1 ± 3.0	20.0	3_6
HW53	16.7452	-73.5779	21.99 ± 0.08	5.5 ± 2.9	2.9 ± 2.0	22.04 ± 0.07	7.3 ± 2.8	14.3 ± 4.9	8.0	3_6
HW54	16.8157	-72.1007	21.94 ± 0.30	6.2 ± 4.9	2.0 ± 1.2	-	-	-	25.0	4_6
HW55	16.8292	-73.3783	22.17 ± 0.17	6.9 ± 4.2	2.0 ± 1.1	22.42 ± 0.08	17.6 ± 8.7	30.7 ± 10.2	20.0	3_6
HW59	17.2230	-73.2419	-	-	-	20.03 ± 0.23	2.1 ± 0.6	3.3 ± 0.1	3.0	3_6
HW61	17.4270	-72.2952	21.02 ± 0.19	6.5 ± 4.7	2.3 ± 1.7	21.11 ± 0.10	12.2 ± 4.7	21.3 ± 4.2	16.0	4_6
HW68	18.4701	-73.4165	21.19 ± 0.46	2.2 ± 1.5	2.0 ± 0.8	21.62 ± 0.39	4.1 ± 2.4	24.4 ± 22.2	12.0	3_6
HW74	19.2002	-73.1601	22.02 ± 0.24	8.4 ± 6.5	2.3 ± 1.7	22.10 ± 0.19	12.3 ± 5.7	38.5 ± 17.0	25.0	3_7
HW78	20.3360	-73.0942	19.49 ± 0.24	4.7 ± 1.4	4.8 ± 1.2	19.41 ± 0.34	2.6 ± 0.7	20.2 ± 3.2	16.0	3_7
HW8	8.4446	-73.6333	19.51 ± 0.28	3.4 ± 1.1	2.0 ± 0.3	19.66 ± 0.31	4.5 ± 1.2	100.9 ± 48.6	50.0	3_3
HW82	21.1158	-73.1707	19.25 ± 0.30	1.9 ± 0.6	2.0 ± 0.2	19.56 ± 0.29	2.7 ± 0.6	57.1 ± 26.5	25.0	3_7
HW9	9.1051	-73.0011	22.03 ± 0.15	4.0 ± 1.4	2.0 ± 0.5	22.22 ± 0.17	6.8 ± 2.4	28.1 ± 13.3	16.0	3_4
IC1611	14.9513	-72.3340	18.73 ± 0.09	6.5 ± 1.0	2.3 ± 0.2	18.73 ± 0.10	6.2 ± 0.6	184.5 ± 89.8	50.0	4_6
IC1612	15.0079	-72.3700	20.74 ± 0.18	11.0 ± 6.6	2.0 ± 1.0	21.07 ± 0.14	28.0 ± 19.4	72.7 ± 61.1	40.0	4_6
IC1624	16.3380	-72.0434	19.23 ± 0.06	12.1 ± 1.5	3.5 ± 0.4	19.21 ± 0.07	8.9 ± 0.8	70.1 ± 9.2	40.0	4_6
IC1662	18.1363	-73.4569	20.88 ± 0.15	11.8 ± 3.8	3.4 ± 1.0	20.87 ± 0.16	9.0 ± 1.9	72.7 ± 24.9	40.0	3_6
K1	5.3578	-73.7486	22.65 ± 0.08	38.3 ± 12.7	3.7 ± 1.4	22.65 ± 0.08	29.9 ± 6.0	160.6 ± 61.5	80.0	3_3
K11	9.1131	-72.4786	22.06 ± 0.10	18.6 ± 4.9	5.0 ± 1.5	22.03 ± 0.11	11.5 ± 1.9	58.6 ± 9.8	40.0	4_4
K13	8.9196	-73.5981	22.60 ± 0.17	19.9 ± 14.0	2.0 ± 1.3	22.84 ± 0.10	63.1 ± 50.0	90.0 ± 35.5	64.0	3_4
K15	10.0556	-72.6988	20.16 ± 0.05	6.3 ± 0.6	2.2 ± 0.1	20.16 ± 0.05	5.8 ± 0.4	223.6 ± 109.6	40.0	4_4
K16	10.1389	-72.7400	21.81 ± 0.07	12.5 ± 5.4	5.2 ± 3.2	21.81 ± 0.08	9.5 ± 2.3	26.8 ± 7.0	16.0	4_4
K17	10.2544	-72.5728	19.54 ± 0.07	7.7 ± 0.8	2.6 ± 0.1	19.50 ± 0.08	6.1 ± 0.5	169.4 ± 39.7	64.0	4_4
K21	10.3532	-72.8890	21.77 ± 0.08	27.3 ± 6.9	2.0 ± 0.4	21.81 ± 0.09	35.5 ± 6.5	292.0 ± 138.4	127.0	4_4
K25	12.0063	-73.4861	20.20 ± 0.22	6.0 ± 2.9	2.0 ± 0.7	20.35 ± 0.25	9.1 ± 3.6	59.4 ± 40.2	32.0	3_4
K27	12.0579	-73.8614	21.16 ± 0.08	12.0 ± 2.5	2.0 ± 0.3	21.27 ± 0.12	17.0 ± 3.5	132.5 ± 59.1	64.0	3_4
K28	12.9233	-71.9998	20.97 ± 0.05	20.1 ± 2.5	2.6 ± 0.3	20.96 ± 0.05	17.2 ± 1.4	272.6 ± 100.6	80.0	4_5
K30	13.1499	-72.1920	21.43 ± 0.14	21.9 ± 9.7	2.0 ± 0.7	21.51 ± 0.15	32.9 ± 10.7	176.5 ± 92.7	100.0	4_5
K31	13.2541	-72.8978	21.56 ± 0.09	43.7 ± 21.1	2.0 ± 1.0	21.61 ± 0.10	68.5 ± 26.8	230.5 ± 130.3	127.0	4_5
K34	13.8875	-72.8330	19.38 ± 0.04	16.9 ± 2.4	5.1 ± 0.9	19.36 ± 0.04	11.1 ± 0.8	47.5 ± 3.3	32.0	4_5
K38	14.4478	-73.4204	22.36 ± 0.10	41.6 ± 20.5	2.0 ± 1.0	22.42 ± 0.10	65.0 ± 24.5	228.3 ± 124.9	127.0	3_5
K4	5.7610	-73.6702	22.56 ± 0.07	14.6 ± 3.1	2.1 ± 0.3	22.60 ± 0.07	17.6 ± 2.5	181.8 ± 88.3	64.0	3_3
K42	15.1420	-72.3658	17.75 ± 0.13	2.6 ± 0.4	2.3 ± 0.2	17.73 ± 0.13	2.4 ± 0.3	80.4 ± 37.0	20.0	4_6
K43	15.2033	-73.3491	20.73 ± 0.12	7.8 ± 2.2	2.0 ± 0.4	20.87 ± 0.16	11.6 ± 3.1	76.5 ± 35.6	40.0	3_5
K44	15.5264	-73.9253	22.73 ± 0.09	52.7 ± 20.3	3.3 ± 1.4	22.73 ± 0.09	43.8 ± 10.5	254.2 ± 127.1	127.0	3_6
K45w	15.6973	-73.7384	20.63 ± 0.17	8.3 ± 3.3	4.1 ± 1.7	20.68 ± 0.15	7.4 ± 1.7	26.4 ± 4.0	20.0	3_6
K47	15.7982	-72.2721	18.88 ± 0.13	9.6 ± 2.5	4.6 ± 1.2	18.86 ± 0.16	6.0 ± 1.2	36.2 ± 6.4	25.0	4_6
K5	6.1770	-73.7546	20.85 ± 0.06	14.2 ± 1.8	2.6 ± 0.3	20.84 ± 0.06	12.3 ± 1.0	187.6 ± 55.1	64.0	3_3
K50	16.1512	-72.1611	19.73 ± 0.08	11.2 ± 4.8	3.1 ± 1.6	19.75 ± 0.08	11.3 ± 3.2	41.1 ± 19.4	20.0	4_6
K53	16.5568	-73.2973	20.62 ± 0.23	7.5 ± 4.6	2.0 ± 1.0	20.90 ± 0.07	27.5 ± 7.0	33.9 ± 1.6	32.0	3_6
K54	16.6988	-72.2725	19.67 ± 0.16	17.0 ± 6.2	5.1 ± 2.0	19.65 ± 0.19	10.2 ± 2.5	56.1 ± 12.7	40.0	4_6
K55	16.8846	-73.1217	20.89 ± 0.16	8.9 ± 2.8	2.3 ± 0.5	20.93 ± 0.17	9.6 ± 2.1	110.9 ± 55.1	50.0	3_6
K56	16.8670	-72.4927	20.61 ± 0.14	7.3 ± 2.5	2.1 ± 0.5	20.70 ± 0.13	10.3 ± 2.4	61.9 ± 24.4	32.0	4_6
K57	17.0552	-73.2583	21.41 ± 0.14	8.0 ± 4.7	2.0 ± 1.2	21.54 ± 0.12	13.8 ± 7.0	39.5 ± 27.7	20.0	3_6
K61	17.2663	-73.0870	20.86 ± 0.18	6.5 ± 3.2	2.0 ± 0.8	21.14 ± 0.12	16.6 ± 7.0	33.2 ± 8.4	25.0	3_6
K63	17.6987	-72.7935	20.39 ± 0.21	5.1 ± 2.2	2.0 ± 0.6	20.56 ± 0.20	8.0 ± 2.6	45.1 ± 21.1	25.0	4_6
K8	7.0067	-73.3039	21.97 ± 0.11	8.1 ± 2.2	2.0 ± 0.4	22.08 ± 0.13	11.3 ± 2.6	86.3 ± 42.7	40.0	3_3
K9	7.5033	-73.3790	22.44 ± 0.19	9.6 ± 4.6	2.0 ± 0.7	22.80 ± 0.13	20.6 ± 6.9	91.7 ± 48.6	50.0	3_3

			EFF			KING				
ID	R.A. (J2000)	Dec (J2000)	μ_0 (mag/arcsec^2)	α (arcsec)	γ	μ_0 (mag/arcsec^2)	r_c (arcsec)	r_t (arcsec)	r_f (arcsec)	Tile
L14	8.1683	-72.5803	22.43 ± 0.13	10.2 ± 3.5	2.3 ± 0.6	22.48 ± 0.13	12.3 ± 3.0	78.9 ± 35.4	40.0	4_4
L19	9.4240	-73.9055	22.72 ± 0.20	14.8 ± 13.7	2.0 ± 1.9	-	-	-	40.0	3_4
L28	10.7481	-72.5890	19.35 ± 0.12	5.4 ± 0.8	2.7 ± 0.2	19.32 ± 0.10	4.4 ± 0.4	73.3 ± 11.1	40.0	4_4
L31	11.6503	-72.7419	20.37 ± 0.08	5.7 ± 0.8	2.2 ± 0.2	20.38 ± 0.08	5.6 ± 0.5	124.3 ± 59.1	32.0	4_5
L33	11.8541	-72.8415	20.19 ± 0.17	6.5 ± 2.0	2.6 ± 0.6	20.21 ± 0.18	6.3 ± 1.4	64.7 ± 27.5	32.0	4_5
L48	13.3672	-71.3989	18.90 ± 0.14	9.6 ± 1.8	5.0 ± 0.8	18.85 ± 0.18	5.2 ± 0.8	38.7 ± 3.6	32.0	5_5
L51	13.7271	-72.1141	18.92 ± 0.17	4.8 ± 1.5	2.2 ± 0.5	18.99 ± 0.17	5.5 ± 1.2	56.3 ± 27.7	26.0	4_5
L52	13.8220	-73.5071	19.38 ± 0.07	4.6 ± 0.6	2.7 ± 0.2	19.35 ± 0.08	3.7 ± 0.3	54.3 ± 14.1	20.0	3_5
L56	14.3753	-72.2648	16.58 ± 0.11	5.7 ± 0.7	3.9 ± 0.3	16.46 ± 0.20	3.2 ± 0.5	41.6 ± 4.1	32.0	4_5
L65	15.2521	-72.7498	20.65 ± 0.31	6.7 ± 4.3	2.0 ± 0.8	21.11 ± 0.28	15.2 ± 9.2	72.4 ± 66.7	40.0	4_6
L66	15.4374	-72.5643	17.31 ± 0.12	7.1 ± 1.4	4.7 ± 0.9	17.24 ± 0.11	4.3 ± 0.5	26.3 ± 2.0	20.0	4_6
L80	16.8675	-72.7694	20.87 ± 0.11	10.6 ± 3.1	2.0 ± 0.4	20.97 ± 0.13	15.5 ± 3.6	94.0 ± 37.3	50.0	4_6
L91	18.2130	-73.1198	21.89 ± 0.09	15.1 ± 6.3	2.8 ± 1.3	21.92 ± 0.09	17.2 ± 5.1	57.1 ± 22.5	32.0	3_6
L93	18.2029	-73.4744	22.12 ± 0.06	15.5 ± 3.7	3.3 ± 0.9	22.11 ± 0.06	12.6 ± 1.8	77.6 ± 28.6	32.0	3_6
NGC152	8.2329	-73.1159	21.20 ± 0.07	24.4 ± 4.4	2.5 ± 0.4	21.20 ± 0.07	22.1 ± 2.6	320.0 ± 157.9	100.0	3_3
NGC176	8.9929	-73.1659	20.18 ± 0.11	16.4 ± 4.9	4.1 ± 1.3	20.17 ± 0.12	11.4 ± 2.2	67.9 ± 18.5	40.0	3_4
NGC220	10.1280	-73.4027	19.53 ± 0.09	11.4 ± 2.0	2.5 ± 0.3	19.52 ± 0.10	9.7 ± 1.2	200.0 ± 96.4	70.0	3_4
NGC222	10.1838	-73.3839	19.54 ± 0.17	8.0 ± 2.5	2.0 ± 0.4	19.62 ± 0.17	10.5 ± 2.2	132.2 ± 60.7	70.0	3_4
NGC231	10.2770	-73.3514	20.08 ± 0.16	9.4 ± 2.9	2.0 ± 0.4	20.25 ± 0.20	14.0 ± 3.6	152.9 ± 74.0	80.0	3_4
NGC241	10.8827	-73.4397	19.22 ± 0.16	7.4 ± 1.9	2.7 ± 0.5	19.19 ± 0.16	6.0 ± 1.1	91.8 ± 38.7	40.0	3_4
NGC242	10.9026	-73.4436	19.10 ± 0.19	4.6 ± 1.3	2.0 ± 0.3	19.27 ± 0.19	6.3 ± 1.3	86.7 ± 39.6	40.0	3_4
NGC256	11.4753	-73.5069	18.49 ± 0.11	14.1 ± 4.7	8.3 ± 3.7	18.57 ± 0.09	9.9 ± 1.4	21.9 ± 0.9	20.0	3_4
NGC265	11.7984	-73.4775	19.22 ± 0.06	12.8 ± 1.7	3.2 ± 0.4	19.20 ± 0.07	9.8 ± 0.9	96.7 ± 17.4	50.0	3_4
NGC269	12.0892	-73.5303	19.09 ± 0.04	7.0 ± 0.5	2.6 ± 0.1	19.07 ± 0.04	5.9 ± 0.3	119.4 ± 20.5	40.0	3_5
NGC290	12.8113	-73.1615	17.27 ± 0.22	2.3 ± 0.6	2.0 ± 0.2	17.49 ± 0.25	3.1 ± 0.7	77.7 ± 37.6	32.0	3_5
NGC294	13.2736	-73.3803	18.74 ± 0.03	11.4 ± 0.7	3.8 ± 0.2	18.71 ± 0.05	7.8 ± 0.4	62.3 ± 4.0	40.0	3_5
NGC299	13.3533	-72.1970	17.12 ± 0.12	6.5 ± 1.4	4.0 ± 0.8	17.06 ± 0.12	4.4 ± 0.6	30.7 ± 4.0	20.0	4_5
NGC306	13.5617	-72.2418	18.62 ± 0.17	8.3 ± 3.5	3.7 ± 1.7	18.75 ± 0.13	9.6 ± 2.3	24.7 ± 3.0	20.0	4_5
NGC330	14.0764	-72.4636	17.10 ± 0.10	13.3 ± 1.9	2.9 ± 0.3	17.07 ± 0.12	9.8 ± 1.1	185.6 ± 37.4	100.0	4_5
NGC361	15.5451	-71.6060	20.38 ± 0.05	19.2 ± 2.2	2.7 ± 0.3	20.38 ± 0.04	16.6 ± 1.1	196.7 ± 38.4	80.0	5_6
NGC376	15.9732	-72.8260	17.88 ± 0.19	12.5 ± 3.5	4.0 ± 0.9	17.85 ± 0.22	7.9 ± 1.7	69.5 ± 13.0	50.0	4_6
NGC416	16.9963	-72.3552	18.57 ± 0.09	9.2 ± 1.3	2.4 ± 0.2	18.54 ± 0.10	7.6 ± 0.8	286.0 ± 136.7	80.0	4_6
NGC419	17.0730	-72.8844	18.16 ± 0.04	15.1 ± 0.9	2.8 ± 0.1	18.11 ± 0.06	10.9 ± 0.6	240.3 ± 25.0	127.0	4_6
OGLE132	15.5551	-72.9679	-	-	-	21.29 ± 0.25	8.2 ± 6.2	20.8 ± 15.1	12.0	3_6
OGLE172	10.4508	-73.3919	20.87 ± 0.35	3.3 ± 2.4	5.3 ± 4.7	21.22 ± 0.08	5.5 ± 1.5	5.5 ± 0.2	5.0	3_4
OGLE28	11.3667	-72.8199	20.80 ± 0.30	1.9 ± 0.9	2.0 ± 0.6	21.19 ± 0.29	3.7 ± 1.9	13.6 ± 8.0	8.0	4_4
OGLE5	9.8419	-73.2580	22.16 ± 0.22	3.1 ± 2.0	4.2 ± 3.1	22.38 ± 0.09	5.5 ± 2.0	6.0 ± 0.5	5.0	3_4
OGLE53	12.3182	-73.2116	20.33 ± 0.17	3.0 ± 2.1	2.0 ± 1.5	20.56 ± 0.08	8.0 ± 6.0	10.2 ± 3.9	6.0	3_5
OGLE6	9.8885	-73.1815	19.62 ± 0.65	0.6 ± 0.3	2.0 ± 0.2	20.34 ± 0.42	1.1 ± 0.4	14.3 ± 6.2	6.0	3_4
RZ140	15.6803	-71.4808	22.04 ± 0.27	4.1 ± 2.2	2.0 ± 0.7	22.23 ± 0.26	6.5 ± 2.5	36.3 ± 20.3	20.0	5_6
RZ82	13.2911	-71.9957	21.75 ± 0.12	4.3 ± 1.2	2.6 ± 0.7	21.80 ± 0.12	4.4 ± 0.9	26.7 ± 10.0	12.0	4_5

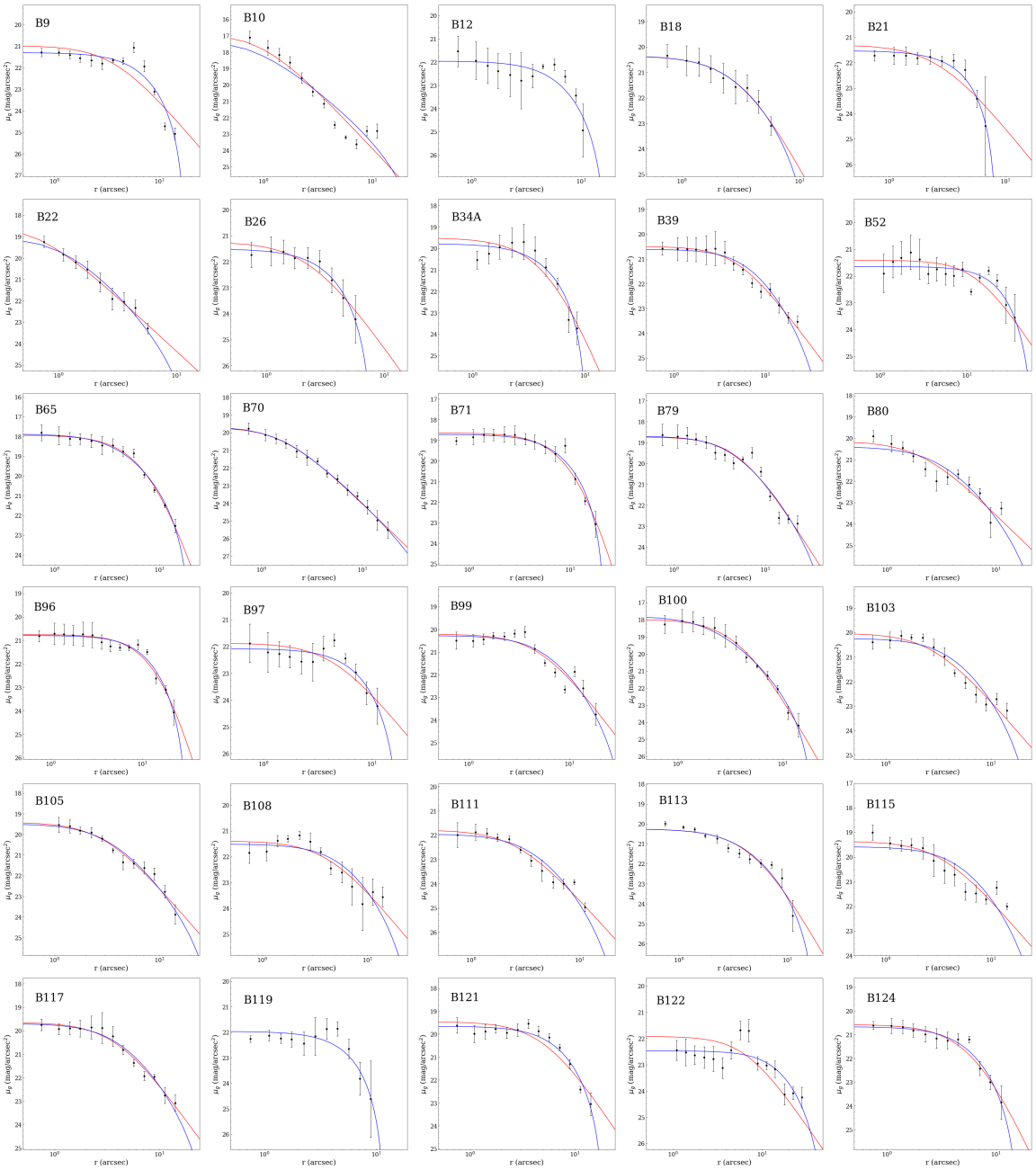

Figure C.2: SBPs derived as described in Sec.7.2. The red and blue lines represent the best fit obtained through the EFF and King's profiles, respectively.

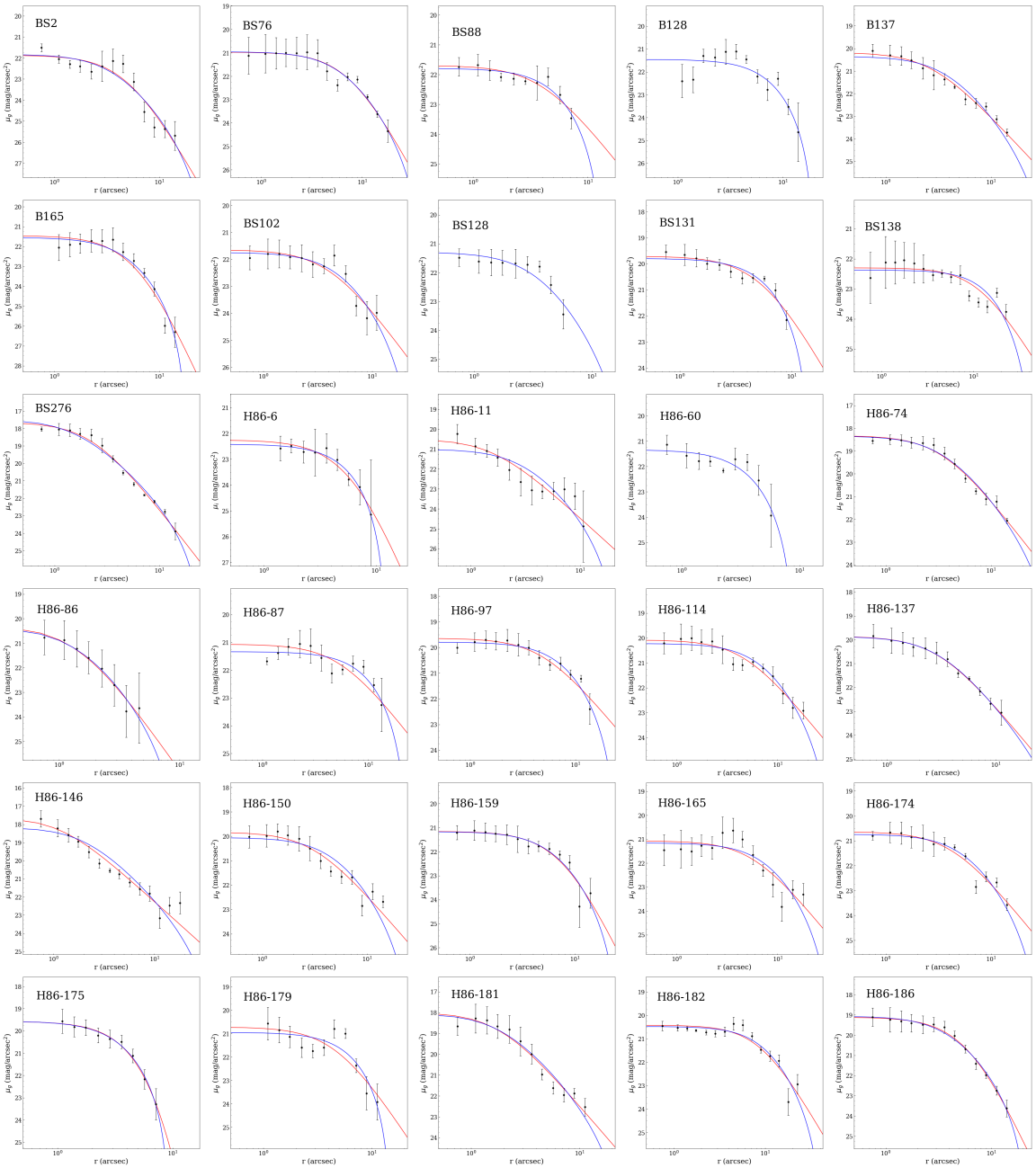
BS2
BS76
BS88
B128
B137
B165
BS102
BS128
BS131
BS138
BS276
H86-6
H86-11
H86-60
H86-74
H86-86
H86-87
H86-97
H86-114
H86-137
H86-146
H86-150
H86-159
H86-165
H86-174
H86-175
H86-179
H86-181
H86-182
H86-186
r (arcsec)

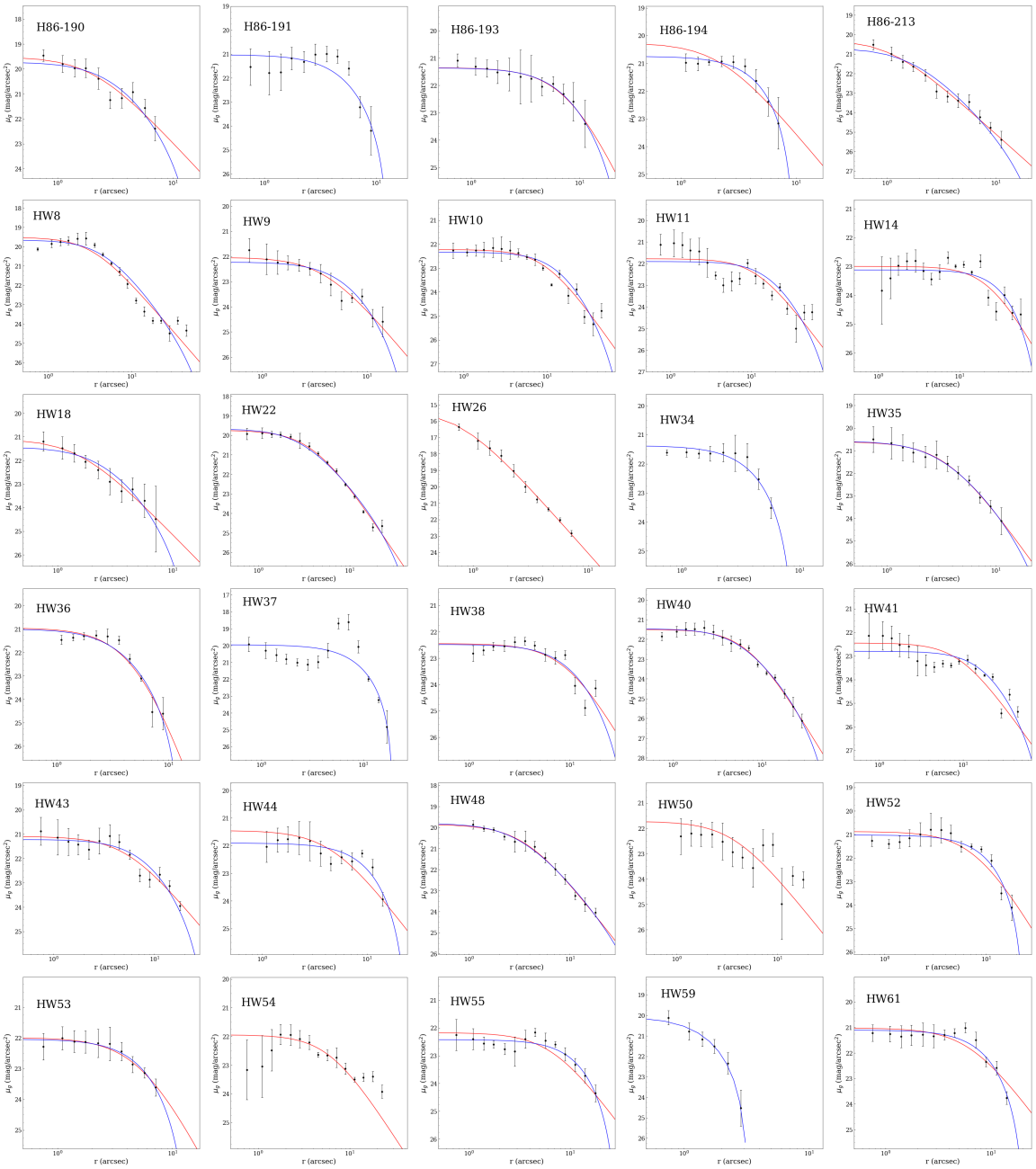
H86-190
H86-191
H86-193
H86-194
H86-213
HW8
HW9
HW10
HW11
HW14
HW18
HW22
HW26
HW34
HW35
HW36
HW37
HW38
HW40
HW41
HW43
HW44
HW48
HW50
HW52
HW53
HW54
HW55
HW59
HW61
r (arcsec)
μ_g (mag/arcsec^2)

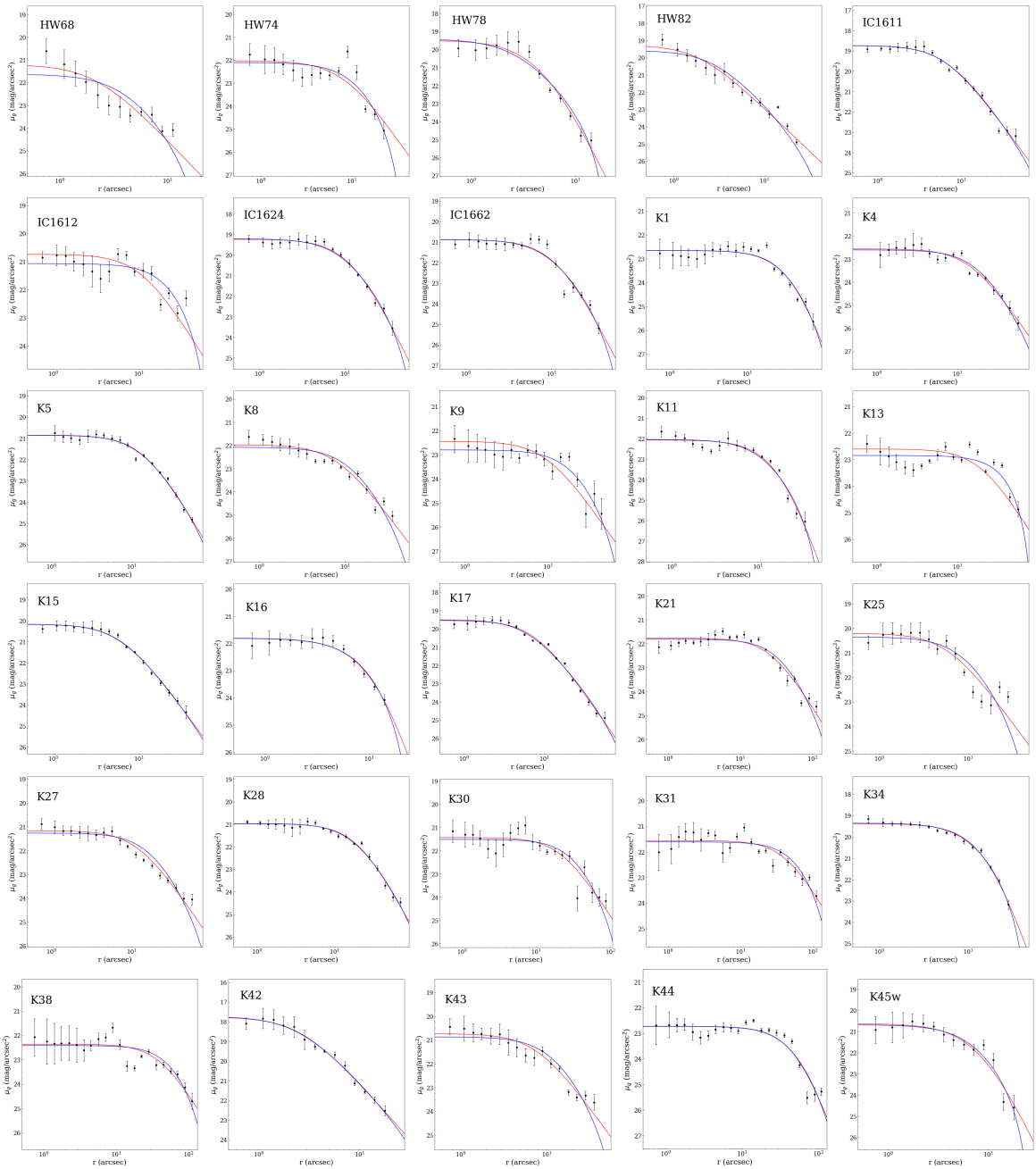
HW68
HW74
HW78
HW82
IC1611
IC1612
IC1624
IC1662
K1
K4
K5
K8
K9
K11
K13
K15
K16
K17
K21
K25
K27
K28
K30
K31
K34
K38
K42
K43
K44
K45w
r (arcsec)
μ_g (mag/arcsec^2)

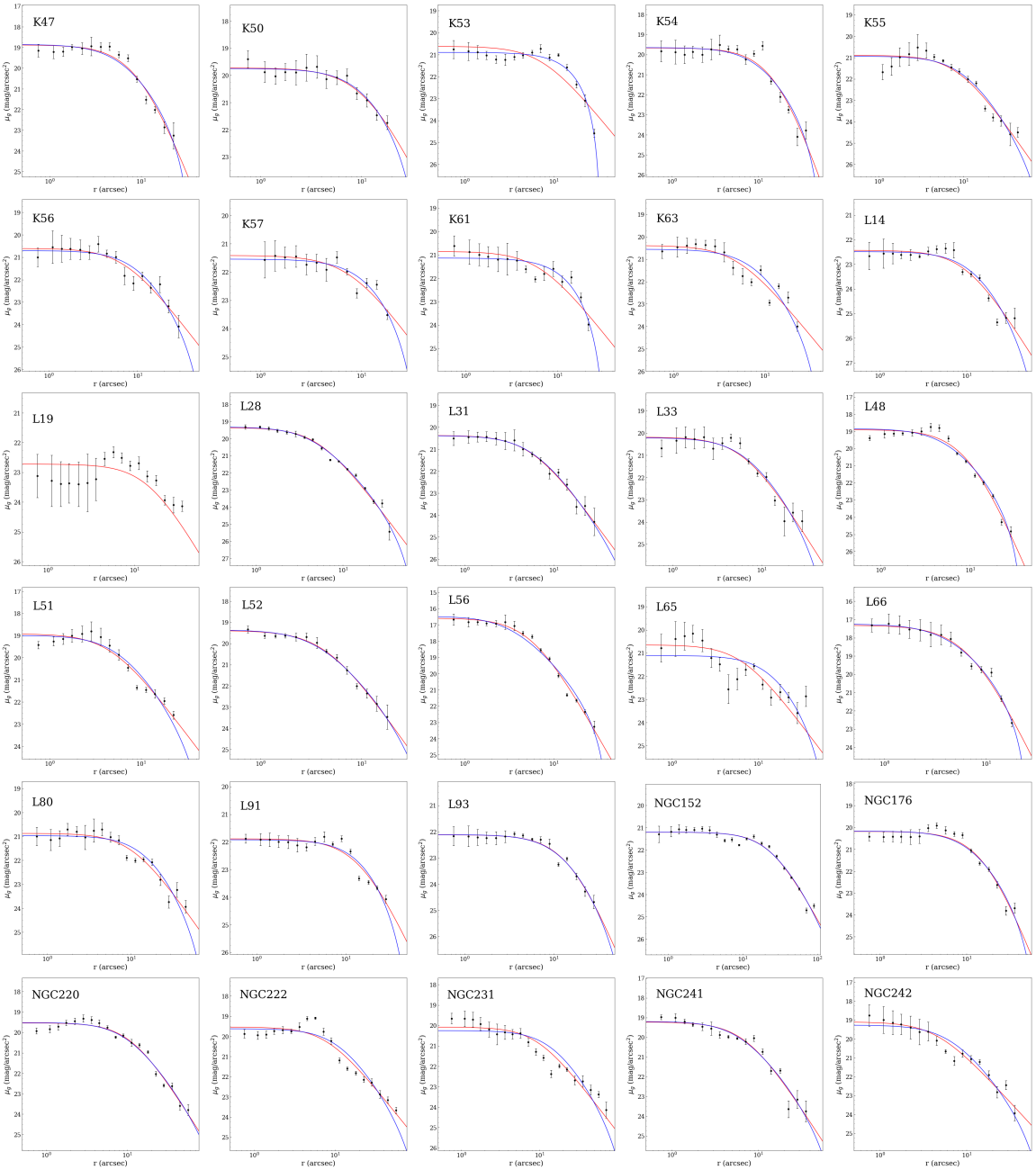
K47
K50
K53
K54
K55
K56
K57
K61
K63
L14
L19
L28
L31
L33
L48
L51
L52
L56
L65
L66
L80
L91
L93
NGC152
NGC176
NGC220
NGC222
NGC231
NGC241
NGC242
r (arcsec)

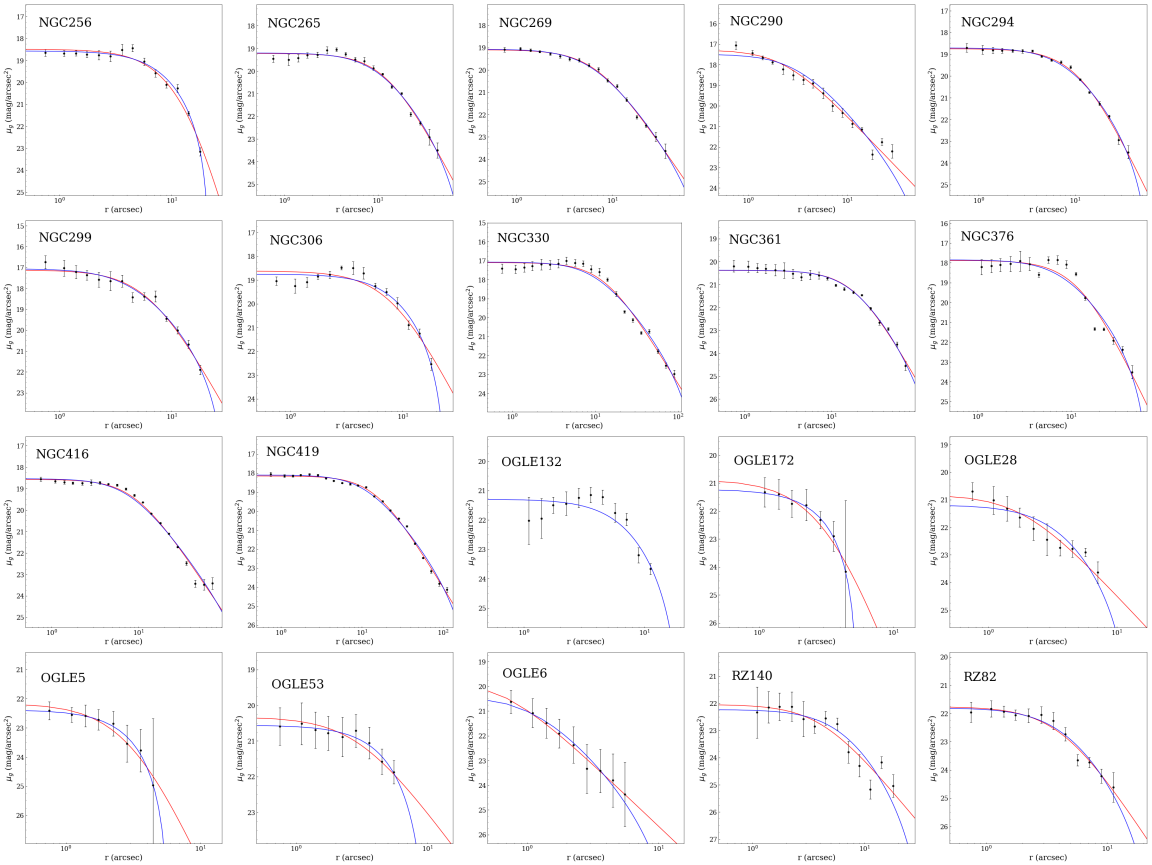
NGC256
NGC265
NGC269
NGC290
NGC294
NGC299
NGC306
NGC330
NGC361
NGC376
NGC416
NGC419
OGLE132
OGLE172
OGLE28
OGLE5
OGLE53
OGLE6
RZ140
RZ82
r (arcsec)

Appendix D

Supplementary material to the Chapter 8

In the following the query we made on the *Gaia* EDR3 dataset:

```
SELECT
source_id,ra,dec,phot_g_mean_mag,phot_bp_mean_mag,phot_rp_mean_mag,bp_rp,parallax,parallax_erro
pmra,pmra_error,pmdec,pmdec_error,l,b,1.085736/phot_g_mean_flux_over_error,
1.085736/phot_bp_mean_flux_over_error,1.085736/phot_rp_mean_flux_over_error
FROM gaiaedr3.gaia_source
WHERE
abs(parallax)<3.0*parallax_error
AND
l>200 AND l<360 AND b<-10 AND b>-90
AND
pmra>-0.5 AND pmra < 3.0 AND pmdec > -2.2 AND pmdec < 2.2
AND
pmra_error<0.2 AND pmdec_error<0.2
AND
phot_bp_rp_excess_factor < 1.3+0.06*power(phot_bp_mean_mag-phot_rp_mean_mag,2)
AND
phot_bp_rp_excess_factor > 1.0+0.015*power(phot_bp_mean_mag-phot_rp_mean_mag,2)
```

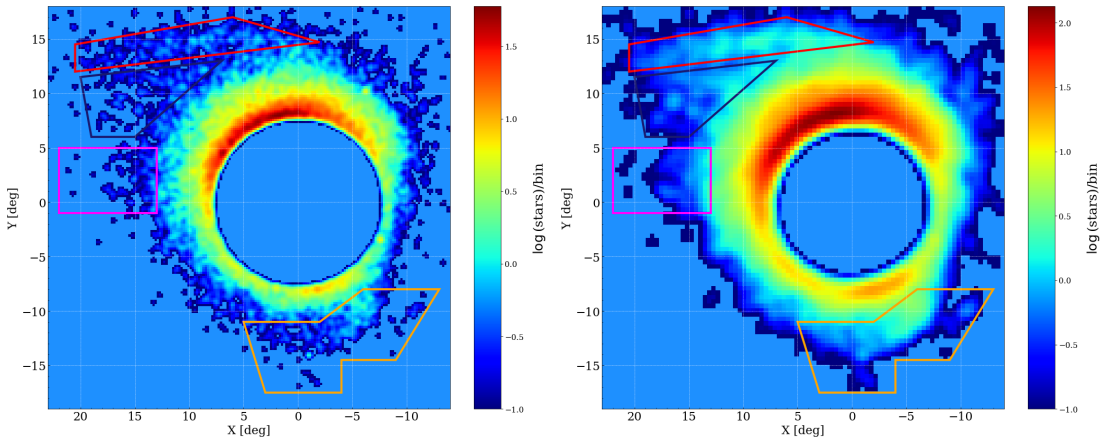

Figure D.1: Same as in Fig.8.4, but with a bin size of $0.2° \times 0.2°$ smoothed with a Gaussian kernel of $\sigma = 0.2°$ (top panel) and a bin size of $0.4° \times 0.4°$ smoothed with a Gaussian kernel of $\sigma = 0.5°$ (bottom panel).

```
AND
ruwe<1.3
AND
astrometric_excess_noise_sig<2
```

The following describes the polygon edges used to select RGB and RC stars by means of TOPCAT:

```
isInside(bp0-rp0, g0, 1.0, 18.35, 1.1, 17.5, 1.25, 16.7, 1.65, 15.50, 2.1,
15.50, 1.6, 16.60, 1.35, 17.65, 1.15, 18.9, 0.9, 18.90, 0.9, 18.35)
```

D.1 Density maps of the outer LMC

In this section we show the density map of the LMC as depicted in Fig.8.4, with different choices of bin size and width of the kernel function. To enhance the small substructures we adopted narrower kernel function, while to have a global view of the outer LMC we set a larger bin size and shallower kernel function.

Bibliography

N. C. Amorisco. Globular cluster populations and the kinematical fingerprints of minor mergers. *Monthly Notices of the Royal Astronomical Society*, 482:2978–2990, Jan. 2019. doi: 10.1093/mnras/sty2927.

N. C. Amorisco, N. W. Evans, and G. van de Ven. The remnant of a merger between two dwarf galaxies in Andromeda II. *Nature*, 507(7492):335–337, Mar. 2014. doi: 10.1038/nature12995.

F. Annibali, C. Nipoti, L. Ciotti, M. Tosi, A. Aloisi, M. Bellazzini, M. Cignoni, F. Cusano, D. Paris, and E. Sacchi. DDO 68: A Flea with Smaller Fleas that on Him Prey. *The Astrophysical Journal Letters*, 826(2):L27, Aug. 2016. doi: 10.3847/2041-8205/826/2/L27.

B. Armstrong and K. Bekki. Formation of a counter-rotating stellar population in the Large Magellanic Cloud: a Magellanic triplet system? *Monthly Notices of the Royal Astronomical Society*, 480(1):L141–L145, Oct. 2018. doi: 10.1093/mnrasl/sly143.

M. Arnaboldi, J. A. L. Aguerri, N. R. Napolitano, O. Gerhard, K. C. Freeman, J. Feldmeier, M. Capaccioli, R. P. Kudritzki, and R. H. Méndez. Intracluster Planetary Nebulae in Virgo: Photometric Selection, Spectroscopic Validation, and Cluster Depth. *The Astronomical Journal*, 123(2):760–771, Feb. 2002. doi: 10.1086/338313.

M. Arnaboldi, O. Gerhard, J. A. L. Aguerri, K. C. Freeman, N. R. Napolitano, S. Okamura, and N. Yasuda. The Line-of-Sight Velocity Distributions of Intracluster Planetary Nebulae in the Virgo Cluster Core. *The astrophysical journal, Letters*, 614:L33–L36, Oct. 2004. doi: 10.1086/425417.

M. Arnaboldi, G. Ventimiglia, E. Iodice, O. Gerhard, and L. Coccato. A tale of two tails and an off-centered envelope: diffuse light around the cD galaxy NGC 3311 in the Hydra I cluster. *Astronomy and Astrophysics*, 545:A37, Sept. 2012. doi: 10.1051/0004-6361/201116752.

K. M. Ashman and S. E. Zepf. *Globular Cluster Systems*. 2008.

G. Bagheri, M. R. L. Cioni, and R. Napiwotzki. The detection of an older population in the Magellanic Bridge. *Astronomy & Astrophysics*, 551:A78, Mar. 2013. doi: 10.1051/0004-6361/201118236.

E. Balbinot, B. X. Santiago, L. Girardi, A. Pieres, L. N. da Costa, M. A. G. Maia, R. A. Gruendl, A. R. Walker, B. Yanny, A. Drlica-Wagner, A. Benoit-Levy, T. M. C. Abbott, S. S. Allam, J. Annis, J. P. Bernstein, R. A. Bernstein, E. Bertin, D. Brooks, E. Buckley-Geer, A. C. Rosell, C. E. Cunha, D. L. DePoy, S. Desai, H. T. Diehl, P. Doel, J. Estrada, A. E. Evrard, A. F. Neto, D. A. Finley, B. Flaugher, J. A. Frieman, D. Gruen, K. Honscheid, D. James, K. Kuehn, N. Kuropatkin, O. Lahav, M. March, J. L. Marshall, C. Miller, R. Miquel, R. Ogando, J. Peoples, A. Plazas, V. Scarpine, M. Schubnell, I. Sevilla-Noarbe, R. C. Smith, M. Soares-Santos, E. Suchyta, M. E. C. Swanson, G. Tarle, D. L. Tucker, R. Wechsler, and J. Zuntz. The LMC geometry and outer stellar populations from early DES data. *Monthly Notices of the Royal Astronomical Society*, 449(1):1129–1145, May 2015. doi: 10.1093/mnras/stv356.

S. Banerjee and P. Kroupa. How can young massive clusters reach their present-day sizes? *Astronomy & Astrophysics*, 597:A28, Jan. 2017. doi: 10.1051/0004-6361/201526928.

J. Barnes and P. Hut. A hierarchical O(N log N) force-calculation algorithm. *Nature*, 324(6096): 446–449, Dec 1986. doi: 10.1038/324446a0.

L. P. Bassino, F. R. Faifer, J. C. Forte, B. Dirsch, T. Richtler, D. Geisler, and Y. Schuberth. Large-scale study of the NGC 1399 globular cluster system in Fornax. *Astronomy & Astrophysics*, 451(3):789–796, June 2006. doi: 10.1051/0004-6361:20054563.

N. Bastian, M. Gieles, S. P. Goodwin, G. Trancho, L. J. Smith, I. Konstantopoulos, and Y. Efremov. The early expansion of cluster cores. *Monthly Notices of the Royal Astronomical Society*, 389(1):223–230, Sept. 2008. doi: 10.1111/j.1365-2966.2008.13547.x.

N. Bastian, A. Adamo, M. Gieles, E. Silva-Villa, H. J. G. L. M. Lamers, S. S. Larsen, L. J. Smith, I. S. Konstantopoulos, and E. Zackrisson. Stellar clusters in M83: formation, evolution, disruption and the influence of the environment. *Monthly Notices of the Royal Astronomical Society*, 419(3):2606–2622, Jan. 2012. doi: 10.1111/j.1365-2966.2011.19909.x.

H. Baumgardt and M. Hilker. A catalogue of masses, structural parameters, and velocity dispersion profiles of 112 Milky Way globular clusters. *Monthly Notices of the Royal Astronomical Society*, 478(2):1520–1557, Aug. 2018. doi: 10.1093/mnras/sty1057.

H. Baumgardt and P. Kroupa. A comprehensive set of simulations studying the influence of gas expulsion on star cluster evolution. *Monthly Notices of the Royal Astronomical Society*, 380 (4):1589–1598, Oct. 2007. doi: 10.1111/j.1365-2966.2007.12209.x.

H. Baumgardt and J. Makino. Dynamical evolution of star clusters in tidal fields. *Monthly Notices of the Royal Astronomical Society*, 340(1):227–246, Mar 2003. doi: 10.1046/j.1365-8711.2003.06286.x.

H. Baumgardt, P. Hut, and D. C. Heggie. Long-term evolution of isolated N-body systems. *Monthly Notices of the Royal Astronomical Society*, 336(4):1069–1081, Nov 2002. doi: 10.1046/j.1365-8711.2002.05736.x.

H. Baumgardt, J. Makino, and T. Ebisuzaki. Massive Black Holes in Star Clusters. I. Equal-Mass Clusters. *The Astrophysical Journal*, 613(2):1133–1142, Oct. 2004a. doi: 10.1086/423298.

H. Baumgardt, J. Makino, and T. Ebisuzaki. Massive Black Holes in Star Clusters. II. Realistic Cluster Models. *The Astrophysical Journal*, 613(2):1143–1156, Oct. 2004b. doi: 10.1086/423299.

H. Baumgardt, G. Parmentier, P. Anders, and E. K. Grebel. The star cluster formation history of the LMC. *Monthly Notices of the Royal Astronomical Society*, 430(1):676–685, 2013. ISSN 00358711. doi: 10.1093/mnras/sts667.

K. Bechtol, A. Drlica-Wagner, E. Balbinot, A. Pieres, J. D. Simon, B. Yanny, B. Santiago, R. H. Wechsler, J. Frieman, A. R. Walker, P. Williams, E. Rozo, E. S. Rykoff, A. Queiroz, E. Luque, A. Benoit-Lévy, D. Tucker, I. Sevilla, R. A. Gruendl, L. N. da Costa, A. Fausti Neto, M. A. G. Maia, T. Abbott, S. Allam, R. Armstrong, A. H. Bauer, G. M. Bernstein, R. A. Bernstein, E. Bertin, D. Brooks, E. Buckley-Geer, D. L. Burke, A. Carnero Rosell, F. J. Castander, R. Covarrubias, C. B. D'Andrea, D. L. DePoy, S. Desai, H. T. Diehl, T. F. Eifler, J. Estrada, A. E. Evrard, E. Fernandez, D. A. Finley, B. Flaugher, E. Gaztanaga, D. Gerdes, L. Girardi, M. Gladders, D. Gruen, G. Gutierrez, J. Hao, K. Honscheid, B. Jain, D. James, S. Kent, R. Kron, K. Kuehn, N. Kuropatkin, O. Lahav, T. S. Li, H. Lin, M. Makler, M. March, J. Marshall, P. Martini, K. W. Merritt, C. Miller, R. Miquel, J. Mohr, E. Neilsen, R. Nichol,

B. Nord, R. Ogando, J. Peoples, D. Petravick, A. A. Plazas, A. K. Romer, A. Roodman, M. Sako, E. Sanchez, V. Scarpine, M. Schubnell, R. C. Smith, M. Soares-Santos, F. Sobreira, E. Suchyta, M. E. C. Swanson, G. Tarle, J. Thaler, D. Thomas, W. Wester, J. Zuntz, and DES Collaboration. Eight New Milky Way Companions Discovered in First-year Dark Energy Survey Data. *The Astrophysical Journal*, 807(1):50, July 2015. doi: 10.1088/0004-637X/807/1/50.

K. Bekki and M. Chiba. Formation and evolution of the Magellanic Clouds - I. Origin of structural, kinematic and chemical properties of the Large Magellanic Cloud. *Monthly Notices of the Royal Astronomical Society*, 356(2):680–702, Jan 2005. doi: 10.1111/j.1365-2966.2004.08510.x.

M. Bellazzini, E. Pancino, F. R. Ferraro, and P. B. Stetson. Confirming Bologna A: An Old Star Cluster in the SMC. *Research Notes of the American Astronomical Society*, 3(3):47, Mar. 2019. doi: 10.3847/2515-5172/ab0c0d.

V. Belokurov and S. E. Koposov. Stellar streams around the Magellanic Clouds. *Monthly Notices of the Royal Astronomical Society*, 456(1):602–616, Feb. 2016. doi: 10.1093/mnras/stv2688.

V. Belokurov, D. B. Zucker, N. W. Evans, G. Gilmore, S. Vidrih, D. M. Bramich, H. J. Newberg, R. F. G. Wyse, M. J. Irwin, M. Fellhauer, P. C. Hewett, N. A. Walton, M. I. Wilkinson, N. Cole, B. Yanny, C. M. Rockosi, T. C. Beers, E. F. Bell, J. Brinkmann, Ž. Ivezić, and R. Lupton. The Field of Streams: Sagittarius and Its Siblings. *The Astrophysical Journal Letters*, 642(2): L137–L140, May 2006. doi: 10.1086/504797.

V. Belokurov, D. Erkal, N. W. Evans, S. E. Koposov, and A. J. Deason. Co-formation of the disc and the stellar halo. *Monthly Notices of the Royal Astronomical Society*, 478(1):611–619, July 2018. doi: 10.1093/mnras/sty982.

V. Belokurov, A. J. Deason, D. Erkal, S. E. Koposov, J. A. Carballo-Bello, M. C. Smith, P. Jethwa, and C. Navarrete. The Pisces Plume and the Magellanic wake. *Monthly Notices of the Royal Astronomical Society*, 488(1):L47–L52, Sept. 2019. doi: 10.1093/mnrasl/slz101.

V. A. Belokurov and D. Erkal. Clouds in arms. *Monthly Notices of the Royal Astronomical Society*, 482(1):L9–L13, Jan 2019. doi: 10.1093/mnrasl/sly178.

G. Besla, N. Kallivayalil, L. Hernquist, B. Robertson, T. J. Cox, R. P. van der Marel, and C. Alcock. Are the Magellanic Clouds on Their First Passage about the Milky Way? *The Astrophysical Journal*, 668(2):949–967, Oct 2007. doi: 10.1086/521385.

G. Besla, N. Kallivayalil, L. Hernquist, R. P. van der Marel, T. J. Cox, and D. Kereš. Simulations of the Magellanic Stream in a First Infall Scenario. *The Astrophysical Journal Letters*, 721(2): L97–L101, Oct 2010. doi: 10.1088/2041-8205/721/2/L97.

G. Besla, N. Kallivayalil, L. Hernquist, R. P. van der Marel, T. J. Cox, and D. Kereš. The role of dwarf galaxy interactions in shaping the Magellanic System and implications for Magellanic Irregulars. *Monthly Notices of the Royal Astronomical Society*, 421(3):2109–2138, Apr 2012. doi: 10.1111/j.1365-2966.2012.20466.x.

G. Besla, D. Martínez-Delgado, R. P. van der Marel, Y. Beletsky, M. Seibert, E. F. Schlafly, E. K. Grebel, and F. Neyer. Low Surface Brightness Imaging of the Magellanic System: Imprints of Tidal Interactions between the Clouds in the Stellar Periphery. *The Astrophysical Journal*, 825(1):20, July 2016. doi: 10.3847/0004-637X/825/1/20.

E. Bica, D. Geisler, H. Dottori, J. J. Clariá, A. E. Piatti, and J. Santos, João F. C. Ages and Metallicities of Star Clusters and Surrounding Fields in the Outer Disk of the Large Magellanic Cloud. *The Astronomical Journal*, 116(2):723–737, Aug. 1998. doi: 10.1086/300448.

E. Bica, C. Bonatto, C. M. Dutra, and J. F. Santos. A general catalogue of extended objects in the Magellanic system. *Monthly Notices of the Royal Astronomical Society*, 389(2):678–690, sep 2008. ISSN 00358711. doi: 10.1111/j.1365-2966.2008.13612.x.

E. Bica, B. Santiago, C. Bonatto, R. Garcia-Dias, L. Kerber, B. Dias, B. Barbuy, and E. Balbinot. Bridge over troubled gas: clusters and associations under the SMC and LMC tidal stresses. *Monthly Notices of the Royal Astronomical Society*, 453(3):3190–3202, Nov. 2015. doi: 10.1093/mnras/stv1720.

E. Bica, P. Westera, L. d. O. Kerber, B. Dias, F. Maia, J. Santos, João F. C., B. Barbuy, and R. A. P. Oliveira. An Updated Small Magellanic Cloud and Magellanic Bridge Catalog of Star Clusters, Associations, and Related Objects. *The Astronomical Journal*, 159(3):82, Mar. 2020. doi: 10.3847/1538-3881/ab6595.

J. P. Blakeslee, A. Jordán, S. Mei, P. Côté, L. Ferrarese, L. Infante, E. W. Peng, J. L. Tonry, and M. J. West. The ACS Fornax Cluster Survey. V. Measurement and Recalibration of Surface Brightness Fluctuations and a Precise Value of the Fornax-Virgo Relative Distance. *The Astrophysical Journal*, 694(1):556–572, Mar. 2009. doi: 10.1088/0004-637X/694/1/556.

A. Bluck, C. Conselice, F. Buitrago, R. Grútzbauch, C. Hoyos, A. Mortlock, and A. Bauer. The structures and total (minor + major) merger histories of massive galaxies up to $z \sim 3$ in the hst goods nicmos survey: A possible solution to the size evolution problem. *The astrophysical journal*, 747:34, mar 2012. doi: 10.1088/0004-637X/747/1/34.

C. Bonatto and E. Bica. The nature of the young and low-mass open clusters Pismis5, vdB80, NGC1931 and BDSB96. *Monthly Notices of the Royal Astronomical Society*, 397(4):1915–1925, Aug 2009. doi: 10.1111/j.1365-2966.2009.14877.x.

C. Bonatto and E. Bica. VizieR Online Data Catalog: Clusters and associations in SMC and LMC. *VizieR Online Data Catalog*, art. J/MNRAS/403/996, Sep 2010.

M. Boylan-Kolchin, G. Besla, and L. Hernquist. Dynamics of the Magellanic Clouds in a Lambda cold dark matter universe. *Monthly Notices of the Royal Astronomical Society*, 414(2):1560–1572, June 2011. doi: 10.1111/j.1365-2966.2011.18495.x.

L. Bradley, B. Sipőcz, T. Robitaille, E. Tollerud, Z. Vinícius, C. Deil, K. Barbary, T. J. Wilson, I. Busko, H. M. Günther, M. Cara, S. Conseil, M. Droettboom, A. Bostroem, E. M. Bray, L. A. Bratholm, P. L. Lim, M. Craig, G. Barentsen, S. Pascual, A. Donath, J. Greco, G. Perren, W. Kerzendorf, M. de Val-Borro, N. Dencheva, L. de Albernaz Ferreira, H. Souchereau, F. D'Eugenio, and B. A. Weaver. astropy/photutils: v0.7.2, Dec. 2019. URL `https://doi.org/10.5281/zenodo.3568287`.

A. Bressan, P. Marigo, L. Girardi, B. Salasnich, C. Dal Cero, S. Rubele, and A. Nanni. PARSEC: stellar tracks and isochrones with the PAdova and TRieste Stellar Evolution Code. *Monthly Notices of the Royal Astronomical Society*, 427(1):127–145, Nov 2012. doi: 10.1111/j.1365-2966.2012.21948.x.

C. Brüns, J. Kerp, L. Staveley-Smith, U. Mebold, M. E. Putman, R. F. Haynes, P. M. W. Kalberla, E. Muller, and M. D. Filipovic. The Parkes H I Survey of the Magellanic System. *Astronomy & Astrophysics*, 432(1):45–67, Mar 2005. doi: 10.1051/0004-6361:20040321.

F. Buitrago, I. Trujillo, C. J. Conselice, R. J. Bouwens, M. Dickinson, and H. Yan. Size evolution of the most massive galaxies at $1.7 < z < 3$ from goods nicmos survey imaging. *The Astrophysical Journal*, 687, 11 2008. doi: 10.1086/592836. URL `http://gen.lib.rus.ec/scimag/index.php?s=10.1086/592836`.

J. S. Bullock and K. V. Johnston. Tracing Galaxy Formation with Stellar Halos. I. Methods. *The Astrophysical Journal*, 635:931–949, Dec. 2005. doi: 10.1086/497422.

M. Cantiello, A. Venhola, A. Grado, M. Paolillo, R. D'Abrusco, G. Raimondo, M. Quintini, M. Hilker, S. Mieske, C. Tortora, M. Spavone, M. Capaccioli, E. Iodice, R. Peletier, J. F. Barroso, L. Limatola, N. Napolitano, P. Schipani, G. van de Ven, F. Gentile, and G. Covone. The Fornax Deep Survey with VST. IX. Catalog of sources in the FDS area with an example study for globular clusters and background galaxies. *Astronomy & Astrophysics*, 639:A136, July 2020. doi: 10.1051/0004-6361/202038137.

M. Capaccioli and P. Schipani. The VLT Survey Telescope Opens to the Sky: History of a Commissioning. *The Messenger*, 146:2–7, Dec 2011.

R. Carini, K. Biazzo, E. Brocato, L. Pulone, and L. Pasquini. MUSE Observations of NGC330 in the Small Magellanic Cloud: Helium Abundance of Bright Main-sequence Stars. *The Astronomical Journal*, 159(4):152, Apr. 2020. doi: 10.3847/1538-3881/ab7334.

J. L. Carlin and D. J. Sand. Boötes III is a Disrupting Dwarf Galaxy Associated with the Styx Stellar Stream. *The Astrophysical Journal*, 865(1):7, Sept. 2018. doi: 10.3847/1538-4357/aad8c1.

R. Carrera, C. Gallart, A. Aparicio, and E. Hardy. Metallicities, Age-Metallicity Relationships, and Kinematics of Red Giant Branch Stars in the Outer Disk of the Large Magellanic Cloud. *The Astronomical Journal*, 142(2):61, Aug 2011. doi: 10.1088/0004-6256/142/2/61.

R. Carrera, B. C. Conn, N. E. D. Noël, J. I. Read, and Á. R. López Sánchez. The Magellanic Inter-Cloud Project (MAGIC) III: first spectroscopic evidence of a dwarf stripping a dwarf. *Monthly Notices of the Royal Astronomical Society*, 471(4):4571–4578, Nov. 2017. doi: 10.1093/mnras/stx1932.

L. Carvalho, T. A. Saurin, E. Bica, C. Bonatto, and A. A. Schmidt. Structures in surface-brightness profiles of LMC and SMC star clusters: evidence of mergers? *Astronomy & Astrophysics*, 485(1):71–80, July 2008. doi: 10.1051/0004-6361:20079298.

P. Cassata, M. Giavalisco, C. C. Williams, Y. Guo, B. Lee, A. Renzini, S. F. Ferguson, H.and Faber, G. Barro, D. H. McIntosh, Y. Lu, E. F. Bell, D. C. Koo, C. J. Papovich, R. E. Ryan, C. J. Conselice, N. Grogin, A. Koekemoer, and N. P. Hathi. Constraining the assembly of normal and compact passively evolving galaxies from redshift z = 3 to the present

with candels. *The Astrophysical Journal*, 775, 10 2013. doi: 10.1088/0004-637X/775/2/106. URL `http://gen.lib.rus.ec/scimag/index.php?s=10.1088/0004-637X/775/2/106`.

R. Chandar, B. C. Whitmore, D. Dinino, R. C. Kennicutt, L. H. Chien, E. Schinnerer, and S. Meidt. The Age, Mass, and Size Distributions of Star Clusters in M51. *The Astrophysical Journal*, 824(2):71, June 2016. doi: 10.3847/0004-637X/824/2/71.

I. V. Chilingarian, P. Di Matteo, F. Combes, A. L. Melchior, and B. Semelin. The GalMer database: galaxy mergers in the virtual observatory. *Astronomy & Astrophysics*, 518:A61, July 2010. doi: 10.1051/0004-6361/200912938.

E. Chiosi, A. Vallenari, E. V. Held, L. Rizzi, and A. Moretti. Age distribution of young clusters and field stars in the Small Magellanic Cloud. *Astronomy & Astrophysics*, 452(1):179–193, June 2006. doi: 10.1051/0004-6361:20054559.

Y. Choi, D. L. Nidever, K. Olsen, G. Besla, R. D. Blum, D. Zaritsky, M.-R. L. Cioni, R. P. van der Marel, E. F. Bell, L. C. Johnson, A. K. Vivas, A. R. Walker, T. J. L. de Boer, N. E. D. Noël, A. Monachesi, C. Gallart, M. Monelli, G. S. Stringfellow, P. Massana, D. Martinez-Delgado, and R. R. Muñoz. SMASHing the LMC: Mapping a Ring-like Stellar Overdensity in the LMC Disk. *The Astrophysical Journal*, 869(2):125, Dec. 2018a. doi: 10.3847/1538-4357/aaed1f.

Y. Choi, D. L. Nidever, K. Olsen, R. D. Blum, G. Besla, D. Zaritsky, R. P. van der Marel, E. F. Bell, C. Gallart, M.-R. L. Cioni, L. C. Johnson, A. K. Vivas, A. Saha, T. J. L. de Boer, N. E. D. Noël, A. Monachesi, P. Massana, B. C. Conn, D. Martinez-Delgado, R. R. Muñoz, and G. S. Stringfellow. SMASHing the LMC: A Tidally Induced Warp in the Outer LMC and a Large-scale Reddening Map. *The Astrophysical Journal*, 866(2):90, Oct 2018b. doi: 10.3847/1538-4357/aae083.

Y. Choi, K. A. G. Olsen, G. Besla, R. P. van der Marel, P. Zivick, N. Kallivayalil, and D. L. Nidever. The recent LMC-SMC collision: Timing and impact parameter constraints from comparison of Gaia LMC disk kinematics and N-body simulations. *arXiv e-prints*, art. arXiv:2201.04648, Jan. 2022.

S. Choudhury, A. Subramaniam, and A. A. Cole. Photometric metallicity map of the Large Magellanic Cloud. *Monthly Notices of the Royal Astronomical Society*, 455(2):1855–1880, Jan. 2016. doi: 10.1093/mnras/stv2414.

S. Choudhury, R. de Grijs, K. Bekki, M.-R. L. Cioni, V. D. Ivanov, J. T. van Loon, A. E. Miller, F. Niederhofer, J. M. Oliveira, V. Ripepi, N.-C. Sun, and S. Subramanian. The VMC survey - XLIV: mapping metallicity trends in the large magellanic cloud using near-infrared passbands. *Monthly Notices of the Royal Astronomical Society*, 507(4):4752–4763, Nov. 2021. doi: 10.1093/mnras/stab2446.

M. Cignoni, A. A. Cole, M. Tosi, J. S. Gallagher, E. Sabbi, J. Anderson, E. K. Grebel, and A. Nota. Mean Age Gradient and Asymmetry in the Star Formation History of the Small Magellanic Cloud. *The Astrophysical Journal*, 775(2):83, Oct 2013. doi: 10.1088/0004-637X/775/2/83.

M. Cignoni, E. Sabbi, R. P. van der Marel, D. J. Lennon, M. Tosi, E. K. Grebel, I. Gallagher, J. S., A. Aloisi, G. de Marchi, D. A. Gouliermis, S. Larsen, N. Panagia, and L. J. Smith. Hubble Tarantula Treasury Project V. The Star Cluster Hodge 301: The Old Face of 30 Doradus. *The Astrophysical Journal*, 833(2):154, Dec. 2016. doi: 10.3847/1538-4357/833/2/154.

M. . R. L. Cioni, J. Storm, C. P. M. Bell, B. Lemasle, F. Niederhofer, J. M. Bestenlehner, D. El Youssoufi, S. Feltzing, C. González-Fernández, E. K. Grebel, D. Hobbs, M. Irwin, P. Jablonka, A. Koch, O. Schnurr, T. Schmidt, and M. Steinmetz. 4MOST Consortium Survey 9: One Thousand and One Magellanic Fields (1001MC). *The Messenger*, 175:54–57, Mar. 2019. doi: 10.18727/0722-6691/5128.

M. R. L. Cioni. The metallicity gradient as a tracer of history and structure: the Magellanic Clouds and M33 galaxies. *Astronomy & Astrophysics*, 506(3):1137–1146, Nov 2009. doi: 10.1051/0004-6361/200912138.

M. R. L. Cioni, G. Clementini, L. Girardi, R. Guand alini, M. Gullieuszik, B. Miszalski, M. I. Moretti, V. Ripepi, S. Rubele, G. Bagheri, K. Bekki, N. Cross, W. J. G. de Blok, R. de Grijs, J. P. Emerson, C. J. Evans, B. Gibson, E. Gonzales-Solares, M. A. T. Groenewegen, M. Irwin, V. D. Ivanov, J. Lewis, M. Marconi, J. B. Marquette, C. Mastropietro, B. Moore, R. Napiwotzki, T. Naylor, J. M. Oliveira, M. Read, E. Sutorius, J. T. van Loon, M. I. Wilkinson, and P. R. Wood. The VMC survey. I. Strategy and first data. *Astronomy & Astrophysics*, 527: A116, Mar 2011. doi: 10.1051/0004-6361/201016137.

J. J. Clariá, A. E. Piatti, J. Santos, J. F. C., E. Bica, A. V. Ahumada, and M. C. Parisi. Spectroscopic study of star clusters in the Small Magellanic Cloud: star formation history. *Boletin de la Asociacion Argentina de Astronomia La Plata Argentina*, 48:140–145, Jan 2005.

G. Clementini, V. Ripepi, R. Molinaro, A. Garofalo, T. Muraveva, L. Rimoldini, L. P. Guy, G. Jevardat de Fombelle, K. Nienartowicz, O. Marchal, M. Audard, B. Holl, S. Leccia, M. Marconi, I. Musella, N. Mowlavi, I. Lecoeur-Taibi, L. Eyer, J. De Ridder, S. Regibo, L. M. Sarro, L. Szabados, D. W. Evans, and M. Riello. Gaia Data Release 2. Specific characterisation and validation of all-sky Cepheids and RR Lyrae stars. *Astronomy & Astrophysics*, 622:A60, Feb. 2019. doi: 10.1051/0004-6361/201833374.

L. Coccato, M. Arnaboldi, and O. Gerhard. Signatures of accretion events in the haloes of early-type galaxies from comparing PNe and GCs kinematics. *Monthly Notices of the RAS*, 436: 1322–1334, Dec. 2013. doi: 10.1093/mnras/stt1649.

T. W. Connors, D. Kawata, S. T. Maddison, and B. K. Gibson. High-Resolution N-body Simulations of Galactic Cannibalism: The Magellanic Stream. *Publications of the Astron. Soc. of Australia*, 21(2):222–227, Jan 2004. doi: 10.1071/AS04014.

T. W. Connors, D. Kawata, and B. K. Gibson. N-body simulations of the Magellanic stream. *Monthly Notices of the Royal Astronomical Society*, 371(1):108–120, Sep 2006. doi: 10.1111/j.1365-2966.2006.10659.x.

C. Conroy, R. P. Naidu, N. Garavito-Camargo, G. Besla, D. Zaritsky, A. Bonaca, and B. D. Johnson. All-sky dynamical response of the Galactic halo to the Large Magellanic Cloud. *Nature*, 592(7855):534–536, Apr. 2021. doi: 10.1038/s41586-021-03385-7.

A. Cooper, S. Cole, C. Frenk, S. White, J. Helly, A. Benson, G. De Lucia, A. Helmi, A. Jenkins, J. Navarro, V. Springel, and J. Wang. Galactic stellar haloes in the CDM model. *Monthly notices of the royal astronomical society*, 406:744–766, Aug. 2010. doi: 10.1111/j.1365-2966.2010.16740.x.

A. P. Cooper, L. Gao, Q. Guo, C. S. Frenk, A. Jenkins, V. Springel, and S. D. M. White. Surface photometry of brightest cluster galaxies and intracluster stars in ΛCDM. *Monthly Notices of the Royal Astronomical Society*, 451(3):2703–2722, Aug. 2015. doi: 10.1093/mnras/stv1042.

A. Cortesi, M. R. Merrifield, M. Arnaboldi, O. Gerhard, I. Martinez-Valpuesta, K. Saha, L. Coccato, S. Bamford, N. R. Napolitano, P. Das, N. G. Douglas, A. J. Romanowsky, K. Kuijken, M. Capaccioli, and K. C. Freeman. Unravelling the origins of S0 galaxies using maximum likelihood analysis of planetary nebulae kinematics. *Monthly Notices of the Royal Astronomical Society*, 414:642–651, June 2011. doi: 10.1111/j.1365-2966.2011.18429.x.

L. R. Cullinane, A. D. Mackey, G. S. Da Costa, D. Erkal, S. E. Koposov, and V. Belokurov. The Magellanic Edges Survey - II. Formation of the LMC's northern arm. *Monthly Notices of the Royal Astronomical Society*, 510(1):445–468, Feb. 2022. doi: 10.1093/mnras/stab3350.

F. Cusano, M. I. Moretti, G. Clementini, V. Ripepi, M. Marconi, M. R. L. Cioni, S. Rubele, A. Garofalo, R. de Grijs, M. A. T. Groenewegen, J. M. Oliveira, S. Subramanian, N. C. Sun, and J. T. van Loon. The VMC Survey - XLII. Near-infrared period-luminosity relations for RR Lyrae stars and the structure of the Large Magellanic Cloud. *Monthly Notices of the Royal Astronomical Society*, 504(1):1–15, June 2021. doi: 10.1093/mnras/stab901.

G. S. Da Costa. The Age-Abundance Relations and Age Distributions for the Star Clusters of the Magellanic Clouds. In R. Haynes and D. Milne, editors, *The Magellanic Clouds*, volume 148 of *IAU Symposium*, page 183, Jan 1991.

G. S. Da Costa. The Star Cluster Systems of the Magellanic Clouds. In D. P. Geisler, E. K. Grebel, and D. Minniti, editors, *Extragalactic Star Clusters*, volume 207, page 83, Jan. 2002.

G. S. Da Costa and D. Hatzidimitriou. Ca II Triplet Spectroscopy of Giants in Small Magellanic Cloud Star Clusters: Abundances, Velocities, and the Age-Metallicity Relation. *The Astronomical Journal*, 115(5):1934–1945, May 1998. doi: 10.1086/300340.

R. D'Abrusco, M. Cantiello, M. Paolillo, V. Pota, N. R. Napolitano, L. Limatola, M. Spavone, A. Grado, E. Iodice, M. Capaccioli, R. Peletier, G. Longo, M. Hilker, S. Mieske, E. K. Grebel, T. Lisker, C. Wittmann, G. van de Ven, P. Schipani, and G. Fabbiano. The Extended Spatial Distribution of Globular Clusters in the Core of the Fornax Cluster. *Astrophysical Journal, Letters*, 819:L31, Mar. 2016. doi: 10.3847/2041-8205/819/2/L31.

Dark Energy Survey Collaboration, T. Abbott, F. B. Abdalla, J. Aleksić, S. Allam, A. Amara, D. Bacon, E. Balbinot, M. Banerji, K. Bechtol, A. Benoit-Lévy, G. M. Bernstein, E. Bertin, J. Blazek, C. Bonnett, S. Bridle, D. Brooks, R. J. Brunner, E. Buckley-Geer, D. L. Burke, G. B. Caminha, D. Capozzi, J. Carlsen, A. Carnero-Rosell, M. Carollo, M. Carrasco-Kind, J. Carretero, F. J. Castander, L. Clerkin, T. Collett, C. Conselice, M. Crocce, C. E. Cunha, C. B. D'Andrea, L. N. da Costa, T. M. Davis, S. Desai, H. T. Diehl, J. P. Dietrich, S. Dodelson, P. Doel, A. Drlica-Wagner, J. Estrada, J. Etherington, A. E. Evrard, J. Fabbri, D. A. Finley, B. Flaugher, R. J. Foley, P. Fosalba, J. Frieman, J. García-Bellido, E. Gaztanaga, D. W. Gerdes, T. Giannantonio, D. A. Goldstein, D. Gruen, R. A. Gruendl, P. Guarnieri, G. Gutierrez, W. Hartley, K. Honscheid, B. Jain, D. J. James, T. Jeltema, S. Jouvel, R. Kessler, A. King,

D. Kirk, R. Kron, K. Kuehn, N. Kuropatkin, O. Lahav, T. S. Li, M. Lima, H. Lin, M. A. G. Maia, M. Makler, M. Manera, C. Maraston, J. L. Marshall, P. Martini, R. G. McMahon, P. Melchior, A. Merson, C. J. Miller, R. Miquel, J. J. Mohr, X. Morice-Atkinson, K. Naidoo, E. Neilsen, R. C. Nichol, B. Nord, R. Ogando, F. Ostrovski, A. Palmese, A. Papadopoulos, H. V. Peiris, J. Peoples, W. J. Percival, A. A. Plazas, S. L. Reed, A. Refregier, A. K. Romer, A. Roodman, A. Ross, E. Rozo, E. S. Rykoff, I. Sadeh, M. Sako, C. Sánchez, E. Sanchez, B. Santiago, V. Scarpine, M. Schubnell, I. Sevilla-Noarbe, E. Sheldon, M. Smith, R. C. Smith, M. Soares-Santos, F. Sobreira, M. Soumagnac, E. Suchyta, M. Sullivan, M. Swanson, G. Tarle, J. Thaler, D. Thomas, R. C. Thomas, D. Tucker, J. D. Vieira, V. Vikram, A. R. Walker, R. H. Wechsler, J. Weller, W. Wester, L. Whiteway, H. Wilcox, B. Yanny, Y. Zhang, and J. Zuntz. The Dark Energy Survey: more than dark energy - an overview. *Monthly Notices of the Royal Astronomical Society*, 460(2):1270–1299, Aug. 2016. doi: 10.1093/mnras/stw641.

R. de Grijs and G. Bono. Clustering of Local Group Distances: Publication Bias or Correlated Measurements? III. The Small Magellanic Cloud. *The Astronomical Journal*, 149:179, June 2015. doi: 10.1088/0004-6256/149/6/179.

R. de Grijs, N. Bastian, and H. J. G. L. M. Lamers. The Missing Link in Star Cluster Evolution. *The Astrophysical Journal Letters*, 583(1):L17–L20, Jan. 2003. doi: 10.1086/367928.

R. de Grijs, J. E. Wicker, and G. Bono. Clustering of Local Group Distances: Publication Bias or Correlated Measurements? I. The Large Magellanic Cloud. *The Astronomical Journal*, 147: 122, May 2014. doi: 10.1088/0004-6256/147/5/122.

M. De Leo, R. Carrera, N. E. D. Noël, J. I. Read, D. Erkal, and C. Gallart. Revealing the tidal scars of the Small Magellanic Cloud. *Monthly Notices of the Royal Astronomical Society*, 495 (1):98–113, June 2020. doi: 10.1093/mnras/staa1122.

G. De Lucia and J. Blaizot. The hierarchical formation of the brightest cluster galaxies. *Monthly Notices of the Royal Astronomical Society*, 375:2–14, Feb. 2007. doi: 10.1111/j.1365-2966.2006.11287.x.

G. De Marchi, F. Paresce, N. Panagia, G. Beccari, L. Spezzi, M. Sirianni, M. Andersen, M. Mutchler, B. Balick, M. A. Dopita, J. A. Frogel, B. C. Whitmore, H. Bond, D. Calzetti, C. M. Carollo, M. J. Disney, D. N. B. Hall, J. A. Holtzman, R. A. Kimble, P. J. McCarthy, R. W. O'Connell, A. Saha, J. I. Silk, J. T. Trauger, A. R. Walker, R. A. Windhorst, and E. T.

Young. Star Formation in 30 Doradus. *The Astrophysical Journal*, 739(1):27, Sept. 2011. doi: 10.1088/0004-637X/739/1/27.

G. de Vaucouleurs. Recherches sur les Nebuleuses Extragalactiques. *Annales d'Astrophysique*, 11:247, Jan. 1948.

G. de Vaucouleurs. Studies of Magellanic Clouds. I. Dimensions and structure of the Large Cloud. *The Astronomical Journal*, 60:126, May 1955. doi: 10.1086/107173.

G. de Vaucouleurs and K. C. Freeman. Structure and dynamics of barred spiral galaxies, in particular of the Magellanic type. *Vistas in Astronomy*, 14(1):163–294, Jan 1972a. doi: 10.1016/0083-6656(72)90026-8.

G. de Vaucouleurs and K. C. Freeman. Structure and dynamics of barred spiral galaxies, in particular of the Magellanic type. *Vistas in Astronomy*, 14(1):163–294, Jan. 1972b. doi: 10.1016/0083-6656(72)90026-8.

A. J. Deason, V. Belokurov, S. E. Koposov, and L. Lancaster. Apocenter Pile-up: Origin of the Stellar Halo Density Break. *The Astrophysical Journal Letters*, 862(1):L1, July 2018. doi: 10.3847/2041-8213/aad0ee.

S. Deb, H. P. Singh, S. Kumar, and S. M. Kanbur. Morphology and metallicity of the Small Magellanic Cloud using RRab stars. *Monthly Notices of the Royal Astronomical Society*, 449 (3):2768–2783, May 2015. doi: 10.1093/mnras/stv358.

S. Demers and P. Battinelli. The Young Intercloud Population. I. Distances and Ages. *The Astronomical Journal*, 115(1):154–161, Jan. 1998. doi: 10.1086/300183.

E. M. Di Teodoro, N. M. McClure-Griffiths, K. E. Jameson, H. Dénes, J. M. Dickey, S. Stanimirović, L. Staveley-Smith, C. Anderson, J. D. Bunton, A. Chippendale, K. Lee-Waddell, A. MacLeod, and M. A. Voronkov. On the dynamics of the Small Magellanic Cloud through high-resolution ASKAP H I observations. *Monthly Notices of the Royal Astronomical Society*, 483(1):392–406, Feb. 2019. doi: 10.1093/mnras/sty3095.

B. Dias, L. O. Kerber, B. Barbuy, B. Santiago, S. Ortolani, and E. Balbinot. Self-consistent physical parameters for five intermediate-age SMC stellar clusters from CMD modelling. *Astronomy & Astrophysics*, 561:A106, Jan. 2014. doi: 10.1051/0004-6361/201322092.

B. Dias, L. Kerber, B. Barbuy, E. Bica, and S. Ortolani. SMC west halo: a slice of the galaxy that is being tidally stripped?. Star clusters trace age and metallicity gradients. *Astronomy & Astrophysics*, 591:A11, June 2016. doi: 10.1051/0004-6361/201527558.

J. D. Diaz and K. Bekki. The Tidal Origin of the Magellanic Stream and the Possibility of a Stellar Counterpart. *The Astrophysical Journal*, 750(1):36, May 2012. doi: 10.1088/0004-637X/750/1/36.

S. Djorgovski. Surface photometry of globular clusters. In J. E. Grindlay and A. G. D. Philip, editors, *The Harlow-Shapley Symposium on Globular Cluster Systems in Galaxies*, volume 126 of *IAU Symposium*, pages 333–345, jan 1988.

S. G. Djorgovski. Correlations of Globular Cluster Properties as Constraints for Dynamical Evolution Models. In P. Hut and J. Makino, editors, *Dynamical Evolution of Star Clusters: Confrontation of Theory and Observations*, volume 174 of *IAU Symposium*, page 9, jan 1996.

P. D. Dobbie, A. A. Cole, A. Subramaniam, and S. Keller. Red giants in the Small Magellanic Cloud - I. Disc and tidal stream kinematics. *Monthly Notices of the Royal Astronomical Society*, 442(2):1663–1679, Aug. 2014. doi: 10.1093/mnras/stu910.

A. E. Dolphin. The star formation histories of two northern LMC fields. *Monthly Notices of the Royal Astronomical Society*, 313(2):281–290, Apr. 2000. doi: 10.1046/j.1365-8711.2000.03197.x.

E. D'Onghia and A. J. Fox. The Magellanic Stream: Circumnavigating the Galaxy. *Annual Review of Astronomy & Astrophysics*, 54:363–400, Sept. 2016. doi: 10.1146/annurev-astro-081915-023251.

E. D'Onghia and G. Lake. Small Dwarf Galaxies within Larger Dwarfs: Why Some Are Luminous while Most Go Dark. *The Astrophysical Journal Letters*, 686(2):L61, Oct. 2008. doi: 10.1086/592995.

M. A. Dopita, G. H. Jacoby, and E. Vassiliadis. A Theoretical Calibration of the Planetary Nebular Cosmic Distance Scale. *The Astrophysical Journal*, 389:27, Apr. 1992. doi: 10.1086/171186.

N. G. Douglas, N. R. Napolitano, A. J. Romanowsky, L. Coccato, K. Kuijken, M. R. Merrifield, M. Arnaboldi, O. Gerhard, K. C. Freeman, H. R. Merrett, E. Noordermeer, and M. Capaccioli. The PN.S Elliptical Galaxy Survey: Data Reduction, Planetary Nebula Catalog,

and Basic Dynamics for NGC 3379. *The astrophysical journal*, 664:257–276, July 2007. doi: 10.1086/518358.

M. J. Drinkwater, M. D. Gregg, and M. Colless. Substructure and Dynamics of the Fornax Cluster. *The Astrophysical Journal Letters*, 548(2):L139–L142, Feb. 2001. doi: 10.1086/319113.

A. Drlica-Wagner, K. Bechtol, E. S. Rykoff, E. Luque, A. Queiroz, Y. Y. Mao, R. H. Wechsler, J. D. Simon, B. Santiago, B. Yanny, E. Balbinot, S. Dodelson, A. Fausti Neto, D. J. James, T. S. Li, M. A. G. Maia, J. L. Marshall, A. Pieres, K. Stringer, A. R. Walker, T. M. C. Abbott, F. B. Abdalla, S. Allam, A. Benoit-Lévy, G. M. Bernstein, E. Bertin, D. Brooks, E. Buckley-Geer, D. L. Burke, A. Carnero Rosell, M. Carrasco Kind, J. Carretero, M. Crocce, L. N. da Costa, S. Desai, H. T. Diehl, J. P. Dietrich, P. Doel, T. F. Eifler, A. E. Evrard, D. A. Finley, B. Flaugher, P. Fosalba, J. Frieman, E. Gaztanaga, D. W. Gerdes, D. Gruen, R. A. Gruendl, G. Gutierrez, K. Honscheid, K. Kuehn, N. Kuropatkin, O. Lahav, P. Martini, R. Miquel, B. Nord, R. Ogando, A. A. Plazas, K. Reil, A. Roodman, M. Sako, E. Sanchez, V. Scarpine, M. Schubnell, I. Sevilla-Noarbe, R. C. Smith, M. Soares-Santos, F. Sobreira, E. Suchyta, M. E. C. Swanson, G. Tarle, D. Tucker, V. Vikram, W. Wester, Y. Zhang, J. Zuntz, and DES Collaboration. Eight Ultra-faint Galaxy Candidates Discovered in Year Two of the Dark Energy Survey. *The Astrophysical Journal*, 813(2):109, Nov. 2015. doi: 10.1088/0004-637X/813/2/109.

P. R. Durrell, J. C. Mihos, J. J. Feldmeier, G. H. Jacoby, and R. Ciardullo. Kinematics of Planetary Nebulae in M51's Tidal Debris. *The Astrophysical Journal*, 582:170–183, Jan. 2003. doi: 10.1086/344612.

P. Eigenthaler, T. H. Puzia, M. A. Taylor, Y. Ordenes-Briceño, R. P. Muñoz, K. X. Ribbeck, K. A. Alamo-Martínez, H. Zhang, S. Ángel, M. Capaccioli, P. Côté, L. Ferrarese, G. Galaz, E. K. Grebel, M. Hempel, M. Hilker, A. Lançon, S. Mieske, B. Miller, M. Paolillo, M. Powalka, T. Richtler, J. Roediger, Y. Rong, R. Sánchez-Janssen, and C. Spengler. The Next Generation Fornax Survey (NGFS). II. The Central Dwarf Galaxy Population. *The Astrophysical Journal*, 855:142, Mar. 2018. doi: 10.3847/1538-4357/aaab60.

D. El Youssoufi, M.-R. L. Cioni, C. P. M. Bell, S. Rubele, K. Bekki, R. de Grijs, L. Girardi, V. D. Ivanov, G. Matijevic, F. Niederhofer, J. M. Oliveira, V. Ripepi, S. Subramanian, and J. T. van Loon. The VMC survey - XXXIV. Morphology of stellar populations in the Magellanic

Clouds. *Monthly Notices of the Royal Astronomical Society*, 490(1):1076–1093, Nov. 2019. doi: 10.1093/mnras/stz2400.

D. El Youssoufi, M.-R. L. Cioni, C. P. M. Bell, R. de Grijs, M. A. T. Groenewegen, V. D. Ivanov, G. Matijevǐc, F. Niederhofer, J. M. Oliveira, V. Ripepi, T. Schmidt, S. Subramanian, N.-C. Sun, and J. T. van Loon. Stellar substructures in the periphery of the Magellanic Clouds with the VISTA hemisphere survey from the red clump and other tracers. *Monthly Notices of the Royal Astronomical Society*, 505(2):2020–2038, Aug. 2021. doi: 10.1093/mnras/stab1075.

R. A. W. Elson. The Structure and Evolution of Rich Star Clusters in the Large Magellanic Cloud. *The Astrophysical Journal Supplementary Material*, 76:185, May 1991. doi: 10.1086/191568.

R. A. W. Elson. Surface brightness profiles for five rich star clusters in the Large Magellanic Cloud. *Monthly Notices of the Royal Astronomical Society*, 256:515–518, June 1992. doi: 10.1093/mnras/256.3.515.

R. A. W. Elson, S. M. Fall, and K. C. Freeman. The Structure of Young Star Clusters in the Large Magellanic Cloud. *The Astrophysical Journal*, 323:54, Dec. 1987. doi: 10.1086/165807.

R. A. W. Elson, K. C. Freeman, and T. R. Lauer. Core Expansion in Young Clusters in the Large Magellanic Cloud. *The Astrophysical Journal Letters*, 347:L69, Dec. 1989. doi: 10.1086/185610.

S. M. Faber and R. E. Jackson. Velocity dispersions and mass-to-light ratios for elliptical galaxies. *The Astrophysical Journal*, 204:668–683, Mar. 1976. doi: 10.1086/154215.

K. Fahrion, M. Lyubenova, M. Hilker, G. van de Ven, J. Falcón-Barroso, R. Leaman, I. Martín-Navarro, A. Bittner, L. Coccato, E. M. Corsini, D. A. Gadotti, E. Iodice, R. M. McDermid, F. Pinna, M. Sarzi, S. Viaene, P. T. de Zeeuw, and L. Zhu. The Fornax 3D project: Globular clusters tracing kinematics and metallicities. *Astronomy & Astrophysics*, 637:A26, May 2020. doi: 10.1051/0004-6361/202037685.

J. J. Feldmeier, R. Ciardullo, G. H. Jacoby, and P. R. Durrell. Intracluster Planetary Nebulae in the Virgo Cluster. III. Luminosity of the Intracluster Light and Tests of the Spatial Distribution. *The Astrophysical Journal*, 615:196–208, Nov. 2004. doi: 10.1086/424372.

J. G. Fernández-Trincado, D. Minniti, S. O. Souza, T. C. Beers, D. Geisler, C. Moni Bidin, S. Villanova, S. R. Majewski, B. Barbuy, A. Pérez-Villegas, L. Henao, M. Romero-Colmenares,

A. Roman-Lopes, and R. R. Lane. VVV CL001: Likely the Most Metal-poor Surviving Globular Cluster in the Inner Galaxy. *The Astrophysical Journal Letters*, 908(2):L42, Feb. 2021. doi: 10.3847/2041-8213/abdf47.

D. A. Forbes, L. R. Spitler, J. Strader, A. J. Romanowsky, J. P. Brodie, and C. Foster. Evidence for two phases of galaxy formation from radial trends in the globular cluster system of NGC 1407. *Monthly Notices of the RAS*, 413:2943–2949, June 2011. doi: 10.1111/j.1365-2966.2011.18373.x.

C. Foster, H. Lux, A. J. Romanowsky, D. Martínez-Delgado, S. Zibetti, J. A. Arnold, J. P. Brodie, R. Ciardullo, R. J. GaBany, M. R. Merrifield, N. Singh, and J. Strader. Kinematics and simulations of the stellar stream in the halo of the Umbrella Galaxy. *Monthly Notices of the RAS*, 442:3544–3564, Aug. 2014. doi: 10.1093/mnras/stu1074.

M. Fouesneau and A. Lançon. Accounting for stochastic fluctuations when analysing the integrated light of star clusters. I. First systematics. *Astronomy & Astrophysics*, 521:A22, Oct. 2010. doi: 10.1051/0004-6361/201014084.

M. Fouesneau, L. C. Johnson, D. R. Weisz, J. J. Dalcanton, E. F. Bell, L. Bianchi, N. Caldwell, D. A. Gouliermis, P. Guhathakurta, J. Kalirai, S. S. Larsen, H.-W. Rix, A. C. Seth, E. D. Skillman, and B. F. Williams. The Panchromatic Hubble Andromeda Treasury. V. Ages and Masses of the Year 1 Stellar Clusters. *The Astrophysical Journal*, 786(2):117, May 2014. doi: 10.1088/0004-637X/786/2/117.

Gaia Collaboration, A. G. A. Brown, A. Vallenari, T. Prusti, J. H. J. de Bruijne, F. Mignard, R. Drimmel, C. Babusiaux, C. A. L. Bailer-Jones, U. Bastian, M. Biermann, D. W. Evans, L. Eyer, F. Jansen, C. Jordi, D. Katz, S. A. Klioner, U. Lammers, L. Lindegren, X. Luri, W. O'Mullane, C. Panem, D. Pourbaix, S. Randich, P. Sartoretti, H. I. Siddiqui, C. Soubiran, V. Valette, F. van Leeuwen, N. A. Walton, C. Aerts, F. Arenou, M. Cropper, E. Høg, M. G. Lattanzi, E. K. Grebel, A. D. Holland, C. Huc, X. Passot, M. Perryman, L. Bramante, C. Cacciari, J. Castañeda, L. Chaoul, N. Cheek, F. De Angeli, C. Fabricius, R. Guerra, J. Hernández, A. Jean-Antoine-Piccolo, E. Masana, R. Messineo, N. Mowlavi, K. Nienartowicz, D. Ordóñez-Blanco, P. Panuzzo, J. Portell, P. J. Richards, M. Riello, G. M. Seabroke, P. Tanga, F. Thévenin, J. Torra, S. G. Els, G. Gracia-Abril, G. Comoretto, M. Garcia-Reinaldos, T. Lock, E. Mercier, M. Altmann, R. Andrae, T. L. Astraatmadja, I. Bellas-Velidis, K. Benson, J. Berthier, R. Blomme, G. Busso, B. Carry, A. Cellino, G. Clementini, S. Cowell,

O. Creevey, J. Cuypers, M. Davidson, J. De Ridder, A. de Torres, L. Delchambre, A. Dell'Oro, C. Ducourant, Y. Frémat, M. García-Torres, E. Gosset, J. L. Halbwachs, N. C. Hambly, D. L. Harrison, M. Hauser, D. Hestroffer, S. T. Hodgkin, H. E. Huckle, A. Hutton, G. Jasniewicz, S. Jordan, M. Kontizas, A. J. Korn, A. C. Lanzafame, M. Manteiga, A. Moitinho, K. Muinonen, J. Osinde, E. Pancino, T. Pauwels, J. M. Petit, A. Recio-Blanco, A. C. Robin, L. M. Sarro, C. Siopis, M. Smith, K. W. Smith, A. Sozzetti, W. Thuillot, W. van Reeven, Y. Viala, U. Abbas, A. Abreu Aramburu, S. Accart, J. J. Aguado, P. M. Allan, W. Allasia, G. Altavilla, M. A. Álvarez, J. Alves, R. I. Anderson, A. H. Andrei, E. Anglada Varela, E. Antiche, T. Antoja, S. Antón, B. Arcay, N. Bach, S. G. Baker, L. Balaguer-Núñez, C. Barache, C. Barata, A. Barbier, F. Barblan, D. Barrado y Navascués, M. Barros, M. A. Barstow, U. Becciani, M. Bellazzini, A. Bello García, V. Belokurov, P. Bendjoya, A. Berihuete, L. Bianchi, O. Bienaymé, F. Billebaud, N. Blagorodnova, S. Blanco-Cuaresma, T. Boch, A. Bombrun, R. Borrachero, S. Bouquillon, G. Bourda, H. Bouy, A. Bragaglia, M. A. Breddels, N. Brouillet, T. Brüsemeister, B. Bucciarelli, P. Burgess, R. Burgon, A. Burlacu, D. Busonero, R. Buzzi, E. Caffau, J. Cambras, H. Campbell, R. Cancelliere, T. Cantat-Gaudin, T. Carlucci, J. M. Carrasco, M. Castellani, P. Charlot, J. Charnas, A. Chiavassa, M. Clotet, G. Cocozza, R. S. Collins, G. Costigan, F. Crifo, N. J. G. Cross, M. Crosta, C. Crowley, C. Dafonte, Y. Damerdji, A. Dapergolas, P. David, M. David, P. De Cat, F. de Felice, P. de Laverny, F. De Luise, R. De March, D. de Martino, R. de Souza, J. Debosscher, E. del Pozo, M. Delbo, A. Delgado, H. E. Delgado, P. Di Matteo, S. Diakite, E. Distefano, C. Dolding, S. Dos Anjos, P. Drazinos, J. Duran, Y. Dzigan, B. Edvardsson, H. Enke, N. W. Evans, G. Eynard Bontemps, C. Fabre, M. Fabrizio, S. Faigler, A. J. Falcão, M. Farràs Casas, L. Federici, G. Fedorets, J. Fernández-Hernández, P. Fernique, A. Fienga, F. Figueras, F. Filippi, K. Findeisen, A. Fonti, M. Fouesneau, E. Fraile, M. Fraser, J. Fuchs, M. Gai, S. Galleti, L. Galluccio, D. Garabato, F. García-Sedano, A. Garofalo, N. Garralda, P. Gavras, J. Gerssen, R. Geyer, G. Gilmore, S. Girona, G. Giuffrida, M. Gomes, A. González-Marcos, J. González-Núñez, J. J. González-Vidal, M. Granvik, A. Guerrier, P. Guillout, J. Guiraud, A. Gúrpide, R. Gutiérrez-Sánchez, L. P. Guy, R. Haigron, D. Hatzidimitriou, M. Haywood, U. Heiter, A. Helmi, D. Hobbs, W. Hofmann, B. Holl, G. Holland, J. A. S. Hunt, A. Hypki, V. Icardi, M. Irwin, G. Jevardat de Fombelle, P. Jofré, P. G. Jonker, A. Jorissen, F. Julbe, A. Karampelas, A. Kochoska, R. Kohley, K. Kolenberg, E. Kontizas, S. E. Koposov, G. Kordopatis, P. Koubsky, A. Krone-Martins, M. Kudryashova, I. Kull, R. K. Bachchan, F. Lacoste-Seris, A. F. Lanza, J. B. Lavigne, C. Le Poncin-Lafitte, Y. Lebreton, T. Lebzelter, S. Leccia, N. Leclerc, I. Lecoeur-Taibi, V. Lemaitre,

H. Lenhardt, F. Leroux, S. Liao, E. Licata, H. E. P. Lindstrøm, T. A. Lister, E. Livanou, A. Lobel, W. Löffler, M. López, D. Lorenz, I. MacDonald, T. Magalhães Fernandes, S. Managau, R. G. Mann, G. Mantelet, O. Marchal, J. M. Marchant, M. Marconi, S. Marinoni, P. M. Marrese, G. Marschalkó, D. J. Marshall, J. M. Martín-Fleitas, M. Martino, N. Mary, G. Matijevič, T. Mazeh, P. J. McMillan, S. Messina, D. Michalik, N. R. Millar, B. M. H. Miranda, D. Molina, R. Molinaro, M. Molinaro, L. Molnár, M. Moniez, P. Montegriffo, R. Mor, A. Mora, R. Morbidelli, T. Morel, S. Morgenthaler, D. Morris, A. F. Mulone, T. Muraveva, I. Musella, J. Narbonne, G. Nelemans, L. Nicastro, L. Noval, C. Ordénovic, J. Ordieres-Meré, P. Osborne, C. Pagani, I. Pagano, F. Pailler, H. Palacin, L. Palaversa, P. Parsons, M. Pecoraro, R. Pedrosa, H. Pentikäinen, B. Pichon, A. M. Piersimoni, F. X. Pineau, E. Plachy, G. Plum, E. Poujoulet, A. Prša, L. Pulone, S. Ragaini, S. Rago, N. Rambaux, M. Ramos-Lerate, P. Ranalli, G. Rauw, A. Read, S. Regibo, C. Reylé, R. A. Ribeiro, L. Rimoldini, V. Ripepi, A. Riva, G. Rixon, M. Roelens, M. Romero-Gómez, N. Rowell, F. Royer, L. Ruiz-Dern, G. Sadowski, T. Sagristà Sellés, J. Sahlmann, J. Salgado, E. Salguero, M. Sarasso, H. Savietto, M. Schultheis, E. Sciacca, M. Segol, J. C. Segovia, D. Segransan, I. C. Shih, R. Smareglia, R. L. Smart, E. Solano, F. Solitro, R. Sordo, S. Soria Nieto, J. Souchay, A. Spagna, F. Spoto, U. Stampa, I. A. Steele, H. Steidelmüller, C. A. Stephenson, H. Stoev, F. F. Suess, M. Süveges, J. Surdej, L. Szabados, E. Szegedi-Elek, D. Tapiador, F. Taris, G. Tauran, M. B. Taylor, R. Teixeira, D. Terrett, B. Tingley, S. C. Trager, C. Turon, A. Ulla, E. Utrilla, G. Valentini, A. van Elteren, E. Van Hemelryck, M. van Leeuwen, M. Varadi, A. Vecchiato, J. Veljanoski, T. Via, D. Vicente, S. Vogt, H. Voss, V. Votruba, S. Voutsinas, G. Walmsley, M. Weiler, K. Weingrill, T. Wevers, Ł. Wyrzykowski, A. Yoldas, M. Žerjal, S. Zucker, C. Zurbach, T. Zwitter, A. Alecu, M. Allen, C. Allende Prieto, A. Amorim, G. Anglada-Escudé, V. Arsenijevic, S. Azaz, P. Balm, M. Beck, H. H. Bernstein, L. Bigot, A. Bijaoui, C. Blasco, M. Bonfigli, G. Bono, S. Boudreault, A. Bressan, S. Brown, P. M. Brunet, P. Bunclark, R. Buonanno, A. G. Butkevich, C. Carret, C. Carrion, L. Chemin, F. Chéreau, L. Corcione, E. Darmigny, K. S. de Boer, P. de Teodoro, P. T. de Zeeuw, C. Delle Luche, C. D. Domingues, P. Dubath, F. Fodor, B. Frézouls, A. Fries, D. Fustes, D. Fyfe, E. Gallardo, J. Gallegos, D. Gardiol, M. Gebran, A. Gomboc, A. Gómez, E. Grux, A. Gueguen, A. Heyrovsky, J. Hoar, G. Iannicola, Y. Isasi Parache, A. M. Janotto, E. Joliet, A. Jonckheere, R. Keil, D. W. Kim, P. Klagyivik, J. Klar, J. Knude, O. Kochukhov, I. Kolka, J. Kos, A. Kutka, V. Lainey, D. LeBouquin, C. Liu, D. Loreggia, V. V. Makarov, M. G. Marseille, C. Martayan, O. Martinez-Rubi, B. Massart, F. Meynadier, S. Mignot, U. Munari, A. T. Nguyen, T. Nordlander, P. Ocvirk, K. S. O'Flaherty, A. Olias Sanz, P. Ortiz,

J. Osorio, D. Oszkiewicz, A. Ouzounis, M. Palmer, P. Park, E. Pasquato, C. Peltzer, J. Peralta, F. Péturaud, T. Pieniluoma, E. Pigozzi, J. Poels, G. Prat, T. Prod'homme, F. Raison, J. M. Rebordao, D. Risquez, B. Rocca-Volmerange, S. Rosen, M. I. Ruiz-Fuertes, F. Russo, S. Sembay, I. Serraller Vizcaino, A. Short, A. Siebert, H. Silva, D. Sinachopoulos, E. Slezak, M. Soffel, D. Sosnowska, V. Straižys, M. ter Linden, D. Terrell, S. Theil, C. Tiede, L. Troisi, P. Tsalmantza, D. Tur, M. Vaccari, F. Vachier, P. Valles, W. Van Hamme, L. Veltz, J. Virtanen, J. M. Wallut, R. Wichmann, M. I. Wilkinson, H. Ziaeepour, and S. Zschocke. Gaia Data Release 1. Summary of the astrometric, photometric, and survey properties. *Astronomy & Astrophysics*, 595:A2, Nov. 2016. doi: 10.1051/0004-6361/201629512.

Gaia Collaboration, A. G. A. Brown, A. Vallenari, T. Prusti, J. H. J. de Bruijne, C. Babusiaux, C. A. L. Bailer-Jones, M. Biermann, D. W. Evans, L. Eyer, F. Jansen, C. Jordi, S. A. Klioner, U. Lammers, L. Lindegren, X. Luri, F. Mignard, C. Panem, D. Pourbaix, S. Randich, P. Sartoretti, H. I. Siddiqui, C. Soubiran, F. van Leeuwen, N. A. Walton, F. Arenou, U. Bastian, M. Cropper, R. Drimmel, D. Katz, M. G. Lattanzi, J. Bakker, C. Cacciari, J. Castañeda, L. Chaoul, N. Cheek, F. De Angeli, C. Fabricius, R. Guerra, B. Holl, E. Masana, R. Messineo, N. Mowlavi, K. Nienartowicz, P. Panuzzo, J. Portell, M. Riello, G. M. Seabroke, P. Tanga, F. Thévenin, G. Gracia-Abril, G. Comoretto, M. Garcia-Reinaldos, D. Teyssier, M. Altmann, R. Andrae, M. Audard, I. Bellas-Velidis, K. Benson, J. Berthier, R. Blomme, P. Burgess, G. Busso, B. Carry, A. Cellino, G. Clementini, M. Clotet, O. Creevey, M. Davidson, J. De Ridder, L. Delchambre, A. Dell'Oro, C. Ducourant, J. Fernández-Hernández, M. Fouesneau, Y. Frémat, L. Galluccio, M. García-Torres, J. González-Núñez, J. J. González-Vidal, E. Gosset, L. P. Guy, J. L. Halbwachs, N. C. Hambly, D. L. Harrison, J. Hernández, D. Hestroffer, S. T. Hodgkin, A. Hutton, G. Jasniewicz, A. Jean-Antoine-Piccolo, S. Jordan, A. J. Korn, A. Krone-Martins, A. C. Lanzafame, T. Lebzelter, W. Löffler, M. Manteiga, P. M. Marrese, J. M. Martín-Fleitas, A. Moitinho, A. Mora, K. Muinonen, J. Osinde, E. Pancino, T. Pauwels, J. M. Petit, A. Recio-Blanco, P. J. Richards, L. Rimoldini, A. C. Robin, L. M. Sarro, C. Siopis, M. Smith, A. Sozzetti, M. Süveges, J. Torra, W. van Reeven, U. Abbas, A. Abreu Aramburu, S. Accart, C. Aerts, G. Altavilla, M. A. Álvarez, R. Alvarez, J. Alves, R. I. Anderson, A. H. Andrei, E. Anglada Varela, E. Antiche, T. Antoja, B. Arcay, T. L. Astraatmadja, N. Bach, S. G. Baker, L. Balaguer-Núñez, P. Balm, C. Barache, C. Barata, D. Barbato, F. Barblan, P. S. Barklem, D. Barrado, M. Barros, M. A. Barstow, S. Bartholomé Muñoz, J. L. Bassilana, U. Becciani, M. Bellazzini, A. Berihuete, S. Bertone, L. Bianchi, O. Bi-

enaymé, S. Blanco-Cuaresma, T. Boch, C. Boeche, A. Bombrun, R. Borrachero, D. Bossini, S. Bouquillon, G. Bourda, A. Bragaglia, L. Bramante, M. A. Breddels, A. Bressan, N. Brouillet, T. Brüsemeister, E. Brugaletta, B. Bucciarelli, A. Burlacu, D. Busonero, A. G. Butkevich, R. Buzzi, E. Caffau, R. Cancelliere, G. Cannizzaro, T. Cantat-Gaudin, R. Carballo, T. Carlucci, J. M. Carrasco, L. Casamiquela, M. Castellani, A. Castro-Ginard, P. Charlot, L. Chemin, A. Chiavassa, G. Cocozza, G. Costigan, S. Cowell, F. Crifo, M. Crosta, C. Crowley, J. Cuypers, C. Dafonte, Y. Damerdji, A. Dapergolas, P. David, M. David, P. de Laverny, F. De Luise, R. De March, D. de Martino, R. de Souza, A. de Torres, J. Debosscher, E. del Pozo, M. Delbo, A. Delgado, H. E. Delgado, P. Di Matteo, S. Diakite, C. Diener, E. Distefano, C. Dolding, P. Drazinos, J. Durán, B. Edvardsson, H. Enke, K. Eriksson, P. Esquej, G. Eynard Bontemps, C. Fabre, M. Fabrizio, S. Faigler, A. J. Falcão, M. Farràs Casas, L. Federici, G. Fedorets, P. Fernique, F. Figueras, F. Filippi, K. Findeisen, A. Fonti, E. Fraile, M. Fraser, B. Frézouls, M. Gai, S. Galleti, D. Garabato, F. García-Sedano, A. Garofalo, N. Garralda, A. Gavel, P. Gavras, J. Gerssen, R. Geyer, P. Giacobbe, G. Gilmore, S. Girona, G. Giuffrida, F. Glass, M. Gomes, M. Granvik, A. Gueguen, A. Guerrier, J. Guiraud, R. Gutiérrez-Sánchez, R. Haigron, D. Hatzidimitriou, M. Hauser, M. Haywood, U. Heiter, A. Helmi, J. Heu, T. Hilger, D. Hobbs, W. Hofmann, G. Holland, H. E. Huckle, A. Hypki, V. Icardi, K. Janßen, G. Jevardat de Fombelle, P. G. Jonker, Á. L. Juhász, F. Julbe, A. Karampelas, A. Kewley, J. Klar, A. Kochoska, R. Kohley, K. Kolenberg, M. Kontizas, E. Kontizas, S. E. Koposov, G. Kordopatis, Z. Kostrzewa-Rutkowska, P. Koubsky, S. Lambert, A. F. Lanza, Y. Lasne, J. B. Lavigne, Y. Le Fustec, C. Le Poncin-Lafitte, Y. Lebreton, S. Leccia, N. Leclerc, I. Lecoeur-Taibi, H. Lenhardt, F. Leroux, S. Liao, E. Licata, H. E. P. Lindstrøm, T. A. Lister, E. Livanou, A. Lobel, M. López, S. Managau, R. G. Mann, G. Mantelet, O. Marchal, J. M. Marchant, M. Marconi, S. Marinoni, G. Marschalkó, D. J. Marshall, M. Martino, G. Marton, N. Mary, D. Massari, G. Matijevič, T. Mazeh, P. J. McMillan, S. Messina, D. Michalik, N. R. Millar, D. Molina, R. Molinaro, L. Molnár, P. Montegriffo, R. Mor, R. Morbidelli, T. Morel, D. Morris, A. F. Mulone, T. Muraveva, I. Musella, G. Nelemans, L. Nicastro, L. Noval, W. O'Mullane, C. Ordénovic, D. Ordóñez-Blanco, P. Osborne, C. Pagani, I. Pagano, F. Pailler, H. Palacin, L. Palaversa, A. Panahi, M. Pawlak, A. M. Piersimoni, F. X. Pineau, E. Plachy, G. Plum, E. Poggio, E. Poujoulet, A. Prša, L. Pulone, E. Racero, S. Ragaini, N. Rambaux, M. Ramos-Lerate, S. Regibo, C. Reylé, F. Riclet, V. Ripepi, A. Riva, A. Rivard, G. Rixon, T. Roegiers, M. Roelens, M. Romero-Gómez, N. Rowell, F. Royer, L. Ruiz-Dern, G. Sadowski, T. Sagristà Sellés, J. Sahlmann, J. Salgado, E. Salguero, N. Sanna, T. Santana-Ros, M. Sarasso, H. Savi-

etto, M. Schultheis, E. Sciacca, M. Segol, J. C. Segovia, D. Ségransan, I. C. Shih, L. Siltala, A. F. Silva, R. L. Smart, K. W. Smith, E. Solano, F. Solitro, R. Sordo, S. Soria Nieto, J. Souchay, A. Spagna, F. Spoto, U. Stampa, I. A. Steele, H. Steidelmüller, C. A. Stephenson, H. Stoev, F. F. Suess, J. Surdej, L. Szabados, E. Szegedi-Elek, D. Tapiador, F. Taris, G. Tauran, M. B. Taylor, R. Teixeira, D. Terrett, P. Teyssandier, W. Thuillot, A. Titarenko, F. Torra Clotet, C. Turon, A. Ulla, E. Utrilla, S. Uzzi, M. Vaillant, G. Valentini, V. Valette, A. van Elteren, E. Van Hemelryck, M. van Leeuwen, M. Vaschetto, A. Vecchiato, J. Veljanoski, Y. Viala, D. Vicente, S. Vogt, C. von Essen, H. Voss, V. Votruba, S. Voutsinas, G. Walmsley, M. Weiler, O. Wertz, T. Wevers, Ł. Wyrzykowski, A. Yoldas, M. Žerjal, H. Ziaeepour, J. Zorec, S. Zschocke, S. Zucker, C. Zurbach, and T. Zwitter. Gaia Data Release 2. Summary of the contents and survey properties. *Astronomy & Astrophysics*, 616:A1, Aug. 2018a. doi: 10.1051/0004-6361/201833051.

Gaia Collaboration, A. Helmi, F. van Leeuwen, P. J. McMillan, D. Massari, T. Antoja, A. C. Robin, L. Lindegren, U. Bastian, F. Arenou, C. Babusiaux, M. Biermann, M. A. Breddels, D. Hobbs, C. Jordi, E. Pancino, C. Reylé, J. Veljanoski, A. G. A. Brown, A. Vallenari, T. Prusti, J. H. J. de Bruijne, C. A. L. Bailer-Jones, D. W. Evans, L. Eyer, F. Jansen, S. A. Klioner, U. Lammers, X. Luri, F. Mignard, C. Panem, D. Pourbaix, S. Randich, P. Sartoretti, H. I. Siddiqui, C. Soubiran, N. A. Walton, M. Cropper, R. Drimmel, D. Katz, M. G. Lattanzi, J. Bakker, C. Cacciari, J. Castañeda, L. Chaoul, N. Cheek, F. De Angeli, C. Fabricius, R. Guerra, B. Holl, E. Masana, R. Messineo, N. Mowlavi, K. Nienartowicz, P. Panuzzo, J. Portell, M. Riello, G. M. Seabroke, P. Tanga, F. Thévenin, G. Gracia-Abril, G. Comoretto, M. Garcia-Reinaldos, D. Teyssier, M. Altmann, R. Andrae, M. Audard, I. Bellas-Velidis, K. Benson, J. Berthier, R. Blomme, P. Burgess, G. Busso, B. Carry, A. Cellino, G. Clementini, M. Clotet, O. Creevey, M. Davidson, J. De Ridder, L. Delchambre, A. Dell'Oro, C. Ducourant, J. Fernández-Hernández, M. Fouesneau, Y. Frémat, L. Galluccio, M. García-Torres, J. González-Núñez, J. J. González-Vidal, E. Gosset, L. P. Guy, J. L. Halbwachs, N. C. Hambly, D. L. Harrison, J. Hernández, D. Hestroffer, S. T. Hodgkin, A. Hutton, G. Jasniewicz, A. Jean-Antoine-Piccolo, S. Jordan, A. J. Korn, A. Krone-Martins, A. C. Lanzafame, T. Lebzelter, W. Löffler, M. Manteiga, P. M. Marrese, J. M. Martín-Fleitas, A. Moitinho, A. Mora, K. Muinonen, J. Osinde, T. Pauwels, J. M. Petit, A. Recio-Blanco, P. J. Richards, L. Rimoldini, L. M. Sarro, C. Siopis, M. Smith, A. Sozzetti, M. Süveges, J. Torra, W. van Reeven, U. Abbas, A. Abreu Aramburu, S. Accart, C. Aerts, G. Altavilla, M. A. Álvarez,

R. Alvarez, J. Alves, R. I. Anderson, A. H. Andrei, E. Anglada Varela, E. Antiche, B. Arcay, T. L. Astraatmadja, N. Bach, S. G. Baker, L. Balaguer-Núñez, P. Balm, C. Barache, C. Barata, D. Barbato, F. Barblan, P. S. Barklem, D. Barrado, M. Barros, M. A. Barstow, S. Bartholomé Muñoz, J. L. Bassilana, U. Becciani, M. Bellazzini, A. Berihuete, S. Bertone, L. Bianchi, O. Bienaymé, S. Blanco-Cuaresma, T. Boch, C. Boeche, A. Bombrun, R. Borrachero, D. Bossini, S. Bouquillon, G. Bourda, A. Bragaglia, L. Bramante, A. Bressan, N. Brouillet, T. Brüsemeister, E. Brugaletta, B. Bucciarelli, A. Burlacu, D. Busonero, A. G. Butkevich, R. Buzzi, E. Caffau, R. Cancelliere, G. Cannizzaro, T. Cantat-Gaudin, R. Carballo, T. Carlucci, J. M. Carrasco, L. Casamiquela, M. Castellani, A. Castro-Ginard, P. Charlot, L. Chemin, A. Chiavassa, G. Cocozza, G. Costigan, S. Cowell, F. Crifo, M. Crosta, C. Crowley, J. Cuypers, C. Dafonte, Y. Damerdji, A. Dapergolas, P. David, M. David, P. de Laverny, F. De Luise, R. De March, D. de Martino, R. de Souza, A. de Torres, J. Debosscher, E. del Pozo, M. Delbo, A. Delgado, H. E. Delgado, P. Di Matteo, S. Diakite, C. Diener, E. Distefano, C. Dolding, P. Drazinos, J. Durán, B. Edvardsson, H. Enke, K. Eriksson, P. Esquej, G. Eynard Bontemps, C. Fabre, M. Fabrizio, S. Faigler, A. J. Falcão, M. Farràs Casas, L. Federici, G. Fedorets, P. Fernique, F. Figueras, F. Filippi, K. Findeisen, A. Fonti, E. Fraile, M. Fraser, B. Frézouls, M. Gai, S. Galleti, D. Garabato, F. García-Sedano, A. Garofalo, N. Garralda, A. Gavel, P. Gavras, J. Gerssen, R. Geyer, P. Giacobbe, G. Gilmore, S. Girona, G. Giuffrida, F. Glass, M. Gomes, M. Granvik, A. Gueguen, A. Guerrier, J. Guiraud, R. Gutiérrez-Sánchez, W. Hofmann, G. Holland, H. E. Huckle, A. Hypki, V. Icardi, K. Janßen, G. Jevardat de Fombelle, P. G. Jonker, Á. L. Juhász, F. Julbe, A. Karampelas, A. Kewley, J. Klar, A. Kochoska, R. Kohley, K. Kolenberg, M. Kontizas, E. Kontizas, S. E. Koposov, G. Kordopatis, Z. Kostrzewa-Rutkowska, P. Koubsky, S. Lambert, A. F. Lanza, Y. Lasne, J. B. Lavigne, Y. Le Fustec, C. Le Poncin-Lafitte, Y. Lebreton, S. Leccia, N. Leclerc, I. Lecoeur-Taibi, H. Lenhardt, F. Leroux, S. Liao, E. Licata, H. E. P. Lindstrøm, T. A. Lister, E. Livanou, A. Lobel, M. López, S. Managau, R. G. Mann, G. Mantelet, O. Marchal, J. M. Marchant, M. Marconi, S. Marinoni, G. Marschalkó, D. J. Marshall, M. Martino, G. Marton, N. Mary, G. Matijevič, T. Mazeh, S. Messina, D. Michalik, N. R. Millar, D. Molina, R. Molinaro, L. Molnár, P. Montegriffo, R. Mor, R. Morbidelli, T. Morel, D. Morris, A. F. Mulone, T. Muraveva, I. Musella, G. Nelemans, L. Nicastro, L. Noval, W. O'Mullane, C. Ordénovic, D. Ordóñez-Blanco, P. Osborne, C. Pagani, I. Pagano, F. Pailler, H. Palacin, L. Palaversa, A. Panahi, M. Pawlak, A. M. Piersimoni, F. X. Pineau, E. Plachy, G. Plum, E. Poggio, E. Poujoulet, A. Prša, L. Pulone, E. Racero, S. Ragaini, N. Rambaux, M. Ramos-Lerate, S. Regibo, F. Riclet, V. Ripepi, A. Riva, A. Rivard,

G. Rixon, T. Roegiers, M. Roelens, M. Romero-Gómez, N. Rowell, F. Royer, L. Ruiz-Dern, G. Sadowski, T. Sagristà Sellés, J. Sahlmann, J. Salgado, E. Salguero, N. Sanna, T. Santana-Ros, M. Sarasso, H. Savietto, M. Schultheis, E. Sciacca, M. Segol, J. C. Segovia, D. Ségransan, I. C. Shih, L. Siltala, A. F. Silva, R. L. Smart, K. W. Smith, E. Solano, F. Solitro, R. Sordo, S. Soria Nieto, J. Souchay, A. Spagna, F. Spoto, U. Stampa, I. A. Steele, H. Steidelmüller, C. A. Stephenson, H. Stoev, F. F. Suess, J. Surdej, L. Szabados, E. Szegedi-Elek, D. Tapiador, F. Taris, G. Tauran, M. B. Taylor, R. Teixeira, D. Terrett, P. Teyssandier, W. Thuillot, A. Titarenko, F. Torra Clotet, C. Turon, A. Ulla, E. Utrilla, S. Uzzi, M. Vaillant, G. Valentini, V. Valette, A. van Elteren, E. Van Hemelryck, M. van Leeuwen, M. Vaschetto, A. Vecchiato, Y. Viala, D. Vicente, S. Vogt, C. von Essen, H. Voss, V. Votruba, S. Voutsinas, G. Walmsley, M. Weiler, O. Wertz, T. Wevems, Ł. Wyrzykowski, A. Yoldas, M. Žerjal, H. Ziaeepour, J. Zorec, S. Zschocke, S. Zucker, C. Zurbach, and T. Zwitter. Gaia Data Release 2. Kinematics of globular clusters and dwarf galaxies around the Milky Way. *Astronomy & Astrophysics*, 616:A12, Aug. 2018b. doi: 10.1051/0004-6361/201832698.

Gaia Collaboration, A. G. A. Brown, A. Vallenari, T. Prusti, J. H. J. de Bruijne, C. Babusiaux, M. Biermann, O. L. Creevey, D. W. Evans, L. Eyer, A. Hutton, F. Jansen, C. Jordi, S. A. Klioner, U. Lammers, L. Lindegren, X. Luri, F. Mignard, C. Panem, D. Pourbaix, S. Randich, P. Sartoretti, C. Soubiran, N. A. Walton, F. Arenou, C. A. L. Bailer-Jones, U. Bastian, M. Cropper, R. Drimmel, D. Katz, M. G. Lattanzi, F. van Leeuwen, J. Bakker, C. Cacciari, J. Castañeda, F. De Angeli, C. Ducourant, C. Fabricius, M. Fouesneau, Y. Frémat, R. Guerra, A. Guerrier, J. Guiraud, A. Jean-Antoine Piccolo, E. Masana, R. Messineo, N. Mowlavi, C. Nicolas, K. Nienartowicz, F. Pailler, P. Panuzzo, F. Riclet, W. Roux, G. M. Seabroke, R. Sordo, P. Tanga, F. Thévenin, G. Gracia-Abril, J. Portell, D. Teyssier, M. Altmann, R. Andrae, I. Bellas-Velidis, K. Benson, J. Berthier, R. Blomme, E. Brugaletta, P. W. Burgess, G. Busso, B. Carry, A. Cellino, N. Cheek, G. Clementini, Y. Damerdji, M. Davidson, L. Delchambre, A. Dell'Oro, J. Fernández-Hernández, L. Galluccio, P. García-Lario, M. Garcia-Reinaldos, J. González-Núñez, E. Gosset, R. Haigron, J. L. Halbwachs, N. C. Hambly, D. L. Harrison, D. Hatzidimitriou, U. Heiter, J. Hernández, D. Hestroffer, S. T. Hodgkin, B. Holl, K. Janßen, G. Jevardat de Fombelle, S. Jordan, A. Krone-Martins, A. C. Lanzafame, W. Löffler, A. Lorca, M. Manteiga, O. Marchal, P. M. Marrese, A. Moitinho, A. Mora, K. Muinonen, P. Osborne, E. Pancino, T. Pauwels, J. M. Petit, A. Recio-Blanco, P. J. Richards, M. Riello, L. Rimoldini, A. C. Robin, T. Roegiers, J. Rybizki, L. M. Sarro, C. Siopis,

M. Smith, A. Sozzetti, A. Ulla, E. Utrilla, M. van Leeuwen, W. van Reeven, U. Abbas, A. Abreu Aramburu, S. Accart, C. Aerts, J. J. Aguado, M. Ajaj, G. Altavilla, M. A. Álvarez, J. Álvarez Cid-Fuentes, J. Alves, R. I. Anderson, E. Anglada Varela, T. Antoja, M. Audard, D. Baines, S. G. Baker, L. Balaguer-Núñez, E. Balbinot, Z. Balog, C. Barache, D. Barbato, M. Barros, M. A. Barstow, S. Bartolomé, J. L. Bassilana, N. Bauchet, A. Baudesson-Stella, U. Becciani, M. Bellazzini, M. Bernet, S. Bertone, L. Bianchi, S. Blanco-Cuaresma, T. Boch, A. Bombrun, D. Bossini, S. Bouquillon, A. Bragaglia, L. Bramante, E. Breedt, A. Bressan, N. Brouillet, B. Bucciarelli, A. Burlacu, D. Busonero, A. G. Butkevich, R. Buzzi, E. Caffau, R. Cancelliere, H. Cánovas, T. Cantat-Gaudin, R. Carballo, T. Carlucci, M. I. Carnerero, J. M. Carrasco, L. Casamiquela, M. Castellani, A. Castro-Ginard, P. Castro Sampol, L. Chaoul, P. Charlot, L. Chemin, A. Chiavassa, M. R. L. Cioni, G. Comoretto, W. J. Cooper, T. Cornez, S. Cowell, F. Crifo, M. Crosta, C. Crowley, C. Dafonte, A. Dapergolas, M. David, P. David, P. de Laverny, F. De Luise, R. De March, J. De Ridder, R. de Souza, P. de Teodoro, A. de Torres, E. F. del Peloso, E. del Pozo, M. Delbo, A. Delgado, H. E. Delgado, J. B. Delisle, P. Di Matteo, S. Diakite, C. Diener, E. Distefano, C. Dolding, D. Eappachen, B. Edvardsson, H. Enke, P. Esquej, C. Fabre, M. Fabrizio, S. Faigler, G. Fedorets, P. Fernique, A. Fienga, F. Figueras, C. Fouron, F. Fragkoudi, E. Fraile, F. Franke, M. Gai, D. Garabato, A. Garcia-Gutierrez, M. García-Torres, A. Garofalo, P. Gavras, E. Gerlach, R. Geyer, P. Giacobbe, G. Gilmore, S. Girona, G. Giuffrida, R. Gomel, A. Gomez, I. Gonzalez-Santamaria, J. J. González-Vidal, M. Granvik, R. Gutiérrez-Sánchez, L. P. Guy, M. Hauser, M. Haywood, A. Helmi, S. L. Hidalgo, T. Hilger, N. Hładczuk, D. Hobbs, G. Holland, H. E. Huckle, G. Jasniewicz, P. G. Jonker, J. Juaristi Campillo, F. Julbe, L. Karbevska, P. Kervella, S. Khanna, A. Kochoska, M. Kontizas, G. Kordopatis, A. J. Korn, Z. Kostrzewa-Rutkowska, K. Kruszyńska, S. Lambert, A. F. Lanza, Y. Lasne, J. F. Le Campion, Y. Le Fustec, Y. Lebreton, T. Lebzelter, S. Leccia, N. Leclerc, I. Lecoeur-Taibi, S. Liao, E. Licata, E. P. Lindstrøm, T. A. Lister, E. Livanou, A. Lobel, P. Madrero Pardo, S. Managau, R. G. Mann, J. M. Marchant, M. Marconi, M. M. S. Marcos Santos, S. Marinoni, F. Marocco, D. J. Marshall, L. Martin Polo, J. M. Martín-Fleitas, A. Masip, D. Massari, A. Mastrobuono-Battisti, T. Mazeh, P. J. McMillan, S. Messina, D. Michalik, N. R. Millar, A. Mints, D. Molina, R. Molinaro, L. Molnár, P. Montegriffo, R. Mor, R. Morbidelli, T. Morel, D. Morris, A. F. Mulone, D. Munoz, T. Muraveva, C. P. Murphy, I. Musella, L. Noval, C. Ordénovic, G. Orrù, J. Osinde, C. Pagani, I. Pagano, L. Palaversa, P. A. Palicio, A. Panahi, M. Pawlak, X. Peñalosa Esteller, A. Penttilä, A. M. Piersimoni, F. X. Pineau, E. Plachy, G. Plum, E. Poggio, E. Poretti, E. Poujoulet,

A. Prša, L. Pulone, E. Racero, S. Ragaini, M. Rainer, C. M. Raiteri, N. Rambaux, P. Ramos, M. Ramos-Lerate, P. Re Fiorentin, S. Regibo, C. Reylé, V. Ripepi, A. Riva, G. Rixon, N. Robichon, C. Robin, M. Roelens, L. Rohrbasser, M. Romero-Gómez, N. Rowell, F. Royer, K. A. Rybicki, G. Sadowski, A. Sagristà Sellés, J. Sahlmann, J. Salgado, E. Salguero, N. Samaras, V. Sanchez Gimenez, N. Sanna, R. Santoveña, M. Sarasso, M. Schultheis, E. Sciacca, M. Segol, J. C. Segovia, D. Ségransan, D. Semeux, S. Shahaf, H. I. Siddiqui, A. Siebert, L. Siltala, E. Slezak, R. L. Smart, E. Solano, F. Solitro, D. Souami, J. Souchay, A. Spagna, F. Spoto, I. A. Steele, H. Steidelmüller, C. A. Stephenson, M. Süveges, L. Szabados, E. Szegedi-Elek, F. Taris, G. Tauran, M. B. Taylor, R. Teixeira, W. Thuillot, N. Tonello, F. Torra, J. Torra, C. Turon, N. Unger, M. Vaillant, E. van Dillen, O. Vanel, A. Vecchiato, Y. Viala, D. Vicente, S. Voutsinas, M. Weiler, T. Wevers, Ł. Wyrzykowski, A. Yoldas, P. Yvard, H. Zhao, J. Zorec, S. Zucker, C. Zurbach, and T. Zwitter. Gaia Early Data Release 3. Summary of the contents and survey properties. *Astronomy & Astrophysics*, 649:A1, May 2021a. doi: 10.1051/0004-6361/202039657.

Gaia Collaboration, X. Luri, L. Chemin, G. Clementini, H. E. Delgado, P. J. McMillan, M. Romero-Gómez, E. Balbinot, A. Castro-Ginard, R. Mor, V. Ripepi, L. M. Sarro, M. R. L. Cioni, C. Fabricius, A. Garofalo, A. Helmi, T. Muraveva, A. G. A. Brown, A. Vallenari, T. Prusti, J. H. J. de Bruijne, C. Babusiaux, M. Biermann, O. L. Creevey, D. W. Evans, L. Eyer, A. Hutton, F. Jansen, C. Jordi, S. A. Klioner, U. Lammers, L. Lindegren, F. Mignard, C. Panem, D. Pourbaix, S. Randich, P. Sartoretti, C. Soubiran, N. A. Walton, F. Arenou, C. A. L. Bailer-Jones, U. Bastian, M. Cropper, R. Drimmel, D. Katz, M. G. Lattanzi, F. van Leeuwen, J. Bakker, J. Castañeda, F. De Angeli, C. Ducourant, M. Fouesneau, Y. Frémat, R. Guerra, A. Guerrier, J. Guiraud, A. Jean-Antoine Piccolo, E. Masana, R. Messineo, N. Mowlavi, C. Nicolas, K. Nienartowicz, F. Pailler, P. Panuzzo, F. Riclet, W. Roux, G. M. Seabroke, R. Sordo, P. Tanga, F. Thévenin, G. Gracia-Abril, J. Portell, D. Teyssier, M. Altmann, R. Andrae, I. Bellas-Velidis, K. Benson, J. Berthier, R. Blomme, E. Brugaletta, P. W. Burgess, G. Busso, B. Carry, A. Cellino, N. Cheek, Y. Damerdji, M. Davidson, L. Delchambre, A. Dell'Oro, J. Fernández-Hernández, L. Galluccio, P. García-Lario, M. Garcia-Reinaldos, J. González-Núñez, E. Gosset, R. Haigron, J. L. Halbwachs, N. C. Hambly, D. L. Harrison, D. Hatzidimitriou, U. Heiter, J. Hernández, D. Hestroffer, S. T. Hodgkin, B. Holl, K. Janßen, G. Jevardat de Fombelle, S. Jordan, A. Krone-Martins, A. C. Lanzafame, W. Löffler, A. Lorca, M. Manteiga, O. Marchal, P. M. Marrese, A. Moitinho, A. Mora, K. Muinonen, P. Os-

borne, E. Pancino, T. Pauwels, A. Recio-Blanco, P. J. Richards, M. Riello, L. Rimoldini, A. C. Robin, T. Roegiers, J. Rybizki, C. Siopis, M. Smith, A. Sozzetti, A. Ulla, E. Utrilla, M. van Leeuwen, W. van Reeven, U. Abbas, A. Abreu Aramburu, S. Accart, C. Aerts, J. J. Aguado, M. Ajaj, G. Altavilla, M. A. Álvarez, J. Álvarez Cid-Fuentes, J. Alves, R. I. Anderson, E. Anglada Varela, T. Antoja, M. Audard, D. Baines, S. G. Baker, L. Balaguer-Núñez, Z. Balog, C. Barache, D. Barbato, M. Barros, M. A. Barstow, S. Bartolomé, J. L. Bassilana, N. Bauchet, A. Baudesson-Stella, U. Becciani, M. Bellazzini, M. Bernet, S. Bertone, L. Bianchi, S. Blanco-Cuaresma, T. Boch, A. Bombrun, D. Bossini, S. Bouquillon, A. Bragaglia, L. Bramante, E. Breedt, A. Bressan, N. Brouillet, B. Bucciarelli, A. Burlacu, D. Busonero, A. G. Butkevich, R. Buzzi, E. Caffau, R. Cancelliere, H. Cánovas, T. Cantat-Gaudin, R. Carballo, T. Carlucci, M. I. Carnerero, J. M. Carrasco, L. Casamiquela, M. Castellani, P. Castro Sampol, L. Chaoul, P. Charlot, A. Chiavassa, G. Comoretto, W. J. Cooper, T. Cornez, S. Cowell, F. Crifo, M. Crosta, C. Crowley, C. Dafonte, A. Dapergolas, M. David, P. David, P. de Laverny, F. De Luise, R. De March, J. De Ridder, R. de Souza, P. de Teodoro, A. de Torres, E. F. del Peloso, E. del Pozo, A. Delgado, J. B. Delisle, P. Di Matteo, S. Diakite, C. Diener, E. Distefano, C. Dolding, D. Eappachen, H. Enke, P. Esquej, C. Fabre, M. Fabrizio, S. Faigler, G. Fedorets, P. Fernique, A. Fienga, F. Figueras, C. Fouron, F. Fragkoudi, E. Fraile, F. Franke, M. Gai, D. Garabato, A. Garcia-Gutierrez, M. García-Torres, P. Gavras, E. Gerlach, R. Geyer, P. Giacobbe, G. Gilmore, S. Girona, G. Giuffrida, A. Gomez, I. Gonzalez-Santamaria, J. J. González-Vidal, M. Granvik, R. Gutiérrez-Sánchez, L. P. Guy, M. Hauser, M. Haywood, S. L. Hidalgo, T. Hilger, N. Hładczuk, D. Hobbs, G. Holland, H. E. Huckle, G. Jasniewicz, P. G. Jonker, J. Juaristi Campillo, F. Julbe, L. Karbevska, P. Kervella, S. Khanna, A. Kochoska, M. Kontizas, G. Kordopatis, A. J. Korn, Z. Kostrzewa-Rutkowska, K. Kruszyńska, S. Lambert, A. F. Lanza, Y. Lasne, J. F. Le Campion, Y. Le Fustec, Y. Lebreton, T. Lebzelter, S. Leccia, N. Leclerc, I. Lecoeur-Taibi, S. Liao, E. Licata, H. E. P. Lindstrøm, T. A. Lister, E. Livanou, A. Lobel, P. Madrero Pardo, S. Managau, R. G. Mann, J. M. Marchant, M. Marconi, M. M. S. Marcos Santos, S. Marinoni, F. Marocco, D. J. Marshall, L. Martin Polo, J. M. Martín-Fleitas, A. Masip, D. Massari, A. Mastrobuono-Battisti, T. Mazeh, S. Messina, D. Michalik, N. R. Millar, A. Mints, D. Molina, R. Molinaro, L. Molnár, P. Montegriffo, R. Morbidelli, T. Morel, D. Morris, A. F. Mulone, D. Munoz, C. P. Murphy, I. Musella, L. Noval, C. Ordénovic, G. Orrù, J. Osinde, C. Pagani, I. Pagano, L. Palaversa, P. A. Palicio, A. Panahi, M. Pawlak, X. Peñalosa Esteller, A. Penttilä, A. M. Piersimoni, F. X. Pineau, E. Plachy, G. Plum, E. Poggio, E. Poretti, E. Poujoulet, A. Prša, L. Pulone, E. Racero, S. Ra-

gaini, M. Rainer, C. M. Raiteri, N. Rambaux, P. Ramos, M. Ramos-Lerate, P. Re Fiorentin, S. Regibo, C. Reylé, A. Riva, G. Rixon, N. Robichon, C. Robin, M. Roelens, L. Rohrbasser, N. Rowell, F. Royer, K. A. Rybicki, G. Sadowski, A. Sagristà Sellés, J. Sahlmann, J. Salgado, E. Salguero, N. Samaras, V. S. Gimenez, N. Sanna, R. Santoveña, M. Sarasso, M. Schultheis, E. Sciacca, M. Segol, J. C. Segovia, D. Ségransan, D. Semeux, H. I. Siddiqui, A. Siebert, L. Siltala, E. Slezak, R. L. Smart, E. Solano, F. Solitro, D. Souami, J. Souchay, A. Spagna, F. Spoto, I. A. Steele, H. Steidelmüller, C. A. Stephenson, M. Süveges, L. Szabados, E. Szegedi-Elek, F. Taris, G. Tauran, M. B. Taylor, R. Teixeira, W. Thuillot, N. Tonello, F. Torra, J. Torra, C. Turon, N. Unger, M. Vaillant, E. van Dillen, O. Vanel, A. Vecchiato, Y. Viala, D. Vicente, S. Voutsinas, M. Weiler, T. Wevers, Ł. Wyrzykowski, A. Yoldas, P. Yvard, H. Zhao, J. Zorec, S. Zucker, C. Zurbach, and T. Zwitter. Gaia Early Data Release 3. Structure and properties of the Magellanic Clouds. *Astronomy & Astrophysics*, 649:A7, May 2021b. doi: 10.1051/0004-6361/202039588.

J. Gallagher, III and J. Ostriker. A note on mass loss during collisions between galaxies and the formation of giant systems. *The astrophysical journal*, 77:288, may 1972. doi: 10.1086/111280.

J. S. Gallagher, J. R. Mould, E. de Feijter, J. Holtzman, B. Stappers, A. Watson, J. Trauger, G. E. Ballester, C. J. Burrows, S. Casertano, J. T. Clarke, D. Crisp, R. E. Griffiths, J. J. Hester, J. Hoessel, J. Krist, L. D. Matthews, P. A. Scowen, K. R. Stapelfeld, and J. A. Westphal. Main-Sequence Stars and the Star Formation History of the Outer Disk in the Large Magellanic Cloud. *The Astrophysical Journal*, 466:732, Aug. 1996. doi: 10.1086/177546.

N. Garavito-Camargo, G. Besla, C. F. P. Laporte, K. V. Johnston, F. A. Gómez, and L. L. Watkins. Hunting for the Dark Matter Wake Induced by the Large Magellanic Cloud. *The Astrophysical Journal*, 884(1):51, Oct. 2019. doi: 10.3847/1538-4357/ab32eb.

L. T. Gardiner and M. R. S. Hawkins. Stellar populations and large-scale structure of the SMC - III. The geometry of the northern and north-western outlying regions. *Monthly Notices of the Royal Astronomical Society*, 251:174, July 1991. doi: 10.1093/mnras/251.1.174.

L. T. Gardiner and M. Noguchi. N-body simulations of the Small Magellanic Cloud and the Magellanic Stream. *Monthly Notices of the Royal Astronomical Society*, 278(1):191–208, Jan 1996. doi: 10.1093/mnras/278.1.191.

L. T. Gardiner, T. Sawa, and M. Fujimoto. Numerical simulations of the Magellanic system - I.

Orbits of the Magellanic Clouds and the global gas distribution. *Monthly Notices of the Royal Astronomical Society*, 266:567–582, Feb 1994. doi: 10.1093/mnras/266.3.567.

M. Gatto, V. Ripepi, M. Bellazzini, M. Cignoni, M. R. L. Cioni, M. Dall'Ora, G. Longo, M. Marconi, P. Schipani, and M. Tosi. A search for star clusters in the outskirts of the Large Magellanic Cloud: indication of clusters in the age gap. *Monthly Notices of the Royal Astronomical Society*, 499(3):4114–4139, Dec. 2020. doi: 10.1093/mnras/staa3003.

M. Gatto, V. Ripepi, M. Bellazzini, M. Tosi, C. Tortora, M. Cignoni, M. Spavone, M. Dall'ora, G. Clementini, F. Cusano, G. Longo, I. Musella, M. Marconi, and P. Schipani. YMCA-1: A New Remote Star Cluster of the Milky Way? *Research Notes of the American Astronomical Society*, 5(7):159, July 2021. doi: 10.3847/2515-5172/ac14bf.

M. C. Geha, J. A. Holtzman, J. R. Mould, I. Gallagher, John S., A. M. Watson, A. A. Cole, C. J. Grillmair, K. R. Stapelfeldt, G. E. Ballester, C. J. Burrows, J. T. Clarke, D. Crisp, R. W. Evans, R. E. Griffiths, J. J. Hester, P. A. Scowen, J. T. Trauger, and J. A. Westphal. Stellar Populations in Three Outer Fields of the Large Magellanic Cloud. *The Astronomical Journal*, 115(3):1045–1056, Mar. 1998. doi: 10.1086/300252.

D. Geisler, E. Bica, H. Dottori, J. J. Claria, A. E. Piatti, and J. Santos, Joao F. C. A Search for Old Star Clusters in the Large Magellanic Cloud. *The Astronomical Journal*, 114:1920, Nov. 1997. doi: 10.1086/118614.

D. Geisler, E. Bica, H. Dottori, J. J. Clariá, A. E. Piatti, and J. Santos, J. F. C. Ages and Metallicities of LMC Clusters and Their Surrounding Fields. In Y. H. Chu, N. Suntzeff, J. Hesser, and D. Bohlender, editors, *New Views of the Magellanic Clouds*, volume 190, page 431, Jan. 1999.

R. A. Gingold and J. J. Monaghan. Kernel estimates as a basis for general particle methods in hydrodynamics. *Journal of Computational Physics*, 46:429–453, Jun 1982. doi: 10.1016/0021-9991(82)90025-0.

L. Girardi and P. Marigo. The TP-AGB phase. Lifetimes from C and M star counts in Magellanic Cloud clusters. *Astronomy & Astrophysics*, 462(1):237–243, Jan. 2007. doi: 10.1051/0004-6361:20065249.

K. Glatt, I. Gallagher, John S., E. K. Grebel, A. Nota, E. Sabbi, M. Sirianni, G. Clementini, M. Tosi, D. Harbeck, A. Koch, and M. Cracraft. An Accurate Age Determination for the Small

Magellanic Cloud Star Cluster NGC 121 with the Hubble Space Telescope/Advanced Camera for Surveys. *The Astronomical Journal*, 135(4):1106–1116, Apr. 2008a. doi: 10.1088/0004-6256/135/4/1106.

K. Glatt, E. K. Grebel, E. Sabbi, I. Gallagher, John S., A. Nota, M. Sirianni, G. Clementini, M. Tosi, D. Harbeck, A. Koch, A. Kayser, and G. Da Costa. Age Determination of Six Intermediate-Age Small Magellanic Cloud Star Clusters with HST/ACS. *The Astronomical Journal*, 136(4):1703–1727, Oct. 2008b. doi: 10.1088/0004-6256/136/4/1703.

K. Glatt, E. K. Grebel, I. Gallagher, John S., A. Nota, E. Sabbi, M. Sirianni, G. Clementini, G. Da Costa, M. Tosi, D. Harbeck, A. Koch, and A. Kayser. Structural Parameters of Seven Small Magellanic Cloud Intermediate-Age and Old Star Clusters. *The Astronomical Journal*, 138(5):1403–1416, Nov. 2009. doi: 10.1088/0004-6256/138/5/1403.

K. Glatt, E. K. Grebel, and A. Koch. Ages and luminosities of young SMC/LMC star clusters and the recent star formation history of the Clouds. *Astronomy and Astrophysics*, 517:A50, 2010. ISSN 0004-6361. doi: 10.1051/0004-6361/201014187.

K. Glatt, E. K. Grebel, K. Jordi, I. Gallagher, John S., G. Da Costa, G. Clementini, M. Tosi, D. Harbeck, A. Nota, E. Sabbi, and M. Sirianni. Present-day Mass Function of Six Small Magellanic Cloud Intermediate-age and Old Star Clusters. *The Astronomical Journal*, 142(2): 36, Aug. 2011. doi: 10.1088/0004-6256/142/2/36.

O. Y. Gnedin and J. P. Ostriker. Destruction of the Galactic Globular Cluster System. *The Astrophysical Journal*, 474(1):223–255, Jan. 1997. doi: 10.1086/303441.

I. Gonidakis, E. Livanou, E. Kontizas, U. Klein, M. Kontizas, M. Belcheva, P. Tsalmantza, and A. Karampelas. Structure of the SMC. Stellar component distribution from 2MASS data. *Astronomy & Astrophysics*, 496(2):375–380, Mar. 2009. doi: 10.1051/0004-6361/200809828.

R. E. González, A. V. Kravtsov, and N. Y. Gnedin. Satellites in Milky-Way-like Hosts: Environment Dependence and Close Pairs. *The Astrophysical Journal*, 770(2):96, June 2013. doi: 10.1088/0004-637X/770/2/96.

S. P. Goodwin and N. Bastian. Gas expulsion and the destruction of massive young clusters. *Monthly Notices of the Royal Astronomical Society*, 373(2):752–758, Dec. 2006. doi: 10.1111/j.1365-2966.2006.11078.x.

K. D. Gordon, C. Bot, E. Muller, K. A. Misselt, A. Bolatto, J. P. Bernard, W. Reach, C. W. Engelbracht, B. Babler, S. Bracker, M. Block, G. C. Clayton, J. Hora, R. Indebetouw, F. P. Israel, A. Li, S. Madden, M. Meade, M. Meixner, M. Sewilo, B. Shiao, L. J. Smith, J. T. van Loon, and B. A. Whitney. The Dust-to-Gas Ratio in the Small Magellanic Cloud Tail. *The Astrophysical Journal Letters*, 690(1):L76–L80, Jan 2009. doi: 10.1088/0004-637X/690/1/L76.

D. Graczyk, G. Pietrzyński, I. B. Thompson, W. Gieren, B. Zgirski, S. Villanova, M. Górski, P. Wielgórski, P. Karczmarek, W. Narloch, B. Pilecki, M. Taormina, R. Smolec, K. Suchomska, A. Gallenne, N. Nardetto, J. Storm, R.-P. Kudritzki, M. Kałuszyński, and W. Pych. A Distance Determination to the Small Magellanic Cloud with an Accuracy of Better than Two Percent Based on Late-type Eclipsing Binary Stars. *The Astrophysical Journal*, 904(1):13, Nov. 2020. doi: 10.3847/1538-4357/abbb2b.

A. Grado, M. Capaccioli, L. Limatola, and F. Getman. VST processing facility: first astronomical applications. *Memorie della Societa Astronomica Italiana Supplementi*, 19:362, Jan 2012.

J. Grady, V. Belokurov, and N. W. Evans. Magellanic Mayhem: Metallicities and Motions. *The Astrophysical Journal*, 909(2):150, Mar. 2021. doi: 10.3847/1538-4357/abd4e4.

G. Green. dustmaps: A Python interface for maps of interstellar dust. *The Journal of Open Source Software*, 3(26):695, Jun 2018. doi: 10.21105/joss.00695.

M. J. Gregg, Michael D.; West. *Nature*, 396, 12 1998. doi: 10.1038/25078. URL `http://gen.lib.rus.ec/scimag/index.php?s=10.1038/25078`.

L. Hagen, E. Hoversten, C. Gronwall, C. Wolf, M. Siegel, M. Page, and A. Hagen. The evolution of the far-uv luminosity function and star formation rate density of the chandra deep field south from z = 0.2 to 1.2 with swift/uvot. *The astrophysical journal*, 808:178, aug 2015. doi: 10.1088/0004-637X/808/2/178.

J. Harris. The Magellanic Bridge: The Nearest Purely Tidal Stellar Population. *The Astrophysical Journal*, 658(1):345–357, Mar. 2007. doi: 10.1086/511816.

J. Harris and D. Zaritsky. The Star Formation History of the Small Magellanic Cloud. *The Astronomical Journal*, 127(3):1531–1544, Mar 2004. doi: 10.1086/381953.

J. Harris and D. Zaritsky. The star formation history of the large magellanic cloud. *Astronomical Journal*, 138(5):1243–1260, 2009. ISSN 00046256. doi: 10.1088/0004-6256/138/5/1243.

W. E. Harris. A Catalog of Parameters for Globular Clusters in the Milky Way. *The Astronomical Journal*, 112:1487, Oct. 1996. doi: 10.1086/118116.

R. Haschke, E. K. Grebel, and S. Duffau. Three-dimensional Maps of the Magellanic Clouds using RR Lyrae Stars and Cepheids. II. The Small Magellanic Cloud. *The Astronomical Journal*, 144(4):107, Oct. 2012. doi: 10.1088/0004-6256/144/4/107.

M. Haywood, P. Di Matteo, M. D. Lehnert, O. Snaith, S. Khoperskov, and A. Gómez. In Disguise or Out of Reach: First Clues about In Situ and Accreted Stars in the Stellar Halo of the Milky Way from Gaia DR2. *The Astrophysical Journal*, 863(2):113, Aug. 2018. doi: 10.3847/1538-4357/aad235.

P. Heller and K. Rohlfs. The dynamical evolution of the Magellanic System. *Astronomy & Astrophysics*, 291:743–753, Nov 1994.

A. Helmi and S. D. M. White. Building up the stellar halo of the Galaxy. *Monthly Notices of the Royal Astronomical Society*, 307(3):495–517, Aug. 1999. doi: 10.1046/j.1365-8711.1999.02616.x.

A. Helmi, C. Babusiaux, H. H. Koppelman, D. Massari, J. Veljanoski, and A. G. A. Brown. The merger that led to the formation of the Milky Way's inner stellar halo and thick disk. *Nature*, 563(7729):85–88, Oct. 2018. doi: 10.1038/s41586-018-0625-x.

D. Hendel, K. V. Johnston, R. K. Patra, and B. Sen. A machine-vision method for automatic classification of stellar halo substructure. *Monthly Notices of the Royal Astronomical Society*, 486(3):3604–3616, July 2019. doi: 10.1093/mnras/stz1107.

L. Hernquist. An Analytical Model for Spherical Galaxies and Bulges. *The Astrophysical Journal*, 356:359, June 1990. doi: 10.1086/168845.

A. Hill and D. Zaritsky. The Star Clusters of the Small Magellanic Cloud: Structural Parameters. *The Astronomical Journal*, 131(1):414–430, Jan. 2006. doi: 10.1086/498647.

J. V. Hindman, F. J. Kerr, and R. X. McGee. A Low Resolution Hydrogen-line Survey of the Magellanic System. II. Interpretation of Results. *Australian Journal of Physics*, 16:570, Jan. 1963. doi: 10.1071/PH630570.

B. Holl, M. Audard, K. Nienartowicz, G. Jevardat de Fombelle, O. Marchal, N. Mowlavi, G. Clementini, J. De Ridder, D. W. Evans, L. P. Guy, A. C. Lanzafame, T. Lebzelter, L. Ri-

moldini, M. Roelens, S. Zucker, E. Distefano, A. Garofalo, I. Lecoeur-Taïbi, M. Lopez, R. Molinaro, T. Muraveva, A. Panahi, S. Regibo, V. Ripepi, L. M. Sarro, C. Aerts, R. I. Anderson, J. Charnas, F. Barblan, S. Blanco-Cuaresma, G. Busso, J. Cuypers, F. De Angeli, F. Glass, M. Grenon, Á. L. Juhász, A. Kochoska, P. Koubsky, A. F. Lanza, S. Leccia, D. Lorenz, M. Marconi, G. Marschalkó, T. Mazeh, S. Messina, F. Mignard, A. Moitinho, L. Molnár, S. Morgenthaler, I. Musella, C. Ordenovic, D. Ordóñez, I. Pagano, L. Palaversa, M. Pawlak, E. Plachy, A. Prša, M. Riello, M. Süveges, L. Szabados, E. Szegedi-Elek, V. Votruba, and L. Eyer. Gaia Data Release 2. Summary of the variability processing and analysis results. *Astronomy & Astrophysics*, 618:A30, Oct. 2018. doi: 10.1051/0004-6361/201832892.

J. A. Holtzman, I. Gallagher, John S., A. A. Cole, J. R. Mould, C. J. Grillmair, G. E. Ballester, C. J. Burrows, J. T. Clarke, D. Crisp, R. W. Evans, R. E. Griffiths, J. J. Hester, J. G. Hoessel, P. A. Scowen, K. R. Stapelfeldt, J. T. Trauger, and A. M. Watson. Observations and Implications of the Star Formation History of the Large Magellanic Cloud. *The Astronomical Journal*, 118(5):2262–2279, Nov. 1999. doi: 10.1086/301097.

D. A. Hunter, B. G. Elmegreen, T. J. Dupuy, and M. Mortonson. Cluster Mass Functions in the Large and Small Magellanic Clouds: Fading and Size-of-Sample Effects. *The Astronomical Journal*, 126(4):1836–1848, Oct 2003. doi: 10.1086/378056.

R. Ibata, M. Irwin, G. Lewis, A. M. N. Ferguson, and N. Tanvir. A giant stream of metal-rich stars in the halo of the galaxy M31. *Nature*, 412(6842):49–52, July 2001a.

R. Ibata, M. Irwin, G. F. Lewis, and A. Stolte. Galactic Halo Substructure in the Sloan Digital Sky Survey: The Ancient Tidal Stream from the Sagittarius Dwarf Galaxy. *Astrophysical Journal, Letters*, 547:L133–L136, Feb. 2001b. doi: 10.1086/318894.

R. A. Ibata, R. F. G. Wyse, G. Gilmore, M. J. Irwin, and N. B. Suntzeff. The Kinematics, Orbit, and Survival of the Sagittarius Dwarf Spheroidal Galaxy. *Astronomical Journal*, 113:634–655, Feb. 1997. doi: 10.1086/118283.

E. Iodice, M. Spavone, M. Cantiello, R. D'Abrusco, M. Capaccioli, M. Hilker, S. Mieske, N. R. Napolitano, R. F. Peletier, L. Limatola, A. Grado, A. Venhola, M. Paolillo, G. V. d. Ven, and P. Schipani. Intracluster patches of baryons in the core of the fornax cluster. *The Astrophysical Journal*, 851, 12 2017. doi: 10.3847/1538-4357/aa9b30. URL `http://gen.lib.rus.ec/scimag/index.php?s=10.3847/1538-4357/aa9b30`.

M. Iodice, E.; Capaccioli, A. Grado, L. Limatola, M. Spavone, N. R. Napolitano, M. Paolillo, R. F. Peletier, M. Cantiello, T. Lisker, C. Wittmann, A. Venhola, M. Hilker, R. D'Abrusco, V. Pota, and P. Schipani. The fornax deep survey with vst. i. the extended and diffuse stellar halo of ngc 1399 out to 192 kpc. *The Astrophysical Journal*, 820, 03 2016. doi: 10.3847/0004-637x/820/1/42. URL `http://gen.lib.rus.ec/scimag/index.php?s=10.3847/0004-637x/820/1/42`.

M. J. Irwin, W. E. Kunkel, and S. Demers. A blue stellar population in the HI bridge between the two Magellanic Clouds. *Nature*, 318(6042):160–161, Nov. 1985. doi: 10.1038/318160a0.

V. D. Ivanov, A. E. Piatti, J.-c. Beamín, D. Minniti, J. Borissova, R. Kurtev, M. Hempel, and R. K. Saito. Astrophysics Candidate star clusters toward the inner Milky Way discovered on deep-stacked K S -band images from the VVV Survey. 112:1–8, 2017.

A. M. Jacyszyn-Dobrzeniecka, D. M. Skowron, P. Mróz, J. Skowron, I. Soszyński, A. Udalski, P. Pietrukowicz, S. Kozłowski, Ł. Wyrzykowski, R. Poleski, M. Pawlak, M. K. Szymański, and K. Ulaczyk. OGLE-ing the Magellanic System: Three-Dimensional Structure of the Clouds and the Bridge Using Classical Cepheids. *Acta Astronomica*, 66(2):149–196, June 2016.

A. M. Jacyszyn-Dobrzeniecka, D. M. Skowron, P. Mróz, I. Soszyński, A. Udalski, P. Pietrukowicz, J. Skowron, R. Poleski, S. Kozłowski, Ł. Wyrzykowski, M. Pawlak, M. K. Szymański, and K. Ulaczyk. OGLE-ing the Magellanic System: Three-Dimensional Structure of the Clouds and the Bridge using RR Lyrae Stars. *Acta Astronomica*, 67(1):1–35, Mar. 2017. doi: 10.32023/0001-5237/67.1.1.

D. James, S. Subramanian, A. O. Omkumar, A. Mary, K. Bekki, M.-R. L. Cioni, R. de Grijs, D. El Youssoufi, S. S. Kartha, F. Niederhofer, and J. T. van Loon. Presence of red giant population in the foreground stellar substructure of the Small Magellanic Cloud. *Monthly Notices of the Royal Astronomical Society*, 508(4):5854–5863, Dec. 2021. doi: 10.1093/mnras/stab2873.

J. Jensen, J. Mould, and N. Reid. The Continuity of Cluster Formation in the Large Magellanic Cloud. *The Astrophysical Journal Supplementary Material*, 67:77, May 1988. doi: 10.1086/191266.

K. V. Johnston, J. S. Bullock, S. Sharma, A. Font, B. E. Robertson, and S. N. Leitner. Tracing Galaxy Formation with Stellar Halos. II. Relating Substructure in Phase and Abun-

dance Space to Accretion Histories. *The Astrophysical Journal*, 689:936–957, Dec. 2008. doi: 10.1086/592228.

E. Kado-Fong, J. E. Greene, D. Hendel, A. M. Price-Whelan, J. P. Greco, A. D. Goulding, S. Huang, K. V. Johnston, Y. Komiyama, C. H. Lee, N. B. Lust, M. A. Strauss, and M. Tanaka. Tidal Features at $0.05 < z < 0.45$ in the Hyper Suprime-Cam Subaru Strategic Program: Properties and Formation Channels. *The Astrophysical Journal*, 866(2):103, Oct. 2018. doi: 10.3847/1538-4357/aae0f0.

N. Kallivayalil, R. P. van der Marel, and C. Alcock. Is the SMC Bound to the LMC? The Hubble Space Telescope Proper Motion of the SMC. *The Astrophysical Journal*, 652(2):1213–1229, Dec 2006a. doi: 10.1086/508014.

N. Kallivayalil, R. P. van der Marel, C. Alcock, T. Axelrod, K. H. Cook, A. J. Drake, and M. Geha. The Proper Motion of the Large Magellanic Cloud Using HST. *The Astrophysical Journal*, 638(2):772–785, Feb 2006b. doi: 10.1086/498972.

N. Kallivayalil, R. P. van der Marel, G. Besla, J. Anderson, and C. Alcock. Third-epoch Magellanic Cloud Proper Motions. I. Hubble Space Telescope/WFC3 Data and Orbit Implications. *The Astrophysical Journal*, 764(2):161, Feb 2013. doi: 10.1088/0004-637X/764/2/161.

N. Kallivayalil, L. V. Sales, P. Zivick, T. K. Fritz, A. Del Pino, S. T. Sohn, G. Besla, R. P. van der Marel, J. F. Navarro, and E. Sacchi. The Missing Satellites of the Magellanic Clouds? Gaia Proper Motions of the Recently Discovered Ultra-faint Galaxies. *The Astrophysical Journal*, 867(1):19, Nov. 2018. doi: 10.3847/1538-4357/aadfee.

F. J. Kerr, J. F. Hindman, and B. J. Robinson. Observations of the 21 cm Line from the Magellanic Clouds. *Australian Journal of Physics*, 7:297, Jan. 1954. doi: 10.1071/PH540297.

D. Kim and H. Jerjen. Horologium II: A Second Ultra-faint Milky Way Satellite in the Horologium Constellation. *The Astrophysical Journal Letters*, 808(2):L39, Aug. 2015. doi: 10.1088/2041-8205/808/2/L39.

I. King. The structure of star clusters. I. an empirical density law. *The Astronomical Journal*, 67:471, Oct. 1962. doi: 10.1086/108756.

S. Koposov, J. T. A. de Jong, V. Belokurov, H. W. Rix, D. B. Zucker, N. W. Evans, G. Gilmore, M. J. Irwin, and E. F. Bell. The Discovery of Two Extremely Low Luminosity Milky Way Globular Clusters. *The Astrophysical Journal*, 669(1):337–342, Nov. 2007. doi: 10.1086/521422.

S. E. Koposov, V. Belokurov, G. Torrealba, and N. W. Evans. Beasts of the Southern Wild: Discovery of Nine Ultra Faint Satellites in the Vicinity of the Magellanic Clouds. *The Astrophysical Journal*, 805(2):130, June 2015. doi: 10.1088/0004-637X/805/2/130.

E. Kourkchi, H. G. Khosroshahi, D. Carter, A. M. Karick, E. Mármol-Queraltó, K. Chiboucas, R. B. Tully, B. Mobasher, R. Guzmán, A. Matković, and N. Gruel. Dwarf galaxies in the Coma cluster - I. Velocity dispersion measurements. *Monthly Notices of the Royal Astronomical Society*, 420(4):2819–2834, Mar. 2012. doi: 10.1111/j.1365-2966.2011.19899.x.

P. Kroupa. On the variation of the initial mass function. *Monthly Notices of the Royal Astronomical Society*, 322(2):231–246, Apr. 2001. doi: 10.1046/j.1365-8711.2001.04022.x.

P. Kroupa, S. Aarseth, and J. Hurley. The formation of a bound star cluster: from the Orion nebula cluster to the Pleiades. *Monthly Notices of the Royal Astronomical Society*, 321(4): 699–712, Mar. 2001. doi: 10.1046/j.1365-8711.2001.04050.x.

J. M. D. Kruijssen, J. L. Pfeffer, M. Reina-Campos, R. A. Crain, and N. Bastian. The formation and assembly history of the Milky Way revealed by its globular cluster population. *Monthly Notices of the Royal Astronomical Society*, 486(3):3180–3202, July 2019. doi: 10.1093/mnras/sty1609.

M. R. Krumholz, M. Fumagalli, R. L. da Silva, T. Rendahl, and J. Parra. SLUG - stochastically lighting up galaxies - III. A suite of tools for simulated photometry, spectroscopy, and Bayesian inference with stochastic stellar populations. *Monthly Notices of the Royal Astronomical Society*, 452(2):1447–1467, Sept. 2015. doi: 10.1093/mnras/stv1374.

M. R. Krumholz, C. F. McKee, and J. Bland-Hawthorn. Star Clusters Across Cosmic Time. *Annual Review of Astronomy & Astrophysics*, 57:227–303, Aug. 2019. doi: 10.1146/annurev-astro-091918-104430.

K. Kuijken. OmegaCAM: ESO's Newest Imager. *The Messenger*, 146:8–11, Dec 2011.

C. Lacey and S. Cole. Merger rates in hierarchical models of galaxy formation. *Monthly Notices of the Royal Astronomical Society*, 262(3):627–649, June 1993. doi: 10.1093/mnras/262.3.627.

C. J. Lada and E. A. Lada. Embedded Clusters in Molecular Clouds. *Annual Review of Astronomy & Astrophysics*, 41:57–115, Jan. 2003. doi: 10.1146/annurev.astro.41.011802.094844.

B. P. M. Laevens, N. F. Martin, E. J. Bernard, E. F. Schlafly, B. Sesar, H.-W. Rix, E. F. Bell, A. M. N. Ferguson, C. T. Slater, W. E. Sweeney, R. F. G. Wyse, A. P. Huxor, W. S. Burgett, K. C. Chambers, P. W. Draper, K. A. Hodapp, N. Kaiser, E. A. Magnier, N. Metcalfe, J. L. Tonry, R. J. Wainscoat, and C. Waters. Sagittarius II, Draco II and Laevens 3: Three New Milky Way Satellites Discovered in the Pan-STARRS 1 3π Survey. *The Astrophysical Journal*, 813(1):44, Nov. 2015. doi: 10.1088/0004-637X/813/1/44.

H. J. G. L. M. Lamers, M. Gieles, and S. F. Portegies Zwart. Disruption time scales of star clusters in different galaxies. *Astronomy & Astrophysics*, 429:173–179, Jan 2005. doi: 10.1051/0004-6361:20041476.

A. Lançon and M. Mouhcine. *Stochastic Fluctuations in the Spectrophotometric Properties of Star Clusters*, volume 211 of *Astronomical Society of the Pacific Conference Series*, page 34. 2000.

A. Lapi, C. Mancuso, A. Bressan, and L. Danese. Stellar Mass Function of Active and Quiescent Galaxies via the Continuity Equation. *The Astrophysical Journal*, 847(1):13, Sept. 2017. doi: 10.3847/1538-4357/aa88c9.

H. S. Leavitt and E. C. Pickering. Periods of 25 Variable Stars in the Small Magellanic Cloud. *Harvard College Observatory Circular*, 173:1–3, Mar. 1912.

T. Lebzelter and P. R. Wood. The AGB stars of the intermediate-age LMC cluster NGC 1846. Variability and age determination. *Astronomy & Astrophysics*, 475(2):643–650, Nov. 2007. doi: 10.1051/0004-6361:20078395.

T. Lebzelter, M. T. Lederer, S. Cristallo, K. H. Hinkle, O. Straniero, and B. Aringer. AGB stars of the intermediate-age LMC cluster NGC 1846. II. Dredge up along the AGB. *Astronomy & Astrophysics*, 486(2):511–521, Aug. 2008. doi: 10.1051/0004-6361:200809363.

D. N. C. Lin and D. Lynden-Bell. On the proper motion of the Magellanic Clouds and the halo mass of our galaxy. *Monthly Notices of the Royal Astronomical Society*, 198:707–721, Feb 1982. doi: 10.1093/mnras/198.3.707.

D. N. C. Lin, B. F. Jones, and A. R. Klemola. The Motion of the Magellanic Clouds, Origin of the Magellanic Stream, and the Mass of the Milky Way. *The Astrophysical Journal*, 439:652, Feb 1995. doi: 10.1086/175205.

L. Lindegren, U. Lammers, U. Bastian, J. Hernández, S. Klioner, D. Hobbs, A. Bombrun, D. Michalik, M. Ramos-Lerate, A. Butkevich, G. Comoretto, E. Joliet, B. Holl, A. Hutton, P. Parsons, H. Steidelmüller, U. Abbas, M. Altmann, A. Andrei, S. Anton, N. Bach, C. Barache, U. Becciani, J. Berthier, L. Bianchi, M. Biermann, S. Bouquillon, G. Bourda, T. Brüsemeister, B. Bucciarelli, D. Busonero, T. Carlucci, J. Castañeda, P. Charlot, M. Clotet, M. Crosta, M. Davidson, F. de Felice, R. Drimmel, C. Fabricius, A. Fienga, F. Figueras, E. Fraile, M. Gai, N. Garralda, R. Geyer, J. J. González-Vidal, R. Guerra, N. C. Hambly, M. Hauser, S. Jordan, M. G. Lattanzi, H. Lenhardt, S. Liao, W. Löffler, P. J. McMillan, F. Mignard, A. Mora, R. Morbidelli, J. Portell, A. Riva, M. Sarasso, I. Serraller, H. Siddiqui, R. Smart, A. Spagna, U. Stampa, I. Steele, F. Taris, J. Torra, W. van Reeven, A. Vecchiato, S. Zschocke, J. de Bruijne, G. Gracia, F. Raison, T. Lister, J. Marchant, R. Messineo, M. Soffel, J. Osorio, A. de Torres, and W. O'Mullane. Gaia Data Release 1. Astrometry: one billion positions, two million proper motions and parallaxes. *Astronomy & Astrophysics*, 595:A4, Nov. 2016. doi: 10.1051/0004-6361/201628714.

F. S. Liu, F. J. Lei, X. M. Meng, and D. F. Jiang. Ongoing growth of the brightest cluster galaxies via major dry mergers in the last ∼6 Gyr. *Monthly Notices of the Royal Astronomical Society*, 447(2):1491–1497, Feb. 2015. doi: 10.1093/mnras/stu2543.

L. Liu, B. F. Gerke, R. H. Wechsler, P. S. Behroozi, and M. T. Busha. How Common are the Magellanic Clouds? *The Astrophysical Journal*, 733(1):62, May 2011. doi: 10.1088/0004-637X/733/1/62.

N. Longeard, N. Martin, R. A. Ibata, M. L. M. Collins, B. P. M. Laevens, E. Bell, and D. Mackey. Detailed study of the Milky Way globular cluster Laevens 3. *Monthly Notices of the Royal Astronomical Society*, 490(2):1498–1508, Dec. 2019. doi: 10.1093/mnras/stz2592.

A. Longobardi, M. Arnaboldi, O. Gerhard, and J. C. Mihos. The build-up of the cD halo of M 87: evidence for accretion in the last Gyr. *Astronomy & Astrophysics*, 579:L3, July 2015. doi: 10.1051/0004-6361/201526282.

L. B. Lucy. A numerical approach to the testing of the fission hypothesis. *The Astronomical Journal*, 82:1013–1024, Dec 1977. doi: 10.1086/112164.

D. Lynden-Bell. Dwarf galaxies and globular clusters in high velocity hydrogen streams. *Monthly Notices of the Royal Astronomical Society*, 174:695–710, Mar. 1976. doi: 10.1093/mnras/174.3.695.

A. D. Mackey and G. F. Gilmore. Surface brightness profiles and structural parameters for 53 rich stellar clusters in the Large Magellanic Cloud. *Monthly Notices of the Royal Astronomical Society*, 338(1):85–119, Jan. 2003a. doi: 10.1046/j.1365-8711.2003.06021.x.

A. D. Mackey and G. F. Gilmore. Surface brightness profiles and structural parameters for 10 rich stellar clusters in the Small Magellanic Cloud. *Monthly Notices of the Royal Astronomical Society*, 338(1):120–130, Jan. 2003b. doi: 10.1046/j.1365-8711.2003.06022.x.

A. D. Mackey and G. F. Gilmore. Photometry of Magellanic Cloud clusters with the Advanced Camera for Surveys - I. The old Large Magellanic Cloud clusters NGC 1928, 1939 and Reticulum. *Monthly Notices of the Royal Astronomical Society*, 352(1):153–167, July 2004. doi: 10.1111/j.1365-2966.2004.07908.x.

A. D. Mackey, M. J. Payne, and G. F. Gilmore. Photometry of Magellanic Cloud clusters with the Advanced Camera for Surveys - II. The unique LMC cluster ESO 121-SC03. *Monthly Notices of the Royal Astronomical Society*, 369(2):921–932, June 2006. doi: 10.1111/j.1365-2966.2006.10342.x.

A. D. Mackey, M. I. Wilkinson, M. B. Davies, and G. F. Gilmore. The effect of stellar-mass black holes on the structural evolution of massive star clusters. *Monthly Notices of the Royal Astronomical Society*, 379(1):L40–L44, July 2007. doi: 10.1111/j.1745-3933.2007.00330.x.

A. D. Mackey, M. I. Wilkinson, M. B. Davies, and G. F. Gilmore. Black holes and core expansion in massive star clusters. *Monthly Notices of the Royal Astronomical Society*, 386(1):65–95, May 2008. doi: 10.1111/j.1365-2966.2008.13052.x.

A. D. Mackey, S. E. Koposov, D. Erkal, V. Belokurov, G. S. Da Costa, and F. A. Gómez. A 10 kpc stellar substructure at the edge of the Large Magellanic Cloud: perturbed outer disc or evidence for tidal stripping? *Monthly Notices of the Royal Astronomical Society*, 459(1): 239–255, June 2016. doi: 10.1093/mnras/stw497.

A. D. Mackey, S. E. Koposov, G. S. Da Costa, V. Belokurov, D. Erkal, F. Fraternali, N. M. McClure-Griffiths, and M. Fraser. Structured star formation in the Magellanic inter-Cloud region. *Monthly Notices of the Royal Astronomical Society*, 472(3):2975–2989, Dec. 2017. doi: 10.1093/mnras/stx2035.

D. Mackey, S. Koposov, G. Da Costa, V. Belokurov, D. Erkal, and P. Kuzma. Substructures and

Tidal Distortions in the Magellanic Stellar Periphery. *The Astrophysical Journal Letters*, 858 (2):L21, May 2018. doi: 10.3847/2041-8213/aac175.

F. F. S. Maia, A. E. Piatti, and J. F. C. Santos. Mass distribution and structural parameters of Small Magellanic Cloud star clusters. *Monthly Notices of the Royal Astronomical Society*, 437 (2):2005–2016, Jan. 2014. doi: 10.1093/mnras/stt2039.

F. F. S. Maia, B. Dias, J. F. C. Santos, L. d. O. Kerber, E. Bica, A. E. Piatti, B. Barbuy, B. Quint, L. Fraga, D. Sanmartim, M. S. Angelo, J. A. Hernandez-Jimenez, O. J. Katime Santrich, R. A. P. Oliveira, A. Pérez-Villegas, S. O. Souza, R. G. Vieira, and P. Westera. The VISCACHA survey - I. Overview and first results. *Monthly Notices of the Royal Astronomical Society*, 484(4):5702–5722, Apr. 2019. doi: 10.1093/mnras/stz369.

S. R. Majewski, M. F. Skrutskie, M. D. Weinberg, and J. C. Ostheimer. A Two Micron All Sky Survey View of the Sagittarius Dwarf Galaxy. I. Morphology of the Sagittarius Core and Tidal Arms. *The astrophysical journal*, 599:1082–1115, Dec. 2003. doi: 10.1086/379504.

K. Malhan and R. A. Ibata. STREAMFINDER - I. A new algorithm for detecting stellar streams. *Monthly Notices of the Royal Astronomical Society*, 477(3):4063–4076, July 2018. doi: 10.1093/mnras/sty912.

E. Malumuth and D. Richstone. The evolution of clusters of galaxies. ii - tidal stripping versus mergers as a function of richness. *The astrophysical journal*, 276:413–422, jan 1984. doi: 10.1086/161626.

N. F. Martin, R. A. Ibata, G. F. Lewis, A. McConnachie, A. Babul, N. F. Bate, E. Bernard, S. C. Chapman, M. M. L. Collins, A. R. Conn, D. Crnojević, M. A. Fardal, A. M. N. Ferguson, M. Irwin, A. D. Mackey, B. McMonigal, J. F. Navarro, and R. M. Rich. The PAndAS View of the Andromeda Satellite System. II. Detailed Properties of 23 M31 Dwarf Spheroidal Galaxies. *The Astrophysical Journal*, 833(2):167, Dec. 2016a. doi: 10.3847/1538-4357/833/2/167.

N. F. Martin, V. Jungbluth, D. L. Nidever, E. F. Bell, G. Besla, R. D. Blum, M.-R. L. Cioni, B. C. Conn, C. C. Kaleida, C. Gallart, S. Jin, S. R. Majewski, D. Martinez-Delgado, A. Monachesi, R. R. Muñoz, N. E. D. Noël, K. Olsen, G. S. Stringfellow, R. P. van der Marel, A. K. Vivas, A. R. Walker, and D. Zaritsky. SMASH 1: A Very Faint Globular Cluster Disrupting in the Outer Reaches of the LMC? *The Astrophysical Journal Letters*, 830(1):L10, Oct. 2016b. doi: 10.3847/2041-8205/830/1/L10.

D. Martínez-Delgado, A. K. Vivas, E. K. Grebel, C. Gallart, A. Pieres, C. P. M. Bell, P. Zivick, B. Lemasle, L. Clifton Johnson, J. A. Carballo-Bello, N. E. D. Noël, M.-R. L. Cioni, Y. Choi, G. Besla, J. Schmidt, D. Zaritsky, R. A. Gruendl, M. Seibert, D. Nidever, L. Monteagudo, M. Monelli, B. Hubl, R. van der Marel, F. J. Ballesteros, G. Stringfellow, A. Walker, R. Blum, E. F. Bell, B. C. Conn, K. Olsen, N. Martin, Y.-H. Chu, L. Inno, T. J. L. Boer, N. Kallivayalil, M. De Leo, Y. Beletsky, F. Neyer, and R. R. Muñoz. Nature of a shell of young stars in the outskirts of the Small Magellanic Cloud. *Astronomy & Astrophysics*, 631:A98, Nov. 2019. doi: 10.1051/0004-6361/201936021.

P. Massana, N. E. D. Noël, D. L. Nidever, D. Erkal, T. J. L. de Boer, Y. Choi, S. R. Majewski, K. Olsen, A. Monachesi, C. Gallart, R. P. v. d. Marel, T. Ruiz-Lara, D. Zaritsky, N. F. Martin, R. R. Muñoz, M.-R. L. Cioni, C. P. M. Bell, E. F. Bell, G. S. Stringfellow, V. Belokurov, M. Monelli, A. R. Walker, D. Martínez-Delgado, A. K. Vivas, and B. C. Conn. SMASHing the low surface brightness SMC. *Monthly Notices of the Royal Astronomical Society*, 498(1): 1034–1049, Oct. 2020. doi: 10.1093/mnras/staa2451.

C. Mastropietro, B. Moore, L. Mayer, J. Wadsley, and J. Stadel. The gravitational and hydrodynamical interaction between the Large Magellanic Cloud and the Galaxy. *Monthly Notices of the Royal Astronomical Society*, 363(2):509–520, Oct 2005. doi: 10.1111/j.1365-2966.2005.09435.x.

M. Mateo, P. Hodge, and R. A. Schommer. CCD Photometry of Large Magellanic Cloud Clusters. III. The Unique, Remote Cluster ESO 121-SC03. *The Astrophysical Journal*, 311:113, Dec. 1986. doi: 10.1086/164757.

D. S. Mathewson, M. N. Cleary, and J. D. Murray. The Magellanic Stream. *The Astrophysical Journal*, 190:291–296, June 1974. doi: 10.1086/152875.

A. Mazzi, L. Girardi, S. Zaggia, G. Pastorelli, S. Rubele, A. Bressan, M.-R. L. Cioni, G. Clementini, F. Cusano, J. P. Rocha, M. Gullieuszik, L. Kerber, P. Marigo, V. Ripepi, K. Bekki, C. P. M. Bell, R. de Grijs, M. A. T. Groenewegen, V. D. Ivanov, J. M. Oliveira, N.-C. Sun, and J. T. van Loon. The VMC survey - XLIII. The spatially resolved star formation history across the Large Magellanic Cloud. *Monthly Notices of the Royal Astronomical Society*, 508 (1):245–266, Nov. 2021. doi: 10.1093/mnras/stab2399.

A. W. McConnachie, M. J. Irwin, R. A. Ibata, J. Dubinski, L. M. Widrow, N. F. Martin, P. Côté, A. L. Dotter, J. F. Navarro, A. M. N. Ferguson, T. H. Puzia, G. F. Lewis, A. Babul, P. Barmby,

O. Bienaymé, S. C. Chapman, R. Cockcroft, M. L. M. Collins, M. A. Fardal, W. E. Harris, A. Huxor, A. D. Mackey, J. Peñarrubia, R. M. Rich, H. B. Richer, A. Siebert, N. Tanvir, D. Valls-Gabaud, and K. A. Venn. The remnants of galaxy formation from a panoramic survey of the region around M31. *Nature*, 461:66–69, Sept. 2009. doi: 10.1038/nature08327.

J. P. McFarland, G. Verdoes-Kleijn, G. Sikkema, E. M. Helmich, D. R. Boxhoorn, and E. A. Valentijn. The Astro-WISE optical image pipeline. Development and implementation. *Experimental Astronomy*, 35(1-2):45–78, Jan. 2013. doi: 10.1007/s10686-011-9266-x.

D. E. McLaughlin and R. P. van der Marel. Resolved Massive Star Clusters in the Milky Way and Its Satellites: Brightness Profiles and a Catalog of Fundamental Parameters. *The Astrophysical Journal Supplementary Material*, 161(2):304–360, Dec. 2005. doi: 10.1086/497429.

R. J. McLure, J. S. Pearce, H. J.and Dunlop, M. Cirasuolo, E. Curtis-Lake, V. A. Bruce, K. I. Caputi, O. Almaini, D. G. Bonfield, E. J. Bradshaw, F. Buitrago, R. Chuter, S. Foucaud, W. G. Hartley, and M. J. Jarvis. The sizes, masses and specific star formation rates of massive galaxies at $1.3 < z < 1.5$: strong evidence in favour of evolution via minor mergers. *Monthly Notices of the Royal Astronomical Society*, 428, 01 2013. doi: 10.1093/mnras/sts092. URL `http://gen.lib.rus.ec/scimag/index.php?s=10.1093/mnras/sts092`.

R. G. McMahon, M. Banerji, E. Gonzalez, S. E. Koposov, V. J. Bejar, N. Lodieu, R. Rebolo, and VHS Collaboration. First Scientific Results from the VISTA Hemisphere Survey (VHS). *The Messenger*, 154:35–37, Dec. 2013.

A. Mellinger. A Color All-Sky Panorama Image of the Milky Way. *Publications of the Astronomical Society of the Pacific*, 121(885):1180, Nov. 2009. doi: 10.1086/648480.

H. R. Merrett, K. Kuijken, M. R. Merrifield, A. J. Romanowsky, N. G. Douglas, N. R. Napolitano, M. Arnaboldi, M. Capaccioli, K. C. Freeman, O. Gerhard, N. W. Evans, M. I. Wilkinson, C. Halliday, T. J. Bridges, and D. Carter. Tracing the star stream through M31 using planetary nebula kinematics. *Monthly Notices of the Royal Astronomical Society*, 346:L62–L66, Dec. 2003. doi: 10.1111/j.1365-2966.2003.07367.x.

H. R. Merrett, M. R. Merrifield, N. G. Douglas, K. Kuijken, A. J. Romanowsky, N. R. Napolitano, M. Arnaboldi, M. Capaccioli, K. C. Freeman, O. Gerhard, L. Coccato, D. Carter, N. W. Evans, M. I. Wilkinson, C. Halliday, and T. J. Bridges. A deep kinematic survey of planetary nebulae

in the Andromeda galaxy using the Planetary Nebula Spectrograph. *Monthly Notices of the Royal Astronomical Society*, 369(1):120–142, Jun 2006. doi: 10.1111/j.1365-2966.2006.10268.x.

D. Merritt. Relaxation and tidal stripping in rich clusters of galaxies. iii - growth of a massive central galaxy. *The astrophysical journal*, 289:18–32, feb 1985. doi: 10.1086/162860.

D. Merritt, S. Piatek, S. Portegies Zwart, and M. Hemsendorf. Core Formation by a Population of Massive Remnants. *The Astrophysical Journal Letters*, 608(1):L25–L28, June 2004. doi: 10.1086/422252.

K. J. Mighell, A. Sarajedini, and R. S. French. WFPC2 Observations of Star Clusters in the Magellanic Clouds. II. The Oldest Star Clusters in the Small Magellanic Cloud. *The Astronomical Journal*, 116(5):2395–2414, Nov. 1998. doi: 10.1086/300591.

J. C. Mihos, P. Harding, J. J. Feldmeier, C. Rudick, S. Janowiecki, H. Morrison, C. Slater, and A. Watkins. The Burrell Schmidt Deep Virgo Survey: Tidal Debris, Galaxy Halos, and Diffuse Intracluster Light in the Virgo Cluster. *The Astrophysical Journal*, 834:16, Jan. 2017. doi: 10.3847/1538-4357/834/1/16.

D. Minniti, T. Palma, I. Dékány, M. Hempel, M. Rejkuba, J. Pullen, J. Alonso-García, R. Barbá, B. Barbuy, E. Bica, C. Bonatto, J. Borissova, M. Catelan, J. A. Carballo-Bello, A. N. Chene, J. J. Clariá, R. E. Cohen, R. Contreras Ramos, B. Dias, J. Emerson, D. Froebrich, A. S. M. Buckner, D. Geisler, O. A. Gonzalez, F. Gran, G. Hajdu, M. Irwin, V. D. Ivanov, R. Kurtev, P. W. Lucas, D. Majaess, F. Mauro, C. Moni-Bidin, C. Navarrete, S. Ramírez Alegría, R. K. Saito, E. Valenti, and M. Zoccali. FSR 1716: A New Milky Way Globular Cluster Confirmed Using VVV RR Lyrae Stars. *The Astrophysical Journal Letters*, 838(1):L14, Mar. 2017. doi: 10.3847/2041-8213/838/1/L14.

A. Mok, R. Chandar, and S. M. Fall. Feedback in Forming Star Clusters: The Mass-Radius Relation and Mass Function of Molecular Clumps in the Large Magellanic Cloud. *arXiv e-prints*, art. arXiv:2101.12260, Jan. 2021.

B. Moore and M. Davis. The origin of the Magellanic Stream. *Monthly Notices of the Royal Astronomical Society*, 270:209–221, Sep 1994. doi: 10.1093/mnras/270.2.209.

B. Moore, N. Katz, G. Lake, A. Dressler, and A. Oemler. Galaxy harassment and the evolution of clusters of galaxies. *Nature*, 379, 1996. doi: 10.1038/379613a0. URL `http://gen.lib.rus.ec/scimag/index.php?s=10.1038/379613a0`.

A. Mucciarelli, F. R. Ferraro, L. Origlia, and F. Fusi Pecci. The Globular Cluster NGC 1978 in the Large Magellanic Cloud. *The Astronomical Journal*, 133(5):2053–2060, May 2007. doi: 10.1086/513076.

A. Mucciarelli, D. Massari, A. Minelli, D. Romano, M. Bellazzini, F. R. Ferraro, F. Matteucci, and L. Origlia. A relic from a past merger event in the Large Magellanic Cloud. *Nature Astronomy*, 5:1247–1254, Oct. 2021. doi: 10.1038/s41550-021-01493-y.

R. P. Munoz, P. Eigenthaler, T. H. Puzia, M. A. Taylor, Y. Ordenes-Briceño, K. Alamo-Martínez, K. X. Ribbeck, S. Ángel, M. Capaccioli, P. Côté, L. Ferrarese, G. Galaz, M. Hempel, M. Hilker, A. Jordán, A. Lançon, S. Mieske, M. Paolillo, T. Richtler, R. Sánchez-Janssen, and H. Zhang. Unveiling a Rich System of Faint Dwarf Galaxies in the Next Generation Fornax Survey. *The astrophysical journal, Letters*, 813:L15, Nov. 2015. doi: 10.1088/2041-8205/813/1/L15.

T. Murai and M. Fujimoto. The Magellanic stream and the galaxy with a massive halo. *Publications of the ASJ*, 32:581–603, Jan 1980.

T. Muraveva, S. Subramanian, G. Clementini, M. R. L. Cioni, M. Palmer, J. T. van Loon, M. I. Moretti, R. de Grijs, R. Molinaro, V. Ripepi, M. Marconi, J. Emerson, and V. D. Ivanov. The VMC survey - XXVI. Structure of the Small Magellanic Cloud from RR Lyrae stars. *Monthly Notices of the Royal Astronomical Society*, 473(3):3131–3146, Jan. 2018. doi: 10.1093/mnras/stx2514.

T. Naab, P. H. Johansson, J. P. Ostriker, and G. Efstathiou. Formation of Early-Type Galaxies from Cosmological Initial Conditions. *The Astrophysical Journal*, 658:710–720, Apr. 2007. doi: 10.1086/510841.

T. Naab, P. H. Johansson, and J. P. Ostriker. Minor Mergers and the Size Evolution of Elliptical Galaxies. *The Astrophysical Journal Letters*, 699:L178–L182, July 2009. doi: 10.1088/0004-637X/699/2/L178.

N. R. Napolitano, M. Arnaboldi, K. C. Freeman, and M. Capaccioli. Planetary nebulae as mass tracers of their parent galaxies: Biases in the estimate of the kinematical quantities. *Astronomy & Astrophysics*, 377:784–800, Oct. 2001. doi: 10.1051/0004-6361:20011106.

N. R. Napolitano, M. Arnaboldi, and M. Capaccioli. NGC 1399: A complex dynamical case. *Astronomy and Astrophysics*, 383:791–800, Mar. 2002. doi: 10.1051/0004-6361:20011795.

N. R. Napolitano, M. Pannella, M. Arnaboldi, O. Gerhard, J. A. L. Aguerri, K. C. Freeman, M. Capaccioli, S. Ghigna, F. Governato, T. Quinn, and J. Stadel. Intracluster stellar population properties from n -body cosmological simulations. i. constraints at z = 0. *The Astrophysical Journal*, 594, 09 2003. doi: 10.1086/376860. URL `http://gen.lib.rus.ec/scimag/index.php?s=10.1086/376860`.

N. R. Napolitano, A. J. Romanowsky, L. Coccato, M. Capaccioli, N. G. Douglas, E. Noordermeer, O. Gerhard, M. Arnaboldi, F. de Lorenzi, K. Kuijken, M. R. Merrifield, E. O'Sullivan, A. Cortesi, P. Das, and K. C. Freeman. The Planetary Nebula Spectrograph elliptical galaxy survey: the dark matter in NGC 4494. *Monthly Notices of the RAS*, 393:329–353, Feb. 2009. doi: 10.1111/j.1365-2966.2008.14053.x.

N. R. Napolitano, A. J. Romanowsky, M. Capaccioli, N. G. Douglas, M. Arnaboldi, L. Coccato, O. Gerhard, K. Kuijken, M. R. Merrifield, S. P. Bamford, A. Cortesi, P. Das, and K. C. Freeman. The PN.S Elliptical Galaxy Survey: a standard ΛCDM halo around NGC 4374? *Monthly Notices of the Royal Astronomical Society*, 411(3):2035–2053, Mar 2011. doi: 10.1111/j.1365-2966.2010.17833.x.

N. R. Napolitano, M. Gatto, C. Spiniello, M. Cantiello, M. Hilker, M. Arnaboldi, C. Tortora, A. Chaturvedi, R. D'Abrusco, R. Li, M. Paolillo, R. Peletier, T. Saifollahi, M. Spavone, A. Venhola, M. Capaccioli, and G. Longo. The Fornax Cluster VLT Spectroscopic Survey. IV. Cold kinematical substructures in the Fornax core from COSTA. *Astronomy & Astrophysics*, 657: A94, Jan. 2022. doi: 10.1051/0004-6361/202141872.

J. F. Navarro, C. S. Frenk, and S. D. M. White. A Universal Density Profile from Hierarchical Clustering. *The Astrophysical Journal*, 490(2):493–508, Dec. 1997. doi: 10.1086/304888.

P. K. Nayak, A. Subramaniam, S. Choudhury, G. Indu, and R. Sagar. Star clusters in the Magellanic Clouds - I. Parametrization and classification of 1072 clusters in the LMC. *Monthly Notices of the Royal Astronomical Society*, 463(2):1446–1461, dec 2016. ISSN 13652966. doi: 10.1093/mnras/stw2043.

P. K. Nayak, A. Subramaniam, S. Choudhury, and R. Sagar. Star clusters in the Magellanic Clouds. II. Age-dating, classification, and spatio-temporal distribution of the SMC clusters. *Astronomy & Astrophysics*, 616:A187, Sept. 2018. doi: 10.1051/0004-6361/201732227.

M. Nichols, J. Colless, M. Colless, and J. Bland-Hawthorn. Accretion of the Magellanic System onto the Galaxy. *The Astrophysical Journal*, 742(2):110, Dec. 2011. doi: 10.1088/0004-637X/742/2/110.

D. L. Nidever, S. R. Majewski, W. Butler Burton, and L. Nigra. The 200° Long Magellanic Stream System. *The Astrophysical Journal*, 723(2):1618–1631, Nov. 2010. doi: 10.1088/0004-637X/723/2/1618.

D. L. Nidever, A. Monachesi, E. F. Bell, S. R. Majewski, R. R. Muñoz, and R. L. Beaton. A Tidally Stripped Stellar Component of the Magellanic Bridge. *The Astrophysical Journal*, 779 (2):145, Dec. 2013. doi: 10.1088/0004-637X/779/2/145.

D. L. Nidever, K. Olsen, A. R. Walker, A. K. Vivas, R. D. Blum, C. Kaleida, Y. Choi, B. C. Conn, R. A. Gruendl, E. F. Bell, G. Besla, R. R. Muñoz, C. Gallart, N. F. Martin, E. W. Olszewski, A. Saha, A. Monachesi, M. Monelli, T. J. L. de Boer, L. C. Johnson, D. Zaritsky, G. S. Stringfellow, R. P. van der Marel, M.-R. L. Cioni, S. Jin, S. R. Majewski, D. Martinez-Delgado, L. Monteagudo, N. E. D. Noël, E. J. Bernard, A. Kunder, Y.-H. Chu, C. P. M. Bell, F. Santana, J. Frechem, G. E. Medina, V. Parkash, J. C. S. Navarrete, and C. Hayes. SMASH: Survey of the MAgellanic Stellar History. *The Astronomical Journal*, 154(5):199, Nov. 2017. doi: 10.3847/1538-3881/aa8d1c.

D. L. Nidever, K. Olsen, Y. Choi, T. J. L. de Boer, R. D. Blum, E. F. Bell, D. Zaritsky, N. F. Martin, A. Saha, B. C. Conn, G. Besla, R. P. van der Marel, N. E. D. Noël, A. Monachesi, G. S. Stringfellow, P. Massana, M.-R. L. Cioni, C. Gallart, M. Monelli, D. Martinez-Delgado, R. R. Muñoz, S. R. Majewski, A. K. Vivas, A. R. Walker, C. Kaleida, and Y.-H. Chu. Exploring the Very Extended Low-surface-brightness Stellar Populations of the Large Magellanic Cloud with SMASH. *The Astrophysical Journal*, 874(2):118, Apr. 2019. doi: 10.3847/1538-4357/aafaf7.

C. Nipoti. The special growth history of central galaxies in groups and clusters. *Monthly Notices of the Royal Astronomical Society*, 467(1):661–673, May 2017. doi: 10.1093/mnras/stx112.

N. E. D. Noël, B. C. Conn, R. Carrera, J. I. Read, H. W. Rix, and A. Dolphin. The MAGellanic Inter-Cloud Project (MAGIC). I. Evidence for Intermediate-age Stellar Populations in between the Magellanic Clouds. *The Astrophysical Journal*, 768(2):109, May 2013. doi: 10.1088/0004-637X/768/2/109.

N. E. D. Noël, B. C. Conn, J. I. Read, R. Carrera, A. Dolphin, and H. W. Rix. The MAGellanic Inter-Cloud (MAGIC) project - II. Slicing up the Bridge. *Monthly Notices of the Royal Astronomical Society*, 452(4):4222–4235, Oct. 2015. doi: 10.1093/mnras/stv1614.

K. Olsen, P. Szkody, M.-R. Cioni, M. Di Criscienzo, I. Musella, V. Ripepi, F. Borsa, M. Marconi, L. Girardi, G. Pastorelli, M. Trabucchi, P. Ventura, and M. Moniez. Mapping the Periphery and Variability of the Magellanic Clouds. *arXiv e-prints*, art. arXiv:1812.03139, Dec. 2018.

K. A. G. Olsen. Star Formation Histories from Hubble Space Telescope Color-Magnitude Diagrams of Six Fields of the Large Magellanic Cloud. *The Astronomical Journal*, 117(5):2244–2267, May 1999. doi: 10.1086/300854.

K. A. G. Olsen and C. Salyk. A Warp in the Large Magellanic Cloud Disk? *The Astronomical Journal*, 124(4):2045–2053, Oct. 2002. doi: 10.1086/342739.

K. A. G. Olsen, P. W. Hodge, M. Mateo, E. W. Olszewski, R. A. Schommer, N. B. Suntzeff, and A. R. Walker. HSTcolour-magnitude diagrams of six old globular clusters in the LMC. *Monthly Notices of the Royal Astronomical Society*, 300(3):665–685, Nov. 1998. doi: 10.1046/j.1365-8711.1998.01860.x.

K. A. G. Olsen, D. Zaritsky, R. D. Blum, M. L. Boyer, and K. D. Gordon. A Population of Accreted Small Magellanic Cloud Stars in the Large Magellanic Cloud. *The Astrophysical Journal*, 737(1):29, Aug. 2011. doi: 10.1088/0004-637X/737/1/29.

E. W. Olszewski, R. A. Schommer, N. B. Suntzeff, and H. C. Harris. Spectroscopy of Giants in LMC Clusters. I. Velocities, Abundances, and the Age-Metallicity Relation. *The Astronomical Journal*, 101:515, Feb. 1991. doi: 10.1086/115701.

A. O. Omkumar, S. Subramanian, F. Niederhofer, J. Diaz, M.-R. L. Cioni, D. El Youssoufi, K. Bekki, R. de Grijs, and J. T. van Loon. Gaia view of a stellar sub-structure in front of the Small Magellanic Cloud. *Monthly Notices of the Royal Astronomical Society*, 500(3):2757–2776, Jan. 2021. doi: 10.1093/mnras/staa3085.

L. Oser, J. P. Ostriker, T. Naab, P. H. Johansson, and A. Burkert. The Two Phases of Galaxy Formation. *The Astrophysical Journal*, 725:2312–2323, Dec. 2010. doi: 10.1088/0004-637X/725/2/2312.

L. Oser, T. Naab, J. P. Ostriker, and P. H. Johansson. The Cosmological Size and Velocity Dispersion Evolution of Massive Early-type Galaxies. *The Astrophysical Journal*, 744:63, Jan. 2012. doi: 10.1088/0004-637X/744/1/63.

J. Ostriker and S. Tremaine. Another evolutionary correction to the luminosity of giant galaxies. *The astrophysical journal*, 202:L113–L117, dec 1975. doi: 10.1086/181992.

A. B. Pace and T. S. Li. Proper Motions of Milky Way Ultra-faint Satellites with Gaia DR2 × DES DR1. *The Astrophysical Journal*, 875(1):77, Apr. 2019. doi: 10.3847/1538-4357/ab0aee.

T. Palma, L. V. Gramajo, J. J. Clariá, M. Lares, D. Geisler, and A. V. Ahumada. Catalogue of Large Magellanic Cloud star clusters observed in the Washington photometric system. *Astronomy & Astrophysics*, 586:A41, Feb. 2016. doi: 10.1051/0004-6361/201527305.

S. A. Pardy, E. D'Onghia, and A. J. Fox. Models of Tidally Induced Gas Filaments in the Magellanic Stream. *The Astrophysical Journal*, 857(2):101, Apr 2018. doi: 10.3847/1538-4357/aab95b.

S. A. Pardy, E. D'Onghia, J. F. Navarro, R. Grand, F. A. Gómez, F. Marinacci, R. Pakmor, C. Simpson, and V. Springel. Satellites of Satellites: The Case for Carina and Fornax. *Monthly Notices of the Royal Astronomical Society*, 492(2):1543–1549, Feb. 2020. doi: 10.1093/mnras/stz3192.

M. C. Parisi, D. Geisler, J. J. Clariá, S. Villanova, N. Marcionni, A. Sarajedini, and A. J. Grocholski. Ca II Triplet Spectroscopy of Small Magellanic Cloud Red Giants. III. Abundances and Velocities for a Sample of 14 Clusters. *The Astronomical Journal*, 149(5):154, May 2015. doi: 10.1088/0004-6256/149/5/154.

S. Parsa, J. S. Dunlop, R. J. McLure, and A. Mortlock. The galaxy uv luminosity function at z $\sim$ 2–4; new results on faint-end slope and the evolution of luminosity density. *Monthly Notices of the Royal Astronomical Society*, 456, 03 2016. doi: 10.1093/mnras/stv2857. URL `http://gen.lib.rus.ec/scimag/index.php?s=10.1093/mnras/stv2857`.

E. Patel, N. Kallivayalil, N. Garavito-Camargo, G. Besla, D. R. Weisz, R. P. van der Marel, M. Boylan-Kolchin, M. S. Pawlowski, and F. A. Gómez. The Orbital Histories of Magellanic Satellites Using Gaia DR2 Proper Motions. *The Astrophysical Journal*, 893(2):121, Apr. 2020. doi: 10.3847/1538-4357/ab7b75.

D. B. Pavani, L. O. Kerber, E. Bica, and W. J. Maciel. Diagnostic tool to analyse colour-magnitude diagrams of poorly populated stellar concentrations. *Monthly Notices of the Royal Astronomical Society*, 412(3):1611–1626, Apr 2011. doi: 10.1111/j.1365-2966.2010.17999.x.

F. Pedregosa, G. Varoquaux, A. Gramfort, V. Michel, B. Thirion, O. Grisel, M. Blondel, P. Prettenhofer, R. Weiss, V. Dubourg, J. Vanderplas, A. Passos, D. Cournapeau, M. Brucher, M. Perrot, and E. Duchesnay. Scikit-learn: Machine learning in Python. *Journal of Machine Learning Research*, 12:2825–2830, 2011.

E. W. Peng, H. C. Ford, and K. C. Freeman. The Planetary Nebula System and Dynamics in the Outer Halo of NGC 5128. *The Astrophysical Journal*, 602(2):685–704, Feb. 2004. doi: 10.1086/381160.

G. I. Perren, R. A. Vázquez, and A. E. Piatti. ASteCA: Automated Stellar Cluster Analysis. *Astronomy & Astrophysics*, 576:A6, Apr. 2015. doi: 10.1051/0004-6361/201424946.

G. I. Perren, A. E. Piatti, and R. A. Vázquez. Astrophysical properties of star clusters in the Magellanic Clouds homogeneously estimated by ASteCA. *Astronomy & Astrophysics*, 602: A89, Jun 2017. doi: 10.1051/0004-6361/201629520.

M. S. Petersen, J. Peñarrubia, and E. Jones. Tidally stripped halo stars from the Large Magellanic Cloud in the Galactic North. *arXiv e-prints*, art. arXiv:2106.13770, June 2021.

A. E. Piatti. Stellar Cluster Candidates Discovered in the Magellanic System. *The Astrophysical Journal Letters*, 834(2):L14, Jan 2017a. doi: 10.3847/2041-8213/834/2/L14.

A. E. Piatti. The real population of star clusters in the bar of the Large Magellanic Cloud. *Astronomy & Astrophysics*, 606:A21, Sep 2017b. doi: 10.1051/0004-6361/201731246.

A. E. Piatti. Astrophysical properties of newly discovered Magellanic Cloud star clusters. *Astronomy & Astrophysics*, 647:A47, Mar. 2021a. doi: 10.1051/0004-6361/202039729.

A. E. Piatti. Revisiting Newly Large Magellanic Cloud Age-gap Star Clusters. *The Astronomical Journal*, 161(4):199, Apr. 2021b. doi: 10.3847/1538-3881/abe545.

A. E. Piatti. The structure of Small Magellanic Cloud star clusters. *Astronomy & Astrophysics*, 647:A11, Mar. 2021c. doi: 10.1051/0004-6361/202039888.

A. E. Piatti. Revisiting a detached stellar structure in the outer north-eastern region of the Small Magellanic Cloud. *Monthly Notices of the Royal Astronomical Society*, 509(3):3462–3469, Jan. 2022a. doi: 10.1093/mnras/stab3190.

A. E. Piatti. A genuine Large Magellanic Cloud age gap star cluster. *arXiv e-prints*, art. arXiv:2201.09926, Jan. 2022b.

A. E. Piatti and E. Bica. Washington photometry of candidate star clusters in the Small Magellanic Cloud. *Monthly Notices of the Royal Astronomical Society*, 425(4):3085–3093, 2012. ISSN 13652966. doi: 10.1111/j.1365-2966.2012.21694.x.

A. E. Piatti and D. Geisler. The age-metallicity relationship of the large magellanic cloud field star population from wide-field washington photometry. *Astronomical Journal*, 145(1), jan 2013. ISSN 00046256. doi: 10.1088/0004-6256/145/1/17.

A. E. Piatti and A. D. Mackey. Evidence of differential tidal effects in the old globular cluster population of the Large Magellanic Cloud. *Monthly Notices of the Royal Astronomical Society*, 478(2):2164–2176, Aug. 2018. doi: 10.1093/mnras/sty1048.

A. E. Piatti, J. Santos, J. F. C., J. J. Clariá, E. Bica, A. V. Ahumada, and M. C. Parisi. Integrated spectral analysis of 18 concentrated star clusters in the Small Magellanic Cloud. *Astronomy & Astrophysics*, 440(1):111–120, Sept. 2005. doi: 10.1051/0004-6361:20052982.

A. E. Piatti, D. Geisler, A. Sarajedini, and C. Gallart. Washington photometry of five star clusters in the Large Magellanic Cloud. *Astronomy & Astrophysics*, 501(2):585–593, July 2009. doi: 10.1051/0004-6361/200912223.

A. E. Piatti, R. Guandalini, V. D. Ivanov, S. Rubele, M. R. L. Cioni, R. De Grijs, B. Q. For, G. Clementini, V. Ripepi, P. Anders, and J. M. Oliveira. The VMC survey: XII. Star cluster candidates in the large magellanic cloud. *Astronomy and Astrophysics*, 570, oct 2014. ISSN 14320746. doi: 10.1051/0004-6361/201424175.

A. E. Piatti, R. de Grijs, V. Ripepi, V. D. Ivanov, M. R. L. Cioni, M. Marconi, S. Rubele, K. Bekki, and B. Q. For. The VMC survey - XVI. Spatial variation of the cluster formation activity in the innermost regions of the Large Magellanic Cloud. *Monthly Notices of the Royal Astronomical Society*, 454(1):839–848, 2015a. ISSN 13652966. doi: 10.1093/mnras/stv2054.

A. E. Piatti, R. de Grijs, S. Rubele, M. R. L. Cioni, V. Ripepi, and L. Kerber. The VMC survey - XV. The Small Magellanic Cloud-Bridge connection history as traced by their star cluster

populations. *Monthly Notices of the Royal Astronomical Society*, 450(1):552–563, 2015b. ISSN 13652966. doi: 10.1093/mnras/stv635.

A. E. Piatti, V. D. Ivanov, S. Rubele, M. Marconi, V. Ripepi, M. R. L. Cioni, J. M. Oliveira, and K. Bekki. The VMC Survey - XXI. New star cluster candidates discovered from infrared photometry in the Small Magellanic Cloud. *Monthly Notices of the Royal Astronomical Society*, 460(1):383–395, 2016. ISSN 13652966. doi: 10.1093/mnras/stw1000.

A. E. Piatti, A. A. Cole, and B. Emptage. Star cluster formation history along the minor axis of the Large Magellanic Cloud. *Monthly Notices of the Royal Astronomical Society*, 473(1): 105–115, 2018. ISSN 13652966. doi: 10.1093/mnras/stx2418.

A. Pieres, B. Santiago, E. Balbinot, E. Luque, A. Queiroz, L. N. da Costa, M. A. G. Maia, A. Drlica-Wagner, A. Roodman, T. M. C. Abbott, S. Allam, A. Benoit-Lévy, E. Bertin, D. Brooks, E. Buckley-Geer, D. L. Burke, A. Carnero Rosell, M. Carrasco Kind, J. Carretero, C. E. Cunha, S. Desai, H. T. Diehl, T. F. Eifler, D. A. Finley, B. Flaugher, P. Fosalba, J. Frieman, D. W. Gerdes, D. Gruen, R. A. Gruendl, G. Gutierrez, K. Honscheid, D. J. James, K. Kuehn, N. Kuropatkin, O. Lahav, T. S. Li, J. L. Marshall, P. Martini, C. J. Miller, R. Miquel, R. C. Nichol, B. Nord, R. Ogando, A. A. Plazas, A. K. Romer, E. Sanchez, V. Scarpine, M. Schubnell, I. Sevilla-Noarbe, R. C. Smith, M. Soares-Santos, F. Sobreira, E. Suchyta, M. E. C. Swanson, G. Tarle, J. Thaler, D. Thomas, D. L. Tucker, and A. R. Walker. Physical properties of star clusters in the outer LMC as observed by the DES. *Monthly Notices of the Royal Astronomical Society*, 461(1):519–541, Sep 2016. doi: 10.1093/mnras/stw1260.

A. Pieres, B. X. Santiago, A. Drlica-Wagner, K. Bechtol, R. P. v. d. Marel, G. Besla, N. F. Martin, V. Belokurov, C. Gallart, D. Martinez-Delgado, J. Marshall, N. E. D. Nöel, S. R. Majewski, M. R. L. Cioni, T. S. Li, W. Hartley, E. Luque, B. C. Conn, A. R. Walker, E. Balbinot, G. S. Stringfellow, K. A. G. Olsen, D. Nidever, L. N. da Costa, R. Ogando, M. Maia, A. F. Neto, T. M. C. Abbott, F. B. Abdalla, S. Allam, J. Annis, A. Benoit-Lévy, A. C. Rosell, M. C. Kind, J. Carretero, C. E. Cunha, C. B. D'Andrea, S. Desai, H. T. Diehl, P. Doel, B. Flaugher, P. Fosalba, J. García-Bellido, D. Gruen, R. A. Gruendl, J. Gschwend, G. Gutierrez, K. Honscheid, D. James, K. Kuehn, N. Kuropatkin, F. Menanteau, R. Miquel, A. A. Plazas, A. K. Romer, M. Sako, E. Sanchez, V. Scarpine, M. Schubnell, I. Sevilla-Noarbe, R. C. Smith, M. Soares-Santos, F. Sobreira, E. Suchyta, M. E. C. Swanson, G. Tarle, D. L. Tucker, and W. Wester. A

stellar overdensity associated with the Small Magellanic Cloud. *Monthly Notices of the Royal Astronomical Society*, 468(2):1349–1360, June 2017. doi: 10.1093/mnras/stx507.

G. Pietrzyński and A. Udalski. The optical gravitational lensing experiment. Multiple cluster candidates in the small magellanic cloud. *Acta Astronomica*, 49(2):165–169, 1999. ISSN 00015237.

G. Pietrzyński and A. Udalski. The optical gravitational lensing experiment. Ages of about 600 star clusters from the LMC. *Acta Astronomica*, 50(3):337–354, 2000. ISSN 00015237.

G. Pietrzyński, D. Graczyk, A. Gallenne, W. Gieren, I. B. Thompson, B. Pilecki, P. Karczmarek, M. Górski, K. Suchomska, M. Taormina, B. Zgirski, P. Wielgórski, Z. Kołaczkowski, P. Konorski, S. Villanova, N. Nardetto, P. Kervella, F. Bresolin, R. P. Kudritzki, J. Storm, R. Smolec, and W. Narloch. A distance to the Large Magellanic Cloud that is precise to one per cent. *Nature*, 567(7747):200–203, Mar 2019. doi: 10.1038/s41586-019-0999-4.

Planck Collaboration, N. Aghanim, Y. Akrami, M. Ashdown, J. Aumont, C. Baccigalupi, M. Ballardini, A. J. Banday, R. B. Barreiro, N. Bartolo, S. Basak, R. Battye, K. Benabed, J. P. Bernard, M. Bersanelli, P. Bielewicz, J. J. Bock, J. R. Bond, J. Borrill, F. R. Bouchet, F. Boulanger, M. Bucher, C. Burigana, R. C. Butler, E. Calabrese, J. F. Cardoso, J. Carron, A. Challinor, H. C. Chiang, J. Chluba, L. P. L. Colombo, C. Combet, D. Contreras, B. P. Crill, F. Cuttaia, P. de Bernardis, G. de Zotti, J. Delabrouille, J. M. Delouis, E. Di Valentino, J. M. Diego, O. Doré, M. Douspis, A. Ducout, X. Dupac, S. Dusini, G. Efstathiou, F. Elsner, T. A. Enßlin, H. K. Eriksen, Y. Fantaye, M. Farhang, J. Fergusson, R. Fernandez-Cobos, F. Finelli, F. Forastieri, M. Frailis, A. A. Fraisse, E. Franceschi, A. Frolov, S. Galeotta, S. Galli, K. Ganga, R. T. Génova-Santos, M. Gerbino, T. Ghosh, J. González-Nuevo, K. M. Górski, S. Gratton, A. Gruppuso, J. E. Gudmundsson, J. Hamann, W. Handley, F. K. Hansen, D. Herranz, S. R. Hildebrandt, E. Hivon, Z. Huang, A. H. Jaffe, W. C. Jones, A. Karakci, E. Keihänen, R. Keskitalo, K. Kiiveri, J. Kim, T. S. Kisner, L. Knox, N. Krachmalnicoff, M. Kunz, H. Kurki-Suonio, G. Lagache, J. M. Lamarre, A. Lasenby, M. Lattanzi, C. R. Lawrence, M. Le Jeune, P. Lemos, J. Lesgourgues, F. Levrier, A. Lewis, M. Liguori, P. B. Lilje, M. Lilley, V. Lindholm, M. López-Caniego, P. M. Lubin, Y. Z. Ma, J. F. Macías-Pérez, G. Maggio, D. Maino, N. Mandolesi, A. Mangilli, A. Marcos-Caballero, M. Maris, P. G. Martin, M. Martinelli, E. Martínez-González, S. Matarrese, N. Mauri, J. D. McEwen, P. R. Meinhold, A. Melchiorri, A. Mennella, M. Migliaccio, M. Millea, S. Mitra, M. A. Miville-Deschênes,

D. Molinari, L. Montier, G. Morgante, A. Moss, P. Natoli, H. U. Nørgaard-Nielsen, L. Pagano, D. Paoletti, B. Partridge, G. Patanchon, H. V. Peiris, F. Perrotta, V. Pettorino, F. Piacentini, L. Polastri, G. Polenta, J. L. Puget, J. P. Rachen, M. Reinecke, M. Remazeilles, A. Renzi, G. Rocha, C. Rosset, G. Roudier, J. A. Rubiño-Martín, B. Ruiz-Granados, L. Salvati, M. Sandri, M. Savelainen, D. Scott, E. P. S. Shellard, C. Sirignano, G. Sirri, L. D. Spencer, R. Sunyaev, A. S. Suur-Uski, J. A. Tauber, D. Tavagnacco, M. Tenti, L. Toffolatti, M. Tomasi, T. Trombetti, L. Valenziano, J. Valiviita, B. Van Tent, L. Vibert, P. Vielva, F. Villa, N. Vittorio, B. D. Wandelt, I. K. Wehus, M. White, S. D. M. White, A. Zacchei, and A. Zonca. Planck 2018 results. VI. Cosmological parameters. *Astronomy & Astrophysics*, 641:A6, Sept. 2020. doi: 10.1051/0004-6361/201833910.

H. C. Plummer. On the problem of distribution in globular star clusters. *Monthly Notices of the Royal Astronomical Society*, 71:460–470, Mar. 1911. doi: 10.1093/mnras/71.5.460.

B. Popescu, M. M. Hanson, and B. G. Elmegreen. Age and Mass for 920 Large Magellanic Cloud Clusters Derived from 100 Million Monte Carlo Simulations. *The Astrophysical Journal*, 751 (2):122, Jun 2012. doi: 10.1088/0004-637X/751/2/122.

V. Pota, D. A. Forbes, A. J. Romanowsky, J. P. Brodie, L. R. Spitler, J. Strader, C. Foster, J. A. Arnold, A. Benson, C. Blom, K. L. Hargis, J. R.and Rhode, and C. Usher. The sluggs survey: kinematics for over 2500 globular clusters in 12 early-type galaxies. *Monthly Notices of the Royal Astronomical Society*, 428, 01 2013. doi: 10.1093/mnras/sts029. URL `http://gen.lib.rus.ec/scimag/index.php?s=10.1093/mnras/sts029`.

V. Pota, N. R. Napolitano, M. Hilker, M. Spavone, C. Schulz, M. Cantiello, C. Tortora, E. Iodice, M. Paolillo, R. D'Abrusco, M. Capaccioli, T. Puzia, R. F. Peletier, A. J. Romanowsky, G. van de Ven, C. Spiniello, M. Norris, T. Lisker, R. Munoz, P. Schipani, P. Eigenthaler, M. A. Taylor, R. Sánchez-Janssen, and Y. Ordenes-Briceño. The Fornax Cluster VLT Spectroscopic Survey - I. VIMOS spectroscopy of compact stellar systems in the Fornax core region. *Monthly Notices of the RAS*, 481:1744–1756, Dec. 2018. doi: 10.1093/mnras/sty2149.

M. E. Putman, B. K. Gibson, L. Staveley-Smith, G. Banks, D. G. Barnes, R. Bhatal, M. J. Disney, R. D. Ekers, K. C. Freeman, R. F. Haynes, P. Henning, H. Jerjen, V. Kilborn, B. Koribalski, P. Knezek, D. F. Malin, J. R. Mould, T. Oosterloo, R. M. Price, S. D. Ryder, E. M. Sadler, I. Stewart, F. Stootman, R. A. Vaile, R. L. Webster, and A. E. Wright. Tidal disruption

of the Magellanic Clouds by the Milky Way. *Nature*, 394(6695):752–754, Aug. 1998. doi: 10.1038/29466.

M. E. Putman, L. Staveley-Smith, K. C. Freeman, B. K. Gibson, and D. G. Barnes. The Magellanic Stream, High-Velocity Clouds, and the Sculptor Group. *The Astrophysical Journal*, 586(1):170–194, Mar. 2003. doi: 10.1086/344477.

M. A. Raj, E. Iodice, N. R. Napolitano, M. Hilker, M. Spavone, R. F. Peletier, H. S. Su, J. Falcón-Barroso, G. van de Ven, M. Cantiello, D. Kleiner, A. Venhola, S. Mieske, M. Paolillo, M. Capaccioli, and P. Schipani. The Fornax Deep Survey with VST. X. The assembly history of the bright galaxies and intra-group light in the Fornax A subgroup. *Astronomy & Astrophysics*, 640:A137, Aug. 2020. doi: 10.1051/0004-6361/202038043.

J. I. Read, M. I. Wilkinson, N. W. Evans, G. Gilmore, and J. T. Kleyna. The tidal stripping of satellites. *Monthly Notices of the Royal Astronomical Society*, 366, 2006. doi: 10.1111/j.1365-2966.2005.09861.x. URL `http://gen.lib.rus.ec/scimag/index.php?s=10.1111/j.1365-2966.2005.09861.x`.

R. M. Rich, M. Shara, S. M. Fall, and D. Zurek. Two Groups of Nearly Coeval Star Clusters in the Small Magellanic Cloud. *The Astronomical Journal*, 119(1):197–206, Jan. 2000. doi: 10.1086/301156.

R. M. Rich, M. M. Shara, and D. Zurek. New Photometry for the Intermediate-Age Large Magellanic Cloud Globular Cluster NGC 2121 and the Nature of the LMC Age Gap. *The Astronomical Journal*, 122(2):842–848, Aug 2001. doi: 10.1086/321164.

T. Richtler, R. Salinas, I. Misgeld, M. Hilker, G. K. T. Hau, A. J. Romanowsky, Y. Schuberth, and M. Spolaor. The dark halo of the Hydra I galaxy cluster: core, cusp, cosmological? Dynamics of NGC 3311 and its globular cluster system. *Astronomy & Astrophysics*, 531:A119, July 2011. doi: 10.1051/0004-6361/201015948.

A. G. Riess, S. Casertano, W. Yuan, J. B. Bowers, L. Macri, J. C. Zinn, and D. Scolnic. Cosmic Distances Calibrated to 1% Precision with Gaia EDR3 Parallaxes and Hubble Space Telescope Photometry of 75 Milky Way Cepheids Confirm Tension with ΛCDM. *The Astrophysical Journal Letters*, 908(1):L6, Feb. 2021. doi: 10.3847/2041-8213/abdbaf.

V. Ripepi, M. Cignoni, M. Tosi, M. Marconi, I. Musella, A. Grado, L. Limatola, G. Clementini, E. Brocato, M. Cantiello, M. Capaccioli, E. Cappellaro, M. R. L. Cioni, F. Cusano,

M. Dall'Ora, J. S. Gallagher, E. K. Grebel, A. Nota, F. Palla, D. Romano, G. Raimondo, E. Sabbi, F. Getman, N. R. Napolitano, P. Schipani, and S. Zaggia. STEP: the VST survey of the SMC and the Magellanic Bridge - I. Overview and first results. *Monthly Notices of the Royal Astronomical Society*, 442(3):1897–1921, Aug 2014. doi: 10.1093/mnras/stu918.

V. Ripepi, M.-R. L. Cioni, M. I. Moretti, M. Marconi, K. Bekki, G. Clementini, R. de Grijs, J. Emerson, M. A. T. Groenewegen, V. D. Ivanov, R. Molinaro, T. Muraveva, J. M. Oliveira, A. E. Piatti, S. Subramanian, and J. T. van Loon. The VMC survey - XXV. The 3D structure of the Small Magellanic Cloud from Classical Cepheids. *Monthly Notices of the Royal Astronomical Society*, 472(1):808–827, Nov. 2017. doi: 10.1093/mnras/stx2096.

V. Ripepi, G. Catanzaro, R. Molinaro, M. Gatto, G. De Somma, M. Marconi, M. Romaniello, S. Leccia, I. Musella, E. Trentin, G. Clementini, V. Testa, F. Cusano, and J. Storm. Cepheid metallicity in the Leavitt law (C-metall) survey - I. HARPS-N@TNG spectroscopy of 47 classical Cepheids and 1 BL Her variables. *Monthly Notices of the Royal Astronomical Society*, 508(3):4047–4071, Dec. 2021. doi: 10.1093/mnras/stab2460.

J. C. Roediger and S. Courteau. On the uncertainties of stellar mass estimates via colour measurements. *Monthly Notices of the Royal Astronomical Society*, 452(3):3209–3225, Sept. 2015. doi: 10.1093/mnras/stv1499.

A. J. Romanowsky, N. G. Douglas, M. Arnaboldi, K. Kuijken, M. R. Merrifield, N. R. Napolitano, M. Capaccioli, and K. C. Freeman. A Dearth of Dark Matter in Ordinary Elliptical Galaxies. *Science*, 301:1696–1698, Sept. 2003. doi: 10.1126/science.1087441.

A. J. Romanowsky, J. Strader, J. P. Brodie, J. C. Mihos, L. R. Spitler, D. A. Forbes, C. Foster, and J. A. Arnold. The Ongoing Assembly of a Central Cluster Galaxy: Phase-space Substructures in the Halo of M87. *The astrophysical journal*, 748:29, Mar. 2012. doi: 10.1088/0004-637X/748/1/29.

M. Rosenblatt. a Central Limit Theorem and a Strong Mixing Condition. *Proceedings of the National Academy of Science*, 42(1):43–47, Jan 1956. doi: 10.1073/pnas.42.1.43.

N. Roy, N. Napolitano, F. La Barbera, C. Tortora, F. Getman, M. Radovich, M. Capaccioli, M. Brescia, S. Cavuoti, G. Longo, M. Raj, E. Puddu, G. Covone, V. Amaro, C. Vellucci, A. Grado, K. Kuijken, G. Verdoes Kleijn, and E. Valentijn. Evolution of galaxy size-stellar

mass relation from the kilo-degree survey. *Monthly Notices of the Royal Astronomical Society*, 480:1057–1080, 10 2018. doi: 10.1093/mnras/sty1917.

S. Rubele, L. Kerber, L. Girardi, M. R. Cioni, P. Marigo, S. Zaggia, K. Bekki, R. de Grijs, J. Emerson, M. A. T. Groenewegen, M. Gullieuszik, V. Ivanov, B. Miszalski, J. M. Oliveira, B. Tatton, and J. T. van Loon. The VMC survey. IV. The LMC star formation history and disk geometry from four VMC tiles. *Astronomy & Astrophysics*, 537:A106, Jan. 2012. doi: 10.1051/0004-6361/201117863.

S. Rubele, L. Girardi, L. Kerber, M.-R. L. Cioni, A. E. Piatti, S. Zaggia, K. Bekki, A. Bressan, G. Clementini, R. de Grijs, J. P. Emerson, M. A. T. Groenewegen, V. D. Ivanov, M. Marconi, P. Marigo, M.-I. Moretti, V. Ripepi, S. Subramanian, B. L. Tatton, and J. T. van Loon. The VMC survey - XIV. First results on the look-back time star formation rate tomography of the Small Magellanic Cloud. *Monthly Notices of the Royal Astronomical Society*, 449(1):639–661, May 2015. doi: 10.1093/mnras/stv141.

S. Rubele, G. Pastorelli, L. Girardi, M.-R. L. Cioni, S. Zaggia, P. Marigo, K. Bekki, A. Bressan, G. Clementini, R. de Grijs, J. Emerson, M. A. T. Groenewegen, V. D. Ivanov, T. Muraveva, A. Nanni, J. M. Oliveira, V. Ripepi, N.-C. Sun, and J. T. van Loon. The VMC survey - XXXI: The spatially resolved star formation history of the main body of the Small Magellanic Cloud. *Monthly Notices of the Royal Astronomical Society*, 478(4):5017–5036, Aug. 2018. doi: 10.1093/mnras/sty1279.

M. Ruszkowski and V. Springel. The Role of Dry Mergers for the Formation and Evolution of Brightest Cluster Galaxies. *The Astrophysical Journal*, 696:1094–1102, May 2009. doi: 10.1088/0004-637X/696/2/1094.

J. E. Ryon, N. Bastian, A. Adamo, I. S. Konstantopoulos, J. S. Gallagher, S. Larsen, K. Hollyhead, E. Silva-Villa, and L. J. Smith. Sizes and shapes of young star cluster light profiles in M83. *Monthly Notices of the Royal Astronomical Society*, 452(1):525–539, Sept. 2015. doi: 10.1093/mnras/stv1282.

J. E. Ryon, J. S. Gallagher, L. J. Smith, A. Adamo, D. Calzetti, S. N. Bright, M. Cignoni, D. O. Cook, D. A. Dale, B. E. Elmegreen, M. Fumagalli, D. A. Gouliermis, K. Grasha, E. K. Grebel, H. Kim, M. Messa, D. Thilker, and L. Ubeda. Effective Radii of Young, Massive Star Clusters in Two LEGUS Galaxies. *The Astrophysical Journal*, 841(2):92, June 2017. doi: 10.3847/1538-4357/aa719e.

J. Ryu and M. G. Lee. Discovery of Two New Globular Clusters in the Milky Way. *The Astrophysical Journal Letters*, 863(2):L38, Aug. 2018. doi: 10.3847/2041-8213/aad8b7.

A. Saha, E. W. Olszewski, B. Brondel, K. Olsen, P. Knezek, J. Harris, C. Smith, A. Subramaniam, J. Claver, A. Rest, P. Seitzer, K. H. Cook, D. Minniti, and N. B. Suntzeff. First Results from the NOAO Survey of the Outer Limits of the Magellanic Clouds. *The Astronomical Journal*, 140(6):1719–1738, Dec 2010. doi: 10.1088/0004-6256/140/6/1719.

L. V. Sales, J. F. Navarro, A. P. Cooper, S. D. M. White, C. S. Frenk, and A. Helmi. Clues to the 'Magellanic Galaxy' from cosmological simulations. *Monthly Notices of the Royal Astronomical Society*, 418(1):648–658, Nov. 2011. doi: 10.1111/j.1365-2966.2011.19514.x.

I. San Roman, A. Sarajedini, J. A. Holtzman, and D. R. Garnett. Newly identified star clusters in M33 - III. Structural parameters. *Monthly Notices of the Royal Astronomical Society*, 426 (3):2427–2440, Nov. 2012. doi: 10.1111/j.1365-2966.2012.21400.x.

J. Santos, João F. C., F. F. S. Maia, B. Dias, L. d. O. Kerber, A. E. Piatti, E. Bica, M. S. Angelo, D. Minniti, A. Pérez-Villegas, A. Roman-Lopes, P. Westera, L. Fraga, B. Quint, and D. Sanmartim. The VISCACHA survey - II. Structure of star clusters in the Magellanic Clouds periphery. *Monthly Notices of the Royal Astronomical Society*, 498(1):205–222, Oct. 2020. doi: 10.1093/mnras/staa2425.

A. Sarajedini. Three Populous Clusters Discovered in the Large Magellanic Cloud Age Gap. *The Astronomical Journal*, 116(2):738–747, Aug. 1998. doi: 10.1086/300472.

E. F. Schlafly and D. P. Finkbeiner. Measuring Reddening with Sloan Digital Sky Survey Stellar Spectra and Recalibrating SFD. *The Astrophysical Journal*, 737(2):103, Aug 2011. doi: 10.1088/0004-637X/737/2/103.

D. J. Schlegel, D. P. Finkbeiner, and M. Davis. Maps of Dust Infrared Emission for Use in Estimation of Reddening and Cosmic Microwave Background Radiation Foregrounds. *The Astrophysical Journal*, 500(2):525–553, June 1998. doi: 10.1086/305772.

T. Schmidt, M.-R. L. Cioni, F. Niederhofer, K. Bekki, C. P. M. Bell, R. de Grijs, J. Diaz, D. El Youssoufi, J. Emerson, M. A. T. Groenewegen, V. D. Ivanov, G. Matijevic, J. M. Oliveira, M. G. Petr-Gotzens, A. B. A. Queiroz, V. Ripepi, and J. T. van Loon. The VMC survey. XXXVIII. Proper motion of the Magellanic Bridge. *Astronomy & Astrophysics*, 641:A134, Sept. 2020. doi: 10.1051/0004-6361/202037478.

D. Schönberner, R. Jacob, C. Sandin, and M. Steffen. The evolution of planetary nebulae. VII. Modelling planetary nebulae of distant stellar systems. *Astronomy & Astrophysics*, 523:A86, Nov. 2010. doi: 10.1051/0004-6361/200913427.

Y. Schuberth, T. Richtler, M. Hilker, B. Dirsch, L. P. Bassino, A. J. Romanowsky, and L. Infante. The globular cluster system of NGC 1399. V. dynamics of the cluster system out to 80 kpc. *Astronomy and Astrophysics*, 513:A52, Apr. 2010. doi: 10.1051/0004-6361/200912482.

V. Scowcroft, W. L. Freedman, B. F. Madore, A. Monson, S. E. Persson, J. Rich, M. Seibert, and J. R. Rigby. The Carnegie Hubble Program: The Distance and Structure of the SMC as Revealed by Mid-infrared Observations of Cepheids. *The Astrophysical Journal*, 816(2):49, Jan. 2016. doi: 10.3847/0004-637X/816/2/49.

H. Shapley. An Extension of the Small Magellanic Cloud. *Harvard College Observatory Bulletin*, 914:8–9, Dec. 1940.

M. M. Shara, S. M. Fall, R. M. Rich, and D. Zurek. Hubble Space Telescope Observations of NGC 121: First Detection of Blue Stragglers in an Extragalactic Globular Cluster. *The Astrophysical Journal*, 508(2):570–575, Dec. 1998. doi: 10.1086/306423.

A. Sheardown, E. Roediger, Y. Su, R. P. Kraft, T. Fish, J. A. ZuHone, W. R. Forman, C. Jones, E. Churazov, and P. E. J. Nulsen. The Recent Growth History of the Fornax Cluster Derived from Simultaneous Sloshing and Gas Stripping: Simulating the Infall of NGC 1404. *The Astrophysical Journal*, 865(2):118, Oct. 2018. doi: 10.3847/1538-4357/aadc0f.

H.-Y. Shih and R. H. Méndez. Possible Stellar Streams in the Edge-on Spiral NGC 891 Discovered from Kinematics of Planetary Nebulae. *The Astrophysical Journal Letters*, 725:L97–L100, Dec. 2010. doi: 10.1088/2041-8205/725/1/L97.

E. Silva-Villa and S. S. Larsen. The star cluster - field star connection in nearby spiral galaxies. II. Field star and cluster formation histories and their relation. *Astronomy & Astrophysics*, 529:A25, May 2011. doi: 10.1051/0004-6361/201016206.

J. D. Simon. The Faintest Dwarf Galaxies. *Annual Review of Astronomy & Astrophysics*, 57: 375–415, Aug. 2019. doi: 10.1146/annurev-astro-091918-104453.

M. Sitek, M. K. Szymański, D. M. Skowron, A. Udalski, Z. Kostrzewa-Rutkowska, J. Skowron, P. Karczmarek, M. Cieślar, Ł. Wyrzykowski, S. Kozłowski, P. Pietrukowicz, I. Soszyński,

P. Mróz, M. Pawlak, R. Poleski, and K. Ulaczyk. OGLE Collection of Star Clusters. New Objects in the Outskirts of the Large Magellanic Cloud. *Acta Astronomica*, 66(3):255–267, Sep 2016.

M. Sitek, M. K. Szymański, A. Udalski, D. M. Skowron, Z. Kostrzewa-Rutkowska, J. Skowron, P. Karczmarek, M. Cieślar, Ł. Wyrzykowski, S. Kozłowski, P. Pietrukowicz, I. Soszyński, P. Mróz, M. Pawlak, R. Poleski, and K. Ulaczyk. OGLE Collection of Star Clusters. New Objects in the Magellanic Bridge and the Outskirts of the Small Magellanic Cloud. *Acta Astronomica*, 67(4):363–378, Dec. 2017. doi: 10.32023/0001-5237/67.4.5.

D. M. Skowron, A. M. Jacyszyn, A. Udalski, M. K. Szymański, J. Skowron, R. Poleski, S. Kozłowski, M. Kubiak, G. Pietrzyński, I. Soszyński, P. Mróz, P. Pietrukowicz, K. Ulaczyk, and Ł. Wyrzykowski. OGLE-ING the Magellanic System: Stellar Populations in the Magellanic Bridge. *The Astrophysical Journal*, 795(2):108, Nov. 2014. doi: 10.1088/0004-637X/795/2/108.

D. M. Skowron, J. Skowron, A. Udalski, M. K. Szymański, I. Soszyński, Ł. Wyrzykowski, K. Ulaczyk, R. Poleski, S. Kozłowski, P. Pietrukowicz, P. Mróz, K. Rybicki, P. Iwanek, M. Wrona, and M. Gromadzki. OGLE-ing the Magellanic System: Optical Reddening Maps of the Large and Small Magellanic Clouds from Red Clump Stars. *The Astrophysical Journal Supplementary Material*, 252(2):23, Feb. 2021. doi: 10.3847/1538-4365/abcb81.

T. A. Smecker-Hane, A. A. Cole, I. Gallagher, John S., and P. B. Stetson. The Star Formation History of the Large Magellanic Cloud. *The Astrophysical Journal*, 566(1):239–244, Feb. 2002. doi: 10.1086/337985.

Y.-Y. Song, M. Mateo, I. Bailey, John I., M. G. Walker, I. U. Roederer, E. W. Olszewski, M. Reiter, and A. Kremin. Dynamical masses and mass-to-light ratios of resolved massive star clusters - II. Results for 26 star clusters in the Magellanic Clouds. *Monthly Notices of the Royal Astronomical Society*, 504(3):4160–4191, July 2021. doi: 10.1093/mnras/stab1065.

C. Spiniello, N. R. Napolitano, M. Arnaboldi, C. Tortora, L. Coccato, M. Capaccioli, O. Gerhard, E. Iodice, M. Spavone, M. Cantiello, R. Peletier, M. Paolillo, and P. Schipani. The Fornax Cluster VLT Spectroscopic Survey II - Planetary Nebulae kinematics within 200 kpc of the cluster core. *Monthly Notices of the RAS*, 477:1880–1892, June 2018. doi: 10.1093/mnras/sty663.

L. Spitzer. *Dynamical evolution of globular clusters.* 1987.

S. Stanimirovic, L. Staveley-Smith, J. M. Dickey, R. J. Sault, and S. L. Snowden. The large-scale HI structure of the Small Magellanic Cloud. *Monthly Notices of the Royal Astronomical Society*, 302(3):417–436, Jan. 1999. doi: 10.1046/j.1365-8711.1999.02013.x.

L. Staveley-Smith, R. J. Sault, D. Hatzidimitriou, M. J. Kesteven, and D. McConnell. An HI aperture synthesis mosaic of the Small Magellanic Cloud. *Monthly Notices of the Royal Astronomical Society*, 289(2):225–252, Aug. 1997. doi: 10.1093/mnras/289.2.225.

P. B. Stetson. DAOPHOT: A Computer Program for Crowded-Field Stellar Photometry. *Publications of the Astronomical Society of the Pacific*, 99:191, Mar 1987. doi: 10.1086/131977.

P. B. Stetson. *More Experiments with DAOPHOT II and WF/PC Images*, volume 25 of *Astronomical Society of the Pacific Conference Series*, page 297. 1992.

P. B. Stetson. The Center of the Core-Cusp Globular Cluster M15: CFHT and HST Observations, ALLFRAME Reductions. *Publications of the Astronomical Society of the Pacific*, 106:250, Mar. 1994. doi: 10.1086/133378.

A. Subramaniam and S. Subramanian. The Mysterious Bar of the Large Magellanic Cloud: What Is It? *The Astrophysical Journal Letters*, 703(1):L37–L40, Sept. 2009. doi: 10.1088/0004-637X/703/1/L37.

S. Subramanian and A. Subramaniam. Depth estimation of the Large and Small Magellanic Clouds. *Astronomy & Astrophysics*, 496(2):399–412, Mar 2009. doi: 10.1051/0004-6361/200811029.

S. Subramanian and A. Subramaniam. The Three-dimensional Structure of the Small Magellanic Cloud. *The Astrophysical Journal*, 744(2):128, Jan. 2012. doi: 10.1088/0004-637X/744/2/128.

M. B. Taylor. STILTS - A Package for Command-Line Processing of Tabular Data. In C. Gabriel, C. Arviset, D. Ponz, and S. Enrique, editors, *Astronomical Data Analysis Software and Systems XV*, volume 351 of *Astronomical Society of the Pacific Conference Series*, page 666, July 2006.

T. Tepper-García, J. Bland-Hawthorn, M. S. Pawlowski, and T. K. Fritz. The Magellanic System: the puzzle of the leading gas stream. *Monthly Notices of the Royal Astronomical Society*, 488 (1):918–938, Sep 2019. doi: 10.1093/mnras/stz1659.

D. Tody. The IRAF Data Reduction and Analysis System. In D. L. Crawford, editor, *Instrumentation in astronomy VI*, volume 627 of *Society of Photo-Optical Instrumentation Engineers (SPIE) Conference Series*, page 733, Jan. 1986. doi: 10.1117/12.968154.

D. Tody. IRAF in the Nineties. In R. J. Hanisch, R. J. V. Brissenden, and J. Barnes, editors, *Astronomical Data Analysis Software and Systems II*, volume 52 of *Astronomical Society of the Pacific Conference Series*, page 173, Jan. 1993.

G. Torrealba, V. Belokurov, S. E. Koposov, K. Bechtol, A. Drlica-Wagner, K. A. G. Olsen, A. K. Vivas, B. Yanny, P. Jethwa, A. R. Walker, T. S. Li, S. Allam, B. C. Conn, C. Gallart, R. A. Gruendl, D. J. James, M. D. Johnson, K. Kuehn, N. Kuropatkin, N. F. Martin, D. Martinez-Delgado, D. L. Nidever, N. E. D. Noël, J. D. Simon, G. S. Stringfellow, and D. L. Tucker. Discovery of two neighbouring satellites in the Carina constellation with MagLiteS. *Monthly Notices of the Royal Astronomical Society*, 475(4):5085–5097, Apr. 2018. doi: 10.1093/mnras/sty170.

M. Tosi. Stellar populations and star formation histories in late-type dwarfs. *Mem. Societa Astronomica Italiana*, 75:103, Jan 2004.

A. V. Tutukov and A. V. Fedorova. The origin of intergalactic stars in galaxy clusters. *Astronomy Reports*, 55(5):383–391, May 2011. doi: 10.1134/S1063772911050076.

A. Udalski, M. Kubiak, and M. Szymanski. Optical Gravitational Lensing Experiment. OGLE-2 – the Second Phase of the OGLE Project. *Acta Astronomica*, 47:319–344, July 1997.

A. Udalski, M. K. Szymański, and G. Szymański. OGLE-IV: Fourth Phase of the Optical Gravitational Lensing Experiment. *Acta Astronomica*, 65(1):1–38, Mar. 2015.

R. P. van der Marel. Magellanic Cloud Structure from Near-Infrared Surveys. II. Star Count Maps and the Intrinsic Elongation of the Large Magellanic Cloud. *The Astronomical Journal*, 122(4):1827–1843, Oct. 2001. doi: 10.1086/323100.

R. P. van der Marel and N. Kallivayalil. Third-epoch Magellanic Cloud Proper Motions. II. The Large Magellanic Cloud Rotation Field in Three Dimensions. *The Astrophysical Journal*, 781 (2):121, Feb. 2014. doi: 10.1088/0004-637X/781/2/121.

R. P. van der Marel and J. Sahlmann. First Gaia Local Group Dynamics: Magellanic Clouds Proper Motion and Rotation. *The Astrophysical Journal Letters*, 832(2):L23, Dec. 2016. doi: 10.3847/2041-8205/832/2/L23.

M. L. van Gelder, L. Kaper, J. Japelj, M. C. Ramírez-Tannus, L. E. Ellerbroek, R. H. Barbá, J. M. Bestenlehner, A. Bik, G. Gräfener, A. de Koter, S. E. de Mink, E. Sabbi, H. Sana, M. Sewiło, J. S. Vink, and N. R. Walborn. VLT/X-shooter spectroscopy of massive young stellar objects in the 30 Doradus region of the Large Magellanic Cloud. *Astronomy & Astrophysics*, 636:A54, Apr. 2020. doi: 10.1051/0004-6361/201936361.

E. Vasiliev, V. Belokurov, and D. Erkal. Tango for three: Sagittarius, LMC, and the Milky Way. *Monthly Notices of the Royal Astronomical Society*, 501(2):2279–2304, Feb. 2021. doi: 10.1093/mnras/staa3673.

A. Venhola, R. Peletier, E. Laurikainen, H. Salo, T. Lisker, E. Iodice, M. Capaccioli, G. Verdois Kleijn, E. Valentijn, S. Mieske, M. Hilker, C. Wittmann, G. van de Ven, A. Grado, M. Spavone, M. Cantiello, N. Napolitano, M. Paolillo, and J. Falcón-Barroso. The Fornax Deep Survey with VST. III. Low surface brightness dwarfs and ultra diffuse galaxies in the center of the Fornax cluster. *Astronomy and Astrophysics*, 608:A142, Dec. 2017. doi: 10.1051/0004-6361/201730696.

K. Vieira, T. M. Girard, W. F. van Altena, N. Zacharias, D. I. Casetti-Dinescu, V. I. Korchagin, I. Platais, D. G. Monet, C. E. López, D. Herrera, and D. J. Castillo. Proper-motion Study of the Magellanic Clouds Using SPM Material. *The Astronomical Journal*, 140(6):1934–1950, Dec. 2010. doi: 10.1088/0004-6256/140/6/1934.

J. Wang, F. Hammer, Y. Yang, V. Ripepi, M.-R. L. Cioni, M. Puech, and H. Flores. Towards a complete understanding of the Magellanic Stream Formation. *Monthly Notices of the Royal Astronomical Society*, 486(4):5907–5916, July 2019. doi: 10.1093/mnras/stz1274.

S. Wang and X. Chen. The Optical to Mid-infrared Extinction Law Based on the APOGEE, Gaia DR2, Pan-STARRS1, SDSS, APASS, 2MASS, and WISE Surveys. *The Astrophysical Journal*, 877(2):116, June 2019. doi: 10.3847/1538-4357/ab1c61.

J. J. Webb and R. G. Carlberg. The likelihood of undiscovered globular clusters in the outskirts of the Milky Way. *Monthly Notices of the Royal Astronomical Society*, 502(3):4547–4557, Apr. 2021. doi: 10.1093/mnras/stab353.

T. Weinzirl, S. Jogee, E. Neistein, S. Khochfar, J. Kormendy, I. Marinova, C. Hoyos, M. Balcells, M. den Brok, D. Hammer, R. F. Peletier, G. Verdoes Kleijn, D. Carter, P. Goudfrooij, J. R. Lucey, B. Mobasher, N. Trentham, P. Erwin, and T. Puzia. The HST/ACS Coma Cluster

Survey - VII. Structure and assembly of massive galaxies in the centre of the Coma cluster. *Monthly Notices of the Royal Astronomical Society*, 441(4):3083–3121, July 2014. doi: 10.1093/mnras/stu731.

D. R. Weisz, A. E. Dolphin, E. D. Skillman, J. Holtzman, J. J. Dalcanton, A. A. Cole, and K. Neary. Comparing the ancient star formation histories of the Magellanic Clouds. *Monthly Notices of the Royal Astronomical Society*, 431(1):364–371, 03 2013. ISSN 0035-8711. doi: 10.1093/mnras/stt165. URL `https://doi.org/10.1093/mnras/stt165`.

D. R. Weisz, S. E. Koposov, A. E. Dolphin, V. Belokurov, M. Gieles, M. L. Mateo, E. W. Olszewski, A. Sills, and M. G. Walker. A Hubble Space Telescope Study of the Enigmatic Milky Way Halo Globular Cluster Crater*. *The Astrophysical Journal*, 822(1):32, May 2016. doi: 10.3847/0004-637X/822/1/32.

F. Werchan and D. Zaritsky. The Star Clusters of the Large Magellanic Cloud: Structural Parameters. *The Astronomical Journal*, 142(2):48, Aug. 2011. doi: 10.1088/0004-6256/142/2/48.

S. D. M. White. The dynamics of rich clusters of galaxies. *Monthly Notices of the Royal Astronomical Society*, 177, 12 1976. doi: 10.1093/mnras/177.3.717. URL `http://gen.lib.rus.ec/scimag/index.php?s=10.1093/mnras/177.3.717`.

S. D. M. White and M. J. Rees. Core condensation in heavy halos - A two-stage theory for galaxy formation and clustering. *Monthly Notices of the Royal Astronomical Society*, 183:341–358, May 1978. doi: 10.1093/mnras/183.3.341.

B. Willman, F. Governato, J. Wadsley, and T. Quinn. The origin and properties of intracluster stars in a rich cluster. *Monthly Notices of the Royal Astronomical Society*, 355, 2004. doi: 10.1111/j.1365-2966.2004.08312.x. URL `http://gen.lib.rus.ec/scimag/index.php?s=10.1111/j.1365-2966.2004.08312.x`.

C. Wolf, C. A. Onken, L. C. Luvaul, B. P. Schmidt, M. S. Bessell, S.-W. Chang, G. S. Da Costa, D. Mackey, T. Martin-Jones, S. J. Murphy, T. Preston, R. A. Scalzo, L. Shao, J. Smillie, P. Tisserand, M. C. White, and F. Yuan. SkyMapper Southern Survey: First Data Release (DR1). *Publications of the Astron. Soc. of Australia*, 35:e010, Feb. 2018. doi: 10.1017/pasa.2018.5.

A. M. Yoshizawa and M. Noguchi. The dynamical evolution and star formation history of the Small Magellanic Cloud: effects of interactions with the Galaxy and the Large Magellanic

Cloud. *Monthly Notices of the Royal Astronomical Society*, 339(4):1135–1154, Mar 2003. doi: 10.1046/j.1365-8711.2003.06263.x.

D. Zaritsky and J. Harris. Quantifying the Drivers of Star Formation on Galactic Scales. I. The Small Magellanic Cloud. *The Astrophysical Journal*, 604(1):167–175, Mar 2004. doi: 10.1086/381795.

D. Zaritsky, J. Harris, and I. Thompson. A digital photometric survey of the magellanic clouds: First results from one million stars. *The Astronomical Journal*, 114:1002–1013, Sep 1997. doi: 10.1086/118531.

D. Zaritsky, J. Harris, E. K. Grebel, and I. B. Thompson. The Morphologies of the Small Magellanic Cloud. *The Astrophysical Journal Letters*, 534(1):L53–L56, May 2000. doi: 10.1086/312649.

Q. Zhang and S. M. Fall. The Mass Function of Young Star Clusters in the "Antennae" Galaxies. *The Astrophysical Journal Letters*, 527(2):L81–L84, Dec 1999. doi: 10.1086/312412.

H. Zhao and N. W. Evans. The So-called "Bar" in the Large Magellanic Cloud. *The Astrophysical Journal Letters*, 545(1):L35–L38, Dec. 2000. doi: 10.1086/317324.

S. Zibetti, S. D. M. White, D. P. Schneider, and J. Brinkmann. Intergalactic stars in z~0.25 galaxy clusters: systematic properties from stacking of Sloan Digital Sky Survey imaging data. *Monthly Notices of the Royal Astronomical Society*, 358(3):949–967, Apr. 2005. doi: 10.1111/j.1365-2966.2005.08817.x.

P. Zivick, N. Kallivayalil, R. P. van der Marel, G. Besla, S. T. Linden, S. Kozłowski, T. K. Fritz, C. S. Kochanek, J. Anderson, S. T. Sohn, M. C. Geha, and C. R. Alcock. The Proper Motion Field of the Small Magellanic Cloud: Kinematic Evidence for Its Tidal Disruption. *The Astrophysical Journal*, 864(1):55, Sep 2018. doi: 10.3847/1538-4357/aad4b0.

P. Zivick, N. Kallivayalil, G. Besla, S. T. Sohn, R. P. van der Marel, A. del Pino, S. T. Linden, T. K. Fritz, and J. Anderson. The Proper-motion Field along the Magellanic Bridge: A New Probe of the LMC-SMC Interaction. *The Astrophysical Journal*, 874(1):78, Mar 2019. doi: 10.3847/1538-4357/ab0554.